

Copyright is owned by the Author of the thesis. Permission is given for a copy to be downloaded by an individual for the purpose of research and private study only. The thesis may not be reproduced elsewhere without the permission of the Author.

Development of a Plasma Gun for application in Magnetized Target Fusion

A Thesis presented in partial fulfilment of the requirements for
the degree of

Doctor of Philosophy
in
Chemistry

Massey University, Albany,
New Zealand

Ian Reginald Roy Shinton

2005

Abstract

A recently proposed route to magnetized target fusion (MTF) has been developed [4] which utilizes an array of high velocity pulsed plasma accelerators, fired in unison at a target plasma. The plasma accelerators are required to be capable of reproducible results of 0.2mg of hydrogen plasma at velocities in excess of 200km/s and be possible of operating at 10Hz. No previously developed pulse plasma accelerator is capable of these results.

The purpose of this thesis was to develop a plasma accelerator for application to the proposed fusion scheme. The previously unexplored possibility of using a piezoelectric valve in these devices was investigated. The piezoelectric valve that was developed is capable of generating reproducible, short, well defined hydrogen pulses with longitudinal temperatures below 2K. Presently the valve can deliver a maximum output of 0.022mg of hydrogen gas.

A unique coaxial plasma accelerator, the Lica was developed that has three main features that set it apart: 1) it uses a piezoelectric valve to deliver short well defined hydrogen pulses into the accelerator, 2) the gas is linearly injected into the device and 3) it uses a novel preionization method. Currently the Lica is unable to offer the performance required for the proposed fusion scheme, the bulk of the plasma generated in this device appears to be travelling the region of 40-50km/s at a temperature of 3000K to 5000K. There are a few anomalies in the operation of this device: 1) it appears to accelerate a series of plasma sheaths in the regions of 40km/s, 50km/s and 60-80km/s, 2) the final plasma velocity appears to be independent of the acceleration distance and in some instances high velocity plasma in the region of 200km/s was observed.

A numerical finite element model (FEM) electromagnetic model called MATAC was developed to try and simulate the operation of the Lica, because it was shown that simple analytical models are inadequate. The preliminary modelling efforts predicted the final velocity of the bulk of the plasma to be 82.6km/s. A spin off from the development of the numerical model was the extension of the upwinding scheme of [157] to quadratic and cubic FEM elements.

Acknowledgements

Throughout this thesis my mentor Dr John Harrison has given me constant guidance, support and intellectual freedom. I am indebted to his enthusiastic efforts in the completion of this research, in particular the construction of the plasma accelerator and the pulsed valve. Special thanks go to Dr Marie-Anne Thelen who worked on the program written in LABVIEW that was used to collect the data from both the plasma accelerator and the pulsed valve. Dr Lutz Gross deserves a special mention for his initial help in the numerical modelling aspects of this research.

I would also like to thank Dr Geoff Dingley for developing some of the equipment used in the plasma accelerator, in particular the voltage driver for the preionizer unit, and Technician Joe Wang for building the devices. In addition I would like to acknowledge the advice and help of Dr Scott Whineray.

I would like to extend my gratitude to the Albany Principal Professor Ian Watson, Pro Vice Chancellor Professor Robert Anderson and Professor Sir Neil Waters for their support and fund raising for this research.

I am indebted to both the Foundation for Research Science and Technology for awarding me with a: Bright Futures Top Achiever Doctoral Scholarship (TAD 680) and the IFS Graduate Research Fund, without whose support this thesis would not have been possible.

Lastly, I would like to acknowledge the makers of the MATLAB, SOLIDWORKS and LABVIEW programs which were used extensively in this thesis.

Contents

Abstract	<u>Pages</u> i
Acknowledgements	ii

Chapter 1: Overview of Magnetized Target Fusion and the operation of plasma accelerators and rail guns

1.1:	Background on Magnetized Target Fusion (MTF).....	1-7
1.2:	Plasma accelerators and rail guns.....	7-13
1.3:	Factors affecting the performance of plasma accelerators and rail guns.....	13-17
1.4:	Overall requirements for designing a plasma accelerator for application to MTF..	17-18

Chapter 2: A piezoelectric pulsed gas source for MTF

2.1:	Overview of the piezoelectric valve – the need for a fast pulse valve.....	19-21
2.1.1:	The piezoelectric valve developed for MTF	21-23
2.2:	Theoretical aspects of molecular beams	
2.2.1:	Maxwell velocity distribution	24-25
2.2.2:	Free jet expansions	26-34
2.3:	Mass output characteristics from the piezoelectric valve	35
2.3.1:	Equipment used to operate the piezoelectric valve	35-36
2.3.2:	Equipment and apparatus used in determining the initial mass output from the valve at its upper limit.....	36-37
2.3.3:	Equipment and apparatus used in determining the mass output from the valve as a function of pressure and driving pulse length.....	35-36 38-39
2.3.4:	Data acquisition relating to the mass output from the valve	39
2.3.5:	Analysis of the data relating to the mass output from the valve	39-40
2.3.6:	Initial mass output results from the valve operating at its upper limit.....	40
2.3.7:	Extended mass output results as a function of pressure and driving pulse length..	40-41
2.3.8:	Discussion on the mass output produced from the piezoelectric valve	41-42
2.4:	Gas pulse characteristics of the piezoelectric valve	43
2.4.1:	Quadrupole mass-spectrometer	43-45
2.4.2:	Equipment used to determine the density profile of the gas pulse produced from the valve without the preionizer attachment.....	45-49
2.4.3:	Equipment used in determining an accurate temperature of short gas pulses produced from the valve without the preionizer attachment.....	49-50
2.4.4:	Equipment used in determining the gas pulse characteristics of the valve with a preionizer attachment	51
2.4.5:	Data acquisition of gas pulses produced from the valve	52
2.4.6:	Determination of the velocity distribution and temperature of the gas pulses produced from the valve	52-55
2.4.7:	Results of the density profile produced from the valve without the preionizer attachment.....	56-63
2.4.8:	Results of the extended density profile used to determine an accurate temperature for gas pulses produced from the valve without the preionizer attachment.....	64-66
2.4.9:	Results of the density profile produced from the valve with the preionizer attachment.....	67-69
2.4.10:	Discussion on the pulse characteristics of the piezoelectric valve	70-74

Chapter 3: A linearly injected coaxial plasma accelerator – the Lica

3.1:	Overview – A new type of plasma accelerator the <u>Lica</u>.....	75-80
3.2:	Background on the generation of plasmas and their electrical properties	
3.2.1:	The electrical breakdown of gases	81-87
3.2.2:	Plasma conductivity expressions	87-95
3.3:	The <u>Lica</u>	96-97
3.3.1:	The <u>Lica</u> apparatus	98-104
3.3.2:	Data acquisition from the <u>Lica</u>	105
3.3.3:	Analysis of the data from the <u>Lica</u>	105-108
3.3.4:	Results of the <u>Lica</u> fitted with a 20cm positive electrode	109-115
3.3.5:	Results of the <u>Lica</u> fitted with a 10cm positive electrode	116-121
3.3.6:	Results of the <u>Lica</u> fitted with a 5cm positive electrode	122-123
3.3.7:	Results observed from Misfires	124-128
3.3.8:	Discussion on the performance of the <u>Lica</u>	129-139

Chapter 4: Modelling the operation of the Lica

4.1:	Overview on modelling techniques used to describe the operation of plasma accelerators and rail guns	140-141
4.1.1:	Description of the problem	141
4.2:	Simple analytical models	
4.2.1:	A basic approach to modelling the problem – a first order model	142-146
4.2.2:	Results of the first order model	146-150
4.2.3:	Discussion on the first order model	151-152
4.3:	Numerical models used to describe the electromagnetic aspects of plasma accelerators and rail guns	153
4.3.1:	The finite element method – FEM	154-160
4.3.2:	Maxwell's equations, and boundary conditions	160-163
4.3.3:	The AVA formulation	163-165
4.3.4:	The problem domain	166
4.3.5:	Numerical problems encountered in the FEM modelling of plasma accelerators and rail guns	166-167
4.3.6:	Singularities close to the axis	167
4.3.7:	Spurious solutions	167-177
4.3.8:	Corner singularities	177-181
4.3.9:	Modelling a moving /deforming system	181-184
4.3.10:	Upwinding – A quadratic and cubic extension to the upwind scheme of Hughes..	184-201
4.3.11:	Boundary conditions for far field and curved boundaries	201-202
4.3.12:	Solving the matrix system of equations	202-203
4.3.13:	Test cases	204-223
4.3.14:	The numerical model used to describe the operation of the <u>Lica</u> – MATAC	224-231
4.3.15:	Results of the numerical model MATAC	231-253
4.3.16:	Discussion on the MATAC numerical model	254-256

Chapter 5: Miscellaneous experiments and procedures

Miscellaneous experiments and procedures.....	257-261
---	---------

Chapter 6: Future directions

		262
6.1:	Future development and experimentation of the piezoelectric valve.....	262-263
6.2:	Future development of the <u>Lica</u>	263-265
6.3:	Future development of the numerical modelling process and the MATAC program.....	265-266

Chapter 7: Conculsions	
Conclusions.....	267-271
 Appendices for Chapter 4	
Appendix 4A: Vector Calculus	272-273
Appendix 4B: Lagrange multipliers	274-275
Appendix 4C: Matrix values for the new cubic upwinding scheme.....	276
Appendix 4D: Bessel functions	282-287
Appendix 4E: Test cases.....	282-287
Appendix 4F: MATAC	288-304
 References	305-314
Bibliographies	315-316

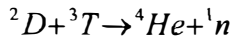
Chapter 1

Overview of Magnetized Target Fusion and the operation of plasma accelerators and rail guns

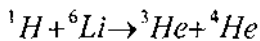
1.1: Background on Magnetized Target Fusion (MTF)

Nuclear fusion is the process of combining of two (or more) light nuclear particles to form a heavier nucleus (or nuclei) [1]. In situations where the product mass is less than the sum of the rest masses of the particles used in its creation, energy is released which is proportional to this mass difference.

This process has long been sought after by mankind as a means of energy production and the possibility of creating new or valuable materials from less expensive ones (Alchemy). One of the simplest fusion reactions is that of the Deuterium – Tritium reaction:



This process is attractive, because (as will be explained later) it requires the least amount of energy to initiate and deuterium can be obtained from water (note there are also further side fusion reactions that occur alongside this reaction [1]). A downside to this reaction is the generation of neutrons. Fusion reactions that generate neutrons are known as first generation fusion reactions, since they are the most likely type of fusion reaction to be first used in fusion energy generation power plants. There are neutron free reactions such as the proton – lithium reaction:



The above reaction also has other possible side fusion reactions all of which are also neutron free [1]. Reactions of this nature require a large amount of energy (high temperatures) to initiate, and because of this these types of reactions are known as advanced fuel or proton based fuels owing to the perceived difficulty in achieving this type of reaction in a fusion energy generation plant.

For a fusion reaction to occur between two nuclei the respective nuclei must overcome the inherent Coulomb repulsion force (between the two nuclei of atomic charge Z_1 and Z_2). The

energy $E_{Coulomb}$ required to overcome this repulsion force is approximated by equation (1.1) [1].

$$E_{Coulomb} = 0.3Z_1Z_2 \text{ (MeV)} \quad (1.1)$$

Using a Maxwell velocity distribution (refer to section 2.2.1 of chapter 2) the mean energy \bar{E} of a gas molecule is described in terms of Boltzmann's constant k and the bulk temperature T as [1]:

$$\bar{E} = \frac{3}{2} kT \quad (1.2)$$

Combining and solving equations (1.1) and (1.2) demonstrates that very high temperatures in the order of millions of degrees are required for the minimum temperature required for fusion to occur; at such high temperatures the gas will be a plasma. For example (using the above equations) the Deuterium – Tritium reaction will require a temperature of $1.39 \times 10^{10} K$. In fusion reactions the energy and temperature are usually given in the units of eV where $1eV = 1.6 \times 10^{-19} J$ and the conversion of the temperature units in Kelvin to eV is $T(K) = 8.61 \times 10^{-5} T(eV)$ [1]. Although it may seem strange to use the units of energy to express temperature, physicists use these units to make the quantities used in fusion reactions more manageable; the unit conversion mentioned above was derived using the relationship of $kT = 1eV$ [1]. The actual temperature at which fusion will begin to occur is a lot less than the approximate value calculated by considering the energy required to overcome the Coulomb repulsion force, because there is a large high velocity tail in the Maxwell velocity distribution (in which some particles may have sufficient energy for the fusion reaction to occur). There are in general two factors which will determine whether or not the reaction will take place: the Bremsstrahlung mechanism and plasma impurities. For the fusion reaction to be self-sustaining the rate of energy generated must be greater than or equal to the rate of energy loss. The majority of energy is lost through Bremsstrahlung radiation [1], in a real plasma there will be other losses such as conduction, diffusion and synchrotron radiation which must also be considered. Assuming the only loss mechanism is that of Bremsstrahlung radiation a minimum temperature can be calculated for the ignition conditions to be reached [1]. This is referred to as the minimum ignition temperature and is shown diagrammatically for the Deuterium – Tritium reaction in figure 1.1, in which the minimum ignition temperature for this reaction is $51.1 \times 10^6 K$.

Impurities in the fusion plasma can prevent the reaction from taking place, because the Bremsstrahlung radiation increases with increasing atomic mass as can be seen schematically in figure 1.2. In figure 1.2 the Bremsstrahlung power loss as a function of temperature is seen to rise when the amount of impurities in the fusion plasma is increased. This power loss is also a function of atomic mass; in figure 1.3 it can be observed that the higher the atomic mass, for a given impurity concentration, the higher the minimum ignition temperature becomes.

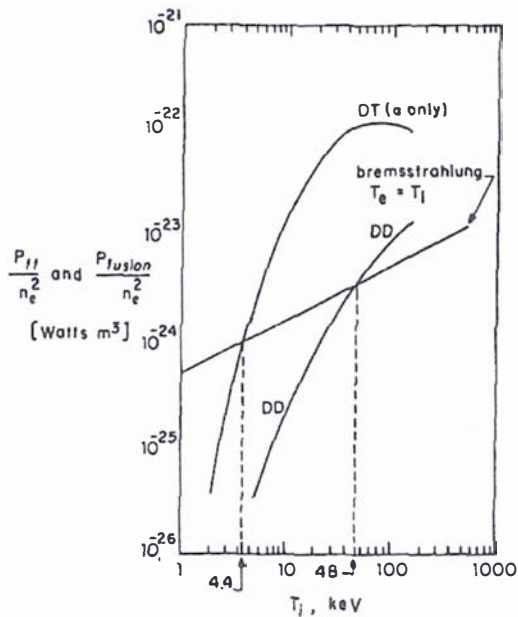


Figure 1.1: Graph of charged particle fusion and Bremsstrahlung power as a function of temperature for the Deuterium – Tritium and the Deuterium – Deuterium fusion reactions [1]

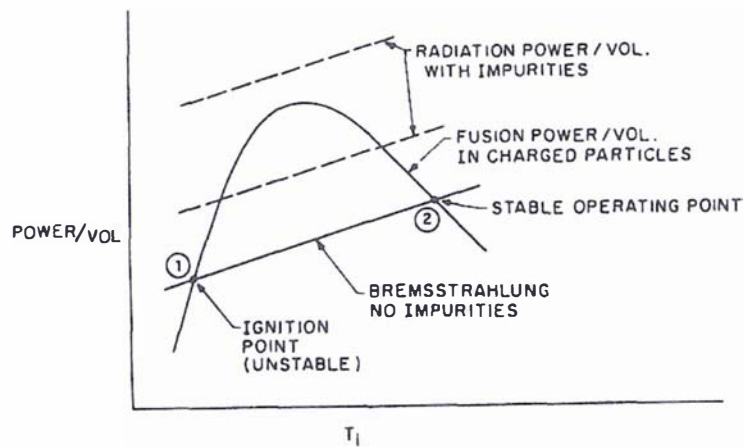


Figure 1.2: Diagrammatic representation of the effect on the Bremsstrahlung power loss as impurities in the fusion plasma are increased [1].

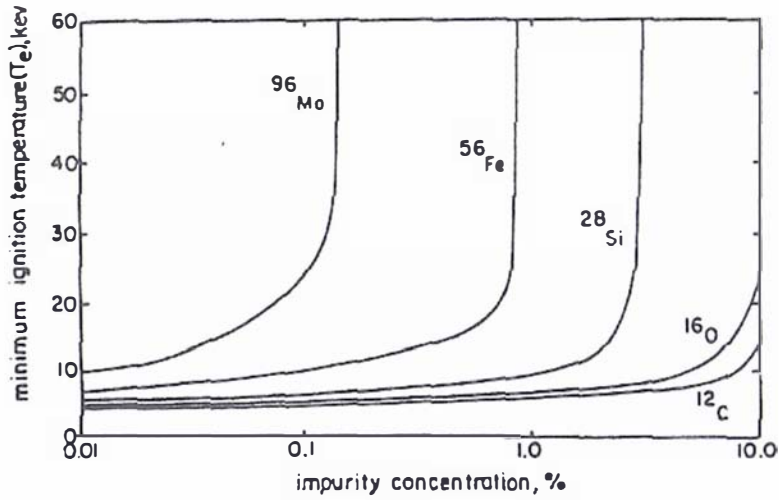


Figure 1.3: A graph of the minimum ignition temperature for the Deuterium – Tritium reaction as a function of impurity concentration for various substances [1].

In addition to the high temperature requirements for a fusion reaction to take place, two other critical parameters, the ion density n and the confinement time τ determine whether or not a self sustained reaction will take place. The confinement time is the time that the interacting ions are maintained at a temperature greater than or equal to the minimum ignition temperature. Lawson’s criteria [1] states that a plasma of a given density must be confined for a minimum length of time to yield a break even energy condition. An example displaying Lawson’s criteria (the break even energy condition) for the Deuterium – Tritium fusion reaction as a function of temperature is shown graphically in figure 1.4 below, from which the conditions for both the minimum ignition temperature and the minimum $n\tau$ value can be determined.

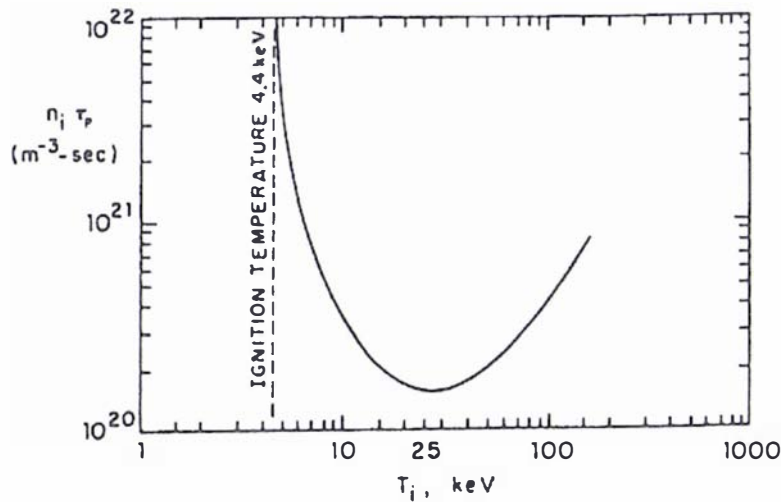


Figure 1.4: A graph showing the Lawson criteria for the Deuterium – Tritium fusion reaction for various values of $n\tau$ and ion temperature T_i [1]

By considering the previously discussed factors affecting a fusion reaction, the Deuterium – Tritium reaction will probably be the first fusion reaction to be used in a fusion power plant, because it has the lowest ignition temperature of $51.1 \times 10^6 \text{ K}$ requiring (at this temperature) a $n\tau$ value of $1 \times 10^{22} \text{ m}^{-3} \text{ s}$ [1]. Under these conditions this reaction releases approximately $3 \times 10^8 \text{ kJ}$ of energy for every 1g of fusion material, which corresponds to the same energy produced from the Hoover dam running at full capacity for one hour [2]. The desired proton – lithium advanced fuel fusion reaction would require a temperature in the region of $3.48 \times 10^9 \text{ K}$ to $1.05 \times 10^{10} \text{ K}$ and a very high $n\tau$ value, these conditions at present are very difficult to achieve [1].

It was recognised over fifty years ago by R.Landshoff that considerable advantages in a fusion reaction are gained if a magnetic field could be used to contain the fusion plasma [3]. This is because a magnetic field would trap the fusion reaction products and reduce their thermal conductivities, this has the effect of dramatically lowering the imploding power required to compress the target to fusion conditions [3]. It has been calculated that the magnetic field required for these benefits to occur will not have a significant effect on the dimensionality of the implosion or cause significant synchrotron radiation losses [3]. The general benefits of MTF over the conventional inertial confinement fusion (ICF) scheme are that it can be achieved using modest values of $n\tau$, the overall implosion process is not as stringent and low implosion velocities are required, meaning less power is needed for the implosion [3].

The basic principles of MTF were demonstrated in an experiment conducted at the Sandia National Laboratory in Albuquerque, New Mexico, USA towards the end of the 1970's. In this experiment, called the Φ - Target experiment, a deuterated polythethylene target was irradiated by two pulses of electron beams. The first pulse, a low-energy beam, called the pre-pulse, was intercepted by a thin metallic foil placed above the target, and charged this foil to a high electrical potential electrically. The negative electrical potential caused an electrical breakdown in the target (which is grounded) producing a linear high-current discharge that produces a magnetic field inside the target. The second pulse is a high-energy relativistic electron beam that penetrates the foil and compresses the target. The compression caused sufficient heating to produce significant fusion reactions, inferred from the number of fusion neutrons detected. When the pre-pulse is not used, no fusion neutrons were detected. Computer simulation of the experiment revealed a consistent picture that the initial magnetic field induced by the pre-pulse provided sufficient magneto-thermal insulation to cause the number of fusion reactions [3].

Recently a new MTF scheme has been proposed by Thio et al [4]. In this scheme it was proposed that a spherical fusion target (made from the combination of two compact toroids [5])

is centred within a large metallic chamber under high vacuum conditions. This fusion target is then imploded to fusion temperatures and pressures by an array of as many as sixty plasma jets that are all generated at approximately the same time with the same (approximately the same) velocity. These plasma jets will be generated several metres away from the fusion target to prevent damage to the equipment when the fusion reaction occurs. The heat generated from the fusion reaction will be radiated and collected by the large metallic vacuum chamber; this heat can then be used to heat water into steam and drive electrical turbines generating power in much the same fashion as any thermal power plant does. The current minimum requirements for the plasma jets to achieve the desired implosion requirements (in this scheme) are that they be composed of 0.2mg of hydrogen plasma, travelling at a velocity in excess of 200km/s and must be capable of a repetitive frequency of 10Hz [4].

It has been suggested that coaxial plasma accelerators (discussed in the next section) be used to generate the required plasma jets in this scheme. Currently the proposed scheme is in its infancy and the first experiments which will be conducted will be compression trials of twelve linearly arranged coaxial plasma accelerators into the large vacuum chamber, as depicted in diagram 1.1. The experiment is referred to as the plasma liner experiment and is depicted schematically in diagram 1.2 where the proposed fusion target has also been included. Compression of cylindrically arranged plasma jets does have a precedence in [6] and suggests the proposed scheme may be possible [4]; however a plasma gun has yet to be constructed that can meet the requirements of the proposed MTF scheme.

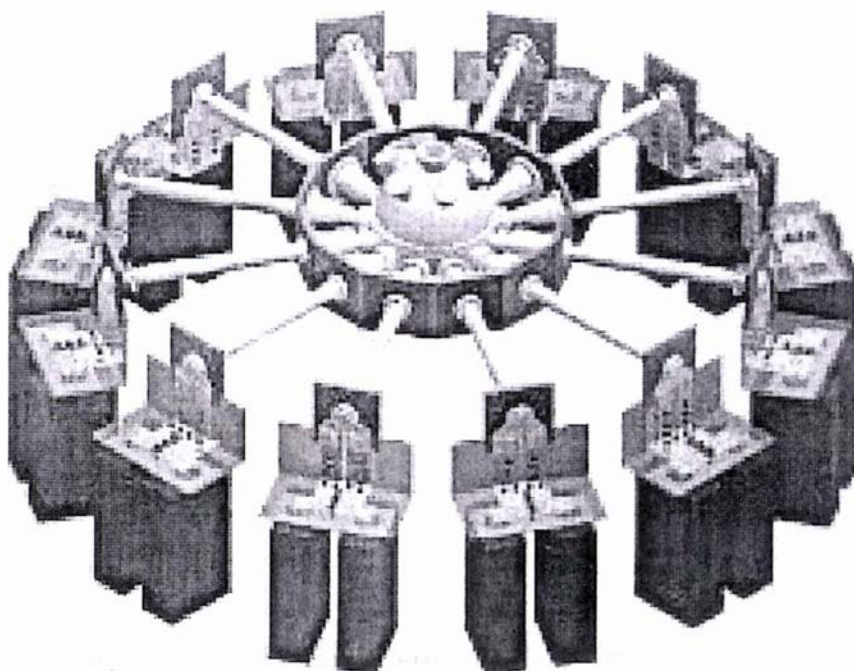


Diagram 1.1: Isometric diagram of the plasma liner experiment [4]

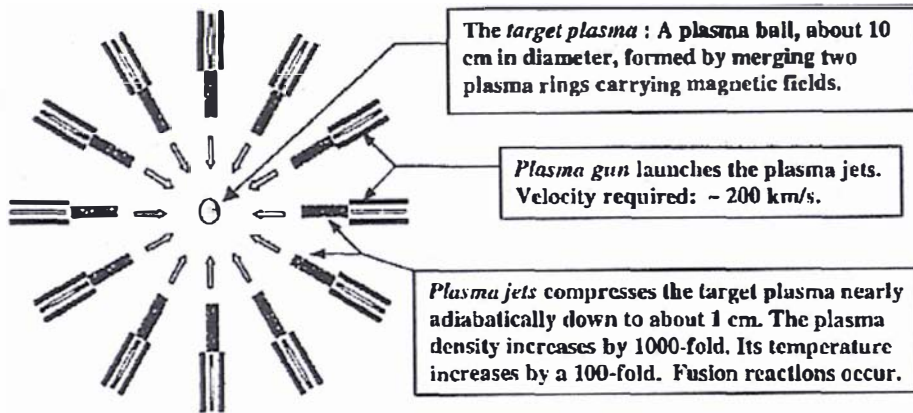


Diagram 1.2: Schematic representation of the plasma liner experiment [4]

1.2: Plasma accelerators and rail guns

A plasma accelerator is any type of device capable of accelerating a quantity of plasma by electromagnetic means. The main difference between an electromagnetic gun and a plasma accelerator is that an electromagnetic gun is used to accelerate a solid armature. The solid armature is either directly accelerated by electromagnetic means or by the acceleration of a plasma armature behind the solid armature.

Plasma accelerators can be broadly classified into either steady state or pulsed operation; steady state plasma accelerators include Hall accelerators [7] and the coaxial plasma accelerators used in HVOF (high velocity oxygen fuel) and HVOF (high velocity air fuel) surface coatings [8]. These types of plasma accelerators produce high temperature plasmas at low velocities, typically in the range of a few hundred meters per second. Pulsed plasma accelerators [7] produce high velocity plasma and can broadly be classified as either electrode or electrodeless accelerators. Electrode pulsed plasma accelerators have four basic geometries: electrode pulsed accelerators, T-tube plasma accelerators, rail plasma accelerators and coaxial plasma accelerators (sometimes known as Marshall accelerators); a general description of these plasma accelerators and the chronological order of their development can be found in [7]. Pulsed electrode plasma accelerators and electromagnetic guns that work with plasma armatures operate by utilising the Lorentz force. The Lorentz force is an electromagnetic force created from mutually perpendicular electric and magnetic fields, usually represented as $\mathbf{J} \times \mathbf{B}$ (in which \mathbf{J} is the current density and \mathbf{B} is the magnetic field). In an ionized gas the Lorentz force creates gradients in the same manner as gradients are created by hydrostatic pressure in a fluid.

This phenomenon is referred to as the magnetic pressure (which is equal to $\frac{B^2}{2\mu_0}$). In instances

where a filament (line or sheet) current is present the Lorentz force can be represented as a function of this magnetic pressure [7], this aspect is employed in some one dimensional plasma accelerator and rail gun models (refer to section 4.2.1).

Plasma accelerators and electromagnetic guns that use plasma armatures operate via one of two modes of operation, either plasma block [9], [10] or snowplough [11]. The difference between the two modes of operation can simply be described using the example of a rail plasma accelerator; this type of plasma accelerator consists of two conducting rails (a cathode and an anode) connected to a fast discharge power source either a capacitor, inductor or some combination of these two power sources. In plasma block mode the entire mass of un-ionized/preionized gas (within the plasma accelerator) is considered to be completely converted into a plasma when the high energy power source is discharged. This plasma is then accelerated as a discrete mass due to the action of the Lorentz force, as shown diagrammatically in diagram 1.3

In snowplough mode the plasma accelerator is initially considered to be full of un-ionized/preionized gas. A thin plasma sheath is formed at the rear of the plasma accelerator when the high energy power source is discharged. The current passing through this sheath rapidly heats it up, resulting in a shockwave that propagates down the length of the plasma accelerator ionizing the gas in front of the plasma sheath adding to the total plasma mass. The resulting plasma is then accelerated down the plasma accelerator though the action of the Lorentz force, the overall snowplough mode of operation is depicted in diagram 1.4.

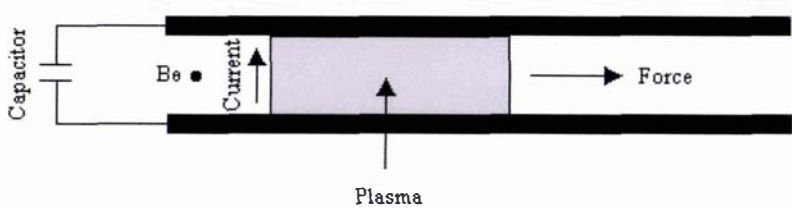


Diagram 1.3: Diagrammatic representation of the plasma block mode of operation within a rail plasma accelerator.

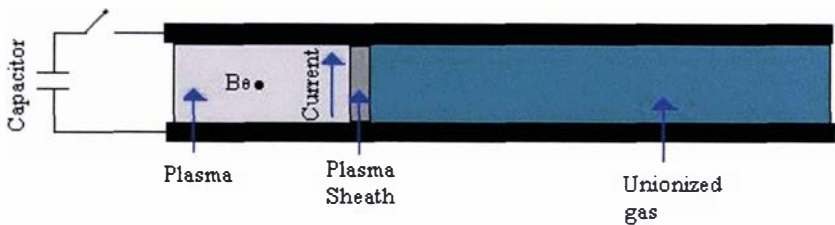


Diagram 1.4: Diagrammatic representation of the snowplough mode of operation within a rail plasma accelerator.

Realistically the operation of a plasma accelerator probably works somewhere in between the two extreme modes of operation. It is expected that the plasma block mode of operation is the most efficient since it does not have to contend with the large shockwave, viscosity and turbulence effects that will be present in the snowplough mode of operation. The snowplough mode of operation is inherently limited, because the mass being accelerated is continually increasing and could lead to a situation where this would severely limit the performance of the accelerator (especially in the case of static fill).

The coaxial plasma accelerator is the most efficient of all the pulsed electrode plasma accelerators with efficiencies of up to fifty percent [7]. The high efficiency of this device can be attributed to the confinement of the plasma within the device, a long accelerating distance and the uniform axisymmetrical accelerating Lorentz force (due to its geometry).

Electrode pulsed plasma accelerators and the T-tube plasma accelerators are only in the order of one percent efficient, primarily owing to a lack of accelerating distance. The rail plasma accelerator offers both plasma confinement and a long accelerating distance; this type of device can reach efficiencies of up to ten percent [7]. The reason why this type of device is much less efficient than the coaxial plasma accelerator is due to its geometry. (Note it is possible to create a symmetric distribution of the Lorentz force across the accelerating mass of plasma [12] within this type of device.)

Pulsed electrodeless plasma accelerators or travelling wave accelerators operate by inductive means [7] and usually have the appearance of large solenoids (they are essentially large inductors), their principle of operation relies on the creation of an azimuthal electric field which then induces an azimuthal current in the plasma. This current interacts with the radial component of the magnetic field resulting in a Lorentz force in the axial direction, accelerating the plasma. There are several variations on this theme [7] and a full review of this extensive research area is beyond the scope of this thesis.

Electromagnetic guns that use plasma armatures can be classified as either rail guns or coil guns. Rail guns can be thought of as being rail plasma accelerators that are used to accelerate a solid armature. An overall history of their development can be found in [13]. Coil guns are essentially the same as travelling wave accelerators, however coil guns typically accelerate a small conducting coil of wire [14] or a ferromagnetic slug [15] rather than a plasma armature.

Pulsed plasma accelerators and electromagnetic guns that use plasma armatures (that have appeared in the literature to-date) typically use solenoid valves to inject a neutral gas pulse into the device, and usually rely on a preionization stage to initiate the breakdown of this gas into a plasma. The preionization stage is commonly a spark gap or Trigatron [16] acting as an electron source, and promoting the breakdown of the gas via the mechanisms discussed in section 3.2.1 of chapter 3.

All pulsed plasma accelerators use high energy fast discharge energy sources to generate the large currents and magnetic fields necessary for their operation. An overview of the different types of power sources (up to the year of 1991) is presented in [17]. Capacitors on the whole offer the greatest energy density for any power source. The power requirements of pulsed plasma accelerators with either a rail or coaxial geometry require a low voltage high current pulse to maximize the accelerating Lorentz force. It is preferable for the current pulse to rise in intensity as the plasma is accelerated down the length of the accelerator [18] to give an ever increasing accelerating force or for the current pulse to be square-wave in nature [19] producing a constant accelerating force. Various types of electrical circuits incorporating capacitors, inductors and crowbar switches (a combination of diodes) have been developed to try and achieve the aforementioned current pulses [18], [19], [20], [21] and [22]. Oscillations in the current pulse will not effect the direction of the force applied to the plasma (confirmed by the simple consideration of the operation of the device), the effects of these oscillations merely produces a corresponding ebb and flow in the force applied to the plasma. Other circuit aspects such as current multipliers [23] and energy recovery circuits [24] as a means of further enhancing the operation of plasma accelerators and rail guns have also been investigated in the literature.

The operation of a coaxial plasma accelerator could be further enhanced by augmentation, compressor coils or aerodynamic nozzles. Augmentation would increase the strength of the magnetic field in the device through the use of external bus bars as shown in diagram 1.5 and hence increase the overall Lorentz force. This form of operational enhancement has only been employed in rail guns [25], [26] and [27] but it could also be applied to coaxial plasma accelerators; however no such augmentation on coaxial plasma accelerators has been reported in the literature.



Diagram 1.5: Diagram of an augmented rail gun

Because the plasma exiting a coaxial plasma accelerator is not in the form of a compact jet (due to the presence of the central electrode) compressor coils have been used to circumvent this problem [28], [29]. The compressor coil is essentially a miniature travelling wave plasma accelerator, with the exception that the accelerating coils are placed in an ever decreasing

circumference creating a magnetic pinch effect compressing the plasma. A diagram of a coaxial plasma accelerator fitted with a compressor coil is shown in diagram 1.6 to illustrate this point.

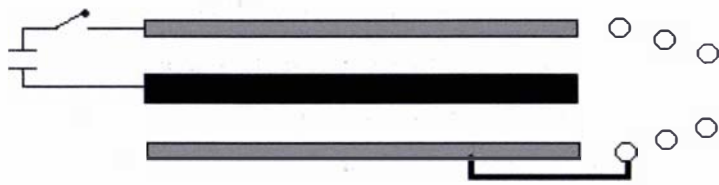


Diagram 1.6: Diagram of a coaxial plasma accelerator with a compressor coil attachment

In contrast to the overall effect of a compressor coil the final velocity produced from a plasma accelerator could be increased if some of the thermal energy of the plasma was converted into kinetic energy through the use of an insulated aerodynamic nozzle [7] shown diagrammatically in diagram 1.7. No use of this type of augmentation has appeared in the literature with respect to coaxial plasma accelerators, and there is no reason why it could not be applied to such devices; however a consequence of this type of augmentation would be a diffuse plasma rather than a compact plasma jet. A variation of the aerodynamic nozzle is that of the converging aerodynamic nozzle, in which the exiting plasma from a device is mechanically compressed. A variation of this type of augmentation, referred to as shaped electrodes, is used in some applications involving coaxial plasma accelerators [30] to form compact plasma jets.

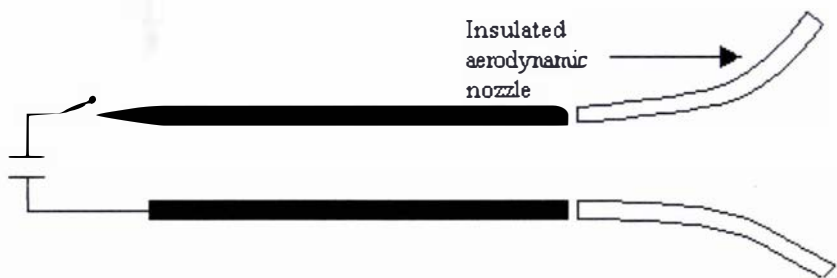


Diagram 1.7: Diagram of a rail gun augmented with an aerodynamic nozzle

Pulsed coaxial plasma accelerators are used in a variety of applications that include: ion engines (or pulsed plasma thrusters) for propulsion systems used in (experimental) space crafts [31] and to keep satellites in geosynchronous orbits [32]; surface coating in manufacturing [33]; and chemical conversion [34]. It is at this point that a distinction must be made between the different types of pulsed plasma accelerators.

The term pulsed plasma accelerator is a generalized term and it does not reflect how the plasma is generated or the operation of the plasma accelerator. The plasma within a coaxial plasma accelerator (or any plasma accelerator for that matter) can be generated using either a gas or a

vaporized material. The latter method is applied in some plasma accelerators [35], in which a thin metallic foil placed between the electrodes at the rear of the accelerator is vaporized (due to ohmic heating) upon the discharge of the high energy power source. Some pulsed plasma thrusters [32] work by ablating a solid fuel. This fuel is traditionally a breech feed Teflon bar. A spark induces an arc (from the discharge of the high energy source) across the surface of the Teflon; the heat from this arc vaporizes the Teflon. Most plasma accelerators use a gas injection system; since the plasma accelerator developed in this thesis (refer to chapter 3) utilizes a gas injection valve (refer to chapter 2), no further emphasis will be devoted to the discussion of plasma accelerators that operate via a vaporized material mechanism.

Pulsed plasma accelerators can be divided into three groups: statically filled, quasi-statically filled and pulse injected. Statically filled pulse plasma accelerators operate by first filling the working volume of the plasma accelerator with gas, at which point the high energy power source is discharged (by an external trigger) and the resulting plasma is accelerated by the snowplough mode of operation.

Quasi-statically filled pulsed plasma accelerators are similar to statically filled pulsed plasma accelerators with the exception that gas is continuously fed into the accelerator throughout the discharge process. A few ion engines and plasma thrusters operate in this fashion [31]. In the coaxial plasma accelerator of [31] (formed from inner and outer electrodes that are 0.37m and 0.56m in diameter respectively and 1m in length) a 10ms long 2MJ discharge was used to accelerate a 2.25g/s helium gas flow to a final velocity of approximately 35km/s, with an experimentally determined electron density of 5×10^{19} electrons/m³ and a calculated electron temperature of approximately 46000K.

Pulsed injected plasma accelerators operate by first injecting a gas pulse into the accelerator and then discharging the high energy source, resulting in the acceleration of the resulting plasma. Pulse injected plasma accelerators offer the potential of being able to operate in the plasma block mode of operation (provided a short enough gas pulse could be injected into the plasma accelerator). Unfortunately there seems to be little in the way of the characterization of the gas pulses injected into these accelerators in the literature. This is an important aspect that has seemingly been overlooked; one of the few pulse injected coaxial plasma accelerators in which the gas pulse has been characterized (to some extent) is that of the LRT accelerator [36]. The LRT accelerator is a very small accelerator of coaxial design consisting of electrodes 16cm in length with a central electrode 1.2cm in diameter and an outer electrode with inner and outer diameters of 3.3cm and 4.4cm respectively. The electrical properties of the LRT plasma accelerator are: 352μF capacitance, a 16kV charging voltage, a resistance of 4.65mΩ and an inductance of 325nH [35]. The LRT accelerator has a radial gas injection system formed from solenoid valves that inject gas towards the back of the plasma accelerator. The injected gas is allowed to uniformly expand (within the accelerator), between 4.1ms and 4.3ms, before the

capacitor is discharged. Since the solenoid valves operate on a millisecond time scale the result is essentially a statically filled accelerator, which probably operates using the snowplough mode of operation. Unfortunately the temperature and mass of the injected gas pulse was not experimentally determined. The LRT accelerator was able to produce Helium plasma pulses with a velocity of 100km/s (although this value is calculated from other experimentally observed parameters rather than being directly measured), a calculated temperature between 10000K and 15000K and a conductivity value (constant conductivity value) of $16000\Omega/\text{m}$ [35].

Plasma accelerators share many common features with rail guns that work with plasma armatures, in particular: the methods of operation, power requirements and the augmentation methods mentioned above. Many of the factors that effect plasma accelerators also affect rail guns using plasma armatures; this aspect is covered in the next section.

1.3: Factors affecting the operation of plasma accelerators and rail guns

The overall factors affecting the performance of plasma accelerators and rail guns (using plasma armatures) are complex and varied in nature, and can be separated into the eight categories of: ablation, the ion gyro radius effect, anode fall, the formation of a boundary layer between the electrodes, resistive heating losses, plasma instabilities, turbulence and the structural response of the device.

The most prevalent effect is that of ablation, in which material from the electrodes of the accelerator is vaporised and forms a region behind the main accelerating plasma, this is bad for two reasons. First it creates drag on the accelerating plasma. The second effect (and consequentially more harmful) is the situation where this region of vaporized material is of sufficient density to initiate breakdown of this material into a plasma (known as plasma restrike), this newly formed plasma region then parasitically steals current from the main accelerating plasma mass [37].

Ablation is caused by the two basic effects of surface heating and arcing. Ablation by surface heating is the direct interaction of the plasma with the surface of the electrodes, since the plasma is very hot (in the order of several thousand degrees centigrade) vaporisation of material from the electrodes is inevitable. The observation of a smooth polished electrode surface would generally result from this effect.

Because the surface of the electrodes is not perfectly smooth, any non-uniformities on the surface will intensify the electric field; since the electric field in a plasma accelerator is very large the electron field emissions from these points will be correspondingly large, leading to Mesyats mechanism [38]; resulting in small regions of the electrode being vaporized, which

would be visible as arc spots on the electrodes. Under the action of high currents if the plasma is not entirely uniform arcing in the regions of higher conductivity may occur, which will be visible as arc traces on the electrodes. Both the Mesyats and high current arcs are classed as ablation by arcing. It is expected that at the start of the acceleration process ablation by surface heating and Mesyats mechanism would be prevalent, because the plasma is moving at a relatively slow speed and there is the presence of a large electric field. As the plasma is accelerated and the current flowing across the plasma increases ablation by high current arcs would become the main ablation mechanism. It is generally very difficult to determine the amount of ablation from an electrode experimentally, so modelling efforts have been used to understand these effects. Analytical ablation models have been developed but they are limited in their scope [39], [40]. A lot of work has been done in numerical modelling to try and simulate the overall ablation process coupled with turbulence, ohmic heating and radiation transport effects [41], [42], [43], [44], and [45]. It has been suggested that ablation by radiation transport is the dominant form of energy transfer in the ablation process [46] and the effect of the plasma composition due to the incorporation of ablated material was considered to be of importance in [47], the electrode spacing has also been suggested as being a dependent factor on the formation of secondary arcs [48].

Ablation has always been considered a materials problem and a variety of materials with superior thermal and electrical properties have been considered in trying to minimise the effects of ablation [49], [50]. A general overview of materials that have been used in electromagnetic guns (up to the year of 1999) can be found in [51]. The prospect of using superconducting materials to augment electromagnetic guns was proposed in [52], in which ablation by arcing could be limited by reducing the current flowing in the rails.

The ion gyro radius effect is caused by the helical motion of charged particles in the presence of a magnetic field. This was considered to be an important effect in [53], where it was shown that if the radial dimensions of the plasma accelerator are less than that of the ion gyro radius then much of the kinetic energy of the plasma will be dissipated on the electrodes.

Anode fall is caused by a reduction in current carriers near the anode due to the Hall effect [33], [7], [38]; this effectively reduces the total current flowing across the plasma, decreasing the acceleration force and the efficiency of the plasma accelerator. This has been shown to be an important effect by the numerical modelling investigation of [33], in which it was suggested that an applied external magnetic field could minimise this effect.

In [54] the boundary layer effect was considered using an analytical approach. It was presented in this paper that at the interface between the plasma and the electrodes a thin, cold, slower moving plasma region is formed. The slower moving plasma is eventually left behind the bulk of the accelerating plasma; this process is repeated as the plasma is accelerated down the length of the accelerator. This cold plasma region would naturally have an effect on the overall

resistance (of the plasma) and the acceleration of the plasma as a whole. However the model used to describe this effect is only a preliminary one and its overall effect on the acceleration of the plasma remains a debateable point.

Because of the high currents normally involved in plasma accelerators and rail guns, ohmic heating of the electrodes and within the plasma will occur. Due to the skin effect, the ohmic heating in the electrodes has been shown by analytical [55] and by numerical means [56], [57] and [58] to be an important effect. It was generally shown in [57] that surface melting of the electrodes was possible (and consequently can be linked as a form of ablation). In [55] and [58] it was demonstrated that large current density gradients occur close to the armature, which could lead to surface melting of the electrodes. However in [58] it was shown that previous models had greatly overestimated the ohmic heating effects in the electrodes, because they had neglected the temperature dependent properties of the materials and the effect of this on the overall current. The effect of resistive heating and the loss of heat energy would of course have a detrimental effect on the performance of any plasma accelerator. In [32] it was discovered (from thermocouple data) that approximately half of the energy of the pulsed plasma thruster described in the paper was lost as heat to the walls (of the thruster). The overall efficiency of the pulsed plasma thruster in [32] was calculated as being (approximately) 10.6 percent as a result of this.

Plasma instabilities (MHD fluid instabilities) can broadly be divided into nine categories [59], [60]: Rayleigh-Taylor (Gravitation or Kruskal-Schwarzschild instabilities), Kelvin-Helmholtz, cylindrical pinch, generalized pinch, space charge, MHD resistive wall, MHD resistive tearing mode, fire-hose, and streaming instabilities. Not all of these plasma instabilities directly apply to the problem of a coaxial plasma accelerator.

The Kelvin-Helmholtz instability is chiefly concerned with the flow of two horizontal ideal MHD plasma streams that share a common horizontal plane. This type of instability can therefore generally be ignored in the operation of pulsed plasma accelerators.

The Fire-hose instability is a pressure based instability (in which the pressure is assumed to be a tensor quantity) which is dependent upon the passing Alfven wave through the plasma accelerator and also does not appear to be of great importance in the literature of plasma accelerators (Alfven waves are magnetic waves caused by small perturbations in the MHD system and are related to the magnetic pressure).

The MHD resistive wall instability is not considered to be a noticeable effect in the literature relating to plasma accelerators, this is probably because this instability is concerned with an ideal incompressible MHD flow and the plasma in plasma accelerators is (essentially) compressible. The MHD resistive tearing mode instability does not appear to be of much concern either, for the same reasons.

1.3: Factors effecting the performance of plasma accelerators and rail guns

The streaming instability (also known as the Buneman instability, the beam plasma instability, or the two stream instability) describes the perturbed motion of ion species within a cold, unmagnetized and unbounded plasma. Since the operation of a plasma accelerator involves the acceleration of a magnetized plasma, this instability has also apparently been ignored in the literature relating to plasma accelerators.

In a coaxial plasma accelerator both the magnetic field and current density are of greatest intensity at the central electrode, and consequently one would expect a generalized pinch instability to be produced. The generalized pinch instability is essentially the same as cylindrical pinch instability except it applies to noncircular geometry. Cylindrical pinch instabilities can be classified as either sausage or kink instabilities. A sausage instability is formed from a region where the azimuthal magnetic field (in relation to the direction of the current) is greater than other regions in the plasma, due to the presence of a higher current density; this enhances the magnetic pressure and results in necking or compression of the plasma in that region. A kink instability results from the deformation of the plasma. The deformation of the plasma (perpendicular to the direction of the current) increases the magnetic pressure in regions where the magnetic field curvature is convex with regard to the rest of the plasma; this simultaneous results in decreasing the magnetic pressure contribution in the concave regions. The overall result forces the plasma to further deform, enhancing the effect of the instability. These two instabilities are probably insignificant compared to the overall deformation caused by the uneven acceleration of the plasma in a coaxial plasma accelerator, and hence have not appeared in the literature of plasma accelerators.

Space-charge instabilities are primarily caused by electron drift. Since the mobility of electrons is much higher than that of the ions, space-charge regions may form in certain areas. The resistive drift instability is a type of space-charge instability and relates to a magnetized plasma, this type of instability is formed at the plasma vacuum interface. Electrons drift diamagnetically along this interface, this results in a space-charge density and a resulting electric field that further enhances this distortion. It was shown in [61] that space-charge instabilities are a limiting factor on the performance of a coaxial magnetoplasma dynamic thrusters (a pulsed plasma thrusters).

The predominant plasma instability that has been of concern in many plasma accelerator and plasma armature rail gun papers is that of the Rayleigh-Taylor instability [38]. A cold magnetized plasma supported by gravity may become unstable due to the effect of ion drift as a result of gravity. The ion drift in a magnetized plasma due to density gradients will result in charge separation, the resulting electric field can interact with the magnetic field ($\mathbf{E} \times \mathbf{B}$, where \mathbf{E} is the electric field) to enhance the distortion. Rayleigh Taylor instabilities have been considered as a possible cause of arcing within plasma accelerators and rail guns as well as affecting the distribution of the current density within the accelerating plasma [62], [63] and

1.3: Factors effecting the performance of plasma accelerators and rail guns

[64]. The effect of these plasma instabilities will be born out in the full solution to the full MHD equations.

Kinetic instabilities have largely been ignored in the plasma accelerator literature, generally because they do not apply to plasma accelerators; for example the bump in the tail instability only applies to un-magnetized plasmas and in most plasma accelerators ohms law is assumed to be valid, so the electron run away instability is ignored.

One would expect turbulent effects to play a certain role in the operation of a plasma accelerator regardless of the mode of operation, because the plasma is likely to be compressible. In [65] a two dimensional study of the dynamics of a pulsed plasma accelerator, operating in snowplough mode, was investigated. This paper showed that instabilities as a result of the acceleration of the plasma (due to pressure and density gradients) leads to noticeable turbulent mixing of the plasma and the magnetic field, resulting in a broadening of the current distribution (current arc) across the plasma.

Plasma accelerators and rail guns must be designed to withstand the expected impulse stresses imposed upon their associated components (conducting plates) as a result of magnetic repulsion during the discharge of the high power energy source. The stresses imposed by the moving armature are only a concern in the design of rail guns [66], because a solid armature is involved.

1.4: Overall requirements for designing a plasma accelerator for application to MTF

The requirements of a plasma accelerator for application to the MTF scheme suggested by Thio et al [4] in section 1.1 are that it be capable of reproducible results of 0.2mg of hydrogen plasma at a velocity in excess of 200km/s at a frequency of 10Hz.

It is of great importance to minimise the effects of ablation, because a large amount of impurities (within the hydrogen plasma) will interfere with the overall fusion process (refer to section 1.1); hence the plasma accelerator should be as efficient as possible.

A coaxial plasma accelerator would be the geometry of choice in the proposed MTF scheme, because of its high efficiency and the high velocities (in the range of 100km/s) that have been reported in the literature [36].

The plasma produced from the plasma accelerators should be dense and at as low an internal temperature as possible to minimise the effects of thermal broadening (in a vacuum), because in the proposed MTF scheme the plasma is required to travel several metres from the plasma accelerators. The augmentation methods discussed in section 1.3 are possible viable methods of optimising the plasma accelerators in achieving the aforementioned aspects, except for the use of a diverging aerodynamic nozzle (because it would result in a diffuse plasma).

1.4: Overall requirements for designing a plasma gun for application to MTF

If possible it would be preferable to operate the plasma accelerator in the plasma block mode of operation for the reasons discussed in section 1.2; however all the (gas) pulsed coaxial plasma accelerators that have appeared in the literature have all operated in snowplough mode, owing to the use of solenoid valves which tend to statically fill the plasma accelerator. Typically, solenoid valves have been tried to achieve the plasma block mode of operation [36]; unfortunately these valves were still too slow for this mode of operation to be realised.

Chapter 2

A piezoelectric pulsed gas source for application to MTF

2.1: Overview of piezoelectric valves – the need for a fast pulsed valve for MTF

The main requirements for the MTF scheme described in section 1.4 of chapter 1 are that the plasma accelerator be capable of reproducible results of 0.2mg hydrogen gas pulses at a frequency of 10Hz. All the pulsed coaxial plasma accelerators and rail guns (using plasma armatures) found in the literature (to date) have used solenoid valves to deliver the gas pulses [36]. These valves work by passing a current through a solenoid, which exerts a Lorentz force on a ferromagnetic poppet [67], [68]. Even though these valves are capable of operating at the mass and frequency required for the proposed MTF scheme [67] these valves operate on a millisecond time scale and will quasi-statically fill the accelerator and some of the vacuum system volume [36], resulting in the snowplough mode of operation (discussed in section 1.2 of chapter 1). This is an undesirable aspect for the proposed MTF scheme primarily because a large quantity of stray gas could interfere and/or neutralise the hydrogen plasma of the two compact toroids, also a large quantity of stray gas would reduce the final velocity and scatter the plasma pulses produced from the plasma accelerators. A fast acting valve is required for the proposed MTF process; three possible candidates are: an electromagnetic hammer valve, current loop actuator valve and a piezoelectric valve. Electromagnetic hammer valves [69] were developed from ballistic valves [69], [70] and their principle of operation relies upon a hammer blow delivered to a spring tensioned poppet to produce a gas pulse (the poppet is sealed against the face plate of the valve with a Teflon gasket). Ballistic valves [70] have pulse durations in the hundreds of microseconds range and are capable of delivering 5mg Deuterium gas pulses (0.3cm³ of Deuterium at standard temperature and pressure). Valves such as these have been used in plasma accelerators [69], [70], although the proper gas pulse characterization of these valves in plasma accelerators has not been undertaken. Despite this fact this type of valve is still a possible candidate for the proposed MTF scheme.

A current loop actuator valve [67] consists of a flexible metal strip placed over a conducting faceplate. When a pulsed current is passed through the flexible metal strip and the conducting faceplate the flexible metallic strip is moved (opening the valve), because of the repulsion caused from the opposing magnetic fields. These valves are generally capable of pulse durations in the range of tens of microseconds and are capable of operating at 10Hz; these valves have not been reported to have been used in any plasma accelerators (in the literature found at the time of the writing of this thesis). But, in order to operate this type of valve fast discharge capacitors

2.1: Overview of piezoelectric valves – the need for a fast pulsed valve for MTF

capable of delivering high currents are required; this makes these types of valves rather complicated and expensive.

A simpler and less expensive alternative would be to use a piezoelectric valve. These valves usually operate in the hundred microsecond to the tens of microseconds range, are capable of operating at 10Hz and produce well defined reproducible pulses. This type of valve is typically used to produce molecular beams [67] and there has been no reported use in the literature of the use of piezoelectric valves in plasma accelerators. Part of this thesis is dedicated to the unexplored possibility of using a piezoelectric valve in a plasma accelerator, with the overall aim of producing a plasma accelerator capable of meeting the demands of the proposed MTF scheme.

The overall design and construction of piezoelectric valves has changed little since their original inception by Auerbach and McDiarmid [71] and in parallel by Cross and Valentini [72]. A typical cross-section of a piezoelectric valve is shown in diagram 2.1. The valve primarily consists of a piezoelectric crystal that has had either a silvered or steel coating applied to the top and bottom surfaces to ensure good electrical contact, as well as an equipotential voltage across the surfaces. Typically the bottom surface of the crystal is grounded through the valve housing and a high voltage potential is applied to the top surface by a connection to the high voltage inlet. The crystal is attached to the valve housing by a series of screws and the crystal is usually tensioned through the use of spring washers. There are variations to this theme, such as the combination of using an O-ring and a tensioned poppet in later designs [73]. Finally, a poppet with an O-ring attachment seals the valve, against a nozzled face plate, from the backing pressure of gas introduced from the gas inlet. The valve operates by applying a voltage pulse to the piezoelectric crystal causing it to mechanically deform, as a result of the inverse piezoelectric effect [74], [75] (and emit a gas pulse).

However once the valve has been assembled it must be adjusted by means of tensioning. If the valve is under-tensioned then it will leak and will not produce well defined gas pulses; on the other hand if it is over-tensioned it may not be able to open properly as the combined force of the backing pressure and tensioning may be greater than the inverse piezoelectric effect. Valve adjustment is individual for every valve; despite this it is quite possible to produce piezoelectric valves that can deliver identical gas pulses [72].

2.1: Overview of piezoelectric valves – the need for a fast pulsed valve for MTF

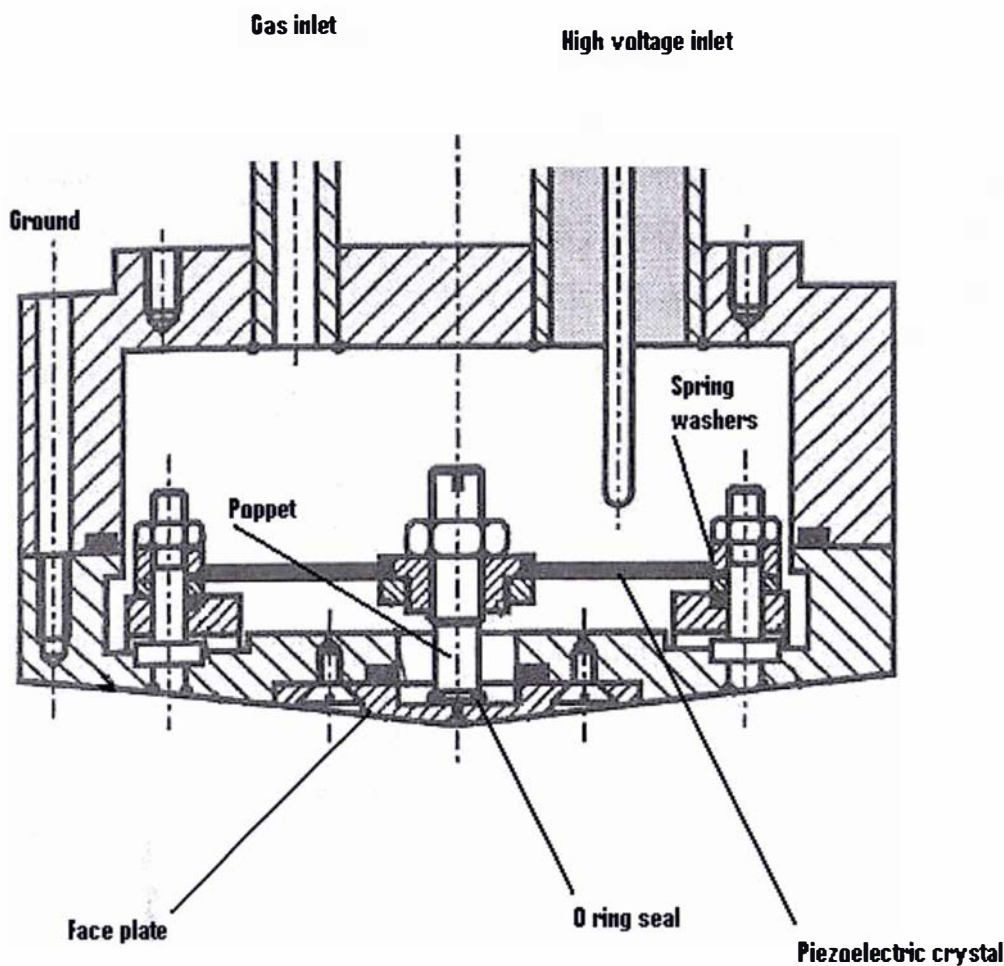


Diagram 2.1: Cross-section of a typical piezoelectric valve (modified from [68])

2.1.1: The piezoelectric valve developed for MTF

A two dimensional cross-sectional view of the piezoelectric valve that was used in this research project is depicted in diagram 2.2. Because of the time limit imposed upon this research project, the valve was constructed by modifying an existing piezoelectric valve using freely obtainable parts. At this stage of development it is merely a prototype that has been used to investigate the feasibility of using such a valve in the proposed MTF scheme.

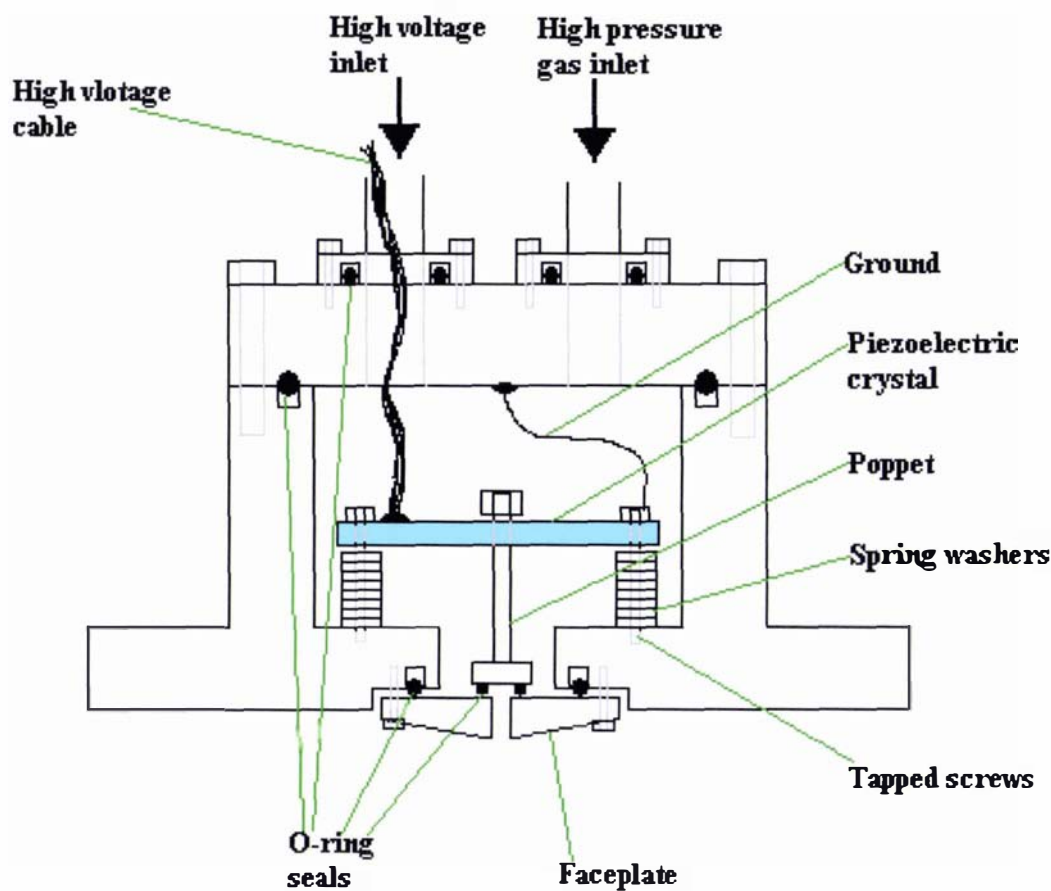


Diagram 2.2: Two dimensional cross-sectional view of the piezoelectric valve used in this research project

The piezoelectric crystal used in the valve was a Physik Intrumete P-286.20 disk translator. This crystal is a high voltage PZT disk translator whose dimensions are given in diagram 2.3 and its main operating parameters, of interest with regard to this thesis, are presented in table 2.1.

Open loop travel 0 to -1000V	100μm
Push/Pull force capacity	20/10N
Maximum operating voltage	-1000V
Standard operating temperature range	-40 to +80 °C

Table 2.1: Operating parameters of a P-286.20 disk translator [75]

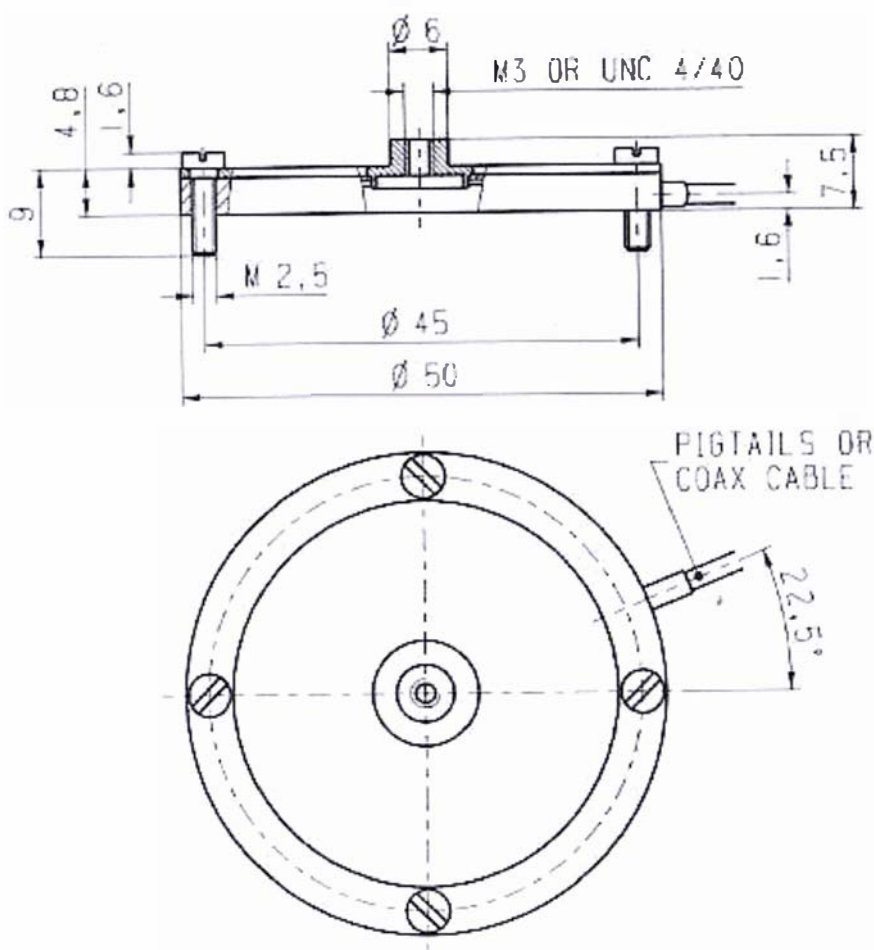


Diagram 2.3: Schematic of the dimensions of a P-286.20 disk translator [75] (dimensions in inches)

This particular type of disk translator was chosen because it offered the greatest deflection amongst the other available disk translators [75]. As seen from table 2.1 the maximum amount of movement that can be produced using this piezoelectric crystal is $100\mu\text{m}$ at the maximum operating voltage of -1000V , however most of this motion will be used in clearing the O-ring seal. It is this, and not the orifice diameter, that limits the amount of gas produced from the valve.

The effective orifice diameter for the valve constructed in this thesis is approximately 0.0204mm . The value was calculated using graph 2.2 (in section 2.2.2), a backing pressure of $6.52 \times 10^5 \text{ Pa}$ and a terminal speed ratio of 23 (these values were taken from the experimental observations reported in section 2.4.8).

2.2: Theoretical aspects of free jet expansions

2.2.1: Maxwell velocity distribution

The Maxwell velocity distribution is the absolute velocity distribution of molecules as the end result of internal collisions. The Maxwell velocity distribution is given by equation (2.1), in which the number of molecules having a speed v is presented as a function of the speed $f(v)$. The derivation of this equation can be found in [68] and in [76].

$$f(v) = \frac{4}{\sqrt{\pi}} \left(\frac{m}{2kT} \right)^{\frac{3}{2}} v^2 e^{\frac{-mv^2}{2kT}} \quad (2.1)$$

It is important to note that the Maxwell velocity distribution is in fact directly derived from the Maxwell – Boltzmann distribution of molecular velocities [76]. The Maxwell – Boltzmann distribution describes the distribution of molecular velocity, while the Maxwell velocity distribution describes the distribution of the velocity of the molecules irrespective of their direction of motion (based upon a three dimensional spherical expansion). The Maxwell – Boltzmann is defined by equation (2.2) where the molecules having a velocity v_z , in the z direction, are described as a function of that velocity $f(v_z)$.

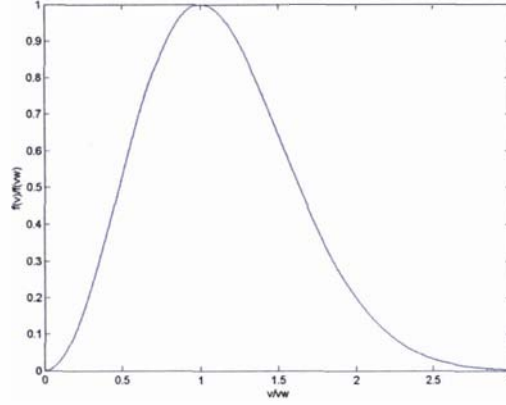
$$f(v_z) = \frac{1}{\sqrt{\pi}} \left(\frac{m}{2kT} \right)^{\frac{1}{2}} e^{\frac{-mv_z^2}{2kT}} \quad (2.2)$$

The most probable speed v_w that a molecule has is determined by the maximum of the Maxwell velocity distribution, this maximum value is derived from equation (2.1) as:

$$v_w = \sqrt{\frac{2kT}{m}} \quad (2.3)$$

A plot of the Maxwell velocity distribution using equation (2.1) is presented below in graph 2.1. The distribution in graph 2.1 is generalised for any temperature and mass value. This is done by presenting both the speed v of a molecule and the number of molecules having this speed $f(v)$ as ratio values of the most probable speed v_w and the maximum value of the distribution

(respectively). As observed in graph 2.1 most of the molecules travel at speeds somewhere between $\frac{v_w}{2}$ and $\frac{3v_w}{2}$, with the majority (over 94%) lying in the region between $\frac{v_w}{4}$ and $2v_w$.



Graph 2.1: Plot of the Maxwell velocity distribution in terms of v / v_w , where the distribution has been normalised with respect to the maximum value of the distribution.

The Maxwell distribution can be used to determine the longitudinal translational temperature of a supersonic molecular beam [77], by using a superimposed stream velocity v_s (which is the average velocity of the beam with respect to the stationary lab frame) with a normalized velocity component (in the direction of the translational velocity). The normalized velocity component is derived by dividing the given velocity v by the velocity at the maximum value of the beam intensity, giving a dimensionless quantity. The normalized Maxwell distribution using a superimposed stream velocity can be expressed as [77]:

$$f(v_{norm}) = C_3 v^2 e^{-\frac{(v-v_s)^2}{\alpha^2}} \quad (2.4)$$

In equation (2.4) C_3 is a normalization constant and the variable α is equal to v_w . Because C_3 is an arbitrary constant, if a graph is plotted of $\ln(f(v_{norm})/v^2)$ as a function of $(v - v_s)^2$ the gradient of the graph will be equal to $-\frac{1}{\alpha^2}$; the longitudinal temperature is then directly obtained

from this gradient value. This method is applied to a selected data range consisting of data values from both the left and right hand sides of the normalised Maxwell distribution until the error in a linear least squares fit of the data is minimised (refer to [78] and [79] for details on the least squares method for linear fits). Generally it is a case of trial and error selecting the data range to minimise the error in the linear least squares fit.

2.2.2: Free jet expansions

A continuum jet expansion is the expansion of a high pressure gas, from a nozzle, into a low pressure background. The physical properties of a continuum jet expansion are described using two properties the Mach number M defined by equation (2.5) and the specific heat ratio γ . In equation (2.5) c is the speed of sound in the gas (of molecular weight W) at a given temperature T . The speed of sound is defined by equation (2.6) in terms of γ .

$$M = \frac{v}{c} \quad (2.5)$$

$$c = \sqrt{\frac{\gamma RT}{W}} \quad (2.6)$$

In a free jet expansion the gas starts at the source with a small velocity value, called the stagnation state, at a pressure P_o and temperature T_o . Because of the pressure difference between the source and the background pressure P_b (where $P_b < P_o$), the gas is accelerated into the low pressure region. If the pressure ratio $\frac{P_o}{P_b}$ exceeds the critical value of G , defined by equation (2.7), the flow will reach supersonic speed; typically the value of G is less than 2.1 for all gases.

$$G = \left(\frac{\gamma + 1}{2} \right)^{\frac{\gamma}{\gamma - 1}} \quad (2.7)$$

If the pressure ratio is less than this critical value the gas will exit at subsonic speeds with an exit pressure almost equal to the background pressure and will not undergo any further expansion. As the pressure ratio increases beyond the critical value the Mach number will equal one at the exit of the source and the exit pressure becomes equal to $\frac{P_o}{G}$ (which is approximately half of the value of the source pressure).

In this research project the source pressure was always above 300KPa and the background pressure (in the high vacuum region) was approximately 13.3×10^{-6} Pa (refer to section 2.4), giving a large pressure ratio (in excess of the critical value) of approximately 22.6×10^9 ; hence all the flows (presented in this thesis) are supersonic in nature.

A supersonic flow has two distinct characteristics. Firstly, it increases in velocity and Mach number as the flow area increases; hence the Mach number exceeds one beyond the source exit. And secondly, the supersonic flow is independent of conditions downstream from it, because while the flow is moving at a velocity less than the speed of sound information within the flow propagates at a velocity in excess of this. Because of this, boundary conditions will be created between the different regions, in which shock waves [68] provide a mechanism of meeting the boundary discontinuities. In particular there will be a shockwave in front of the free jet expansion called the Mach shock disk [67]. The Mach shock disk location given by equation (2.8) is defined in terms of the nozzle diameter and has been found to be insensitive to the specific heat ratio.

$$\frac{x_m}{d} = 0.67 \left(\frac{P_o}{P_b} \right)^{\frac{1}{2}} \quad (2.8)$$

In equation (2.8) x_m is the Mach shock disk location and d is the nozzle diameter. The actual width of the Mach shock disk is a difficult feature to measure and estimate, the width can usually be taken to be between three quarters and one half of the value derived for the Mach shock disk location; however its actual value is dependent upon the pressure ratio and the specific heat ratio [67].

With regard to this research project the Mach disk and any associated shockwave effects [68] are irrelevant, because the Mach disk location is located beyond the boundaries of the vacuum system volume. For example, using equation (2.8) and the experimental parameters given in section 2.4.8 results in a Mach disk location of 3.5m (in which the backing pressure on the valve was 6.52×10^5 Pa, the operational pressure within the main and source chambers (refer to sections 2.4.2 and 2.4.3) of 1×10^{-5} Pa and the effective orifice diameter of 0.0204mm (refer to section 2.1.1)). This distance is well beyond any of the boundaries of the vacuum system volumes (i.e. the main expansion of the gas from the valve into the main chamber) discussed in section 2.4. Because shock waves do not have any influence on any of the free jet expansions covered in this thesis, the free jet expansions can be represented by diagram 2.4, rather than a general free jet expansion [68], [67] (which consists of an isentropic region that is bounded by a shock wave region).

The temperature of a gas in a free jet expansion can be separated into two components, which describe the velocity spread either parallel $T_{||}$ or perpendicular T_{\perp} to the flow direction. A model that is used to describe (or at least approximate) the free jet expansion shown in diagram

2.4 is the “quitting surface” model. In the “quitting surface” model the free jet expansion is divided into two regimes, a continuum isentropic regime where $T_{\parallel} = T_{\perp}$ that is followed by a collision free regime in which T_{\parallel} remains constant “frozen”, because the gas has stopped expanding (translational relaxation). The most probable speed that a molecule will be travelling at within this “frozen” region will be the terminal velocity, which is a fixed quantity [67]. This velocity will be obtained at the point at which the continuum region changes to that of the collision free regime, which is known as the quitting surface. The quitting surface is the minimum point that a skimmer [68] should be placed in order to extract a molecular beam from the isentropic region (also known as the zone of silence).

It is the collision free region that is of most importance to this thesis, in particular the value for the terminal velocity, since it is the maximum mean velocity value that a gas pulse produced from the piezoelectric valve (designed in section 2.1.1) will obtain.

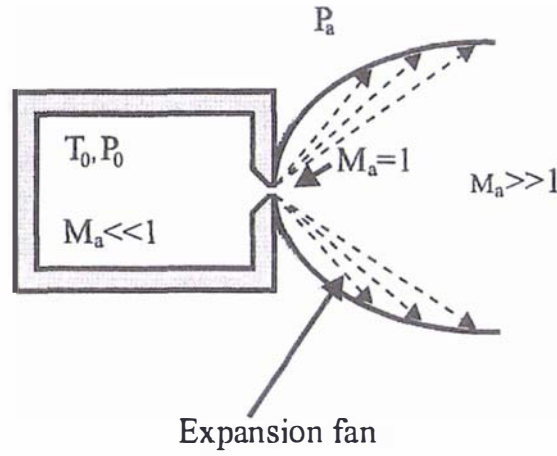


Diagram 2.4: Diagrammatic representation of a free jet expansion in which shockwave effects are irrelevant (modified from [68])

The continuum region is described using the Mach number and the speed ratio S , which is defined by equation (2.9) below.

$$S = \frac{v}{\sqrt{\frac{2kT}{m}}} = \sqrt{\frac{\gamma}{2}} M \quad (2.9)$$

In the continuum region the collisional frequency is sufficient to give an equilibrium where $T_{\parallel} = T_{\perp}$. The most frequently used velocity distribution model in this region is that of the

ellipsoidal drifting Maxwell model [67] (which is a variation of the distribution described in section 2.2.1), given by equation (2.10).

$$f(v) = n \left(\frac{m}{2\pi k T_{\parallel}} \right)^{\frac{1}{2}} \left(\frac{m}{2\pi k T_{\perp}} \right) e^{-\frac{m}{2kT_{\parallel}}(v_{\parallel}-v)^2 - \frac{m}{2kT_{\perp}}v_{\perp}^2} \quad (2.10)$$

If this distribution is used to derive the moments of the Boltzmann equation [67] the resulting energy equation will give a constant enthalpy h_0 condition of:

$$\frac{mv^2}{2} + \frac{3}{2}kT_{\parallel} + kT_{\perp} = h_0 \quad (2.11)$$

At equilibrium (where $T_{\parallel} = T_{\perp}$) this equation reduces to:

$$\frac{mv^2}{2} + \frac{5}{2}kT = h_0 \quad (2.12)$$

So an effective temperature might be defined as [67]:

$$T = \frac{3}{5}T_{\parallel} + \frac{2}{5}T_{\perp} \quad (2.13)$$

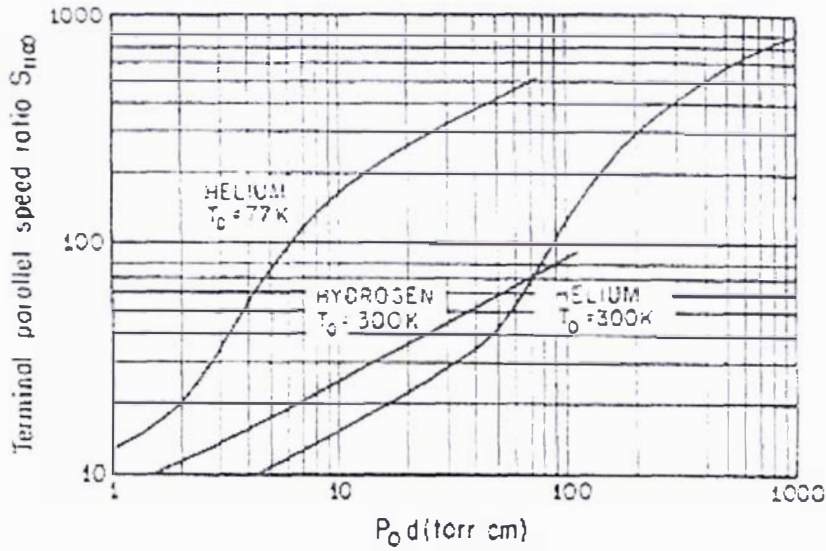
The reason that T_{\parallel} is weighted is that the “flow work” term is included along the streamline [67].

The collision free regime is usually described by only one variable (within this region), the terminal translational speed ratio $S_{\parallel\infty}$, which is defined by using the terminal velocity in equation (2.9). There is no simple empirical equation that can be used to describe the terminal speed ratio [67] for polyatomic gases in which vibrational (CO_2) or rotational (H_2) relaxation occurs in the continuum region long before translational relaxation. Instead experimentally determined values are used, such as the values given for hydrogen in graph 2.2 [67].

The location of the quitting surface is determined from the terminal speed ratio [67] and can be approximated by the empirical equation (2.14), where C_1 is a constant for a given value of γ .

For example given a value of $\gamma = \frac{5}{3}$ C_1 is equal to 3.232 [67]. In terms of the work conducted in this thesis using hydrogen gas, the quitting surface occurs a few centimetres from the (nozzle of the) valve; hence the expanding gas can essentially be considered to be in the collision free “frozen” regime.

$$x_s = d \left[\frac{S_{\parallel\infty} \sqrt{\frac{2}{\gamma}}}{C_1} \right]^{\frac{1}{\gamma-1}} \quad (2.14)$$



Graph 2.2: Terminal speed ratio as a function of the source pressure and nozzle diameter for hydrogen and helium [67]

In the case of a polyatomic gas such as hydrogen (in which rotational relaxation occurs [67]) the terminal velocity can be determined once the internal energy relaxation has been calculated. The simplest linear relaxation model that describes the rotational energy state populations (such as the Boltzmann distribution of particles with a temperature T_r , coupled with a translational temperature T) is that given by equation (2.15).

$$\frac{\partial T_r}{\partial t} = \frac{1}{\tau} (T - T_r) \quad (2.15)$$

In equation (2.15) τ is the relaxation time, which is equal to the collision number divided by the local collision frequency. The rotational energy can be included in the overall energy equation, through the use of the equation of state $P = \rho RT$ to give an energy balance equation that has separate translational and rotational contributions, denoted by the subscripts t and r , as shown in equation (2.16).

$$h_o = h + \frac{1}{2}v^2 = h_t + h_r + \frac{1}{2}v^2 \quad (2.16)$$

If the specific heats are constants then equation (2.16) can be written as (2.17).

$$\left(\frac{5}{2}k + C_r\right)T_o = \frac{5}{2}kT + C_rT_r + \frac{1}{2}mv^2 \quad (2.17)$$

For a diatomic gas $C_r = k$ can be assumed; hence equation (2.17) is simplified to:

$$T_o = \frac{5}{7}T + \frac{2}{7}T_r + \frac{mv^2}{7k} \quad (2.18)$$

A value for T_r can be found using this energy balance equation by measuring T , v^2 and knowing T_o ; however correlating the perpendicular temperature is very difficult, it is most directly determined by measuring the lateral spread of the centreline of a molecular beam (after it has past through a skimmer) [67].

A better way to obtain T_r is to integrate equation (2.15) after a transformation into steady state:

$$\frac{\partial T_r}{\partial t} = v \left(\frac{\partial T_r}{\partial S} \right) \text{ where } S \text{ is the distance along the streamline. The integration is carried out}$$

until T_r "freezes" or the position of the skimmer/diagnostic device is reached. At each integration step the energy balance equation is adjusted, which can be done in one of two ways.

The first by using a $\gamma = \frac{5}{3}$ equilibrium expansion and at each step increasing the total external enthalpy $\left(\frac{1}{2}mv^2 + \frac{5}{2}kT\right)$ by the amount of energy released by the internal energy relaxation.

The second method is to use a $\gamma = \frac{7}{5}$ equilibrium expansion, but to decrease total external

enthalpy by the amount of energy lost to energy relaxation. Both methods work equally well and will produce equation (2.19) [67].

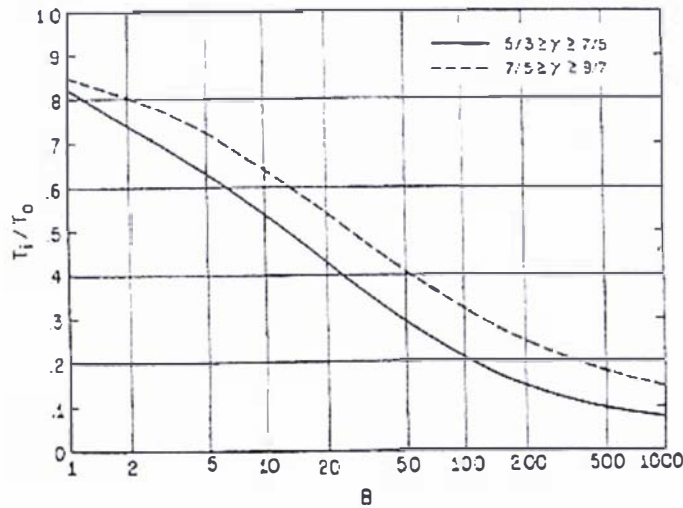
$$\frac{\partial \left(\frac{T_r}{T_o} \right)}{\partial \left(\frac{x}{d} \right)} = \frac{B \left(\frac{T_o^*}{T_o} \right) \left[\left(\frac{T_o^*}{T_o} - \frac{T_r}{T_o} \left(1 + \frac{\gamma-1}{2} M^2 \right) \right) \right]}{\gamma^{\frac{1}{2}} M \left(1 + \frac{\gamma-1}{2} M^2 \right)^{\frac{\gamma}{\gamma-1}}} \quad (2.19)$$

In equation (2.19) the value T_o^* is used to adjust the external flow variables of temperature, velocity, pressure and density before each integration step. B is a dimensionless collision parameter defined by equation (2.20).

$$B = \left(\frac{\pi \sigma^2}{Z} \right) \left(\frac{4}{\sqrt{\pi}} \right) n_o d \quad (2.20)$$

In equation (2.20) Z is the collision number, $\pi \sigma^2$ is the hard sphere cross section and n_o is the number density at the source. In the case of hydrogen gas where rotational relaxation is an important effect, Z is set equal to 300, γ is taken as $\frac{5}{3}$ and the value for σ is 2.76 \AA [67].

Graph 2.3 gives the variation of the terminal value of $\frac{T_r}{T_o}$ as a function of B , in which B has been calculated through a method of characteristics (MOC) [67].



Graph 2.3: Terminal internal temperature as a function of B from MOC calculations [67]

The terminal velocity of a polyatomic gas that has internal energy relaxation (such as H_2) can be calculated as follows [67]. First find the terminal speed ratio using graph 2.2 then calculate a value for B using equation (2.20), knowing B the terminal value of $\frac{T_r}{T_o}$ can be found from graph 2.3. Then assuming that the velocity is obtained in the isentropic regime of the quitting model (where $T_{\parallel} = T_{\perp}$) the following relationship of $T_{\parallel} = T_{\perp} = T$ is derived (obtained from equation (2.13)). Finally, rearranging equation (2.18) and using the constant heat capacity temperature relationship from [67] of $\frac{T}{T_o} = \left(1 - \frac{\gamma-1}{2} M^2\right)^{-1}$ results in equation (2.21) [67].

$$v_{\parallel\infty} = \left(\frac{7kT_o}{m}\right)^{\frac{1}{2}} \left(\frac{1 - \frac{2T_r}{7T_o}}{1 + \frac{5}{2S_{\parallel\infty}}}\right)^{\frac{1}{2}} \quad (2.21)$$

The above approach is rather cumbersome and unfortunately relies upon prior knowledge of the pressure and effective orifice diameter, which in the case of the valve developed for this thesis is an unknown value; hence the value for $S_{\parallel\infty}$ in equation (2.21) will be an unknown. Also the determination of $\frac{T_r}{T_o}$ from graph 2.3 can give misleading results, because graph 2.3 was calculated with the assumption that C_p is a constant. It has been experimentally determined that $\frac{T_r}{T_o}$ is approximately equal to 0.8 [67].

In the case of hydrogen gas it is best to integrate its heat capacity, both translational and rotational, to obtain the correct enthalpy values in the overall energy equation of (2.16). A graph for the heat capacity of various diatomic molecules as a function of temperature is presented in graph 2.4. In graph 2.4 θ_R is the characteristic rotational temperature of a molecule.

There are two forms of the diatomic hydrogen molecule (H_2) with distinct molecular spins, which are defined as either ortho-hydrogen or para-hydrogen. Normal hydrogen consists of 75% ortho-hydrogen and 25% para-hydrogen and is the form always encountered, except in the case of cryogenic temperatures. At cryogenic temperatures the ortho-hydrogen continues to rotate because it cannot exist at an angular momentum J equal to zero; the lowest energy level that ortho-hydrogen can exist is at $J = 1$. Under cryogenic temperatures the ortho-hydrogen will lose its rotational energy and be converted to the para-hydrogen state. This conversion process is very slow and in the molecular beam work conducted in this thesis this conversion process

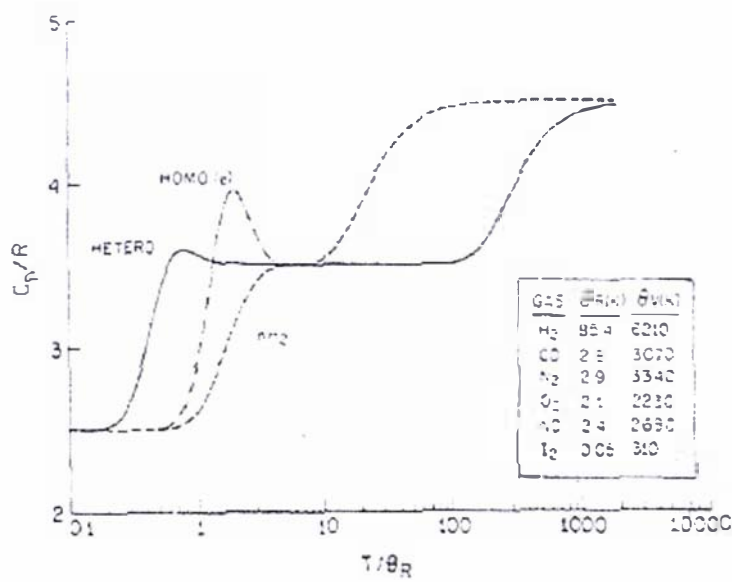
(under cryogenic temperatures) can be ignored; hence it is the heat capacity of the normal form of hydrogen that should be used in the calculation to determine the terminal velocity of hydrogen.

The integration of both the translational and rotational heat capacities, and the various models and approximations that can be used, to calculate the terminal velocity of hydrogen is beyond the scope of this thesis. There is the further consideration that the terminal velocity of hydrogen is essentially an unobtainable upper limit, because it would require the complete conversion of all the translational and rotational energies into the translational kinetic energy of the gas pulse/flow. Because of the last point, it is probably preferable to use the experimentally determined value for the terminal velocity of hydrogen. The terminal velocity of hydrogen was determined in [80] using the standard time of flight (TOF) method, refer to [67] for a detailed description of this method. The experimentally determined value for the terminal velocity of hydrogen [80] is:

$$v_{\infty} = 2659 \text{ m/s}$$

(2.22)

For the remainder of this thesis the terminal velocity of hydrogen will be assumed to be equal to 2660m/s, for sheer convenience. Note the difference of a few 100m/s in the chosen terminal velocity makes little difference to the calculated temperatures (using a Maxwell velocity distribution) in section 2.4.



Graph 2.4: Diatomic heat capacity as a function of temperature for various molecules [67]. Hetero: general heteronuclear diatomic, Homo(e): homonuclear diatomic with only even states, nH_2 : normal hydrogen.

2.3: Mass output characteristics of the piezoelectric valve

The mass output of the (source) valve must be established to give an indication of its performance and whether or not the mass output requirement for the MTF scheme has been satisfied. Before the mass output of the valve was determined the valve was tensioned so that it would operate at its maximum driving voltage of -1000V and as great a backing pressure as possible, to enable the greatest mass output from the valve without an appreciable leak rate. The valve was tensioned until it operated at an upper limit of 750×10^3 Pa, which was the maximum pressure that the pressure regulator and the feed-throughs could withstand.

The mass output produced from the valve was determined by pulsing the valve into a known “working volume” and then measuring the increase in pressure. The mass produced from a single pulse from the valve can then be determined by using the ideal gas law. The “working volume” was deduced by introducing a known amount of gas from a “sample volume” and then measuring the increase in pressure. After subtracting the known background pressure in the “working volume” the value for the “working volume” was calculated by using the ideal gas law. The methodology and related equations to calculating the mass output from the valve are given in section 2.3.5.

The mass output for the valve was initially determined under what had experimentally been found to be the upper limit of its performance; these results are displayed in section 2.3.6. These were only preliminary in nature and a more extensive set of results were generated after experimentation on the plasma accelerator (discussed in chapter 3) was concluded. This extended set of results was concerned with two features of the valves operation. Firstly, establishing the mass output from the valve as a function of backing pressure and driving pulse lengths (for a range of values). And second, to give an indication of any decrease in the performance of the valve after its three year working period.

2.3.1: Equipment used to operate the piezoelectric valve

The equipment, in sequential order, used to operate the piezoelectric valve is shown sequentially in diagram 2.5. At this point it is important to make the distinction between the voltage pulse sent to the valve, which shall be known as the driving pulse, and the actual gas pulse length delivered from the valve. The actual gas pulse length will be referred to as the pulse width and is derived by taking the full width half height (FWHH) of the experimentally observed pulse (using a multichannel scaler).

The driving pulse lengths are set on the SRS model DG535 four channel digital delay/pulse generator; this device generates square wave voltage pulses and can be set to deliver either single or multiple pulses. The pulses generated from this pulse generator can either be internally

2.3.1: Equipment used to operate the piezoelectric valve

(from the device) or externally (from another source) triggered. Note all the experiments carried out within this section used internal triggering on the pulse generator. The driving voltage supplied to the piezoelectric crystal comes from a PI model E-471.00 HVPZT power amplifier, this device supplies -1000V to the crystal.

The operation of the piezoelectric valve starts with a +4V voltage pulse sent from the pulse generator, which is then amplified by a homemade preamplifier with a voltage gain of 2.5. The resulting +10V pulse is then amplified by the E-471.00 HVPZT power amplifier to give a -1000V driving pulse, that is then supplied to the piezoelectric crystal. The resulting voltage pulse that is sent to the crystal is “saw tooth” in nature.

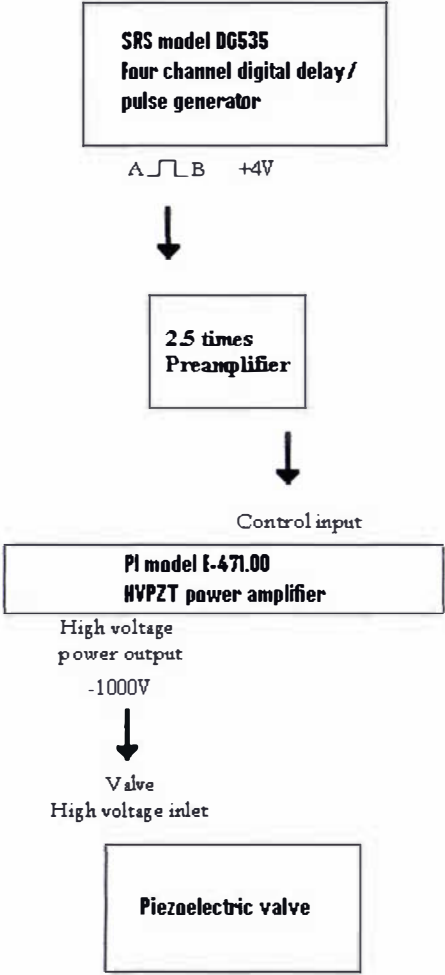


Diagram 2.5: Schematic of equipment and sequence used to operate the piezoelectric valve

2.3.2: Equipment and apparatus used in determining the initial mass output from the valve at its upper operating limit

The apparatus used to determine the initial mass output from the valve is shown in diagram 2.6. The equipment used to operate the piezoelectric valve has been described in the previous section. The rest of the equipment depicted in diagram 2.6 is listed in table 2.2.

2.3.2:Equipment and apparatus used in the determining the initial mass output from the valve at its upper operating limit

In the experimental apparatus depicted in diagram 2.6 the actual volume that the piezoelectric valve was pulsed into consists of the combined volumes highlighted in blue and green, this volume will hence forth be termed as the “working volume”. In order to determine the value of this “working volume” a calibration experiment was conducted using the volume highlighted in green, which shall be called the “sample volume”, the details of this calibration are described in section 2.3.4.

The output from the MKS 622 pressure transducer (with a full scale deflection of 1000Torr) was observed on a Tektronix model THM550 true RMS multimeter/auto ranging scope; the smallest observable pressure on this device was 13.3Pa and can be taken as the experimental error value within the “working volume”. The Edwards model E2M2 roughing pump has a pumping speed of 3.7m³/hr.

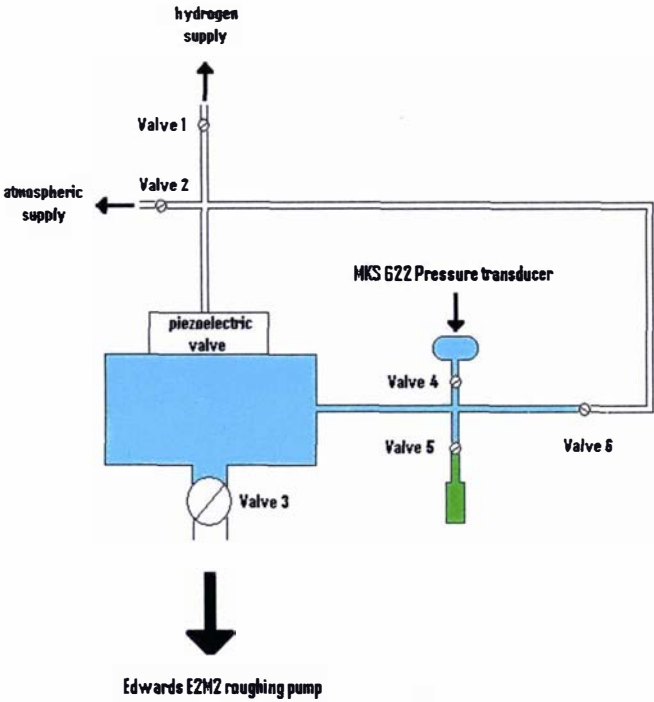


Diagram 2.6: Experimental apparatus used for determining the mass output from the piezoelectric valve

Label	Make/Model
Valve 1	NUPRO: SS 4PT Plug valve
Valve 2	NUPRO: SS 4PT Plug valve
Valve 3	MDC: AV-150M Ball valve
Valve 4	NUPRO: SS 4PT Plug valve
Valve 5	NUPRO: SS 4PT Plug valve
Valve 6	NUPRO: SS 4PT Plug valve

Table 2.2: Description of experimental equipment listed in diagram 2.6

2.3.3: Equipment and apparatus used in determining the mass output from the valve as a function of pressure and driving pulse length

2.3.3: Equipment and apparatus used in determining the mass output from the valve as a function of pressure and driving pulse length

The apparatus used to determine the mass output from the valve as a function of hydrogen backing pressure and driving pulse length is shown in diagram 2.7, this apparatus is a modified version of the apparatus described in section 2.3.2. This apparatus was constructed after the tests on the plasma accelerator, discussed in chapter 3, were completed. The equipment used to operate the piezoelectric valve is described in section 2.3.1. The remaining equipment in diagram 2.7, for which no description has been given, is described in table 2.3. The “working volume” into which the valve was pulsed consists of the combination of the highlighted blue and green volumes, with the “sample volume” being the highlighted green volume in diagram 2.7.

The hydrogen backing pressure upon the piezoelectric valve was measured by a MKS 722 pressure transducer (with a full scale deflection of 10000Torr), and the pressure within the “working volume” was observed by a MKS 622 pressure transducer (with a full scale deflection of 1000Torr). The output from both of these pressure transducers was viewed on a Tektronix model THM550 true RMS multimeter/auto ranging scope, the smallest observable pressure on this device was 13.3Pa and can be taken as the experimental error value within the “working volume” (i.e. the MKS 622 pressure transducer).

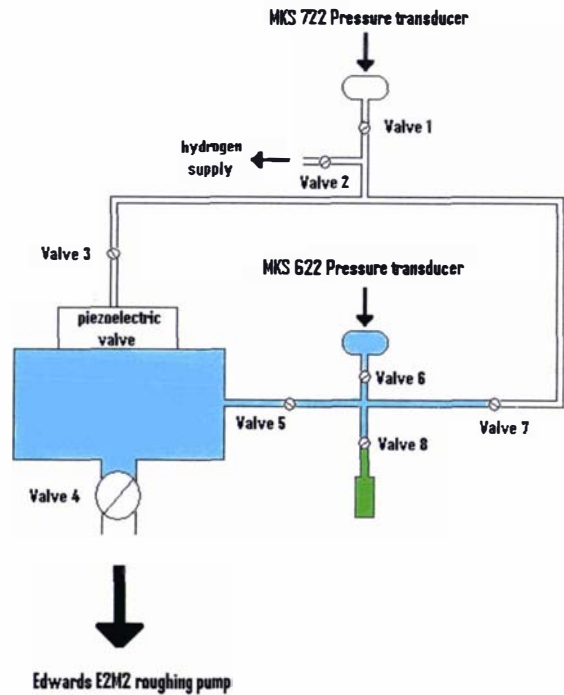


Diagram 2.7: Experimental apparatus used for determining the mass output from the piezoelectric valve as a function of hydrogen backing pressure and driving pulse length

2.3.3:Equipment and apparatus used in determining the mass output from the valve as a function of pressure and driving pulse length

Label	Make/Model
Valve 1	NUPRO: SS-4BT VC bellows valve
Valve 2	NUPRO: SS-4BT VC bellows valve
Valve 3	NUPRO: SS 4PT Plug valve
Valve 4	MDC: AV-150M Ball valve
Valve 5	NUPRO: SS 4PT Plug valve
Valve 6	NUPRO: SS 4PT Plug valve
Valve 7	NUPRO: SS 4PT Plug valve
Valve 8	NUPRO: SS 4PT Plug valve

Table 2.3: Description of experimental equipment listed in diagram 2.7

2.3.4: Data acquisition relating to the mass output from the valve

As alluded to before, the mass output of the valve was determined by pulsing the valve into a known “working volume” (described in sections 2.3.2 and 2.3.3). This “working volume” was determined from a calibration experiment involving a “sample volume”. The “sample volume” was measured by filling it with distilled water (the temperature of the water was also recorded) then subtracting the weight of the evacuated “sample volume”, its volume is then calculated from the known density of water. (This method was found to give reproducible results). The mass produced per gas pulse from the piezoelectric valve (described in section 2.1.1) was determined by pulsing the valve into the evacuated “working volume” (whose background pressure and leak rate of the valve had been noted) and recording the resulting pressure increase and the number of gas pulses used to generate this increase in pressure.

2.3.5: Analysis of the data relating to the mass output from the valve

In the “working volume” calibration experiment both the number of moles and the temperature can be considered constant in the volume of gas contained within the “sample volume” and “working volume”, so the simple relation of equation (2.23) can be derived (from the ideal gas law).

$$V_2 = \frac{P_1 V_1}{P_2} \tag{2.23}$$

In equation (2.23) the suffixes 1 and 2 relate to the “sample volume” and the “working volume” respectively. (Note P_1 , V_1 and P_2 are experimentally measured quantities, refer to

2.3.5: Analysis of the data relating to the mass output from the valve

section 2.3.4.) The total amount of gas produced from the valve is determined using the ideal gas law and the actual pressure increase within the “working volume” (i.e. the amount of gas introduced into the “working volume” solely from the operation of the valve). The actual pressure increase P_a is determined by subtracting the leak rate (from the valve) and the background pressure (within the “working volume”) from the recorded pressure increase (within the “working volume”). The amount of gas produced per pulse m_{pulse} is then simply the total amount of gas produced from the valve divided by the number of gas pulses N_{pulse} (used to generate the total mass):

$$m_{pulse} = \frac{MP_a V}{N_{pulse} RT} \tag{2.24}$$

2.3.6: Initial mass output results from the valve at its upper operating limit

The “sample volume” used to determine the “working volume” was found to be 0.768ml. In the “working volume” calibration experiment the “sample volume” was filled with 750×10^3 Pa of hydrogen. Using equation (2.23) and the data obtained from the calibration experiment the “working volume” was found to be 550ml. The results presented in table 2.4 show the average mass of hydrogen produced per pulse, these results were determined by using the calculated “working volume”, equation (2.24) and the raw experimental data.

	Mass per shot: kg
pulse length: us	Pressure: 750KPa
150	1.54E-08
200	2.17E-08

Table 2.4: Average mass per shot produced from the piezoelectric valve in kg as a function of pulse length, produced from the initial mass output experiment where the hydrogen backing pressure was 750KPa

2.3.7: Extended mass output results as a function of pressure and driving pulse length

The “sample volume” used to extend the initial mass output results was the same as that used in the previous section. The “working volume” was found to be 411 ml, this result was calculated using equation (2.23) and the data obtained from filling the “sample volume” with 807×10^3 Pa of hydrogen gas. The average mass of hydrogen gas produced per pulse from the valve

2.3.7: Extended mass output results as a function of pressure and driving pulse length

presented in table 2.5 were determined from the data obtained by pulsing the valve into the “working volume” and the use of equation (2.24). In table 2.5 the average results are presented with the driving pulse length as a function of hydrogen backing pressure upon the valve. The experimental error on all these results is approximately one percent, and the observed upper and lower (experimentally observed) limits are within twenty percent of the averaged values presented in table 2.5.

	Mass per shot: kg		
pulse length: us	Pressure Pa: 420KPa	Pressure Pa: 543KPa	Pressure Pa: 672KPa
160	2.93E-09	3.39E-09	3.75E-09
180	3.66E-09	4.31E-09	4.84E-09
200	4.54E-09	5.27E-09	5.50E-09
220	5.78E-09	6.50E-09	6.46E-09
240	7.24E-09	8.03E-09	7.98E-09
260	8.38E-09	9.41E-09	9.54E-09
280	9.63E-09	1.10E-08	1.05E-08

Table 2.5: Average mass per shot from the piezoelectric valve in kg as a function of driving pulse length for various hydrogen backing pressures obtained from the extended mass output experiments.

2.3.8: Discussion on the mass output produced from the piezoelectric valve

The maximum output that has been achieved with the current valve is 0.022mg of hydrogen gas (refer to table 2.4), which was produced from the initial experiments upon the piezoelectric valve using a 200us driving pulse length and a driving voltage of -1000V. Although this value is below the required 0.2mg of hydrogen gas for the MTF scheme (that this valve has been designed for), the mass output from the valve could potentially be increased through: cryogenic means, using an array of piezoelectric valves or by increasing the backing pressure behind the piezoelectric crystal. None of these options have yet been fully investigated owing to the time constraints placed upon this research project.

There is a noticeable decrease in the mass output produced from the valve when the initial mass output results of table 2.4 are compared to those obtained from the extended mass output results in table 2.5. Unfortunately, due to the limited scope of the initial mass output experiment, only the 200μs driving gas pulse length can be used to determine decrease in the performance of the valve over its three year working period. There is almost a three-fold decrease in the mass

2.3.8: Discussion on the mass output produced from the piezoelectric valve

output from the valve (if the results from table 2.5 are linearly interpolated to obtain a mass output value at $750 \times 10^3 \text{ Pa}$). Upon examination of the valve, it was discovered that the screws used to tighten the face plate and the spring washers had slightly moved. This can be solely attributed to the operation of the valve and the fact that these screws are not actually locked in place. This problem can easily be fixed by redesigning the valve so that the screws are locked in place, or more simply by cementing the screws in place (although this remedy would prevent any further maintenance/modification of the valve).

The general variation in the results in table 2.5 (the lack of consistency between certain pressure values, for example the difference between the mass output results at $543 \times 10^3 \text{ Pa}$ and $672 \times 10^3 \text{ Pa}$ for a driving pulse length of $280 \mu\text{s}$) can mostly be attributed to the limited scope of the experiment; the experiment was only conducted three times for each pressure and driving pulse length to derive the average value presented in the table.

The initial results of table 2.4 were re-obtained once the loose screws were re-tightened. The results in table 2.5 give an indication of the mass produced per pulse as a function of driving pulse length and backing pressure; however there was not enough time to determine this variation for the re-tensioned valve.

2.4: Gas pulse characteristics

The gas pulse characteristics of the valve that are of interest are the gas pulse width and the temperature of the gas pulse, both of these quantities can be found from the velocity profile. The pulse width is important as it gives the actual length of the gas pulse produced (where the majority of the gas lies); the temperature of the gas pulse is also an indication of the broadness of the gas pulse. This is an important measure of the performance of the valve and is also necessary in determining the properties of the gas pulse when it enters the plasma accelerator (discussed in chapter 3). Only the results relating to hydrogen gas pulses will be presented (hereafter) in this chapter.

The Mass-spectrometer described in section 2.4.1 was used to gather raw data from the gas pulses produced from the valve, in the form of intensity as a function of time; from this the pulse width can easily be determined. The longitudinal temperature of the gas pulses was calculated from the experimental velocity distribution by assuming a Maxwell velocity distribution (refer to section 2.4.6). The initial tests characterising the gas pulse characteristics produced (solely) from the valve were conducted using the apparatus described in section 2.4.2. These initial findings (from this apparatus) showed that the gas pulses had very narrow pulse widths; as a result of this it was not possible to accurately determine a temperature, because of the limited number of data points. So the flight distance between the valve and the Mass-spectrometer was increased to provide enough data points to accurately determine the temperature, the apparatus in section 2.4.3 was used for this purpose.

However the results from these two experiments did not necessarily represent the actual gas pulse characteristics produced from the valve's operation within the plasma accelerator, in which a skimmer and preionizing unit was placed in front of the valve. The skimmer and preionizer might have a considerable flow dynamic effect on the gas pulses. So an experiment was conducted using the apparatus discussed in section 2.4.4. This experiment was conducted after the tests on the plasma accelerator described in chapter 3 were completed. A long flight distance between the valve and the mass-spectrometer was not needed in this experiment, because there were enough data points to accurately determine a temperature for the gas pulses.

2.4.1: Quadrupole mass-spectrometer

The main diagnostic tool used in this research was a SRS RGA200 residual gas analyser which is shown in diagram 2.10, technical details on this device can be found from [81]. This device consists of a quadrupole mass-spectrometer and various ion detectors, most notably a continuous diode electron multiplier (CDEM).

A quadrupole mass-spectrometer consists of four equally spaced rods arranged around a central axis; an ionizer unit in front of the quadrupole ionizes gas as it enters the mass-spectrometer. The rods carry both a DC and a RF voltage component, diametrically opposite rods are held at the same time dependent voltage. Ions travelling along the axis (the z axis) of the Quadrupole experience a time dependent force which is alternatively focused in the perpendicular directions to the central axis (the x and y axes), this causes ions to travel with a helical trajectory. Only ions with stable trajectories (the amplitude of the ion oscillations which are finite for all times) will travel to the end of the quadrupole mass-spectrometer and be detected by the CDEM. A stable trajectory is dependent upon the mass to charge ratio of an ion for a particular voltage amplitude (a function of both the DC and RF voltage), in this way the Quadrupole Mass-spectrometer acts as a mass filter. A detailed description of the principle of operation of this type of Mass-spectrometer can be found in [68]. The distance from the start of the quadrupole and the CDEM is approximately 14.9cm.

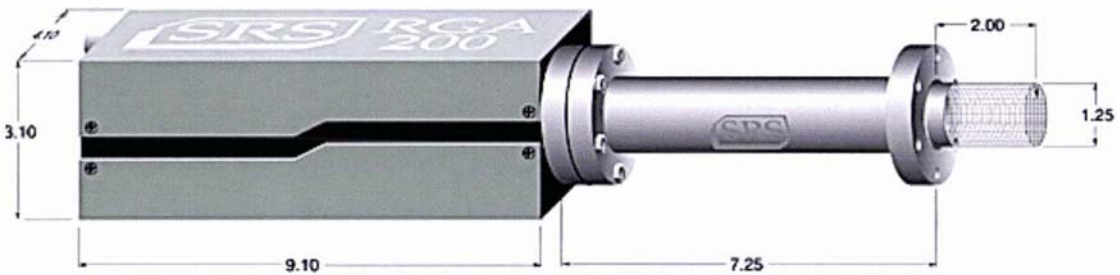


Diagram 2.10: The SRS RGA200 residual gas analyser [81] (dimensions in inches)

A CDEM is an ion detecting device and consists of a hollow circular tube that has a semi-conducting inner surface. A potential difference, typically in the region of 2000V, is applied between the two ends of the device. Ions that enter the device impinge upon the inner surface generating secondary electrons, which are then accelerated until they impinge upon another portion of the curved inner surface. The entire process is repeated and an avalanche effect is produced, the resulting sum of the secondary electrons is collected at the end by an ion collector generating an ion current. A detailed reference on the operation of this device can be found in [68]

The RGA200 was operated as a quadrupole mass-spectrometer in the determination of the gas pulse characteristics of the piezoelectric valve discussed here within section of 2.4 in its entirety; but in the plasma accelerator experiments of chapter 3 the device was used as a CDEM to detect the hydrogen plasma produced from the plasma accelerator.

The main operational settings on this device are ML the mass of the ions that are scanned for, FL the filament current (in mA) used to ionize the gas, EE the electron energy level (in eV)

and HV the voltage potential (in V) set on CDEM. Since only hydrogen gas is used in all the experiments conducted within chapters 2 and 3 $ML = 2.0$, the voltage of the CDEM is typically set to about $HV = -2000V$ and the electron energy is set at $EE = 70eV$. The only difference between the quadrupole mass-spectrometer and CDEM operation of this device is that the filament current is switched on during mass-spectrometer operation, while in CDEM mode it is switched off. Typically the filament current is set in the range of $FL = 0.1mA$ to $FL = 0.8mA$ (the lowest value that the filament current was ever set to was $FL = 0.02mA$), but in the plasma accelerator experiments (in chapter 3) $FL = 0$ was set.

There are two corrections that must be made when analysing the results obtained from this device. First the flight time of the ions through this device must be taken into account for any obtained results, because it is the inherent delay time associated with this device. It is quite small in the order of a few microseconds and can be determined by dividing the distance travelled by the ions through the mass-spectrometer by their velocity v_i . This velocity is determined from equation (2.25) where E is the ion energy and m is the ions mass; by default the ion energy on the SRS RGA200 residual gas analyser is set equal to 12eV.

$$v_i = \sqrt{\frac{2E}{m}} \quad (2.25)$$

Hence using equation (2.25) with the default ion energy of 12eV results in an ion velocity of 33907m/s. Multiplying this value by the known distance from the start of the quadrupole mass-spectrometer to the CDEM results in a time of flight delay of 4.38 μ s.

Secondly the faster the molecules are travelling the less time they will spend in the ionizer at the front of the device; hence the probability of these molecules being ionized will be smaller than that for slower moving molecules. (This is the second correction, which must be considered when analysing the results from this device.)

2.4.2: Equipment used to determine the density profile of the gas pulse produced from the valve without the preionizer attachment

A schematic representation of the apparatus and equipment used to determine the density profile of the gas pulse produced from the valve is shown in diagram 2.11, while an isometric cross sectional view of the apparatus is presented in diagram 2.12. The apparatus consists of three differentially pumped chambers: a source chamber, main chamber and an ultra high vacuum chamber. The piezoelectric valve is centred in the main vacuum chamber within an extension of

2.4.2: Equipment used to determine the density profile of the gas pulse produced from the valve without the preionizer attachment

the source chamber. The valve is on axis with the mass-spectrometer, which is connected to the ultra high vacuum chamber as can be seen in diagram 2.11.

The basic pieces of equipment labelled in diagram 2.11 are listed in table 2.6. Turbo pump 1 is controlled by an Edwards EXC 300M control unit and Turbo pump 2 is controlled by a LH turbotronik NT50 control unit. The operating pressure was approximately 7×10^{-9} Pa within the ultra high vacuum chamber and is in the region of 1×10^{-5} Pa for both the main and source chambers.

The equipment associated with operating the piezoelectric valve remains the same as that discussed in section 2.3.1 and depicted in diagram 2.5, it consists of: the pulse generator, amplifier 2 and the piezo-driver. The pulse generator is a SRS model DG535 four channel digital delay/pulse generator, amplifier 2 is a home made preamplifier with a voltage gain of 2.5 and the piezo-driver is a PI model E-471.00 HVPZT power amplifier.

The diagnostic equipment used with the apparatus depicted in diagram 2.11 are the Mass-spectrometer and the multichannel scaler. The mass-spectrometer is the SRS model RGA200 residual gas analyser discussed in section 2.4.1. The voltage pulses from the Mass-spectrometer are first amplified by a three stage SR445 DC-300MHz amplifier (Amplifier 1 in diagram 2.11) and are then accumulated by a SR 430 multichannel scaler. The setting of the operational parameters and output of the diagnostic equipment was monitored and recorded using a LABVIEW program (version 3.1). The distance from the piezoelectric valve to the mass-spectrometer in this apparatus was 42.9cm.

2.4.2:Equipment used to determine the density profile of the gas pulse produced from the valve without the preionizer attachment

Label	Make/Model	Pumping speed
S1	MDC Bayard-Alpert ion gauge	
S2	Edwards model PRM pressure gauge	
S3	TC1A thermocouple vacuum gauge	
S4	TC1A thermocouple vacuum gauge	
S5	Edwards model 6 pressure gauge	
S6	MDC Bayard-Alpert ion gauge	
V1	MDC: K AV-100 bellows valve	
V2	Edwards model BRV 25 backing/roughing valve	
V3	Generic butterfly valve	
Roughing pump 1	Edwards RV5 roughing pump	5.1 m ³ /hr
Roughing pump 2	Edwards RV5 roughing pump	5.1 m ³ /hr
Roughing pump 3	Edwards E2M18 roughing pump	17 m ³ /hr
Diffusion pump 1	Edwards Diffstak model 100LN2	500 L/s
Diffusion pump 2	CIT-ALCATEL crystal 160E	3000 L/s
Turbo pump 1	Edwards EXT 250M turbo pump	190 L/s (Hydrogen)
Turbo pump 2	LH tubovac 50 tubomolecular pump	33 L/s (Hydrogen)

Table 2.6: Description of experimental equipment listed in diagram 2.11

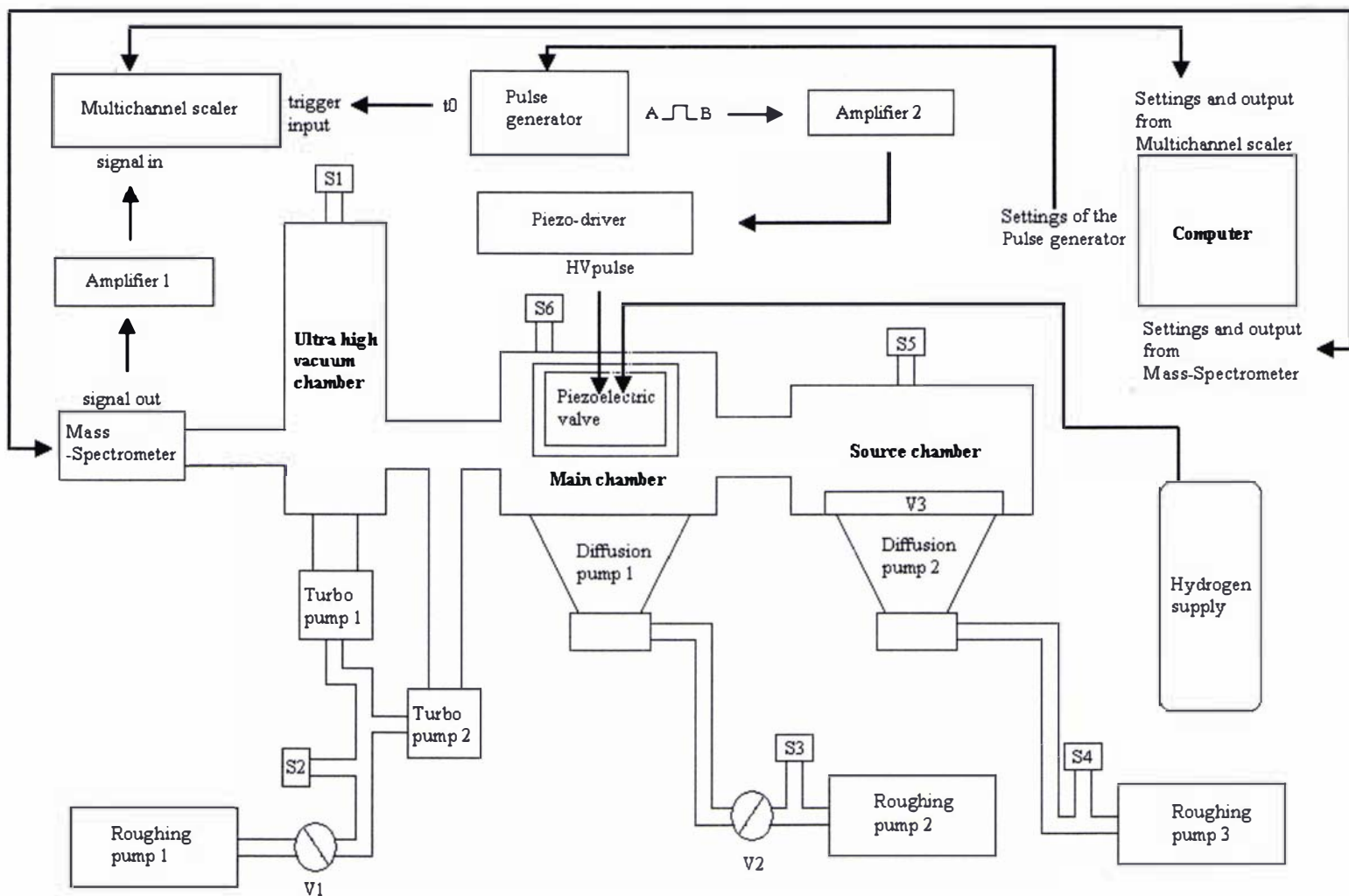


Diagram 2.11: Schematic representation of experimental apparatus used to determine the pulse density profile produced from the piezoelectric valve

2.4.2: Equipment used to determine the density profile of the gas pulse produced from the valve without the preionizer attachment

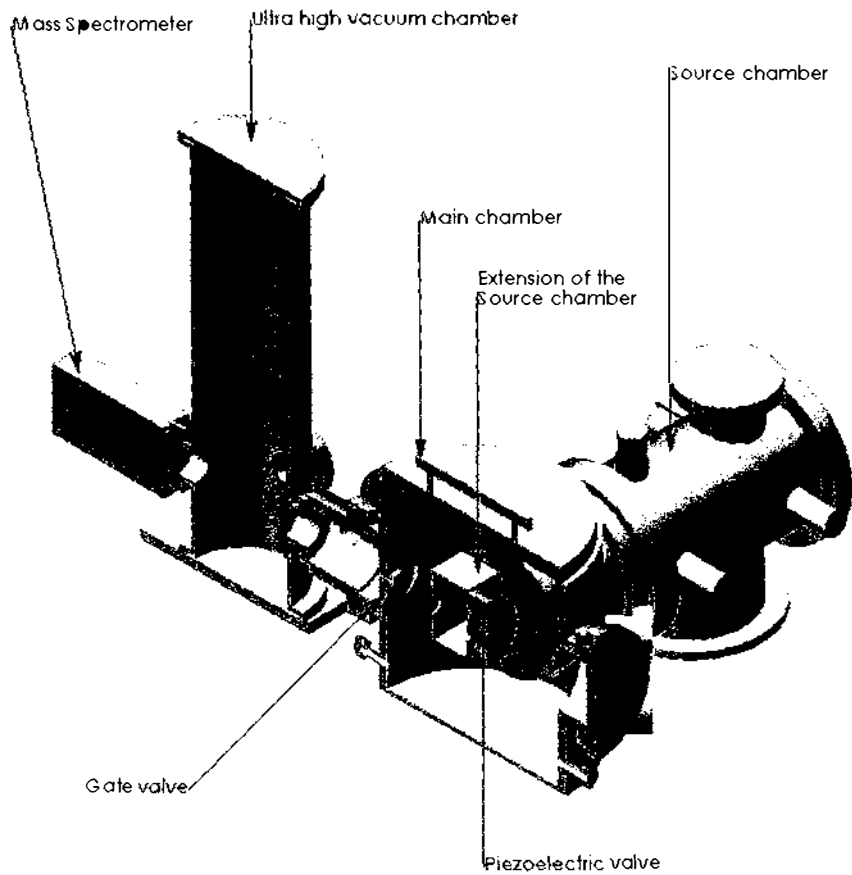


Diagram 2.12: Isometric cross-section of the apparatus used to measure the density profile of the piezoelectric valve

2.4.3: Equipment used in determining an accurate temperature of gas pulses with short pulse widths produced from the valve without the preionizer attachment

The gas pulses generated, from the previously described apparatus, were found to have very narrow pulse widths and because of this there were not enough data points to enable an accurate temperature fit using a Maxwell velocity distribution (refer to section 2.2.1). A modification of the apparatus discussed in the previous section was made to rectify this problem. The flight distance between the piezoelectric valve and the mass-spectrometer was increased by the insertion of a flight tube; this is shown as an isometric cross-section in diagram 2.13. The equipment used in the apparatus depicted in diagram 2.11 remains the same as that described in section 2.4.2 with the exception that the ultra high vacuum chamber, its associated pumping equipment (Turbo pump 1, 2 and roughing pump 1) and the diagnostic equipment are positioned at the end of the flight tube. At the end of the flight tube a conical skimmer, with an aperture diameter of 5.9mm was placed. The flight tube was pumped using a MFG Torr vacuum products model R-420 diffusion pump that has a pumping speed for hydrogen of 1410L/s.

2.4.3: Equipment used in determining accurate temperature of the gas pulses with short pulse widths produced from the valve without the preionizer attachment

Connected to that diffusion pump is an Edwards RV5 roughing pumps that has a pumping speed of 5.1m³/hr. The operational pressure within the flight tube was approximately 1×10^{-4} Pa and the flight distance from the piezoelectric valve to the mass-spectrometer was 4.336m.

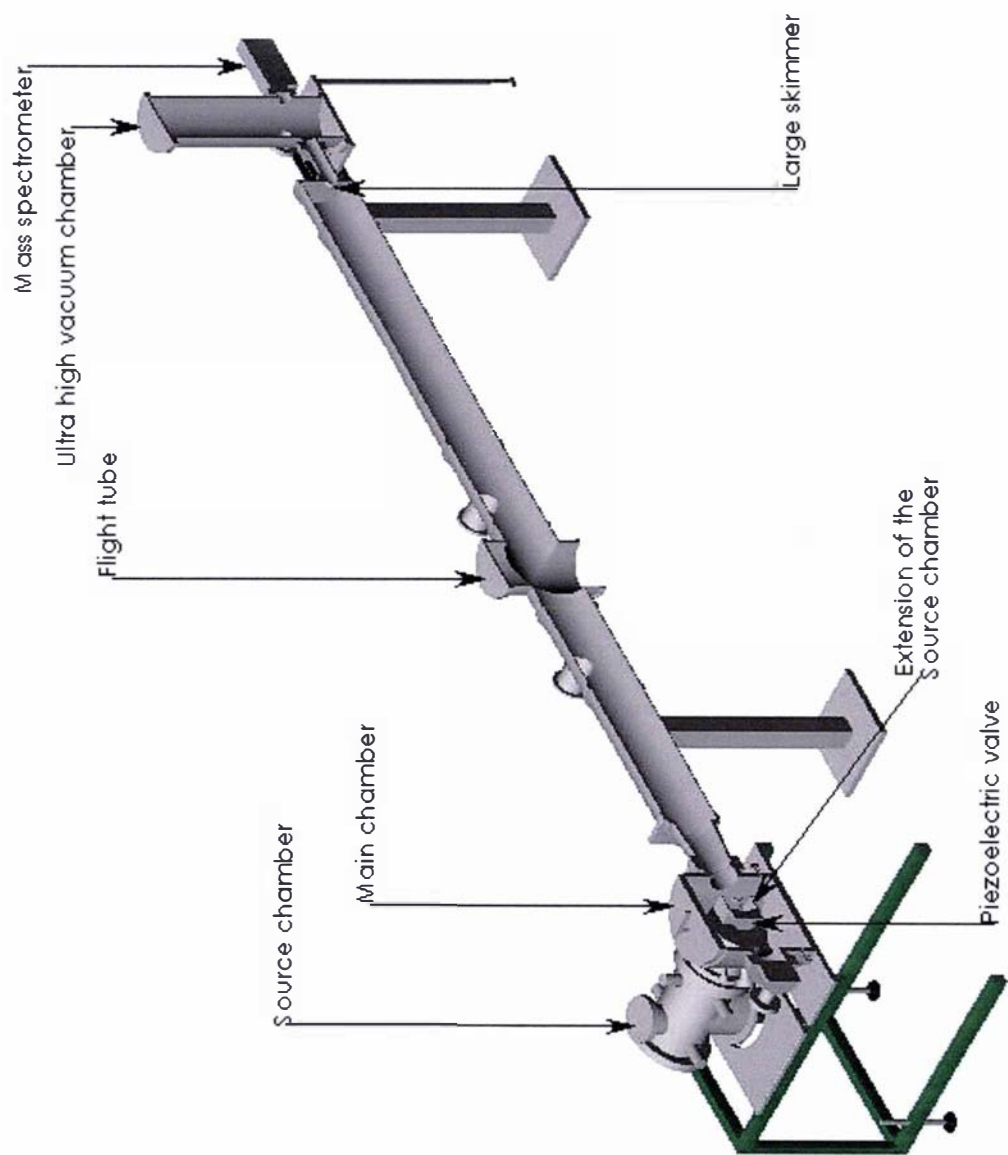


Diagram 2.13: Isometric cross-section of the apparatus used to determine the temperature of gas pulses that have very narrow pulse widths

2.4.4: Equipment used in determining the gas pulse characteristics of the valve with a preionizer attachment

2.4.4: Equipment used in determining the gas pulse characteristics of the valve with a preionizer attachment

The plasma accelerator described in chapter 3 has a skimmer and preionizer attachment placed in front of the valve. The apparatus used to investigate the gas pulse characteristics of the piezoelectric valve as a result of these attachments was made using a modified version of the apparatus described in section 2.4.2. The main modification is that the skimmer and preionizer attachment was placed in front of the piezoelectric valve. This is shown schematically with dimensions in diagram 2.14 and isometrically in diagram 2.15. The other modification was that the distance between the piezoelectric valve and the mass-spectrometer was increased to 52cm.

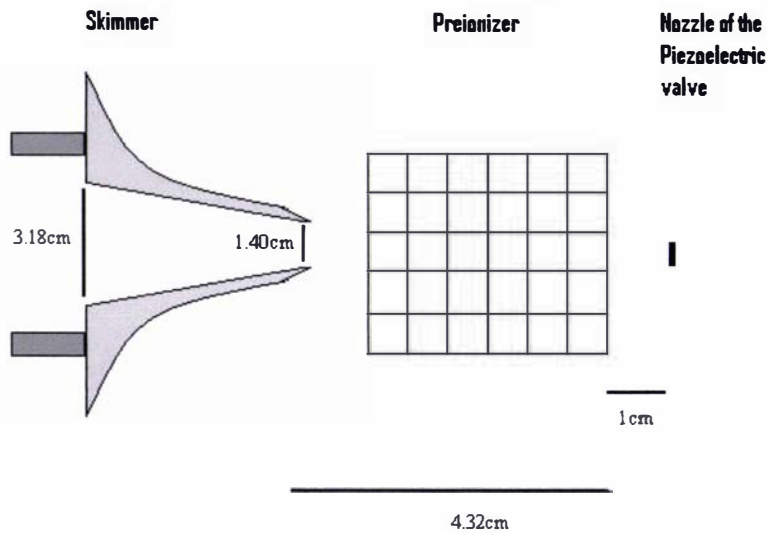


Diagram 2.14: Schematic of the skimmer, preionizer and piezoelectric valve arrangement

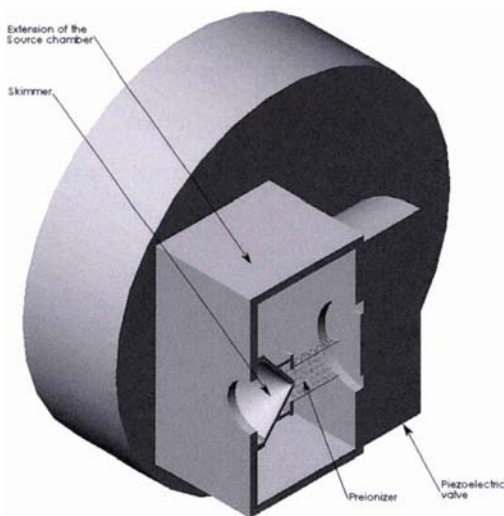


Diagram 2.15: Isometric cross-section of the skimmer, preionizer and piezoelectric valve arrangement

2.4.5: Data acquisition of the gas pulses produced from the valve

The process of obtaining data is shown schematically in diagram 2.11. The data collection and operational settings of the diagnostic equipment were controlled by a computer using a LABVIEW (version 3.1) program over a GPIB link. The driving pulse length for the pulse generator and the bin width on the multichannel scaler are set using the LABVIEW program. The settings on the mass-spectrometer are controlled using its supplied software, in which the mass-spectrometer was operated in mass-spectrometer mode using the operational parameters discussed in section 2.4.1.

Once the operational and diagnostic settings have been programmed the experiment is triggered by a user defined command in the LABVIEW program. This causes the pulse generator to send a driving pulse to the piezoelectric valve using the process discussed in section 2.3.1, which results in the generation of a gas pulse. At the same time a trigger signal is sent from the pulse generator to the multichannel scaler, causing it to start recording the data from the mass-spectrometer. The recorded data from the multichannel scaler is sent to the LABVIEW program where it is recorded as a “dat” file and displayed as a plot of counts as a function of bins.

2.4.6: Determining the velocity distribution and temperature of the gas pulses produced from the valve

The speed distribution and longitudinal temperature of a gas pulse can be calculated from the raw data obtained from the multichannel scaler. The data obtained from the multichannel scaler was not continuous but binned (the data is grouped into specified ranges of the continuous data variable, in this case the bin width). Before the data can be analysed there are a number of corrections that must be accounted for:

- 1) There will be an underlying background intensity (continuous random data)
- 2) The time of flight through the mass-spectrometer (refer to section 2.4.1)
- 3) The flight time of the molecules through the ionizer in front of the mass-spectrometer (refer to section 2.4.1)
- 4) There is a time delay between the signal sent to the piezoelectric valve and it actually opening
- 5) Convolution and expansion of the gas pulse
- 6) Because the data is binned (and involves an inherent loss of information, since the data is grouped), the value for the data and subsequent time at which it is represented should be a linear average of the values of the bin and its adjacent values.

2.4.6: Determination of the velocity distribution and temperature of the gas pulses produced from the valve

The background intensity is determined by taking the mean number of counts over a specified range of bins, far from the perceived gas pulse structure (typically between the fiftieth and two hundredth bin). This background intensity is then subtracted from the raw data values.

The time scale of this data is obtained by assuming the first bin is equal to a time of zero (since it corresponds to the start of the triggered driving pulse sent to the valve) and then adding the value of the bin width for each subsequent bin. This produces a plot of counts as a function of time. It can of course be argued that the time of the first bin should have been set at half the bin width of the first bin; however since the data was recorded over a very long period, the error introduced into the results by neglecting this correction is essentially irrelevant.

Linearly averaging both the bin data values and subsequent times at which they occur was not conducted, instead this shift in the data (of the counts and time) is absorbed into what shall be discussed later as the overall correction function.

The actual flight distance that is used to determine the velocity distribution of the gas pulse is taken the distance from the valve to the mass-spectrometer. It will make little difference to the results if the flight distance is calculated from the quitting surface (which varies based on the source conditions), because the distance between the valve and the mass-spectrometer is very large compared to the quitting distance. This approximation simplifies the problem, not only by removing the need to factor in the quitting surface distance but it also removes the need to factor in the time delay required for the gas pulse to reach the quitting surface and the terminal velocity. Determining the velocity distribution of the gas pulse would now appear to be the simple matter of dividing the distance travelled by the arrival time at the mass-spectrometer, however there are other considerations.

The gas pulse measurements described within this section were not conducted using the standard TOF method; this combined with the inherent time delay between the trigger signal sent to the valve and it opening, which is essentially an experimentally unknown parameter, mean that $t=0$ is unknown. So determining the velocity distribution of the gas pulse is not quite as straight-forward as it would first appear.

What is known is that by the time the gas pulse reaches the mass-spectrometer its mean velocity will be equal to the terminal velocity. So despite the fact that the time delay on the valve is an experimental unknown it can be calculated by adding a user defined time delay to the known time delay of the molecules time of flight through the mass-spectrometer, and then calculating the mean velocity from the resulting velocity distribution. The velocity distribution of the gas pulse is calculated by dividing the flight distance (between the valve and the mass-spectrometer) by the adjusted time (adjusted by the aforementioned time delays) corresponding to each bin. The gas pulse is identified by inspection and its average velocity is calculated by the sum of multiplying the velocity by the number of counts for every value and then dividing

2.4.6: Determination of the velocity distribution and temperature of the gas pulses produced from the valve

this value by the sum of the counts (for all the selected values). The user defined time delay is adjusted, by trial and error, until the mean velocity is equal to the terminal velocity.

The actual velocity distribution fitted to all the data, within this thesis, differs slightly from the discussion in section 2.2.1, which uses the normalized Maxwell velocity distribution given by equation (2.4). As discussed in section 2.2.1 the Maxwell velocity distribution is actually derived from the Maxwell – Boltzmann distribution (equation (2.2)). Equation (2.4) can easily be re-written/simplified into the Maxwell – Boltzmann distribution (by comparing equation (2.1) to (2.2) and using equations (2.4) and (2.3)). The normalized Maxwell – Boltzmann distribution using a superimposed stream velocity is then described as:

$$f(v_{norm}) = C_4 e^{\frac{-(v-v_s)^2}{\alpha^2}} \quad (2.26)$$

In equation (2.26) C_4 is a normalization constant and the variable α is equal to v_w (refer to equation (2.3)). Once the temperature has been determined using the Maxwell – Boltzmann distribution the Maxwell velocity distribution can easily be recovered by using equation (2.4), if so desired. Equation (2.26) was used to determine the temperature of the gas pulses instead of equation (2.4) in order to simplify the problem of accounting for both the convolution and expansion of the gas pulse. The resulting experimental velocity distribution is effectively a convolution of the pieces of equipment in the path of the gas pulse and the expansion of the gas pulse due to the thermal distribution.

In order to find the temperature of the gas pulse first it is assumed that the gas pulse has reached a thermal equilibrium by the time it reaches the mass-spectrometer, so that the Maxwell – Boltzmann distribution can be applied; this in itself is a fair assumption since the flight distance involved is very large. Then a plot is made of $\ln(v_{norm})$ as a function of $\ln((v - v_s)^2)$, the

resulting gradient (of the linear graph) will be equal to $-\frac{1}{\alpha^2}$, from which the temperature can

be calculated. Because the exact effect of the convolution, expansion and effect of the flight time of the ions through the ionizer are unknowns, but are likely to be proportional to some function of the velocity of the gas pulse, the resulting velocity distribution was normalized as a function of the velocity. It was found through trial and error that normalizing the velocity distribution as a function of $\frac{1}{v}$ gave the best linear least squares fits of the data (i.e.

2.4.6: Determination of the velocity distribution and temperature of the gas pulses produced from the valve

$v_{norm} = \frac{f(v)}{v}$). The previously discussed effect of linearly averaging the bin data values is

absorbed into this overall correction function $\frac{1}{v}$.

Once the velocity distribution data has been normalized a linear least squares fit is made of a plot of $\ln(v_{norm})$ as a function of $\ln((v - v_s)^2)$. The data range selected (from both the left and right hand sides of the normalized velocity distribution) is adjusted until the error in the linear least squares fit is minimised, which is a trial and error process. The value for $f(v_{norm})$ is recovered from the linear least squares fit (by taking the exponential of $\ln(v_{norm})$ from the linear fit). These values are then normalized with respect to the experimental $f(v_{norm})$ so that the experimental and the fitted velocity distribution may be graphically compared. The fitted velocity distribution is normalized with respect to the experimental values, by multiplying it by a weighted term derived from taking the ratio of the maximum of $f(v_{norm})$ from the linear least squares fit against an averaged value from the experimental $f(v_{norm})$ data. This average experimental $f(v_{norm})$ value is calculated by taking the sum of two points either side of the maximum value of the distribution and the maximum value itself, and then averaging the result. The normalized least squares fit of $f(v_{norm})$ can then be plotted against the experimental $f(v_{norm})$ values to graphically represent the soundness of the fit. The robustness of the least squares linear fits is determined using a variable called the coefficient of determination R^2 [79], this number lies between the values of 0 and 1, the closer the value of R^2 is to 1 the more reliable the least squares linear fit (i.e. the data being linear in nature).

A program was written on LABVIEW (version 3.1) following the above discussion and procedures to determine the temperature of the gas pulses produced from the valve. This program was used to analyse all the data presented within this section.

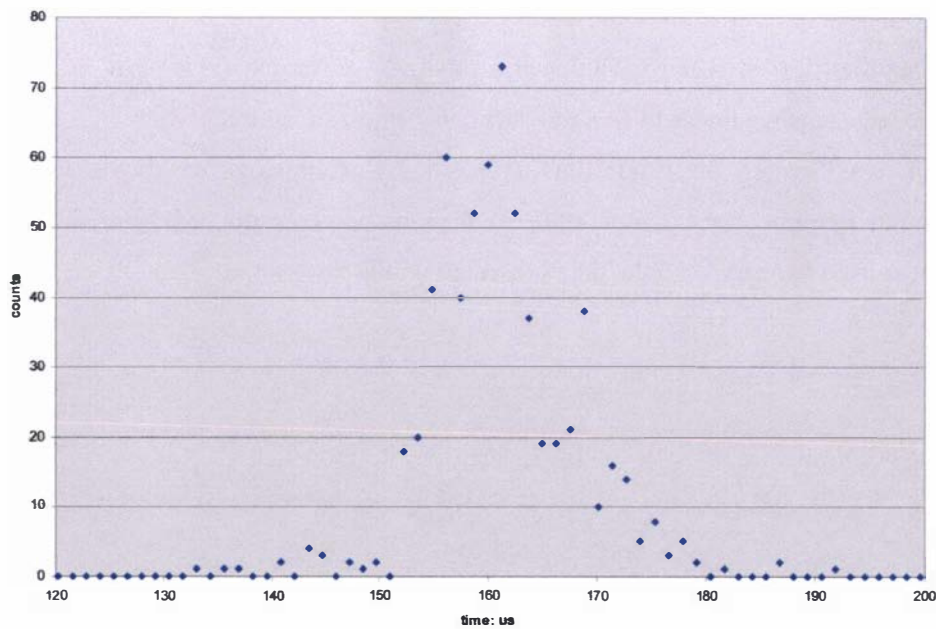
2.4.7: Results of the density profile produced from the valve without the preionizer attachment

These results were generated using a hydrogen backing pressure (on the valve) of 6×10^5 Pa and 100 gas pulses with a bin width setting of $1.28\mu\text{s}$ on the multichannel scaler. The results of hydrogen gas pulses produced from the valve are presented in graphs 2.5 to 2.15 as a function of driving pulses $100\mu\text{s}$ to $300\mu\text{s}$ in length. The time scale presented on the graphs was derived using the method outlined in section 2.4.6, in which the terminal velocity of hydrogen is taken to be 2660m/s (refer to section 2.2.2).

One of the better temperature fits was derived from graph 2.8 and is presented in graph 2.16.a.

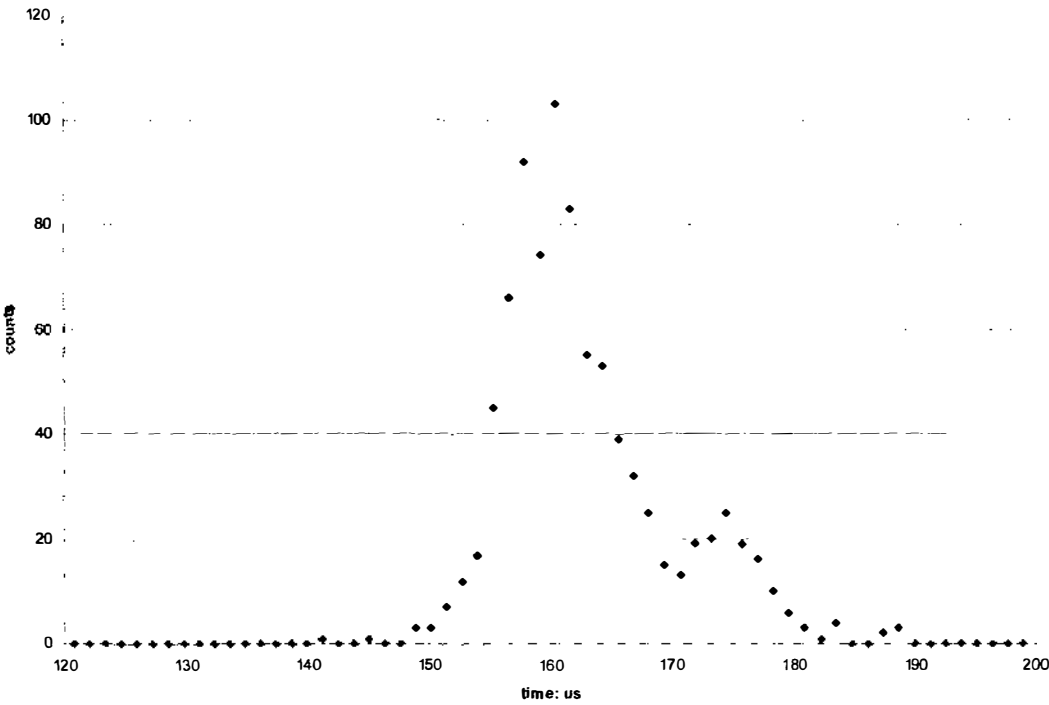
The corresponding least squares fit of $(v - v_w)^2$ as a function of $\ln\left(\frac{\text{counts}}{v}\right)$ used to determine the temperature of the gas pulse (refer to section 2.4.6) of graph 2.16.a is presented in graph 2.16.b, in which the slope, intercept and the coefficient of determination R^2 of the fit have been included.

The results of the calculated temperatures are summarised in table 2.7 where the average R^2 value of these fits was 0.89 which shows a reasonable degree of the robustness for the fits; however since there are a limited number of data points available for the temperature calculation these calculated temperatures are likely to be inaccurate (as well as the estimation of their pulse widths);

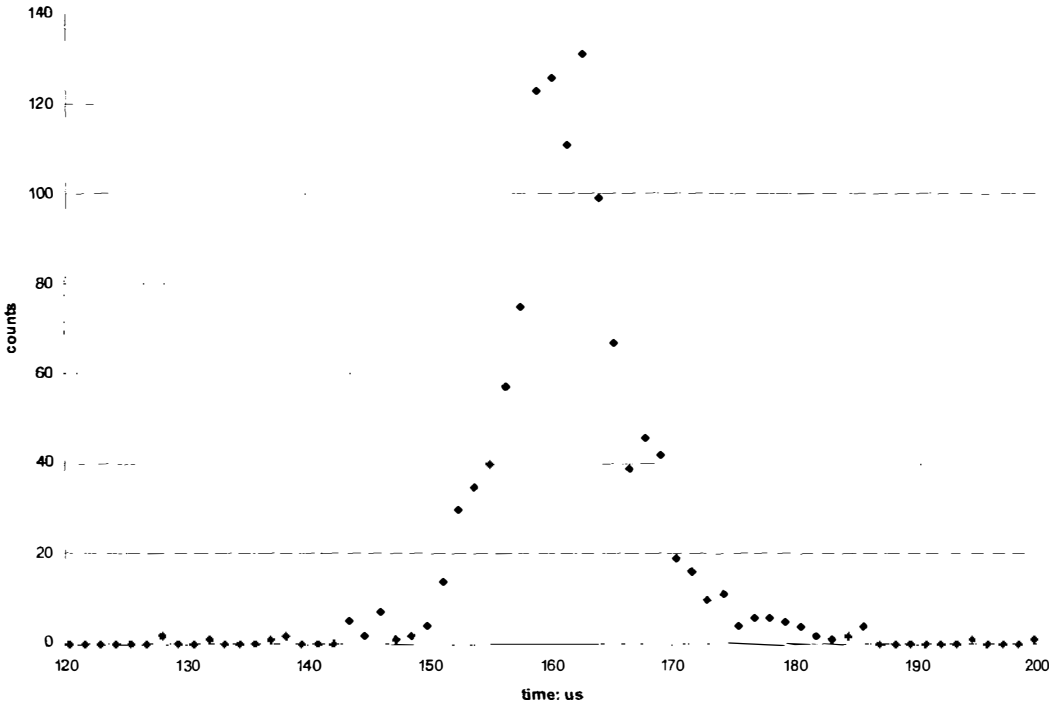


Graph 2.5: Graph of counts as a function of time, for a hydrogen gas pulse with a $10\mu\text{s}$ pulse width produced using $100\mu\text{s}$ driving pulse

2.4.7:Results of the density profile produced from the valve without the preionizer attachment

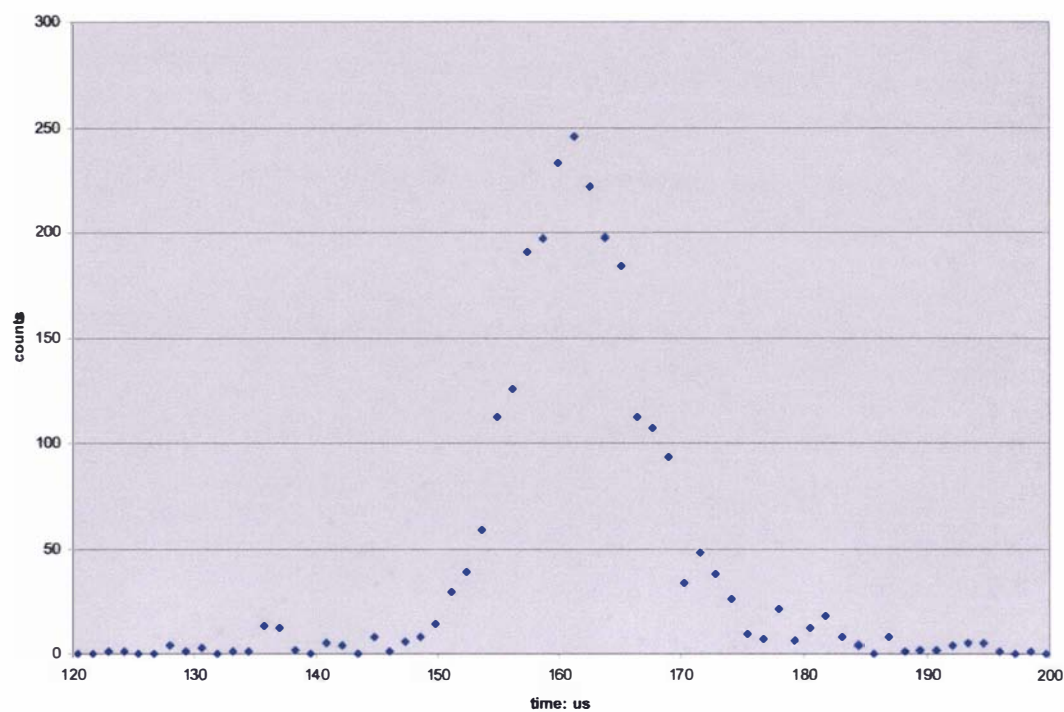


Graph 2.6: Graph of counts as a function of time, for a hydrogen gas pulse with a $10\mu\text{s}$ pulse width produced using $120\mu\text{s}$ driving pulse

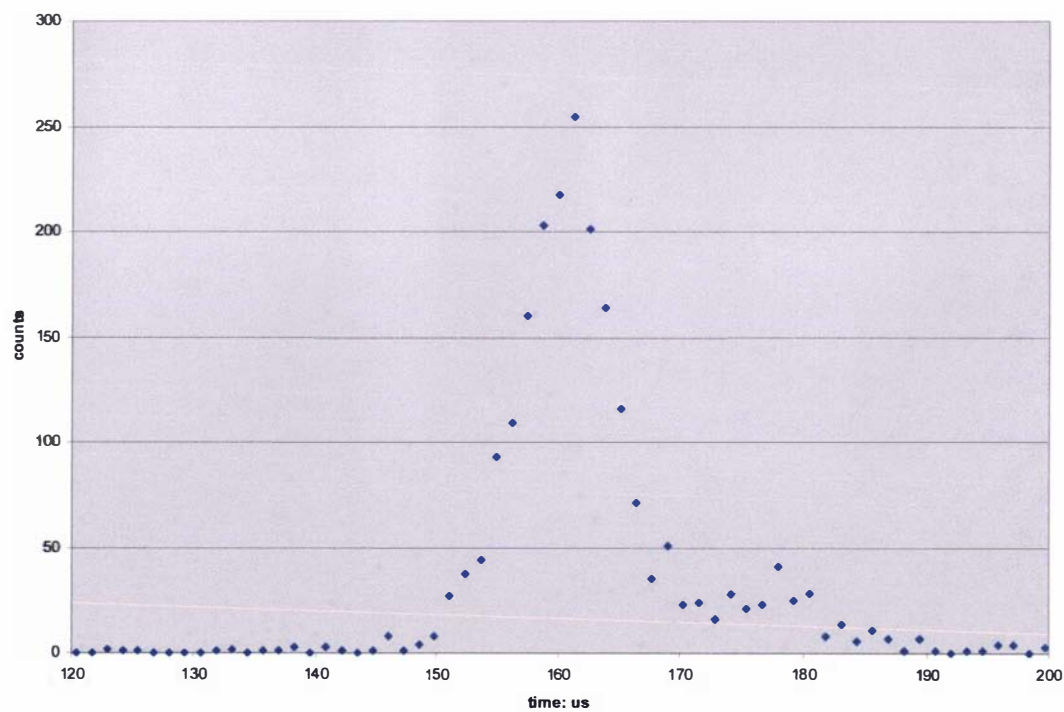


Graph 2.7: Graph of counts as a function of time, for a hydrogen gas pulse with a $10\mu\text{s}$ pulse width produced using $140\mu\text{s}$ driving pulse

2.4.7: Results of the density profile produced from the valve without the preionizer attachment

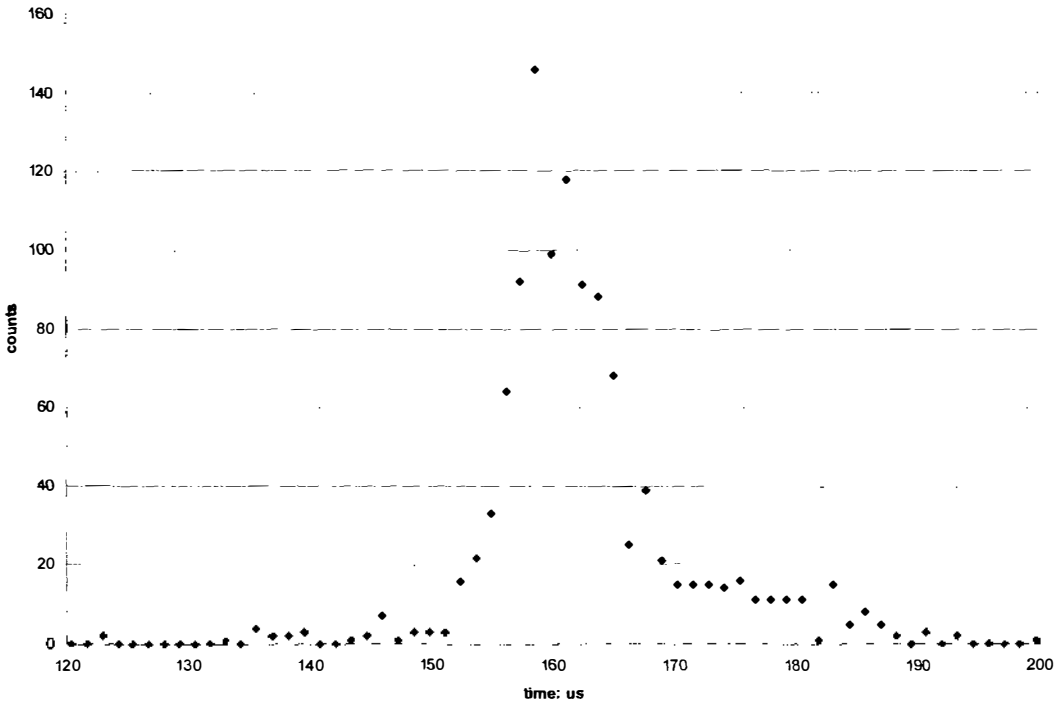


Graph 2.8: Graph of counts as a function of time, for a hydrogen gas pulse with a $10\mu\text{s}$ pulse width produced using $160\mu\text{s}$ driving pulse

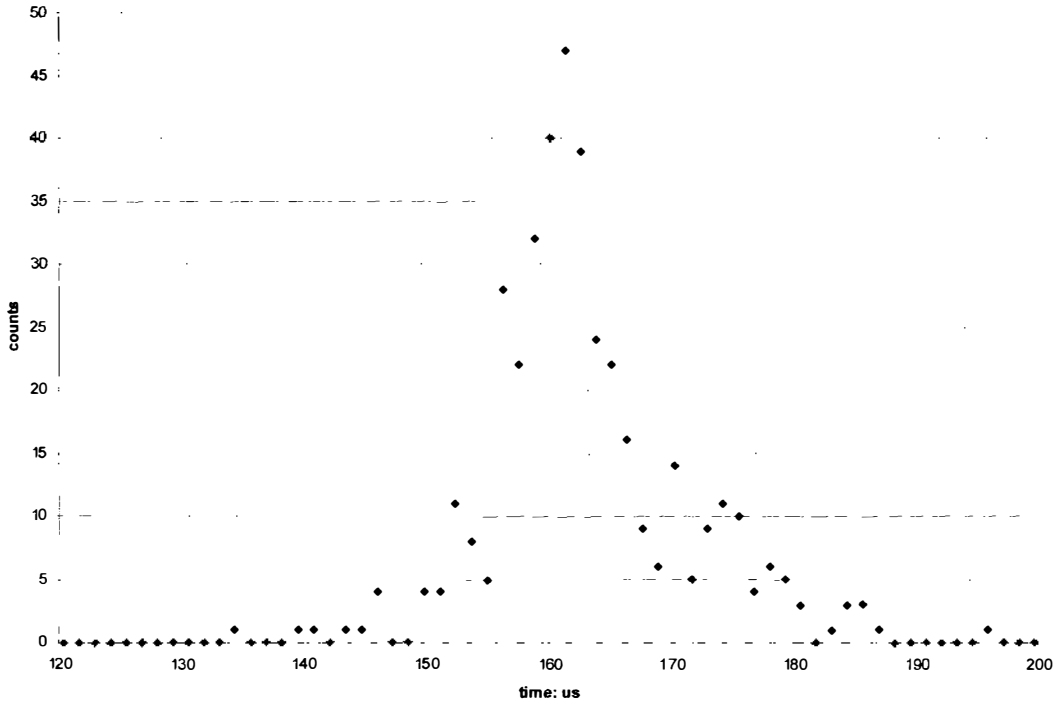


Graph 2.9: Graph of counts as a function of time, for a hydrogen gas pulse with a $10\mu\text{s}$ pulse width produced using $180\mu\text{s}$ driving pulse

2.4.7:Results of the density profile produced from the valve without the preionizer attachment

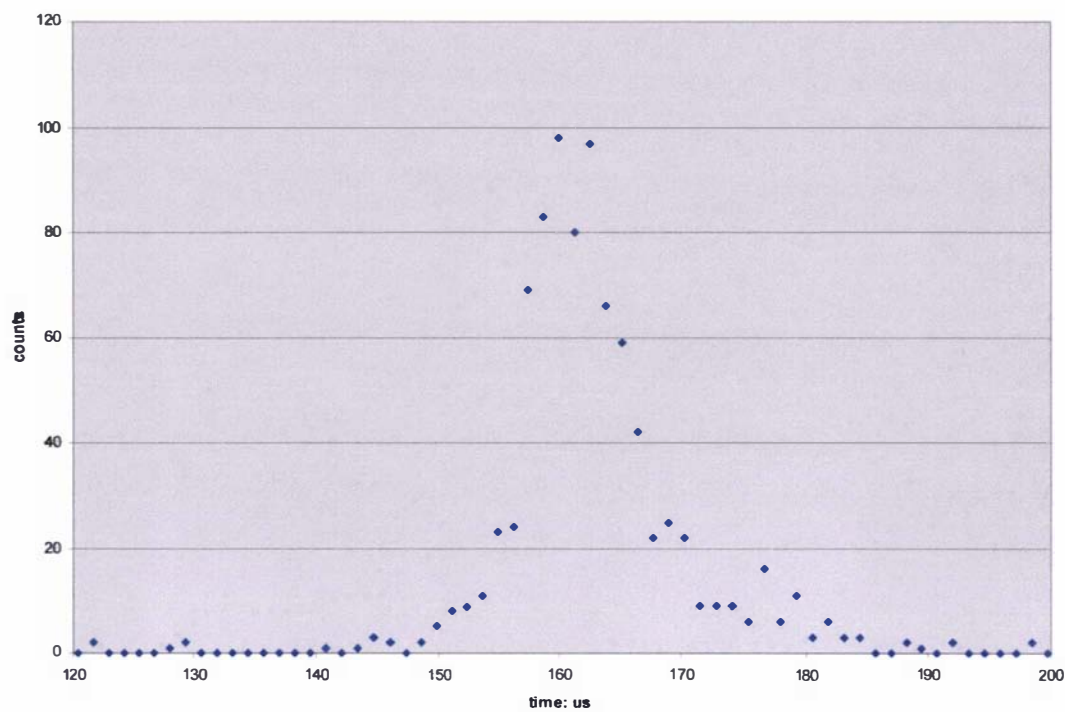


Graph 2.10: Graph of counts as a function of time, for a hydrogen gas pulse with a $10\mu\text{s}$ pulse width produced using $200\mu\text{s}$ driving pulse

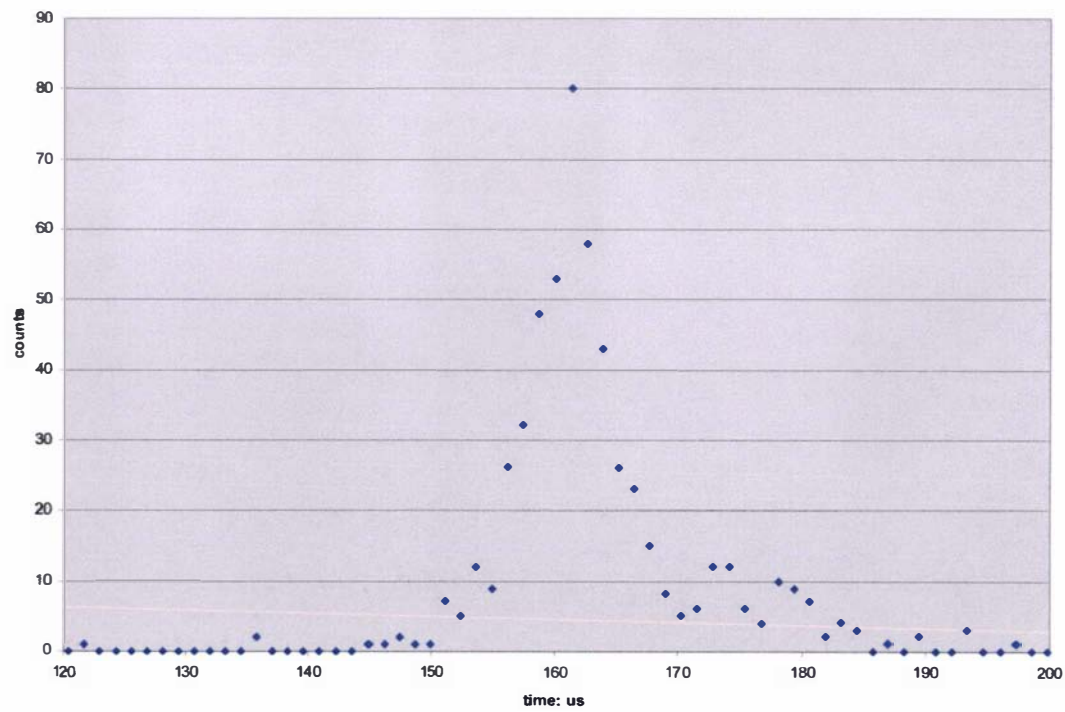


Graph 2.11: Graph of counts as a function of time, for a hydrogen gas pulse with a $10\mu\text{s}$ pulse width produced using $220\mu\text{s}$ driving pulse

2.4.7:Results of the density profile produced from the valve without the preionizer attachment

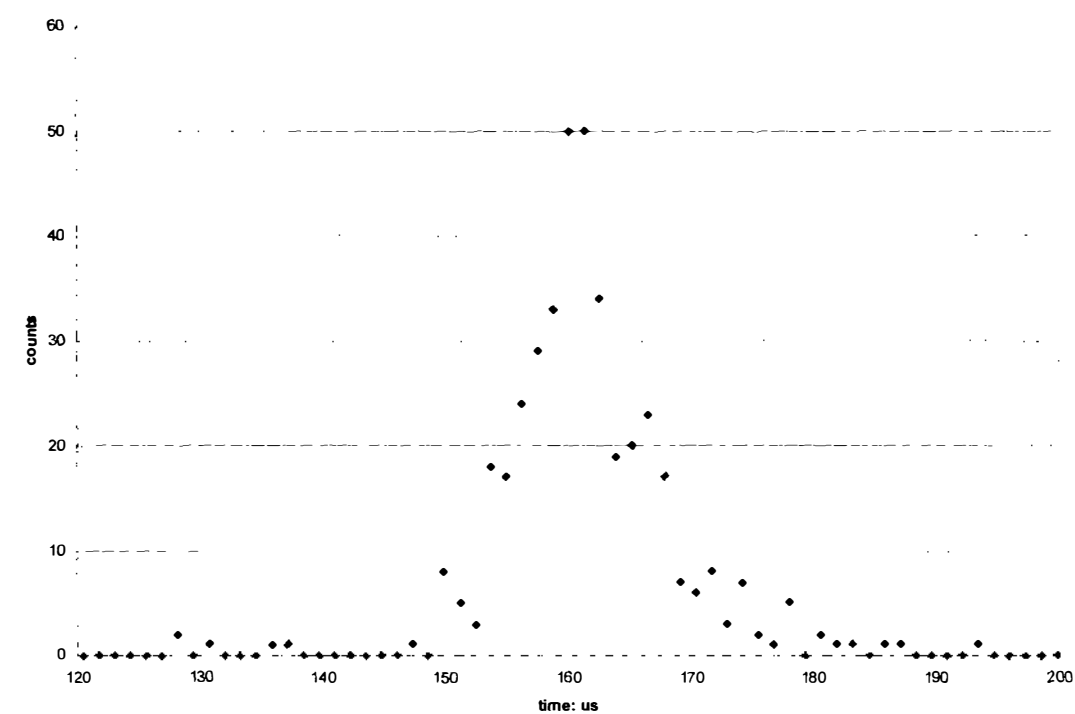


Graph 2.12: Graph of counts as a function of time, for a hydrogen gas pulse with a 10µs pulse width produced using 240µs driving pulse

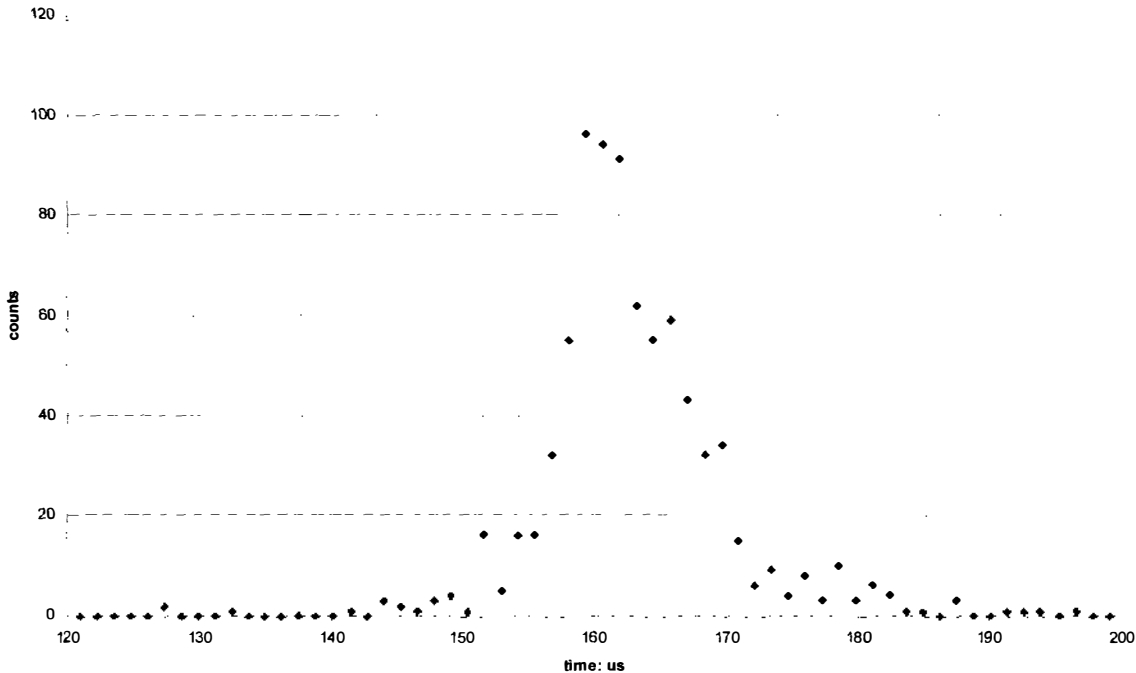


Graph 2.13: Graph of counts as a function of time, for a hydrogen gas pulse with a 10µs pulse width produced using 260µs driving pulse

2.4.7: Results of the density profile produced from the valve without the preionizer attachment

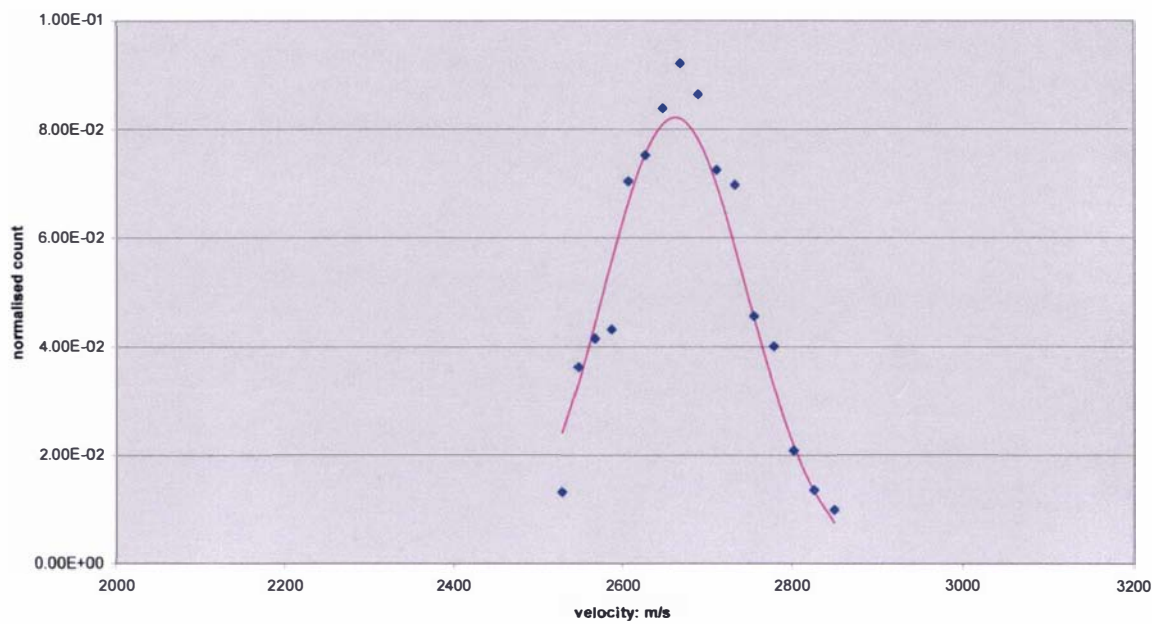


Graph 2.14: Graph of counts as a function of time, for a hydrogen gas pulse with a $10\mu\text{s}$ pulse width produced using $280\mu\text{s}$ driving pulse

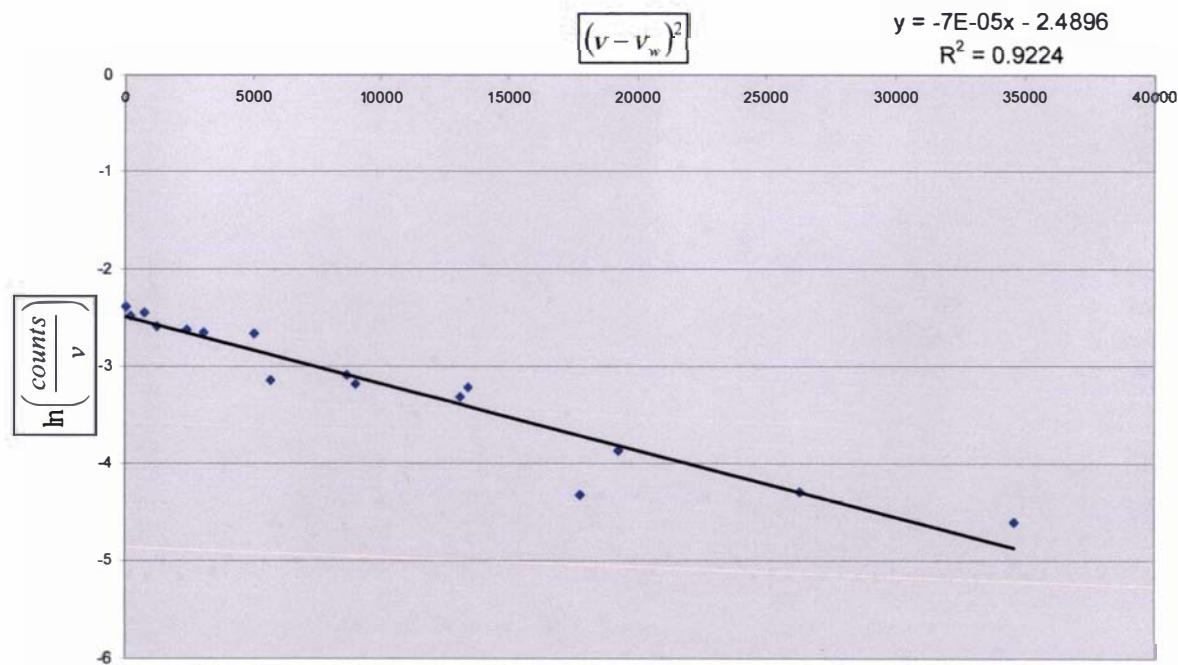


Graph 2.15: Graph of counts as a function of time, for a hydrogen gas pulse with a $10\mu\text{s}$ pulse width produced using $300\mu\text{s}$ driving pulse

2.4.7:Results of the density profile produced from the valve without the preionizer attachment



Graph 2.16.a: Graph of fitted Maxwell velocity distribution and normalised velocity data, for a hydrogen gas pulse with a10µs pulse width produced using 160µs driving pulse



Graph 2.16.b: Graph of the least squares fit of $(v - v_w)^2$ as a function of $\ln\left(\frac{\text{counts}}{v}\right)$ for the data points used in graph 2.16.a. The slope, intercept and R^2 value of the fit are displayed above the graph

pulse length: us	T(K) of fit
100	1.44
120	1.49
140	1.89
160	1.75
180	1.21
200	1.22
220	1.33
240	1.51
260	1.28
280	1.57
300	1.15

Table 2.7: Table of the temperature of gas pulses as a function of driving pulse length obtained by fitting a Maxwell velocity distribution to the data.

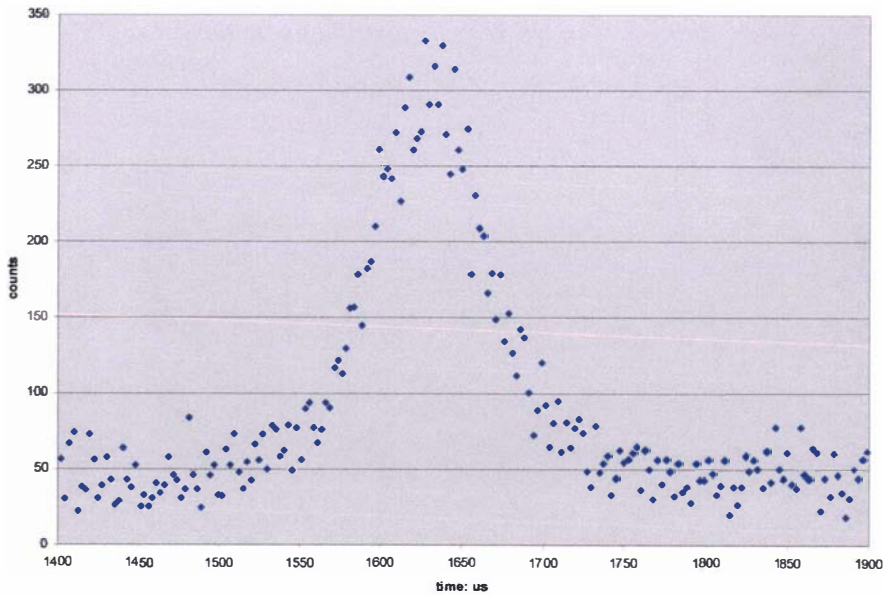
2.4.8:Results of the extended density profile used to determine an accurate temperature for gas pulses produced from the valve without the preionizer attachment

2.4.8: Results of the extended density profile used to determine an accurate temperature for gas pulses produced from the valve without the preionizer attachment

The results of hydrogen gas pulses produced from the valve using a 4.336m long flight tube are presented in graphs 2.17 to 2.19, for driving pulses 100μs, 160μs and 200μs in length. These results were generated using a hydrogen backing pressure on the valve of 6.52×10^5 Pa with a bin width setting of 2.56μs on the multichannel scaler. Graph 2.17 was generated using 200 gas pulses while graphs 2.18 and 2.19 were generated using 1000 gas pulses.

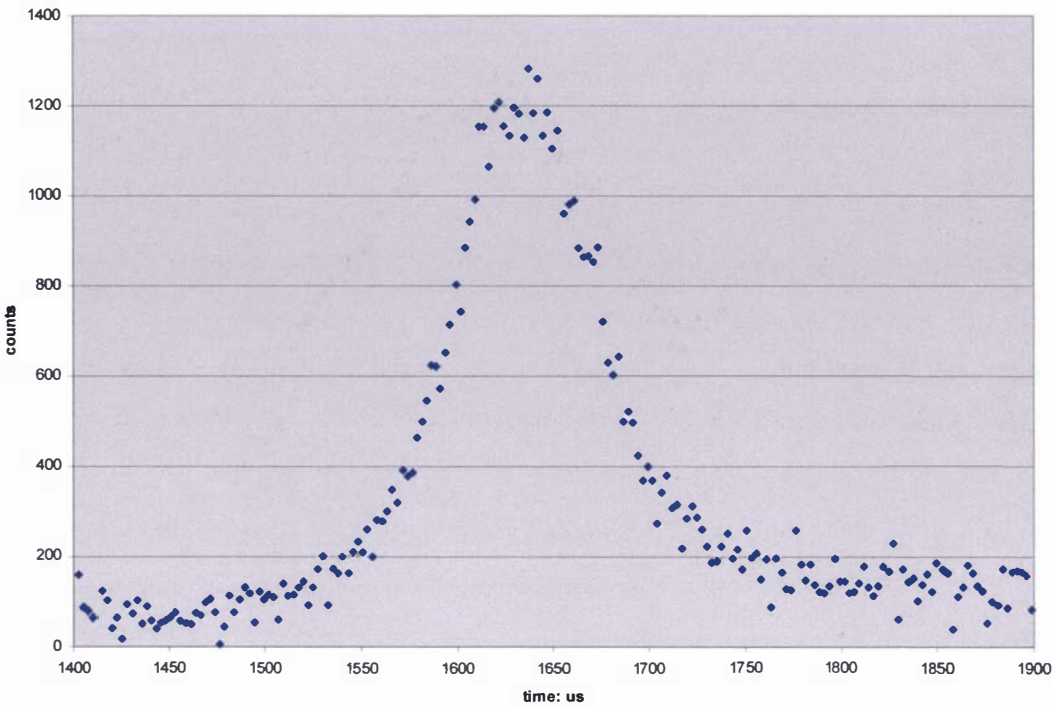
The time scale shown on the respective graphs was derived using the method outlined in section 2.4.6, in which the terminal velocity for hydrogen was taken to be 2660m/s. The calculated temperatures of the gas pulses are presented in table 2.8 with an example of a fitted Maxwell velocity distribution shown in graph 2.20.a. The corresponding least squares fit of $(v - v_w)^2$ as a function of $\ln\left(\frac{\text{counts}}{v}\right)$ used to determine the temperature of the gas pulse (refer to section

2.4.6) of graph 2.20.a is presented in graph 2.20.b, in which the slope, intercept and the coefficient of determination R^2 of the fit have been included. The average R^2 value of the linear least squares fits is 0.92, which shows a reasonably good degree of robustness for the fits. However the temperature results derived from the gas pulse with a driving pulse of 200μs is suspect because of the large amount of background noise present. The speed ratio calculated using equations (2.5), (2.6), (2.9) and the temperature range presented in table 2.8 suggests the terminal speed ratio lies between the values of 23 and 28 for gas pulses produced solely from the valve.

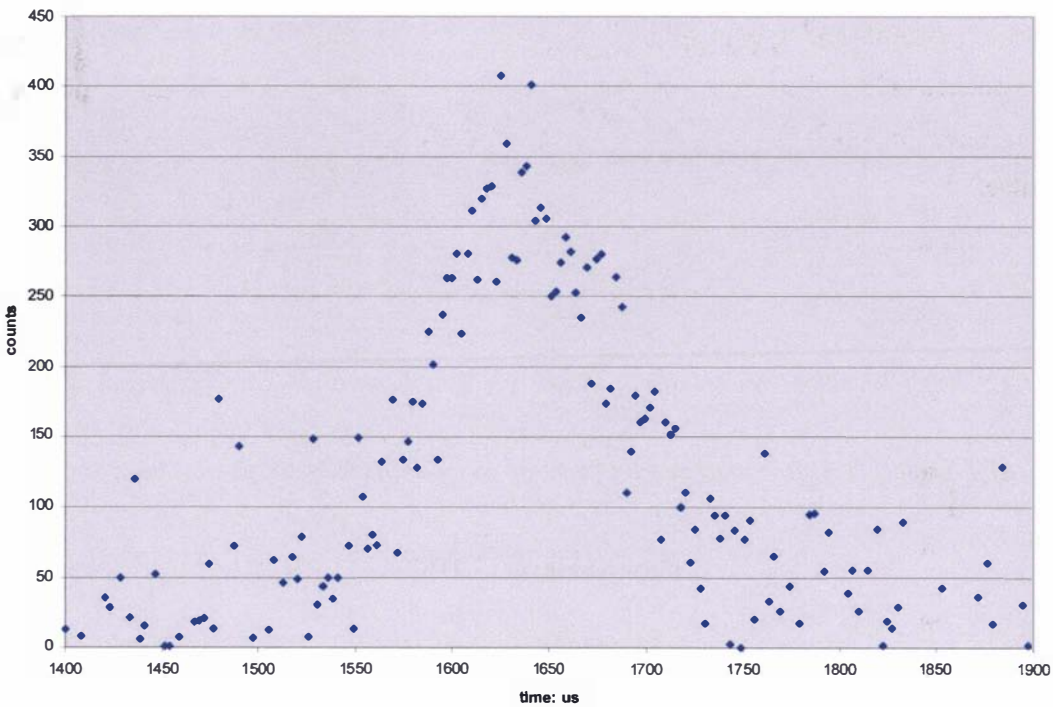


Graph 2.17: Graph of counts as a function of time, for a hydrogen gas pulse with a 82μs pulse width produced using 100μs driving pulse

2.4.8:Results of the extended density profile used to determine an accurate temperature for gas pulses produced from the valve without the preionizer attachment

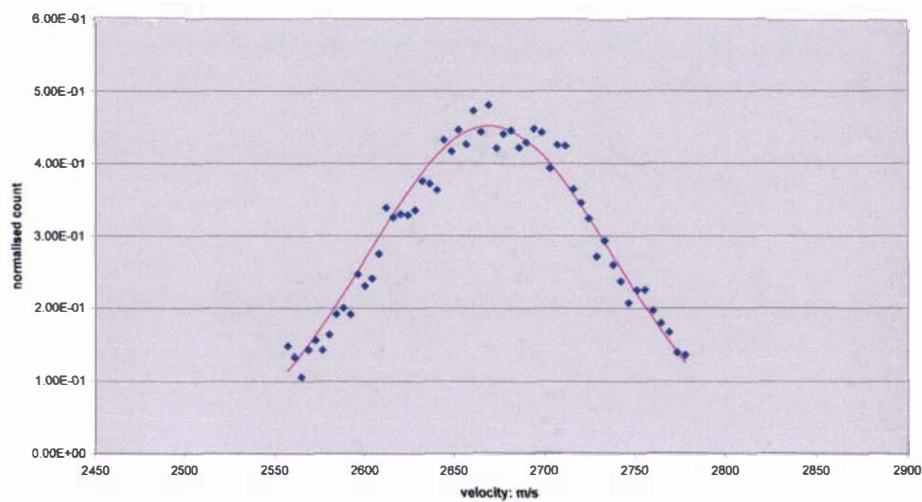


Graph2.18: Graph of counts as a function of time, for a hydrogen gas pulse with a $87\mu\text{s}$ pulse width produced using $160\mu\text{s}$ driving pulse

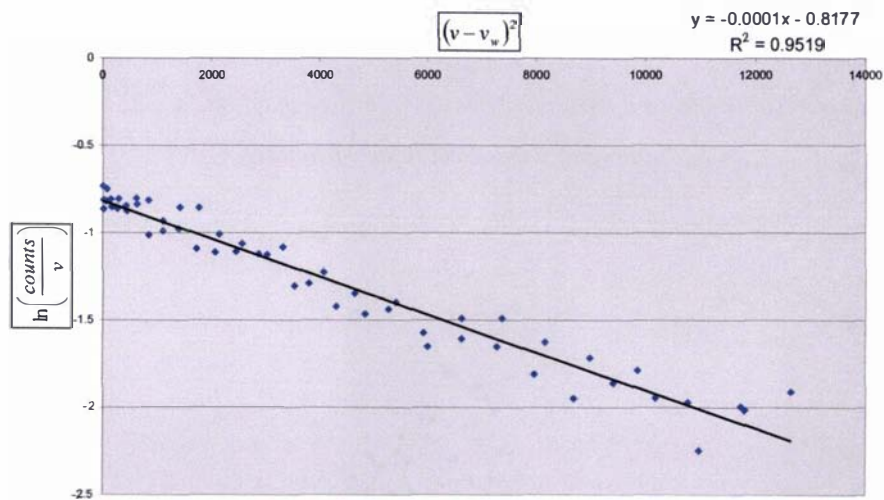


Graph 2.19: Graph of counts as a function of time, for a hydrogen gas pulse with a $92\mu\text{s}$ pulse width produced using $200\mu\text{s}$ driving pulse

2.4.8:Results of the extended density profile used to determine an accurate temperature for gas pulses produced from the valve without the preionizer attachment



Graph 2.20.a: Graph of fitted normalised Maxwell distribution and normalised velocity data for a hydrogen gas pulse with a 87µs pulse width produced from a 160µs driving pulse



Graph 2.20.b: Graph of the least squares fit of $(v - v_w)^2$ as a function of $\ln\left(\frac{\text{counts}}{v}\right)$ for the data points used in graph 2.20.a. The slope, intercept and R^2 value of the fit are displayed above the graph

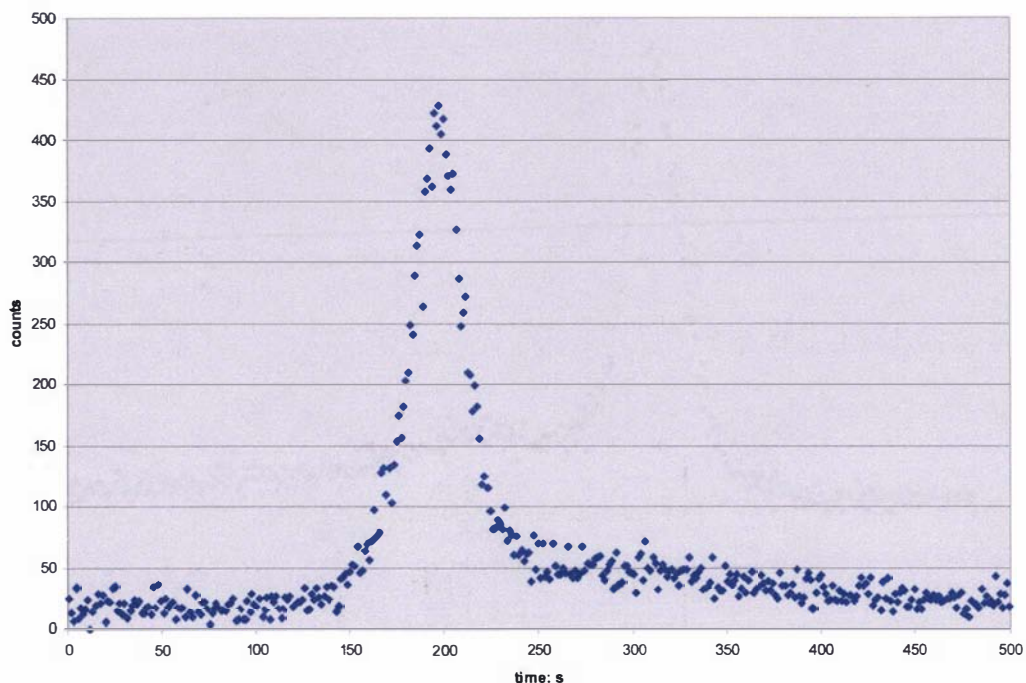
pulse length: us	T(K) of fit
100	0.88
160	1.11
200	1.37

Table 2.8: Table of the temperature of gas pulses as a function of driving pulse length obtained by fitting a Maxwell velocity distribution to the data

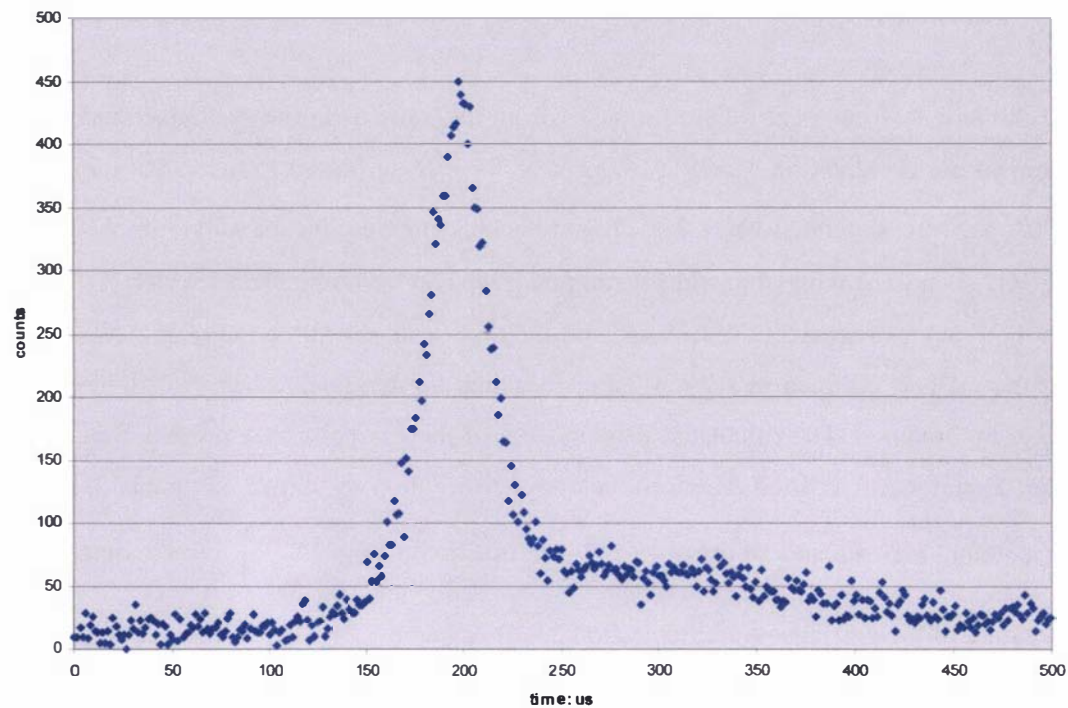
2.4.9: Results of the density profile produced from the valve with the preionizer attachment

The results of hydrogen gas pulses produced from the valve with the preionizer and skimmer attachment are presented in graphs 2.21 to 2.23, for driving pulses 150 μ s to 200 μ s in length. The results were generated using a hydrogen backing pressure on the valve of 5.39×10^5 Pa using 100 gas pulses, with a bin width setting of 1.28 μ s on the multichannel scaler.

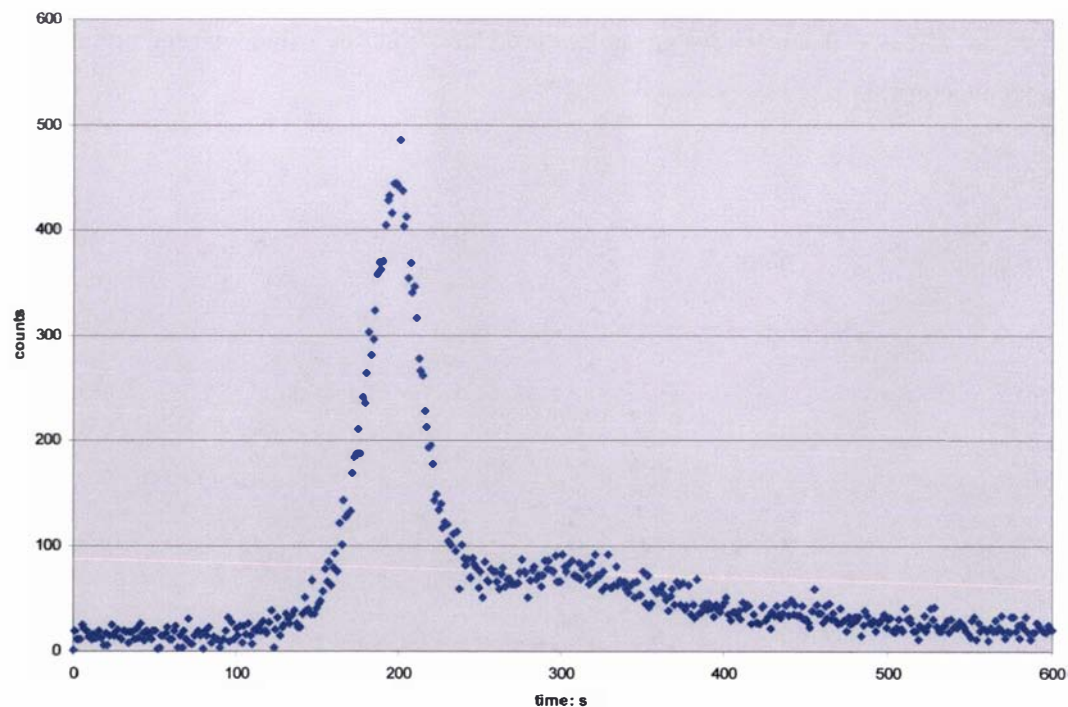
As in the previous sections of 2.4.7 and 2.4.8 the time scale shown on the graphs was obtained using the method outlined in section 2.4.6, in which the terminal velocity for hydrogen was taken to be 2660m/s. The calculated temperatures of the gas pulses are presented in table 2.9 and an example of a fitted Maxwell velocity distribution is shown in graph 2.24.a. The corresponding least squares fit of $(v - v_w)^2$ as a function of $\ln\left(\frac{\text{counts}}{v}\right)$ used to determine the temperature of the gas pulse (refer to section 2.4.6) of graph 2.24.a is presented in graph 2.24.b, in which the slope, intercept and the coefficient of determination R^2 of the linear least squares fit have been included. The average R^2 value for this set of data is 0.94, suggesting a reasonably good robustness for the fits. The speed ratio calculated using equations (2.5), (2.6), (2.9) and the temperature range presented in table 2.9 suggests the terminal speed ratio lies between the values of 8 and 10 for gas pulses produced from the value with the preionizer and skimmer attachment.



Graph 2.21: Graph of counts as a function of time, for a hydrogen gas pulse with a 25 μ s pulse width produced using 150 μ s driving pulse

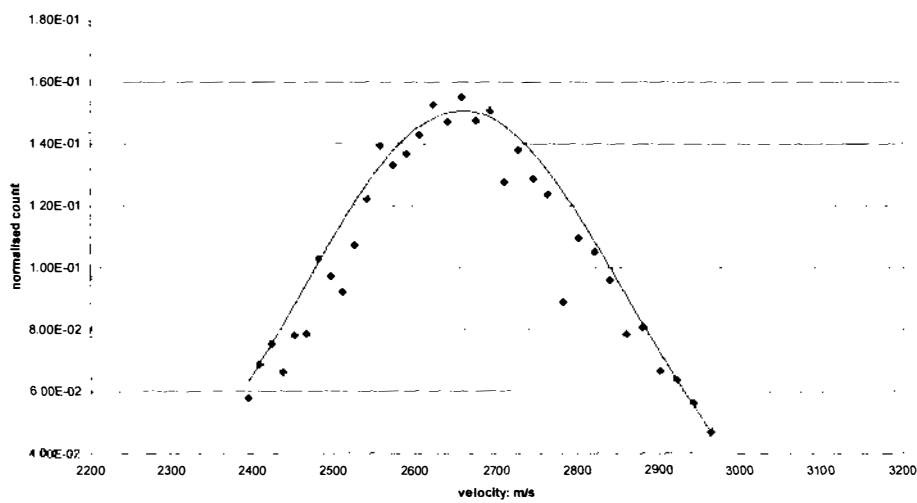


Graph 2.22: Graph of counts as a function of time, for a hydrogen gas pulse with a $29\mu\text{s}$ pulse width produced using $180\mu\text{s}$ driving pulse

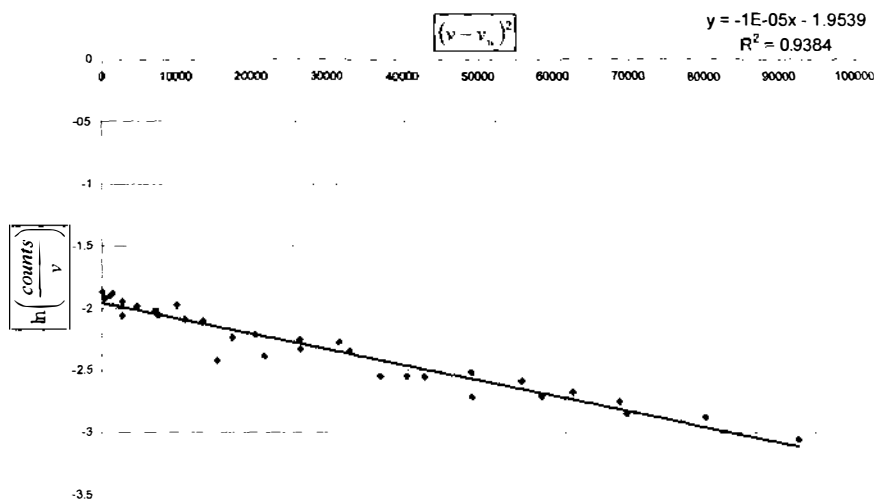


Graph 2.23: Graph of counts as a function of time, for a hydrogen gas pulse with a $34\mu\text{s}$ pulse width produced using $200\mu\text{s}$ driving pulse

2.4.9: Results of the density profile produced from the valve with the preionizer attachment



Graph 2.24: Graph of fitted normalised Maxwell distribution and normalised velocity data, for a hydrogen gas pulse with a 29 μ s pulse width produced from a 180 μ s driving pulse



Graph 2.24.b: Graph of the least squares fit of $(v - v_w)^2$ as a function of $\ln\left(\frac{\text{counts}}{v}\right)$ for the data points used in graph 2.24.a. The slope, intercept and R^2 value of the fit are displayed above the graph

pulse length: μ s	T(K) of fit
150	9.63
180	12.2
200	12.1

Table 2.9: Table of the temperature of gas pulses as a function of driving pulse length obtained by fitting a Maxwell velocity distribution to the data

2.4.10: Discussion on the pulse characteristics of the piezoelectric valve

From the initial results obtained from the currently tensioned valve (without the skimmer and preionizer attachment) it appears that optimum hydrogen gas pulses were obtained for driving pulses within the range of 160 μ s to 200 μ s; since within this range peak splitting is not as pronounced as other values within the investigated range. The peak splitting could be attributed to the bouncing of the O-ring seal (no attempts have been made to investigate this potentially complex phenomena). Another important feature is that the hydrogen gas pulses produced from the valve were very short with an average pulse width of about 10 μ s (over a flight distance of 42.9cm). The extended results produced using a flight tube demonstrated that these gas pulses were very cold with longitudinal temperatures below 2K as seen in table 2.8, with a terminal speed ratio between the values of 23 and 28. No piezoelectric valve in the literature is capable of producing hydrogen gas pulses with all these characteristics.

The skimmer and preionizer attachment was found to have a noticeable effect on the gas pulses produced from the valve. The gas pulses produced in this manner were broader and consequently had higher longitudinal temperatures than those solely produced from the valve (which can be confirmed by comparing tables 2.8 and 2.9). These effects could be contributed to scattered gas from the preionizer attachment, giving broader and hence warmer gas pulses with temperatures in the range of 10K to 12K and a terminal speed ratio between the values of 8 and 10.

The reasonable degree of the robustness of the least squares linear fits (an average value of $R^2 = 0.92$ for the extended results produced using a flight tube and an average value of $R^2 = 0.94$ for the results obtained using the skimmer and preionizer attachment) show that the temperature values obtained by fitting a Maxwell – Boltzmann distribution to the gas pulses are accurate.

Overall, the gas pulses introduced into the plasma accelerator (described in chapter 3) by the valve developed in this thesis are well defined and in the order of a few Kelvin in temperature. This suggests that the prototype valve is superior in its operation compared to the traditionally employed solenoid valves, which tend to quasi-statically fill pulsed plasma accelerators. The gas pulses produced from the piezoelectric valve developed in this thesis could lead to a pulsed plasma accelerator that operates in the plasma block rather than the snow plough mode of operation (as defined in chapter 1).

Gas pulse characteristics of a gas pulse produced from the valve with the skimmer and preionizer attachment at the plasma accelerator

Using the results gained from the experimental investigation of the valve the velocity, density and pressure profiles of gas pulses entering the plasma accelerator can be calculated. These distributions are important for the basic operational calculations of the plasma accelerator used in chapter 3 and initial values used in the numerical model developed in chapter 4.

The actual mass that enters the plasma accelerator is not the total amount that is produced by the valve given in section 2.3, because of the skimmer attachment (described in section 2.4.4) that was placed in front of the valve. Since the gas flow has been assumed to be isotropic, the mass of gas that enters the skimmer can be simply calculated as the total mass multiplied by the volume ratio of gas entering the skimmer. This volume ratio is calculated from the volume of the cone (formed from the expanding gas that enters the skimmer) compared to the volume of a hemisphere formed from the overall expansion of the gas. A volume ratio of 0.00866 is obtained using this assumption and the dimensions given in diagram 2.14 (of section 2.4.4).

The density profile of the gas pulse when it reaches the plasma is required for the calculations conducted in chapter 4. The density profile will have the same form as the velocity profile, which is described by the Maxwell velocity distribution of equation (2.4) (refer to section 2.2). The quitting surface occurs long before the gas pulse reaches the plasma accelerator (as discussed in section 2.2.2) so equation (2.4) can be described in terms of distance from the valve, because the velocity is equal to the distance divided by the time of travel. If it is assumed that the front of the gas pulse is travelling at a velocity of v_{front} , then by time t_o the molecules travelling at this velocity will have reached a distance of z_{front} ; hence equation (2.4) can be written in terms of distance z as equation (2.27).

$$f(z) = C_4 z^2 e^{-\frac{(z-z_s)^2}{t_o^2 \alpha^2}} \quad (2.27)$$

In this equation C_4 is a new normalisation constant and z_s is the distance the mean velocity (the terminal velocity) has travelled in time t_o . Using a cylindrical coordinate system and assuming the density profile is isotropic in both the r and θ coordinates, the density profile as a function of the z coordinate can be expressed as:

$$\rho(z) = C_\rho z^2 e^{-D_\rho (z-z_s)^2} \quad (2.28)$$

In equation (2.28) C_ρ and D_ρ are constants, the value of D_ρ is defined by equation (2.29).

$$D_\rho = \frac{1}{t_o^2 \alpha^2} \quad (2.29)$$

Since the integration of the density over volume will give the value for the total mass of the gas pulse m_T , the value for C_ρ can be calculated using equation (2.30), in which R is the distance between the electrodes of the accelerator.

$$m_T = \pi R^2 \int \rho \partial z \quad (2.30)$$

Substituting equation (2.28) into equation (2.30) and integrating between the back $z = z_{back}$ and the front $z = z_{front}$ of the gas pulse (at time t_o) defines the constant C_ρ as:

$$C_\rho = \frac{m_T}{\pi R^2 \int_{z_{back}}^{z_{front}} z^2 e^{-D_\rho z^2} \partial z} \quad (2.31)$$

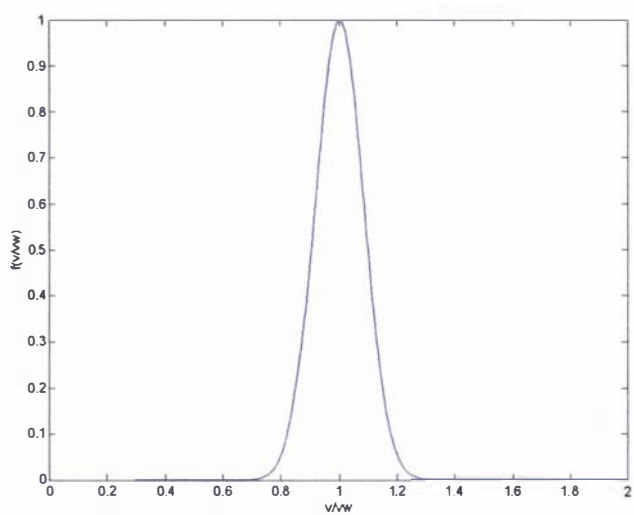
The values of z_{back} and z_{front} are determined using equation (2.4) and a user defined minimum velocity/density ratio (based on a percentage of the mean value). (These values must be user defined because equation (2.4) is an infinite function.). The above process of defining the start and end of the gas pulse is statistically known as thresholding. It can be argued that there are statistical drawbacks in doing this here and instead the density should be integrated between $z = 0$ and $z = \infty$; the overall error introduced by thresholding will not be very significant provided the minimum velocity/density ratio is small; this can be simply justified by considering the form of the Maxwell velocity distribution (refer to section 2.2.1 and graph 2.1). Also the use of thresholding allows the exact position/time that the gas pulse enters the plasma accelerator to be determined and makes defining the gas pulse more manageable.

The integral contained within equation (2.31) can be integrated analytically in terms of the error function; instead the solution of this integral was solved using the numerical Trapezoid rule [78] for all the results presented hereafter. The error introduced into the final answer (for the constant C_ρ) by choosing this method is expected to be insignificant. Once the density profile has been calculated the pressure P profile is calculated as equation (2.32).

$$P(z)=\rho(z)\frac{RT}{M}$$

(2.32)

The plasma accelerator discussed in chapter 3 was investigated using only hydrogen gas pulses generated by a 180μs driving pulse. Using the results obtained in section 2.4.9 and assuming the terminal velocity of hydrogen is 2660m/s (refer to section 2.2.2) the velocity distribution can be calculated using equation (2.1), the result is displayed in graph 2.25. The distance between the plasma accelerator and the valve (ignoring the quitting surface for reasons given in section 2.4.6) is 36.5cm (refer to section 3.3 of chapter 3). Basing an upper and lower limit on the velocity distribution at one hundredth of the maximum count value (in order to define the dimensions of the gas pulse) gives an upper velocity of 3344m/s and a lower velocity of 1988m/s, which means that the gas pulse is 14.8cm in length by the time its leading edge reaches the plasma accelerator. At the FWHH the velocity is between 2397m/s and 2937m/s (the lower and upper velocity values at the FWHH), which means the FWHH length of the gas pulse at the accelerator (where the majority of the mass resides) is 5.89cm. The aforementioned details are summarized in table 2.10.

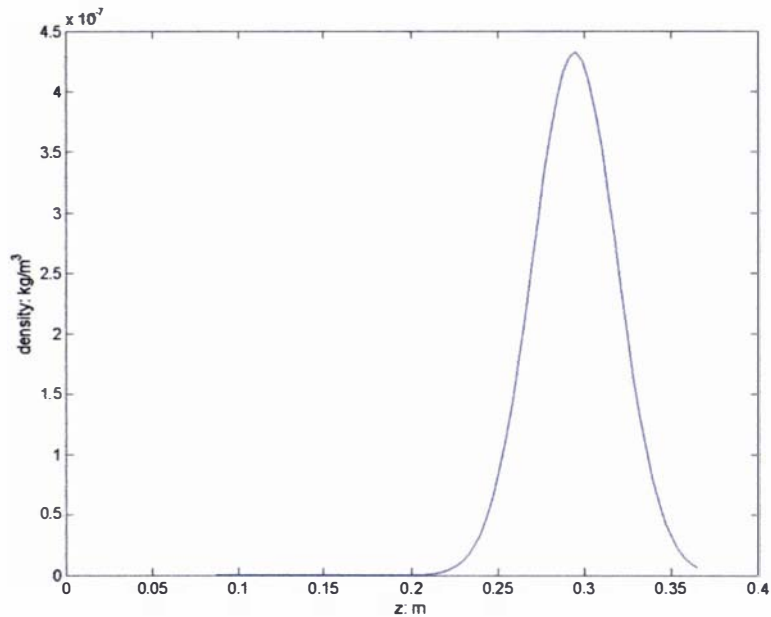


Graph 2.25: Graph of normalized Maxwell velocity distribution for a 12.2K hydrogen gas pulse produced using a 180μs driving pulse with a mean velocity of 2660m/s

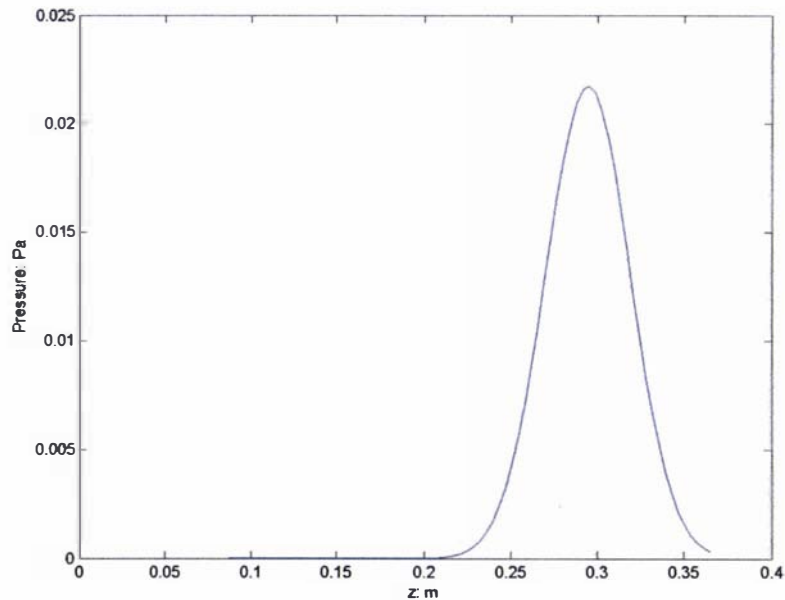
Mean velocity: m/s	2660
Longitudinal temperature: K	12.2
Total length of gas pulse at the plasma accelerator: cm	14.8
FWHH length of the gas pulse at the plasma accelerator: cm	5.89

Table 2.10: Summary of gas pulse properties produced from the piezoelectric valve with the preionizer attachment

The density and pressure profiles of the gas pulses when the leading edge reaches the plasma accelerator can be calculated using equations (2.28) and (2.32). The variables within these equations are calculated based upon the information given in table 2.10, the velocity distribution in graph 2.25, an assumed total gas mass of 21.7×10^{-6} g (refer to table 2.4) and the calculated skimming factor of 0.00866. The density profile is displayed in graph 2.26 and the pressure profile is given by graph 2.27.



Graph 2.26: Calculated density profile as a function of the z coordinate for a hydrogen gas pulse when its leading edge reaches the plasma accelerator, produced using a $180\mu\text{s}$ driving pulse



Graph 2.27: Calculated pressure profile as a function of the z coordinate for a hydrogen gas pulse when its leading edge reaches the plasma accelerator, produced using a $180\mu\text{s}$ driving pulse.

Chapter 3

A linearly injected coaxial plasma accelerator – the Lica

3.1: Overview – A new type of plasma accelerator the Lica

The plasma accelerator required for the MTF scheme discussed in section 1.1 of chapter 1 must be capable of accelerating a 0.2mg hydrogen gas pulse to a velocity in excess of 200km/s, with reproducible results and be able to operate at a firing rate of 10Hz.

The most efficient type of plasma accelerator is that of the coaxial plasma accelerator, as discussed in section 1.2 of chapter 1. No previously designed pulsed coaxial plasma accelerator found in the literature is capable of the performance required for the proposed MTF scheme. All the previously employed pulsed coaxial plasma accelerators have used solenoid valves (refer to section 2.1 of chapter 2) to produce gas pulses [36], and so all of these accelerators have operated in the snowplough mode of operation (described in section 1.2 of chapter 1). Furthermore the valves in these accelerators were angled towards the back of the accelerator; operating the valves in such a manner will not produce a homogenous isotropic gas pulse within the plasma accelerator. This effect (and turbulence effects on the gas pulses produced) has largely been ignored in plasma accelerator design, as has a homogenous preionization of the neutral gas within the plasma accelerators. Typically, a trigatron or a spark gap is used to preionize/breakdown the neutral gas pulses; however the subsequent plasma generated by these means is far from homogenous. It can be hypothesised that a plasma accelerator that operates in the plasma block mode of operation with homogenous isotropic plasma would produce superior results to those gained from the currently designed plasma accelerators.

The pulsed coaxial plasma accelerator developed in this research project is of a unique design that linearly injects a gas pulse with some seed ionization into the plasma accelerator; hence its name Lica, which stands for a linearly injected coaxial accelerator. It has three main features that set it apart from previously designed coaxial plasma accelerators: 1) it uses a piezoelectric valve (developed in chapter 2) to deliver a short well defined gas pulse into the plasma accelerator, giving the possibility of the plasma block mode of operation, 2) the gas is directly injected into the plasma accelerator and 3) it uses a novel preionization method to preionize the neutral gas pulse. The second feature gives the possibility that the plasma pulse produced within the plasma accelerator will be homogenous in nature.

The plasma accelerator is of coaxial design (as shown in diagram 3.1), consisting of the basic components of an anode and a cathode. In this particular type of plasma accelerator the cathode is the grounded electrode and the anode is the positive electrode. The plasma accelerator has

modular components that allow for different material and configurations to be implemented. The present design is unique in the fact that the positive electrode is supported in the centre of the plasma accelerator by four struts, which also serve the purpose of supplying voltage and current to the positive electrode. This design allows gas to be directly injected into the plasma accelerator.

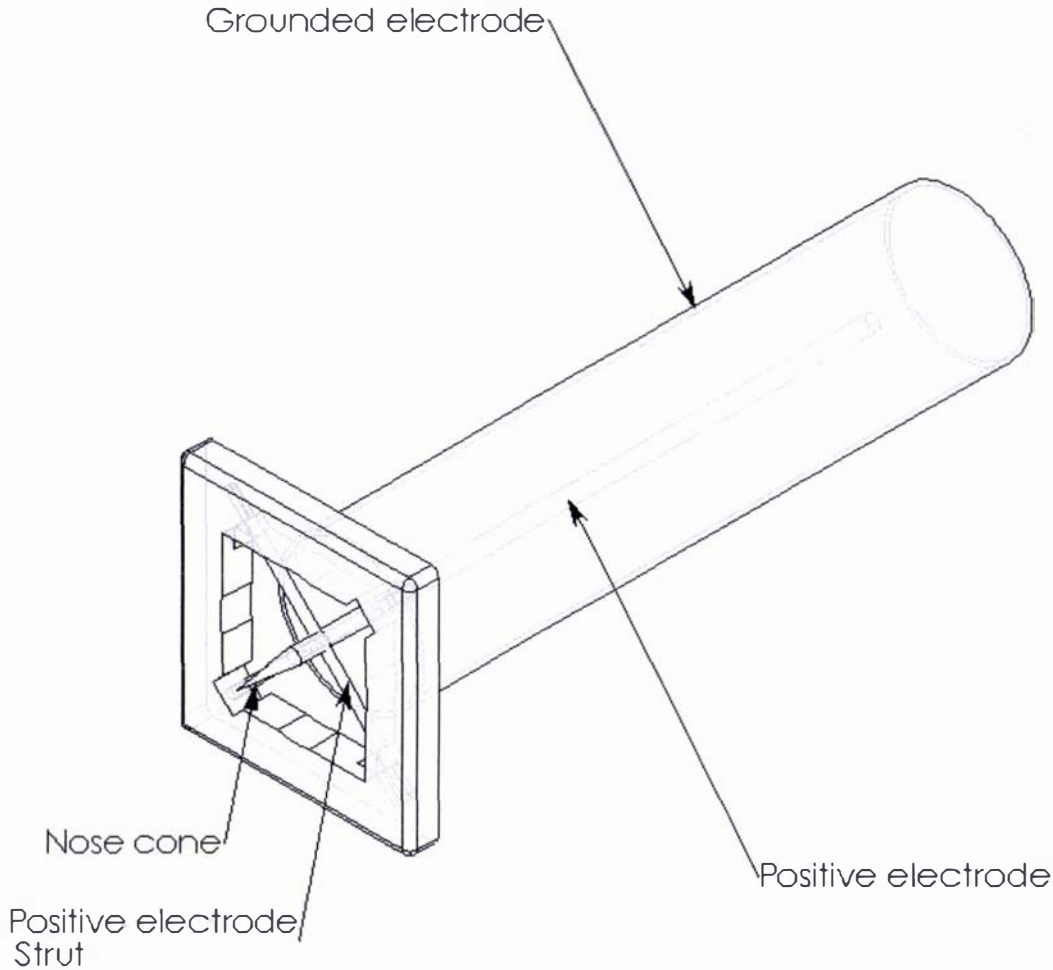


Diagram 3.1: Transparent isometric view of the Plasma accelerator

For the purposes of initial experimentation three different positive electrodes were manufactured at 20cm, 10cm and 5cm in length, all 3cm in diameter and made out of 316 stainless steel. A single anode made out of a seamless 6061T6 Aluminium tube (from NALCO) was manufactured, which was 30cm in length with an outer diameter of 10cm and 3mm in thickness. The struts supporting the positive electrode were made out of 316 stainless steel rods 6mm in thickness and were insulated with an inner sleeve of fibreglass and an outer Teflon casing. A nose cone made out of Teflon was fitted at the back of the positive electrode to minimize shockwave effects encountered when the gas pulse comes into contact with the positive electrode. The positive electrode was machined so that a sharp edge would be present at

3.1: Overview – A new type of plasma accelerator the Lica

its backmost point, as shown diagrammatically in diagram 3.2. This was done to promote a strong electric field gradient (due to a singularity point, refer to section 4.3.6 of chapter 4) in this region, which would encourage the breakdown of preionized gas.

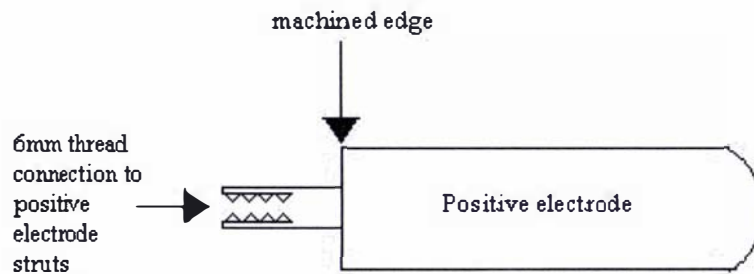


Diagram 3.2: Schematic representation of the positive electrode

The preionization stage, in the plasma accelerator developed in this thesis, is formed from a voltage grid supplied with a positive voltage pulse from a voltage generator. The voltage grid is placed between the grounded piezoelectric valve housing and the plasma accelerator; this is represented diagrammatically in diagram 3.3 and isometrically in diagram 3.4. This preionizer unit works in a similar fashion to a cathode ray tube (CRT) [82], in that an electric field formed between the grounded piezoelectric valve housing and the voltage grid is used to accelerate electrons towards the deflecting electric field inside the plasma accelerator, this is represented diagrammatically in diagram 3.3.

The preionizer unit resides in the extension to the source chamber, refer to diagrams 2.14 and 2.15 in section 2.4.4. This unit comprises of a voltage grid which is directly attached to the skimmer, so that the two are held at the same potential, ceramic spacers separate the skimmer from the walls of the grounded vacuum chamber (the extension to the source chamber).

The operation of this preionizer unit relies upon the breakdown of the residual scattered gas left behind the main gas pulse produced from the piezoelectric valve. Upon a user specified time delay, after the neutral gas pulse has been produced from the valve, a square wave preionizing voltage pulse is sent to the voltage grid. The residual scattered gas then breaks down generating electrons, which are then accelerated towards the plasma accelerator. A short steel tube (with an inner diameter equal to the orifice of the skimmer) attached to the rear of the skimmer and held at the same potential allows the preionizing electrons to be directed towards the plasma accelerator, without being retarded by the electric field generated between the rear of the preionizing unit/skimmer and the grounded walls of the vacuum chamber, refer to diagram 3.3.

The timing of the preionized voltage pulse (sent to the voltage grid) used to preionize the neutral hydrogen gas pulse within the plasma accelerator was experimentally determined

through trial and error; this aspect is discussed in section 3.3. Currently the efficiency of the preionizer device is unknown and remains an aspect of future experimentation. There are two basic possibilities for the preionization of the neutral gas pulse at the plasma accelerator, either the gas pulse can be preionized before it reaches the plasma accelerator or the gas pulse can be preionized some where within the plasma accelerator. Depending upon the timing of the preionization pulse, with respect to the position of the gas pulse, the effect of preionizing different sections of the neutral gas pulse could be investigated; for instance the neutral gas pulse could be preionized just as it enters or leaves the accelerator. The timing of the preionizing pulse used in the experimentation of the Lica is discussed in section 3.3.

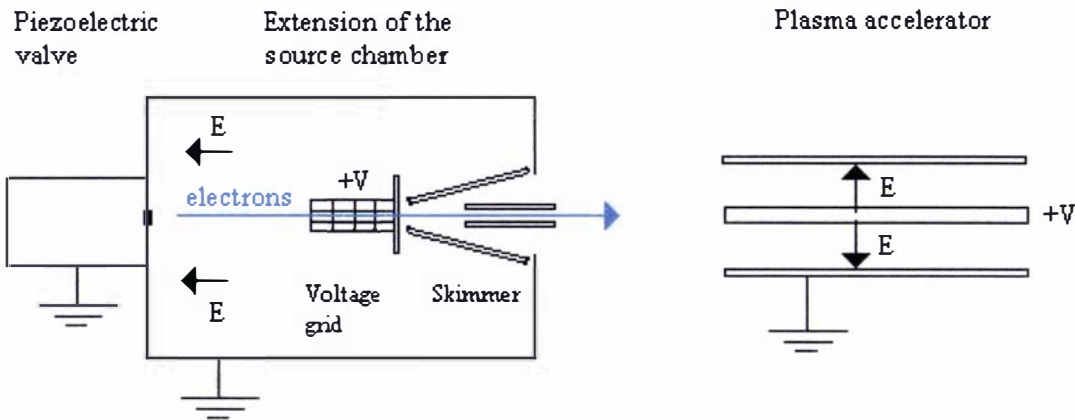


Diagram 3.3: Diagrammatic representation of the preionization process

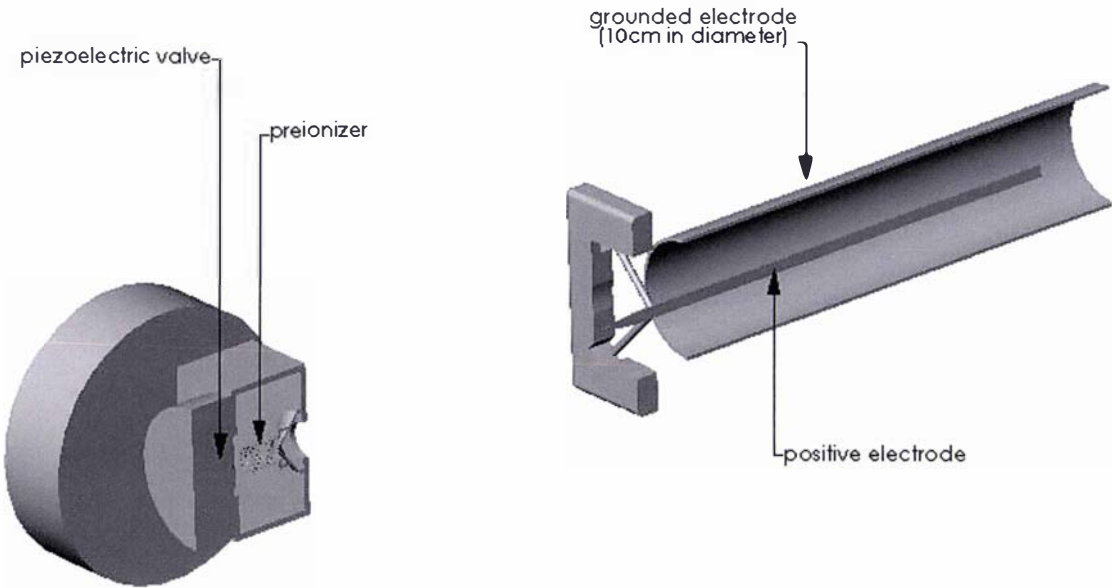


Diagram 3.4: Isometric cross section of the valve, preionizer and the coaxial plasma accelerator

3.1: Overview – A new type of plasma accelerator the Lica

The operation of this plasma accelerator is a five step process: 1) the capacitor is charged, 2) then a gas pulse is produced from the piezoelectric valve, 3) the gas pulse is then preionized (essentially it is a gas with some seed ionization not a plasma), 4) the preionized gas then breaks down in the presence of the high electric field within the plasma accelerator, 5) this causes the capacitor to discharge and the resulting plasma is then accelerated down the plasma gun through the action of the resulting Lorentz force (refer to section 1.2 for a discussion on this acceleration process and to section 1.3 for the various factors effecting the operation of the plasma accelerators).

The Lica was constructed around the experimental apparatus used to investigate the gas pulse characteristics of the piezoelectric valve covered in section 2.4 in its entirety. The Lica consists of a series of differentially pumped chambers: a source chamber, a main chamber, a flight tube and an ultra high vacuum chamber. The entire Lica setup is shown in an isometric cross-sectional view in diagram 3.5. The essential components of the Lica are:

- 1) A high voltage circuit, formed from a high energy capacitor and an energy dump connected to an oscilloscope
- 2) A piezoelectric valve and the pulsed circuit used to operate it
- 3) A preionization unit and a pulsed voltage driver
- 4) A plasma accelerator
- 5) A flight tube
- 6) An ion detector (a CDEM) and a multichannel scaler

These pieces of equipment and the associated devices used to operate them are discussed in section 3.3.1. Both the piezoelectric valve and the preionization unit are centred within the main chamber (facing towards the plasma accelerator) in an extension of the source chamber.

The CDEM and the oscilloscope were the main diagnostic devices used to gather results from the plasma accelerator. The CDEM is used to determine the velocity profile of the plasma pulses produced from the plasma accelerator, by dividing the flight distance between the plasma accelerator and the CDEM by the time that the plasma counts were recorded. The oscilloscope was used to obtain the voltage trace (refer to section 3.3.2) from the capacitor circuit (refer to diagram 3.10 in section 3.3.1).

Photomultipliers were tried as an additional means of measuring the velocity of the resulting plasma. In diagram 3.5 it can be seen that there are two T-pieces separated by a distance of 1 m on the flight tube, it was here that two photomultipliers were attached. The final velocity of the plasma exiting the plasma gun could be determined by the time delay between the signals

generated from these devices as the plasma passes each photomultiplier. Unfortunately the first photomultiplier was placed too close to the plasma accelerator, this resulted in the saturation of the first photomultiplier (refer to chapter 5 for a fuller discussion). So this means of determining the resulting velocity of the plasma could not be used in practice. An interferometer was also tried as a means of measuring the velocity of the plasma. However the vibration of the flight tube from the mechanical pumps (refer to section 3.3.1) was too great for this technique to be used, as all that was observed was the background vibration (refer to chapter 5 for more details). Spectral analysis to provide temperature and ion distributions within the plasma gun was not possible due to the time constraints placed upon this thesis.

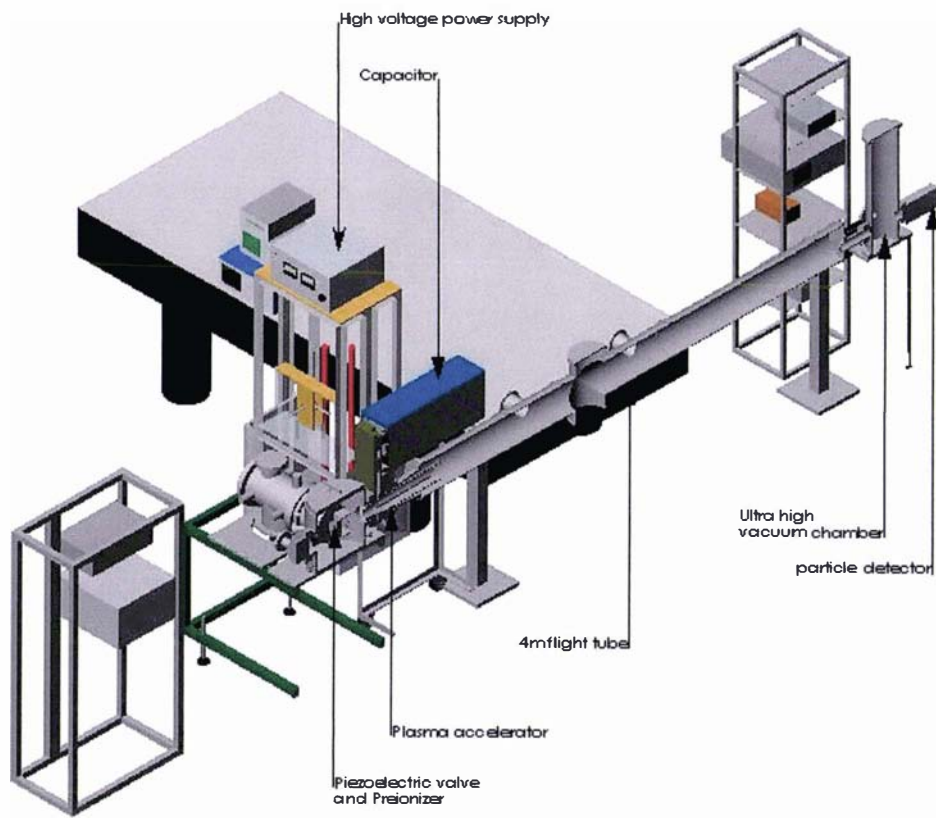


Diagram 3.5: Isometric cross sectional view of the Lica with the main components identified

3.2: Background on the generation of plasmas and their electrical properties

3.2.1: The electrical breakdown of gases

At room temperature and atmospheric pressure gases, in the absence of electric fields, are very good insulators. But in the presence of a high electric field charged particles may gain sufficient energy between collisions to cause neutral molecules or atoms to become ionized upon impact. Electrons in the presence of an electric field lose little energy in an elastic collision with a molecule; instead their kinetic energy is transferred as potential energy that may result in the ionization of the impacted molecule. Because of this electron impact is the primary ionization mechanism in the electrical breakdown of gases, especially in the presence of high electric fields. The probability of ionization by electron impact is dependent upon the energy that the electrons gain in the direction of the applied electric field. The average energy gained ΔW over a distance λ_e is given as [83]:

$$\Delta W = eE\lambda_e \quad (3.1)$$

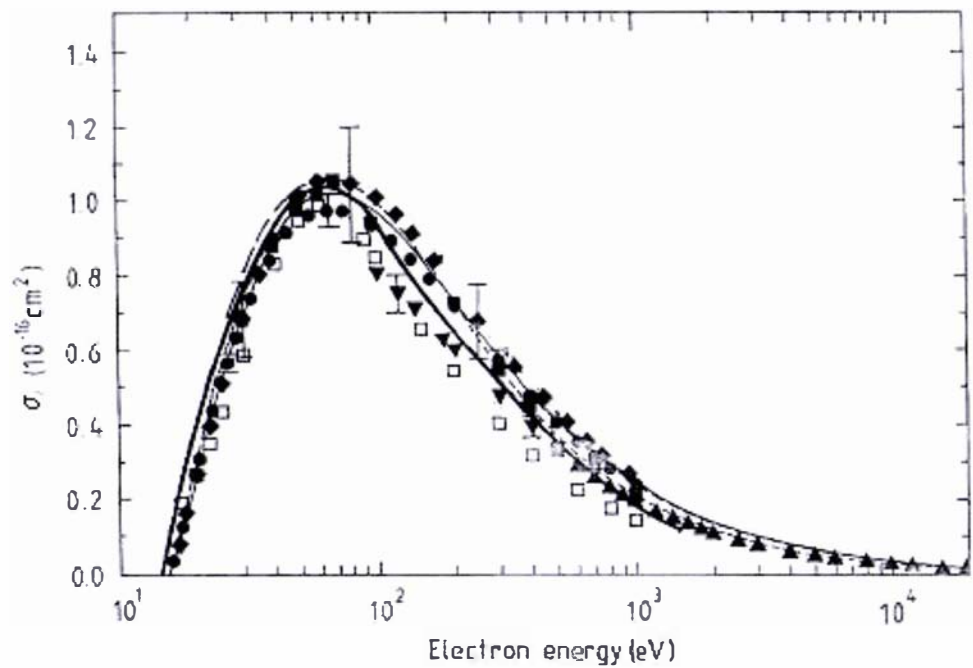
where λ_e is the mean free path of the electron in the direction of the electric field, E is the electric field strength and e is the elementary charge. The value for the mean free path of electrons in a particular gas (assuming all the electrons and molecules are in thermal equilibrium) can be calculated by knowing the mean free path for a molecule of gas λ_g . The relationship between these two quantities is $\lambda_e = 4\sqrt{2}\lambda_g$ [83]. The value for λ_g is directly proportional to the temperature and pressure; hence given the experimentally determined value λ_{g0} at a pressure of P_0 and temperature of T_0 the value for λ_g at a pressure P and temperature

$$T \text{ is given as: } \lambda_g = \lambda_{g0} \frac{P_0}{P} \frac{T}{T_0} \text{ [83].}$$

In order for a molecule to be ionized upon impact the average energy gained must be greater than or equal to the ionization energy of the molecule eV_i , where V_i is the ionization voltage required for breakdown. It should be noted that electrons having energy below the ionization energy of the molecule may still lead to ionization, since if a molecule has impacts with several electrons it may gain enough energy to become ionized. Also, not all electrons that have energy above the ionization energy level will lead to the ionization of a molecule upon impact; this is because the electrical breakdown of a gas is a probability phenomenon and is generally expressed in terms of the ionization cross section σ_i which is a product of the probability of

3.2.1: The electrical breakdown of gases

ionization upon impact P_i and the molecular/atomic cross sectional area [83]. A plot of the ionization cross section as a function of electron energy is shown in graph 3.1 for various gases.



Graph 3.1: Graph of the experimentally measured ionization cross section of hydrogen as a function of electron energy determined by various groups, adapted from [84].

Electrical breakdown in gases can be defined by two distinct classifications: those of a self sustained discharge and that of a breakdown discharge. In a self sustained discharge the current flowing through the ionized gas is solely dependent upon the initial ionization source, while a breakdown discharge is independent of the ionization source. The self sustained discharge can be further subdivided into two main mechanisms: primary ionization (primary ionization is used to describe any mechanism that leads to the (initial) generation of electrons within the gas or gas with some seed ionization) and secondary ionization (secondary ionization is any process/mechanism that generates further electrons from primary ionization). Within the classification of secondary ionization mechanisms there is a special category that is referred to as cathode related effects and relates to any secondary ionization mechanism in which the cathode plays an important role in the mechanism.

Townsend's first ionization coefficient σ_{Town} is used to describe a primary self sustained discharge within a gas in which there is already some seed ionization (i.e. there is already the presence of some ions and more importantly electrons). Townsend's first ionization coefficient is based upon the assumption that the anode and cathode are separated by a distance d with a constant applied electric field and that the seed electrons are accelerated towards the anode. As the seed electrons move towards the anode they will collide with neutral molecules, it is

assumed (in this model) that every electron has enough energy to cause ionization upon impact. After each collision more electrons will be generated and accelerated towards the anode in an ever increasing avalanche effect, which is approximated by an exponential function. Townsend's first ionization coefficient is simply interpreted as the coefficient in the exponential function, which gives the current (or number density of electrons) as a function of distance:

$$i_a = i_0 e^{\sigma_{Town} d} \quad (3.2)$$

In equation (3.2) i_a is the resultant current generated at the anode and i_0 is the initial current generated at the cathode. The formula for Townsend's first ionization coefficient (refer to [83] for the derivation) is given as:

$$\frac{\sigma_{Town}}{P} = A_{Town} e^{-\left(\frac{B_{Town} P}{E}\right)} \quad (3.3)$$

In equation (3.3) A_{Town} and B_{Town} are constants, which are defined as:

$$A_{Town} = \frac{\sigma_i}{kT} \quad (3.4)$$

$$B_{Town} = \frac{\sigma_i V_i}{kT} \quad (3.5)$$

The theoretical value of the Townsend coefficient is not entirely accurate because (in this model) it was assumed that every electron, whose energy exceeds the ionization energy for a molecule, will automatically lead to ionization. However it has been found experimentally that the probability for electrons with energy just above the ionization threshold is small and rises slowly to a maximum value of about 0.5 at 4 to 6 times the ionization energy [83]. Instead experimentally determined values for A_{Town} and B_{Town} are used; however due to the dependence of Townsend's first ionization coefficient upon pressure, electric field and other phenomena the experimentally determined values for these coefficients are only valid within the experimental pressure and electric field range over which they were determined [59], [38]. Townsend's mechanism is not the only mechanism that can lead to a self sustained discharge, there are also secondary ionization mechanisms (stemming from Townsend's mechanism) such as: photoionization, metastable interactions and thermal ionization [83] that can also contribute or be the main driving force of the overall self sustained discharge.

The cathode provides an important role in the discharge process by supplying electrons for the initiation, sustaining and completion of the discharge process. Cathode effects are a special form of secondary ionization and they include the following processes: photoelectronic emission, electron emission by positive ion and excited ion impact, thermionic emission, field emission and Townsend's secondary ionisation mechanism [83]. Townsend's secondary ionisation coefficient γ_{Town} is concerned with the electrons released from the cathode as a result of positive ion bombardment (in which it is assumed that there is secondary electron emission from the cathode as a result of positive ion bombardment). Townsend's second coefficient is derived using the same method that was used to obtain Townsend's first ionization coefficient [83]. The equation giving the anode current as a function of Townsend's second ionization coefficient is:

$$i_a = i_0 \frac{e^{\sigma_{Town}d}}{1 - \gamma_{Town}(e^{\sigma_{Town}d} - 1)} \quad (3.6)$$

The coefficient itself is interpreted as an electron multiplication factor, as can be seen in equation (3.6). Equation (3.6) is the simplest form of Townsend's second ionization coefficient; other secondary effects (due to further effects of this process) can also be incorporated into this equation, such as secondary photon impact at the cathode and electrons produced as a result of electron collisions with positive ions travelling a distance d along the electric field [59].

The transition from a self sustained discharge described using the mechanisms mentioned above to breakdown or what is commonly called the "sparking condition" can be broadly separated into three categories: the Townsend mechanism, the streamer or "Kanal" mechanism, and breakdown in non-uniform fields [83].

Townsend's breakdown mechanism uses equation (3.6) to describe the phenomenon in which the number of secondary electrons produced at the cathode by $e^{\sigma_{Town}d}$ positive ions (and or photons) exceeds (by unity) the number of secondary electrons emitted from the cathode as a result of ions produced from the initial seed electrons (i.e. from Townsend's self sustained discharge mechanism). At this point the anode current predicted in equation (3.6) becomes indeterminate. This will occur if the denominator in equation (3.6) is equal to zero; hence the denominator can be rearranged to give the Townsend's breakdown in terms of the first and second Townsend's ionization coefficients as equation (3.7).

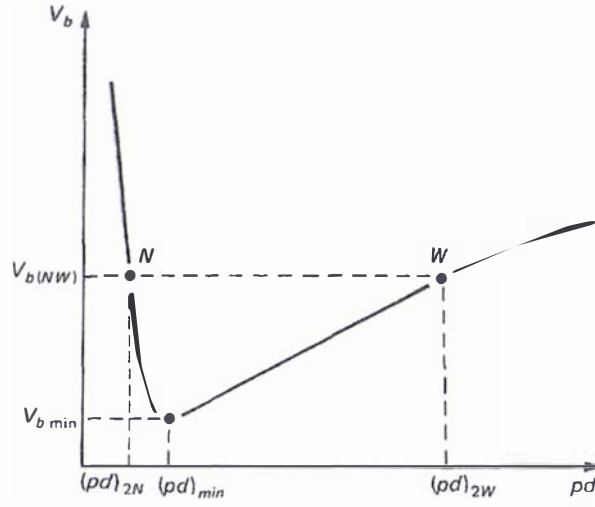
$$\sigma_{Town} d = \ln \left(\frac{1}{\gamma_{Town}} + 1 \right) = K \quad (3.7)$$

In equation (3.7) K can be taken to be between the values of 8 to 10 [83]; equation (3.7) can also be extended to include further effects [59]. Equation (3.7) is of little practical use, because it is not expressed in terms of the field strength and the pressure of the gas between the electrodes. Paschen's law is a practical version of the breakdown phenomena in terms of Townsend's mechanism; it is derived by combining equations (3.7) and equation (3.3) to give the breakdown voltage V_b (in which $V_b = Ed$) as:

$$V_b = \frac{C_2 Pd}{\ln \left(\frac{C_1 Pd}{K} \right)} \quad (3.8)$$

In equation (3.8) C_1 and C_2 are either the experimentally or calculated constants for A_{Town} and B_{Town} . Equation (3.8) is used to generate a Paschen curve, depicted in graph 3.2. The curve passes through a minimum point, known as the sparking voltage. It may be said that there exists two points as a product of pressure and distance which have the same breakdown voltage. This can simply be interpreted as the same breakdown occurring at either a low pressure at a short electrode distance $(pd)_{2N}$ or a high pressure at a long electrode distance $(pd)_{2W}$. Equation (3.8) is a very simple form of Paschen's curve and can be extended to include other effects such as the work function of the cathode material [83].

The exact breakdown mechanism or mechanisms that are present in the operation of the coaxial plasma accelerator, developed during this research, is currently unknown. Without the use of high speed photography to document the breakdown of the gas within the accelerator [83] or the use of spectrographic techniques [85], [86], [87] the breakdown mechanism remains speculative. But, in general, it can be said that the avalanche mechanism will be one of the mechanisms responsible in the breakdown. (Unfortunately no graph was found in the literature relating to breakdown mechanisms of hydrogen gas under the low pressure and temperature conditions produced from the piezoelectric valve, presented in section 2.4.10.)



Graph 3.2: Paschen's curve for hydrogen gas [83]

In non-uniform fields such as those produced by a point plane gap, sphere plane gap or a coaxial cylinder the ionization coefficient will vary across the gap. The electron multiplication under these conditions is then governed by the integral of the ionization coefficient across the gap; hence at low pressures [83] the Townsend sparking condition defined by equation (3.7) is modified to:

$$\int_0^d \sigma_{Town} \partial x = \ln \left(\frac{1}{\gamma_{Town} + 1} \right) = K \quad (3.9)$$

The integration in equation (3.9) should be taken over the highest electric field gradient [83]. The above equation is also valid for higher pressures, provided the field is only slightly non-uniform [83]. In strongly divergent fields large $\frac{E}{P}$ values will exist in which $\frac{\sigma_{Town}}{P} > 0$ (refer to equation (3.3)); however if the field drops below a critical value E_c the integral of $\int \sigma_{Town} \partial x$ will approximately be equal to zero. This condition may occur when the field strength at the cathode is small, in which case the Townsend breakdown mechanism loses its validity when it is solely reliant upon γ_{Town} ; however breakdown may still be possible if photoionization is taken into account [83].

The condition for breakdown in a non-uniform field is typically considered to occur from the initiation of a streamer. The streamer or “Kanal” sparking mechanism assumes that a large space charge region is formed at the front of the electron avalanche, because the electrons have a higher mobility than the positive ions. The overall electric field is modified because of this charge separation. Not only is a high electric field formed in the space charge region but the field is also enhanced in both the region in front of the avalanche (towards the anode) and the region behind the avalanche (towards the cathode). These field distributions become noticeable with a charge carrier number n greater than 1×10^6 , but if the charge carrier number reaches 1×10^8 the space charge field may lead to the initiation of a streamer. A streamer is essentially an ionization channel, a region containing a significant amount of ionized gas.

The name streamer was coined from observations made in breakdown experiments conducted in cloud chambers, in which streams of ionized material were noted. There are two distinct streamer classifications either an “anode directed streamer” or a “cathode directed streamer” (these descriptions are self-explanatory). The streamer mechanism is only a possible sparking mechanism if the critical length x_c of the avalanche, necessary for the formation of a large space charge region, is less than the electrode gap. Unfortunately there are only empirical formulas (generalised under the range of conditions under which they were derived) to describe this critical distance (refer to [83]). The above discussion is a very brief overview of the complex streamer mechanism, for a more detailed discussion refer to [83].

A generalized breakdown formula using the streamer mechanism is that of equation (3.10) [83].

$$\int_0^{x_c} \sigma_{Town} \partial x = K_S \quad (3.10)$$

The value for K_S lies in the range of 18 to 20 (the value of K_S is obtained by taking the logarithm of the charge carrier number in the avalanche i.e. a minimum of 1×10^8 charge carriers are generally required to initiate a streamer).

3.2.2: Plasma conductivity expressions

A plasma is a quasi-neutral gas of charged and neutral particles that share a collective behaviour. A quasi-neutral plasma is neutral enough so that one can assume that $n_i = n_e = n$ (n_i is the number density of ions and n_e is the number density of electrons). A fundamental characteristic of a plasma is its ability to shield itself from external electrical potentials. The Debye length λ_D , defined by equation (3.11) in which T_e is the electron temperature, is the

length of the charge screening (between the electrons and ions within the plasma) in an electron plasma in which the ions are assumed to be stationary.

$$\lambda_D = \left(\frac{\epsilon_o k_B T_e}{n_e e^2} \right)^{\frac{1}{2}} \quad (3.11)$$

Debye shielding is only a statistically valid concept if there are enough particles within the charged particle cloud. This concept is validated by the Debye sphere parameter N_D , which is defined by equation (3.12). Provided $N_D \gg 1$ then the criteria for shielding will be validated.

$$N_D = n_e^{\frac{4}{3}} \pi \lambda_D^3 \quad (3.12)$$

The natural (circular) frequency of charged particles of a plasma consisting of only a single element under a self-consistent electrostatic restoring force, called the plasma frequency w_p , is defined by equation (3.13). In equation (3.13) q_s is the ion charge and m_i is its mass.

$$w_p = \left(\frac{n_e q_s}{\epsilon_o m_i} \right)^{\frac{1}{2}} \quad (3.13)$$

There are three conditions for an ionized gas to be classified as a quasi-neutral plasma [88]:

- 1) $\lambda_D \ll L$
- 2) $N_D \gg 1$
- 3) $w_p \tau > 1$

The first condition is that the ionized gas must be dense enough that the Debye shielding length must be smaller than the dimensions of the system, of length L , used to contain/create the plasma. If L is much greater than λ_D then whenever an external potential is applied or when local charge concentrations arise, these effects will be shielded out leaving the bulk of the ionized gas unaffected. The second condition is the criteria validating the concept of the Debye shielding length. The final condition requires that the motion of the charged particles should be the result of electromagnetic forces rather than hydrodynamic ones. To this end the product of

the plasma frequency and the mean time between collisions with neutral atoms τ must be greater than 1 for this condition to be true.

The conductivity and resistance of the plasma within the plasma accelerator are important for the modelling aspects (of the plasma accelerator) conducted in chapter 4. Plasmas are generally characterised by the dimensionless parameters Γ and θ . Γ defined by equation (3.14) is the non-ideal parameter, it is the ratio of the mean potential energy (thermal energy) and the kinetic energy. θ is the degeneracy parameter and is defined by equation (3.15), this parameter determines what statistical distribution may be used to describe the plasma.

$$\Gamma = \frac{e^2}{4\pi\epsilon_0 k_B T} \left(\frac{4\pi m_e}{3} \right)^{\frac{1}{3}} \quad (3.14)$$

$$\theta = \frac{2m_e k_B T}{\hbar^2} \left(3\pi^2 n_e \right)^{-\frac{2}{3}} \quad (3.15)$$

The non-ideal parameter Γ is used to distinguish the cases of weak and strong coupling of the plasmas ions as: $\Gamma \ll 1$ for an ideal plasma, $\Gamma \leq 1$ for a weakly non-ideal plasma, and $\Gamma > 1$ for a strongly coupled plasma.

The degenerate parameter θ defines two distinct regions: $\theta > 1$ for the non-degenerate plasma domain, and $\theta < 1$ for the degenerate plasma domain. In the non-degenerate plasma domain the classical Boltzmann statistics apply; however in the degenerate plasma domain quantum corrections become important.

There are further plasma parameters which are also used to generally define the physical and electrical properties of a plasma, most notably the density parameter r_s , the degree of ionization ξ and the dimensionless parameter $\Gamma^2 \theta$. Plasmas are classified as being either high density or low density through the use of the r_s parameter: $r_s > 1$ for low density plasmas, and $r_s < 1$ for high density plasmas. The parameter r_s , given in equation (3.18), is defined by the parameters a_e (equation (3.16)) and a_\bullet (equation (3.17)).

$$a_e = \left(\frac{3}{4\pi m_e} \right)^{\frac{1}{3}} \quad (3.16)$$

$$a_o = \frac{4\pi\epsilon_o \hbar^2}{m_e^2} \quad (3.17)$$

$$r_s = \frac{a_e}{a_o} \quad (3.18)$$

The degree of ionization ξ is the ratio of the ion density to the total plasma density; it defines the amount of ionization (the degree of ionization) present in a plasma. The degree of ionization is a function of temperature T , ionization potential U_i , and the pressure P of the plasma. The degree of ionization is derived from Shaha's equation (which describes the thermal ionization of gases) and the assumption that the plasma is a quasi-neutral plasma (i.e. $T_e = T_i = T$) as [89]:

$$\xi = \sqrt{\frac{F}{1+F}} \quad (3.19)$$

where

$$\begin{aligned} F &= \frac{(2\pi m_e)^{\frac{3}{2}} (k_B T)^{\frac{5}{2}}}{P h^3} e^{\frac{-eU_i}{k_B T}} \\ &= 3.33 \times 10^{-7} \frac{T^{\frac{5}{2}}}{P} e^{-11.6 \times 10^3 \left(\frac{U_i}{T} \right)} \end{aligned} \quad (3.20)$$

In equation (3.20) U_i is measured in eV, T in K, and P in bar. The dimensionless parameter of $\Gamma^2 \theta$ is used to divide plasmas, based solely upon temperature, into two further regions. The first region $\Gamma^2 \theta \gg 1$ is used to define what is known as the classical region and $\Gamma^2 \theta \ll 1$ is known as the high temperature region in which the Born approximation holds. The plot of plasma density as a function of temperature in figure 3.1 shows some of the discussed regions above, including a few regions (in terms of density and temperature) where various types of plasmas are defined.

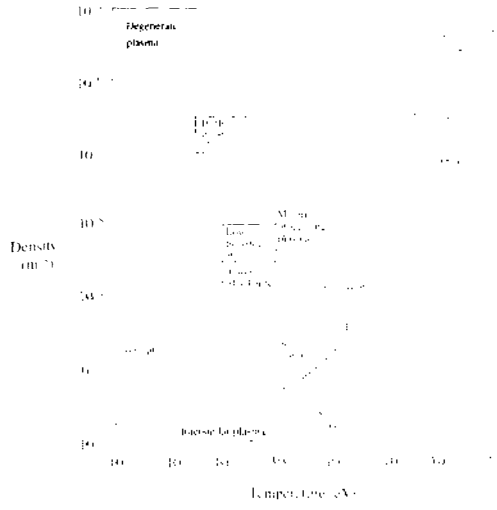


Figure 3.1: Figure showing the plasma density-temperature plane, including a few regions where various types plasmas are defined (adapted from [60]).

The Spitzer conductivity is typically assumed in the majority of papers that deal with the numerical modelling aspects of rail guns that use plasma armatures [41], [42], [44], and [45]. The Spitzer conductivity applies to an ideal plasma (i.e. $\Gamma \ll 1$). The Spitzer conductivity is derived from the assumption that the ions form a stationary, infinitely heavy neutralizing background, and only the mobile electrons interact with these ions; electron-electron interactions as well as the interactions of ions with different species are accommodated in this formula. An empirical expression for the Spitzer conductivity σ_s is defined as [59]:

$$\sigma_s = \left(0.295 + \frac{0.39}{0.85 + Z_{eff}} \right)^{-1} \frac{n_e e^2}{m_e} \tau_e \quad (3.21)$$

In equation (3.21) Z_{eff} is the effective ion charge, defined by equation (3.22), and τ_e is the collision time (for electrons), given by equation (3.23). In equation (3.22) the effective ion charge is summed over all ionic species s with a corresponding charge Z_s .

$$Z_{eff} = \frac{\sum_s n_s Z_s^2}{\sum_s n_s Z_s} \quad (3.22)$$

$$\tau_e = 3(2\pi)^{\frac{3}{2}} \frac{\epsilon_0 m_e^{\frac{1}{2}} (k_B T_e)^{\frac{3}{2}}}{e^4 Z_{eff} n_e \ln(\Lambda)} \quad (3.23)$$

In equation (3.23) $\ln(\Lambda)$ is referred to as the Coulomb logarithm. In a fully ionized plasma it is more likely that an electron will suffer many small angle deflections as a result of encounters with ions of charge q , in which this small angle deflection lies between the maximum (b_{\max}) and minimum (b_{\min}) values:

$$b_{\max} = \lambda_D \quad (3.24)$$

$$b_{\min} = \frac{qe}{12\pi\epsilon_o k_B T} \quad (3.25)$$

The Coulomb logarithm is defined using these deflection angles as:

$$\ln(\Lambda) = \ln\left(\frac{b_{\max}}{b_{\min}}\right) \quad (3.26)$$

As mentioned before the Spitzer conductivity only applies to the situation of $\Gamma \ll 1$. In some coaxial plasma accelerators the electrical conductivity of the plasma has instead been determined to be non-ideal [90], [91] and in these instances non-ideal plasma electrical conductivity interpolation formulas have been used. A general summary of these interpolation formulas (up to the year 2003) is given in [92]; this paper gives a summary of interpolation formulas for $\Gamma^2 \theta \gg 1$, $\Gamma^2 \theta \ll 1$, a classical non-degenerate hydrogen plasma, and a general formula for non-ideal plasmas. In [90] and [91] the conductivity of the plasma was determined using the low density approximation of G.Ropke [93], which was derived from a high density expression. The high density behaviour of [93] was derived by considering such effects as Bogoliubov-Born-Green-Kirkwood-Yvon hierarchy (BBGKY) (to describe the kinetic effects), long range Coulomb interactions and the Debye Onsager relaxation. The high density conductivity is determined by numerical means; however a simplified analytical expression for the low density behaviour σ_{Low1} was derived and is given by equation (3.27).

$$\sigma_{Low1} = 0.591 \frac{(4\pi\epsilon_o)^2 (k_B T)^{\frac{3}{2}}}{e^2 m_e^{\frac{1}{2}}} \left[\ln \Gamma^{\frac{-3}{2}} + 1.124 + \frac{1}{\sqrt{6} + \sqrt{3}} \Gamma^{\frac{3}{2}} \ln \Gamma^{\frac{-3}{2}} \right]^{-1} \quad (3.27)$$

The range for equation (3.27) is restricted to $\Gamma < 1$, $\theta \gg 1$ and the condition that $\theta \gg \Gamma^{-2}$. Another widely non-ideal plasma electrical conductivity interpolation formula is that of S.Ichimarui and S.Tanaka [94]. The formulation of [94] concerns itself with the strong Coulomb

coupling effects as the result of electron degeneracy and local field corrections, in which the analytical formula for the low density plasma conductivity σ_{Low2} , given by equation (3.28), was derived using a generalized Coulomb logarithmic function. Equation (3.28) is restricted to $0.003 \leq \Gamma \leq 2$ and $\theta \geq 0.1$.

$$\sigma_{Low} = 1.97 \left[\frac{3\pi}{2} \right]^{\frac{1}{2}} \frac{w_p}{4\pi\Gamma^{\frac{3}{2}} L_{IT}} \quad (3.28)$$

where

$$w_p = \left(\frac{16\pi^2 \epsilon_0 n_e e^2}{m_e} \right)^{\frac{1}{2}} \quad (3.29)$$

$$L_{IT} = \frac{a(\theta) \ln \Gamma + b(\theta) + c(\theta) \Gamma}{1 + d(\theta) \Gamma^3} \quad (3.30)$$

In equation (3.30) $a(\theta)$, $b(\theta)$, $c(\theta)$ and $d(\theta)$ are defined by equations (3.31) to (3.34)

$$a(\theta) = \frac{-\theta^{\frac{3}{2}}}{2\theta^{\frac{3}{2}} - 0.57923\theta + 0.23272\theta^2 + 1.4853} \quad (3.31)$$

$$b(\theta) = \frac{\theta^3 \left(\frac{1}{2} \ln \theta - 0.18603 \right) + 1.2704\theta^{\frac{3}{2}}}{\theta^3 + 1.8993\theta^2 + 4.3243\theta + 1} \quad (3.32)$$

$$c(\theta) = \theta^{\frac{3}{2}} \frac{0.69460\theta^{\frac{1}{2}} + 0.2428}{\theta^2 + 1.7768} \quad (3.33)$$

$$d(\theta) = \theta^{\frac{3}{2}} \frac{0.13550\theta^{\frac{1}{2}} + 0.083521}{\theta^2 + 0.36797} \quad (3.34)$$

There is a general inconstancy between the two formulations (3.28) and (3.27), both should have the same form and yet it is not possible to derive equation (3.28) from the simplifications made to the high density conductivity expressions of [93]. This is because equation (3.28) has been partially derived using empirical means. It should also be noted that the 1.97 term in equation (3.28) is an interpolation factor and in fact should not be a constant, but should be

dependent upon the degree of degeneration (as can be observed in [94] for the case of Xe plasma). In essence, equation (3.28) is generally the more accurate of the two formulas when compared to experimental values (although there is question on the accuracy of the experimental results [94], [93]), but in general both formulas give reasonable results.

The above conductivity expressions, including the Spitzer formula, are used to describe un-magnetised plasmas. In plasma accelerators and rail guns, that use plasma armatures, large magnetic fields are present; these fields are of important consideration in terms of the electrical conductivity of the plasma. In the absence of a magnetic field the electrical conductivity of a plasma is a scalar quantity; however in the presence of a magnetic field the electrical conductivity will be a tensor quantity [7], [38], [59], [38], [60], which is a function of the magnetic field, and the collision times and frequencies of both the ions and electrons. This means that an electric current can occur in directions in which the electric field is zero, and this is born out in such effects as the Hall effect [7], [38]. In such a situation (in which the plasma may be considered to be magnetized) the use of Braginskii transport analysis [59] would be appropriate; note this formula assumes that the equilibrium distribution for ions and electrons is the Maxwell distribution, although T_i is not necessarily equal to T_e . For the present the effects of the magnetic field on the conductivity of the plasma will be neglected, to simplify the initial modelling efforts of chapter 4.

An expression for the conductivity profile of the plasma inside the plasma accelerator can be calculated using the following assumptions. Firstly, the plasma will be assumed to be obtained directly from the neutral hydrogen gas pulse (from the piezoelectric valve), to this end the plasma will be assumed to be entirely composed of hydrogen. Secondly, assume for initial purposes that the plasma density profile is the same as that for the un-ionized gas pulse given by equation (2.28) (section 2.4.10 of chapter 2). Thirdly, it will be assumed that the plasma is in a thermal equilibrium i.e. $T_e = T_i = T$. And finally, it will be assumed that the temperature across the plasma has a constant value, derived from the average experimentally determined temperature value of the plasma (from the plasma accelerator). Using these assumptions the number density of electrons n_e as a function of distance can be derived by dividing the density profile by the molar mass, multiplying this value by Avogadro's number, and finally multiplying the end result by the degree of ionization defined by equations (3.19) and (3.20).

There are, of course, some ad hoc elements to these assumptions. The resulting plasma, will of course, initially expand due to the process of converting the gas with some seed ionization into a plasma. The temperature of the resulting plasma will not be a constant value but will be a factor of the density, pressure and energy distribution across the plasma and a function of time.

Also, assuming that the temperature (the bulk temperature) of the resulting plasma is that of the experimentally determined temperature (at the end of the plasma flight tube) is erroneous, because by the time the plasma has reached the detector some of its thermal energy will have been radiated as black body energy; but more notably the resulting plasma produced from the plasma accelerator would have had heating effects as a result of resistive heating and compression. A detailed ion model would be required to model such effects, but for the initial purposes of providing a preliminary investigation of the plasma accelerator the above assumptions are adequate.

Once the conductivity distribution has been calculated, the overall resistance of the plasma can be calculated (or any portion of the plasma can have its overall resistance calculated). The overall resistance of the plasma is necessary for calculation of the circuit equations relating to the charge, current and voltage of the plasma accelerator. The resistance of the plasma is calculated by first assuming steady state conditions (for the current density) across the plasma in the coaxial accelerator so that Ohms law can be applied; this equation is then expanded using the expression for the current density given by equation (4.55) (from section 4.3.2 of chapter 4), in which the velocity term has been neglected. Since a steady state has been assumed, the electric field will be constant across the length of the plasma. Using these assumptions the equation for the resistance of the plasma in cylindrical coordinates (r, θ, z) for an element of infinitesimal thickness in the r direction is given as:

$$\partial R = \frac{\partial r}{2\pi \int \sigma \partial z} \quad (3.35)$$

Integrating equation (3.35) between the lower and upper electrodes ($R_1 \geq r \geq R_2$) results in:

$$R = \frac{1}{2\pi \int \sigma \partial z} \ln \left(\frac{R_2}{R_1} \right) \quad (3.36)$$

The integration of the conductivity can be done by Trapezoid or Simpson's integration [78], because a total value for the resistance is required rather than an expression for its distribution as a function of distance z . (Equation (3.36) can be extended to accommodate an assumed skin effect, instead of integrating over the entire length of the plasma).

3.3: The Lica

The Lica accelerator described in section 3.1 was investigated using the pieces of equipment discussed in section 3.3.1. The initial tests conducted using this apparatus were to prove that it was possible to accelerate a plasma using this new unique type of plasma accelerator. The plasma accelerator has not yet been fully optimized and only the effect of changing the positive electrode length upon the velocity profile of the plasma pulse was examined; in which 20 cm, 10 cm and 5 cm in length positive electrodes were investigated, the results of which are shown in sections 3.3.4, 3.3.5 and 3.3.6 respectively. As discussed in section 3.1 it is possible to preionize the neutral gas pulse (produced from the piezoelectric valve) before it enters or at some position within the plasma accelerator. It is not possible to tell exactly the point at which the gas pulse is preionized, because the exact time delay upon the piezoelectric valve is unknown. The time delay placed upon the preionization trigger (used in the initial experiments on the Lica) was between $270\mu\text{s}$ to $300\mu\text{s}$ (taken from the time that a trigger pulse was sent to the piezoelectric valve) with a preionization pulse length of between $30\mu\text{s}$ to $60\mu\text{s}$, to give a total time of $330\mu\text{s}$.

These time delays are shown diagrammatically in diagram 3.6, in which the voltage pulse (of length $t=t_1$) sent to the piezoelectric causes it to deform to its maximum deflection at time t_2 . (The time t_2 was always found to occur after the voltage pulse sent to the valve had finished (at $t=t_1$); for example for a $180\mu\text{s}$ voltage pulse ($t_1=180\mu\text{s}$) it was experimentally determined that $t_2=191\mu\text{s}$). After a user defined time $t=t_3$ a voltage pulse of t_4 minus t_3 in duration is sent to the preionization unit, preionizing the neutral gas pulse.

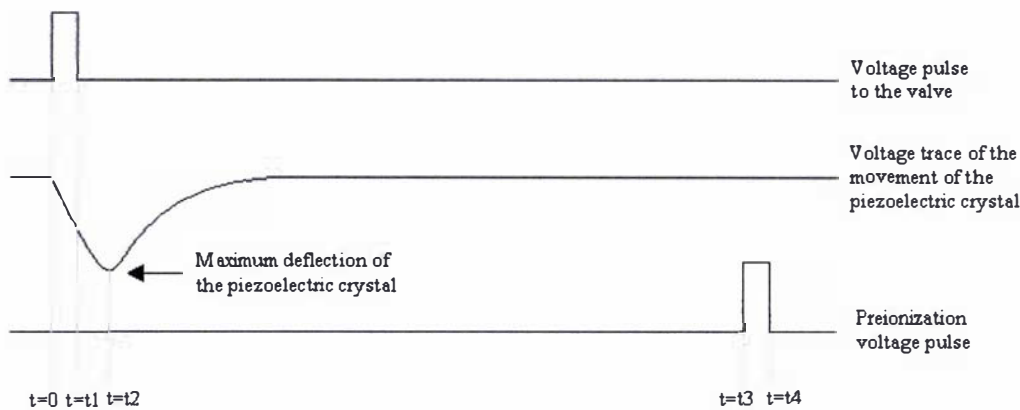


Diagram 3.6: Diagram representing the timing of various voltage pulses, all referenced from $t=0$ (the time when a voltage pulse is sent from the pulse generator to the valve).

It was experimentally found from the experiments conducted in section 2.4 of chapter 2 that the overall time delay on the valve (refer to section 2.4.6) was approximately $188\mu\text{s}$ for the initially tightened valve. This was the time delay required to match the calculated mean (experimental) velocity to the terminal velocity of hydrogen created for a $180\mu\text{s}$ driving pulse. Assuming that the bulk of the neutral hydrogen gas is travelling at 2660m/s a rough estimate of where the neutral gas pulse is preionized can be calculated. The maximum distance that the bulk of the neutral gas is preionized is equal to the mean velocity multiplied by the sum of the maximum preionization pulse time ($330\mu\text{s}$) minus the minimum experimental time delay of $188\mu\text{s}$, which gives a distance of 0.378m . The minimum distance that the bulk of the neutral gas is preionized is calculated in much the same fashion, with the exception that the start time of the preionization pulse is used (i.e. $300\mu\text{s}$, the upper limit to the minimum preionization pulse initiation time), which results in a distance of 0.298m . Hence it can be claimed that the bulk of the neutral hydrogen gas pulse is preionized either just before or just as it enters the plasma accelerator.

The possibility of the repetitive firing of the Lica was briefly investigated using 10cm and 20cm long positive electrodes, the results of which are presented in sections 3.3.4 and 3.3.5. The use of a higher charging voltage on the capacitor was also briefly investigated, the results of which are presented in section 3.3.4 for a single test shot. During some of the experimental tests it was found that high velocity pulses of hydrogen plasma could be generated, this anomaly will be referred to as a “misfire”, the results of these anomalies are presented in section 3.3.7.

The Lica was in full operation for over a year and several hundred experiments conducted, investigating various aspects of the operation of the apparatus. These experiments covered such effects as various charging voltages on the capacitor from 1kV to 14kV , which lead to the development of the preionizer unit (in its final form). Many experiments were conducted using what will be referred to as “burst mode” in which two or more gas pulses are introduced into the plasma accelerator allowing a lower charging voltage on the capacitor to be used. These miscellaneous experiments are discussed in chapter 5.

The results presented in this section represent a small sample of the typical results from the operation of the Lica in its intended role for MTF, in which a single gas pulse produced from the valve (refer to diagram 3.6) is accelerated.

The Lica is a prototype pulsed coaxial plasma accelerator that has been developed for use in the MTF scheme discussed in chapter 1 (refer to section 1.1) and its performance is yet to be fully optimised (due to the time constraints placed upon this thesis). Future aspects and plans for this apparatus are discussed in chapter 6.

3.3.1: The Lica apparatus

A schematic representation of the Lica and its associated pieces of equipment is presented in diagram 3.7 and isometrically in diagram 3.8. The Lica was constructed using the existing experimental equipment used to determine the gas pulse characteristics of gas pulses produced from the valve, discussed in section 2.4 (in its entirety) of chapter 2 (with the use of diagram 2.11). The new pieces of equipment that were added to the existing experiment (discussed in section 2.4, in its entirety) to construct the Lica include: a preionizing unit, a high voltage power supply, a capacitor, the plasma accelerator, the energy dump, an oscilloscope and a flight tube that is pumped by a diffusion pump connected to a roughing pump, all of which are labelled in diagram 3.7. The basic pieces of equipment listed in diagram 3.7 are described in table 3.1.

The operational pressure within the main, source and ultra high vacuum chambers were the same as that given in section 2.4.2 of chapter 2. Within the flight tube the operational pressure was approximately 1×10^{-4} Pa. The equipment associated with the operation of the valve: the pulse generator, amplifier 2 and the piezoelectric driver remains the same as that discussed in sections 2.4.2 and 2.3.1 (with the aid of diagram 2.5). The preionizer described in section 3.1 was built from the ionizing grid taken from a Vacuum Generators Ltd ion gauge. The preionizer is driven by the preionizer driver, which delivers a positive 760V square wave pulse to the unit; the length of the preionizing pulse is controlled by the pulse generator.

The capacitor is a custom made capacitor from General Atomics, capacitor model number 32891, it is a low inductance high energy capacitor that has the following electrical characteristics: a 17 μ F capacitance, a 40nH inductance and at its maximum charge of 40kV it is capable of producing a maximum of 450kA. The capacitor was charged using the high voltage power supply, which was a Spellman RH5R50 P50/200 high voltage power supply, capable of a maximum voltage output of 60kV.

Label	Make/Model	Pumping speed
S1	MDC Bayard-Alpert ion gauge	
S2	Edwards model PRM pressure gauge	
S3	TCIA thermocouple vacuum gauge	
S4	TCIA thermocouple vacuum gauge	
S5	Edwards model 6 pressure gauge	
S6	MDC Bayard-Alpert ion gauge	
S7	Edwards model 6 pressure gauge	
V1	MDC KVA-100 bellows valve	
V2	Edwards model BRV 25/backing roughing valve	
V3	Generic butterfly valve	
V4	Generic ball valve	
V5	Generic butterfly valve	
Roughing pump 1	Edwards RV5 roughing pump	5.1m ³ /h
Roughing pump 2	Edwards RV5 roughing pump	5.1m ³ /h
Roughing pump 3	Edwards E2M18 roughing pump	17m ³ /h
Roughing pump 4	Edwards RV5 roughing pump	5.1m ³ /h
Diffusion pump 1	Edwards Diffstak model 100LN2	500L/s
Diffusion pump 2	CIT-ALCATEL crystal 160E	3000L/s
Diffusion pump 3	MFG Torr vacuum products: R-420 diffusion pump	1410L/s
Turbo pump 1	Edwards EXT 250M turbo pump	190L/s
Turbo pump 2	LH turbovac 50 turbomolecular pump	33L/s

Table 3.1: Description of experimental equipment listed in diagram 3.7

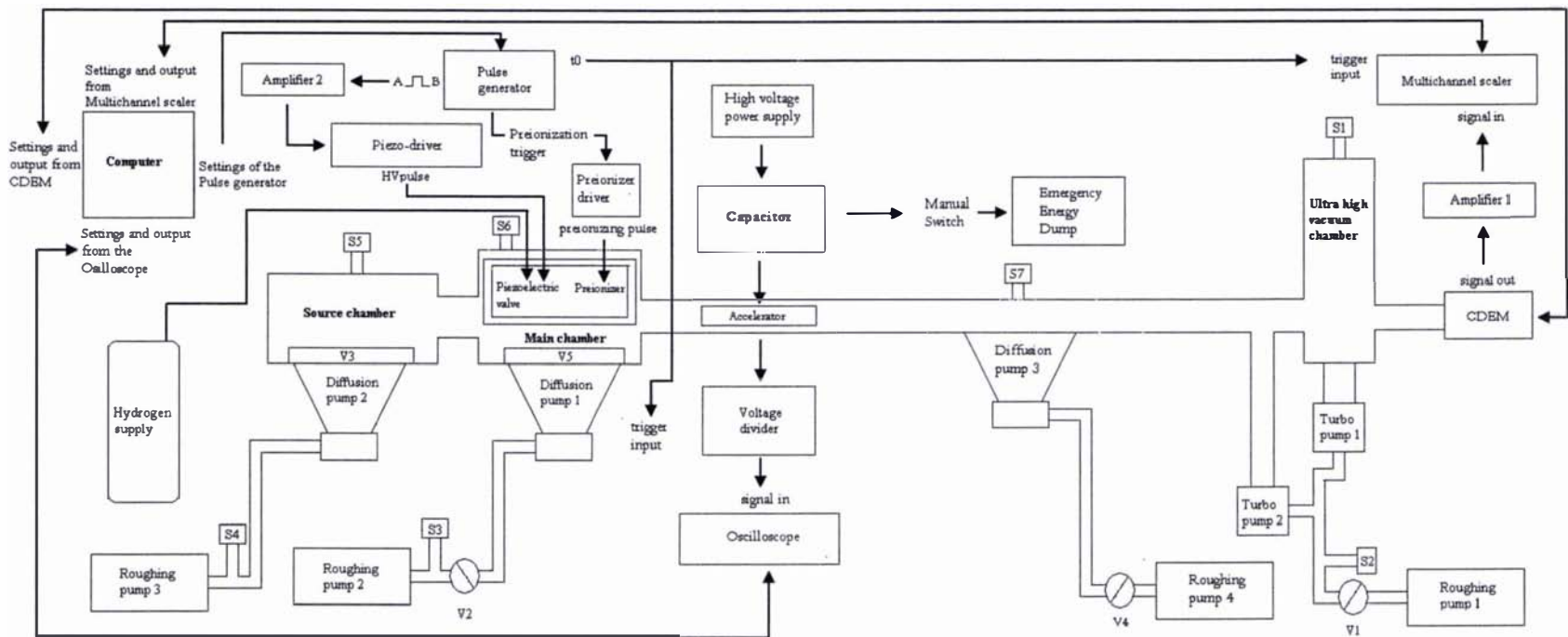


Diagram 3.7: Schematic representation of the Lica plasma accelerator, with it associated pieces of equipment

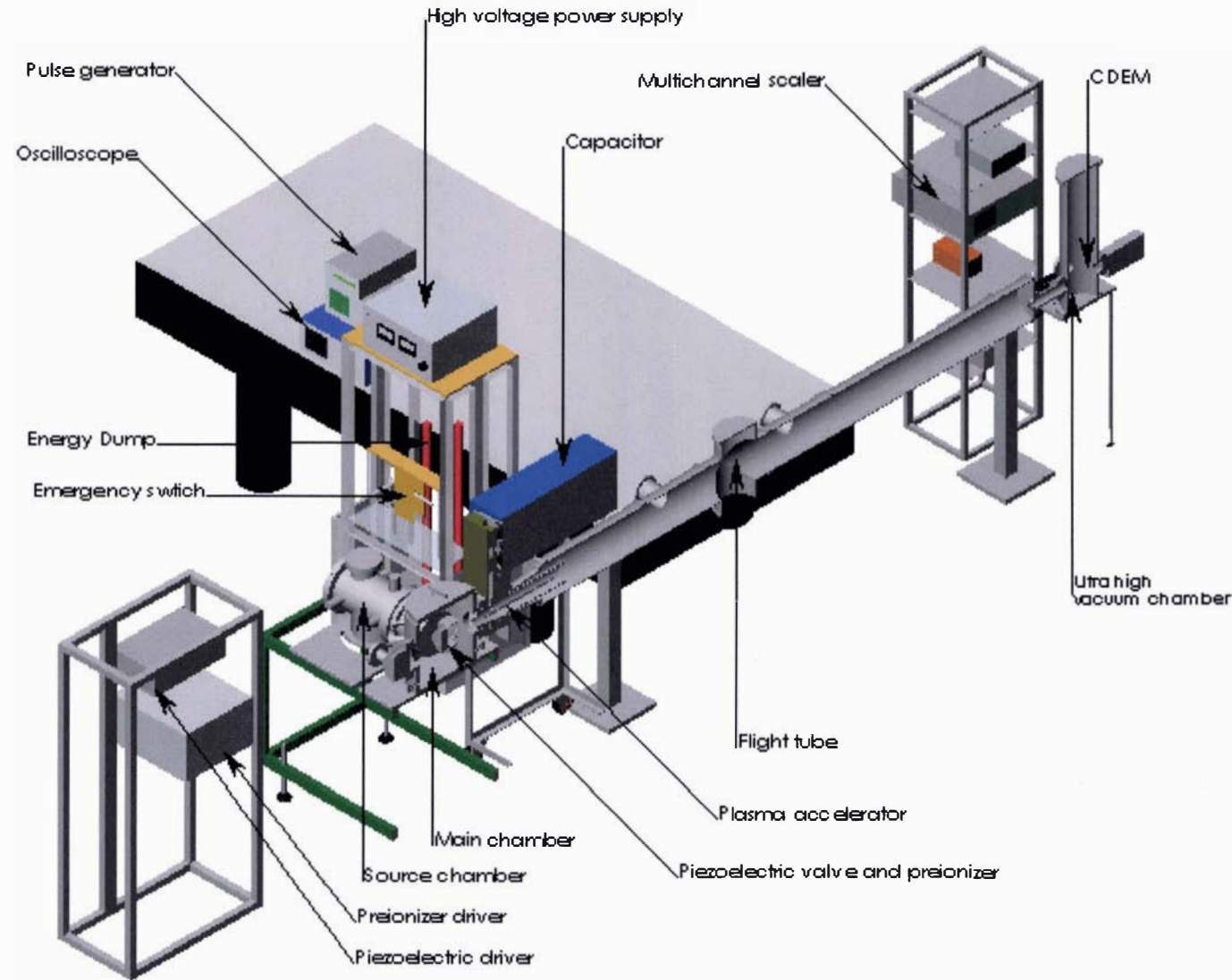


Diagram 3.8: Isometric cross section of the *Lica* plasma accelerator, with it associated pieces of equipment

The plasma accelerator is that described in section 3.1. The connection of the plasma accelerator to the capacitor is shown as a side profile in diagram 3.9, in which the insulation about the plasma accelerator has been removed for viewing purposes and the interior sections are shown in grey. The plasma accelerator is directly connected to the capacitor by two 6061T6 aluminium plates that are 20mm in thickness. The positive plate is 510mm in length and 160mm in width and the grounded plate is 577mm in length and 270mm in width, these two plates are separated by two layers of Teflon (sheet) 1.5mm in thickness. The plasma accelerator is connected to these plates via aluminium connections; a series of O-rings ensures that a vacuum seal is maintained. The plasma accelerator is linked to the main chamber by a thick Nylon connector; this connector serves the purpose of electrical insulation preventing arcing from the plasma accelerator to the main chamber, preionizer or the piezoelectric valve, and also forms a vacuum seal between the main chamber and the grounded plate. The nylon connector has an angled interior of 7.5 degrees to ensure the smooth expansion of the expanding gas, limiting the amount of scattered gas (from the walls of the nylon connector) that enters the plasma accelerator. A Pyrex tube 5mm in thickness with an inner diameter of 11cm surrounds the plasma accelerator, electrically insulating it from the flight tube. The electrically (exposed) conducting regions of the plasma accelerator and its connections to the capacitor were insulated using 2cm thick Tufnol Whale brand phenolic plate insulation. Finally, a Faraday cage was formed about the plasma accelerator and the capacitor out of 1.5mm thick 6061T6 aluminium. This was constructed to prevent current being induced in the electrical cables (associated with the electrical equipment used in the Lica) as well as shielding the diagnostic equipment from any electromagnetic noise that would be produced when the capacitor discharged. (Neither the insulation nor the Faraday cage are shown in either diagram 3.8 or 3.11).

The energy dump mentioned in section 3.1 consists of a voltage divider and an emergency (manual) energy dump. The energy dump (in its entirety) is shown in diagram 3.10, in which the voltage divider consists of a 9.58M Ω KOA model PSN6 resistor and a 4.56K Ω off the shelf resistor. The voltage divider is permanently connected to the capacitor as a safety precaution, ensuring that the capacitor will always discharge (the time scale for this to occur is approximately two minutes). The manual emergency switch is a simple 6061T6 aluminium rod that is unevenly pivoted, so that when it is released from rest it forms a circuit between the capacitor and the emergency energy dump. The energy dump consists of a single 60K Ω KOA model PSN6 resistor. The temperature rise from dumping the fully charged capacitor (approximately 14KJ) into the emergency energy dump will result in a 25°C temperature rise (so this component will survive the possible surge conditions placed upon it).

3.3.1: The Lica apparatus

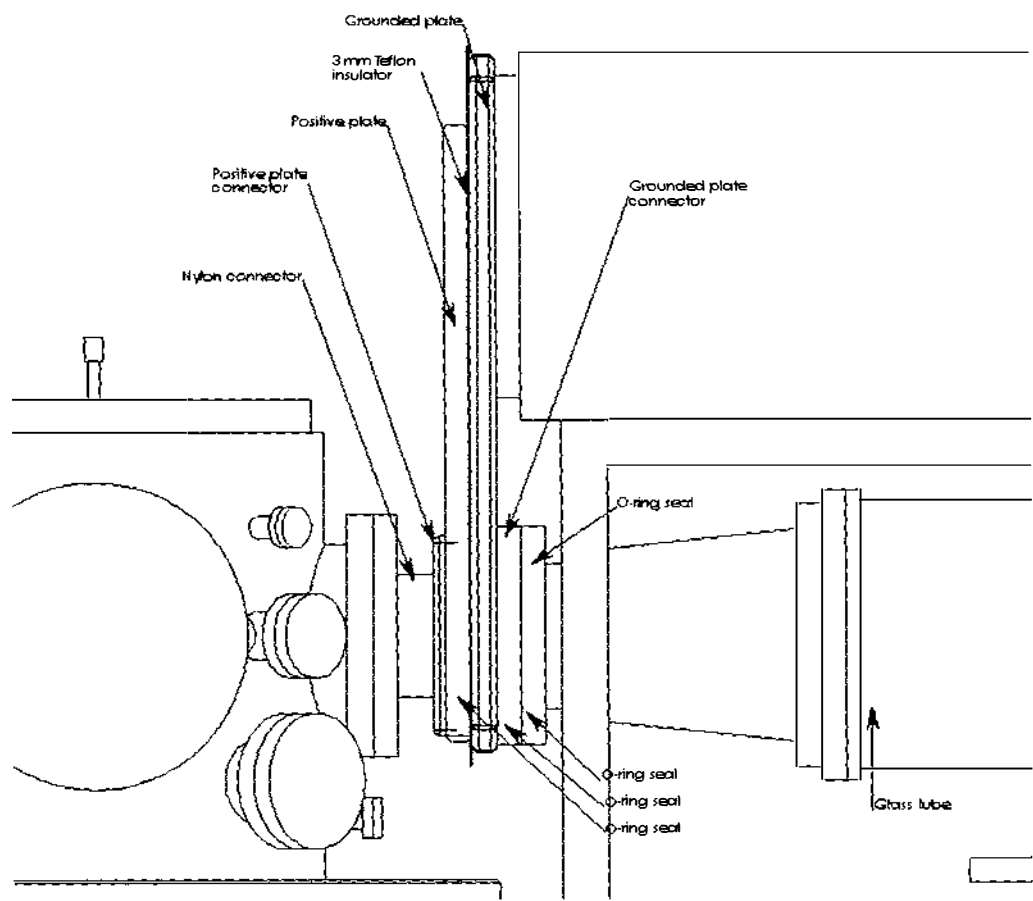


Diagram 3.9: Side view of the plasma accelerator and its connection to the capacitor and vacuum system; the interior sections are shown in grey.

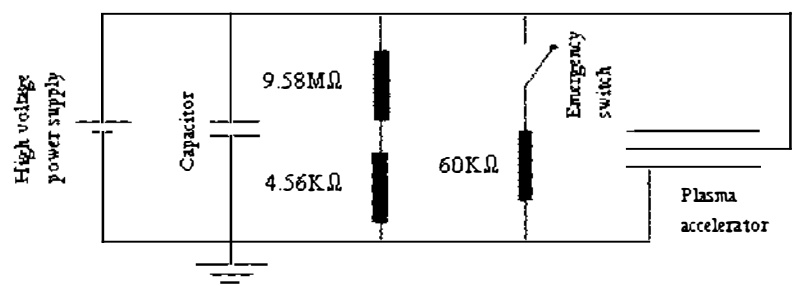


Diagram 3.10: Schematic representation of the capacitor circuit

The diagnostic equipment used to gather data from the Lica are the oscilloscope, multichannel scaler and the CDEM. The CDEM shown in diagram 3.7 is a component of the SRS RGA200 residual gas analyser discussed in section 2.4.1, the operational settings of this device were also covered in that section. The multichannel scaler is a SRS 430 multichannel scaler, this device

and details of amplifier 1 (a SRS model SRS445 DC-300MHz amplifier) are discussed in section 2.4.2 of chapter 2. The oscilloscope is a Tektronix TDS 524A digital oscilloscope, this device was used to obtain voltage traces (refer to section 3.3.2) from the circuit depicted in diagram 3.10; the oscilloscope measured the voltage of this circuit across the $4.56\text{K}\Omega$ resistor. The flight distance from the back of the plasma accelerator to the CDEM was 4.147m and the distance between the piezoelectric valve and the back of the plasma accelerator was 0.365m , both these distances are shown in a two dimensional cross-sectional view of the Lica in diagram 3.11. Note the CDEM was placed 3cm off axis (as can be seen in diagram 3.11) so that a portion of the resulting plasma could be viewed.

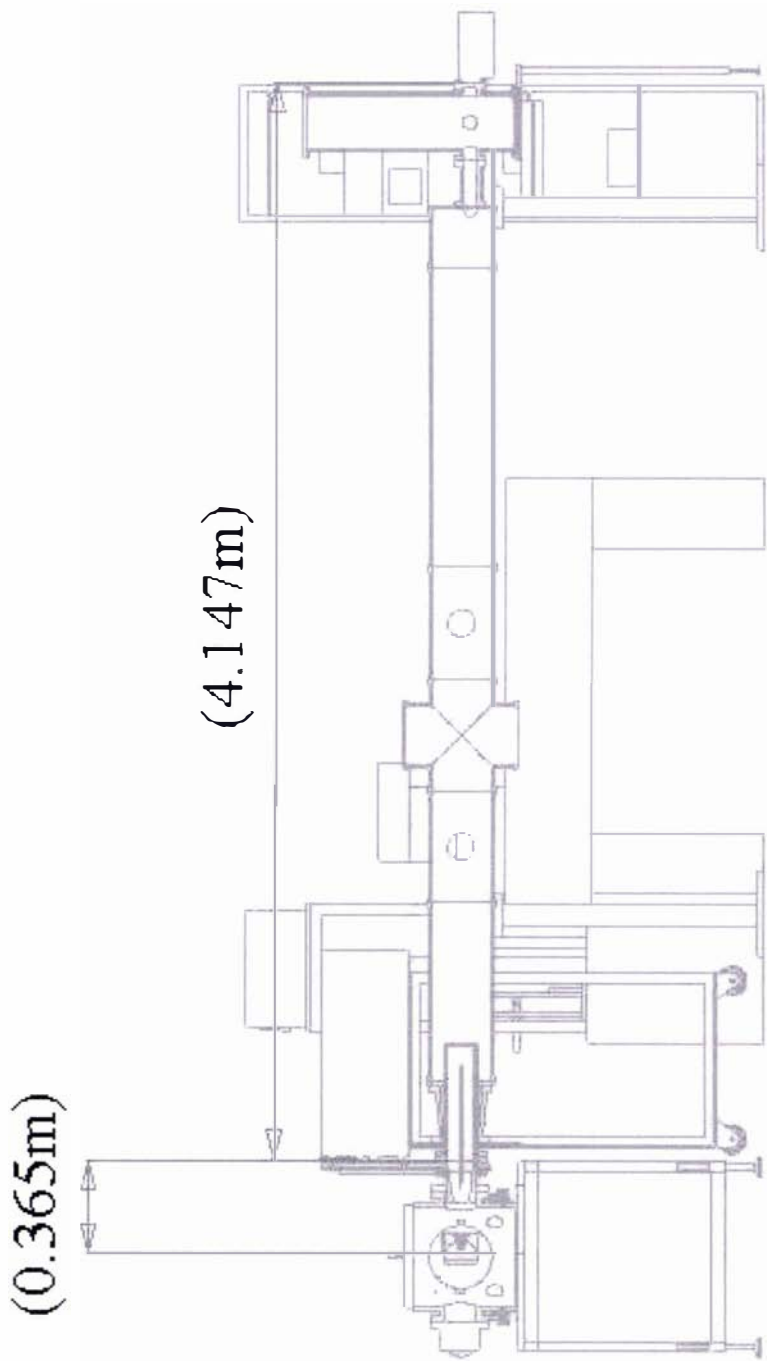


Diagram 3.11: Two dimensional cross section of the Lica plasma accelerator, showing the distances involved.

3.3.2: Data acquisition from the Lica

Data acquisition from the Lica is shown schematically in diagram 3.7, in which a LABVIEW program (run on a computer using LABVIEW version 3.1) controls the operational settings on the diagnostic (the CDEM, multichannel scaler and the oscilloscope) and driving equipment (the pulse generator) as well as recording the data produced from the diagnostic equipment (the multichannel scaler and the oscilloscope). The LABVIEW program is used to set the driving pulse length of the piezoelectric valve and the length of the preionization pulse. The bin width of the multichannel scaler and the sampling rate of the oscilloscope were also set using the program. The settings on the CDEM were controlled using its supplied software, the operational parameters that were used can be found in section 2.4.1 of chapter 2.

After the operational settings were set the experiments were started by using a manual trigger on the pulse generator. Once the trigger had been activated the pulse generator sends a driving pulse to the piezoelectric valve using the process discussed in section 2.3.1 of chapter 2. This results in a gas pulse being generated. At the time the piezoelectric valve is triggered a trigger signal is sent to both the multichannel scaler and the oscilloscope. This causes the multichannel scaler to start recording data from the CDEM and the oscilloscope to start recording the voltage trace (the voltage trace is a plot of the voltage measured across the $4.56\text{K}\Omega$ resistor, refer to section 3.3.1 and diagram 3.10, as a function of time) of the plasma accelerator circuit depicted in diagram 3.10 (of section 3.3.1). After a specified time the pulse generator sends a preionization pulse to the preionizer driver, which then delivers a 760V square wave voltage pulse to the preionizer. The preionizing voltage pulse preionizes the neutral gas pulse produced from the valve, using the mechanism discussed in section 3.1. The preionized gas would then break down within the plasma accelerator generating a plasma, which then discharges the capacitor. The resulting plasma is then accelerated down the plasma accelerator by the Lorentz force (refer to section 1.2) and would then be detected by the CDEM at the end of the flight tube. The data recorded from the multichannel scalar and the oscilloscope was recorded as “dat” files in the LABVIEW program. After the capacitor had discharged the high voltage power supply was turned off and the remaining energy in the capacitor was discharged using the emergency energy dump.

3.3.3: Analysis of the data from the Lica

There is a small peak on the raw data obtained from the multichannel scaler which is coincident with the initial drop in the voltage recorded on the oscilloscope (as the current begins to flow). This peak can be taken to correspond to the breakdown of the preionized gas inside the plasma accelerator and is recorded by the CDEM because the breakdown of hydrogen gas produces a

large amount of ultra-violet light. The presence of this peak is confirmed by the large over voltage present in the voltage trace from the oscilloscope, which can be considered to be point where the preionized gas breaks down into a plasma [83].

There was neither enough time nor funding for equipment to experimentally determine the temperature of the resulting plasma (i.e. diffraction gratings) [85], [86], [87]; so instead the temperature (longitudinal) was established using a Maxwell – Boltzmann velocity distribution (refer to section 2.2.1 and 2.4.6 of chapter 2). By assuming this distribution it is implied that the plasma has had sufficient time to come to a thermal equilibrium; it is unclear whether or not this assumption is true.

The longitudinal temperature of the plasma is found by making the assumption that it is a hydrogen plasma (in its entirety), using the same method described in section 2.4.6 and equations (2.26) and (2.3), with the exception that none of the following corrections need to be accounted for in analysing the multichannel scaler data:

- 1) The time of flight of the molecules through the ionizer in front of the mass-spectrometer (refer to section 2.4.1)
- 2) The time delay between the signal sent to the piezoelectric valve and it actually opening.

Taking the start of the small peak on the multichannel scaler to correspond to a zero time value, since it has been determined to be the point where the preionized gas breakdown inside the plasma accelerator, the time scale of this data is then derived by adding the value of the bin width (of the multichannel scaler) to this value for each subsequent bin. Linearly averaging the bin data and subsequent time values was not conducted, neither was taking $t=0$ at half the bin width (of the small peak on the multichannel scaler) because of the reasons discussed in section 2.4.6.

The velocity distribution of the plasma pulse is calculated by dividing the distance travelled by the plasma pulse, assuming that the plasma is generated at the back of the plasma accelerator (refer to section 3.3.1), by the times corresponding to the recorded counts.

The effect of convolution and expansion of the plasma pulse was accounted for using the same method as in section 2.4.6, in which the velocity distribution is normalized as a function of $\frac{1}{v}$

The fitting of the Maxwell – Boltzmann distribution is made from inspection of the velocity distribution. It can be argued from the velocity distributions presented in the following sections 3.3.4, 3.3.4, 3.3.5 and 3.3.6 that there is either a single peak structure as shown in diagram 3.12 or what appear to be a series of peaks as represented in diagram 3.13.

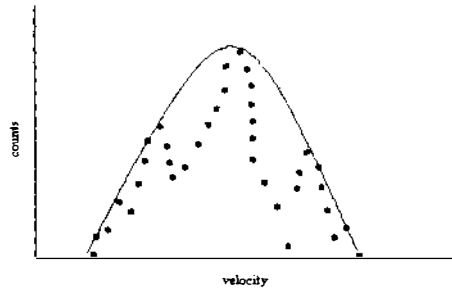


Diagram 3.12: Diagrammatic example of the fitting of a Maxwell velocity distribution across the entire velocity data range.

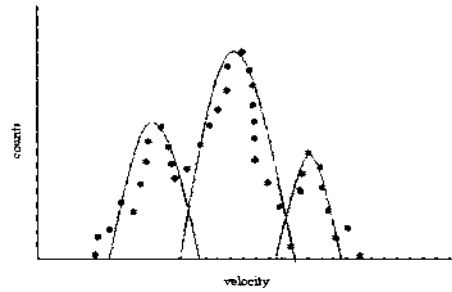


Diagram 3.13: Diagrammatic example of the fitting of several Maxwell velocity distributions about the perceived peaks in the velocity data range.

In any given experimental measurement there will be an amount of statistical uncertainty that will arise, not from a lack in the precision of the instruments, but from the overall statistical fluctuations in collecting a finite number of counts over a finite interval of time [79]. This statistical uncertainty can be analytically estimated from the standard deviation of a Poisson distribution. If the same measurement is repeatedly conducted, the data obtained would be distributed about a Poisson distribution. The use of this distribution can be justified because it is expected that the distribution will be related to a binomial distribution with the boundary conditions that any positive number of counts and no fewer than zero counts can be collected within any time interval [79]. The standard deviation σ of the Poisson distribution is derived from the mean μ of the distribution as equation (3.23).

$$\sigma = \sqrt{\mu} \quad (3.23)$$

In most of the velocity graphs presented in this section it can be argued that there is a distinct peak structure. This statement can be justified by relating the uncertainty in the peaks (determined by using equation (3.23)) to the peak structure, and noting that the data points in the perceived peak structure are greater than this level of uncertainty. The most obvious examples that show a definite peak structure are those of graphs 3.7.c and 3.11.c. Based on this

observation it will be assumed (as it appears to be the case in most of the graphs) that the plasma accelerator produces a series of plasma pulses, and that there is some degree of the merging of these plasma pulses in all the results. Most of the Maxwell – Boltzmann fits applied to the plasma distributions were not completely satisfactory; it was generally found that applying a peak structure to the velocity distributions gave more favourable fits than fitting a single peak. Because there were often only a few data points within the identified plasma peaks to apply the Maxwell – Boltzmann distribution to, the weighted term used to graphically compare the experimental and least squares velocity distributions (refer to section 2.4.6) was calculated using the average of the mean experimental $f(v_{norm})$ value and the immediate values either side of it.

The data obtained from the oscilloscope (measured voltage across the voltage divider as a function of time) are presented as voltage plots as a function of time, referred to as voltage traces. First it must be mentioned that the actual voltage values presented on the voltage traces have not been corrected to show the actual voltage values (from the plasma accelerator, rather they show the voltage values across the voltage divider, refer to section 3.3.1); instead the voltage traces are used to determine the resonant frequency of the plasma accelerator circuit and the length of time that the plasma remains in the plasma accelerator.

Finally, it should be noted that the voltage traces contain a certain amount of noise (inductive noise) due to the discharge of the capacitor inducing inductive noise/ringing in some of the coaxial cables connecting the various pieces of equipment in the plasma accelerator circuit (in particular the cables connecting the energy dump and the voltage divider). This inductive noise is present in the voltage trace and will be especially noticeable as part of the large overvoltage.

The time scale on the voltage traces presented in sections 3.3.4, 3.3.5, 3.3.6 and 3.3.7 have been altered to correspond to the zero time value used to determine the velocity profile of the plasma pulses from the multichannel scaler.

The length of time that the plasma remains in the plasma accelerator, or at least as long as the plasma accelerator is in operation, is determined by the presence of the RLC (resistance, inductance and capacitor) ringing of the plasma accelerator circuit before the voltage trace reverts to the RC (resistance and capacitor) circuit being charged by the high voltage power supply (refer to section 3.3.1). The period of oscillation of the RLC circuit is determined directly from the voltage trace by measuring the time between the maximum amplitudes of the first two peaks (after the large overvoltage), with the assumption that both the resistance and inductance of the plasma accelerator remain constant. It is ad hoc to assume that both the resistance and inductance of the plasma accelerator remain constant, since they are both time dependent properties (due to the motion and position of the plasma). For initial purposes and without exact knowledge of the plasma and its acceleration this assumption will have to stand.

3.3.4: Results of the Lica fitted with a 20cm positive electrode

3.3.4: Results of the Lica fitted with a 20cm positive electrode

Some of the results from the plasma accelerator fitted with a 20cm in length, 3cm in diameter 316 stainless steel positive electrode are presented in graphs 3.4 to 3.7; the experimental settings used to generate these results are presented in table 3.2. The settings on the CDEM are those discussed in section 2.4.1 of chapter 2. Unfortunately the scale on the oscilloscope was incorrectly set (the scale for the amplitude on the oscilloscope was set too low) and only a portion of the amplitude of the voltage traces were recorded for the results presented in graphs 3.4 to 3.7; the period of oscillation of the RLC (resistor, inductor and capacitor) circuit and the time period that the plasma remains inside the plasma accelerator can still be determined from the voltage trace.

Shot number	Hydrogen backing pressure: kPa	Driving pulse length: μ s	Preionization time delay: μ s	Preionization length: μ s	Capacitor voltage: kV	Multichannel scaler bin width: μ s	Oscilloscope sampling frequency: MHz
Shot 1	480	180	270	60	10	1.26	2.5
Shot 2	480	180	270	60	10	1.26	2.5
Shot 3	480	180	270	60	10	1.26	2.5
Shot 4	500	180	270	60	14	1.26	2.5

Table 3.2: Settings on the various pieces of experimental equipment used to conduct tests on the Lica fitted with a 20cm long positive electrode.

The effect of repetitive firing was investigated for two sequential shots, which will be referred to as shot one and shot two of scenario one, were investigated using the experimental procedure described in section 3.3.2; with the exception that after the first shot was fired instead of turning off the high voltage power supply and discharging the capacitor (using the emergency energy dump) the capacitor was allowed to charge up to 10kV. There was a few minutes delay time between the shots to allow the capacitor to charge (the exact charging time taken was not recorded). The results of these two sequential shots were analysed using the methods described in section 3.3.3. The resulting raw data as a function of time, the obtained voltage trace and the calculated velocity distribution are presented for the first shot in graphs 3.4.a, 3.4.b and 3.4.c, and for the second shot in graphs 3.5.a, 3.5.b and 3.5.c. Upon inspection of the positive electrode it was found that there were small arc traces, arc spots and what appeared to be polished regions extending over half the length of the positive electrode. Most notably there were two deep arc traces approximately 1cm in length both originating from the same position at the back of the positive electrode and the sharp edge at the back of the positive electrode

3.3.4: Results of the Lica fitted with a 20cm positive electrode

(refer to section 3.1) showed signs of arc spots and melting in places. The positive electrode was polished and reinstalled in the plasma accelerator. The ground electrode showed little sign of damage, so it was not polished.

Then a single shot (using the previous conditions) was conducted which will be know as shot 3 of scenario two. The resulting raw data as a function of time, the voltage plot and the calculated velocity distribution for this experiment are presented in graphs 3.6.a, 3.6.b and 3.6.c. Upon inspection of the positive electrode very little damage was found, only the presence of arc traces, arc spots and polished regions within the back 5cm were noted. The ground electrode showed little signs of damage as before. The positive electrode was polished and then reinstalled in the plasma accelerator.

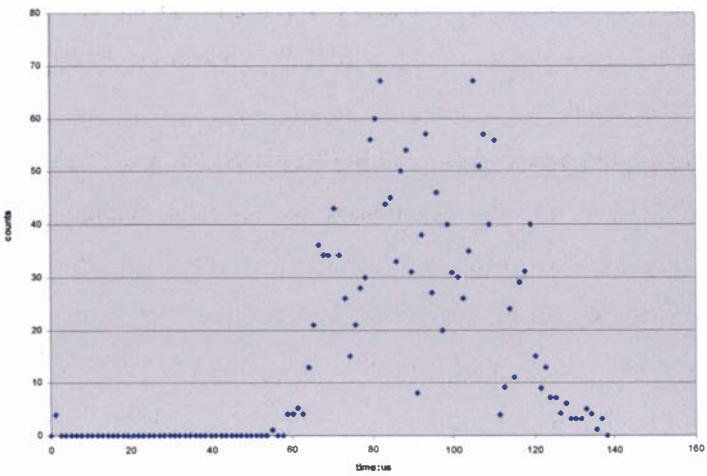
It was found that from initial tests that a minimum voltage of 10kV on the capacitor was required for the preionized gas to breakdown, so a test was conducted at a higher voltage to investigate the effects of this upon the resulting plasma and damage to the accelerator, this experiment will be referred to as shot 4 of scenario three. The raw data as a function of time, the voltage trace and the calculated velocity distribution are given for this scenario in graphs 3.7.a, 3.7.b and 3.7.c. When the positive electrode was inspected only a small amount of surface melting was observed at the start of the positive electrode and faint arc traces were present over a 5cm region at its rear. The grounded electrode still appeared undamaged.

The calculation of the temperature of the plasma using a Maxwell velocity distribution proved difficult; there were only a few data points present in all the velocity distribution graphs. The fittings of a Maxwell distribution, whether based on an overall fit of the data (i.e. considering a single peak for the data set) or individual peaks (based upon inspection) was generally unsatisfactory. It is possible to claim that there are at least three main peaks present in the velocity distributions in the vicinity of 40km/s, 50km/s and 60km/s. The fitting of a Maxwell distribution assuming that there are least three main peaks gave the best results. One of the better fits is shown in graph 3.8.a, it was derived from the velocity distribution of graph 3.4.c in which the temperature was calculated as being 3273K. The corresponding least squares fit of

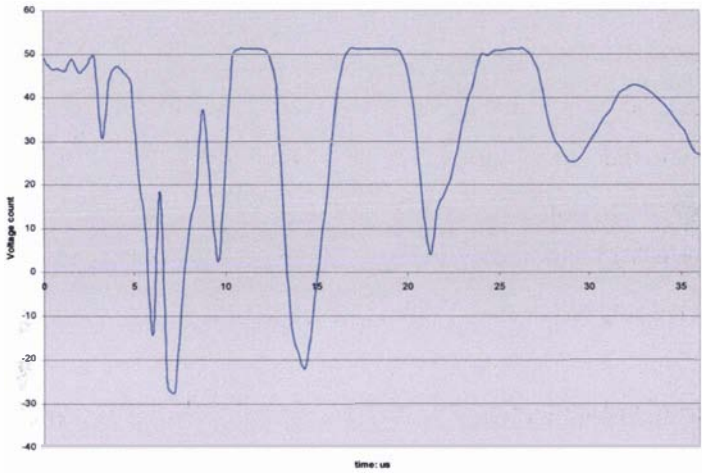
$(v - v_w)^2$ as a function of $\ln\left(\frac{counts}{v}\right)$ used to determine the temperature of the plasma peak

(refer to section 3.3.3) in graph 3.8.a is presented in graph 3.8.b, in which the slope, intercept and the coefficient of determination R^2 of the least squares linear fit have been included. The average R^2 value of the better linear least squares fits is about 0.75, showing that the robustness of these fits is not very satisfactory. The better fits, assuming there are at least three main peaks, suggest that the temperature of the plasma pulses are approximately between 3000K and 7000K.

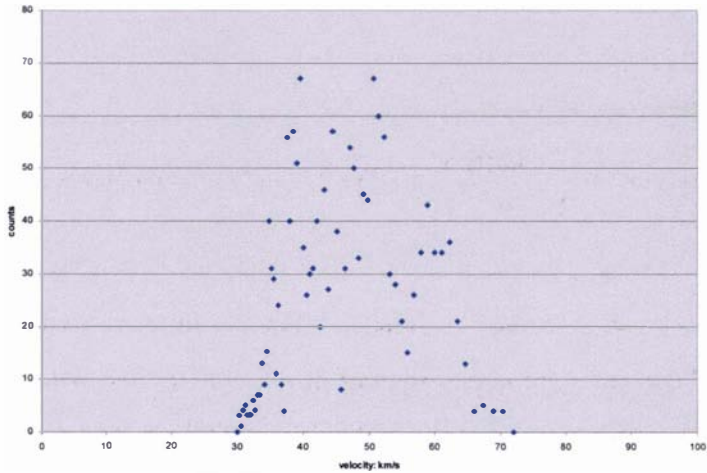
3.3.4: Results of the Lica fitted with a 20cm positive electrode



Graph 3.4.a: Graph of raw data as a function of time for shot 1 of scenario one

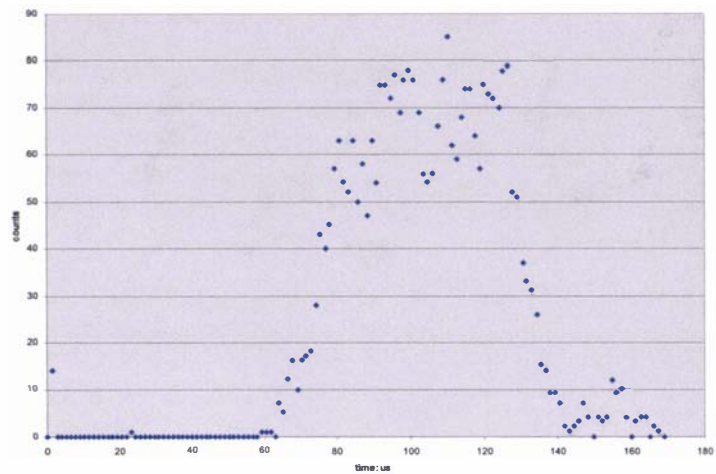


Graph 3.4.b: Graph of the voltage trace as a function of time for shot 1 of scenario one

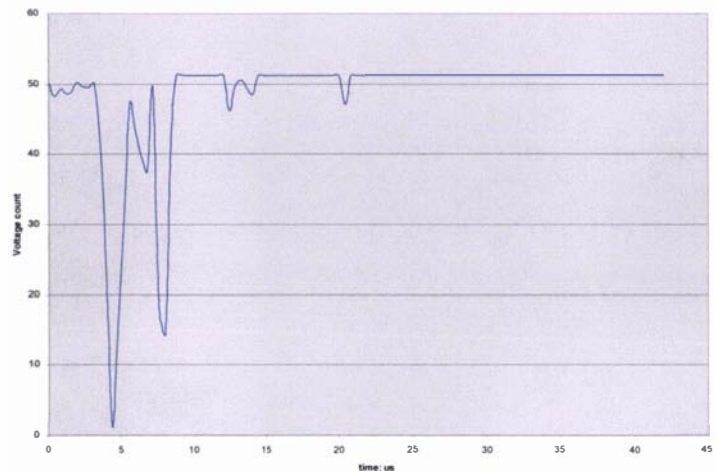


Graph 3.4.c: Graph of the velocity distribution of the plasma as a function of time for shot 1 of scenario one

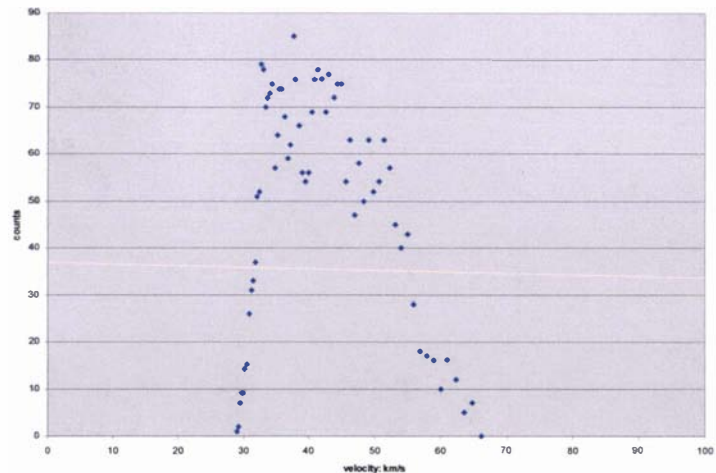
3.3.4: Results of the Lica fitted with a 20cm positive electrode



Graph 3.5.a: Graph of raw data as a function of time for shot 2 of scenario one

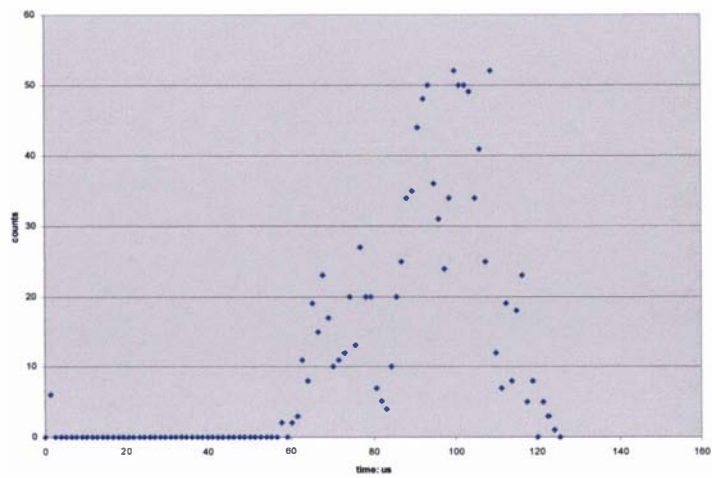


Graph 3.5.b: Graph of the voltage trace as a function of time for shot 2 of scenario one

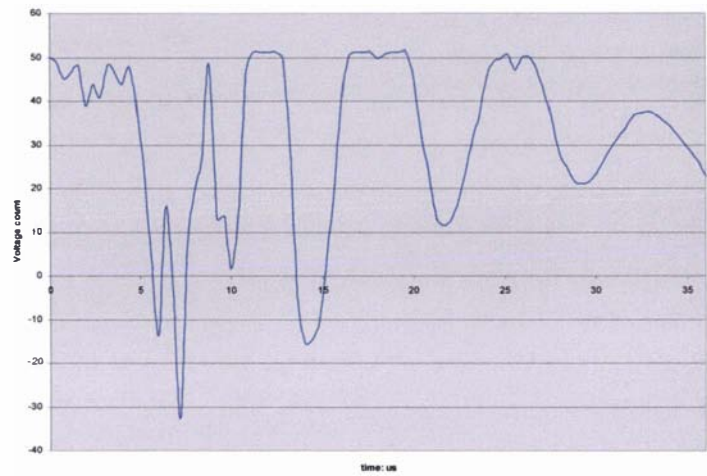


Graph 3.5.c: Graph of the velocity distribution of the plasma as a function of time for shot 2 of scenario one

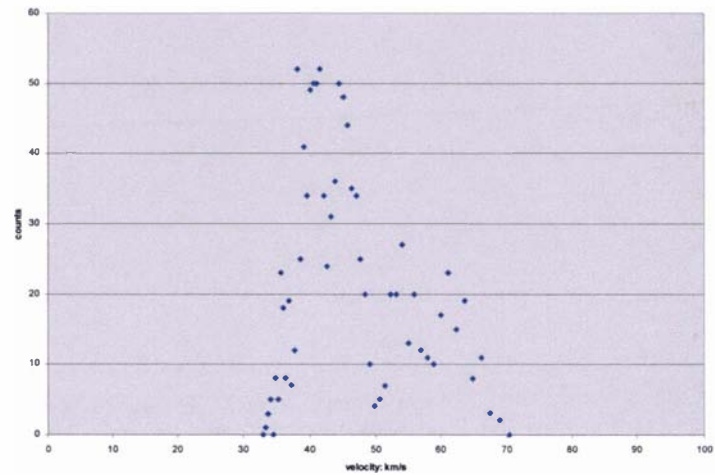
3.3.4: Results of the Lica fitted with a 20cm positive electrode



Graph 3.6.a: Graph of raw data as a function of time for shot 3 of scenario two

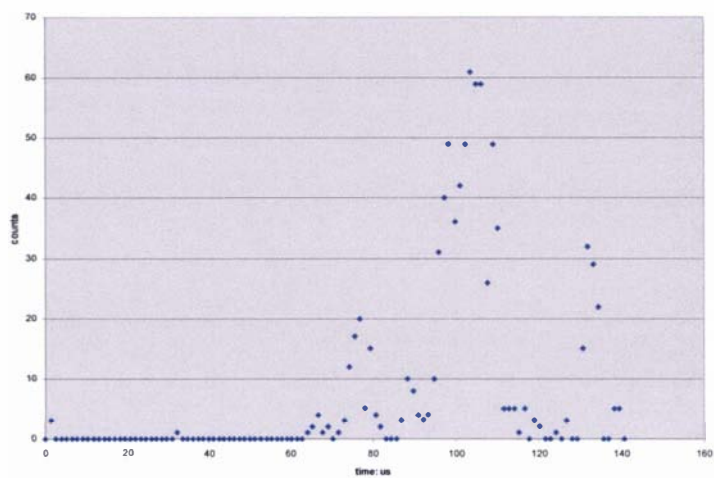


Graph 3.6.b: Graph of the voltage trace as a function of time for shot 3 of scenario two

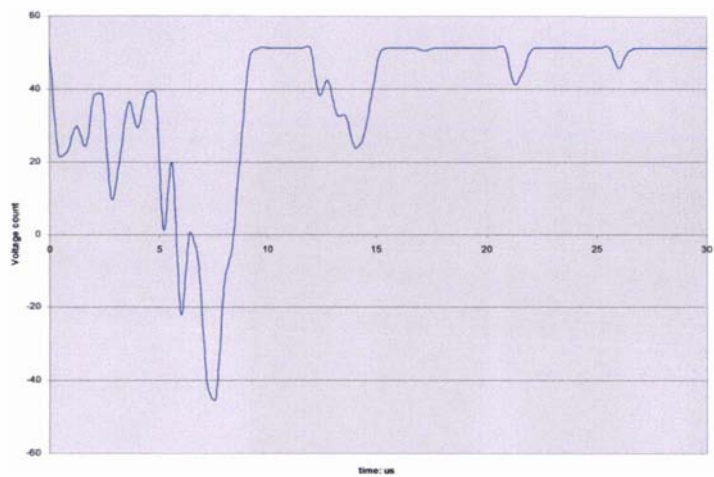


Graph 3.6.c: Graph of the velocity distribution of the plasma as a function of time for shot 3 of scenario two

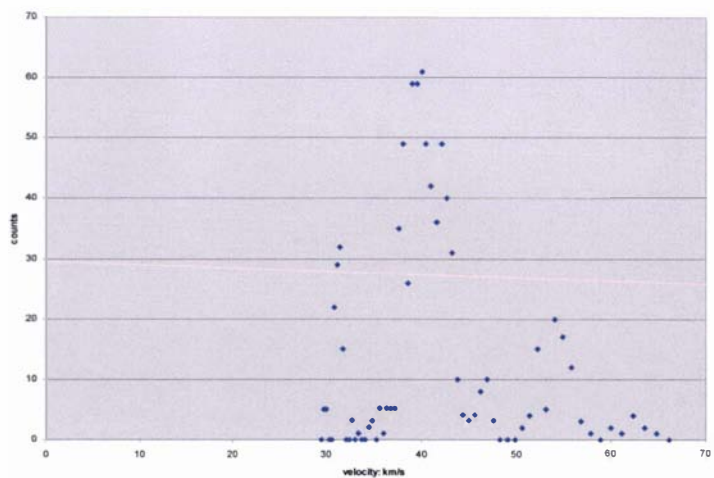
3.3.4: Results of the Lica fitted with a 20cm positive electrode



Graph 3.7.a: Graph of raw data as a function of time for shot 4 of scenario three

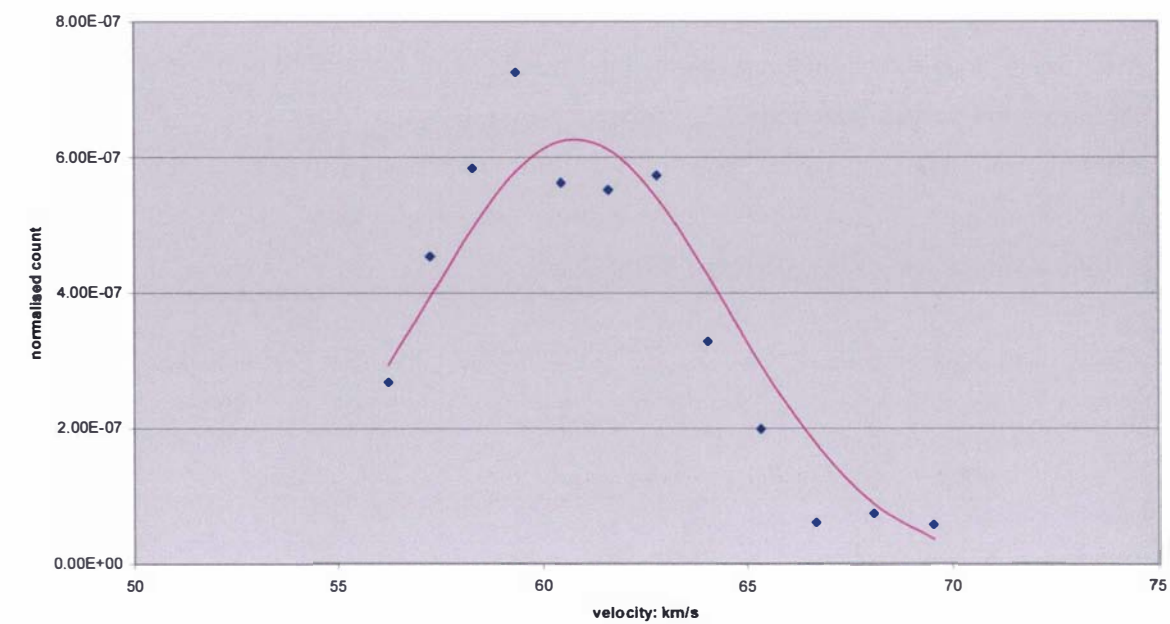


Graph 3.7.b: Graph of the voltage trace as a function of time for shot 4 of scenario three

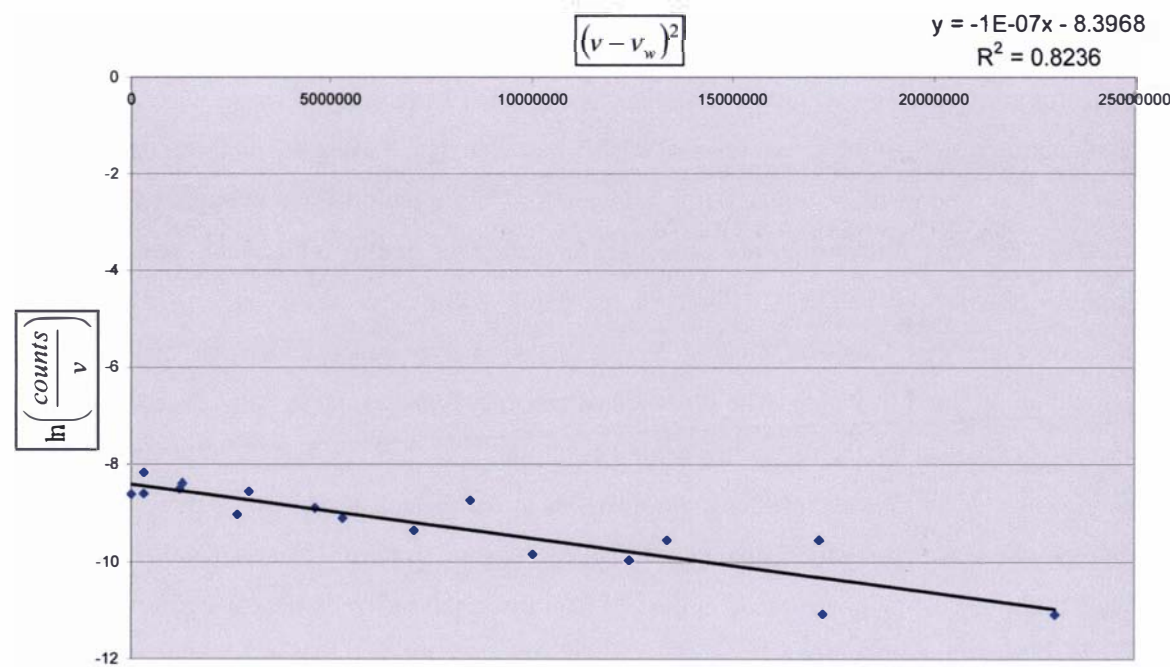


Graph 3.7.c: Graph of the velocity distribution of the plasma as a function of time for shot 4 of scenario three

3.3.4: Results of the Lica fitted with a 20cm positive electrode



Graph 3.8.a: Graph of the Maxwell velocity distribution, fitted by inspection, for the peak in the 60km/s velocity range of graph 3.4.c



Graph 3.8.b: Graph of the least squares fit of $(v - v_w)^2$ as a function of $\ln\left(\frac{\text{counts}}{v}\right)$ for the data points used in graph 3.8.a. The slope, intercept and R^2 value of the fit are displayed above the graph

3.3.5: Results of the Lica fitted with a 10cm positive electrode

3.3.5: Results of the Lica fitted with a 10cm positive electrode

After the tests on the plasma accelerator fitted with a 20cm in length positive electrode were completed the positive electrode was replaced with a 10cm in length, 3cm in diameter 316 stainless steel positive electrode, some of the results are presented in graphs 3.9 to 3.11. The experimental settings used to generate these results are given in table 3.3. The settings on the CDEM are those discussed in section 2.4.1 of chapter 2.

Shot number	Hydrogen backing pressure: kPa	Driving pulse length: μ s	Preionization time delay: μ s	Preionization length: μ s	Capacitor voltage: kV	Multichannel scaler bin width: μ s	Oscilloscope sampling frequency: MHz
Shot 5	477	180	270	60	10	1.26	2.5
Shot 6	477	180	270	60	10	1.26	2.5
Shot 7	499	180	300	30	10	1.26	2.5

Table 3.3: Settings on the various pieces of experimental equipment used to conduct tests on the Lica fitted with a 10cm long positive electrode.

The effect of repetitive firing was reinvestigated using the new positive electrode for two sequential shots, which shall be referred to as shot 5 and shot 6 of scenario four. The two sequential shots were investigated using the same method as outlined in the previous section of 3.3.4 and the results of these two sequential shots were analysed using the methods described in section 3.3.3. The resulting raw data as a function of time, the obtained voltage trace and the calculated velocity distribution are presented for shot 5 in graphs 3.9.a, 3.9.b and 3.9.c, and graphs 3.10.a, 3.10.b and 3.10.c for shot 6. At the sharp edge at the back of the positive electrode there was localized melting in places, and the presence of a small melted patch approximately 5mm in length. The presence of arc traces and arc spots were observable from 1.5cm to 9cm along the length of the positive electrode.

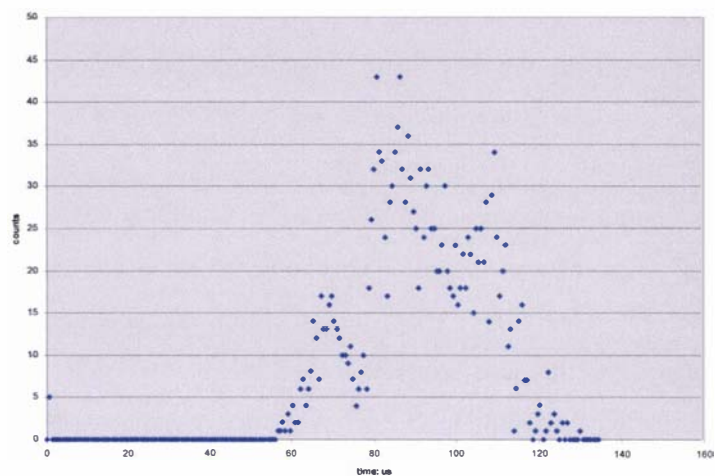
The positive electrode was polished and reinstalled in the plasma accelerator, a new experiment using only a single shot which shall be termed as shot 7 of scenario five was conducted. Using the methods discussed in section 3.3.3 the raw data was analysed to produce a graph of raw data as a function of time, a voltage trace and a calculated velocity distribution, which are shown in graphs 3.11.a, 3.11.b and 3.11.c. The results of the visual inspection of the positive electrode were not recorded before it was re-polished.

As discovered in the previous section of 3.3.4 the calculation of the temperature of the plasma by fitting a Maxwell velocity distribution to the data was difficult, due to the limited number of data points. Fitting a distribution to all the data points present in the velocity distributions did

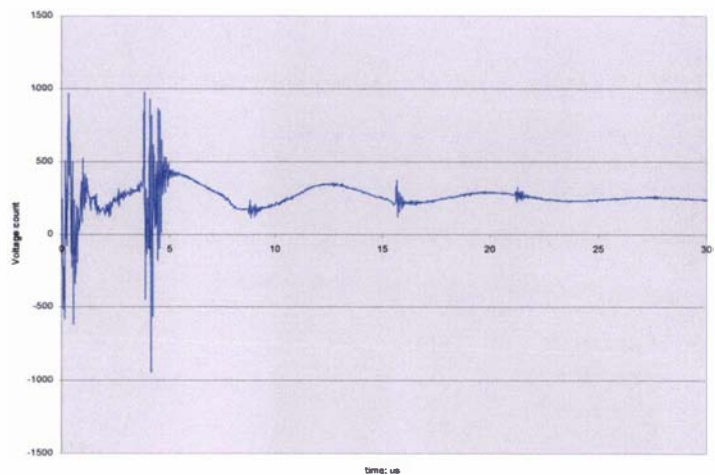
3.3.5: Results of the Lica fitted with a 10cm positive electrode

not give satisfactory results. It can be argued, as in the previous section, that there are at least three main peaks present in the velocity distributions in the regions of 40km/s, 50km/s and 60km/s, with the possibility of a further peak in the region of 70km/s. The peak in the 70km/s is most notably present in graph 3.10.c and can also be identified in graphs 3.9.c and 3.11.c; however in these two graphs the peaks in this region are so small that they could be construed as part of the statistical error of the graphs. The fitting of Maxwell distributions using the assumption that there are at least three main peaks gave reasonable results for some of the identified peaks, suggesting that the temperature of the plasma pulses are approximately between 1000K and 5600K. An example of one of the better fits is shown in graph 3.12.a; it was derived from the velocity distribution of graph 3.11.c, in which the temperature of the plasma was calculated to be approximately 1078K. The corresponding least squares fit of $(v - v_w)^2$ as a function of $\ln\left(\frac{\text{counts}}{v}\right)$ (including the slope, intercept and the coefficient of determination R^2 of the least squares linear fit) used to determine the temperature of the plasma peak in graph 3.12.a is presented in graph 3.12.b (refer to section 3.3.3 for a description of the method used to determine the temperature of the plasma peaks). The average R^2 value of the better linear least squares fits is about 0.75, showing that the robustness of these fits is again not very satisfactory.

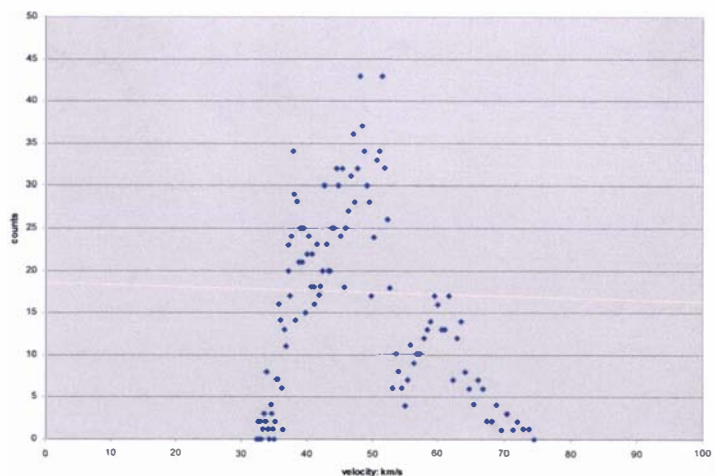
3.3.5: Results of the Lica fitted with a 10cm positive electrode



Graph 3.9.a: Graph of raw data as a function of time for shot 5 of scenario four

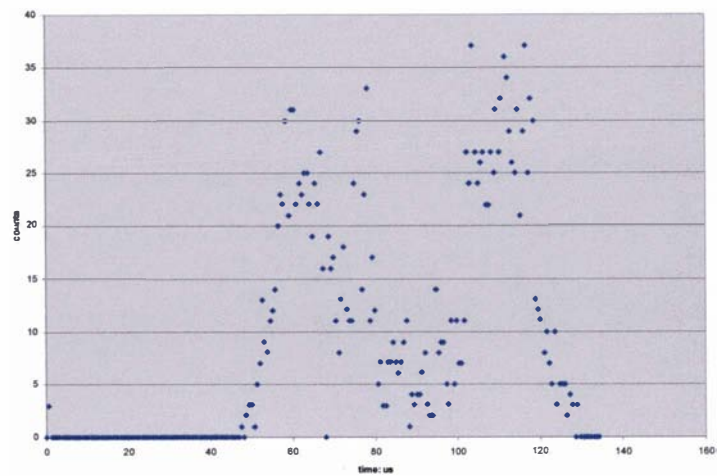


Graph 3.9.b: Graph of the voltage trace as a function of time for shot 5 of scenario four

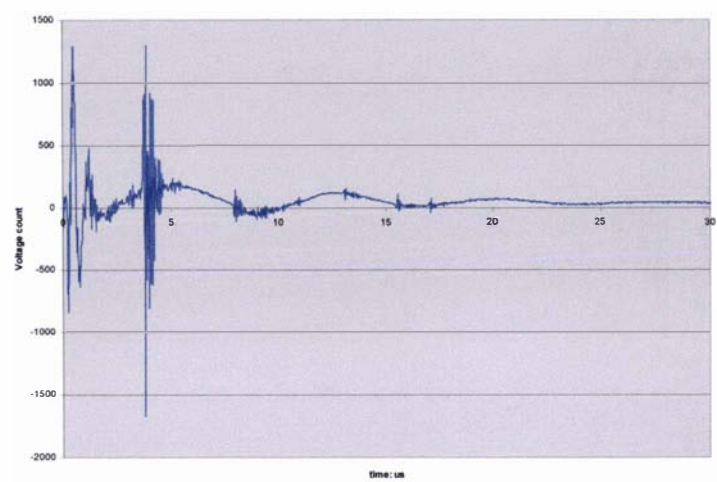


Graph 3.9.c: Graph of the velocity distribution of the plasma as a function of time for shot 5 of scenario four

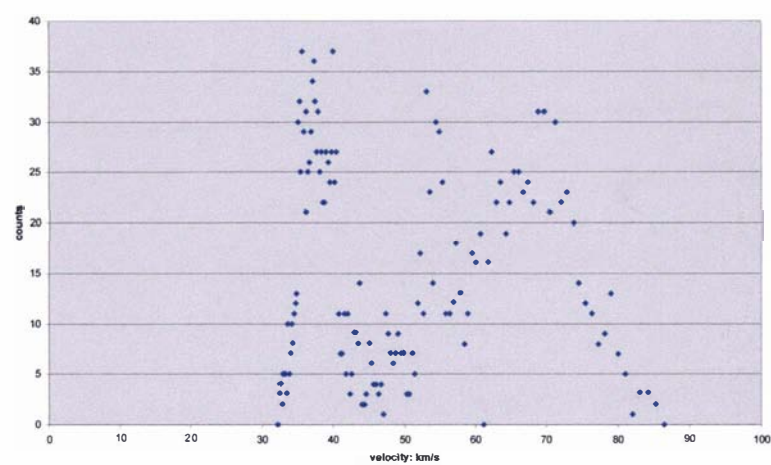
3.3.5: Results of the Lica fitted with a 10cm positive electrode



Graph 3.10.a: Graph of raw data as a function of time for shot 6 of scenario four

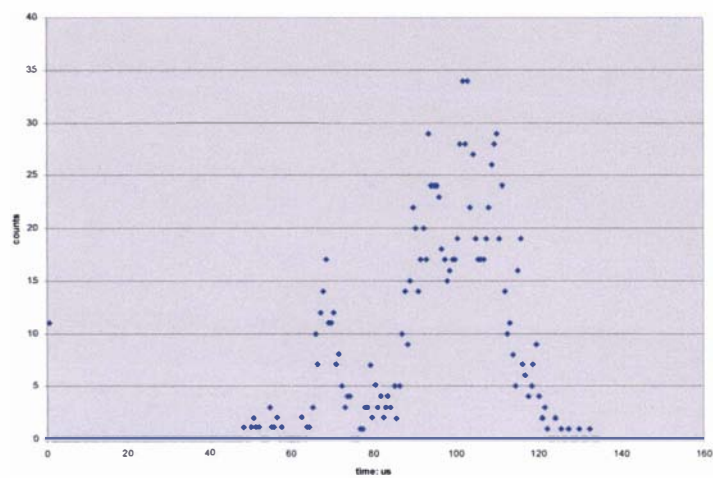


Graph 3.10.b: Graph of the voltage trace as a function of time for shot 6 of scenario four

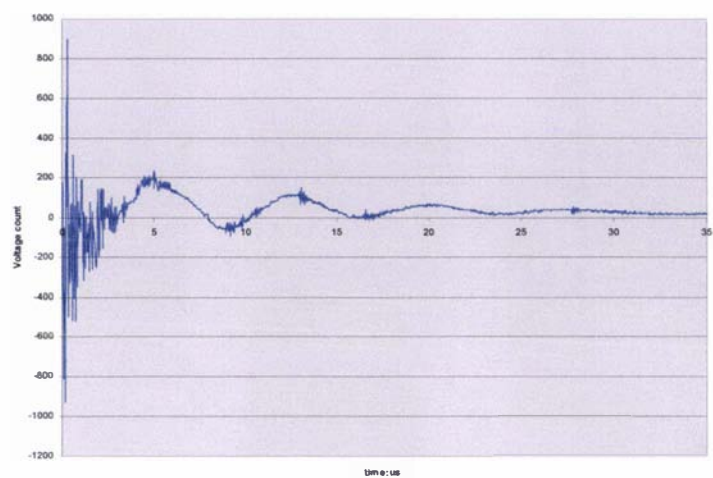


Graph 3.10.c: Graph of the velocity distribution of the plasma as a function of time for shot 6 of scenario four

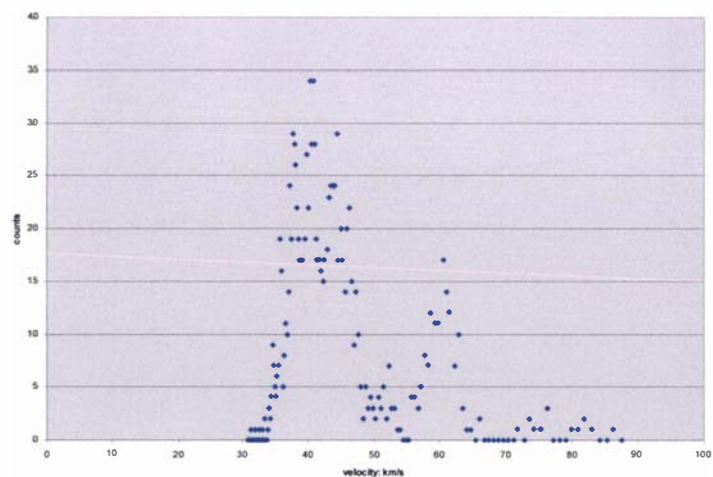
3.3.5: Results of the Lica fitted with a 10cm positive electrode



Graph 3.11.a: Graph of raw data as a function of time for shot 7 of scenario five

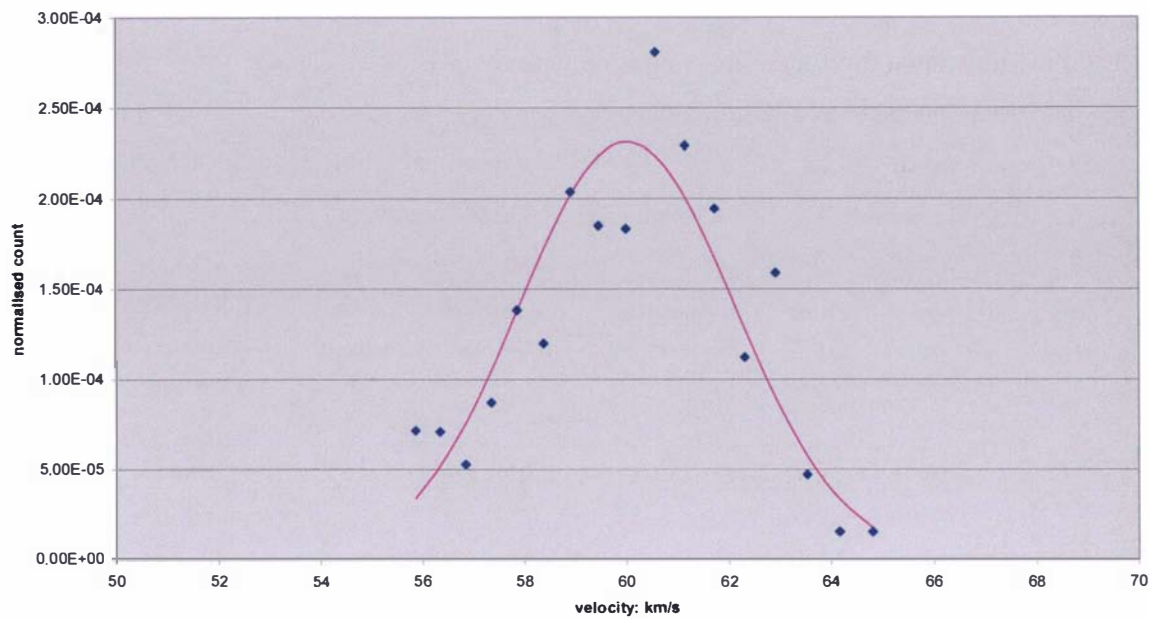


Graph 3.11.b: Graph of the voltage trace as a function of time for shot 7 of scenario five

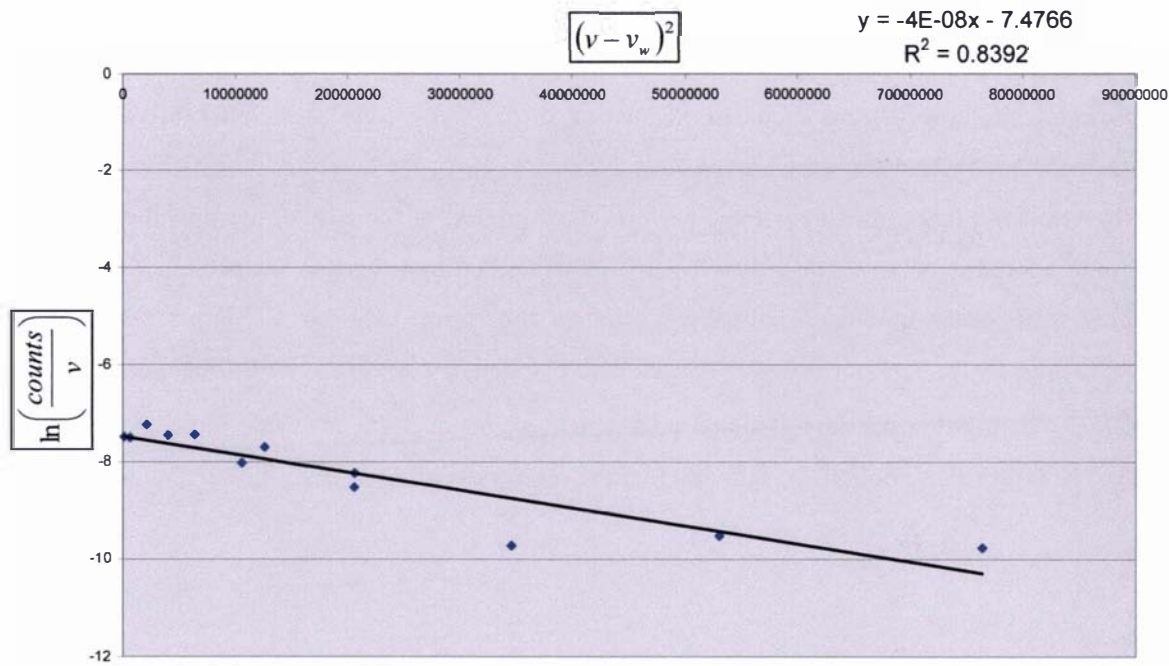


Graph 3.11.c: Graph of the velocity distribution of the plasma as a function of time for shot 7 of scenario five

3.3.5: Results of the Lica fitted with a 10cm positive electrode



Graph 3.12.a: Graph of the Maxwell velocity distribution, fitted by inspection, for the peak in the 60km/s velocity range of graph 3.11.c



Graph 3.12.b: Graph of the least squares fit of $(v - v_w)^2$ as a function of $\ln\left(\frac{\text{counts}}{v}\right)$ for the data points used in graph 3.12.a. The slope, intercept and R^2 value of the fit are displayed above the graph

3.3.6: Results of the Lica fitted with a 5cm positive electrode

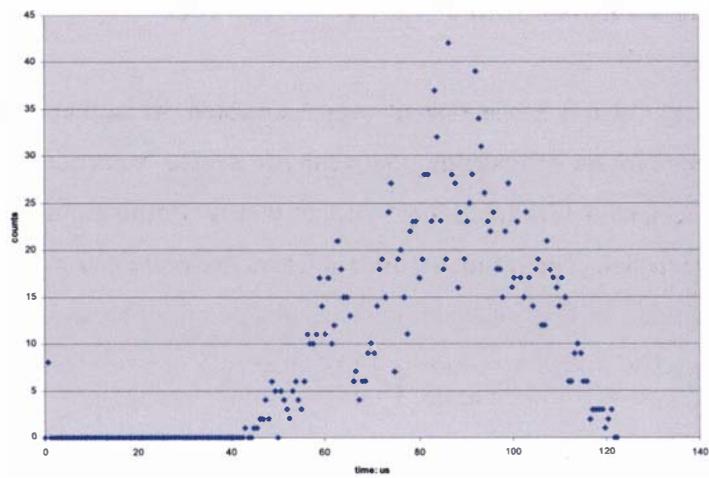
The final tests upon the Lica were conducted with the plasma accelerator fitted with a 5cm in length, 3cm in diameter 316 stainless steel positive electrode, the results of which are presented for a single shot in graphs 3.13.a to 3.13.c. The experimental settings used to generate these results are given in table 3.4. The settings on the CDEM are covered in section 2.4.1.

Shot number	Hydrogen backing pressure: kPa	Driving pulse length: μ s	Preionization time delay: μ s	Preionization length: μ s	Capacitor voltage: kV	Multichannel scaler bin width: μ s	Oscilloscope sampling frequency: MHz
Shot 8	511	180	300	30	10	1.26	2.5

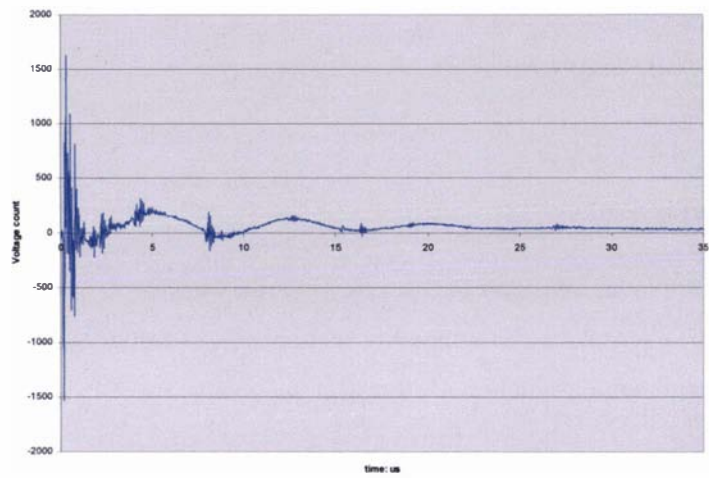
Table 3.4: Settings on the various pieces of experimental equipment used to conduct initial tests on the Lica fitted with a 5cm long positive electrode.

The results of a single shot, which shall be known as shot 8 of scenario six, were analysed using the methods outlined in section 3.3.3. The raw data as a function of time, the voltage trace and the calculated velocity distribution are given in graphs 3.13.a, 3.13.b and 3.13.c. A second shot was conducted after the first shot but it produced a misfire; the results of this second shot are presented in section of 3.3.7. After the second shot was conducted the positive electrode was inspected, it showed signs of localised melting of the sharp edge at the back of the positive electrode and there were some arc traces and arc spots along the length of the positive electrode. Most notably, large polished/melted regions were present at the rear of the positive electrode (some approximately 1.5cm in length). It can be argued that there is the presence of at least three main peaks in the velocity distribution in the region of 45km/s, 75km/s and 85km/s. Unfortunately, it was not possible to satisfactorily derive a temperature by fitting a Maxwell velocity distribution for any assumed peak structure; the average R^2 value of the better linear least squares fits is about 0.53, showing that the robustness of these fits is unsatisfactory.

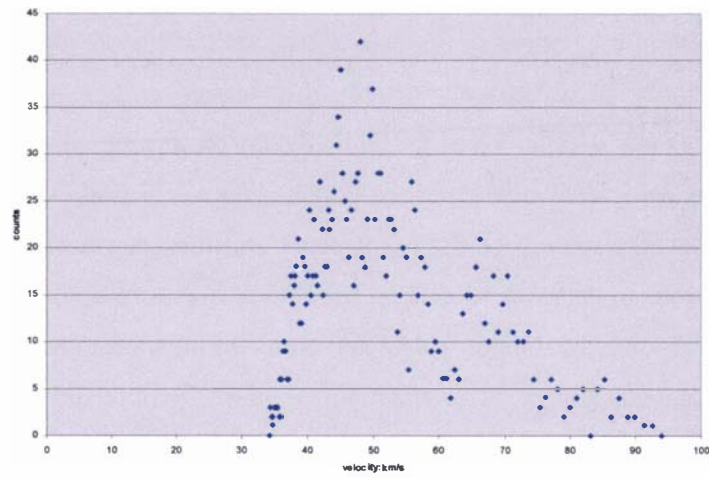
3.3.6: Results of the Lica fitted with a 5cm positive electrode



Graph 3.13.a: Graph of raw data as a function of time for shot 8 of scenario six



Graph 3.13.b: Graph of the voltage trace as a function of time for shot 8 of scenario six



Graph 3.13.c: Graph of the velocity distribution of the plasma as a function of time for shot 8 of scenario six

3.3.7: Results observed from misfires

In some instances high velocity plasma pulses were generated, which have been referred to as “misfires”. During the process of obtaining the results presented in sections 3.3.5 and 3.3.6 (in which the plasma accelerator was fitted with a 10cm then a 5cm in length positive electrode) two misfires were generated. The results of these misfires are presented in graphs 3.14 to 3.15. The experimental settings used to generate these results are presented in table 3.5; the settings on the CDEM are those discussed in section 2.4.1 of chapter 2.

Shot number	Positive electrode length: cm	Hydrogen backing pressure: kPa	Driving pulse length: μ s	Preionization time delay: μ s	Preionization length: μ s	Capacitor voltage: kV	Multichannel scaler bin width: μ s	Oscilloscope sampling frequency: MHz
Shot 9	5	511	180	300	30	10	1.26	2.5
Shot10	10	501	180	300	30	10	1.26	2.5

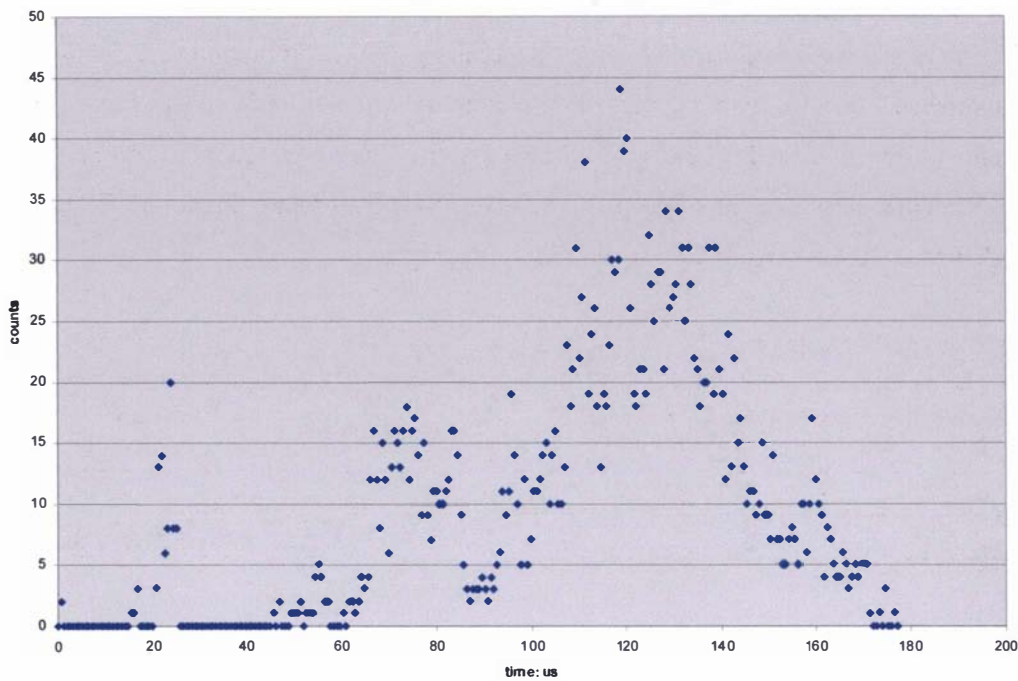
Table 3.5: Settings on the various pieces of experimental equipment used in the operation of the Lica, in which misfires were observed

A misfire occurred on the second shot of the experiment conducted in section 3.3.6 this will be referred to as shot 9. The results of this misfire were analysed using the methods discussed in section 3.3.3; the raw data as a function of time and the voltage trace are given in graphs 3.14.a and 3.14.b. The calculated velocity distribution is classified as two distinct regions: one containing what appears to be the typically observed velocity distribution presented in graph 3.14.c, and a high velocity plasma region shown in graph 3.14.d. In the typically observed velocity distribution (3.14.c) it can be argued (as noted before in section 3.3.6) that there are at least three main peaks in the regions of 35km/s, 55km/s and 75km/s. Unfortunately, it was not possible to satisfactorily fit a Maxwell velocity distribution to these results for either the typically observed velocity distribution or the high velocity plasma region.

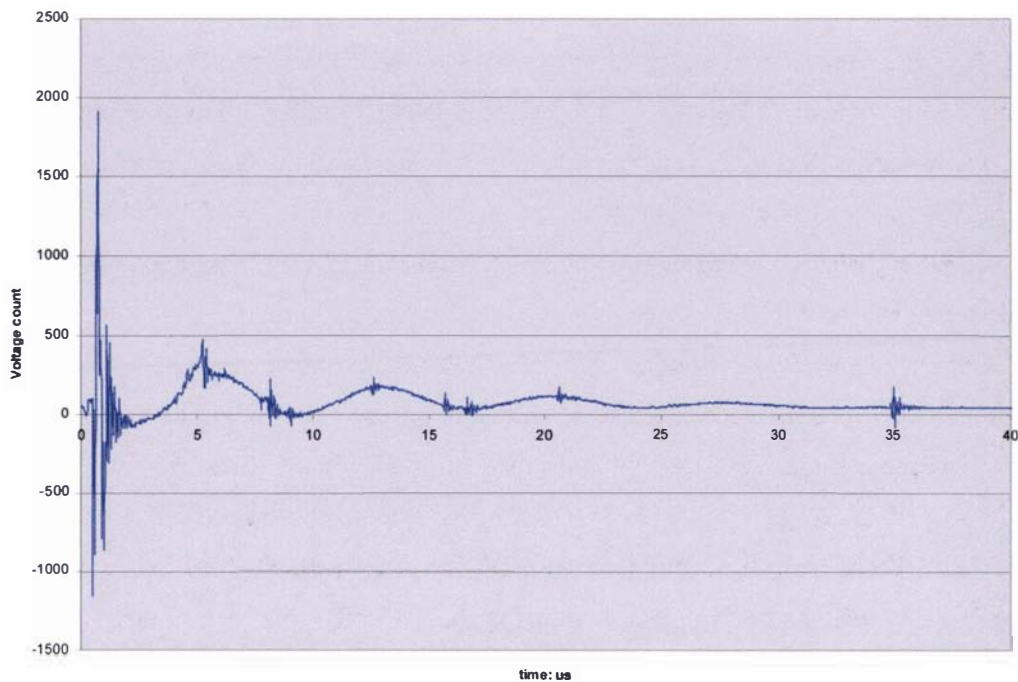
The misfire that was generated on the 10cm in length positive electrode shall be referred to as shot 10. Unfortunately, the settings on the oscilloscope (for this set of results) were incorrectly set and no useable voltage data was recorded. The raw data as a function of time is shown in graph 3.15.a. The velocity distribution calculated from the method given in section 3.3.3 is presented as two distinct regions, one containing the typically observed velocity distribution shown in graph 3.15.c and a high velocity plasma region presented in graph 3.15.d. It was not possible to estimate the temperature of the high velocity plasma region as there were not enough data points to do so. It is possible to distinguish at least two main peaks in graph 3.15.c, in the regions of 45km/s and 55km/s. Assuming this peak structure, it was possible to fit a Maxwell

3.3.7: Results observed from misfires

velocity distribution, which gave an approximate temperature value of 3000K and 1000K for the respective peaks.

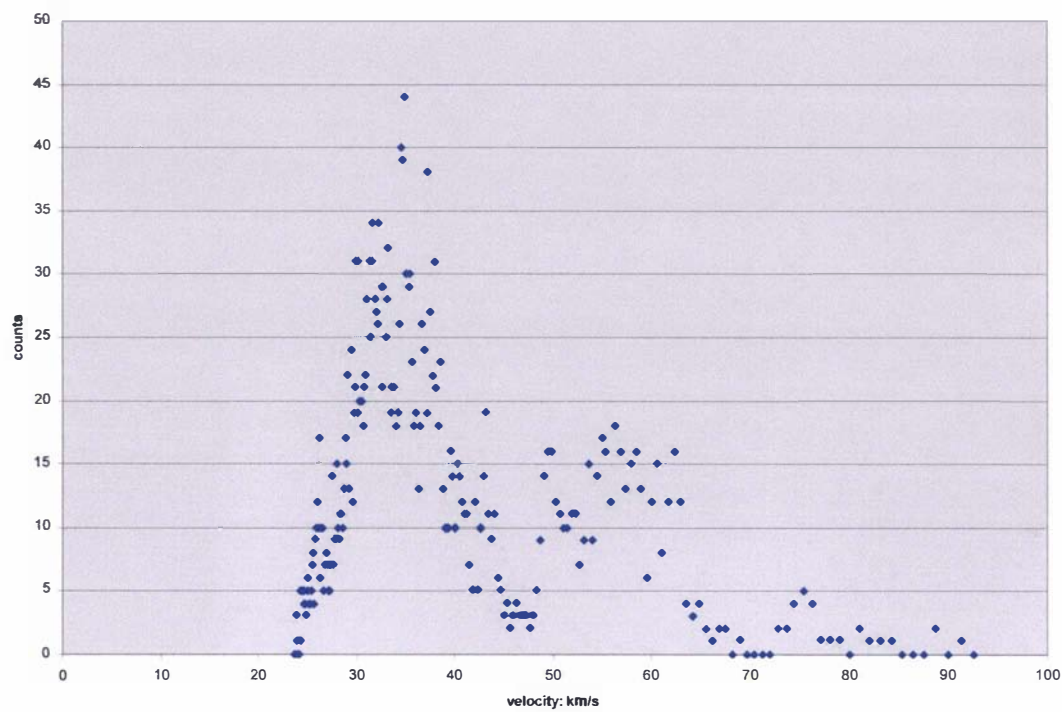


Graph 3.14.a: Graph of raw data as a function of time for a misfire, generated with the plasma accelerator fitted with a 5cm positive electrode (shot 9).

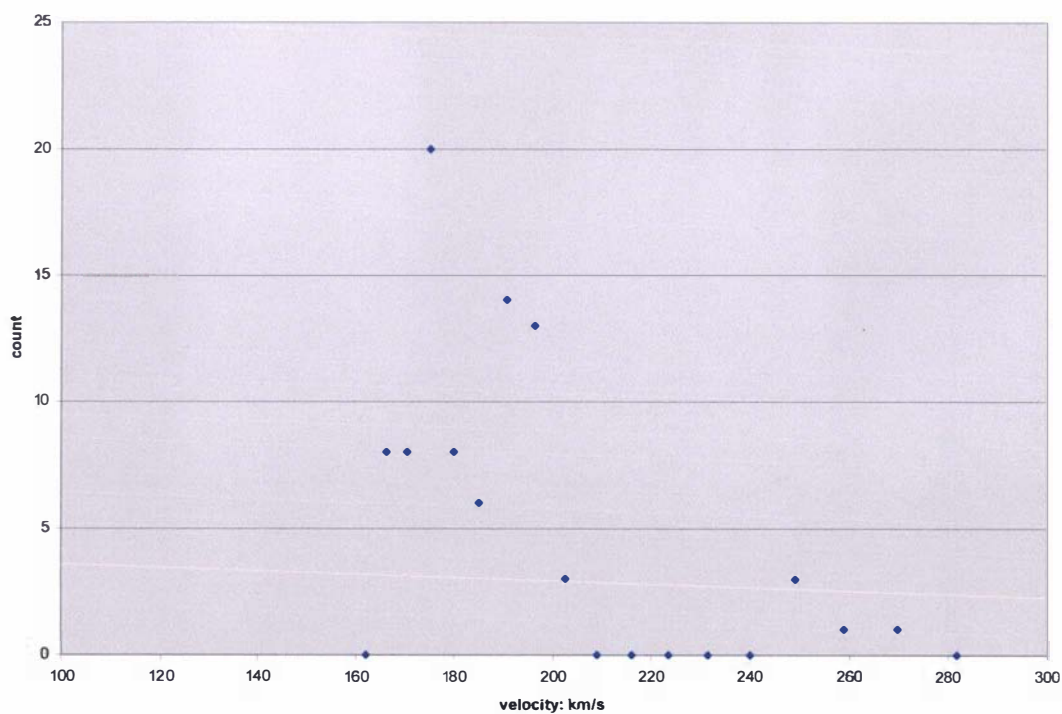


Graph 3.14.b: Graph of the voltage trace as a function of time for a misfire, generated with the plasma accelerator fitted with a 5cm electrode (shot 9)

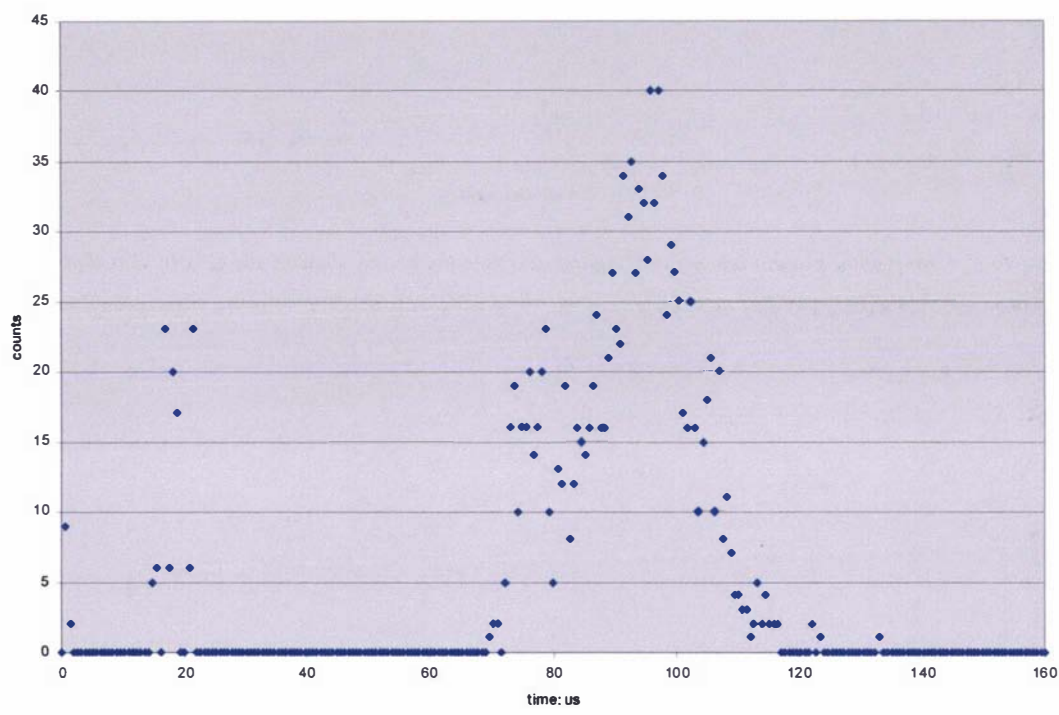
3.3.7: Results observed from misfires



Graph 3.14.c: Graph of the plasma velocity distribution as a function of time showing the velocity distribution below 100km/s for a misfire, generated with the plasma accelerator fitted with a 5cm positive electrode (shot 9)

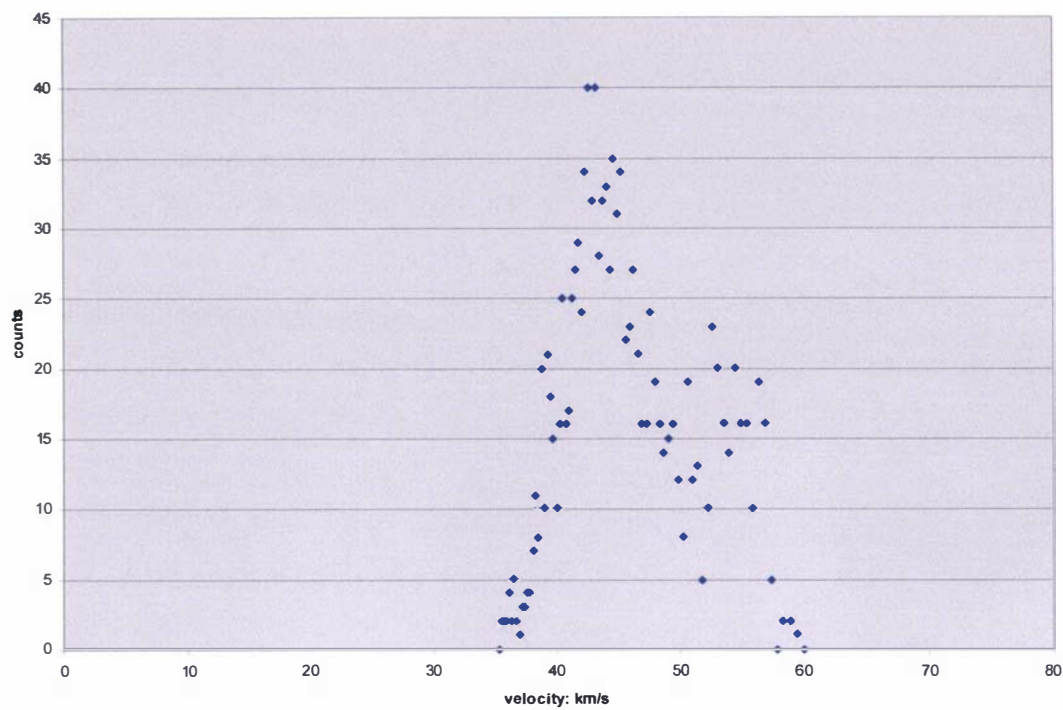


Graph 3.14.d: Graph of plasma the velocity distribution as a function of time showing the velocity distribution above 100km/s for a misfire, generated with the plasma accelerator fitted with a 5cm positive electrode (shot 9)

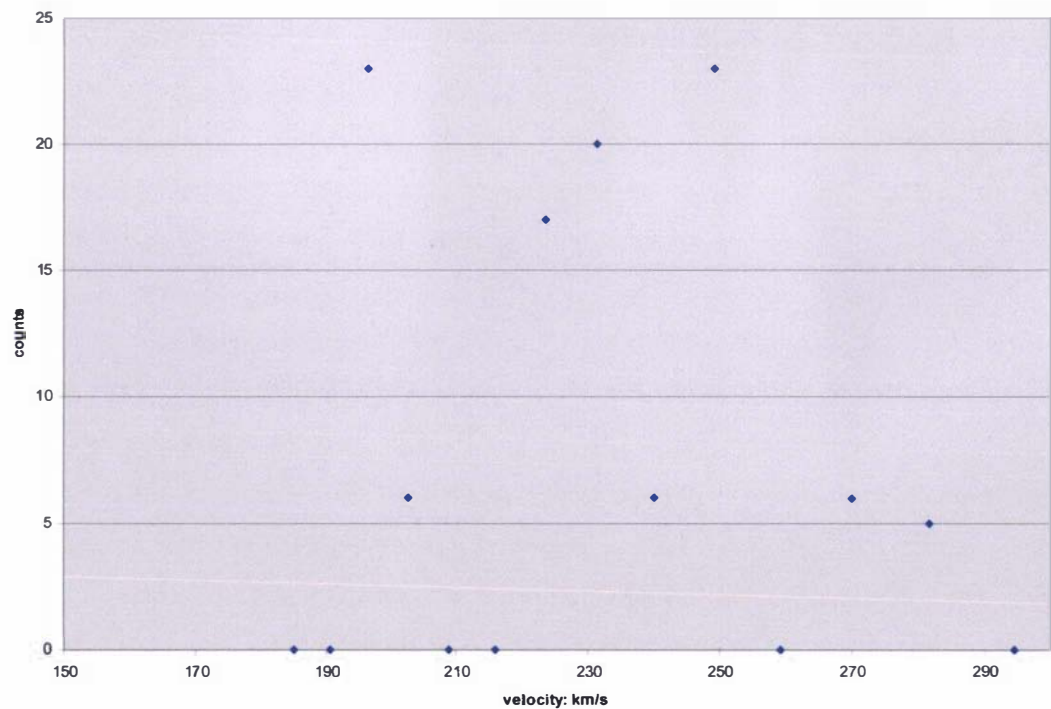


Graph 3.15.a: Graph of raw data as a function of time for a misfire, generated with the plasma accelerator fitted with a 10cm positive electrode (shot 10)

3.3.7: Results observed from misfires



Graph 3.15.c: Graph of the plasma velocity distribution as a function of time showing the velocity distribution below 100km/s for a misfire, generated with the plasma accelerator fitted with a 10cm positive electrode (shot 10)



Graph 3.15.d: Graph of the plasma velocity distribution as a function of time showing the velocity distribution above 100km/s for a misfire, generated with the plasma accelerator fitted with a 10cm positive electrode (shot 10)

3.3.8: Discussion on the performance of the Lica

Firstly, it can be claimed that the Lica is a working plasma accelerator from the fact that the CDEM was able to detect the presence of ionized material, as seen in the results generated in sections 3.3.4, 3.3.5, 3.3.6 and 3.3.7. Secondly, the novel preionization method and the unique linearly injected plasma accelerator are both practical options in the construction of a plasma accelerator, even though at this stage of development the Lica is only a prototype and has yet to be fully optimised. The Lica is yet to achieve the main aim of this research, that of the construction of a plasma accelerator that is capable of accelerating 0.2mg of hydrogen plasma at velocities in excess of 200km/s and be capable at operating at a frequency of 10Hz. Currently, because of the skimmer placed in front of the valve, the actual total mass that is being accelerated, as discussed in section 2.4.10, is 1.88×10^{-4} mg. The upper velocity limit under typical conditions that has been recorded so far is 80km/s, however the bulk of the plasma appears to be travelling (on average) in approximately the range of 40km/s to 50km/s. The prospect of repetitive operation at 10Hz has yet to be investigated.

From the results presented in sections 3.3.4, 3.3.5 and 3.3.6 there is a strange anomaly, it is expected that the results gained from the accelerator fitted with a longer positive electrode should show a faster overall velocity distribution than those with a shorter positive electrode. However in the experimental results it appears that the length of the positive electrode has little effect on the velocity distribution of the plasma, suggesting the possibility that the acceleration of the plasma occurs in the first five centimetres. It also appears that there is more than one plasma peak present (refer to the discussion given in section 3.3.3), in general it appears that there are at least three peaks in the approximate regions of 40km/s, 50km/s and 60km/s to 80km/s, with the bulk of the plasma travelling in the region of 40km/s to 50km/s. It is possible to hypothesize that as it has been assumed that the neutral gas pulse is preionized just before or just as it enters the plasma accelerator (as discussed in section 3.3.1) that a series of plasma pulses are being accelerated rather than a distinct plasma mass, in which a portion of the preionized gas breaks down (satisfying the breakdown conditions discussed in sections 3.3.1) and is accelerated until it either leaves the accelerator or another portion of the preionized gas (within the plasma accelerator) satisfies the breakdown conditions. This process is repeated until either all the preionized gas has been accelerated or the point at which either the capacitor is drained of energy or no longer has enough voltage to initiate the formation of further plasma sheaths. A further possibility is that due to the evidence of ablation present on the electrodes the Lica has in fact been accelerating a series of plasma pulses consisting primarily of ablated material; however without experimental analysis of the plasma the exact composition of the plasma being accelerated remains unknown. The effect of plasma instabilities and other factors,

discussed in section 1.3, on the performance of the plasma accelerator also remains unknown due to the lack of experimental equipment.

The temperature of the plasma estimated by fitting a Maxwell – Boltzmann distribution, with the assumption that the plasma is a hydrogen plasma, was difficult because there were limited data points available and it was not always possible to satisfactorily fit a Maxwell distribution to the data. The fitting of a several Maxwell distributions to the data, assuming that there were several peaks rather than a single peak structure gave the best fits, gave an average R^2 value of about 0.75 showing that the robustness of the linear least squares fit although not completely satisfactory gives a rough fit. It is still unclear as to whether or not the assumption that the plasma has had enough time to come to a thermal equilibrium is justified because: fitting a Maxwell – Boltzmann distribution gives a rough fit to the data, there are often only a few points to fit the distribution to (especially for the plasma in the region above 60km/s) and there is a certain degree of the merging of the plasma peaks in most of the distributions making individual fits difficult. The longitudinal temperature of the plasma calculated in this fashion was found to be somewhere in the range of 1000K to 7000K, with the majority of the Maxwell – Boltzmann fits suggesting that the average temperature of the plasma lies between 3000K and 5000K. Spectrographic equipment was not available to experimentally determine the temperature of the plasma so at present this remains the only way of determining the temperature based on the limited information available. The calculated temperature of the plasma from the Lica is much colder than that observed from other coaxial plasma accelerators, such as the LRT accelerator [35] in which the temperature of the plasma was calculated to be in the region of 15000K (this accelerator was operated in the snow plough mode of operation). The coldness of the plasma generated in the Lica could be attributed to the low densities involved, rather than its method of operation.

The voltage traces from sections 3.3.4, 3.3.5 and 3.3.6 show that the entire acceleration process within the Lica is finished within 22 μ s to 32 μ s. The voltage traces all contain a large over voltage, except for the results generated for the Lica fitted with a 20cm in length positive electrode; due to incorrect settings on the oscilloscope for this set of results it is not possible to see the over voltage (as stated before in section 3.3.3). This over voltage has been assumed to correspond to the initial breakdown of the preionized hydrogen gas; this seems to be confirmed by the corresponding presence of a small peak on the multichannel scaler at the same time. The small peak observed on the multichannel scaler can be attributed to photoionization effects upon the CDEM from the large amount of ultra violet light released from the breakdown of the preionized gas (as mentioned in section 3.3.3).

All the voltage traces show that there are between three and four voltage cycles decreasing in amplitude (although it is a little hard to see on some of the voltage traces in section 3.3.4) giving a period of oscillation of approximately 7 μ s. The exact breakdown mechanism within the Lica

remains unknown, because high speed photography and spectrographic equipment were not available to analyse the formation of the hydrogen plasma; all that can be said on this point is that a minimum voltage of 10kV was required on the capacitor to initiate the breakdown of the preionized gas under the conditions used in experiments presented in sections 3.3.4 to 3.3.7.

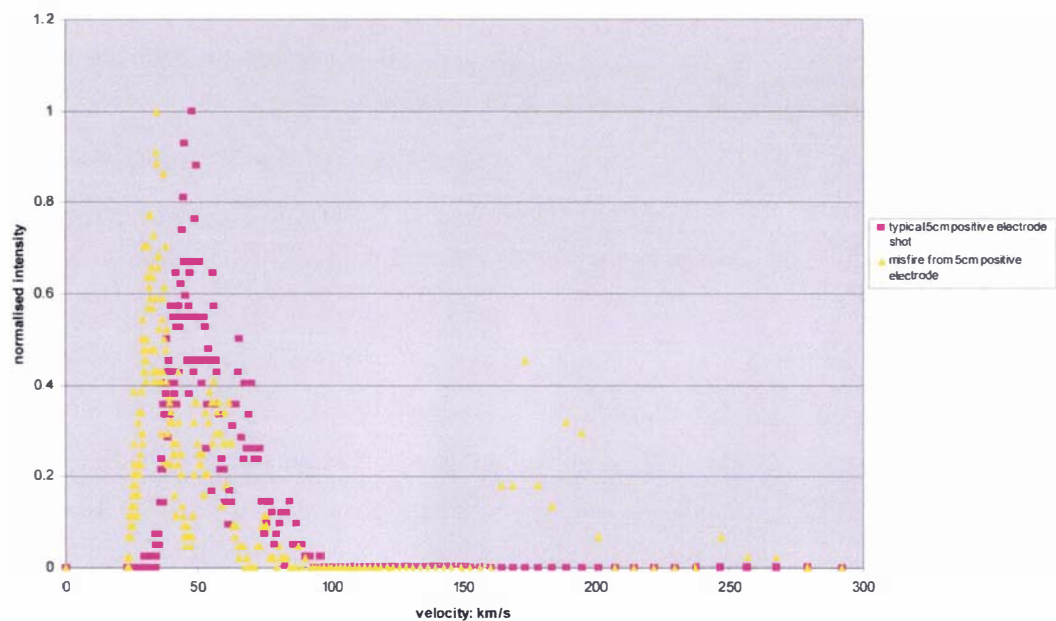
The observed damage on the positive electrode of melted/polished surfaces, arc traces and spots are the typical damage associated with ablation as discussed in section 1.3 of chapter 1. It was expected that the positive electrode would show more signs of damage than the grounded electrode, because there is a higher electric field gradient present at the positive electrode compared to the grounded electrode (due to the geometry of the plasma accelerator being coaxial). The presence of this large electric field would increase the damage on the positive electrode from electron bombardment (due to the acceleration of electrons towards it), because one of the breakdown mechanisms of the preionized gas is likely to be an electron avalanche mechanism (refer to section 3.2.1). It appears that ablation occurred in every shot conducted in the Lica; the effects of this ablation appear to be confined to the back regions of the positive electrodes within a length of 5cm to 10cm. The problem of ablation needs to be minimised to optimise the performance of the plasma accelerator. The 316 stainless steel currently used as a positive electrode material needs to be either replaced by a more durable electrically conducting material that has higher melting/vaporisation characteristics or coated by such a material, this remains an aspect for future research.

The anomaly of misfires remains speculative at this point, because the exact breakdown mechanism remains unknown. In general it was found that misfires occurred in the situations where sequential shots were fired (the actual time between shots required to recharge the capacitor, although not properly recorded, was in the order of a few minutes).

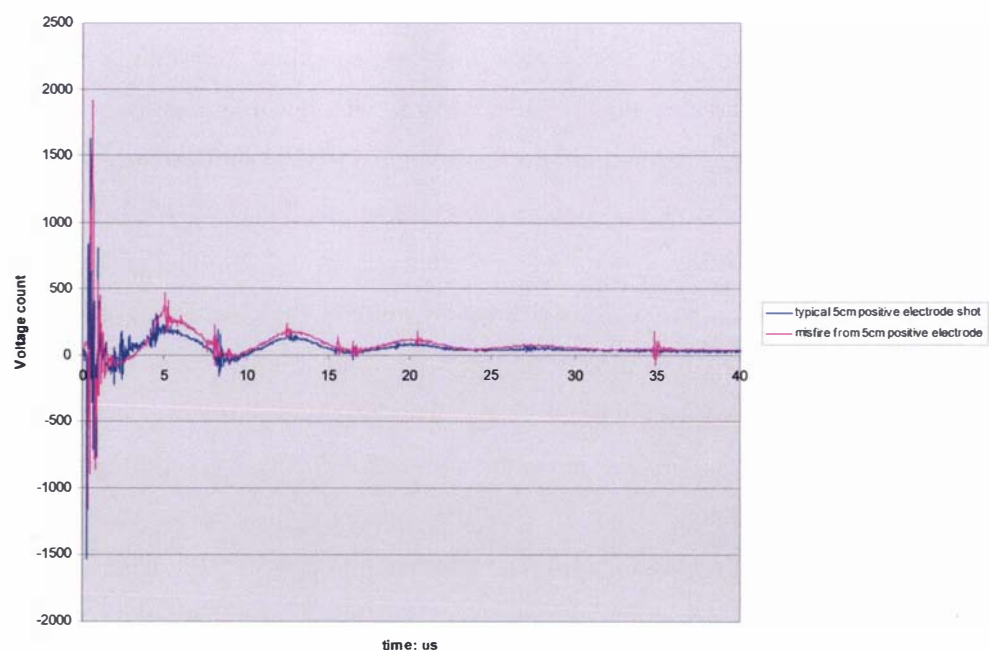
A comparison of the velocity distribution of a misfire and a typical shot produced using a 5cm in length 3cm in diameter positive electrode is presented in graph 3.15.a. Graph 3.15.a is made from the combination of graphs 3.14.c, 3.14.d (from section 3.3.7) and graph 3.13.c (from section 3.3.6). A combination of the voltage traces relating to these results is shown in graph 3.15.b. The comparison between a misfire and a typical shot from a 10cm in length 3cm in diameter positive electrode is given in graph 3.16.a. This graph was made by combining graphs 3.14.c, 3.14.d (of section 3.3.7) and graph 3.9.c (of section 3.3.5). There appears to be little difference between the voltage trace of a misfire and a typical shot, and the velocity distributions seem to show a region very similar in structure to that obtained from a typical shot. Unfortunately, there were only a few instances of misfires to compare with the typically obtained results; this limits the general comparisons that can be made. All that can be claimed at this point is the presence of high speed plasma in the range of 150km/s to 280km/s was observed in some instances.

3.3.8: Discussion on the performance of the Lica

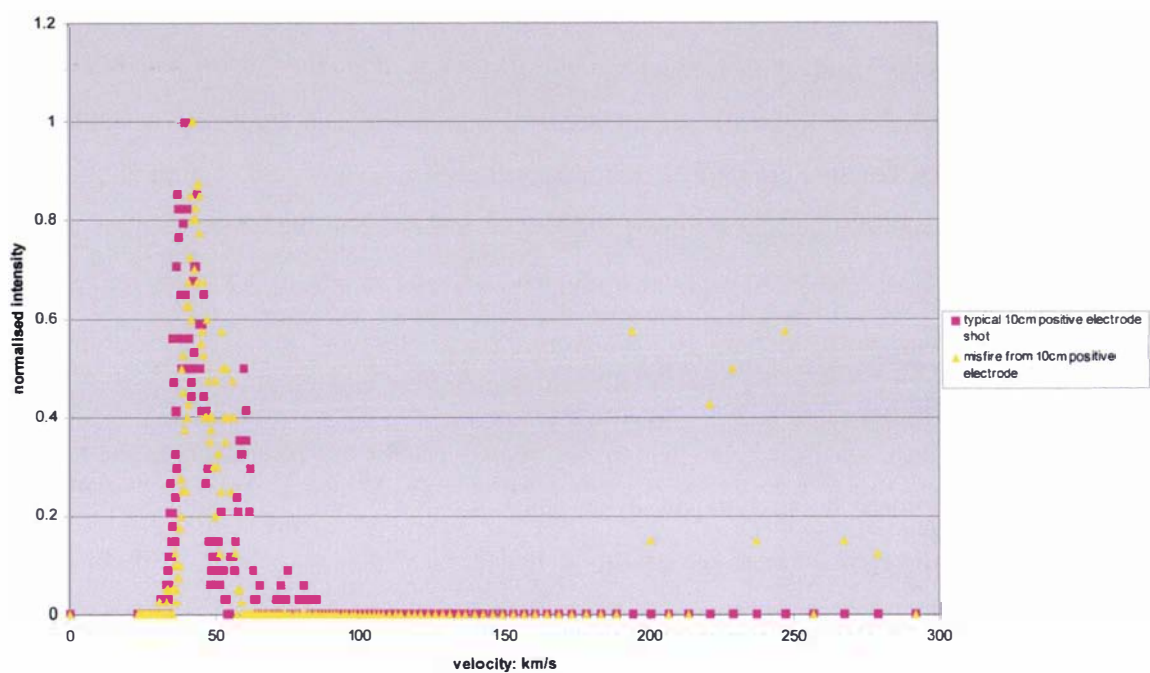
Only one test was conducted at a higher voltage of 14kV (graphs 3.7.a, 3.7.b and 3.7.c). The results of this test show a more separated peak structure compared to the results generated using a charging voltage of 10kV, but since only one test was conducted under these conditions there is not enough evidence to make this claim. More tests need to be conducted to establish the effect of driving pulse length and the effect of higher voltages on the operation of the Lica.



Graph 3.15.a: Graph of the comparison of the plasma velocity distribution between a typical shot and a misfire as a function of time, for the plasma accelerator fitted with a 5cm positive electrode



Graph 3.15.b: Graph of the comparison between the voltage traces for a typical shot and a misfire as a function of adjusted time, for the plasma accelerator fitted with a 5cm positive electrode



Graph 3.16.a: Graph of the comparison the of plasma velocity distribution between a typical shot and a misfire as a function of time, for the plasma accelerator fitted with a 10cm positive electrode

Calculated effects

The first question that must be asked is, is the ionized gas a plasma and if so what type of plasma is it? Before the ionized gas can be classified as a plasma it must fulfil the three conditions discussed in section 3.2.2. The degree of ionization and the number density must be calculated first so that the variables associated with these conditions can be determined.

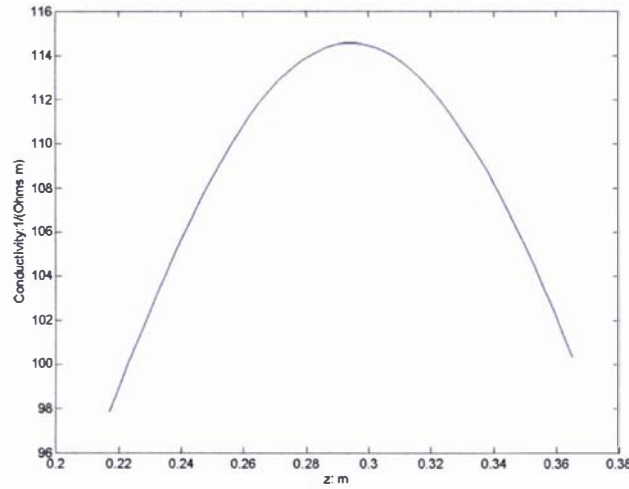
The average experimentally determined temperature, of the ionized gas, from the plasma accelerator has been found to be between 3000K and 5000K. Using these temperatures and the assumption that the pressure of the ionized gas is equal to the average pressure (the pressure at FWHH) of the neutral hydrogen gas pulse from the valve (refer to section 2.4.10), the respective degrees of ionization can be calculated through the use of equations (3.19) and (3.20). The degree of ionization is calculated as being 4.2×10^{-9} at 3000K and 1.2×10^{-3} at 5000K; full ionization (at the assumed pressure) is not achieved until a temperature of 10000K has been reached (i.e. $\xi = 0.999$). The calculated degrees of ionization listed above suggest that the density of the plasma (bounded by value at the FWHH, refer to section 3.2.2) lies in the range of 3.1×10^{11} electrons/m³ to 6.3×10^{11} electrons/m³ at 3000K, and 8.9×10^{16} electrons/m³ to 1.8×10^{17} electrons/m³ at 5000K.

Now the question of whether or not the ionized gas is a plasma can be answered. The first and second conditions can be analysed by using equations (3.11) and (3.12) and the previously determined temperature, degree of ionization and density ranges; hence at 3000K λ_D is calculated as being in the range of 6.8×10^{-3} m to 4.3×10^{-3} m, and at 5000K λ_D is in the range of 1.6×10^{-5} m to 1.2×10^{-5} m. This satisfies that the first two conditions classifying the ionized gas as a plasma ($\lambda_D \ll L$, where $L = 3.2$ cm (refer to section 3.1), and $N_D \gg 1$). The third condition ($w_p \tau > 1$) is also satisfied for both the temperatures (3000K and 5000K), in which τ was taken from Spitzer's conductivity expression, equation (3.23) (note this assumption is not strictly true, because τ is dependent upon the chosen conductivity regime, but it does give an indication that $w_p \tau \gg 1$). So the assumption that the ionized gas within the plasma accelerator is a plasma has been verified, and according to figure 3.1 the plasma can be likened to being similar to either the plasma in the Ionosphere (for the parameters of the plasma at 3000K) or close to a low pressure arc (using the plasma parameters calculated at 5000K).

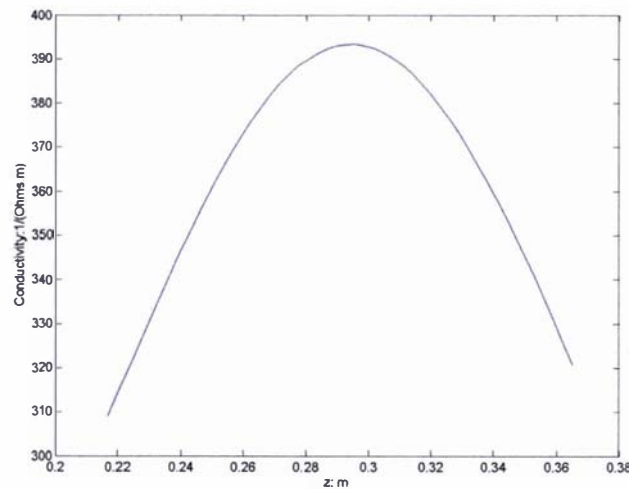
The plasma's electrical properties can now be defined, first it should be noted that the plasma is a low density plasma at both 3000K and 5000K, this assertion is based upon the results for the density parameter r_s calculated by using equations (3.16) to (3.18) and the previously

determined density ranges (i.e. $r_s \gg 1$). The plasma was determined to be an ideal, non-degenerate plasma using the parameters Γ (equation (3.14)) and θ (equation (3.15)); at 3000K $6.1 \times 10^{-5} \leq \Gamma \leq 7.7 \times 10^{-5}$ and $9.6 \times 10^9 \leq \theta \leq 1.5 \times 10^{10}$, while at 5000K $2.4 \times 10^{-3} \leq \Gamma \leq 3.0 \times 10^{-3}$ and $3.7 \times 10^6 \leq \theta \leq 5.9 \times 10^6$. The electrical conductivity of the plasma in the Lica is best described using the Spitzer formula (equation (3.21)) because $\Gamma \ll 1$, rather than the weakly non-ideal plasma electrical conductivity interpolation formulas defined by equations (3.27) and (3.28).

The conductivity profiles of the plasma at 3000K and 5000K, calculated using the Spitzer formula and the method outlined in section 3.2.2, are displayed in graphs 3.17 and 3.18. It makes little difference to the calculated conductivity profile whether or not the entire gas pulse is assumed to be within the plasma accelerator or just before it.



Graph 3.17: Graph of the calculated conductivity profile of the plasma as a function of distance z from the valve, using the assumed density profile, the Spitzer conductivity formula [59] and a plasma temperature of 3000K.



Graph 3.18: Graph of the calculated conductivity profile of the plasma as a function of distance z from the valve, using the assumed density profile, the Spitzer conductivity formula [59] and a plasma temperature of 5000K.

Because the Lica is of coaxial design the electric field (the static electric field) before the preionized gas breaks down will be described, in terms of the cylindrical r coordinate, by equation (3.37).

$$E = \frac{V}{r \log\left(\frac{R_2}{R_1}\right)} \quad (3.37)$$

In equation (3.37) V is the applied voltage, R_1 is the radius of the inner electrode, and R_2 is the inner radius of the outer electrode. Since the initial static electric field within the Lica is non-uniform either Townsend's sparking condition, implied by equation (3.9), or the streamer breakdown mechanism, equation (3.10), will be possible breakdown mechanisms for this device. Expanding equation (3.9) using equations (3.37), (3.3) and assuming a K value of 8 (the lower limit for Townsend's sparking limit) results in equation (3.38).

$$\frac{V}{B_{Town} P \ln\left(\frac{R_2}{R_1}\right)} e^{\frac{-B_{Town} P \ln\left(\frac{R_2}{R_1}\right) R_1}{V}} - \frac{V}{B_{Town} P \ln\left(\frac{R_2}{R_1}\right)} e^{\frac{-B_{Town} P \ln\left(\frac{R_2}{R_1}\right) R_2}{V}} - \frac{8}{PA_{Town}} = 0 \quad (3.38)$$

Expanding equation (3.10) using equation (3.3), the definition for the electric field given by equation (3.37), the assumption that the maximum length possible for the critical stream formation is equal to the gap length between the electrodes d , and a value for K_s equal to 18 gives:

$$\frac{V}{B_{Town} P \ln\left(\frac{R_2}{R_1}\right)} e^{\frac{-B_{Town} P \ln\left(\frac{R_2}{R_1}\right) R_1}{V}} - \frac{V}{B_{Town} P \ln\left(\frac{R_2}{R_1}\right)} e^{\frac{-B_{Town} P \ln\left(\frac{R_2}{R_1}\right) R_2}{V}} - \frac{18}{PA_{Town}} = 0 \quad (3.39)$$

Upon inspection of the two equations (equations (3.38) and (3.39)) it would appear that equation (3.38) would give a lower breakdown pressure value. This is true, because both formulas are calculated using essentially the same equation except different values for the right hand sides have been used (i.e. K and K_s). But as the critical streamer length cannot be calculated (and can be considered to be a scenario of "a thousand monkeys on a thousand typewriters") equation (3.38) will have to be used as a means of determining the approximate

breakdown point for the preionized gas. In fact, under the present low pressure conditions and the coaxial geometry of the accelerator Townsend's sparking condition, equation (3.38), will be a more likely candidate for breakdown than the streamer mechanism given by equation (3.39) [83].

The mean free path for hydrogen at 288K and a pressure of 101KPa has been experimentally determined as $11.8 \times 10^{-8} \text{ m}$ [83]. Taking the maximum pressure as being 0.02Pa from the pressure distribution of graph 2.27 (in section 2.4.10 of chapter 2) and the experimentally determined temperature of 12.2K (for the 180 μ s gas pulse produced using the preionizer attachment in front of the valve, refer to section 2.4.9 of chapter 2) the mean free path for hydrogen is calculated as being 2cm. This gives the mean free path for an electron as being equal to 11cm. It is quite evident that this distance is far in excess of the electrode gap of 3.2cm and suggests a greater pressure within the electrode gap is required for breakdown to occur. This is confirmed by the solution to equation (3.38).

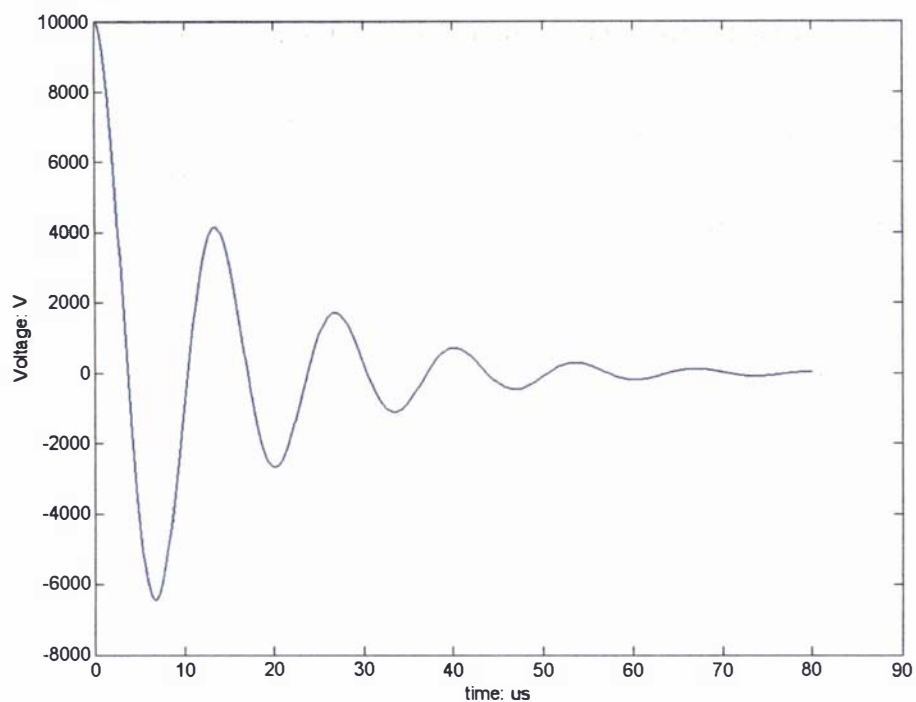
From the calculated values presented above and given the charging voltage on the capacitor of 10kV the electron energy is calculated from equation (3.1) as being 32104eV (using the mean electric field value of equation (3.37)); this value corresponds to an ionization cross section of approximately $1 \times 10^{-22} \text{ m}^2$ (from interpolation of the values given in graph 3.1). Using the value determined for the ionization cross section and a value of 15.4V for the ionization potential V_i of hydrogen [83], the values for A_{Town} and B_{Town} can be calculated from equations (3.4) and (3.5). Using these values and the previously assumed conditions equation (3.38) can be used to check whether or not the preionized gas will breakdown. Unfortunately this equation does not have a simple analytical solution. But an approximate solution can be found by inserting a value for the pressure between the maximum pressure and the pressure at the front of the gas pulse into equation (3.35) and using the bisection root finding method for a non-linear equation [78]. Using the above values it was found that the preionized gas would not breakdown under Townsend's non-uniform breakdown mechanism (equation (3.38)). (Note as discussed in section 3.2.1 the theoretically calculated values of A_{Town} and B_{Town} are also likely to be higher than those experimentally. But as no experimentally determined values, within the pressure and electric field range used in this research, were found in the literature these calculated values remain the only means for calculating the breakdown characteristics of the gas via an avalanche mechanism.) Note, even if the maximum ionization cross section value is used in the calculation presented above, the preionized gas still will not breakdown under Townsend's non-uniform breakdown mechanism.

Because the preionized gas is known to breakdown, as shown in the results generated in sections 3.3.4 to 3.3.7, the above calculations using the non-uniform Townsend's breakdown mechanism suggest two possibilities. Either the gas released from the valve does not undergo an

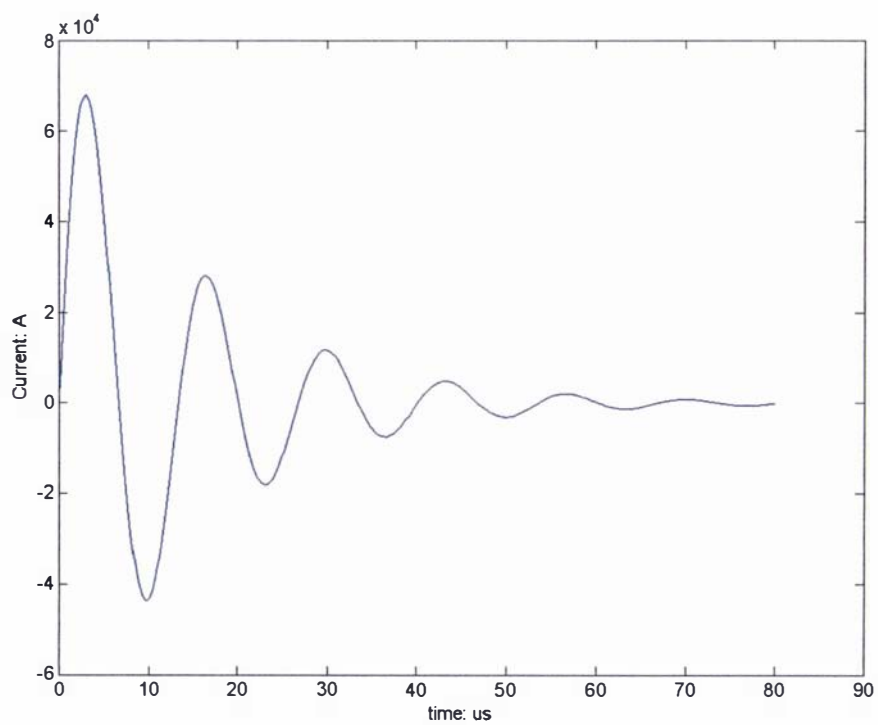
ideal isotropic expansion meaning a greater amount of gas enters the skimmer than previously calculated (which is unlikely), or a secondary ionization mechanism is responsible for the breakdown. This secondary ionization mechanism is likely to be a combination of photoionization (refer to [83] and the modified Townsend's equation given in [59]) and secondary electrons generated from the preionization pulse (refer to section 3.1) as a result of electron impact either with the anode or within the neutral gas pulse. However calculating the contributions of these effects on Townsend's breakdown mechanism is difficult, especially the secondary electrons generated from the preionization pulse. So the hypothesis that the Lica operates by accelerating a series of plasma sheaths remains unproven, as does the exact breakdown mechanism.

Since the breakdown mechanism is unknown the circuit parameters for the plasma accelerator will have to be calculated using the entire plasma mass, or at least the FWHH to ensure that the gas pulse fits within the accelerator for the positive electrode lengths of 5cm and 10cm.

Given the calculated plasma conductivity the resistance of the plasma can be calculated using the method outlined in section 3.2.2. Once the resistance of a plasma has been determined the circuit parameters of charge, current and voltage as a function of time can be calculated. The acceleration of the plasma is investigated by modelling means in chapter 4, but for initial purposes the resistance and inductance will be assumed to be constants; hence the resistance of the plasma is calculated as being $8.2\text{m}\Omega$ using the conductivity profile calculated at 5000K (graph 3.18). The total resistance and inductance of the plasma accelerator and its associated components (shown in diagram 3.5) were calculated using equations given in [82], [95] in which the skin effect was also considered [96]. This gave the calculated resistance of the conducting plates connecting the capacitor to the accelerator as being $0.26\text{m}\Omega$ with an inductance of 3.14nH . The resistance and inductance of the positive and grounded electrodes were calculated over a distance of 5cm, because this was the minimum distance over which damage on the positive electrodes was observed, under this assumption the resistances of the positive and grounded electrodes were calculated as $59.6\mu\Omega$ and $30\mu\Omega$ and the inductance of the plasma accelerator calculated as 11.4nH . As the capacitor has such a large capacitance compared to the other components, the capacitance of the system will be taken as being equal to this value. The inductance of the capacitor was also included as part of the total inductance of the system. Combining all these values with the calculated resistance value for the plasma (calculated at 5000K) produces the plots of voltage and current as a function of time presented in graphs 3.19 and 3.20. It can be seen that the voltage trace given in graph 3.19 shows a resemblance to the voltage traces obtained experimentally, but this is only a preliminary view of the situation as the motion of the plasma and other effects have not been considered.



Graph 3.19: Graph of calculated voltage as a function of time using the assumed plasma resistance calculated from the conductivity profile at 5000K



Graph 3.20: Graph of calculated current as a function of time using the assumed plasma resistance calculated from the conductivity profile at 5000K

Chapter 4

Modelling the operation of the Lica

4.1: Overview on modelling techniques used to describe the operation of plasma accelerators and rail guns

The operation of a plasma accelerator or rail gun is described by the coupled Maxwell and Magnetohydrodynamic (MHD) equations. Maxwell's equations describe electromagnetic effects and their interactions (this set of equations is discussed in section 4.3.2), while the MHD equations apply to motional aspects [7]. Both sets of equations are time dependent and form a complex system in three dimensions. Analytically this set of coupled equations is exceedingly difficult to solve, only simple one or two dimensional steady state problems can be fully solved [7], [97].

In trying to model either a plasma accelerator or rail gun a numerical approach is typically employed, because of the aforementioned complexities. One dimensional analytical models have been derived for coaxial plasma accelerators in both the plasma block and snowplough modes of operation, but these models are based on a gross simplification of the problem, in which the plasma is accelerated by a filament current. The initial results from the Lica analysed by a one dimensional model are discussed in section 4.2 (in its entirety), in which several different assumptions are investigated to try and reproduce/understand the experimental results. Because of the limitations of the one dimensional model a two dimensional numerical electromagnetic model was developed. This electromagnetic model and the techniques used in its creation are discussed in section 4.3 (in its entirety). A program called MATAC was produced using these techniques; this program provides a platform to which other aspects such as MHD, ablation and ion models could be added.

The coupled Maxwell and MHD equations form the basic set of equations that describe the motion of plasma within the accelerator or plasma armature rail gun; but there are other important aspects such as the breakdown of preionized gas (discussed in section 3.2.1), ablation (refer to section 1.3), the properties of the plasma and its interaction with ablated material. These are important aspects which are best described through the use of an ion model [98], [99], [100], [101], [102], [103], but due to the preliminary nature of the modelling process (presented here) these aspects will be neglected.

Some people will raise the question as to why one would want to develop their own numerical model to describe the operation of a coaxial plasma accelerator, when there are already specially written or commercially available programs that could be used.

Firstly, it must be pointed out that specially written programs such as MACH3 are export controlled and ordinarily cannot be obtained. Secondly, many of the freeware rail gun programs are inadequate and are not as advanced as MATAC. And finally, the commercially available programs that can be used for either electromagnetic (PDEase) or fluid flow calculations (PHOENICS, FLUENT or PHYSICA+) are either very expensive (to obtain a licence) or they are unable to be applied to the plasma accelerator problem, because they cannot model or account for certain aspects. Most commercially available programs have the added difficulty that they are essentially “black box” in nature and do not allow access or additions to the source code.

4.1.1: Description of the problem

The problem of modelling the operation of a coaxial plasma accelerator will be treated simply, so that a preliminary set of working results can be obtained. The plasma block mode of operation will be assumed (since it is the preferred mode of operation), in which the plasma will be assumed to be incompressible. These assumptions are made to simplify the MHD equations to a simple force equation, in which the acceleration of the plasma is equal to the action of the Lorentz force across it (refer to section 1.2). The properties of the plasma (i.e. its conductivity, density, pressure and temperature) will also be assumed to be constant.

The plasma accelerator is of coaxial design as discussed in section 3.3 and is surrounded by a large vacuum region, essentially in all directions, only the electric and magnetic fields produced from the accelerator (and their interactions) will be considered in the modelling process. Due to the symmetry of the coaxial plasma accelerator the problem will be considered in a cylindrical coordinate system, as shown in diagram 4.1. In order to further simplify the problem, the properties of the plasma will be assumed to be axisymmetrical (constant in the θ direction); hence the problem is simplified to a two dimensional problem measured from the central axis of the accelerator.

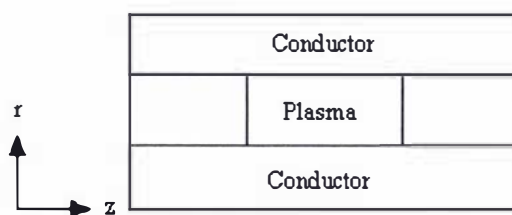


Diagram 4.1: Diagram of plasma accelerator and the two dimensional cylindrical coordinate system used to describe it

4.2.1: A basic approach to modelling the problem – a first order model

4.2: Simple analytical models

4.2.1: A basic approach to modelling the problem – a first order model

A simple analytical model is required for the preliminary analysis of the plasma accelerator. Because the voltage trace from the experimental results in sections 3.3.4 to 3.3.6 of chapter 3 shows the electrical circuit as being underdamped, the derived analytical model is only required to reflect this behaviour.

A full nonsteady state solution to Maxwell's equations (discussed in section 4.3.2) cannot be made, but a simple "lump sum" analytical model based on a few assumptions can be derived. Most of the analytical models that have been derived in the literature were created during the 1960 to 1970 period. Even though both the plasma block [9] and the snowplough [10] models have been considered, the majority of the models that have been derived are mainly concerned with the properties of the circuit rather than the motion of the plasma and are often limited to specific ranges; however in [11] it was the motion of the plasma that was of prime interest.

In [11], which is a one dimensional model, a filament current was assumed to be accelerated by the action of the magnetic pressure upon it, accreting mass as it was accelerated down the length of the plasma accelerator in the snowplough mode of operation (as discussed in section 1.2 of chapter 1). In this model the equations of motion were derived by solving the circuit equation for charge q , substituting this result into the equation of force and then integrating the resulting acceleration equation with respect to both volume and time. Using this model as a basis, a one dimensional plasma block model for an underdamped system can be derived. The first step involves solving the circuit equation for charge:

$$\ddot{q} + \frac{R_o}{L_o} \dot{q} + \frac{1}{L_o C} q = 0 \quad (4.1)$$

In equation (4.1) R_o is the resistance, L_o is the inductance and C is the capacitance of the circuit. The underdamped solution to equation (4.1) is given as:

$$q = Q e^{\left(-\frac{R_o t}{2L_o}\right)} \cos(\Omega t) + Q \left(\frac{R_o}{2\Omega L_o}\right) e^{\left(-\frac{R_o t}{2L_o}\right)} \sin(\Omega t) \quad (4.2)$$

In equation (4.2) Q is the initial charge on the capacitor and Ω is defined by equation (4.3).

4.2.1: A basic approach to modelling the problem – a first order model

$$\Omega = \sqrt{\left(\frac{1}{L_o C}\right) - \left(\frac{R_o^2}{4L_o^2}\right)} \quad (4.3)$$

The current i is defined as:

$$i = -\frac{\partial q}{\partial t} = -\dot{q} \quad (4.4)$$

Substituting equation (4.2) into equation (4.3) results in:

$$i = Q\Omega e^{\left(\frac{R_o t}{2L_o}\right)} \sin(\Omega t) + Q\left(\frac{R_o^2}{4\Omega L_o^2}\right) e^{\left(\frac{R_o t}{2L_o}\right)} \sin(\Omega t) \quad (4.5)$$

The force F on the plasma sheath in [11] was derived from the magnetic pressure on a filament current (refer to section 1.1), as shown in equation (4.6) below (where r_i and r_o are the inner and outer radii of the coaxial electrodes).

$$F = \left(\frac{2\pi}{2u_o}\right) \int_{r_i}^{r_o} B^2(r) dr = \left[\left(\frac{u_o}{4\pi}\right) \ln\left(\frac{r_o}{r_i}\right)\right] \dot{q}^2 = f \dot{q}^2 \quad (4.6)$$

Because the plasma block mode of operation is being considered the mass of the plasma m can be assumed to be a constant property, it is at this point that the derivation (of the simple first order plasma block model) departs from that described in [11]; the equation of motion in the z direction (the positive direction of motion along the electrodes) for the plasma block mode of operation is simply derived from Newton's law as:

$$F = m \ddot{z} \quad (4.7)$$

The acceleration \ddot{z} is then derived by combining equations (4.6) and (4.7) to obtain:

$$\ddot{z} = \frac{f}{m} \dot{q}^2 \quad (4.8)$$

4.2.1: A basic approach to modelling the problem – a first order model

Integrating this equation with respect to both volume and time, in which v_o is defined as the initial velocity and the terms d and D are constants given by equations (4.9) and (4.10), results in the velocity (of the plasma mass) $v(t)$ being defined by equation (4.11).

$$d = \frac{R_o}{L_o} \quad (4.9)$$

$$D = Q^2 \Omega^2 + \frac{Q^2 R_o^2}{2L_o^2} + \frac{Q^2 R_o^4}{16\Omega^2 L_o^4} \quad (4.10)$$

$$\Rightarrow v(t) = v_o + \frac{fD}{m} \left(\frac{1}{2d} - \frac{1}{2d} e^{-dt} + \frac{e^{-dt}}{2(d^2 + 4\Omega^2)} (d \cos 2\Omega t - 2\Omega \sin 2\Omega t) - \frac{d}{2(d^2 + 4\Omega^2)} \right) \quad (4.11)$$

Integrating this velocity equation with respect to time produces equation (4.12), which is the equation for the distance travelled by the plasma block $z(t)$ as a function of time.

$$z(t) = v_o t + \frac{fD}{m} \left(\left(\frac{1}{2d} - \frac{d}{2(d^2 + 4\Omega^2)} \right) t + \frac{1}{2d^2} e^{-dt} - \frac{1}{2d^2} + \frac{de^{-dt}}{2(d^2 + 4\Omega^2)^2} (2\Omega \sin 2\Omega t - d \cos 2\Omega t) \right. \\ \left. + \frac{d^2}{2(d^2 + 4\Omega^2)^2} + \frac{\Omega e^{-dt}}{(d^2 + 4\Omega^2)^2} (d \sin 2\Omega t + 2\Omega \cos 2\Omega t) - \frac{2\Omega^2}{(d^2 + 4\Omega^2)^2} \right) \quad (4.12)$$

The derived plasma block model has a terminal velocity, which is realised when the value for time t approaches infinity. The terminal velocity and distance for the plasma block model are then derived as equations (4.13) and (4.14).

$$v(t \rightarrow \infty) = v_o + \frac{fD}{m} \left(\frac{1}{2d} - \frac{d}{2(d^2 + 4\Omega^2)} \right) \quad (4.13)$$

$$z(t \rightarrow \infty) = v_o t + \frac{fD}{m} \left(\left(\frac{1}{2d} - \frac{d}{2(d^2 + 4\Omega^2)} \right) t - \frac{1}{2d^2} + \frac{d^2}{2(d^2 + 4\Omega^2)^2} - \frac{2\Omega^2}{(d^2 + 4\Omega^2)^2} \right) \quad (4.14)$$

Equation (4.13) gives an upper limit for the velocity, which would result if the acceleration distance was infinite. The derived plasma block model has inherent limitations due to the simplifications made in its derivation. It does not have the correct current and magnetic field distribution across the plasma, magnetohydrodynamic effects resulting from the compression of

4.2.1: A basic approach to modelling the problem – a first order model

the plasma have been neglected and the effects of ablation have not been considered. These simplifications mean that the velocity predicted by this model will probably be higher than the experimentally obtained values.

The analytical plasma block model is further limited by the assumption that the circuit has constant resistance and inductance. These values are time dependent quantities, which are dependent upon the position of the plasma block within the plasma accelerator, especially the resistance of the plasma as it exits the plasma accelerator. The resistance of the plasma will increase as the plasma exits the accelerator, because there will be less surface area (and conducting mass) to conduct across.

Because of the above limitations, and the perceived difficulty of analytically deriving a model that takes into account these limitations, a numerical approach is required. A Runge-Kutta solver is typically used to solve the simultaneous equations of (4.1), (4.4), (4.8) and the velocity equation (4.15) [4] to obtain a simple first order one dimensional numerical model.

$$v = \frac{\partial z}{\partial t} \quad (4.15)$$

Using a fifth order Runge-Kutta scheme [78], the numerical procedure begins with specifying the initial conditions for charge, current, velocity and distance travelled by the plasma block. Then the system of equations is solved for a given time step, the results are extracted and the initial conditions are reset using the newly calculated values. The process is repeated until the plasma has left the plasma accelerator. Most mathematical package programs such as MATLAB contain a variety of Runge-Kutta solvers. Using the above procedure with a program written in MATLAB equations (4.11) and (4.12) were confirmed as being the correct analytical answers.

Ablation is likely to be the biggest factor affecting the performance of the plasma accelerator, rather than the time dependent circuit parameters of resistance and inductance. A simple ablation model was proposed in [40] and [104], where the ablated mass from the electrodes is assumed to be equal to the energy flowing in these conductors multiplied by an ablation constant α . The ablation constant is a material dependent property and is equal to the reciprocal of the energy required to ionize one gram of material. Since the dominant factor in determining the ablation constant will be proportional to the average atomic weight of the material being ablated, the ablation constant in [40] and [104] was approximated by the following equation:

$$\alpha = \frac{3M_r}{4} \quad (4.16)$$

4.2.1: A basic approach to modelling the problem – a first order model

In equation (4.16) M_r is the average atomic weight and α has the units of g/MJ. The ablated mass m_a removed from the electrodes as a function of time (assuming this proposed mechanism) given in equation (4.17) was derived by considering the electrical power dissipated in the electrodes at any given instant.

$$\frac{\partial m_a}{\partial t} = \alpha_1 I^2 R_{electrode1} + \alpha_2 I^2 R_{electrode2} \quad (4.17)$$

In equation (4.17) subscripts 1 and 2 relate to the positive and negative electrodes of the accelerator and $R_{electrode}$ is the resistance of an electrode. This resistance will be taken as a fixed value (for preliminary purposes) calculated over the entire length of the plasma accelerator. Rewriting equation (4.17) in terms of charge, as equation (4.18), allows it to be directly used in the one dimensional numerical model.

$$\frac{\partial m_a}{\partial t} = \alpha_1 \dot{q}^2 R_{electrode1} + \alpha_2 \dot{q}^2 R_{electrode2} \quad (4.18)$$

The effect of this ablated mass will be considered in terms of the worst case scenario, in which the ablated mass is directly incorporated into the plasma mass m_p [40]; hence equation (4.8) is modified to

$$\ddot{z} = \frac{f \dot{q}^2}{(m_p + m_a)} \quad (4.19)$$

The effects of arcing/plasma restrike [41], [45] are beyond the scope of the proposed model, because a detailed ion/breakdown model would be required to model such effects.

4.2.2: Results of the first order model

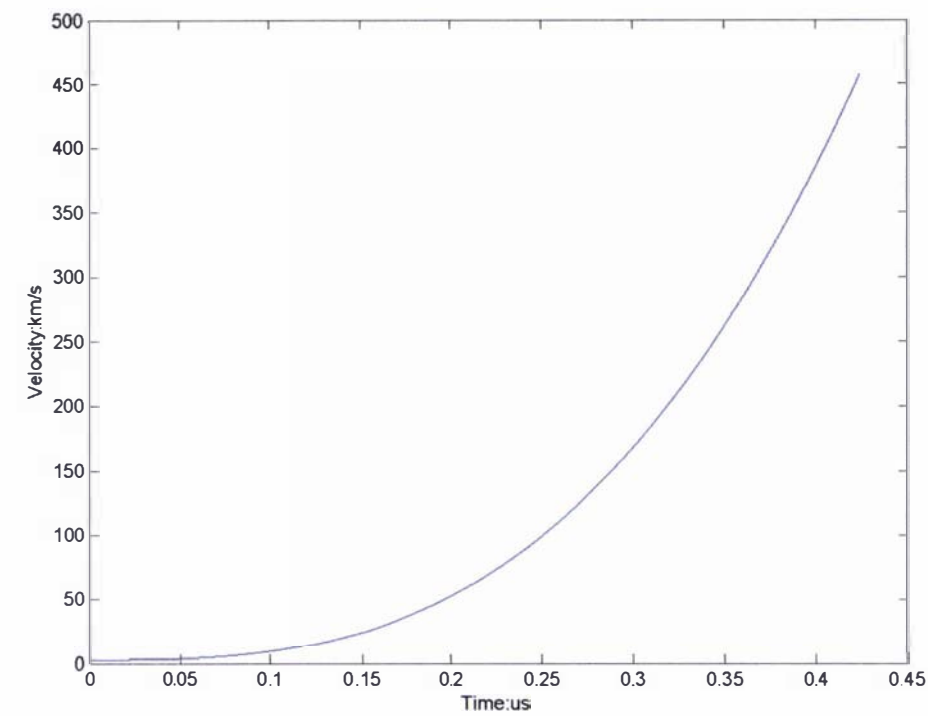
The Lica was modelled using both the analytical plasma block and the one dimensional ablation plasma block model, in an attempt to explain the experimental results. In both models the resistance and inductance were calculated using the known dimensions of the plasma accelerator and its associated components (mentioned in section 3.3.1), including the material properties (at room temperature) in which the skin effect was taken into account [96]. The

resistance R_o and inductance L_o of the plasma accelerator were calculated as constant values (using the equations for a coaxial cable given in [82], [95]), taken over the entire plasma acceleration distance. The resistance of the plasma was calculated in accordance to the method described in section 3.2.2, in which the conductivity profile calculated in section 3.3.8 at 5000K (graph 3.18) was used in the calculation. The acceleration distance mentioned in tables 4.1 and 4.2 relates to the distance over which the plasma block was accelerated over. The calculations in both models were conducted until the rear of the plasma block had reached this distance, effectively leaving the accelerator.

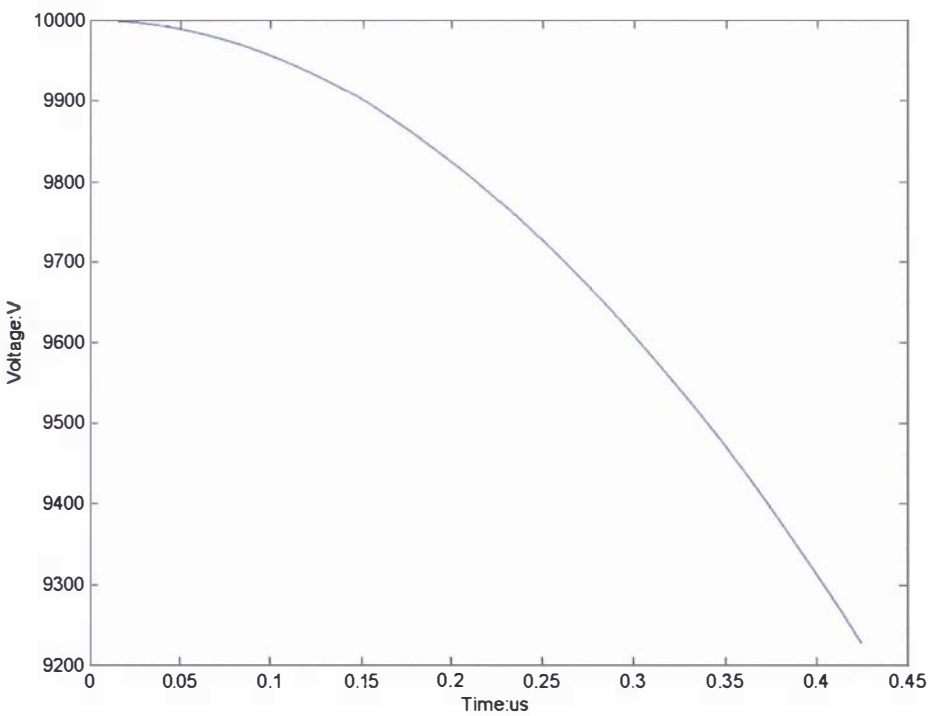
The results from the analytical plasma block model (equations (4.11) and (4.12)) are presented in table 4.1, together with the parameters used to generate them. The calculated velocity and voltage trace for the acceleration distance of 0.05m are shown in graphs 4.1 and 4.2 respectively.

Acceleration distance: m	Mass: mg	Final velocity: km/s	Ro: Ω	Lo: nH	C: μ F	Charging voltage: V	Time period of the acceleration: μ s
0.05	0.00014	456	0.0086	64.6	17.5	10000	0.42
0.1	0.00014	705	0.0087	76.0	17.5	10000	0.55
0.2	0.00014	1027	0.0089	98.8	17.5	10000	0.75

Table 4.1: Results from the analytical plasma block model, obtained using the stated parameters



Graph 4.1: Graph of velocity as a function of time for the analytical model, created using the parameters given in table 4.1 for an acceleration distance of 0.05m.

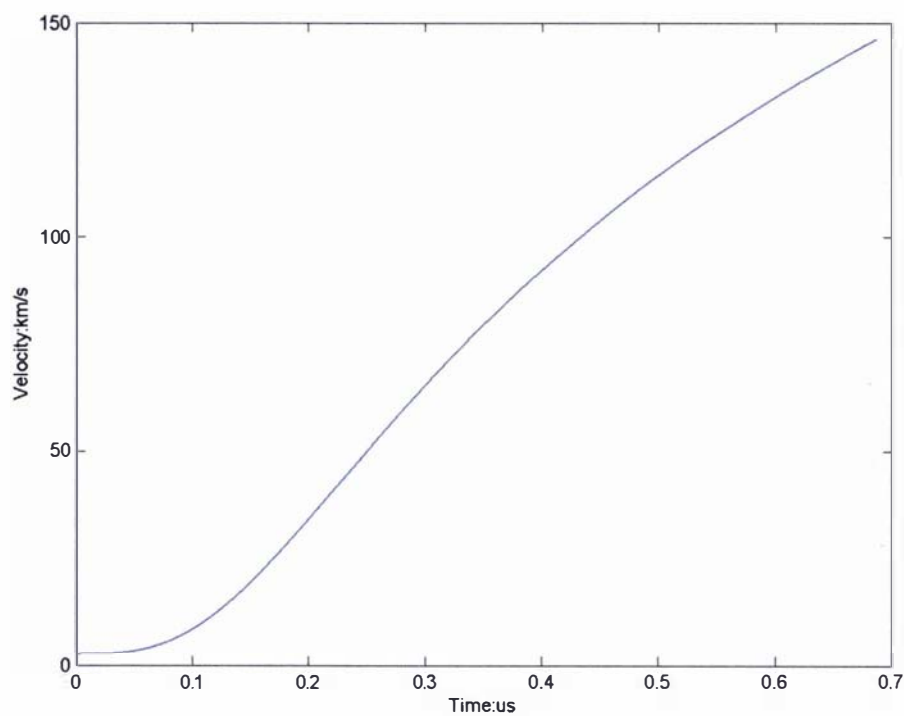


Graph 4.2: Graph of voltage as a function of time for the analytical model, created using the parameters given in table 4.1 for an acceleration distance of 0.05m.

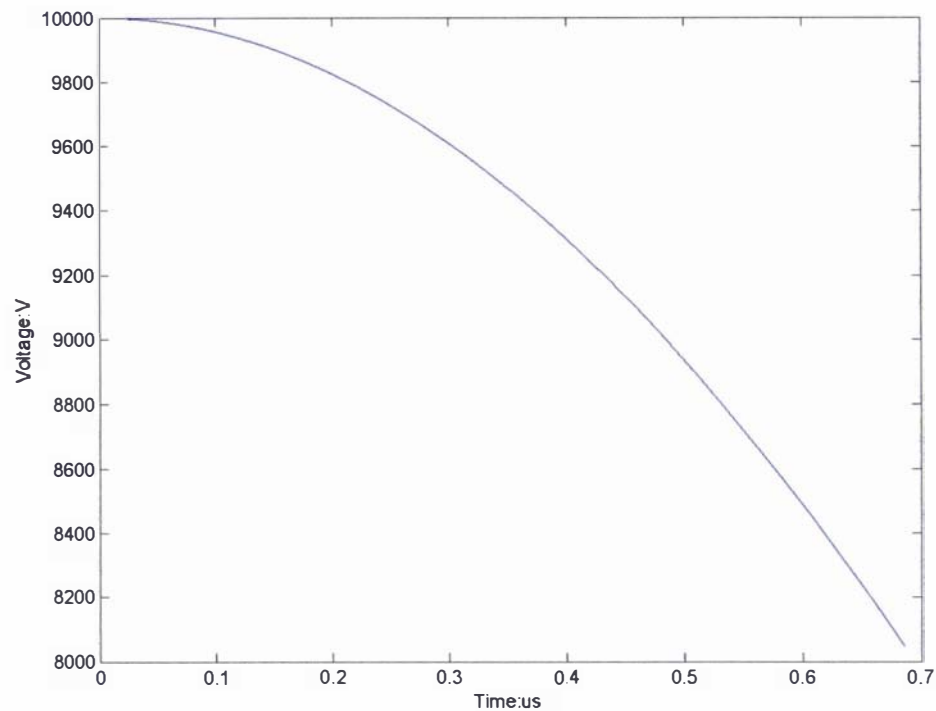
The results from the one dimensional numerical ablation plasma block model (equations (4.1), (4.4), (4.15) and (4.19)) and the parameters used to generate these results are presented in table 4.2. The resistances for the steel (RFeElectrode) and aluminium (RAIElectrode) electrodes are also presented in this table; these values are used in the assumed ablation model described by equations (4.16) and (4.18). The resistance of the electrodes was calculated as a constant, taken over the entire acceleration distance (including the skin effect). The calculated velocity and voltage trace using this model are shown in graphs 4.3 and 4.4 for an acceleration distance of 0.05m.

Acceleration distance: m	Mass: mg	Final velocity km/s	Ro: Ω	RFeElectrode: $\mu\Omega$	RAIElectrode: $\mu\Omega$	Lo: nH	C: μ F	Charging voltage: V	Time period of the acceleration: μ s	Total ablated mass: mg
0.05	0.00014	146	0.0086	59.6	30.0	64.6	17.5	10000	0.69	0.0069
0.1	0.00014	115	0.0087	119	60.0	76.0	17.5	10000	1.39	0.064
0.2	0.00014	75	0.0089	239	120	98.8	17.5	10000	3.46	0.37

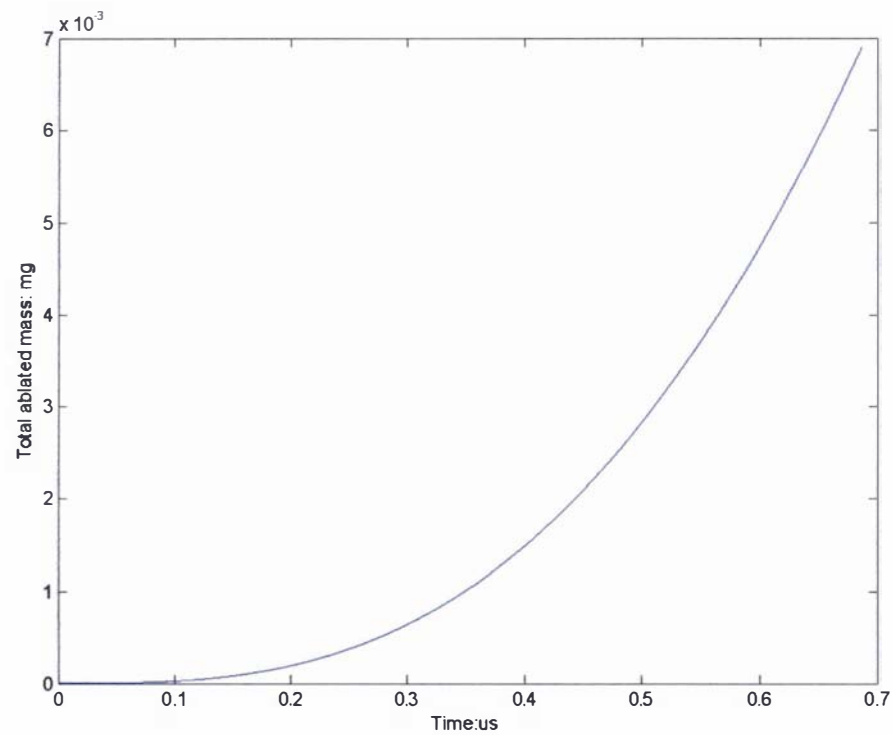
Table 4.2: Results from the one dimensional numerical ablation plasma block model, obtained using the stated parameters.



Graph 4.3: Graph of velocity as a function of time for the numerical one dimensional ablation model, created using the parameters given in table 4.2 for an acceleration distance of 0.05m.



Graph 4.4: Graph of voltage as a function of time for the numerical one dimensional ablation model, created using the parameters given in table 4.2 for an acceleration distance of 0.05m.



Graph 4.5: Graph of ablated mass as a function of time for the numerical one dimensional ablation model, created using the parameters given in table 4.2 for an acceleration distance of 0.05m.

4.2.3: Discussion on the first order model

The results from the initial first order model (i.e. the results shown in table 4.1) are several orders of magnitude greater than the experimental results. These results fail to adequately represent the operation of the Lica and do not explain either the time scale observed in the experimental voltage traces (i.e. a $22\mu\text{s}$ to $32\mu\text{s}$ in duration overdamped experimental voltage trace, refer to section 3.3.8) or the strange anomaly of the final velocity of the hydrogen plasma (apparent bulk of the plasma) being independent of the positive electrode length (refer to section 3.3.8).

The failings of the first order model can be attributed to its derivation being based upon a filament current. By assuming that the Lorentz force across the plasma is solely the product of this assumption, the effects of the current density and magnetic field distributions have been neglected. If the circuit parameters are held constant and the conductivity of the plasma is either increased or decreased one would expect a noticeable effect on the performance of the accelerator; the first order model is unable to correctly model this effect and other effects such as the velocity skin effect.

The addition of a simple ablation model to the derived first order model demonstrated (as expected) that ablation would have the greatest effect on the performance of the plasma accelerator (as can be seen from the results presented in table 4.2). Unfortunately the addition of the simple ablation model still does not explain the operation of the Lica; in fact the simple ablation model suggests the final velocity of the bulk of the hydrogen plasma decreases with an ever increasing electrode length; hence given an infinite acceleration length the simple ablation model would imply that the final velocity of the plasma will tend towards 0km/s . This is because the simple ablation model directly incorporates the ablated material into the accelerated plasma mass and neglects any physical interactions this would have on the plasma, its properties and other effects such as plasma restrike (refer to section 1.3).

Overall it can be said that the first order model is inadequate to accurately model the complex time dependent system of the pulsed coaxial plasma accelerator. The initial first order model described by equations (4.11) and (4.12) represents an upper limit to the operation of a coaxial plasma accelerator operating in plasma block mode. These results would be attainable if all the factors effecting the operation of a plasma accelerator (most are mentioned in section 1.3) could be neglected and the plasma was conductive enough that essentially a filament current would be in effect. Such models can only give accurate answers for simple steady state problems, such as the examples given in [7]. In order to accurately model the operation of the Lica a numerical approach must be used, which will consist of three linked modelling processes: an electromagnetic model, a magnetohydrodynamic model, and an ion model. The electromagnetic

model is necessary to account for the electromagnetic effects i.e. Maxwell's equations (refer to section 4.3.2). The magnetohydrodynamic model is required to describe the motional aspects of the plasma i.e. the velocity and compressional effects. And finally, an ion model is necessary to describe the plasma and its interactions i.e. breakdown processes, conductivity calculations, ablation, plasma restrike et cetera.

The remainder of this chapter, section 4.3 in its entirety, is concerned with the development of an initial numerical model to simulate the electromagnetic aspects of the plasma accelerator.

4.3: Numerical models used to describe the electromagnetic aspects of plasma accelerators and rail guns

The finite element method (FEM) is the currently accepted approach to solving electromagnetic problems [105], [106], [107]. It is preferred over the previously favoured finite difference (FD) approach, because of its adaptability in the discretization of complex shaped problems and its far greater accuracy [108]; an overview of the history and development of FEM in electromagnetics can be found in [109]. Finite difference methods [110], [111], [112] are very simple to understand and implement compared to FEM; because of this they are still employed in the modelling of plasma accelerators [90], [91]. Other schemes that are typically used in the solution of fluid flow problems (Navier Stokes) such as the finite volume method (FV or FVM) [113], [114] have also been used to solve the electromagnetic aspects of rail guns [115].

In this thesis FEM was used as the method of choice, because of its general acceptance and the large amount of published literature relating to its implementation. The finite element method is discussed in section 4.3.1, the associated numerical problems (and solutions to these problems) encountered in modelling a coaxial plasma accelerator using this method are covered in sections 4.3.5 to 4.3.11. Isoparametric cubic serendipity finite elements [108] were used in the numerical program known as MATAC (that was developed to describe the operation of the Lica, refer to section 4.3.14); these elements give superior solutions in regions containing large gradients compared to lower order elements, as is demonstrated in the test problems presented in section 4.3.13.

The use of edge elements [105], [106], [116], [117] (which are a special vector oriented form of isoparametric elements) to model the problem was considered. Edge elements reduce the problem of singularities near re-entrant corners (singularities at re-entrant corners are discussed in section 4.3.8) [118], [119], [120]. Edge elements can also be formulated to prevent spurious solutions (spurious solutions are discussed in section 4.3.7); however this is only true for Cartesian coordinates (easily justified by considering the divergence in terms of cylindrical coordinates for the rectangular edge element given in [106]) and would require the plasma accelerator to be considered in three dimensions (requiring a prohibitive amount of computer memory and time).

The main reason why edge elements were not used is because only tangential boundaries/boundary conditions can be used. If edge elements were applied the problem of the coaxial plasma accelerator, imposing the normal current density boundary condition (refer to section 4.3.2) would not be possible and instead the tangential component would have to be specified, which is essentially an unknown, on some conducting surfaces.

4.3.1: The finite element method – FEM

The finite element method is a numerical technique, which is used to obtain approximate solutions to a set of equations with known boundary conditions. In the finite element method the problem domain is broken up into a series of elements. The elements consist of a series of specified points called nodes or nodal points; the solution to the problem is calculated at these points. The overall structure formed by the elements is referred to as a mesh. There are several finite element schemes: the variational method, the Ritz method and the Galerkin method (also known as the method of weighted residuals) [108], [121]. The Galerkin method is perhaps the easiest of all the methods to apply and for this reason it will be used as the method of choice to model the electromagnetic aspects of the plasma accelerator. In this approach the equation (to be integrated over the computational domain) is multiplied by a trial function (also referred to as an interpolation, test or shape function). The trial function is taken to be equal to the sought after solution to the problem and is typically represented by a polynomial function. The trial function is required to fulfill two conditions. Firstly, the order of the polynomial function chosen must be equal to the degrees of freedom of the element; in other words the polynomial must contain enough terms to define a set of equations in terms of the sought after solution for all the nodes of an element. Secondly, the continuity of the trial function must be the same as the equation being solved. This point is discussed in a practical approach in [108] and in a theoretical sense in [122]. In simple terms, if a polynomial trial function is used it will have what is known as C_0 continuity (the solution is guaranteed to be continuous across an element surface); hence it will be sufficient to give a unique variation of the derivative of the solution across the element surface. The highest order derivative that can be solved with C_0 continuity is a first order derivative. Due to this second requirement if a polynomial trial function is used then the equations to be solved must be simplified using integration by parts and the vector relationships in appendix 4A to derive derivative terms no higher than first order. Providing these requirements have been fulfilled the resulting equations (simplified by integration by parts if necessary) are integrated with respect to the computational volume and the resulting matrix is solved using the known boundary conditions.

The following example using a linear trial function across a one dimensional problem domain will be used to demonstrate the method by integrating equation (4.20) in the range of $0 < x < 1$.

$$\frac{\partial^2 u}{\partial x^2} = u \quad (4.20)$$

Subject to the boundary conditions

$$u(0) = 1 \quad (4.21)$$

$$u(1) = e^1 \quad (4.22)$$

First equation (4.20) is rearranged, then multiplied by the trial function w

$$\int_0^1 \left(w \frac{\partial^2 u}{\partial x^2} - wu \right) dx = 0 \quad (4.23)$$

Integration by parts on the above equation is used to produce what is known as a weak formulation or weak form of the problem:

$$\int_0^1 \left(- \frac{\partial w}{\partial x} \frac{\partial u}{\partial x} - wu \right) dx = - \left[w \frac{\partial u}{\partial x} \right]_0^1 \quad (4.24)$$

Let the assumed linear trial function be in the form of:

$$u = ax + b, \quad (4.25)$$

where a and b are constants. The elements across the problem domain can be expressed graphically as shown in diagram 4.2 below.

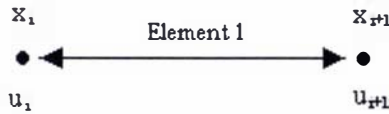


Diagram 4.2: Diagrammatic representation of a linear finite element

In diagram 4.2 x_i and x_{i+1} are two adjacent nodes used in the construction of an element, which have solutions of u_i and u_{i+1} respectfully:

$$u_i = ax_i + b \quad (4.26)$$

$$u_{i+1} = ax_{i+1} + b \quad (4.27)$$

Rearranging equations (4.26) and (4.27) gives the values for the constants a and b as:

$$a = \frac{u_{i+1} - u_i}{x_{i+1} - x_i} \quad (4.28)$$

$$b = \frac{u_i x_{i+1} - u_{i+1} x_i}{x_{i+1} - x_i} \quad (4.29)$$

Substituting equation (4.28) and (4.29) into equations (4.26) and (4.27) produces a linear solution for u across the element as:

$$u = H_1 u_i + H_2 u_{i+1} \quad (4.30)$$

, where

$$H_1 = \frac{x_{i+1} - x}{hi} \quad (4.31)$$

$$H_2 = \frac{x - x_i}{hi} \quad (4.32)$$

$$hi = x_{i+1} - x_i \quad (4.33)$$

Since the trial function is assumed to be the approximate solution to the problem (i.e. $w = u$), substituting equation (4.30) into the left hand side of equation (4.24) results in expression (4.34).

$$- \int_{x_i}^{x_{i+1}} \left(\begin{pmatrix} \dot{H}_1 \\ \dot{H}_2 \end{pmatrix} \begin{pmatrix} H_1, H_2 \end{pmatrix} + \begin{pmatrix} \dot{H}_1 \\ \dot{H}_2 \end{pmatrix} (H_1, H_2) \right) \partial x \begin{Bmatrix} u_i \\ u_{i+1} \end{Bmatrix} \quad (4.34)$$

, in which

$$\dot{H}_1 = -\frac{1}{hi} \quad (4.35)$$

$$\dot{H}_2 = \frac{1}{hi} \quad (4.36)$$

Integrating expression (4.34) results in the following matrix:

$$-\begin{bmatrix} \frac{1}{hi} + \frac{hi}{3}, -\frac{1}{hi} + \frac{hi}{6} \\ -\frac{1}{hi} + \frac{hi}{6}, \frac{1}{hi} + \frac{hi}{3} \end{bmatrix} \begin{Bmatrix} u_i \\ u_{i+1} \end{Bmatrix} \quad (4.37)$$

If the problem domain is considered to consist of two elements as shown in diagram 4.3.

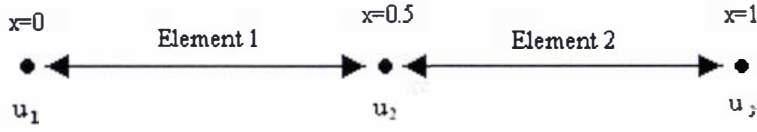


Diagram 4.3: Problem domain with two elements in the range of $0 < x < 1$

Using expression (4.37) the first element is written as expression (4.38) and the second element is written as being expression (4.39).

$$\begin{bmatrix} -2.1667, 1.9167 \\ 1.9167, -2.1667 \end{bmatrix} \begin{Bmatrix} u_1 \\ u_2 \end{Bmatrix} \quad (4.38)$$

$$\begin{bmatrix} -2.1667, 1.9167 \\ 1.9167, -2.1667 \end{bmatrix} \begin{Bmatrix} u_2 \\ u_3 \end{Bmatrix} \quad (4.39)$$

Directly adding the expressions for first and second elements results in what is known as the system matrix, combining the system matrix with the natural boundary conditions arising from the term on the right hand side of equation (4.24) (in which the test function w is equal to 1 at the first and last node, this can be verified by the reader) results in:

$$\begin{bmatrix} -2.1667, & 1.9167 & , & 0 \\ 1.9167, & -4.3333 & , & 1.9167 \\ 0 & , & 1.9167 & , & 2.1667 \end{bmatrix} \begin{Bmatrix} u_1 \\ u_2 \\ u_3 \end{Bmatrix} = \begin{bmatrix} u(0) \\ 0 \\ -u(1) \end{bmatrix} \quad (4.40)$$

Substituting the values for the known Dirichlet boundary conditions (equations (4.21) and (4.22)) into the above equation gives the following matrix, equation (4.41).

$$\begin{bmatrix} 1 & , & 0 & , & 0 \\ 1.9167, -4.3333, 1.9167 \\ 0 & , & 0 & , & 1 \end{bmatrix} \begin{Bmatrix} u_1 \\ u_2 \\ u_3 \end{Bmatrix} = \begin{bmatrix} 1 \\ 0 \\ e^1 \end{bmatrix} \quad (4.41)$$

The above system can be written in the more compact form of equation (4.42).

$$Ku = F \quad (4.42)$$

The solution u in equation (4.42) is calculated from the inversion of the system matrix K over the system vector F i.e.

$$u = K^{-1}F \quad (4.43)$$

This results in the values of $u_1 = 1$, $u_2 = 1.64$ and $u_3 = e^1$. The actual solution at $x = 0.5$ is 1.65, so the difference between the analytical and the numerical answer for this example is approximately 0.61 percent. The more elements that are used in the calculation the more accurate the final solution (as a general rule of thumb).

The above discussion is somewhat over simplified; a good reference discussing the above points in detail is [108]. It is possible to use functions other than polynomials that have higher degrees of continuity, such as Hermite polynomials [108]; however in this thesis only C_0 continuity elements are required (as seen from inspection of equations (4.69) and (4.70) in section 4.3.3), so this point will be discussed no further.

The above example used analytically calculated trial functions; this approach is cumbersome and rather limited in scope. A better, and widely accepted, approach is to use isometric elements [108], [121], in which the trial functions can be calculated numerically using Legendre-Gauss integration of Lagrange polynomials [108]. Isoparmetric elements are integrated in a normalised coordinate system (usually between the dimensionless points of -1 and 1), which has been derived from the physical coordinate system using a Jacobian. Isoparametric elements have great versatility in being able to represent curved surfaces and still give accurate results when deformed or compressed [108], [123]. There is a variation on the traditional finite elements, derived from Lagrange polynomials (which have internal nodes within the elements), known as Serendipity elements. These elements are particularly advantageous for high order trial

functions, because they only contain exterior nodes (nodes on elemental surfaces) reducing the computational memory and time required to obtain a solution compared to the traditional isoparametric elements.

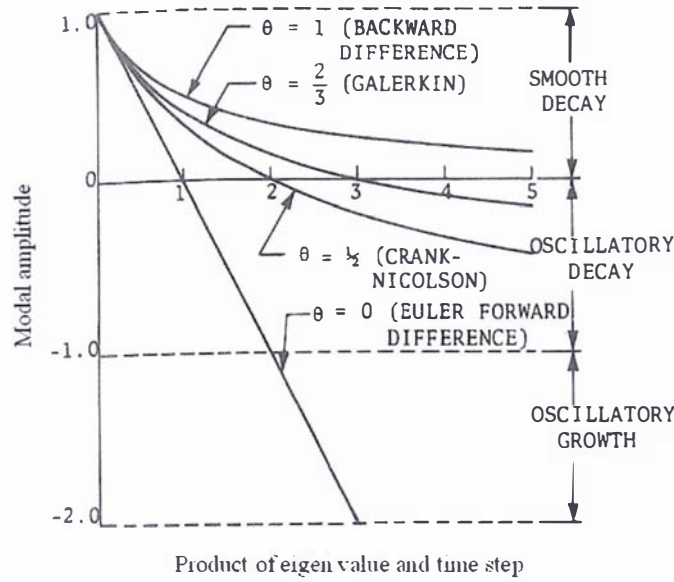
For problems in the finite element method that involve both a spatial and temporal dependence there are two techniques that can be used to find the transient response of a system, either the mode of superposition or a time marching scheme [108]. The mode of superposition uses eigenvalue analysis; this method is computationally (very) expensive and is traditionally used in solving second order equations encountered in structural analysis [108]. A time marching scheme was chosen as the method of choice, because of its simplicity and ease of implementation. A time marching scheme relies on deriving recursion formulas which relate the solution at one instance of time t to the solution at a later time $t + \Delta t$, based on a finite time step Δt . In the Galerkin method the temporal domain is treated in the same manner as the spatial domain [108], [121] and the temporal derivatives are multiplied by a trial function in much the same manner (with the same restrictions being placed upon the trial function as discussed previously). The only difference is that the sort after solution is in both time and space; this results in the following representation:

$$M \dot{u} + Ku = F \quad (4.44)$$

In equation (4.44) M is the temporal variation matrix (containing the integrated trial function and temporal derivative terms), K is the system matrix, and F is the system vector. The generalised form of a time marching scheme [108], obtained using a finite difference approximation, is given by equation (4.45) below:

$$\left[\theta K + \frac{1}{\Delta t} M \right] u_{t+\Delta t} = \left[-(1-\theta)K + \frac{1}{\Delta t} M \right] u_t + (1-\theta)F_t + \theta F_{t+\Delta t} \quad (4.45)$$

The subscripts in equation (4.45) represent the solutions/matrices at a given point in time. Equation (4.45) represents a family of recurrence relationships; the particular algorithm chosen depends upon the value of θ (a dimensionless constant). The following algorithms are available: the forward difference method if $\theta = 0$, the Crank-Nicolson method if $\theta = \frac{1}{2}$, the Galerkin method (not to be confused with the Galerkin finite element method) if $\theta = \frac{2}{3}$ and the backwards difference method if $\theta = 1$. Graph 4.6 shows the stability of these algorithms.



Graph 4.6: Graph showing stability behaviour of recurrence formula, using eigenvalue analysis [108]

The forward difference method is an explicit method (conditionally stable), whose stability is dependent upon the size of the time step that is used; the other methods are implicit (unconditionally stable). Although the Crank-Nicolson method is a second order accurate scheme, giving the least error for any of the implicit schemes, the backwards difference method always gives a smooth decay rate. This allows the backwards difference method to be applied to very fast changing systems with a time step of any size without the concern of oscillations appearing in the solution, as might happen if one of the other implicit schemes were used.

Finally, the finite element method will only produce a unique solution if the uniqueness theorem is satisfied [107], [112]. The uniqueness theorem guarantees that the problem will give a unique solution. A vector quantity will only be uniquely defined if both its curl and divergence are defined and either its Dirichlet or Flux boundary conditions (arising from the weak formulation) are satisfied on the boundaries. A scalar quantity is only uniquely defined if either its gradient or value is specified on the boundaries.

4.3.2: Maxwell's equations and boundary conditions

The mathematical formulas that describe the electromagnetic effects in a plasma accelerator system are those of Maxwell's equations: Gauss's law, Gauss's law of magnetism, Faraday's law of induction, and Ampere's law.

Gauss's law, equation (4.46), states that the total electric flux D through any closed surface must equal the net charge q inside that surface

$$\nabla \cdot D = q \quad (4.46)$$

The electric flux is defined in terms of the electric field E and the total polarisation p by equation (4.47).

$$D = \varepsilon_o E + p \quad (4.47)$$

Gauss's law in magnetism, equation (4.48), states that the net magnetic flux B through any closed surface must equal zero.

$$\nabla \cdot B = 0 \quad (4.48)$$

Faraday's law of induction, equation (4.49), states that the line integral of the electric field E through any closed path must equal the change in magnetic flux through any surface bound by that path.

$$\nabla \times E = -\frac{\partial B}{\partial t} \quad (4.49)$$

Ampere's law, equation (4.50) in which \dot{J} is the current density, describes the line integral of the magnetic field H around any closed path and is determined by the sum of the conduction current through that path plus the rate of change of electric flux through any surface bounded by that path.

$$\nabla \times H = \dot{J} + \frac{\partial D}{\partial t} \quad (4.50)$$

The magnetic field in equation (4.50) is described in terms of the magnetic flux by equation (4.51), where M is the magnetic moment (the helical motion of charges in a magnetic field). The magnetic moment can be considered to be the gyro radius effect mentioned in section 1.3.

$$H = \frac{1}{\mu_o} B + M \quad (4.51)$$

The current density term \vec{J}^* , in equation (4.50), is comprised of the conduction current \vec{J} and the convection current $q\vec{v}$ (which is the current flow due to the transport of excess charges) [7].

The conduction current is described through the use of an equation of state known as Ohm's law, given by equation (4.52) below, in which the effects of ion slip [7], [124] have been ignored. In equation (4.52) β is Hall's constant [7], $\beta \vec{J} \times \vec{B}$ is the Hall conduction current and ∇P_e is the electron pressure.

$$\vec{J} = \sigma(\vec{E} + \vec{v} \times \vec{B} + \beta(\vec{J} \times \vec{B} - \nabla P_e)) \quad (4.52)$$

Maxwell's equations can be simplified through the use of the magnetohydrodynamic approximation [7]. It has been assumed for the current analysis of the plasma that Polarisation effects are unimportant, so this term is neglected in equation (4.47). The ion gyro radius effect will not be considered an important factor so \vec{M} will be neglected in equation (4.51). The generalised equation for Ohm's law is simplified for the case of a conducting plasma because $\beta \sim 0$; hence the two terms on the right hand side of equation (4.52) disappear. The displacement current term in equation (4.50) can be neglected, because of the proof provided in [7]. The current density \vec{J}^* can be set equal to the conductor current \vec{J} , because the convection current $q\vec{v}$ is very small, as explained from the proof given in [7]. Finally, Gauss's law (equation (4.46)) is simplified for the case of a current carrying conductor which does not have any surface charge present. The simplified Maxwell equations are then given as:

$$\nabla \times \vec{E} = -\frac{\partial \vec{B}}{\partial t} \quad (4.53)$$

$$\frac{1}{\mu_o} \nabla \times \vec{B} = \vec{J} \quad (4.54)$$

$$\vec{J} = \sigma(\vec{E} + \vec{v} \times \vec{B}) \quad (4.55)$$

$$\nabla \cdot \vec{B} = 0 \quad (4.56)$$

$$\nabla \cdot \vec{E} = 0 \quad (4.57)$$

$$\vec{H} = \frac{1}{\mu_o} \vec{B} \quad (4.58)$$

$$\vec{D} = \epsilon_o \vec{E} \quad (4.59)$$

4.3.2: Maxwell's equations and boundary conditions

The current continuity equation given by equation (4.60), which was directly derived from equation (4.54), ensures the current is conserved.

$$\nabla \cdot J = 0 \quad (4.60)$$

The property related boundary conditions of Maxwell's equations are covered in any text book that deals with electromagnetics [7], [107], [112]. The most important boundary conditions relating to a plasma accelerator are the normal component of the magnetic flux, the tangential component of the electric field, and the normal component of the current density on the surface of a conductor. The normal component of the magnetic flux across a surface must be continuous, as shown in equation (4.61) where the subscripts represent two different regions.

$$B_1 \cdot n = B_2 \cdot n \quad (4.61)$$

The tangential component of the electric field across a surface must be continuous, as demonstrated by equation (4.62) below where the subscripts represent two different regions.

$$E_1 \times n = E_2 \times n \quad (4.62)$$

And finally the normal component of the current density is zero at the surface of a conductor i.e.

$$J \cdot n = 0 \quad (4.63)$$

4.3.3: The AVA formulation

The simultaneous equations of (4.53) to (4.57) can be formulated into a more compact form using of the magnetic vector potential A , which is defined as:

$$\nabla \times A = B \quad (4.64)$$

Equation (4.53) can be rewritten in terms of A by the substitution of equation (4.64), producing equation (4.65).

$$\nabla \times E = - \left(\nabla \times \frac{\partial A}{\partial t} \right) \quad (4.65)$$

Integrating equation (4.65) results in an expression for the electric field, given by equation (4.66), where the electric scalar potential V arises as an integration constant.

$$\mathbf{E} = -\frac{\partial \mathbf{A}}{\partial t} - \nabla V \quad (4.66)$$

Equations (4.53), (4.54), (4.55), (4.66) and (4.64) can now be combined into a single equation:

$$-\frac{\partial \mathbf{A}}{\partial t} = \frac{1}{\sigma \mu_o} \nabla \times (\nabla \times \mathbf{A}) + \nabla V - \mathbf{v} \times (\nabla \times \mathbf{A}) \quad (4.67)$$

An equation describing the electric scalar potential in terms of the magnetic vector potential is obtained by combining equations (4.60), (4.55), (4.64) and (4.66) to give:

$$\nabla \cdot \left(\sigma \frac{\partial \mathbf{A}}{\partial t} + \sigma \nabla V - \sigma \mathbf{v} \times (\nabla \times \mathbf{A}) \right) = 0 \quad (4.68)$$

Equations (4.67) and (4.68) are referred to as the AVA formulation [125], where the magnetic vector potential exists in both conducting and non-conducting regions and the electric scalar potential exists only in the conducting regions. There are several variations of the AVA formulation, such as the modified magnetic vector potential [125], [126] and the AVA ϕ formulation [125], [127].

The AVA formulation is relatively simple to implement and is capable of solving multi-connected conductive and non-conductive regions. Regions of discontinuous or varying conductivity can be solved through the use of equation (4.68), which also ensures that the current continuity is always satisfied [125], [107]. Both time dependent and steady state problems can be solved; however a loss in the accuracy of the solution is often apparent at high and low frequencies, because the equations become badly structured [107].

The main advantages of the modified magnetic vector potential are a reduction in computer memory from the exclusion of the electric scalar potential variable and its ease of implementation. However the formulation is restricted to calculations in conductive regions and can cause problems, because unknown boundary conditions may have to be applied to conductive surfaces. But the main drawback of the formulation is that the current continuity is only weakly implied, because of this the formulation cannot be used in regions of varying conductivity [107], [128], [129].

The AVA ϕ formulation has the same properties as the AVA formulation; however it has the advantage of reducing the number of variables in non-conductive regions from three components to one. The AVA ϕ has altered boundary conditions compared to the standard AVA formulation for the magnetic vector potential at conductive surfaces, because the magnetic field is a continuous function and is described by the magnetic vector potential in conductive regions and the magnetic scalar potential ϕ in non-conductive regions [125]. The altered boundary conditions in themselves are not a problem, however in a situation that has a time dependent distribution of conducting and non-conducting regions such a formulation becomes a hindrance [90], because the scheme requires a constant re-evaluation of the magnetic vector potential and magnetic scalar potential regions as well as their initial values (in a time marching scheme). Despite the obvious problem associated with the AVA ϕ formulation a variation of the formulation has been derived [130] that has the advantage that the standard conductor boundary condition of $A \cdot n = 0$ is replaced by $V = 0$. This is particularly advantageous in cases of a deformed boundary (refer to section 4.3.11) where it is difficult to set $A \cdot n = 0$.

The modelling of a plasma accelerator is a time dependent problem with variable conductivity in the plasma region and time dependent/deforming boundaries. The modified magnetic vector potential formulation cannot be used to model such a problem, because it will be unable to handle the variable conductivity within the plasma and the setting of the boundary conditions for the magnetic vector potential upon deformed boundaries would be problematic.

The AVA ϕ formulation could be used, but it would be a hindrance due to the (possibility of) changing regions of conductivity from either the re-meshing of the computational domain as a result of the compression of the plasma or from the addition of conductive ablated material. This leaves the standard AVA formulation as the only available formulation that is able to model the problem of the plasma accelerator.

The weak AVA formulation [125], equations (4.69) and (4.70), used in the Galerkin residual finite element method is derived by multiplying equations (4.67) and (4.68) by their respective test functions, integrating over the entire computational region and then simplifying the resulting equations using the vector relationships in appendix 4A.

$$\int \frac{1}{\mu_0} \nabla \times W \cdot \nabla \times A \partial \Omega + \int \sigma W \cdot \frac{\partial A}{\partial t} \partial \Omega - \int \sigma W \cdot v \times (\nabla \times A) \partial \Omega - \int \frac{1}{\mu_0} W \cdot (\nabla \times A) \times n \partial \Gamma = 0 \quad (4.69)$$

$$\begin{aligned} & \int \sigma \nabla W \cdot \frac{\partial A}{\partial t} \partial \Omega - \int \sigma \nabla W v \times (\nabla \times A) \partial \Omega + \int \sigma \nabla W \cdot \nabla V \partial \Omega - \int \sigma W \cdot \frac{\partial A}{\partial t} \cdot n \partial \Gamma \\ & + \int \sigma W v \times (\nabla \times A) \cdot n \partial \Gamma - \int \sigma W \nabla V \cdot n \partial \Gamma = 0 \end{aligned} \quad (4.70)$$

4.3.4: The problem domain

Because of the symmetry of the problem (as discussed in section 4.1.1), the discretization of the overall problem is represented diagrammatically in diagram 4.4 below.

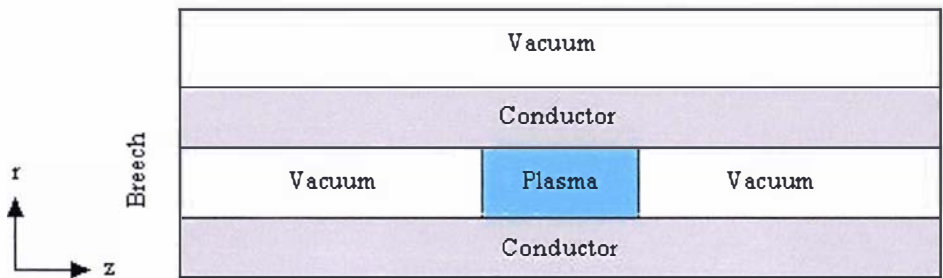


Diagram 4.4: Diagram of two dimensional problem domain (in cylindrical coordinates) used in the numerical electromagnetic model

The conductivity of the plasma is calculated using the conductivity profile given in section 3.3.8 (graph 3.18) and is used to calculate the resistance of the plasma. This resistance is combined with the calculated resistance and inductance of the plasma accelerator (and its associated components) and is used to solve the equation of charge (equation (4.1)), in which all the circuit parameters are assumed to be constant. The resulting calculated current is used as a known boundary condition at the breech of the plasma accelerator. The normal current density component is set equal to zero on all conducting surfaces. The vacuum region around the plasma accelerator is suitably large enough that far field boundary conditions can be set (these boundary conditions are discussed in section 4.3.11); hence the magnetic field at the breech (as the sole result of current flowing in the electrodes) can be set. The plasma block is accelerated (under these boundary conditions) until a user defined distance has been covered.

The above discussion is only a general description of how the problem and its boundary conditions are used in terms of the numerical model MATAC. These aspects are discussed in full, together with the techniques used in dealing with encountered numerical problems, in section 4.3.14.

4.3.5: Numerical problems encountered in the FEM modelling of plasma accelerators and rail guns

There are six numerical problems associated with trying to model the electromagnetics of a coaxial plasma accelerator: singularities close to the axis, spurious solutions of the magnetic

4.3.5: Numerical problems encountered in the FEM modelling of plasma accelerators and rail guns

vector potential, corner singularities, modelling a moving/deforming system, upwinding to prevent numerical oscillations from unsymmetrical matrix terms, and boundary conditions for far field and curved/deforming boundaries. These numerical issues are discussed in the following sections 4.3.6 to 4.3.11.

4.3.6: Singularities close to the axis

Singularities close to the axis arise from terms proportional to $\frac{1}{r}$ and $\frac{1}{r^2}$ in the cylindrical form of the weak AVA formulation, obtained from expanding equations (4.69) and (4.70) using the cylindrical coordinate relationships given in appendix 4A. As r goes to zero these terms become infinite. A simple way of rectifying this problem is to use a coordinate transformation [105], [107], [90] to remove these terms. The following coordinate transformation will remove these singularities [90]:

$$(A_r, A_\theta, A_z) \rightarrow (rA_r, rA_\theta, A_z) \quad (4.71)$$

The above transformation removes all terms inversely proportional to r from the formulation. Others have argued for a more strenuous approach [105], by transformations involving higher powers of r ; some have reported instances where simple transformations result in poor accuracy close to the axis and suggest transforming the potential variable and applying a coordinate transformation [107]. The simple coordinate transformation given by equation (4.71) was chosen as the method of choice, because of its simplicity and the general accuracy obtained from using it in the test problems of section 4.3.13.

4.3.7: Spurious solutions

A vector is not uniquely defined unless both its curl and divergence are defined. If a vector is not uniquely defined then there may be a series of solutions that fit the given equations, referred to as spurious solutions. Problems that do not contain uniquely defined vectors are often referred to as ill posed problems, where several solutions including the sought after solution can combine to give an unphysical solution. In terms of the AVA formulation there are typically two types of gauge that are used to impose the divergence of the magnetic vector potential. The first is the application of the Coulomb gauge [107] defined as:

$$\nabla \cdot \mathbf{A} = 0 \quad (4.72)$$

The second is the use of the Lorentz gauge [107], [131], [132], [133]:

$$\nabla \cdot \mathbf{A} = -\mu_o \sigma V \quad (4.73)$$

If the Lorentz gauge is used in the AVA formulation equation (4.68) describing the electric scalar potential is instead replaced by equation (4.73). The stationary weak AVA formulation containing the Lorentz gauge, given by equation (4.74), is derived from substituting equation (4.73) into (4.67). Equation (4.74) is presented as a stationary problem ($v = 0$) to make the following discussion simpler.

$$\begin{aligned} & \int \left(\frac{1}{\mu_o} \nabla \times \mathbf{W} \cdot \nabla \times \mathbf{A} + \sigma \mathbf{W} \cdot \frac{\partial \mathbf{A}}{\partial t} + \frac{1}{\mu_o \sigma} (\nabla \cdot \mathbf{A}) \nabla \cdot (\sigma \mathbf{W}) \right) \partial \Omega \\ & + \int \frac{1}{\mu_o} ((\nabla \times \mathbf{A}) \times \mathbf{W}) \cdot \mathbf{n} \partial \Gamma + \int \sigma V \mathbf{W} \cdot \mathbf{n} \partial \Gamma = 0 \end{aligned} \quad (4.74)$$

Equation (4.74) will only be unique if the boundary integrals are known, but because of equation (4.73) there is freedom of choice on conducting surfaces in imposing the zero normal current component condition $\mathbf{J} \cdot \mathbf{n} = 0$. In a stationary situation the current density defined by equation (4.55) gives the boundary condition of:

$$\sigma \frac{\partial \mathbf{A}}{\partial t} \cdot \mathbf{n} + \sigma \nabla V \cdot \mathbf{n} = 0 \quad (4.75)$$

There is flexibility in the above equation in the definition of \mathbf{A} with respect to V ; a suitable choice which reflects the physics of the problem and gives a unique solution is to directly relate $\mathbf{A} \cdot \mathbf{n}$ to V through equation (4.76), in which k^2 is a positive constant [107].

$$\frac{\partial \mathbf{A}}{\partial t} \cdot \mathbf{n} = k^2 \sigma \frac{\partial V}{\partial t} \quad (4.76)$$

Integrating equation (4.76) with respect to time and taking the integration constant to be equal to zero results in:

$$\mathbf{A} \cdot \mathbf{n} = k^2 \sigma V \quad (4.77)$$

This boundary condition will give a unique solution (for equation (4.74)) [107]. This formulation will always produce nonzero values of V , because the values of A and V are related through the choice of k^2 . If k^2 is set to a large number ($>1 \times 10^6$) then the values for V will be comparable to the machine rounding error for single precision, however the larger the value k^2 the more ill conditioned the matrix becomes. This is because the larger the value of k^2 the greater the emphasis that is placed upon the curl of A rather than on the divergence of A leading to spurious solutions [107].

If the conductivity varies between two adjoining conducting surfaces denoted as region 1 and region 2 there will be a jump in the normal component of ∇V across such a surface (because $J \cdot n$ and A are continuous across the surface). This can be represented by expanding equation (4.75) in terms of the different regions:

$$(\sigma_1 - \sigma_2) \frac{\partial A_1}{\partial t} \cdot n + \sigma_1 \nabla V_1 \cdot n - \sigma_2 \nabla V_2 \cdot n = 0 \quad (4.78)$$

(Because A is a continuous function, distinction between the different regions is unnecessary in equation (4.78)). A suitable choice, so that the surface integral of equation (4.78) can be defined to reflect the physical conditions of the problem and the jump conditions in ∇V , would be to relate $A \cdot n$ to V by equation (4.79) [107]:

$$\frac{\partial A}{\partial t} \cdot n = k^2 (\sigma_1 - \sigma_2) \frac{\partial V}{\partial t} \quad (4.79)$$

Integrating equation (4.79) with respect to time, and taking the integration constant to be equal to zero, results in equation (4.80).

$$A \cdot n = k^2 (\sigma_1 - \sigma_2) V \quad (4.80)$$

Although equation (4.80) allows for a unique solution, equation (4.80) must be applied on the surfaces of adjoining finite elements that have different conductivities. In the problem of modelling a plasma accelerator the plasma region has a discontinuous conductivity and equation (4.80) would have to be applied to all the elements in the plasma region. Such a condition becomes difficult to enforce, especially if a large number of elements are employed to model the plasma region.

The Coulomb gauge, in contrast to the Lorentz gauge is very simple to implement. The Coulomb gauge is imposed on equation (4.69) by the addition of the following term [134], [135], [136], [137]:

$$\int \frac{S}{\mu_o} \nabla(\nabla \cdot \mathbf{A}) \partial \Omega \quad (4.90)$$

In expression (4.90) S is a user defined constant known as the penalty parameter. Applying the Galerkin method to expression (4.90) and then integrating over the volume of the computational domain (making use of equations (4.A.7) and (4.A.11) in Appendix 4A) results in:

$$\int \frac{S}{\mu_o} (\nabla \cdot \mathbf{W})(\nabla \cdot \mathbf{A}) \partial \Omega - \int \frac{S}{\mu_o} (\nabla \cdot \mathbf{W}) \mathbf{A} \cdot \mathbf{n} \partial \Gamma \quad (4.91)$$

Provided that the normal component for \mathbf{A} is not set on the domain boundaries the Coulomb gauge will be satisfied over the entire computational region, because of the surface integral in expression (4.91). The magnitude of the penalty parameter determines the amount of emphasis that is placed upon the divergence of the magnetic vector potential.

A good discussion upon the effects of setting the penalty parameter are given in [138]; a simplified discussion can be made from the system of equations and associated boundary conditions, on arbitrary boundaries Γ_D and Γ_N , formed from equations (4.92) to (4.96).

$$\nabla \times \nabla \times \mathbf{H} - S \nabla(\nabla \cdot \mathbf{H}) - K^2 \mathbf{H} = 0 \quad (4.92)$$

$$\mathbf{H} \times \mathbf{n} = 0 \text{ on } \Gamma_D \quad (4.93)$$

$$\nabla \cdot \mathbf{H} = 0 \text{ on } \Gamma_D \quad (4.94)$$

$$\mathbf{H} \cdot \mathbf{n} = 0 \text{ on } \Gamma_N \quad (4.95)$$

$$(\nabla \times \mathbf{H}) \times \mathbf{n} = 0 \text{ on } \Gamma_N \quad (4.96)$$

The solutions to equation (4.92) (where K^2 is a positive constant greater than zero) and its associated boundary conditions (4.93), (4.94), (4.95) and (4.96) are separated into two systems

of equations. First a set of equations that represents the physical (termed as solenoidal) solution to the problem:

$$\nabla \times \nabla \times H - K^2 H = 0 \quad (4.97)$$

$$H \times n = 0 \text{ on } \Gamma_D \quad (4.98)$$

$$(\nabla \times H) \times n = 0 \text{ on } \Gamma_N \quad (4.99)$$

And a second set of equations that have no physical significance (termed as irrotational), the spurious solutions, given as:

$$S \nabla (\nabla \cdot H) + K^2 H = 0 \quad (4.100)$$

$$\nabla \cdot H = 0 \text{ on } \Gamma_D \quad (4.101)$$

$$H \cdot n = 0 \text{ on } \Gamma_N \quad (4.102)$$

The solutions to equation (4.100) are irrotational solutions of (4.92) whose resonant frequencies, of the eigenvalues (which are solutions to the equations), increase linearly with the square root of the penalty parameter [138], [134]. As the penalty parameter S approaches zero there will be an infinite number of such solutions. The larger the value of the penalty parameter the greater the emphasis placed upon the solenoidality of the solution, at the expense of the accuracy of the overall solution. Typically the value for the penalty parameter is set equal to 1 [107], [134].

A good example (with an analytical solution) embodying the above discussion of a situation where spurious solutions can arise is given in [116] and [117]. The problem is treated as a two dimensional problem in Cartesian coordinates using equation (4.103), with the condition of $\nabla \cdot A = 0$, K being a user defined constant and the boundary conditions shown in diagram 4.5.

$$\nabla \times \nabla \times A - K^2 A = 0 \quad (4.103)$$

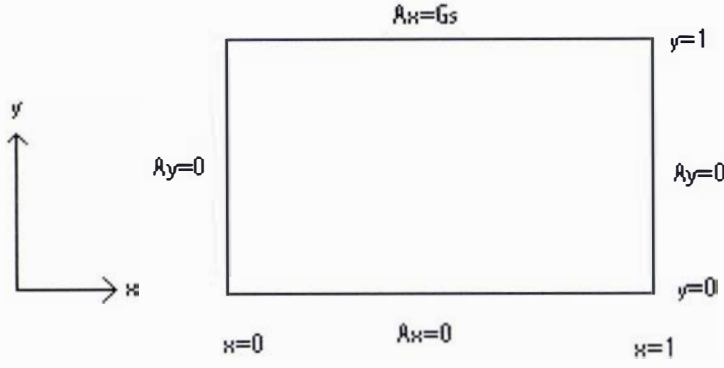


Diagram 4.5: Boundary conditions of the spurious example

The function G_s in diagram 4.5 is defined as $G_s = \cos(4\pi x)$, the solutions to equation (4.103) are presented in equations (4.104) to (4.107) according to the value of K^2 i.e. both the underdamped and overdamped solutions to the problem are displayed.

if $K^2 > 16\pi^2$

$$A_x = \cos(4\pi x) \sin(\sqrt{K^2 - 16\pi^2} y) \left(\frac{1}{\sin(\sqrt{K^2 - 16\pi^2})} \right) \quad (4.104)$$

$$A_y = -4\pi \sin(4\pi x) \cos(\sqrt{K^2 - 16\pi^2} y) \frac{1}{\sqrt{K^2 - 16\pi^2}} \left(\frac{1}{\sin(\sqrt{K^2 - 16\pi^2})} \right) \quad (4.105)$$

and if $K^2 < 16\pi^2$

$$A_x = \cos(4\pi x) \left(\frac{1}{e^\lambda - e^{-\lambda}} e^{\lambda y} - \frac{1}{e^\lambda - e^{-\lambda}} e^{-\lambda y} \right) \quad (4.106)$$

$$A_y = 4\pi \sin(4\pi x) \frac{1}{\lambda} \left(\frac{1}{e^\lambda - e^{-\lambda}} e^{\lambda y} + \frac{1}{e^\lambda - e^{-\lambda}} e^{-\lambda y} \right) \quad (4.107)$$

, where

$$\lambda = \sqrt{-(K^2 - 16\pi^2)} \quad (4.108)$$

Note, the solutions given in [117] only refer to the underdamped solution (equations (4.106) and (4.107)); the above equations represent both the overdamped and underdamped solutions to the system.

Equations (4.104) to (4.107) represent the physical (solenoidal) solutions, but there are an infinite number of non-physical (irrotational) solutions. These non-physical solutions are obtained if equation (4.103) is solved using the Galerkin weighted residual method with too small a value for the penalty factor. The correct physical results are obtained with a penalty parameter equal to one as can be seen in figure 4.1. For this particular problem an over emphasis of the solenoidality of the solution is not observed until the penalty parameter is set higher than 1×10^{14} (for the current mesh and linear elements that have been used). Spurious solutions are observed if the penalty parameter is set equal to zero as demonstrated in figure 4.2.

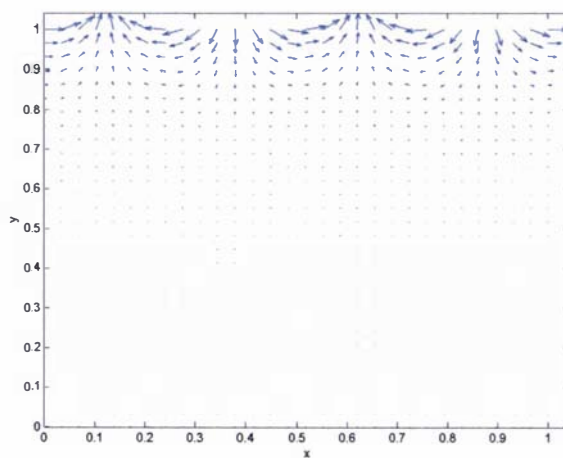


Figure 4.1: Vector plot showing the correct (physical) solution to the problem suggested by [116], with penalty parameter equal to 1, a value for K of 1 and a 30×30 (linear) mesh.

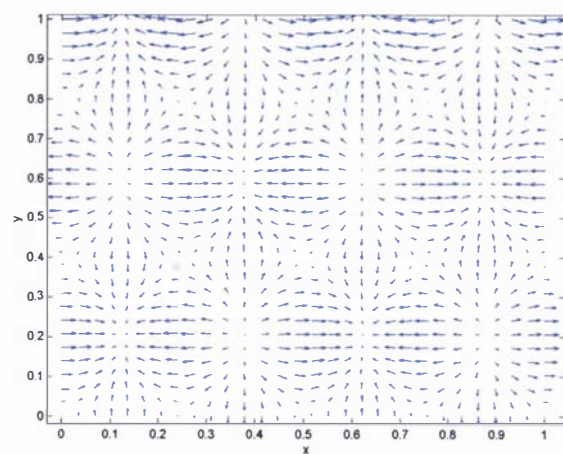


Figure 4.2: Vector plot showing spurious solutions for the problem suggested by [116], with a penalty parameter equal to zero, a value for K of 1 and a 30×30 (linear) mesh.

There are two other ways of imposing the Coulomb gauge on equation (4.72), using either eigenvalue analysis or a Lagrange multiplier. The method of using eigenvalue analysis to impose the Coulomb gauge was proposed in [139], this method has the attractive advantage of setting an individual penalty parameter to each of the solutions arising from equation (4.92). Basically the method works by trying to minimise the function F :

$$F = H^T (A + S_i C - K^2 B) H \quad (4.109)$$

, in which H is treated as a solution vector A, C and B are square matrices derived from the following equations:

$$A = \nabla \times H \cdot \nabla \times H \quad (4.110)$$

$$C = \nabla \cdot H \nabla \cdot H \quad (4.111)$$

$$B = H \cdot H \quad (4.112)$$

S_i is the penalty parameter for the corresponding “ i ” solution, the entire system is solved as an eigenvalue problem using an algorithm similar to that of trace minimisation [140]. After the problem has been solved in the subspace, the penalty parameter for a given solution is increased until the ratio of the curl to the divergence of the solution is below a user defined positive number, in [139] this number was set to 0.1. The entire process is repeated until the algorithm has converged. This method removes spurious solutions and has the added advantage of being able to set the penalty parameter to prevent an overemphasis of the solenoidal solution, but the method is difficult to implement and it requires a lot of computer memory. The other disadvantage is it is not possible to generate a parallel program using this technique. In the problem of modelling a plasma accelerator a lot of elements are required, consequently such an approach would not be practical (as a lot of memory would be required).

The possibility of using a Lagrange multiplier to impose the Coulomb gauge has not been previously investigated, the theory and application of Lagrange multipliers is discussed in Appendix 4B. There is precedence for this approach in [141], where the condition of $\nabla \cdot v = 0$ was applied to an incompressible fluid flow problem. To demonstrate and test the effectiveness of this proposed method, the stationary forms of equations (4.67) and (4.68) will be used. The AVA formulation with the Coulomb gauge introduced by means of the Lagrange multiplier λ is described by equations (4.113) to (4.115)

$$\frac{1}{\mu_o} \nabla \times \nabla \times \mathbf{A} - \sigma \frac{\partial \mathbf{A}}{\partial t} - \sigma \nabla V + \lambda \nabla \cdot \mathbf{A} = 0 \quad (4.113)$$

$$\nabla \cdot \left(\sigma \frac{\partial \mathbf{A}}{\partial t} + \sigma \nabla V \right) = 0 \quad (4.114)$$

$$\nabla \cdot \mathbf{A} = 0 \quad (4.115)$$

Using the Galerkin weighted residual method (in which equations (4.113) and (4.115) are multiplied by a test function for \mathbf{A} and equation (4.114) is multiplied by a test function for V) the following set of equations is derived:

$$\int W \cdot \left(\frac{1}{\mu_o} \nabla \times \nabla \times \mathbf{A} - \sigma \frac{\partial \mathbf{A}}{\partial t} \right) \partial \Omega - \int W \cdot \sigma \nabla V \partial \Omega + \lambda \int W \nabla \cdot \mathbf{A} \partial \Omega = 0 \quad (4.116)$$

$$\int W \nabla \cdot \left(\sigma \frac{\partial \mathbf{A}}{\partial t} + \sigma \nabla V \right) \partial \Omega = 0 \quad (4.117)$$

$$\int W \nabla \cdot \mathbf{A} \partial \Omega = 0 \quad (4.118)$$

The above set of equations (4.116), (4.117) and (4.118) can be written in the form of a matrix as:

$$\begin{bmatrix} L_{11}, L_{12}, g' \\ L_{21}, L_{22}, 0 \\ g, 0, 0 \end{bmatrix} \begin{Bmatrix} \mathbf{A} \\ V \\ \lambda \end{Bmatrix} = 0 \quad (4.119)$$

The terms L_{11} , L_{12} , L_{21} , L_{22} and g in the above matrix are defined by equations (4.120) to (4.124).

$$L_{11} = \int W \cdot \left(\frac{1}{\mu_o} \nabla \times \nabla \times \mathbf{A} - \sigma \frac{\partial \mathbf{A}}{\partial t} \right) \partial \Omega \quad (4.120)$$

$$L_{12} = - \int W \cdot \sigma \nabla V \partial \Omega \quad (4.121)$$

$$L_{21} = \int W \nabla \cdot \sigma \frac{\partial A}{\partial t} \partial \Omega \quad (4.122)$$

$$L_{22} = \int W \nabla \cdot \sigma \nabla V \partial \Omega \quad (4.123)$$

$$g = \int W \nabla \cdot A \partial \Omega \quad (4.124)$$

The Lagrange multiplier technique, with slack variables on the matrix diagonals (refer to appendix 4B), gives similar results to that of using the penalty parameter technique. However the Lagrange multiplier technique requires a lot more memory and computing time than the penalty factor technique (because it requires a larger system matrix). A disadvantage of using this method is that on boundaries where Dirichlet conditions are set the $\nabla \cdot A = 0$ condition no longer applies (upon these boundaries). This is demonstrated in figure 4.3 in which the Lagrange multiplier method has been applied to the test problem of a current carrying coaxial cable, as described in section 4.3.13. The penalty factor technique is more flexible, since the tangential component of A can be set as a Dirichlet condition upon any boundary surface.

The Coulomb gauge is used in the calculations presented here in the modelling of the plasma accelerator, because it is impractical to use the Lorentz gauge due to the discontinuous conductivity of the plasma. The Coulomb gauge is introduced into the AVA formulation using the traditional penalty parameter method. This is because the method of using eigenvalue analysis [139] requires too much memory and computational time and the use of Lagrange multipliers requires more memory, computer time and does not give as good a result as the penalty parameter method.

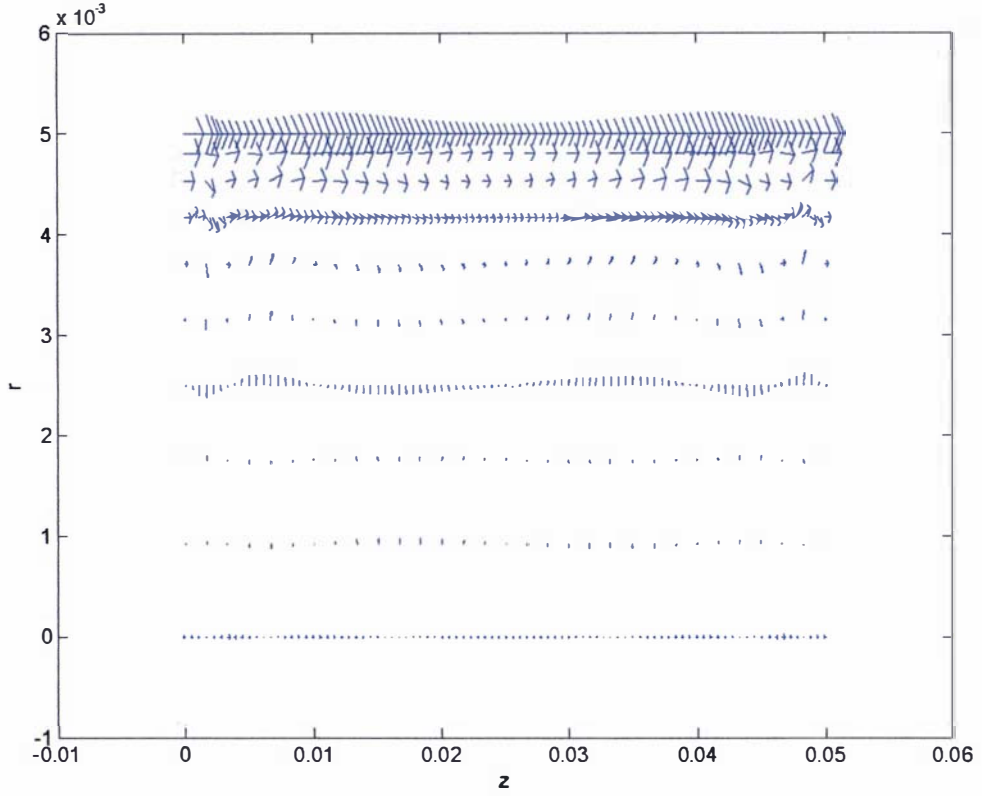


Figure 4.3: Vector plot showing the extracted current density in the cathode region for the problem of a current carrying coaxial cable (refer to section 4.3.13), using the AVA formulation and the Lagrange multiplier technique to impose the Coulomb gauge

4.3.8: Corner singularities

It is well known that any plane (electromagnetic) wave can be decomposed into two distinct planes, a E_z polarized plane having only a “z” component for the electric field and a H_z plane only a “z” component for the magnetic field [106].

The solution to Laplace’s equation in cylindrical coordinates for a two component (r, θ) system yields the following form for the solution of $\nabla^2 \mathcal{G} = 0$ (refer to [107]): $\mathcal{G}(r, \theta) = (cr^m + dr^{-m})(g\cos(m\theta) + h\sin(m\theta))$ where c, d, g and h are constants. The variables in the tangential plane are solved using the previously described equation and boundary conditions. Once the tangential field (i.e. the vector given in the form of $\nabla \mathcal{G}$) has been calculated the transverse field component can be solved using either $E = \frac{1}{j\omega\epsilon_o} \nabla \times H$ or

$H = \frac{1}{j\omega\mu_o} \nabla \times E$ (depending upon the sought after field value), where it has been assumed

that the fields vary in time as a complex exponential function (i.e. $e^{-j\omega t}$, where ω is a

constant) [106]. At re-entrant corners the solution for field variables becomes that of the steady state solution [105], [106], [142]; hence the electric field is described as:

$$E = -\nabla V \quad (4.125)$$

The magnetic field described by the non-conducting region is $\nabla \times B = 0$; therefore the magnetic field around a re-entrant corner is expressed by the magnetic scalar potential φ as:

$$B = -\nabla \varphi \quad (4.126)$$

It is known that the solution of some of the components at a re-entrant corner becomes singular. For this reason the geometry of the problem around a re-entrant corner is best described by the cylindrical coordinate system as shown in diagram 4.6

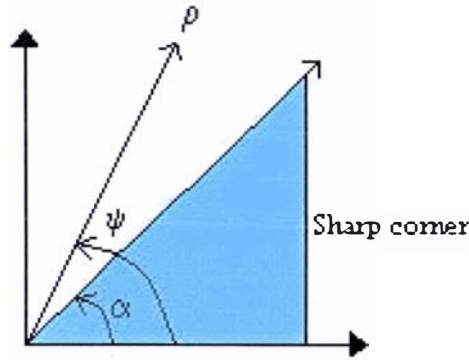


Diagram 4.6: Coordinates for a re-entrant corner describing the singularity

In diagram 4.6 α is the angle of the corner, ρ and ψ are the cylindrical coordinates of the sharp corner. Combining the simplified Gauss's law of equation (4.57) with equation (4.125) gives:

$$\nabla \cdot (\nabla V) = 0 \quad (4.127)$$

Solving the above equation (using the cylindrical coordinates of the sharp corner) gives the equation for the electric scalar potential as:

$$V = A\rho^v \sin(v(\psi + \psi_o)) \quad (4.128)$$

In equation (4.128) the terms A , v and ψ_o are integration constants to be determined by the boundary conditions. Substituting equation (4.128) into equation (4.125) and expanding results in the electric field :

$$E = \left(-Av\rho^{v-1}(\sin(v(\psi + \psi_o))) \right) \mathbf{i} + \left(-Av\rho^{v-1}(\cos(v(\psi + \psi_o))) \right) \mathbf{j} \quad (4.129)$$

The tangential electric field is zero at a perfectly conductive surface; so the values of ψ_o and v are solved as [106]:

$$\psi_o = -\alpha \quad (4.130)$$

$$v = \frac{\pi}{2\pi - \alpha} \quad (4.131)$$

The corresponding magnetic field in the transverse direction z_m is derived as [106]:

$$H_{z_m} = j\omega\epsilon_o A\rho^v \cos(v(\varphi - \alpha)) \quad (4.132)$$

Substituting equation (4.126) into Gauss's law of magnetism (equation (4.56)) produces equation (4.133), which when solved will give both the magnetic field in the $\rho\psi$ plane and the transverse electric field at the singular point.

$$\nabla \cdot (\nabla \varphi) = 0 \quad (4.133)$$

Solving equation (4.133) (using the cylindrical coordinates of the sharp corner) results in:

$$\varphi = A\rho^v \cos(v(\psi + \psi_o)) \quad (4.134)$$

Substituting equation (4.134) into equations (4.126) and (4.58) produces:

$$H = \left(-Av\rho^{v-1}(\cos(v(\psi + \psi_o))) \right) \mathbf{i} + \left(Av\rho^{v-1}(\sin(v(\psi + \psi_o))) \right) \mathbf{j} \quad (4.135)$$

The normal magnetic field is zero at a perfectly conductive surface; therefore the values of ψ_o and v are given by equations (4.130) and (4.131) [106]. Assuming as before that the magnetic

field varies in time as a complex exponential function, the transverse electric field is solved as equation (4.136) [106].

$$E_{z_m} = j\omega\mu_o A\rho^v \text{Sin}(v(\varphi - \alpha)) \quad (4.136)$$

The values for the tangential components of E and H are proportional to ρ^{v-1} , because of this these components will be singular (i.e. infinite) at the corner if the internal angle of the corner is less than π (refer to equation (4.131) (i.e. as ρ goes to zero then $\rho^{v-1} \rightarrow \infty$). However the transverse components H_{z_m} and E_{z_m} are equal to zero at the corner, because these values are proportional to ρ^v .

The above discussion relates only to the case of a conducting corner, but singularities can also be found in dielectric corners and at a dielectric/conductor corner [143].

In the problem of modelling a Plasma accelerator, (which is being treated as a two dimensional axisymmetrical problem as stated in section 4.3.4) there are only E_r and E_z components corresponding to the tangential components given by equation (4.129) together with a H_θ component, which is given by (the transverse component) equation (4.132). At the boundary made between the conducting plasma block and the cathode/anode surface there is a singularity, as can be seen in diagram 4.4 of section 4.3.4; hence at the singular corners the current density, which is a product of E_r and E_z , is infinite.

Traditional finite elements using Lagrange interpolation functions [108] are unable to model the components that are proportional to ρ^{v-1} close to a re-entrant corner. In order to correctly model the singularity using the finite element method, elements containing interpolation functions with the right type of singular derivative must be used. A simple scheme to incorporate this into a conventional finite element scheme was proposed in [142]. In this scheme a singular trial function is added to the standard finite element trial functions in the region of the singularity. However this scheme cannot be used for deformed/deforming isoparametric elements [105], because the scheme relies upon the Jacobian of the coordinate transformation not being distorted; so curvilinear isoparametric elements cannot be used with this scheme.

There is a singular basis function scheme that can be applied to high order isoparametric triangular elements [144], but this method was formulated for the boundary element method and the theory has yet to be extended to rectangular elements. Other possible singular trial functions have been suggested such as [145] and [146]. A different approach is to eliminate the

singularity from the computational domain in an exact fashion [147] instead of adding singular trial functions. The singularity in this method is removed from the computational domain by the use of an artificial boundary; however the method is more complicated to implement than the other methods that simply add a singular trial function to the standard finite elements.

A method that does not require any modification or addition to the standard finite element method is to simply refine the mesh in the area of the singularity [148], since standard finite element interpolation functions are polynomials, the finer the mesh is the more accurate the solution. Although such a method will not remove the error around the singularity it will reduce it, however it is computationally expensive.

It is unclear whether or not any of the techniques discussed above are employed in rail gun and plasma accelerator models. It is probable that they either rely upon node refinement in the region of the singularity [115] or that they simply accept the resulting error at and around the region of the singularity.

4.3.9: Modelling a moving /deforming system

The plasma accelerator consists of a moving plasma being accelerated down a stationary pair of electrodes; there are two types of coordinate systems that could be used to represent this problem: a fixed coordinate system known as an Eulerian system, or a moving coordinate system called a Lagrangian system. Both these systems are shown diagrammatically in diagram 4.7 for a two dimensional problem with respect to the coordinates r and z .

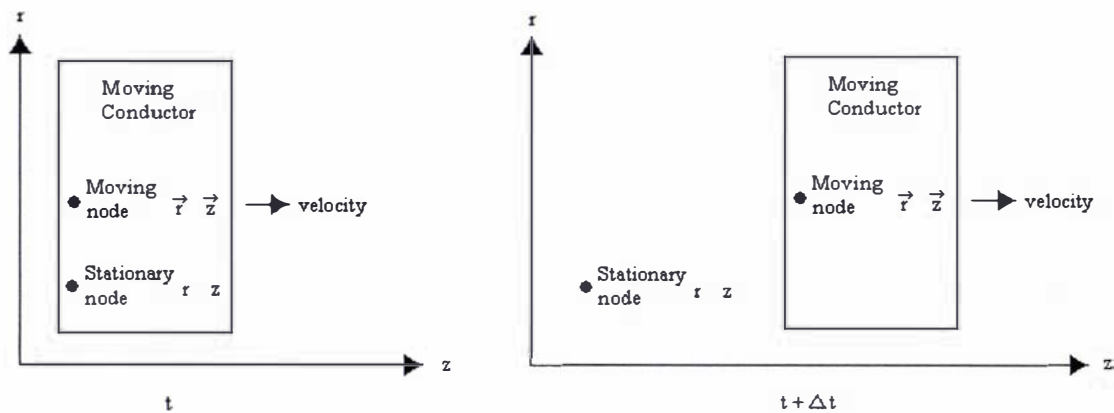


Diagram 4.7: Representation of stationary and moving coordinate systems

In a fixed coordinate system the mesh points are stationary with respect to the reference frame used to measure the velocity. The AVA formulation (given by equations (4.67) and (4.68)) is

rewritten to show the dependence upon the stationary coordinate system r and z by equations (4.137) and (4.138).

$$-\frac{\partial A_{(r,z)}}{\partial t} = \frac{1}{\sigma \mu_o} \nabla \times (\nabla \times A_{(r,z)}) + \nabla V_{(r,z)} - v \times (\nabla \times A_{(r,z)}) \quad (4.137)$$

$$\nabla \cdot \left(\sigma \frac{\partial A_{(r,z)}}{\partial t} + \sigma \nabla V_{(r,z)} - \sigma v \times \nabla \times A_{(r,z)} \right) = 0 \quad (4.138)$$

If this system was used to describe the plasma accelerator then, after each time step, the new position and conducting boundaries of the plasma would have to be re-evaluated, which would involve re-meshing the computational volume. Alternatively, the plasma could be moved through the mesh by the elements themselves; in such an approach the position of the plasma and its conductive boundaries would be represented by full or empty mesh elements as shown in diagram 4.8 below.

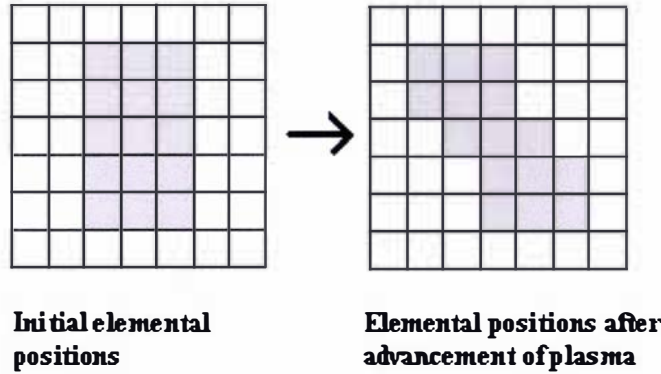


Diagram 4.8: Diagrammatic representation of the plasma mass, in a finite element model, using either full or empty mesh elements. The plasma elements are represented in grey.

At the end of each time step the plasma is advanced according to the calculated velocity distribution, the elements containing plasma are then determined based upon a user defined density threshold [90], [91]. Such a scheme is relatively easy to implement and gives a simple yet crude way to define the normal component of the current density as equalling zero on the conducting plasma boundary; however an exceedingly fine mesh would be required to obtain a truly accurate result.

In a moving coordinate system the mesh points are considered to be moving with a velocity relative to a stationary reference frame. The AVA formulation (given by equations (4.67) and (4.68)) is written in terms of the moving coordinate system \vec{r} and \vec{z} as:

$$-\frac{\partial \mathbf{A}_{(\vec{r}, \vec{z})}}{\partial t} = \frac{1}{\sigma \mu_o} \nabla \times \left(\nabla \times \mathbf{A}_{(\vec{r}, \vec{z})} \right) + \nabla V_{(\vec{r}, \vec{z})} \quad (4.139)$$

$$\nabla \cdot \left(\sigma \frac{\partial \mathbf{A}_{(\vec{r}, \vec{z})}}{\partial t} + \sigma \nabla V_{(\vec{r}, \vec{z})} \right) = 0 \quad (4.140)$$

At the end of each time step the mesh points are then moved to their new positions based upon their calculated velocities. This approach has several beneficial features. Firstly, the moving boundaries can be accurately represented since they are directly associated with the mesh points. And secondly, upwinding (discussed in section 4.3.10) is not required, because the unsymmetrical velocity terms which can lead to numerical oscillations do not appear in the formulation. A major advantage of using a moving coordinate system over a stationary one is that a substantial amount of memory and computational time is saved, because only the moving region is considered in the calculation. It has also been found that the moving coordinate system is superior to that of a stationary coordinate system regarding the accuracy of the solution for moving problems in which the computational mesh does not require re-meshing [149], [150], [151], [152]. However after several time steps the Lagrangian grid may become distorted to such an extent that the results become inaccurate or the nodes are moved beyond neighbouring nodes resulting in elements that are no longer connected by common sides, contravening the FEM approach. In such situations the mesh must be re-meshed to remove these distortions. The transfer of data from the old deformed mesh to the new re-meshed one is usually done through simple interpolation, but in doing this an inherent interpolation error is introduced. If the simulation has to be re-meshed many times the overall solution may produce unphysical results. Re-meshing schemes are commonly used in fluid flow problems [153], [154], [155], [156] and are the object of continued research. Specialised re-meshing programs have been developed that find the new mesh positions from the old ones, by using the old mesh interpolation shape functions to interpolate the dependant variables [156]. An alternative approach to re-meshing is to use a Free-Lagrangian method [155], which has no rigidly defined mesh in the computational region. Instead, at the start of each time step elements are formed from the nodes based on general connectivity of the nearest surrounding nodes; then the system is then solved and the

nodes are then moved to their new positions based upon their calculated velocities, the entire process is then repeated. The computational price of this method is that the interaction of all the nodes needs to be taken into consideration at the start of each time step, requiring a large system matrix.

In trying to model the plasma accelerator problem the use of a fixed coordinate system would be computationally expensive, because the entire region of the accelerator plus far field boundaries would have to be considered. The fixed coordinate system would also ultimately give rise to inaccurate solutions if the mesh was too coarse to account for the new position of the plasma at the end of a time step. Because the plasma is accelerated to a high velocity, of around 100 kms^{-1} [35], either a very fine mesh or very small time steps would be required to avoid this. A simpler solution to such a problem would be to use a moving coordinate system with a region surrounding the plasma sufficiently large enough to satisfy the far field boundary conditions for the magnetic field. To account for the stationary electrodes the reference frame is taken as being the velocity of the accelerating plasma; hence the electrodes will be moving with the negative velocity of the plasma [115]. In such a scheme the equations regarding the plasma and its boundary region are given by equations (4.139) and (4.140) (assuming the plasma is moving as an incompressible plasma mass), the equations for the electrodes will be given essentially by equations (4.137) and (4.138) rewritten to shown the dependence upon the moving reference frame \vec{r} and \vec{z} by equations (4.141) and (4.142).

$$-\frac{\partial \mathbf{A}_{(\vec{r}, \vec{z})}}{\partial t} = \frac{1}{\sigma \mu_o} \nabla \times \left(\nabla \times \mathbf{A}_{(\vec{r}, \vec{z})} \right) + \nabla V_{(\vec{r}, \vec{z})} - \mathbf{v} \times \left(\nabla \times \mathbf{A}_{(\vec{r}, \vec{z})} \right) \quad (4.141)$$

$$\nabla \cdot \left(\sigma \frac{\partial \mathbf{A}_{(\vec{r}, \vec{z})}}{\partial t} + \sigma \nabla V_{(\vec{r}, \vec{z})} - \sigma \mathbf{v} \times \left(\nabla \times \mathbf{A}_{(\vec{r}, \vec{z})} \right) \right) = 0 \quad (4.142)$$

4.3.10: Upwinding – A quadratic and cubic extension to the upwind scheme of Hughes

It has been observed in the literature [157], [158], [159] that the Galerkin weighted residual finite element method can give rise to spurious oscillations in the presence of significant non-symmetrical terms; for example the diffusion term in the diffusion advection equation used in fluid flow problems can lead to the appearance of unphysical numerical oscillations. The

4.3.10: Upwinding – A quadratic and cubic extension to the upwind scheme of Hughes

simplest example used to demonstrate this effect is given by equation (4.143), in which v is the velocity, with the boundary conditions given by equations (4.144) and (4.145).

$$\nabla^2 \phi - v \nabla \phi = 0 \quad (4.143)$$

$$\phi = 1 \quad \text{at} \quad x = 0 \quad (4.144)$$

$$\phi = 0 \quad \text{at} \quad x = 1 \quad (4.145)$$

Equation (4.143) with the associated boundary conditions (4.144) and (4.145) has the analytical solution of:

$$\phi(x) = A_1 + B_1 e^{vx} \quad (4.146)$$

$$\phi(x) = \frac{e^{vx} - e^v}{1 - e^v} \quad (4.147)$$

The weak formulation of equation (4.143) is given by equation (4.148). The surface integrals in this equation are unimportant, because it is a one dimensional problem with Dirichlet conditions applied on all boundaries.

$$\int \nabla \phi \nabla \phi \partial \Omega - \int v \phi \nabla \phi \partial \Omega = 0 \quad (4.148)$$

The spurious oscillations that can arise from this equation are purely numerical in nature and are dependent upon the velocity and the mesh size. It was I.Christie et al [158] who first provided a reason as to why these numerical oscillations occur in certain circumstances. If equation (4.148) is expanded using the linear test and basis functions as described by A.K.Runchal [160] for an internal node i that is between a previous node $i - 1$ and a following node $i + 1$, the resulting equation describing the answer at node i is derived as:

$$\phi = A_2 + B_2 \left[\frac{1 + (1 + A)L}{1 - (1 - A)L} \right]^i \quad (4.149)$$

In equation (4.149) the constants A_2 and B_2 are determined by the boundary conditions, L is called the Peclet number and is a function of the mesh size h and the velocity; the Peclet is defined by equation (4.150).

4.3.10: Upwinding – A quadratic and cubic extension to the upwind scheme of Hughes

$$L = \frac{1}{2}vh \quad (4.150)$$

The variable A in equation (4.150) is a function of the gradients of the test and basis functions at node i . Stability will be guaranteed (i.e. no oscillations) if the second term in equation (4.149) is positive, this will occur if $A \geq 1$ or if:

$$h < \frac{2}{(1-A)v}. \quad (4.151)$$

The term upwinding is derived from the fact that the test and or basis functions are biased in the direction of the velocity term (upwinded) to prevent numerical oscillations.

For the current example, which has been derived using linear test and basis functions, three situations can be derived:

- (i) $A = 1$ backwards difference
- (ii) $A = 0$ central difference
- (iii) $A = -1$ forward difference

No upwinding is applied to the finite element model if the central difference scheme is used (i.e. the use of the standard finite elements without upwinding). If the velocity term is positive then using the backwards difference scheme guarantees stability; while if the velocity term is negative using the forwards difference scheme will guarantee stability.

Unfortunately, the scheme developed by Christie et al [158] is not easy to implement and it is not amenable to extension to two or three dimensions. J.R.Hughes [157] developed a simple upwinded finite element scheme, which encompasses the work done by Christie et al. The scheme is extendable to two and three dimensional finite elements and can easily be added to existing finite element programs; it is this scheme that has been adopted by rail gun and plasma accelerator programs. The [157] scheme uses standard isoparametric linear rectangular finite elements with their associated standard test and basis functions and the integration is conducted using Gaussian integration with the standard integration points and weighting coefficients. The Gaussian integration points in the integral containing the unsymmetrical terms, ξ_e , (which can lead to numerical oscillations) are offset from their traditional positions (note in the upwinding scheme ξ_e still lies in the region of $0 < \xi_e < 1$). Using this scheme the weak formulation of equation (4.148) is expressed as equation (4.152).

4.3.10: Upwinding – A quadratic and cubic extension to the upwind scheme of Hughes

$$\sum v N_i(\xi_e) \nabla N_i(\xi_e) J W \phi' + \sum \nabla N_i(\xi) \nabla N_i(\xi) J W \phi' = 0 \quad (4.152)$$

In equation (4.152) J is the Jacobian, W is the standard Gaussian weighting coefficient, N is the standard isoparametric test function, and ξ is the standard Gaussian integration point. The location of ξ_e determines the amount of upwinding. Consider two adjoining one dimensional elements in the x coordinate that have a shared interior node i that is between a previous node $i-1$ and a following node $i+1$. Assume that the spacing between all the nodes is equal, so that the Jacobian for all elements will be the same, to simplify the following derivation. The solution at point i is expressed using standard 2-point Gaussian quadrature on the second term of the left hand side of equation (4.152) and a 1-point Gaussian quadrature on the first term on the left hand side of equation (4.152) resulting in equation (4.153).

$$\left(-\frac{v}{2}(1+\xi_e) - \frac{1}{h} \right) \phi_{i-1} + \left(v\xi + \frac{2}{h_e} \right) \phi_i + \left(\frac{1}{2}(1+\xi_e) - \frac{1}{h} \right) \phi_{i+1} = 0 \quad (4.153)$$

Equation (4.153) can be simplified by defining the variable $\alpha = \frac{vh}{2}$ resulting in:

$$(1 + \alpha(1 + \xi_e))\phi_{i-1} + (-2 - 2\alpha\xi_e)\phi_i + (1 - \alpha(1 - \xi_e))\phi_{i+1} = 0 \quad (4.154)$$

The solution of ϕ_i can be expressed as:

$$\phi = A + B \left[\frac{1 + (1 + \xi_e)\alpha}{1 - (1 - \xi_e)\alpha} \right]^i \quad (4.155)$$

In equation (4.155) A and B are constants to be determined by the boundary conditions. It can be clearly seen that equation (4.155) has the same form as equation (4.149), thus justifying the method; the numerical scheme is guaranteed to be stable if:

- (iv) $\xi_e = 1$ backwards difference: if v is positive
- (v) $\xi_e = 0$ central difference: using standard Gaussian integration point – if $v = 0$
- (vi) $\xi_e = -1$ forwards difference: if v is negative

4.3.10: Upwinding – A quadratic and cubic extension to the upwind scheme of Hughes

The scheme discussed above is easily extendable to two dimensions, by applying the same procedure to the basis and test functions used in the second dimension as shown in [157]. When applying this upwinding scheme to an existing finite element scheme the system matrix is first constructed using all the terms in the equation except for the unsymmetrical terms. The unsymmetrical terms are then calculated using the upwinded scheme described above and are then added to the system matrix to form the completed algebraic system of equations. Even though the scheme could be extended to higher dimensional elements there is no evidence of this in the literature. For the purposes of this thesis the scheme has been extended to quadratic and cubic elements, because high order FEM elements were used in the numerical model of section 4.3.14.

Extension of the simple upwinding scheme to quadratic elements

In order to extend the scheme of [157] to quadratic elements, first consider equation (4.143) as a one dimensional problem in the x coordinate with two adjoining one dimensional elements that have a shared interior node i . Describing the first element as consisting of nodes $i-1$, $i-\frac{1}{2}$ and i , where $i-\frac{1}{2}$ is an internal node and the nodes $i-1$ and i are integer nodes. The second element is then described as consisting of nodes i , $i+\frac{1}{2}$ and $i+1$, where $i+\frac{1}{2}$ is an internal node and nodes i and $i+1$ are integral nodes. Assume (as in the linear upwinding example) that the spacing between all the nodes is equal, so that the Jacobian for all elements will be the same, to simplify the following derivation. The solution at point i is expressed using standard 3-point Gaussian quadrature on the second part on the left hand side of equation (4.152) and a 2-point Gaussian quadrature on the first part of the left hand side of equation (4.152), which produces equation (4.156). In equation (4.156) $\frac{h}{2}$ is the Jacobian, which in this example is a constant equal to the distance h between the first and last node of an element divided by two.

$$\begin{aligned}
 & \left(\frac{2}{6h} + \frac{\nu}{4}(2\xi_1 - 1)(\xi_1^2 + \xi_1) + \frac{\nu}{4}(2\xi_2 - 1)(\xi_2^2 + \xi_2) \right) \phi_{i-1} + \left(-\frac{8}{3h} - \nu\xi_1(\xi_1^2 + \xi_1) - \nu\xi_2(\xi_2^2 + \xi_2) \right) \phi_{i-\frac{1}{2}} \\
 & + \left(\frac{14}{3h} + \frac{\nu}{4}(2\xi_1 + 1)(\xi_1^2 + \xi_1) + \frac{\nu}{4}(2\xi_2 + 1)(\xi_2^2 + \xi_2) + \frac{\nu}{4}(2\xi_1 - 1)(\xi_1^2 - \xi_1) + \frac{\nu}{4}(2\xi_2 - 1)(\xi_2^2 - \xi_2) \right) \phi_i \\
 & + \left(-\frac{8}{3h} - \nu\xi_1(\xi_1^2 - \xi_1) - \nu\xi_2(\xi_2^2 - \xi_2) \right) \phi_{i+\frac{1}{2}} + \left(\frac{2}{6h} + \frac{\nu}{4}(2\xi_1 + 1)(\xi_1^2 - \xi_1) + \frac{\nu}{4}(2\xi_2 + 1)(\xi_2^2 - \xi_2) \right) \phi_{i+1} \\
 & = 0
 \end{aligned} \tag{4.156}$$

4.3.10: Upwinding – A quadratic and cubic extension to the upwind scheme of Hughes

The solution at internal node $i - \frac{1}{2}$ is given as:

$$\begin{aligned} & \left(-\frac{8}{3h} + \frac{\nu}{2}(2\xi_1 - 1)(1 - \xi_1^2) + \frac{\nu}{2}(2\xi_2 - 1)(1 - \xi_2^2) \right) \phi_{i-1} + \left(\frac{16}{3h} - 2\nu\xi_1(1 - \xi_1^2) - 2\nu\xi_2(1 - \xi_2^2) \right) \phi_{i-\frac{1}{2}} \\ & + \left(-\frac{8}{3h} + \frac{\nu}{2}(2\xi_1 + 1)(1 - \xi_1^2) + \frac{\nu}{2}(2\xi_2 + 1)(1 - \xi_2^2) \right) \phi_i = 0 \end{aligned} \quad (4.157)$$

and the solution at internal node $i + \frac{1}{2}$ is given as:

$$\begin{aligned} & \left(-\frac{8}{3h} + \frac{\nu}{2}(2\xi_1 - 1)(1 - \xi_1^2) + \frac{\nu}{2}(2\xi_2 - 1)(1 - \xi_2^2) \right) \phi_i + \left(\frac{16}{3h} - 2\nu\xi_1(1 - \xi_1^2) - 2\nu\xi_2(1 - \xi_2^2) \right) \phi_{i+\frac{1}{2}} \\ & + \left(-\frac{8}{3h} + \frac{\nu}{2}(2\xi_1 + 1)(1 - \xi_1^2) + \frac{\nu}{2}(2\xi_2 + 1)(1 - \xi_2^2) \right) \phi_{i+1} = 0 \end{aligned} \quad (4.158)$$

In equations (4.156), (4.157) and (4.158) ξ_1 and ξ_2 are the first and second weighted Gaussian integration points for the 2-point Gaussian quadrature. Defining the variable

$\psi = \frac{16}{3h} - 2\nu\xi_1(1 - \xi_1^2) - 2\nu\xi_2(1 - \xi_2^2)$ equations (4.157) and (4.158) can be written as:

$$\begin{aligned} \phi_{i-\frac{1}{2}} &= -\frac{1}{\psi} \left(-\frac{8}{3h} + \frac{\nu}{2}(2\xi_1 - 1)(1 - \xi_1^2) + \frac{\nu}{2}(2\xi_2 - 1)(1 - \xi_2^2) \right) \phi_{i-1} \\ &- \frac{1}{\psi} \left(-\frac{8}{3h} + \frac{\nu}{2}(2\xi_1 + 1)(1 - \xi_1^2) + \frac{\nu}{2}(2\xi_2 + 1)(1 - \xi_2^2) \right) \phi_i \end{aligned} \quad (4.159)$$

and

$$\begin{aligned} \phi_{i+\frac{1}{2}} &= -\frac{1}{\psi} \left(-\frac{8}{3h} + \frac{\nu}{2}(2\xi_1 - 1)(1 - \xi_1^2) + \frac{\nu}{2}(2\xi_2 - 1)(1 - \xi_2^2) \right) \phi_i \\ &- \frac{1}{\psi} \left(-\frac{8}{3h} + \frac{\nu}{2}(2\xi_1 + 1)(1 - \xi_1^2) + \frac{\nu}{2}(2\xi_2 + 1)(1 - \xi_2^2) \right) \phi_{i+1} \end{aligned} \quad (4.160)$$

Substituting equations (4.159) and (4.160) into equation (4.156) results in equation (4.161).

4.3.10: Upwinding – A quadratic and cubic extension to the upwind scheme of Hughes

$$\begin{aligned}
 & \left(\frac{2}{6h} + \frac{v}{4} (2\xi_1 - 1)(\xi_1^2 + \xi_1) + \frac{v}{4} (2\xi_2 - 1)(\xi_2^2 + \xi_2) \right. \\
 & \left. - \left(-\frac{8}{3h} - v\xi_1(\xi_1^2 + \xi_1) - v\xi_2(\xi_2^2 + \xi_2) \right) \frac{1}{\psi} \left(-\frac{8}{3h} + \frac{v}{2} (2\xi_1 - 1)(1 - \xi_1^2) + \frac{v}{2} (2\xi_2 - 1)(1 - \xi_2^2) \right) \right) \phi_{i-1} \\
 & + \left(\frac{14}{3h} + \frac{v}{4} (2\xi_1 + 1)(\xi_1^2 + \xi_1) + \frac{v}{4} (2\xi_2 + 1)(\xi_2^2 + \xi_2) + \frac{v}{4} (2\xi_1 - 1)(\xi_1^2 - \xi_1) + \frac{v}{4} (2\xi_2 - 1)(\xi_2^2 - \xi_2) \right. \\
 & \left. - \left(-\frac{8}{3h} - v\xi_1(\xi_1^2 + \xi_1) - v\xi_2(\xi_2^2 + \xi_2) \right) \frac{1}{\psi} \left(-\frac{8}{3h} + \frac{v}{2} (2\xi_1 + 1)(1 - \xi_1^2) + \frac{v}{2} (2\xi_2 + 1)(1 - \xi_2^2) \right) \right) \phi_i \\
 & + \left(-\left(-\frac{8}{3h} - v\xi_1(\xi_1^2 - \xi_1) - v\xi_2(\xi_2^2 - \xi_2) \right) \frac{1}{\psi} \left(-\frac{8}{3h} + \frac{v}{2} (2\xi_1 - 1)(1 - \xi_1^2) + \frac{v}{2} (2\xi_2 - 1)(1 - \xi_2^2) \right) \right) \phi_{i+1} \\
 & = 0
 \end{aligned} \tag{4.161}$$

From equation (4.161) ϕ_i can be solved as:

$$\phi_i = A + B \left[\frac{\left(\frac{2}{6h} + \frac{v}{4} (2\xi_1 - 1)(\xi_1^2 + \xi_1) + \frac{v}{4} (2\xi_2 - 1)(\xi_2^2 + \xi_2) \right.}{\left(\frac{2}{6h} + \frac{v}{4} (2\xi_1 + 1)(\xi_1^2 - \xi_1) + \frac{v}{4} (2\xi_2 + 1)(\xi_2^2 - \xi_2) \right.} \right. \\
 \left. \left. - \left(-\frac{8}{3h} - v\xi_1(\xi_1^2 + \xi_1) - v\xi_2(\xi_2^2 + \xi_2) \right) \frac{1}{\psi} \left(-\frac{8}{3h} + \frac{v}{2} (2\xi_1 - 1)(1 - \xi_1^2) + \frac{v}{2} (2\xi_2 - 1)(1 - \xi_2^2) \right) \right) \right] \tag{4.162}$$

In equation (4.162) A and B are constants determined by the boundary conditions and the solution for an internal node such as $i + \frac{1}{2}$ is given by equation (4.160). It should be noted that

Christie et al [158] did calculate a similar condition for a quadratic test and basis function, but they did not analyse the function for the cases where stability was guaranteed. Instead they analysed the stability for standard quadratic one dimensional elements in which they derived the following equation for the solution at node i as:

$$\phi_i = A + B \left[\frac{1 + L + \frac{1}{3}L^2}{1 - L + \frac{1}{3}L^2} \right]^i \tag{4.163}$$

4.3.10: Upwinding – A quadratic and cubic extension to the upwind scheme of Hughes

And the solution at an internal node such as $i + \frac{1}{2}$ was determined to be:

$$\phi_{i+\frac{1}{2}} = \frac{1}{2} \left(\left(1 - \frac{1}{2} L \right) \phi_{i-1} + \left(1 + \frac{1}{2} L \right) \phi_{i+1} \right) \quad (4.164)$$

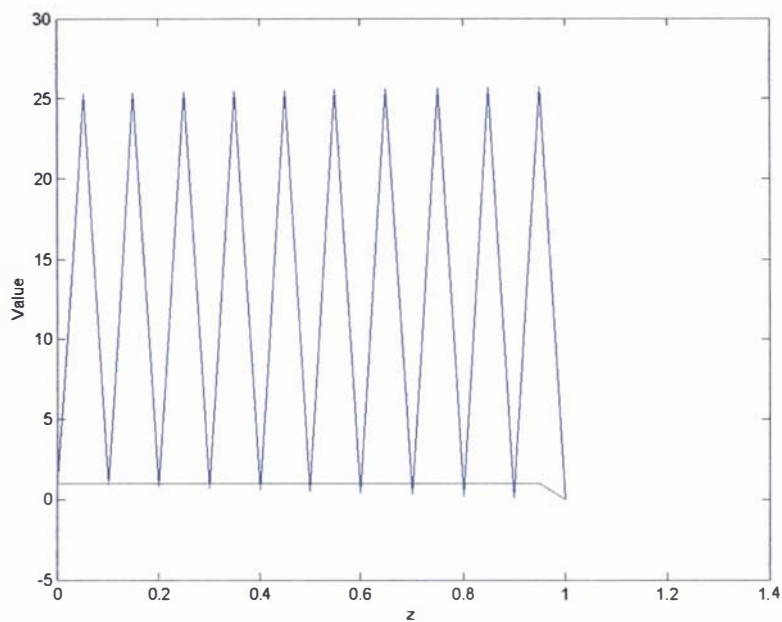
Equations (4.163) and (4.164) are obtained from equation (4.162) by inserting the standard values for the integration points for a 2-point Gaussian quadrature; therefore proving the validity of the derived equations (4.162) and (4.160). It is easily observed that the solution at an integer node given by equation (4.163) is unconditionally stable for all values of L , but the values for the internal nodes given by equation (4.164) will lead to numerical oscillations at these nodes if $L > 2$.

The numerical scheme for a quadratic test function, given by equations (4.162) and (4.160), is guaranteed to be stable if:

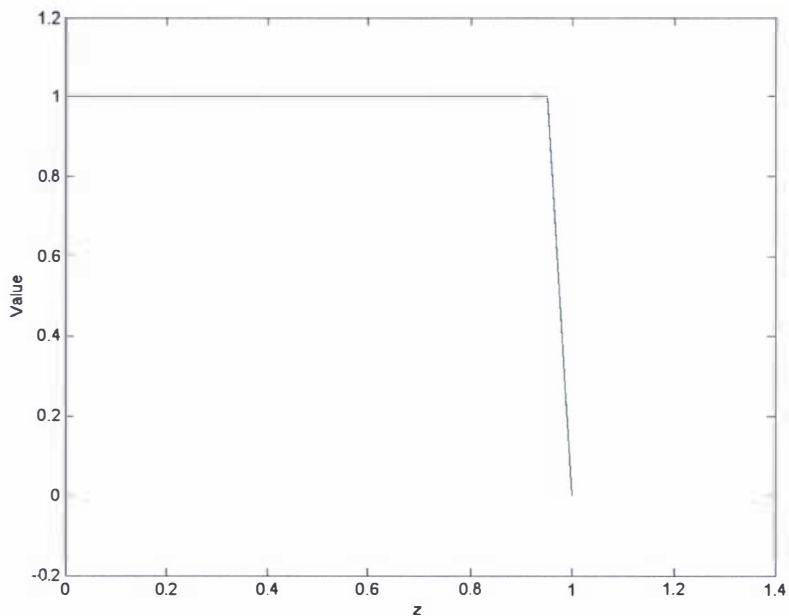
- | | | |
|--------|-------------------------------|--|
| (vii) | $\xi_1 = -\frac{1}{2}$ | backwards difference: if v is positive |
| | $\xi_2 = 1$ | backwards difference: if v is positive |
| (viii) | $\xi_1 = -\frac{1}{\sqrt{3}}$ | central difference: first Gaussian integration point – if $v = 0$ |
| | $\xi_2 = \frac{1}{\sqrt{3}}$ | central difference: second Gaussian integration point – if $v = 0$ |
| (ix) | $\xi_1 = -1$ | forward difference: if v is negative |
| | $\xi_2 = \frac{1}{2}$ | forward difference: if v is negative |

The unconditional stability of the upwinded quadratic scheme is demonstrated in graph 4.8 for the situation of a high Peclet number and a positive velocity value. Graph 4.7 shows the oscillatory behaviour when using standard finite elements for the same problem. The scheme discussed above is easily extendable to two dimensions by applying the same procedure to the basis and test functions used in the second dimension.

4.3.10: Upwinding – A quadratic and cubic extension to the upwind scheme of Hughes



Graph 4.7: Comparison of analytical and numerical answers showing oscillatory behaviour from the use of a high Peclet number in a quadratic finite element scheme. A Peclet number of 50 and a mesh consisting of 19 equally spaced nodes were used to solve equation (4.143) and its boundary conditions.



Graph 4.8: Comparison of analytical and numerical answers for a backwards upwinded scheme from the use of a high Peclet number in a quadratic finite element scheme. A Peclet number of 50 and a mesh consisting of 19 equally spaced nodes were used to solve equation (4.143) and its boundary conditions.

Extension of the simple upwinding scheme to cubic elements

The scheme of [157] can also be extended to cubic elements, by treating equation (4.143) as a one dimensional problem in the x coordinate for two adjoining elements one dimensional elements that have a shared interior node i . Describing the first element as consisting of nodes $i-1, i-\frac{2}{3}, i-\frac{1}{3}$ and i , where $i-\frac{2}{3}$ and $i-\frac{1}{3}$ are integer nodes and the nodes $i-1$ and i are integer nodes. The second element is then described as consisting of nodes $i, i+\frac{1}{3}, i+\frac{2}{3}$ and $i+1$, in which $i+\frac{1}{3}$ and $i+\frac{2}{3}$ are internal nodes and nodes i and $i+1$ are integral nodes. Assume (as in the previous upwinding derivations) that the spacing between all the nodes is equal, so that the Jacobian for all elements will be the same, to simplify the following derivation. The unsymmetrical term on the left hand side of equation (4.152) is expressed using a 3-point Gaussian quadrature as equation (4.165). In equation (4.165) $\frac{h}{2}$ is the Jacobian, which in this example is a constant equal to the distance h between the first and last node of an element divided by two.

$$\int_{-1}^1 \phi \frac{\partial \phi}{\partial x} J d\xi = \sum_{i=1}^3 \phi(\xi_i) \frac{\partial \phi(\xi_i)}{\partial x} \frac{h}{2} W_i \quad (4.165)$$

The right hand side of equation (4.165) can be expressed in the form of a matrix for the four nodes of an element, nodes 1, 2, 3 and 4 as shown in equation (4.166). In equation (4.166) the subscripts relate to the node number in terms of the variable ϕ and the products of the various test function terms for the v variable. The v matrix terms used in the matrix given in equation (4.166) can be found in Appendix 4C.

$$\int_{-1}^1 \phi \frac{\partial \phi}{\partial x} J d\xi = \begin{bmatrix} v_{11}, v_{12}, v_{13}, v_{14} \\ v_{21}, v_{22}, v_{23}, v_{24} \\ v_{31}, v_{32}, v_{33}, v_{34} \\ v_{41}, v_{42}, v_{43}, v_{44} \end{bmatrix} \begin{Bmatrix} \phi_1 \\ \phi_2 \\ \phi_3 \\ \phi_4 \end{Bmatrix} \quad (4.166)$$

Using a standard 4-point Gaussian quadrature on the second part on the left hand side of equation (4.152) and the matrix values given in equation (4.166) the solution at point i is expressed as equation (4.167).

4.3.10: Upwinding – A quadratic and cubic extension to the upwind scheme of Hughes

$$\begin{aligned} & \left(-\frac{13}{40h} + \nu v_{41} \right) \phi_{i-1} + \left(\frac{27}{20h} + \nu v_{42} \right) \phi_{i-\frac{2}{3}} + \left(-\frac{189}{40h} + \nu v_{43} \right) \phi_{i-\frac{1}{3}} + \left(\frac{74}{10h} + \nu(v_{44} + v_{11}) \right) \phi_i \\ & + \left(-\frac{189}{40h} + \nu v_{12} \right) \phi_{i+\frac{1}{3}} + \left(\frac{27}{20h} + \nu v_{13} \right) \phi_{i+\frac{2}{3}} + \left(-\frac{13}{40h} + \nu v_{14} \right) \phi_{i+1} = 0 \end{aligned} \quad (4.167)$$

An equation for internal nodes $i - \frac{2}{3}$ and $i - \frac{1}{3}$ is given as:

$$\left(-\frac{189}{40h} + \nu v_{21} \right) \phi_{i-1} + \left(\frac{54}{5h} + \nu v_{22} \right) \phi_{i-\frac{2}{3}} + \left(-\frac{297}{40h} + \nu v_{23} \right) \phi_{i-\frac{1}{3}} + \left(\frac{27}{20h} + \nu v_{24} \right) \phi_i = 0 \quad (4.168)$$

$$\left(\frac{27}{20h} + \nu v_{31} \right) \phi_{i-1} + \left(-\frac{297}{40h} + \nu v_{32} \right) \phi_{i-\frac{2}{3}} + \left(\frac{54}{5h} + \nu v_{33} \right) \phi_{i-\frac{1}{3}} + \left(-\frac{189}{40h} + \nu v_{34} \right) \phi_i = 0 \quad (4.169)$$

and an equation for internal nodes $i + \frac{1}{3}$ and $i + \frac{2}{3}$ is derived as being:

$$\left(-\frac{189}{40h} + \nu v_{21} \right) \phi_i + \left(\frac{54}{5h} + \nu v_{22} \right) \phi_{i+\frac{1}{3}} + \left(-\frac{297}{40h} + \nu v_{23} \right) \phi_{i+\frac{2}{3}} + \left(\frac{27}{20h} + \nu v_{24} \right) \phi_{i+1} = 0 \quad (4.170)$$

$$\left(\frac{27}{20h} + \nu v_{31} \right) \phi_i + \left(-\frac{297}{40h} + \nu v_{32} \right) \phi_{i+\frac{1}{3}} + \left(\frac{54}{5h} + \nu v_{33} \right) \phi_{i+\frac{2}{3}} + \left(-\frac{189}{40h} + \nu v_{34} \right) \phi_{i+1} = 0 \quad (4.171)$$

Rearranging equation (4.169) for the internal node $i - \frac{1}{3}$ gives:

$$\phi_{i-\frac{1}{3}} = -\frac{1}{\psi_1} \left(\left(\frac{27}{20h} + \nu v_{31} \right) \phi_{i-1} + \left(-\frac{297}{40h} + \nu v_{32} \right) \phi_{i-\frac{2}{3}} + \left(-\frac{189}{40h} + \nu v_{34} \right) \phi_i \right) \quad (4.172)$$

In equation (4.172) ψ_1 is defined by equation (4.173)

$$\psi_1 = \left(\frac{54}{5h} + \nu v_{33} \right) \quad (4.173)$$

4.3.10: Upwinding – A quadratic and cubic extension to the upwind scheme of Hughes

Substituting equation (4.172) and (4.173) into equation (4.168) gives an equation (4.174) for the internal node at $i - \frac{2}{3}$.

$$\phi_{i-\frac{2}{3}} = -\frac{1}{\psi_2} \left[\left(-\frac{189}{40h} + v_{21} - \frac{1}{\psi_1} \left(-\frac{297}{40h} + v_{23} \right) \left(\frac{27}{20h} + v_{31} \right) \right) \phi_{i-1} + \left(\frac{27}{20h} + v_{24} - \frac{1}{\psi_1} \left(-\frac{297}{40h} + v_{23} \right) \left(-\frac{189}{40h} + v_{34} \right) \right) \phi_i \right] \quad (4.174)$$

In equation (4.174) ψ_2 is defined by equation (4.175)

$$\psi_2 = \left(\frac{54}{5h} + v_{22} - \frac{1}{\psi_1} \left(-\frac{297}{40h} + v_{23} \right) \left(-\frac{297}{40h} + v_{32} \right) \right) \quad (4.175)$$

Substituting equation (4.174), (4.175) and (4.173) into equation (4.172) gives the internal node $i - \frac{1}{3}$ in terms of the integer nodes $i - 1$ and i as:

$$\phi_{i-\frac{1}{3}} = \left[\left(-\frac{1}{\psi_1} \left(\frac{27}{20h} + v_{31} \right) + \frac{1}{\psi_1 \psi_2} \left(\frac{297}{40h} + v_{32} \right) \left(\frac{189}{40h} + v_{21} - \frac{1}{\psi_1} \left(-\frac{297}{40h} + v_{23} \right) \left(\frac{27}{20h} + v_{31} \right) \right) \right) \phi_{i-1} + \left(-\frac{1}{\psi_1} \left(-\frac{189}{40h} + v_{34} \right) + \frac{1}{\psi_1 \psi_2} \left(-\frac{297}{40h} + v_{32} \right) \left(\frac{27}{20h} + v_{24} - \frac{1}{\psi_1} \left(-\frac{297}{40h} + v_{23} \right) \left(-\frac{189}{40h} + v_{34} \right) \right) \right) \phi_i \right] \quad (4.176)$$

The values for internal nodes $i + \frac{1}{3}$ and $i + \frac{2}{3}$ can then be derived by replacing i with $i + 1$ in the equations for $i - \frac{2}{3}$ and $i - \frac{1}{3}$. Similar equations are derived for $i - \frac{1}{3}$ and $i + \frac{2}{3}$, $i - \frac{2}{3}$ and $i + \frac{1}{3}$; hence the internal node $i + \frac{1}{3}$ is given as:

$$\phi_{i+\frac{1}{3}} = -\frac{1}{\psi_2} \left[\left(-\frac{189}{40h} + v_{21} - \frac{1}{\psi_1} \left(-\frac{297}{40h} + v_{23} \right) \left(\frac{27}{20h} + v_{31} \right) \right) \phi_i + \left(\frac{27}{20h} + v_{24} - \frac{1}{\psi_1} \left(-\frac{297}{40h} + v_{23} \right) \left(-\frac{189}{40h} + v_{34} \right) \right) \phi_{i+1} \right] \quad (4.177)$$

4.3.10: Upwinding – A quadratic and cubic extension to the upwind scheme of Hughes

The internal node $i + \frac{2}{3}$ is derived as equation (4.178).

$$\phi_{i+\frac{2}{3}} = \left[\left(-\frac{1}{\psi_1} \left(\frac{27}{20h} + v v_{31} \right) + \frac{1}{\psi_1 \psi_2} \left(-\frac{297}{40h} + v v_{32} \right) \left(-\frac{189}{40h} + v v_{21} - \frac{1}{\psi_1} \left(-\frac{297}{40h} + v v_{23} \right) \left(\frac{27}{20h} + v v_{31} \right) \right) \right) \phi_i \right. \\ \left. \left(-\frac{1}{\psi_1} \left(-\frac{189}{40h} + v v_{34} \right) + \frac{1}{\psi_1 \psi_2} \left(-\frac{297}{40h} + v v_{32} \right) \left(\frac{27}{20h} + v v_{24} - \frac{1}{\psi_1} \left(-\frac{297}{40h} + v v_{23} \right) \left(-\frac{189}{40h} + v v_{34} \right) \right) \right) \phi_{i+1} \right] \quad (4.178)$$

Substituting equations (4.178), (4.177), (4.176) and (4.174) into equation (4.167) results in equation (4.179).

$$\left[\begin{aligned} & \left(-\frac{13}{40h} + v v_{41} \right) - \frac{1}{\psi_2} \left(\frac{27}{20h} + v v_{42} \right) \left(-\frac{189}{40h} + v v_{21} - \frac{1}{\psi_1} \left(-\frac{297}{40h} + v v_{23} \right) \left(\frac{27}{20h} + v v_{31} \right) \right) \\ & + \frac{1}{\psi_1 \psi_2} \left(-\frac{189}{40h} + v v_{43} \right) \left(-\frac{297}{40h} + v v_{32} \right) \left(-\frac{189}{40h} + v v_{21} - \frac{1}{\psi_1} \left(-\frac{297}{40h} + v v_{23} \right) \left(\frac{27}{20h} + v v_{31} \right) \right) \\ & - \frac{1}{\psi_1} \left(-\frac{189}{40h} + v v_{43} \right) \left(\frac{27}{20h} + v v_{31} \right) \end{aligned} \right] \phi_{i-1} \\ + \left[\begin{aligned} & -\frac{1}{\psi_2} \left(\frac{27}{20h} + v v_{42} \right) \left(\frac{27}{20h} + v v_{24} - \frac{1}{\psi_1} \left(-\frac{297}{40h} + v v_{23} \right) \left(-\frac{189}{40h} + v v_{34} \right) \right) \\ & - \frac{1}{\psi_1} \left(-\frac{189}{40h} + v v_{43} \right) \left(-\frac{189}{40h} + v v_{34} \right) + \left(\frac{74}{10h} + v(v_{44} + v_{11}) \right) \\ & + \frac{1}{\psi_1 \psi_2} \left(-\frac{189}{40h} + v v_{43} \right) \left(-\frac{297}{40h} + v v_{32} \right) \left(\frac{27}{20h} + v v_{24} - \frac{1}{\psi_1} \left(-\frac{297}{40h} + v v_{23} \right) \left(-\frac{189}{40h} + v v_{34} \right) \right) \\ & - \frac{1}{\psi_2} \left(-\frac{189}{40h} + v v_{12} \right) \left(-\frac{189}{40h} + v v_{21} - \frac{1}{\psi_1} \left(-\frac{297}{40h} + v v_{23} \right) \left(\frac{27}{20h} + v v_{31} \right) \right) \\ & + \frac{1}{\psi_1 \psi_2} \left(\frac{27}{20h} + v v_{13} \right) \left(-\frac{297}{40h} + v v_{32} \right) \left(-\frac{189}{40h} + v v_{21} - \frac{1}{\psi_1} \left(-\frac{297}{40h} + v v_{23} \right) \left(\frac{27}{20h} + v v_{31} \right) \right) \\ & - \frac{1}{\psi_1} \left(\frac{27}{20h} + v v_{13} \right) \left(\frac{27}{20h} + v v_{31} \right) \end{aligned} \right] \phi_i \\ + \left[\begin{aligned} & \frac{1}{\psi_1 \psi_2} \left(\frac{27}{20h} + v v_{13} \right) \left(-\frac{297}{40h} + v v_{32} \right) \left(\frac{27}{20h} + v v_{24} - \frac{1}{\psi_1} \left(-\frac{297}{40h} + v v_{23} \right) \left(-\frac{189}{40h} + v v_{34} \right) \right) \\ & - \frac{1}{\psi_1} \left(\frac{27}{20h} + v v_{13} \right) \left(-\frac{189}{40h} + v v_{34} \right) + \left(-\frac{13}{40h} + v v_{14} \right) \\ & - \frac{1}{\psi_2} \left(-\frac{189}{40h} + v v_{12} \right) \left(\frac{27}{20h} + v v_{24} - \frac{1}{\psi_1} \left(-\frac{297}{40h} + v v_{23} \right) \left(-\frac{189}{40h} + v v_{34} \right) \right) \end{aligned} \right] \phi_{i+1} \\ = 0 \quad (4.179)$$

4.3.10: Upwinding – A quadratic and cubic extension to the upwind scheme of Hughes

From equation (4.179) ϕ_i can be solved as:

$$\phi_i = A + B \left[\begin{array}{l} \left(-\frac{13}{40h} + vv_{41} \right) - \frac{1}{\psi_2} \left(\frac{27}{20h} + vv_{42} \right) \left(-\frac{189}{40h} + vv_{21} - \frac{1}{\psi_1} \left(-\frac{297}{40h} + vv_{23} \right) \left(\frac{27}{20h} + vv_{31} \right) \right) \\ + \frac{1}{\psi_1 \psi_2} \left(-\frac{189}{40h} + vv_{43} \right) \left(-\frac{297}{40h} + vv_{32} \right) \left(-\frac{189}{40h} + vv_{21} - \frac{1}{\psi_1} \left(-\frac{297}{40h} + vv_{23} \right) \left(\frac{27}{20h} + vv_{31} \right) \right) \\ - \frac{1}{\psi_1} \left(-\frac{189}{40h} + vv_{43} \right) \left(\frac{27}{20h} + vv_{31} \right) \\ \frac{1}{\psi_1 \psi_2} \left(\frac{27}{20h} + vv_{13} \right) \left(-\frac{297}{40h} + vv_{32} \right) \left(\frac{27}{20h} + vv_{24} - \frac{1}{\psi_1} \left(-\frac{297}{40h} + vv_{23} \right) \left(-\frac{189}{40h} + vv_{34} \right) \right) \\ - \frac{1}{\psi_2} \left(-\frac{189}{40h} + vv_{12} \right) \left(\frac{27}{20h} + vv_{24} - \frac{1}{\psi_1} \left(-\frac{297}{40h} + vv_{23} \right) \left(-\frac{189}{40h} + vv_{34} \right) \right) \\ - \frac{1}{\psi_1} \left(\frac{27}{20h} + vv_{13} \right) \left(-\frac{189}{40h} + vv_{34} \right) + \left(-\frac{13}{40h} + vv_{14} \right) \end{array} \right]^i \quad (4.180)$$

The solution to internal node $i + \frac{1}{3}$ is given by equation (4.177) and the solution to the internal node $i + \frac{2}{3}$ is given by equation (4.178). It is more difficult to see the behaviour of the cubic upwinded system as compared to the quadratic or linear system. The standard cubic one dimensional elements are stable for values of the Peclet number less than two i.e. $L < 2$. For values of the Peclet number greater than two numerical oscillations are observed, where the oscillatory behaviour is a combination of the oscillatory nature of the linear and quadratic test and basis function schemes, as can be observed in graph 4.9.

4.3.10: Upwinding – A quadratic and cubic extension to the upwind scheme of Hughes

The numerical scheme for a cubic test function given by equation (4.180), (4.177) and (4.178) is guaranteed to be stable if:

(x) $\xi_1 = -\frac{3}{4}$ backwards difference: if v is positive

$\xi_2 = 0$ backwards difference: if v is positive

$\xi_3 = 1$ backwards difference: if v is positive

(xi) $\xi_1 = -\frac{3}{\sqrt{15}}$ central difference: first Gaussian integration point – if $v = 0$

$\xi_2 = 0$ central difference: second Gaussian integration point – if $v = 0$

$\xi_3 = \frac{3}{\sqrt{15}}$ central difference: third Gaussian integration point – if $v = 0$

(xii) $\xi_1 = -1$ forward difference: if v is negative

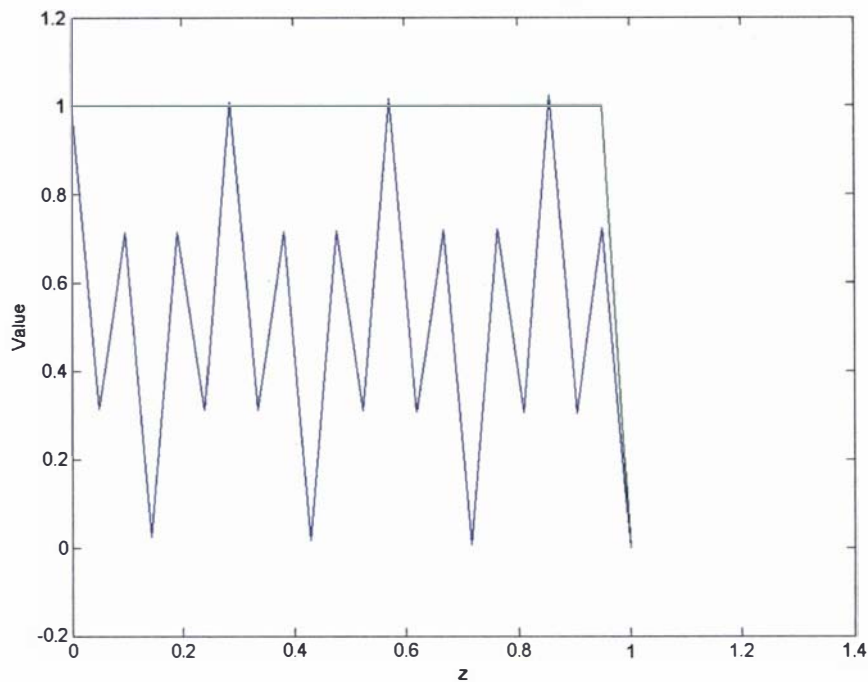
$\xi_2 = 0$ forward difference: if v is negative

$\xi_3 = \frac{3}{4}$ forward difference: if v is negative

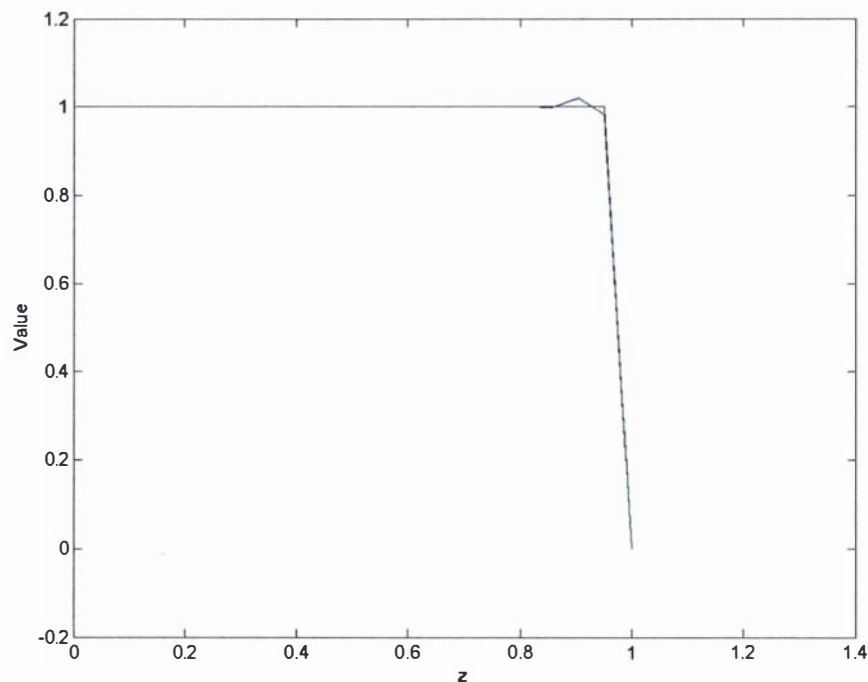
The unconditional stability of the upwinded cubic scheme is shown in graph 4.10 using a high Peclet number and a positive velocity value. Graph 4.9 shows the oscillatory behaviour observed when using standard finite elements.

The one dimensional cubic upwinded scheme discussed above is easily extendable to two dimensions by applying the same procedure to the basis and test functions used in the second dimension.

4.3.10: Upwinding – A quadratic and cubic extension to the upwind scheme of Hughes



Graph 4.9: Comparison of analytical and numerical answers showing oscillatory behaviour from the use of a high Peclet number in a cubic finite element scheme. A Peclet number of 50 and a mesh consisting of 19 equally spaced nodes were used to solve equation (4.143) and its boundary conditions.



Graph 4.10: Comparison of analytical and numerical answers for a backwards upwinded scheme from the use of a high Peclet number in a cubic finite element scheme. A Peclet number of 50 and a mesh consisting of 19 equally spaced nodes were used to solve equation (4.143) and its boundary conditions.

4.3.10: Upwinding – A quadratic and cubic extension to the upwind scheme of Hughes

Numerical results for the linear, quadratic and cubic upwinded schemes

The numerical results of solving equation (4.143) with the associated boundary conditions given by equations (4.144) and (4.145), using the three discussed upwinding schemes are presented in table 4.3 below. These results were calculated over the two dimensional computational volume shown in diagram 4.9, with a fixed mesh size for various values of the Peclet number. The results in table 4.3 were generated using: standard rectangular FEM elements in the linear upwinded scheme; nine node isoparametric quadratic elements in the quadratic upwinded scheme; and cubic serendipity elements [108] in the cubic upwinded scheme.

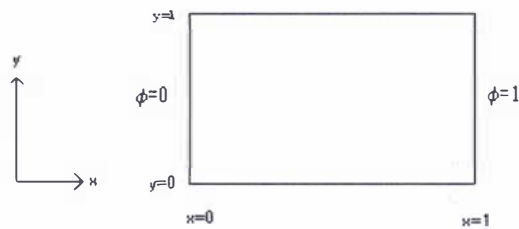


Diagram 4.9: Two dimensional computational region for upwinding problem with associated boundary conditions

Peclet number	Number of nodes used to generate the mesh in terms of number of nodes used along both the x and y axes	Linear upwinded scheme maximum error	Quadratic upwinded scheme maximum error	Cubic upwinded scheme maximum error
0.001	19	0.000423	0.0220	0.0227
0.1	19	2.77	2.75	2.50
1	19	21.0	18.7	15.1
2	19	22.9	22.0	18.3
10	19	9.09	9.93	7.39
50	19	1.96	2.33	3.48
100	19	0.990	1.19	2.70
1000	19	0.0999	0.122	1.94
1000000	19	0.0001	0.000122	1.85

Table 4.3: Table showing maximum percentage error with respect to various Peclet numbers for the linear, quadratic and cubic upwinded schemes for the given diffusion advection problem

It can be seen from table 4.3 that for high Peclet numbers the linear upwinded scheme is the most accurate. As there is little error between the linear and quadratic schemes for high Peclet numbers (as seen in table 4.3) the two schemes can be said to be comparable. The cubic

4.3.10: Upwinding – A quadratic and cubic extension to the upwind scheme of Hughes

upwinded scheme is the least accurate of all the upwinded schemes; however the cubic upwinded scheme gives a consistent percentage error over a range of Peclet numbers. The maximum percentage error in the cubic upwinded scheme is associated with the internal nodes immediately before the high gradient jump in the solution.

4.3.11: Boundary conditions for far field and curved boundaries

Imposing the normal component of the current density being exactly equal to zero on curved and/or deforming conducting surface can be viewed as difficult; however the normal component on a curved/deformed surface can instead be approximated, at a node, by considering the slope between nodes adjacent to it, as shown in diagram 4.10.

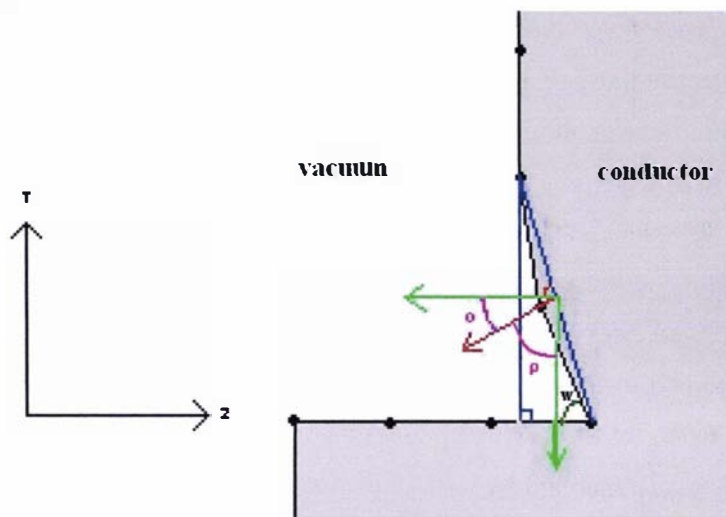


Diagram 4.10: The approximation of the normal component of the current density on a curved boundary

The normal current density component of a node on a curved/deformed surface can be calculated, as a first rough estimate, by considering the positions of the nodes directly adjacent to the node in question. From geometric inspection of diagram 4.10 the angles o and p can be calculated by knowing angle w , forming a triangle from the node in question and its (directly) adjacent nodes, and using simple trigonometry and trigonometric functions. The normal current density at a node is then roughly approximated as:

$$J_z \cos(o) \cdot M_z + J_r \cos(p) \cdot M_r = 0 \quad (4.181)$$

In equation (4.181) o and p are angles and M_r and M_z are unit vectors. The above equation is only an approximation, its accuracy is increased through the use of a finer mesh. This boundary condition could be implemented using the Lagrange multiplier technique discussed in appendix 4B. Because the AVA formulation is being used to model the coaxial plasma

accelerator, the above approximation is the only available method that could be used to approximate a curved/deformed boundary; methods do exist that do not approximate this boundary condition [130] as discussed in section 4.3.3, but they cannot be used without a great deal of difficulty.

Far field boundary conditions are commonly used in numerical electromagnetic modelling problems to provide known boundary conditions. Typically these conditions are approximated by including a large enough region around the modelled area that the magnetic and/or electric field can assumed to be negligible on the boundaries of the computational domain [137]. In most rail gun and plasma accelerator programs this distance is taken to be a few centimetres from the plasma/armature [115], [90], [91]. This method can be computationally expensive if a large region is required to obtain usable far field boundaries. Also some error is introduced into the calculation, because of the finite distance used to describe the far field boundaries.

In the boundary element method BEM [107] the far field boundary conditions are correctly represented (in infinite space) eliminating any error to the final solution from the approximation of these boundaries. It is possible to couple the FEM and BEM schemes [161], which has the added advantage of reducing the computational region required to describe the far field boundary conditions.

In general the perceived error from approximating the field boundary is very small and it is a simple procedure to add to the computational domain rather than using a complicated BEM-FEM method; because of these two points the far field boundary conditions will be approximated in the numerical model constructed in this thesis.

4.3.12: Solving the matrix system of equations

There are three basic methods that can be used to solve the system of linear equations formed from either equation (4.42) or (4.44): Conjugate gradient methods (conjugate gradient, biconjugate gradient and generalized minimum residual method (GRMES) [78]), the mode-of-superposition (eigenvalue analysis [108]), and Matrix algebra (Gauss-Jordan elimination and LU decomposition [78]).

The linear system of equations produced using the AVA formulation (discussed in section 4.3.3) forms a square, sparse matrix. This matrix is unsymmetrical, because of the way in which the velocity of the plasma has been treated. This aspect was discussed in section 4.3.9, in which the electrodes are considered to be moving with a negative velocity relative to the plasma (i.e. equations (4.141) and (4.142)).

Conjugate gradient solvers are attractive, because they can (usually) be used to generate a parallel version of a program. However, because they obtain their results through an iterative process, most of these algorithms are only guaranteed to converge if the system matrix is

square, symmetrical, and positive definite. The conjugate gradient method requires the system matrix to be square, symmetric, and positive definite to guarantee convergence [78] (proof that convergence is guaranteed under these conditions can be found in [111]). The conjugate gradient method was never found to converge for the plasma accelerator problem and this can be attributed to the system matrix being unsymmetrical. The biconjugate gradient method (which is essentially a variation of the conjugate gradient method) did not converge either. Neither did the GRMES algorithm (the GRMES algorithm [162] is guaranteed to converge if the system matrix is both square and symmetrical), which can also be attributed to the system matrix being unsymmetrical. There are conjugate gradient solvers in the literature that are capable of solving ill conditioned and unsymmetrical systems [163]; however these algorithms are somewhat difficult to implement and as the initial aim of the modelling process is to obtain a working numerical model the possibility of using such an algorithm to essentially optimize the problem, through the use of a parallel version, was not of prime concern; therefore application of using a Conjugate gradient method was deferred.

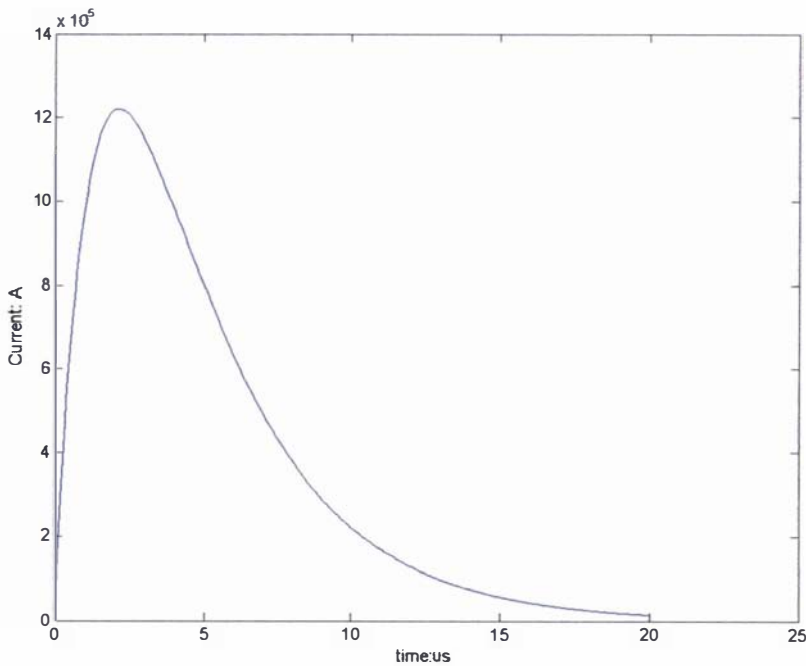
The mode-of-superposition, as discussed in section 4.3.1, could be used to solve the plasma accelerator problem; however this method was not employed, because it is computationally expensive and complex [108] (this method is restricted to solving problems with small system matrices).

The method which was finally chosen to solve the plasma accelerator problem was LU decomposition (a form of basic Matrix algebra). A description of this method can be found in any mathematical or numerical text book such as [78], [111] and most mathematical package programs such as MATLAB contain some form of this algorithm. Despite the fact that this method requires more computational memory than the standard Conjugate gradient methods and on the whole cannot be used in the generation of a parallel version of a program, provided the system matrix is not singular (i.e. has no inverse) or very close to being singular, this method will always give a result.

The system matrix for the plasma accelerator problem was not singular (or even remotely close to being singular) and so this method was always found to generate a result (note there are versions of LU solvers that are capable of solving ill conditioned systems [164]). The MATLAB LU solver “LU” was used to generate the results presented within this thesis relating to all FEM programs. The MATLAB LU solver has the advantage that it is capable of solving sparse matrices [165], [166] (a discussion on LU decomposition on a sparse matrix can be found in [78]). On a commercial 32-bit machine the total amount of available Ram is approximately 6Gbytes (from 4Gbytes Ram and 2Gbytes virtual memory) this limits the size of the (sparse and banded) system matrix that can roughly be solved to a 36722×36722 matrix, which corresponds to a 60×60 mesh generated using cubic serendipity elements (refer to section 4.3) for a two component FEM problem.

4.3.13: Test cases

Three test cases with analytical solutions, which can be found in appendix 4E, were proposed as a means of evaluating the effectiveness of some of the proposed solutions to the six numerical problems encountered when trying to model the electromagnetics of a coaxial plasma accelerator. These three test cases are used to verify that the aforementioned methods used to circumvent singularities close to the axis, spurious solutions, moving systems, upwinding and far field boundary conditions are correct. The three test cases are: Case 1 an infinitely long conductive wire carrying a current, Case 2 an infinitely long conductive coaxial cable carrying a current, and Case 3 an infinitely long conductive wire carrying a current set in a moving reference frame. All three cases will be solved using the finite element method (refer to section 4.3.1) and the AVA formulation (refer to section 4.3.3) as eddy current problems generated from the discharge of a capacitor, with the assumption that the electrical system is overdamped (because of the reasons discussed in appendix 4E). In order to test the effectiveness of the proposed numerical scheme/schemes a rigorous and quickly changing set of boundary conditions (generated from the calculated current) will be required; the current will be calculated using the following circuit parameters (described by equation (4.1)): resistance $R_o = 0.01\Omega$, inductance $L_o = 1 \times 10^{-8} H$, capacitance $C = 5 \times 10^{-4} F$ and a charging voltage of 16000V. A plot of the current as a function of time is presented in graph 4.11.



Graph 4.11: Graph of current as a function of time, which will be used to generate the boundary conditions used in the test cases.

Case 1: an infinitely long conductive wire carrying a current

The simple problem of a infinitely long current carrying wire, of radius R , was solved using the standard weak AVA formulation (equations (4.69) and (4.70)) in which the Coulomb gauge was added to the formulation using a penalty parameter technique (as discussed in section 4.3.7), which results in the following weak formulation:

$$\begin{aligned} & \int \frac{1}{\mu_o} \nabla \times W \cdot \nabla \times A \partial\Omega + \int \frac{S}{\mu_o} \nabla \cdot W \nabla \cdot A \partial\Omega + \int \sigma W \cdot \frac{\partial A}{\partial t} \partial\Omega - \int \sigma W \cdot v \times (\nabla \times A) \partial\Omega \\ & - \int \frac{1}{\mu_o} W \cdot (\nabla \times A) \times n \partial\Gamma - \int \frac{S}{\mu_o} \nabla \cdot W A \cdot n \partial\Gamma = 0 \end{aligned} \quad (4.182)$$

$$\begin{aligned} & \int \sigma \nabla W \cdot \frac{\partial A}{\partial t} \partial\Omega - \int \sigma \nabla W v \times (\nabla \times A) \partial\Omega + \int \sigma \nabla W \cdot \nabla V \partial\Omega - \int \sigma W \frac{\partial A}{\partial t} \cdot n \partial\Gamma \\ & + \int \sigma W v \times (\nabla \times A) \cdot n \partial\Gamma - \int \sigma W \nabla V \cdot n \partial\Gamma = 0 \end{aligned} \quad (4.183)$$

(In equation (4.182) S is the penalty parameter (refer to section 4.3.7).) In order to prevent singularities close to the axis (refer to section 4.3.6) the coordinate transformation given by equation (4.71) was used. The problem domain for this problem is depicted in diagram 4.11 for a section of wire in the regions of $0 \leq r \leq R$ and $0 \leq z \leq R$.

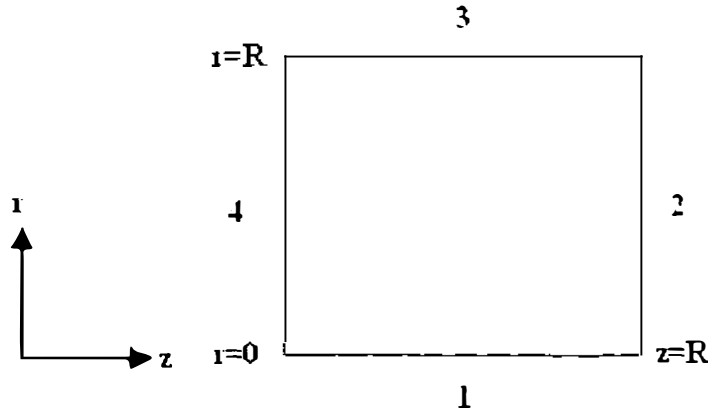


Diagram 4.11: Representation of the problem domain used to solve Test Case 1, showing the computational surface boundaries 1 to 4.

The Coulomb gauge will be satisfied over the entire computational volume provided the normal component for the magnetic vector potential A is not set on any computational surface (refer to the discussion given in section 4.3.7); hence A_r cannot be set on boundaries 1 and 3 and

A_z cannot be set on boundaries 2 and 4. $A_r = 0$ will be set on boundaries 2 and 4 and the flux condition for A_z will be set on boundaries 1 and 4 i.e. $\nabla \times \mathbf{A} = 0$ will be set on boundary 1 and $\nabla \times \mathbf{A} = \frac{\mu_o i_o}{2\pi R}$ will be set on boundary 3 (where i_o is the input current at time t).

The boundary conditions for the electric scalar potential V can be defined by the normal flux condition on the conductive surface boundary i.e. $\nabla V \cdot \mathbf{n} = 0$; however, because of the weak formulation given by equation (4.183) the surface boundary condition Γ_S is defined as:

$$\Gamma_S = -\int \sigma W \frac{\partial A}{\partial t} \cdot \mathbf{n} d\Gamma + \int \sigma W \mathbf{v} \times (\nabla \times \mathbf{A}) \cdot \mathbf{n} d\Gamma - \int \sigma W \nabla V \cdot \mathbf{n} d\Gamma \quad (4.184)$$

Because $\mathbf{v} = 0$ in this particular problem, the above equation is simplified to equation (4.185).

$$\Gamma_S = -\int \sigma W \frac{\partial A}{\partial t} \cdot \mathbf{n} d\Gamma - \int \sigma W \nabla V \cdot \mathbf{n} d\Gamma \quad (4.185)$$

On boundaries 2 and 4 (for this problem) $\int \sigma W \frac{\partial A}{\partial t} \cdot \mathbf{n} d\Gamma \neq 0$ (refer to the analytical solution 4.E.14 in appendix 4E) and this integral must be included as part of the system vector. An alternative to the inclusion of this flux boundary condition is to set $V = 0$ on boundaries 2 and 4 (because the solution to this problem is $V=0$ over the computational region), which will override the flux boundary conditions given in equation (4.185). If the problem consists of a region of constant conductivity, this problematic flux boundary can be entirely eliminated by an alternative weak AVA formulation. If $\int W \nabla \cdot \left(\sigma \frac{\partial \mathbf{A}}{\partial t} \right) \partial \Omega$ is not expanded to produce the typically used volume and surface integrals of $\int \sigma \nabla W \frac{\partial A}{\partial t} \partial \Omega - \int \sigma W \frac{\partial A}{\partial t} \cdot \mathbf{n} d\Gamma$ an alternative weak AVA formulation that consists of solving equations (4.182) and (4.186) is obtained.

$$\begin{aligned} & \int W \nabla \cdot \left(\sigma \frac{\partial \mathbf{A}}{\partial t} \right) \partial \Omega - \int \sigma \nabla W \mathbf{v} \times (\nabla \times \mathbf{A}) \partial \Omega + \int \sigma \nabla W \cdot \nabla V \partial \Omega \\ & + \int \sigma W \mathbf{v} \times (\nabla \times \mathbf{A}) \cdot \mathbf{n} d\Gamma - \int \sigma W \nabla V \cdot \mathbf{n} d\Gamma = 0 \end{aligned} \quad (4.186)$$

If the problem is solved using equations (4.182) and (4.186) then the normal flux boundary condition for V (i.e. $\nabla V \cdot \mathbf{n} = 0$) can be set on any boundary.

Test Case 1 was solved using a 10×10 mesh consisting of cubic isoparametric serendipity elements. A conductivity value of $\sigma = 1 \times 10^7 \text{ } \Omega/\text{m}^2$, the backwards time marching scheme (discussed in section 4.3.1) with a $0.1 \mu\text{s}$ time step for a total of 20 time steps, and a wire radius of $R = 0.005 \text{ m}$ were used to generate the results. The numerical result for the current density is displayed in figure 4.4 with its analytical comparison in figure 4.5. Since there is only a single component for the magnetic field, namely B_θ , the magnetic field will be presented as a vector plot, in which the magnitude of the vector represents the value of B_θ and the direction of the vector represents its sign (i.e. either (positive) in the positive z direction or (negative) in the negative z direction). The numerical result for B_θ is presented in figure 4.6 and its analytical counterpart is given in figure 4.7.

The results presented below were generated using equations (4.182) and (4.186) and the previously discussed boundary conditions, with the exception that $V = 0$ was set on boundary 1 to prevent the system matrix from being close to being singular. A downside to setting a Dirichlet condition for V on any boundary is that $\nabla V \cdot \mathbf{n} = 0$ no longer applies upon those boundaries; so the setting of Dirichlet conditions for this variable should be minimized wherever possible. Traditionally in the literature [125] a value for A_z is required to be set on at least one surface boundary to uniquely define this variable, usually a symmetry boundary (such as boundary 1) has been used to set an arbitrary value of $A_z = 0$. However this boundary condition is incorrect, because $A_z \neq 0$ upon boundary 1 for low conductivity values (refer to equation 4.E.12 in appendix 4E). The only correct boundary conditions on boundaries 1 and 3 for A_z are the flux boundary conditions defined by the magnetic field B_θ (which was used to generate the numerical results); the use of such flux boundary conditions did not cause any adverse effects in this particular problem (such as a singular system matrix).

The backwards time marching scheme was found to be the best of the time marching schemes, because it did not exhibit the oscillatory decay present when higher order implicit schemes were used to solve this problem. The cubic order finite elements were found to give more accurate results than lower order linear and quadratic finite elements in solving this problem. A reasonable degree of accuracy was obtained using the coordinate transformation discussed in section 4.3.6 to remove singularities close to the axis, although as $r \rightarrow 0$ the percentage error between the numerical and analytical results increases (as mentioned in section 4.3.6); however this error, with regard to the overall solution, is small enough to be ignored for this particular problem.

An accurate calculation of ∇V and B_θ was obtained by extracting the values for A and V from the solved AVA system and then using these values in further finite element schemes for

∇V and B_θ (and the boundary conditions used for these values in the AVA scheme). The overall FEM process is shown schematically in diagram 4.12.

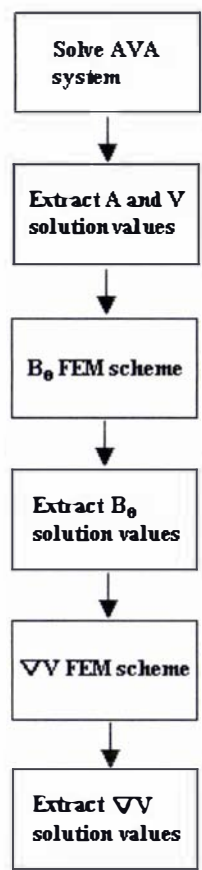


Diagram 4.12: Schematic representation of how the AVA system was solved to determine the current density J and the magnetic field B

Using the process depicted in diagram 4.12 and the previously discussed boundary conditions and circuit parameters the numerically obtained value for the current density of 7.69×10^{10} A/m² was obtained at $r = R$, the corresponding analytical value at this point is 9.60×10^{10} A/m²; this shows a reasonable degree of accuracy for the solution of this problem.

An important point to mention is that because the system being solved with a time marching scheme is both a time dependent problem with time dependent boundaries, any perturbations in the solution at one time step will be carried through to the next time step. If these perturbations are of significant magnitude an avalanche effect of errors will be produced, resulting in a non-physical solution. The errors introduced into the overall solution are from both the spatial discretization of the problem domain and the approximation of the time dependence of the system from the time marching scheme. The problem to be solved must contain both a small enough time step to accurately model the time dependency of the system, and a fine enough

mesh at each time step to accurately solve the problem. Note, if the time dependency of the system is solved using the method of superposition, the errors introduced into the solution by the discretization of the system with respect to time would be minimised [108] (compared to those obtained from using a time marching scheme). A final point to make, in conjunction with the main discussion, is that because a time marching scheme has been used, care must be taken not to use too small a time step (for the given mesh), i.e. refer to equation (4.45) in section 4.31. If too small a time step is used then a situation may occur where the equation being solved is $Mu_{t+\Delta t} = Mu_t + ((1 - \theta)F_t + \theta F_{t+\Delta t})\Delta t$, and would necessitate the use of a finer mesh to circumvent this problem.

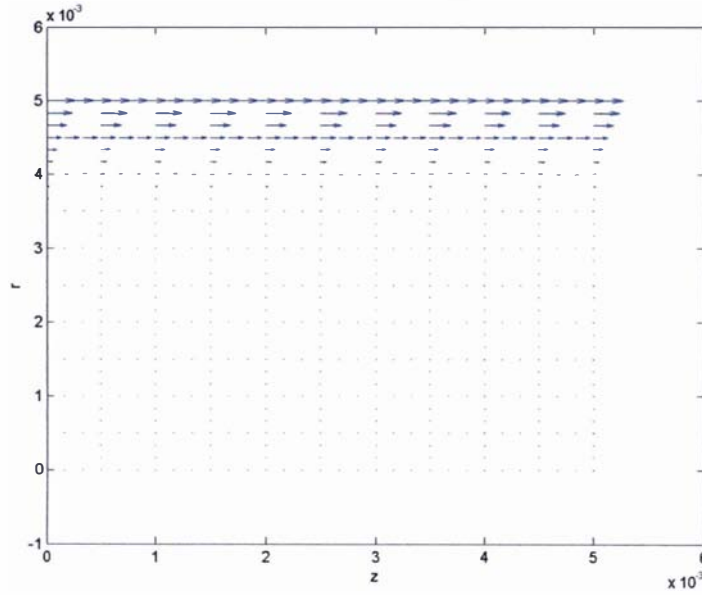


Figure 4.4: Numerical vector plot of the calculated current density for Test Case 1 at $t=2\mu s$, calculated using the AVA formulation on a rough 10×10 mesh of cubic isoparametric elements and the backwards time marching scheme with a $0.1\mu s$ time step for a total of 20 time steps.

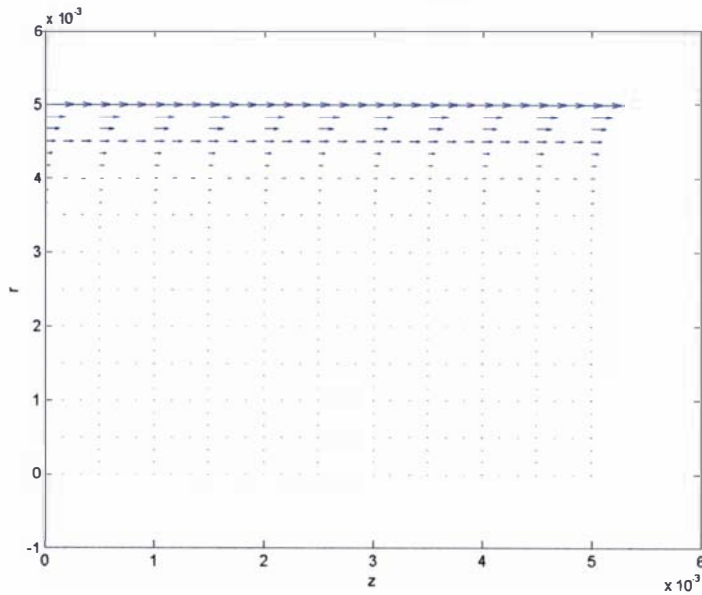


Figure 4.5: Analytical vector plot of the current density for Test Case 1 at $t=2\mu s$

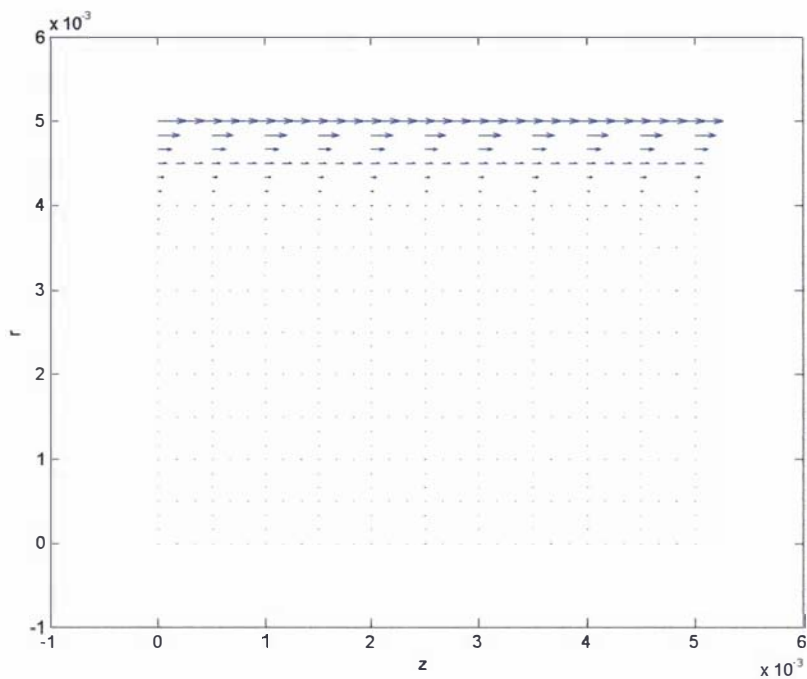


Figure 4.6: Numerical vector plot of the calculated magnetic field for Test Case 1 at $t=2\mu s$, calculated using the AVA formulation on a rough 10×10 mesh of cubic isoparametric elements and the backwards time marching scheme with a $0.1\mu s$ time step for a total of 20 time steps

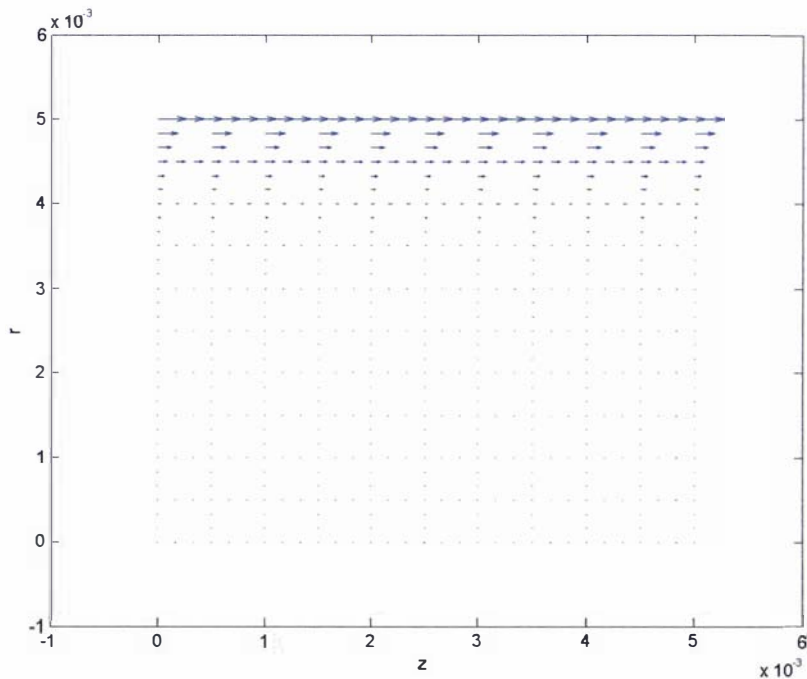


Figure 4.7: Analytical vector plot of the magnetic field for Test Case 1 at $t=2\mu s$

Note for this particular problem, along with the various parameters used to generate the results presented here, it was noticed that meshes rougher than 5x5 generated erroneous results near the axis (errors were seen to form within the numerical answers that grow with time). These numerical errors can be attributed to the general errors introduced into the formulation (near the axis) from the coordinate transformation used to remove singularities close to the axis (refer to section 4.3.6).

The resulting system matrix is unsymmetrical; it is unsymmetrical because the V variable has not been considered as a time dependent variable [125] and equation (4.186) was used instead of equation (4.183). Even though a system matrix could be made symmetrical and allow the use of a biconjugate gradient solver (refer to section 4.3.12) there is little point in doing this because the plasma accelerator problem (because of the way in which it has been formulated) is inherently unsymmetrical (refer to section 4.3.12).

Case 2: an infinitely long coaxial cable carrying a current

The problem of an infinitely long conductive coaxial cable, with a cathode radius of R_1 and an anode with an inner radius of R_2 and an outer radius of R_3 , was next considered as a test case (since it is a simple extension of Test Case 1). The problem domain is depicted in diagram 4.13, in which $0 \leq r \leq R_3$ and $0 \leq z \leq R_3$.

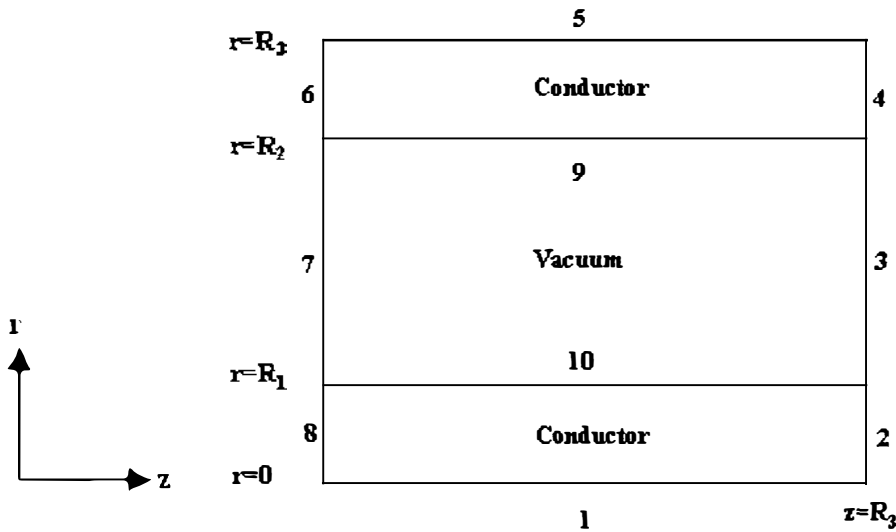


Diagram 4.13: Representation of the problem domain used to solve Test Case 2, showing the computational surface boundaries 1 to 10.

The same techniques used to prevent spurious solutions and singularities close to the axis in Test Case 1 were applied to this problem using isoparametric cubic serendipity elements

(because of their accuracy over lower order elements). The procedure shown schematically in diagram 4.12 was used to solve the problem. The flux boundary conditions for A_z were set on boundaries 1 and 5 (i.e. $\nabla \times A = 0$ on these boundaries). A value of $A_r = 0$ was set on boundaries 2, 4, 6 and 8. Because of the boundary conditions on the surface of a conductor (refer to section 4.3.2) $A_r = 0$ was also set on boundaries 5, 9 and 10. On boundaries 3 and 7 the flux boundary condition of $\nabla \times A = \frac{\mu_o i_o}{2\pi R}$ was set. In order to uniquely define V a value of $V = 0$ was set on boundaries 1 and 5 (because the anode and cathode regions are separate regions). In the B_θ finite element scheme the flux boundary conditions used in the AVA scheme were set i.e. boundaries 1, 3, 5 and 7. While in the ∇V finite element scheme $\nabla V \cdot n = 0$ was set on all conductive boundaries.

The results of solving Test Case 2 using a 30x30 mesh consisting of cubic isoparametric serendipity elements is presented here, in which the numerical current density is given in figure 4.8 and its corresponding analytical solution is shown in figure 4.9. These results were obtained using a conductivity value of $\sigma = 1 \times 10^6 \Omega/\text{m}^2$, the backwards time marching scheme with a $0.1 \mu\text{s}$ time step for a total of 5 time steps, $R_1 = 0.005 \text{ m}$, $R_2 = 0.045 \text{ m}$ and $R_3 = 0.05 \text{ m}$. As this problem only has a single component for the magnetic field (B_θ) the numerically calculated magnetic field is presented as a vector plot in figure 4.10.

In order to improve the solution in the conductor regions, because of the high gradient solutions present in these regions, what shall be referred to as a linear changing mesh was used (as shown in figures 4.8, 4.9 and 4.10). The use of a logarithmic mesh such as that used in [115] was found to give inaccurate results if fine meshes are used, because the jacobain of the isoparametric elements becomes greater than two (a general rule of thumb is that the jacobain of a rectangular element should not exceed a value of two). The linear varying mesh was based upon the solution of the linear change in the r coordinate between adjoining nodes:

$$\nabla r = ax + b \quad (4.187)$$

In equation (4.187) x is node index (the placement between adjacent nodes i.e. a value of $x = 1$ is used to describe the distance between nodes 1 and 2 in the r direction and a value of $x = 2$ is used to describe the distance between nodes 2 and 3), ∇r is the distance between the adjacent nodes indexed by x , and a and b are constants to be determined by the boundary conditions defined within the region in question.

For the cathode region

$$\sum_{x=1}^{x=3} \nabla r = \nabla r_1 \quad (4.188)$$

$$\sum_{x=1}^{x=height1-1} \nabla r = \nabla r_2 = R_1 \quad (4.189)$$

In the boundary condition given by equation (4.188) ∇r_1 is the distance between the first node and the fourth node (in the r direction for a cubic element). In the boundary condition defined by equation (4.189) ∇r_2 is the distance between a node at the position $r = R_1$ and a node at the position $r = 0$ and $height1$ is the total number of nodes in the r direction up to the point $r = R_1$. Using these boundary conditions the values for the constants a and b are derived within this region as:

$$a = \frac{\nabla r_2 - \frac{1}{3} \nabla r_1 (height1 - 1)}{\sum_{x=1}^{height1-1} x - 2(height1 - 1)} \quad (4.190)$$

$$b = \frac{1}{3} \nabla r_1 - 2a \quad (4.191)$$

If $\nabla r_1 = 1.5 \text{elementsidelength}$ (where *elementsidelength* is the typical side length of a rectangular cubic element before the linear changing mesh is applied) then the jacobian of the first element will be equal to 1.5 and the jacobian of the element at $x = height1 - 1$ will be equal to 2.

For the anode region

$$\sum_{x=a_{new}-3}^{x=a_{new}-1} \nabla r = \nabla r_3 \quad (4.192)$$

$$\sum_{x=1}^{x=a_{new}-1} \nabla r = \nabla r_4 = R_3 - R_2 \quad (4.193)$$

In the boundary condition given by equation (4.192) a_{now} is the total number of nodes in the r direction between $R_2 \leq r \leq R_3$ and ∇r_3 is the distance between the node at a_{now} and $a_{now} - 3$. In the boundary condition defined by equation (4.193) ∇r_4 is the distance between the node at R_3 and the node at R_2 . Using these boundary conditions the values for the constants a and b are derived within this region as:

$$a = \frac{\nabla r_4 - \frac{1}{3}\nabla r_3(a_{now} - 1)}{\sum_1^{a_{now}-1} x - \frac{1}{3}(3a_{now} - 6)(a_{now} - 1)} \quad (4.194)$$

$$b = \frac{1}{3}\nabla r_1 - \frac{1}{3}a(3a_{now} - 6) \quad (4.195)$$

If $\nabla r_3 = 1.5 \text{ elements length}$ then the jacobian of the last element in the in the anode region will be equal to 1.5 and the jacobian of the first element in the anode region will be equal to 2.

The numerically obtained values for the current density, in the cathode region, at $r = R_1$ in figure 4.8 is $3.72 \times 10^{10} \text{ A/m}^2$ and its corresponding analytical value is $1.75 \times 10^{10} \text{ A/m}^2$; while the numerically obtained current density value, in the anode region, at $r = R_2$ in figure 4.8 is $-3.14 \times 10^9 \text{ A/m}^2$ and its corresponding analytical value is $-1.63 \times 10^9 \text{ A/m}^2$. The numerical value for B_θ at $r = R_1$, in figure 4.10, is 27.3T and its corresponding analytical value is 25.0T, at $r = R_2$ its numerical value is 3.95T and its corresponding analytical value is 2.77T. These are reasonable values for this particular problem, considering that the problem was solved using a rough mesh (only three elements in the r direction in both the anode and cathode regions).

The previously discussed need to have a fine enough mesh at each time step to prevent an avalanche effect of errors and a small enough time step to accurately model the time dependence of the system (refer to the discussion presented for Test Case 1), naturally also applies to this test case.

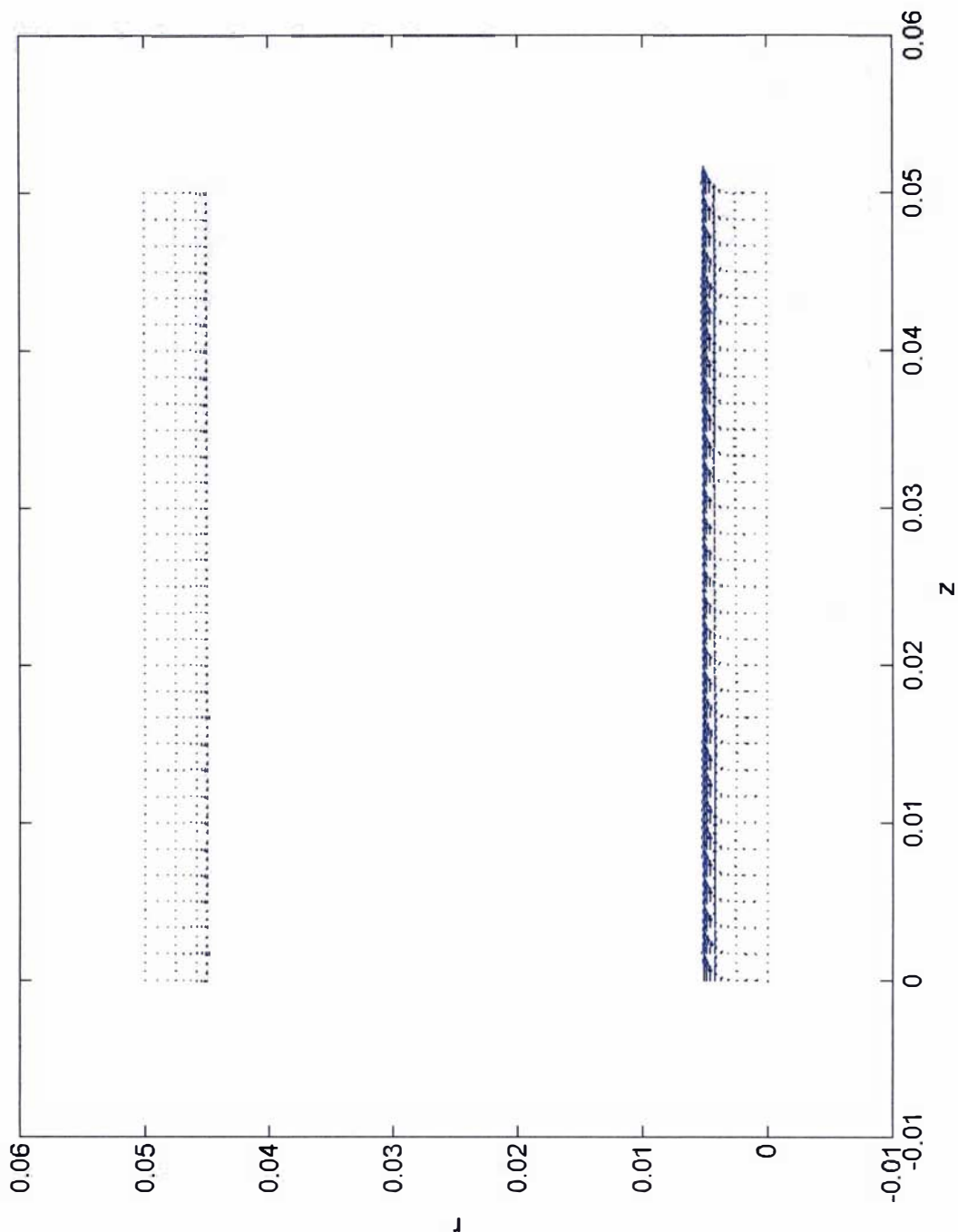


Figure 4.8: Numerical vector plot of the calculated current density for Test Case 2 at $t=0.5\mu s$, calculated using the AVA formulation on a 30×30 mesh of cubic isoparametric elements and the backwards time marching scheme with a $0.1\mu s$ time step for a total of 5 time steps.

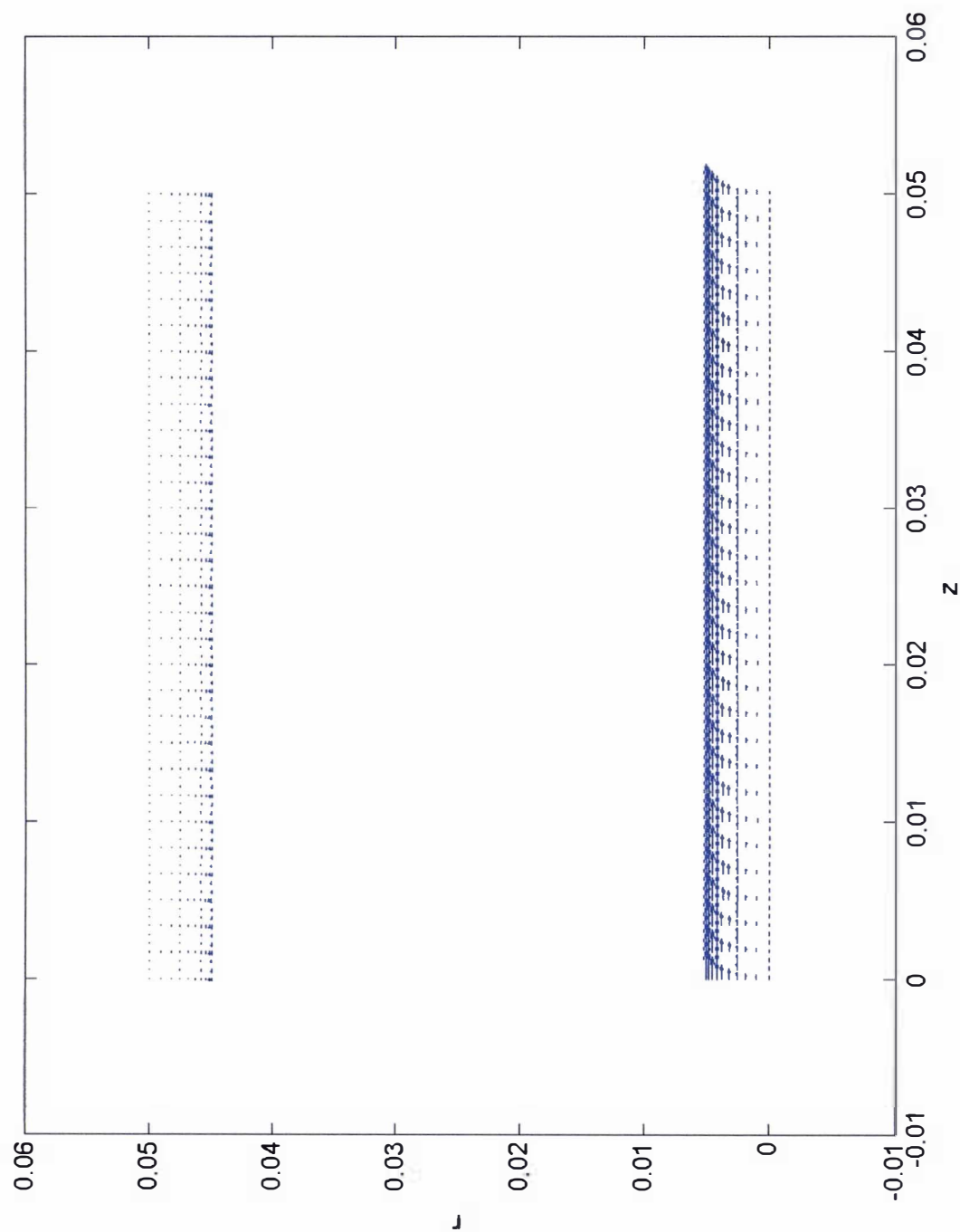


Figure 4.9: Analytical vector plot of the current density for Test Case 2 at $t=0.5\mu s$

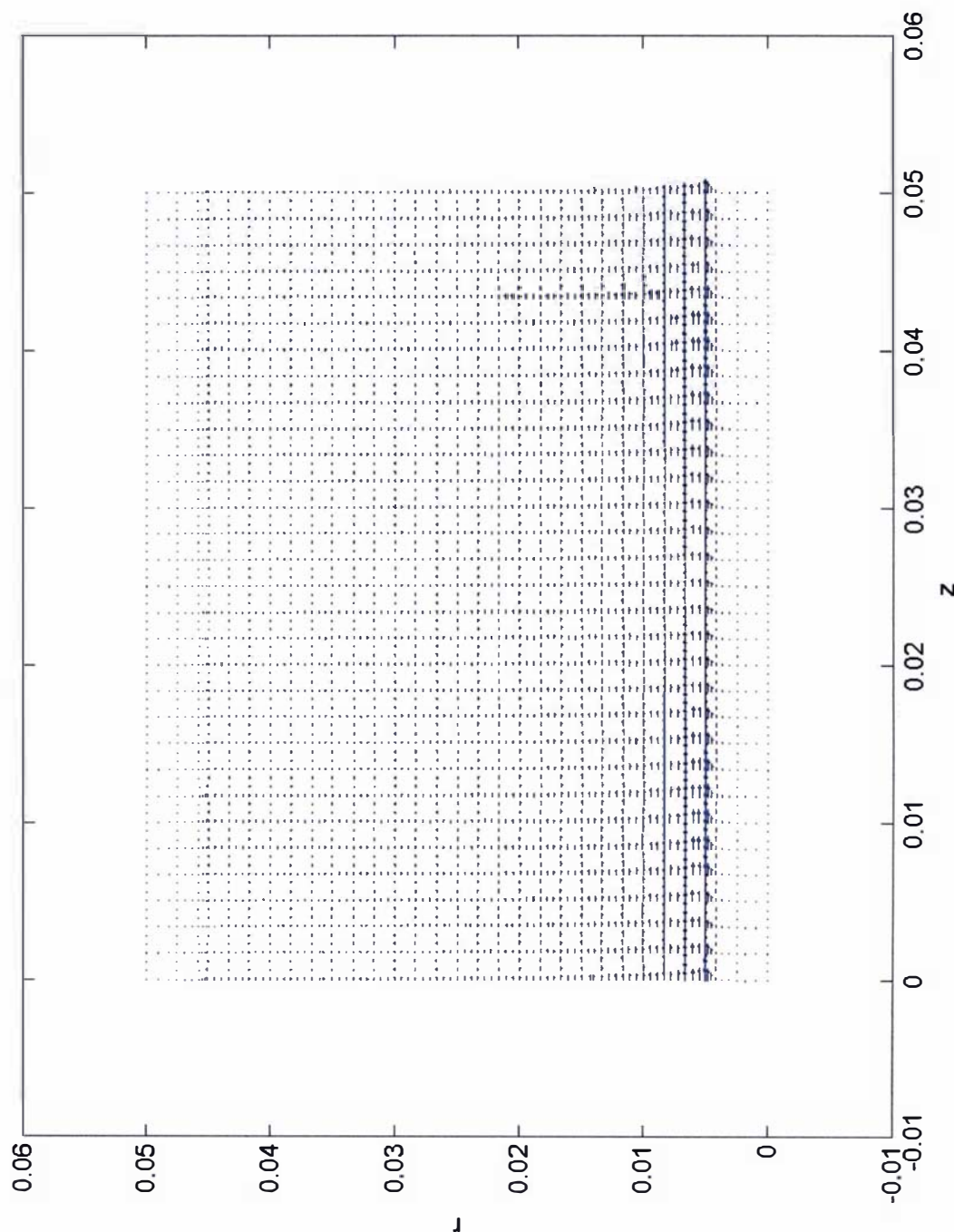


Figure 4.10: Numerical vector plot of the calculated magnetic field for Test Case 2 at $t=0.5\mu\text{s}$, calculated using the AVA formulation on a 30×30 mesh of cubic isoparametric elements and the backwards time marching scheme with a $0.1\mu\text{s}$ time step for a total of 5 time steps.

Given the dimensions and boundary conditions used to generate this test problem it was not possible to conduct accurate calculations for higher conductivity values i.e. $\sigma > 1 \times 10^6 \Omega/\text{m}^2$ on a commercially available 32-bit computer, as unphysical numerical solutions were obtained. This is because of the memory limitation of a maximum of 6Gbytes of Ram (refer to section 4.3.12) available on a commercial 32-bit machine and can also be partially attributed to both a loss in accuracy that is inherently encountered in solving high frequency problems using the AVA formulation (as mentioned in section 4.3.3) and the large number of elements need to accurately model the large gradient solutions present in the anode and cathode regions (for large conductivity values).

The addition of a vacuum region around the anode, to account for the far field boundary conditions (refer to section 4.3.11) and to allow the correct boundary conditions imposed by the use of the penalty factor technique, proved unnecessary. The addition of such a region made little difference to the numerically obtained solution, probably because at the top of the coaxial cable (at $r = R_3$) the far field boundary condition of $B = 0$ has already been reached.

It was also found possible to set the normal component of A on some computational surface boundaries (such as $A_r = 0$ on boundary 5) without adversely effecting the numerical solution, provided that over the majority of the computational surface boundaries the normal component for A is not set.

Case 3: an infinitely long conductive wire carrying a current set in a moving reference frame

The final test problem that was investigated was that of an infinitely long conductive wire carrying a current set in a moving reference frame. The purpose of this test was to investigate any perceived numerical problems that would arise from the addition of a large unsymmetrical velocity term (refer to section 4.3.10). The results from this test case would be very useful in the plasma accelerator problem, because as has been discussed in section 4.3.9 the plasma accelerator will be modelled in a moving reference frame, in which the anode and cathode regions will be considered to be moving with a negative velocity relative to the plasma.

This test problem is essentially the same as that of Test Case 1, with the exception that the problem will be set in a moving reference frame. The problem domain used to model this problem is depicted in diagram 4.14. The equations used to describe this problem are those of equations (4.141) and (4.142) (refer to section 4.3.9); this problem also has an analytical solution which can be found in appendix 4E.

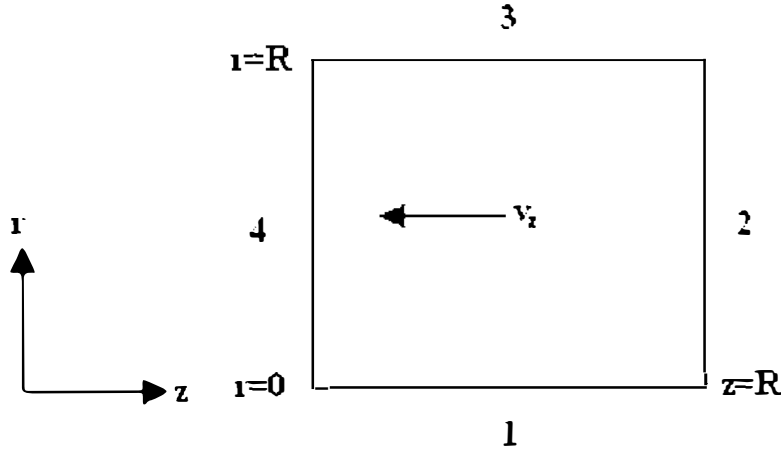


Diagram 4.14: Representation of the problem domain used to solve Test Case 3, showing the computational surface boundaries 1 to 4.

The same techniques employed in Test Case 1 of using the penalty factor technique (to prevent spurious solutions) and the coordinate transformation of equation (4.71) (to remove singularities close to the axis) were also applied to this test problem. However there are two possible choices that can be used to satisfy the analytical solution of $J_r = 0$ within the problem domain, as discussed in appendix 4E. Either equation (4.E.35) can be assumed, which results in equation (4.E.36) for the A_r component and $\nabla V = 0$ over the computational domain, or equation (4.E.37) can be assumed, which results in equation (4.E.38) for $\frac{\partial V}{\partial r}$ and $A_r = 0$ over the computational domain.

Which of these assumptions is chosen, in conjunction with the weak formulation and the boundary conditions, is particularly important in this problem. For example if the traditional weak AVA formulation, given by equations (4.182) and (4.183), is used to solve this test problem then the surface boundary conditions given by equation (4.184) would have to be considered on boundaries 2 and 4. The inclusion of these flux boundary conditions applies to either of the chosen solutions given by equations (4.E.35) or (4.E.38). If the conductivity of the problem region is constant then the alternative weak AVA formulation discussed in Test Case 1, given by equations (4.182) and (4.186), can be used and the surface boundary conditions will be defined by the following equation:

$$\Gamma_S = \int \sigma W \nabla \times \nabla \times A \cdot n \partial \Gamma - \int \sigma W \nabla V \cdot n \partial \Gamma \quad (4.196)$$

Hence if the A_r component, defined by equation (4.E.36) in appendix 4E, is used to ensure $J_r = 0$ on boundaries 2 and 4, then either the flux boundary condition of $\int \sigma W \nabla \times \nabla \times A \cdot n \partial \Gamma$ or A_z must be defined on these boundaries. But instead if the $\frac{\partial V}{\partial r}$ component, defined by equation (4.E.38) in appendix 4E, is used to ensure $J_r = 0$ on boundaries 2 and 4 then the natural flux boundary condition of equation (4.196) will define this component on these boundaries i.e. $\int \sigma W \nabla \times \nabla \times A \cdot n \partial \Gamma - \int \sigma W \nabla V \cdot n \partial \Gamma = 0$. So the use of the $\frac{\partial V}{\partial r}$ component to ensure $J_r = 0$ will be easier to implement compared to using the A_r component. Both conditions were implemented and it was discovered that the use of the $\frac{\partial V}{\partial r}$ component (to ensure $J_r = 0$) was the most effective and accurate method.

It was also discovered that upwinding was not necessary to obtain an accurate solution to this problem and the cubic upwinding scheme suggested in section 4.3.10 proved ineffective when applied to this test case. This can probably be attributed to the fact that the cubic upwinding scheme was based upon preventing numerical oscillations in the convection/diffusion equation of (4.143), but the system that is being solved in this test problem is not of the same form as this equation. Essentially the cubic upwinding scheme developed in section 4.3.10 cannot be applied to this problem and a new (coupled and more complex) stability analysis needs to be conducted with regard to the AVA system used in this test case; however since upwinding appears unnecessary (from the results of this test case) this stability analysis has been deferred.

Test Case 1 was reinvestigated using a moving reference frame travelling at -800000m/s (using the same parameters, techniques, mesh and time step values). The numerical results for the current density are displayed in figure 4.11 together with its analytical comparison in figure 4.12. As there is only a single component for the magnetic field, namely B_θ , the magnetic field will be presented as a vector plot. The numerical results for B_θ are presented in figure 4.13 and its analytical counterpart is given in figure 4.14. It was discovered that the most accurate results were obtained if the magnetic field was included in the AVA system matrix (i.e. included as part of the matrix) rather than calculating this value from the extracted values of the AVA formulation i.e. equations (4.182) and (4.186) are solved in conjunction with the weak formulation of equation (4.197) (in which the coordinate transformation of equation (4.71) has been taken into account).

$$B = \nabla \times A \quad (4.197)$$

The apparent loss in accuracy when the magnetic field is calculated using a separate FEM scheme can probably be attributed to the rounding (machine rounding) of the extracted A values from the solved AVA system. A schematic representation of the process used to generate the numerical results presented below is given in diagram 4.15.

Using the process depicted in diagram 4.15 and the previously discussed boundary conditions and circuit parameters, the numerically obtained value for the current density at $r = R$ was $7.69 \times 10^{10} \text{ A/m}^2$, the corresponding analytical value at this point is $9.60 \times 10^{10} \text{ A/m}^2$; this shows a reasonable degree of accuracy for the solution of this problem using a rough mesh .

Since this test case is also a time dependent problem, the previous discussion on Test case 1 of using a fine enough mesh to prevent the growth of errors within the solution and a small enough time step to accurately model the time dependence of the system also applies to this problem. As observed in Test Case 1, it was found that meshes rougher than 5×5 generated erroneous results near the axis (errors were seen to form within the numerical answers that grow with time). These numerical errors can also be attributed to the general errors introduced into the formulation close to the axis from the coordinate transformation used to remove singularities (refer to section 4.3.6).

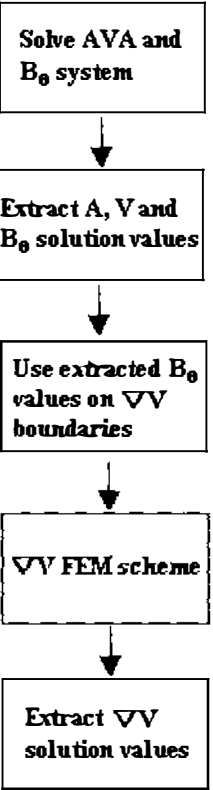


Diagram 4.15: Schematic representation of how the AVA and B system was solved to determine the current density J and the magnetic field B

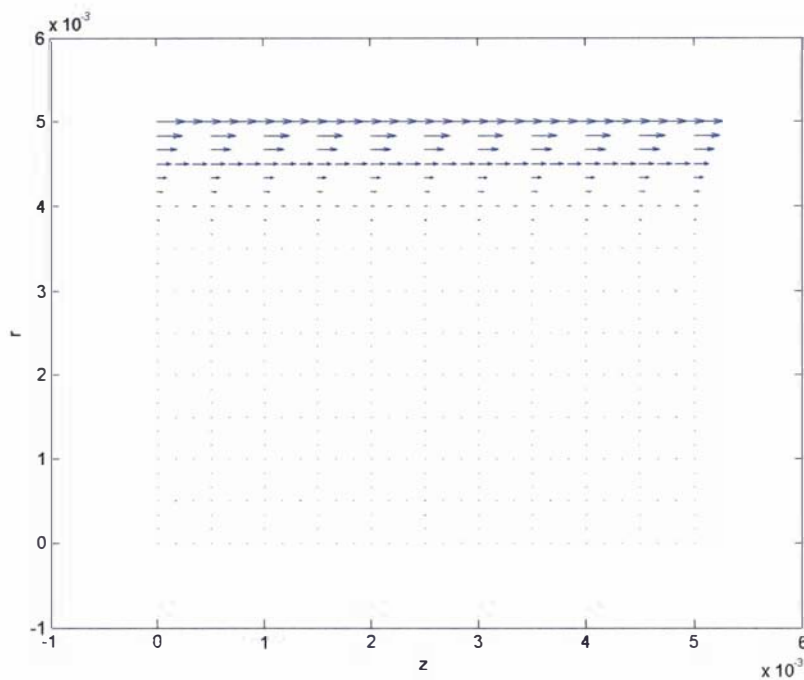


Figure 4.11: Numerical vector plot of the calculated current density for Test Case 3 at $t=2\mu\text{s}$ set in a moving reference frame with a velocity of -80000m/s ; calculated using the AVA formulation on a rough 10×10 mesh of cubic isoparametric elements and the backwards time marching scheme with a $0.1\mu\text{s}$ time step for a total of 20 time steps.

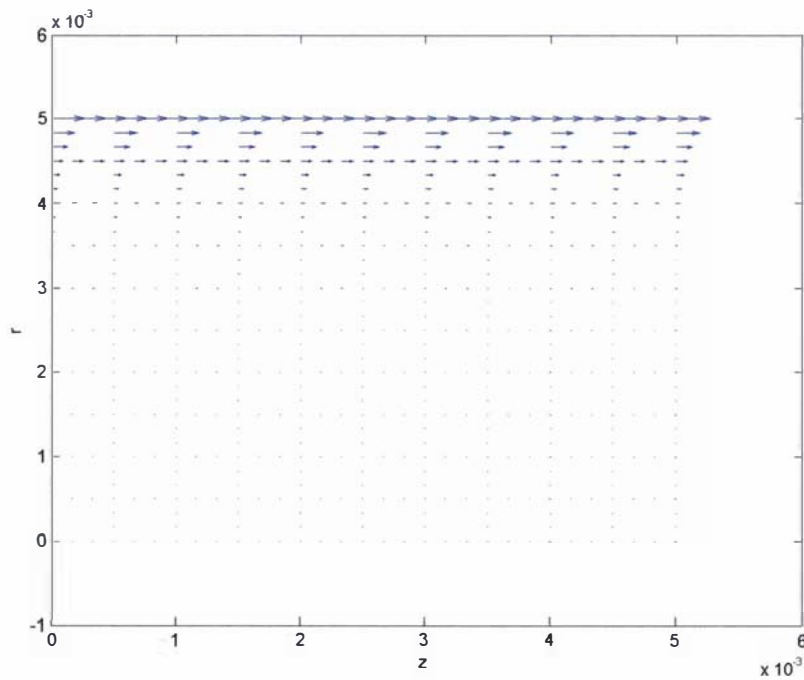


Figure 4.12: Analytical vector plot of the current density for Test Case 3 at $t=2\mu\text{s}$

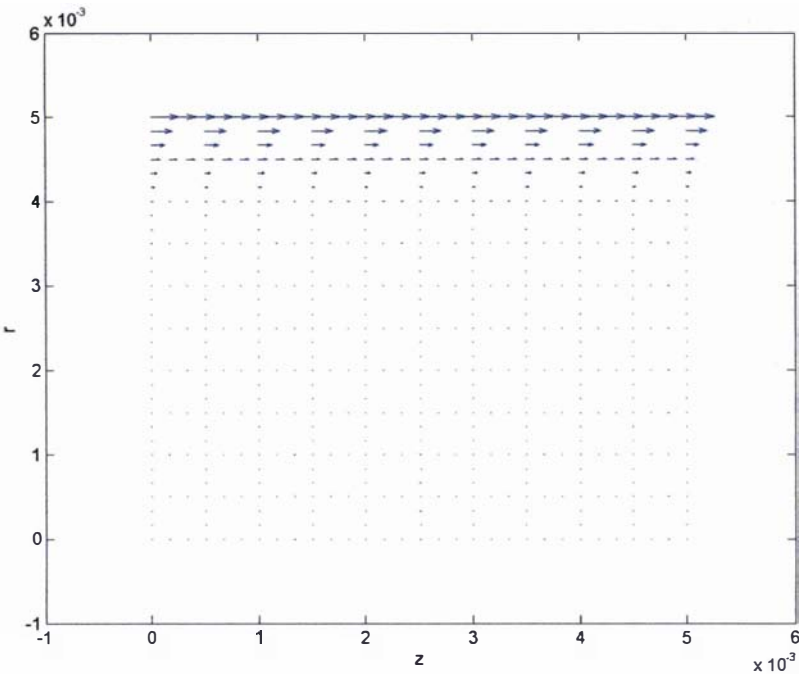


Figure 4.13: Numerical vector plot of the calculated magnetic field for Test Case 3 at $t=2\mu\text{s}$ set in a moving reference frame with a velocity of -80000m/s ; calculated using the AVA formulation on a rough 10×10 mesh of cubic isoparametric elements and the backwards time marching scheme with a $0.1\mu\text{s}$ time step for a total of 20 time steps.

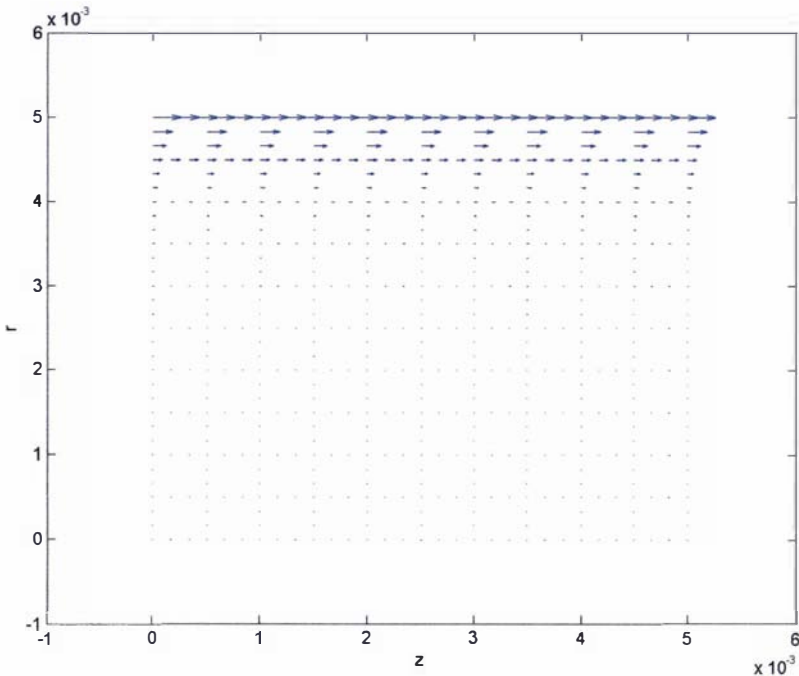


Figure 4.14: Analytical vector plot of the magnetic field for Test Case 3 at $t=2\mu\text{s}$

4.3.14: The numerical model used to describe the operation of the Lica – MATAC

4.3.14: The numerical model used to describe the operation of the Lica – MATAC

A numerical model called MATAC was developed to describe the operation of the Lica, using the techniques discussed in sections 4.3.6 to 4.3.12 and the results of the test cases described in section 4.3.13. MATAC was written using the widely available MATLAB program (version 6.5), because MATLAB is based around and works with sparse matrices and vectors.

MATAC consists of two distinct processes, first the electromagnetic problem is solved using a FEM calculation with cubic isoparametric serendipity elements [108] (because of the greater degree of accuracy these elements offer compared to lower order elements, refer to section 4.3.13), and then the magnetohydrodynamic equations are solved using a FV model. In order to develop a preliminary numerical model the following assumptions were made:

- 1) The plasma block mode of operation is assumed
- 2) The plasma is assumed to be incompressible and moving as a distinct undeforming mass
- 3) Because of assumption 2) the magnetohydrodynamic equations are reduced to the solution of a simple acceleration equation.
- 4) The properties of the plasma will be assumed to be axisymmetrical (i.e. no change in the θ direction), so the geometry of the problem is reduced to a two dimensional axisymmetrical problem with a symmetry plane (refer to section 4.3.4).

The electromagnetic problem is solved using the AVA formulation (refer to section 4.3.3). Because the system that is being solved is an axisymmetrical system, the transformation discussed in section 4.3.6 is used to prevent singularities close to the axis. In order to uniquely define the magnetic vector potential A the Coulomb gauge is introduced into the AVA formulation using the penalty factor method, for the reasons covered in section 4.3.7. The problem of singularities at re-entrant corners of the problem is dealt with by simple node refinement in the region of the singularity (refer to section 4.3.8) with the knowledge that there will be an inherent error in the region of the singularity (refer to section 4.3.8). The plasma accelerator problem is a time dependent, moving problem. In order to account for this fact the reference frame (for this system) is taken as being the velocity of the plasma; hence the electrodes will be considered to be moving with a negative velocity relative to the plasma in essentially a Eulerian system similar to that proposed in [115] (refer to section 4.3.9). In choosing to model the accelerator in this manner a substantial amount of computational time and memory is saved (refer to section 4.3.9). Even though the upwinding scheme that is used in the majority of rail gun programs, (that of Hughes [157], refer to section 4.3.10) was extended

4.3.14: The numerical model used to describe the operation of the Lica – MATAC

to quadratic and cubic FEM elements for use in MATAC, it was discovered that upwinding was unnecessary for the current problem; this assertion is made on the basis of the results given for Test Case 3 in section 4.3.13 (refer to that section for a discussion). Because (for initial purposes) the plasma has been assumed to be an incompressible, undeforming plasma block (refer to assumptions 1 and 2) the problem of defining the normal component of the current density on a curved plasma boundary is not applicable. The far field boundary conditions for this problem, as discussed in section 4.3.11, are treated very simply by including a region around the modelled area large enough that the effects of the magnetic and electric fields produced by the plasma have negligible effect upon the prescribed computational boundaries. This is the standard method used in rail gun and plasma accelerator programs, as discussed in section 4.3.11. In MATAC the far field boundary conditions are assumed to occur a distance of approximately 3cm from the plasma (the choice of this distance was partially chosen because of the memory limitations on a commercial 32-bit machine). Given the calculated current as a function of time presented in section 3.3.8, this distance should be sufficient and is comparable to the distances used in other programs for example [115]. Once the AVA system has been assembled into the temporal system matrix and overall system vector it is solved using the sparse LU solver in MATLAB. The current density and magnetic field are calculated for the current time step and are extracted within the plasma region for use in the FV scheme.

The FV scheme, because of assumptions 1), 2) and 3), is reduced to solving the following equation for the Lorentz force F_L .

$$F_L = \int J \times B d\Omega \quad (4.198)$$

In equation (4.198) the Lorentz force is equal to the sum of $J \times B$ across the volume Ω of the plasma. The value for $J \times B$ at the plasma electrode boundaries should not be included in this calculation.

The FV method [113], [114] is a special method that has been derived from FD methods and shares some common features with the FEM method. In the FV method the problem domain is discretized into a series of elements known as finite volume elements (in a process akin to that of FEM). The equation to be solved is expanded using integration by parts and the resulting surface fluxes on a FV element are discretized by either FD or FEM techniques. Any volume source terms are generally treated by multiplying the known average of the source term by the volume of FV element; this also applies to any linear time derivative terms. Applying the above discussion to the FV element shown in diagram 4.16 and the example equation of (4.199) results in the FV version of this equation given by equation (4.200).

4.3.14: The numerical model used to describe the operation of the Lica – MATAC

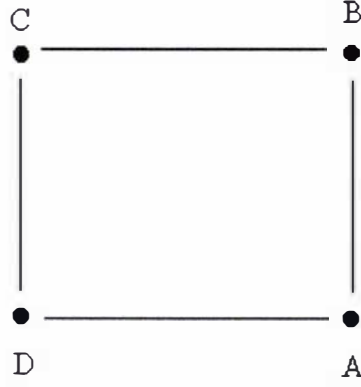


Diagram 4.16: A simple linear FV element in which A, B, C and D are nodal points

$$\frac{\partial}{\partial t} \int U \partial \Omega + \int F \partial \Gamma = \int Q \partial \Omega \quad (4.199)$$

$$\frac{\partial}{\partial t} U_J \Omega_J + \sum_{Sides} (F \cdot S) = Q_J \Omega_J \quad (4.200)$$

In equation (4.199) U is the sought after solution variable (i.e. it is both a spatial and temporal term), F is the flux through the surface of the FV element and Q is the source term. In equation (4.200) Ω_J is the volume of the FV element being calculated, the subscript J relates to the quantity in question for the current element and $\sum_{Sides} (F \cdot S)$ represents the sum of all the fluxes across the sides of the FV element.

The above discussion has been over simplified somewhat and the most significant rule of the FV scheme requiring that the flux contributions be conservative has not been discussed (refer to [114]). But for the purposes of the MATAC program, because of the assumptions that have been made, the FV method is only required to calculate the sum of $J \times B$ across the plasma; so $J \times B$ will be treated as a source term. The finite volume discretion of equation (4.198) is:

$$F_{L_J} = (J_J \times B_J) \Omega_J \quad (4.201)$$

In MATAC only linear rectangular FV elements were used (although higher order FV elements can also be constructed). Since the FV elements are linear rectangular elements the volume of each of these elements Ω_J , given by equation (4.202), was derived using the area formula from [114] (in reference to diagram 4.16). Because the plasma accelerator system is calculated using

4.3.14: The numerical model used to describe the operation of the Lica – MATAC

axisymmetrical coordinates the volume of a FV element in equation (4.202) was obtained by multiplying the area of the element (in the rz plane) by the average r value for the current element (denoted as r_c) and 2π .

$$\Omega_J = r_c \pi (\Delta x_{AC} \Delta y_{BD} - \Delta x_{BD} \Delta y_{AC}) \quad (4.202)$$

In equation (4.202) Δ represents the change in a coordinate (a distance), for example Δx_{AC} represents the difference in the x coordinate between node A and node C (i.e. $\Delta x_{AC} = x_C - x_A$).

Once the sum of $J \times B$ has been calculated across the plasma the velocity v and distance d travelled by the plasma, within the current time step, is determined by solving equations (4.203) and (4.204) using a fifth order Runge-Kutta solver, the ode45 algorithm in MATLAB.

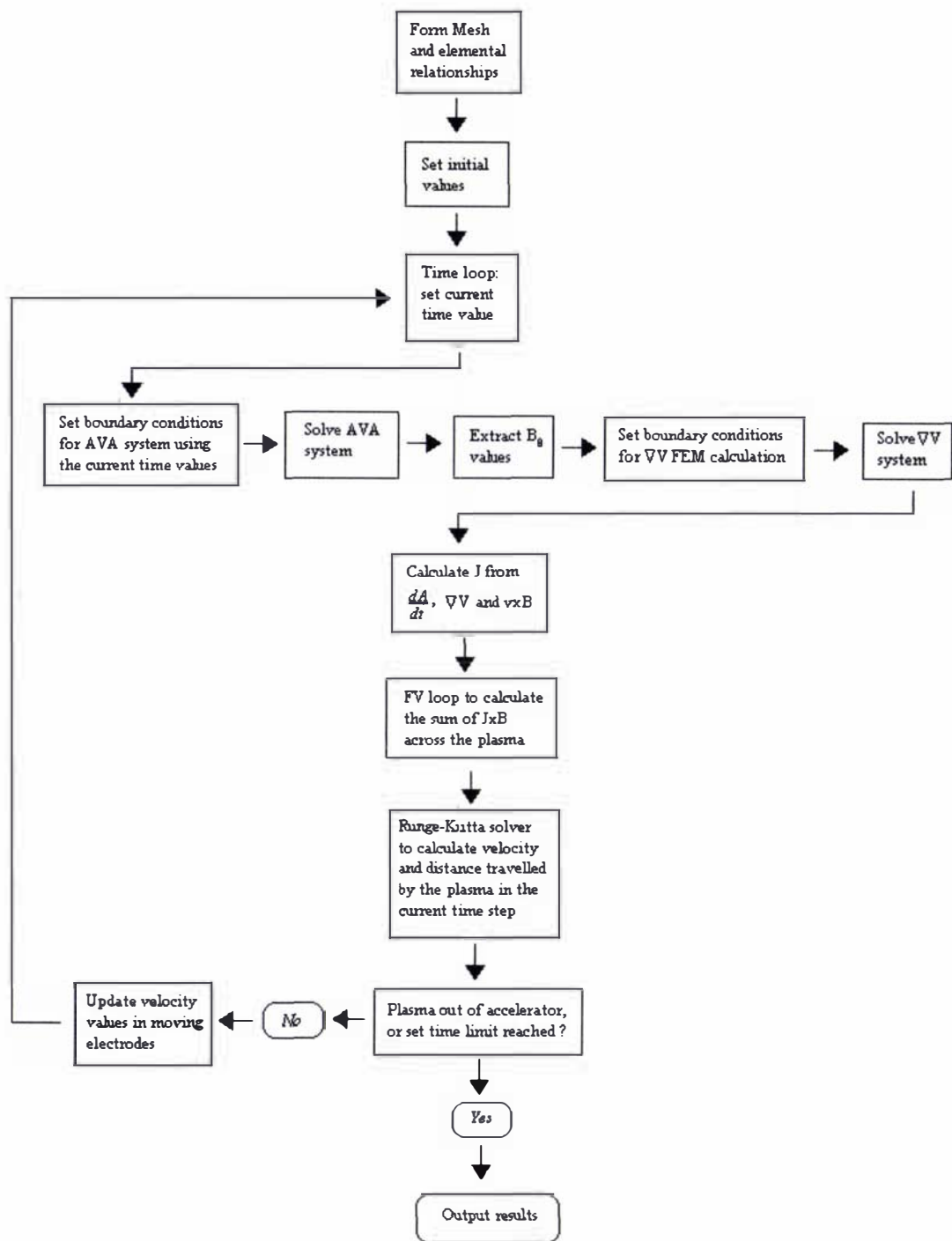
$$\frac{\partial v}{\partial t} = \frac{J \times B}{m} \quad (4.203)$$

$$\frac{\partial d}{\partial t} = v \quad (4.204)$$

After the velocity and distance travelled by the plasma are known, the velocity of the moving electrodes is updated for use in the next time step. The entire process (the FEM, FV and Runge-Kutta calculations) are repeated until either the plasma has left the accelerator or a user defined number of time steps has been reached.

A windows based version of MATAC is included on the disk accompanying this thesis; a general description of the inner workings of the program including excerpts and some of the subroutines is presented in appendix 4F. A diagrammatic representation of the modelling process used in MATAC is presented in flow chart 4.1. Note the calculation of B in MATAC can either be applied as a variable within the AVA formulation (refer to test case 3 of section 4.3.13) or as a separate FEM calculation (refer to test case 1 of section 4.3.13). In the version of MATAC accompany this thesis and all the results presented in preceding section B was calculated as part of the AVA calculation.

4.3.14: The numerical model used to describe the operation of the Lica – MATAC



Flow chart 4.1: Flow chart representing the modelling process in the MATAC program.

4.3.14: The numerical model used to describe the operation of the Lica – MATAC

The problem domain in MATAC is depicted in diagram 4.17 in which R_1 is the radius of the positive electrode; R_2 and R_3 are the inner and outer radii of the grounded electrode; L_1 is the distance from the far field boundary at the breech to the start of the plasma block; L_2 is the distance from the far field boundary at the breech to the end of the plasma block and L_3 is the distance between the two far field boundaries.

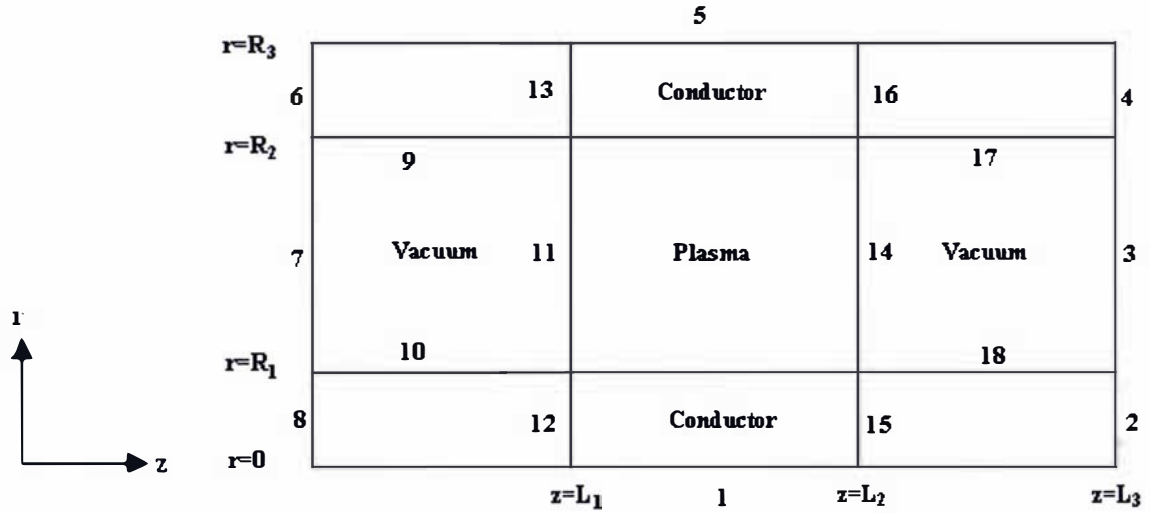


Diagram 4.17: Representation of the problem domain in MATAC, showing the computational surface boundaries 1 to 18.

It was found to be unnecessary to include a vacuum region around the ground electrode to account for the far field boundary conditions, as it made very little difference to the final results. This can be attributed to the coaxial plasma accelerator acting (on the whole) like a coaxial cable (refer to the discussion on test case 2 in section 4.3.13) with the plasma having very little effect on the magnetic field at the outer radius of the grounded electrode.

The overall boundary conditions consist of applying $J \cdot n = 0$ on all conductive surfaces i.e. $A \cdot n = 0$ and $\nabla V \cdot n = 0$, except in regions where there is a velocity component in which case $\nabla V = -v \times B$ is applied on the conductive surface (refer to case 3 in appendix 4E). On boundaries 7 and 3 flux conditions for A are applied i.e. the far field boundary conditions on

boundary 7 of $\nabla \times A = \frac{\mu_o i_o}{2\pi r}$ and on boundary 3 of $\nabla \times A = 0$ are applied. Flux boundary

conditions are also applied on boundaries 1 and 5 (for the reasons discussed on test case 1 in section 4.3.13). The singular points at the re-entrant corners of the plasma-electrode interface can also be set for the A_z and A_r terms. At a re-entrant corner the electric field (and the

4.3.14: The numerical model used to describe the operation of the Lica – MATAC

current density) are described by ∇V (refer to section 4.3.8); this can also be confirmed by the reader by applying either the modified magnetic vector potential (refer to section 4.3.3) or the AVA formulation in which V has not been included to a problem containing a re-entrant corner. Upon doing this one will find that A will tend towards zero at the re-entrant corner. This is yet another reason why the modified magnetic vector potential cannot be used to model the plasma accelerator problem.

In order to model the problem of variable conductivity within the plasma (refer to the calculated conductivity profiles calculated in section 3.3.8) as well as the jump conditions at the plasma-electrode interfaces, the full AVA weak formulation given by equations (4.182) and (4.183) must be solved. If the circuit equation is underdamped then the setting of the surface boundary condition given by equation (4.184) at the breech becomes problematic, because

$$\int \sigma W \frac{\partial A}{\partial t} \cdot n \partial \Gamma \text{ must be included in the surface integral calculation (refer to the discussion on}$$

test case 1 in section 4.3.13). If the circuit equation is underdamped then there is no simple analytical solution for A in the electrodes (refer to appendix 4E); instead a one dimensional numerical calculation will have to be applied to the electrode boundaries at the breech (boundaries 6 and 8) at the start of each time step before the main boundary conditions for the AVA calculation are set.

For the preliminary purposes of testing the MATAC program, to ensure that it is working correctly (i.e. giving physically meaningful results) and as a check on the effectiveness of the chosen techniques used in its creation, the alternative weak AVA formulation equations (4.182) and (4.186) was used (refer to test case 1 in section 4.3.13). However in making this choice the restriction of a constant conductivity within the conductive regions must be applied. This

restriction will be made otherwise the $\int W \nabla \cdot \left(\sigma \frac{\partial A}{\partial t} \right) \partial \Omega$ term would have to be expanded in

terms of $\nabla \sigma$ across either the plasma or a jump condition (i.e. a jump in conductivity), which is very difficult.

Because the Lica has a large positive electrode radius (1.5cm) there are a very large current density and magnetic field gradients within this region, which cannot be accurately calculated given the dimensions and materials of the Lica, because of the memory limitations on a commercially available 32-bit machine (a finer mesh than can be generated is required to adequately solve the problem). So the alternative weak AVA formulation (equations (4.182) and (4.186)) will be (initially) used with constant conductivity within the conductive regions (for the reasons previously discussed).

4.3.14: The numerical model used to describe the operation of the Lica – MATAC

The initial results from MATAC using the above assumptions are presented in the preceding section. Note, if either a parallel version of MATAC or a 64-bit computer was used (on a 64-bit computer the virtual memory is not restricted to 2Gbytes, but can be dumped onto the hard drive) then the typically used weak AVA formulation with a variable conductivity within the plasma region and correct conductivity within the electrodes could be used. The current version of MATAC would have to be altered to be able to use the typical weak AVA formulation, but this is a minor matter. The system and temporal matrices subroutines would have to be altered and the previously discussed one dimensional numerical calculation would have to be included at the breech.

There is one final point that should be made about the MATAC program, it does not contain any error improvement strategy [107] either within the time marching scheme or the mesh. The time step is a user defined, fixed variable and the mesh that is used is a fixed algebraic mesh. A certain amount of error will be included in the overall solution because of this. Because the priority was to develop MATAC rather than to optimise it, the use of error evaluation at half time steps [107] (to improve the accuracy of the time marching scheme) and an adaptive mesh [155] (to improve the solution within the mesh) were deferred. Since MATAC contains no error improvement strategy, special care must be taken by the user (of MATAC) to ensure that a fine enough mesh is used in order to prevent errors of significant magnitude forming within the solution. Care must also be made in choosing a small enough time step to accurately model the time dependence of the system (refer to the discussion of Test case 1 in section 4.3.13 for fuller details on these two aspects).

4.3.15: Results of the numerical model MATAC

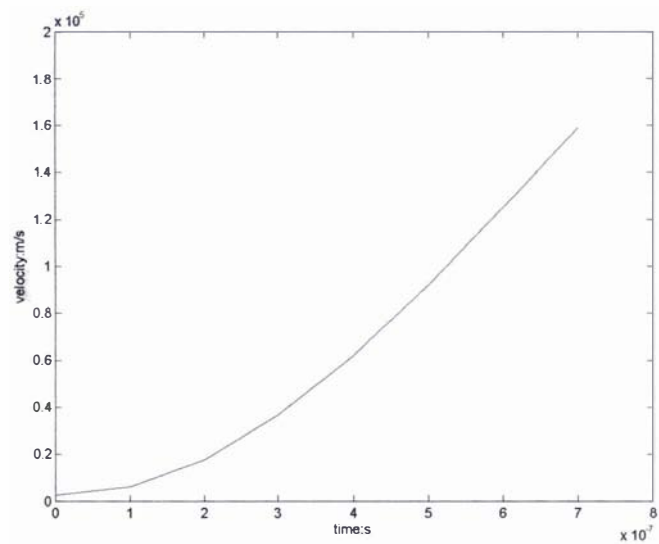
Two initial trial runs of MATAC were conducted, which shall be referred to as numerical test 1 and numerical test 2, using the data contained within table 4.4 in conjunction with the previously discussed assumptions and techniques covered in section 4.3.14.

Numerical test number	Mass: mg	Acceleration distance: m	Plasma Length: cm	Total Ro: Ω	Total Lo: nH	C: μ F	Charging Voltage: V	Conductivity Value: $1/(\Omega m)$	Initial velocity km/s	Time step: μ s
1	0.0003	0.05	2	0.01	10	500	1000	300	2.6	0.1
2	0.0003	0.05	2	0.01	10	500	1000	16000	2.6	0.1

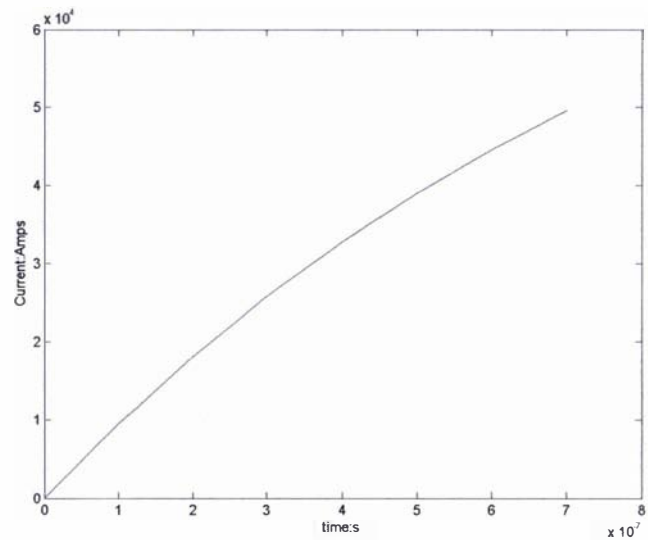
Table 4.4: parameters used to initially test the MATAC program

Results for Numerical test 1

The velocity and current as functions of time are displayed in graphs 4.12 and 4.13. Vector plots of the current density across the plasma are presented for three selected times in figures 4.15 to 4.17. The magnetic field across the plasma is presented as a vector plot (in which the magnitude and sign for B_θ is presented as a vector value in the z direction) for three selected times in figures 4.18 to 4.20. The overall vector plot of the current density is shown for selected times in figures 4.21 and 4.22. The magnetic field within the conductive regions is presented as vector plots in figures 4.23 and 4.24 at the same selected times that were chosen to display the overall current density distribution. Vector plots of A and ∇V within the overall conductive regions at $t=0.7\mu s$ are presented in figures 4.25 and 4.26 respectively.



Graph 4.12: Graph of velocity of the plasma as a function of time, for numerical test 1.



Graph 4.13: Graph of current as a function of time, for numerical test 1

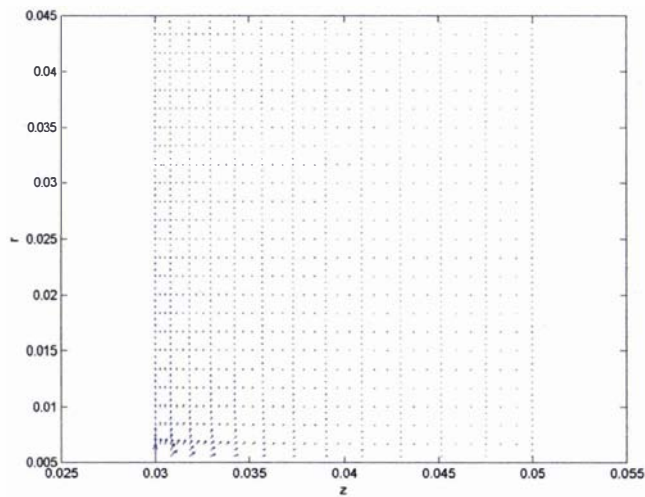


Figure 4.15: Vector plot of the current density across the plasma at $t=0.1\mu\text{s}$, for numerical test 1

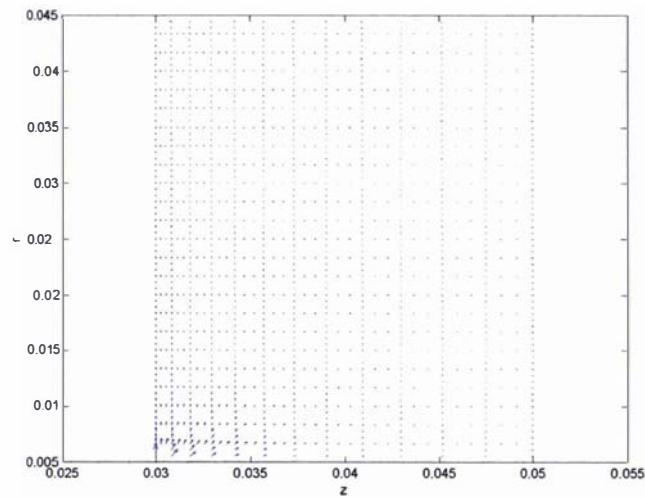


Figure 4.16: Vector plot of the current density across the plasma at $t=0.4\mu\text{s}$, for numerical test 1

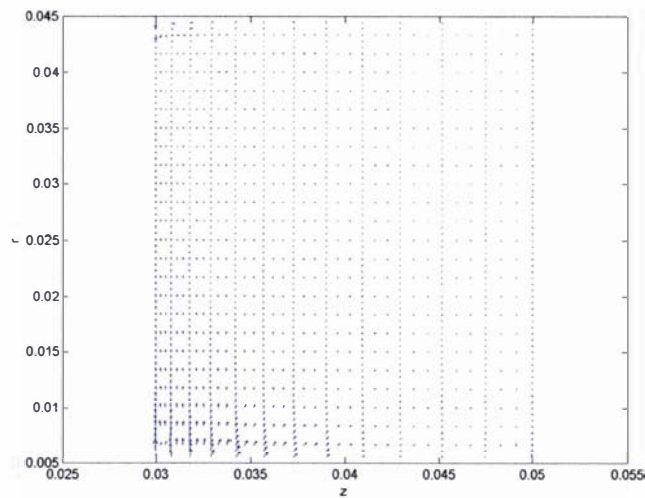


Figure 4.17: Vector plot of the current density across the plasma at $t=0.7\mu\text{s}$, for numerical test 1

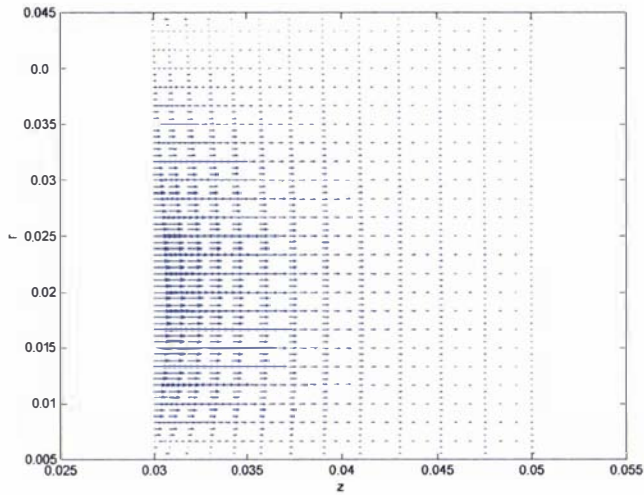


Figure 4.18: Vector plot showing the magnetic field distribution across the plasma at $t=0.1\mu\text{s}$, for numerical test 1.

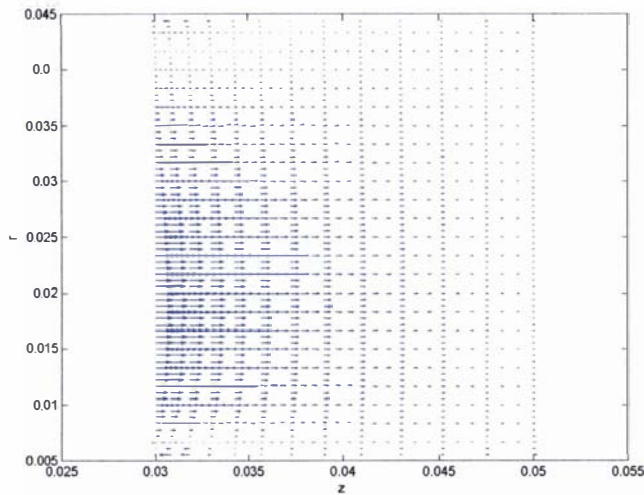


Figure 4.19: Vector plot showing the magnetic field distribution across the plasma at $t=0.4\mu\text{s}$, for numerical test 1.

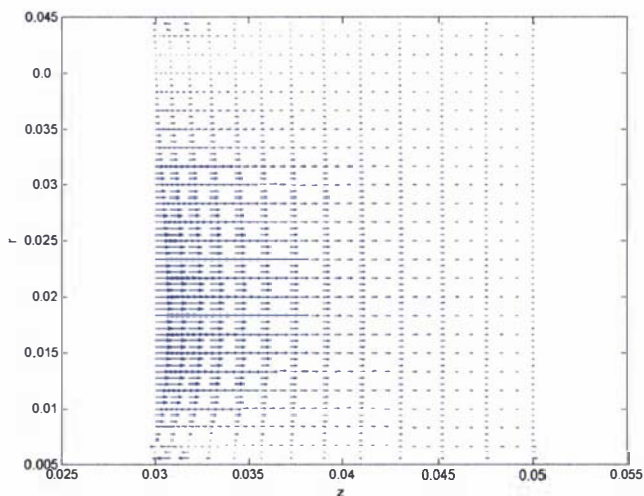


Figure 4.20: Vector plot showing the magnetic field distribution across the plasma at $t=0.7\mu\text{s}$, for numerical test 1.

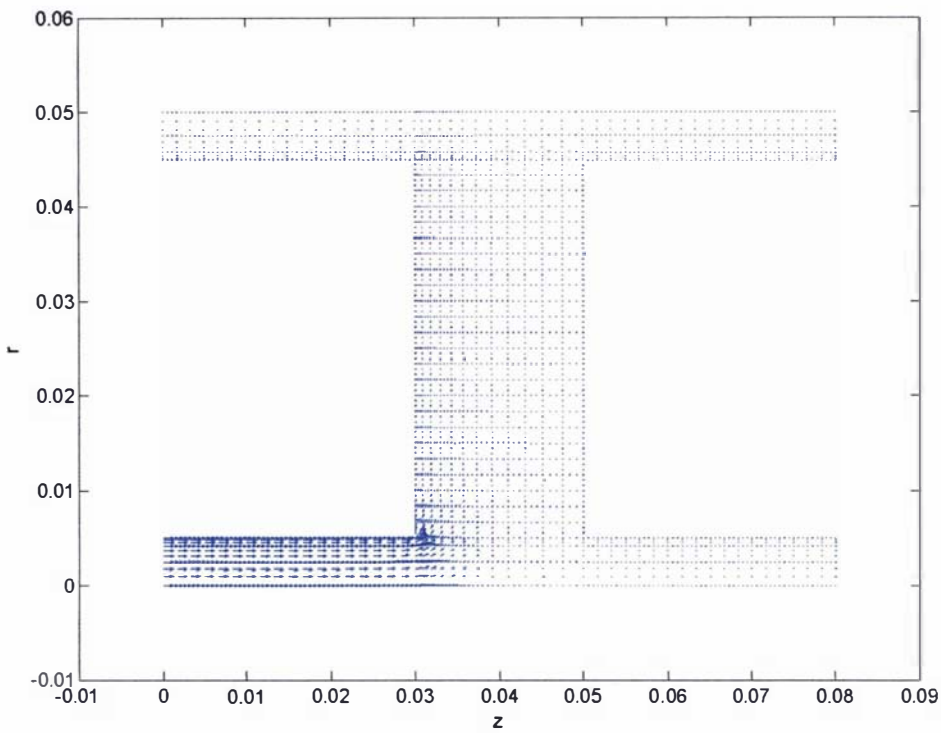


Figure 4.21: Vector plot of the overall current density distribution at $t=0.1\mu s$, for numerical test 1.

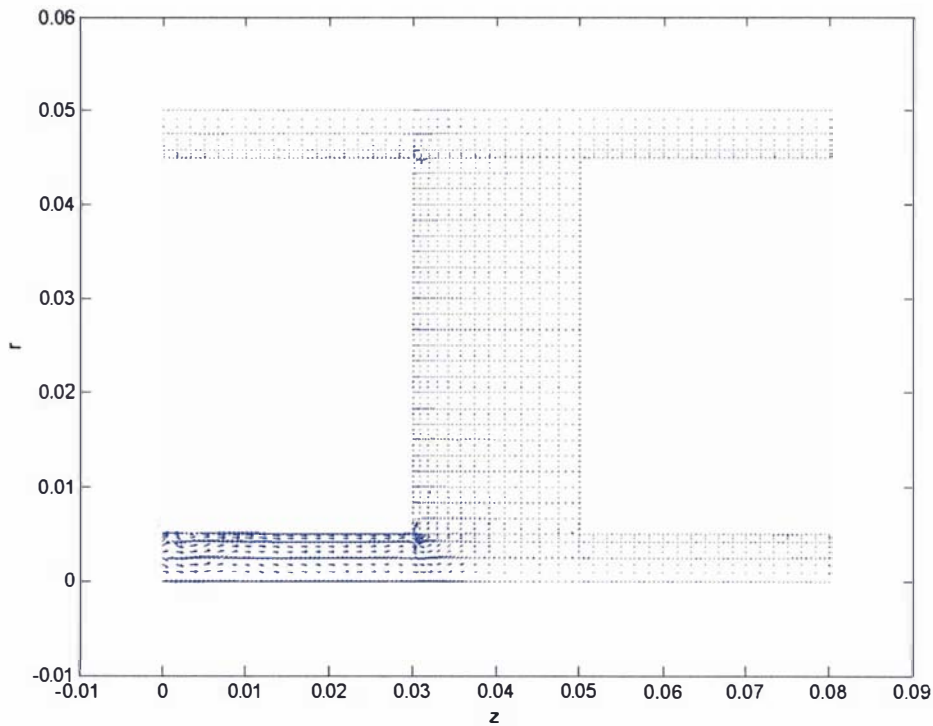


Figure 4.22: Vector plot of the overall current density distribution at $t=0.7\mu s$ showing the formation of errors within the solution, for numerical test 1.

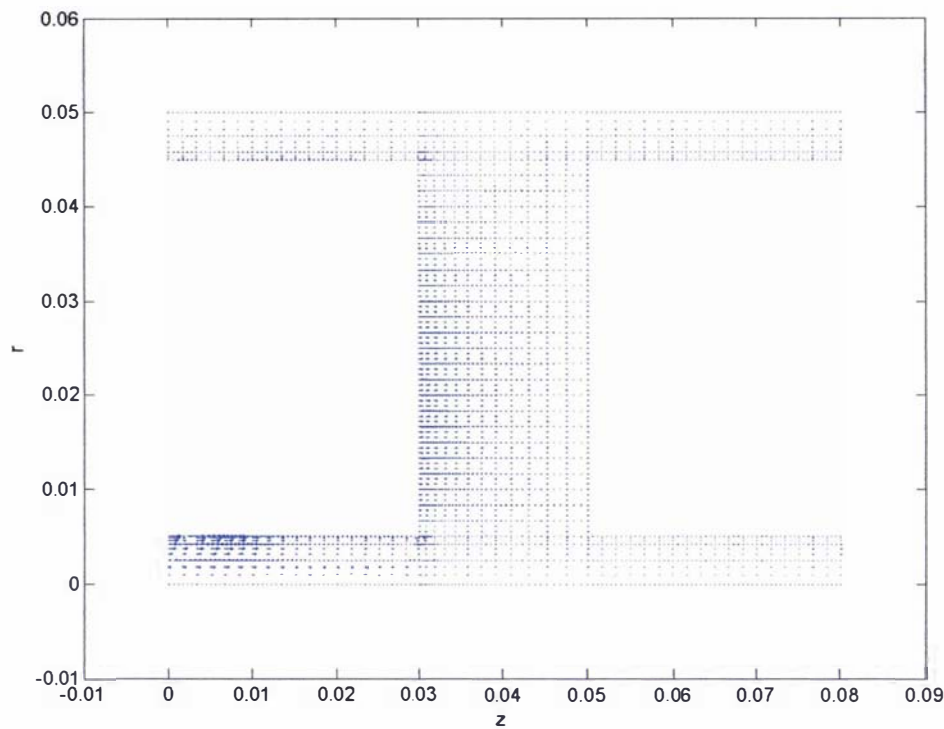


Figure 4.23: Vector plot of the magnetic field within the conductive regions at $t=0.1\mu\text{s}$, for numerical test 1.

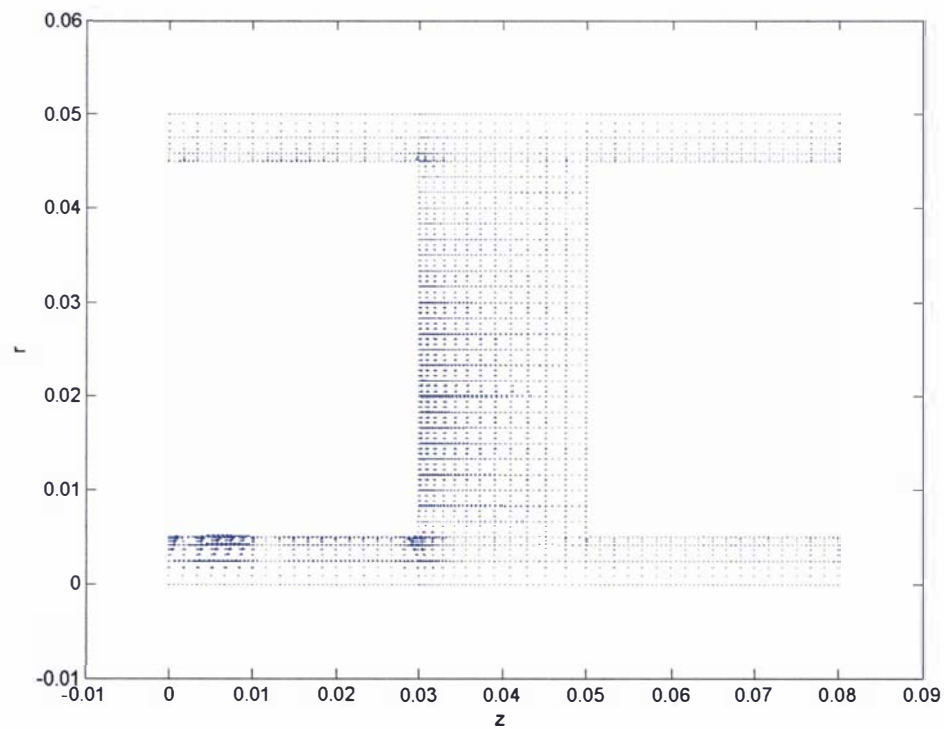


Figure 4.24: Vector plot of the magnetic field within the conductive regions at $t=0.7\mu\text{s}$ showing the formation of errors within the solution, for numerical test 1.

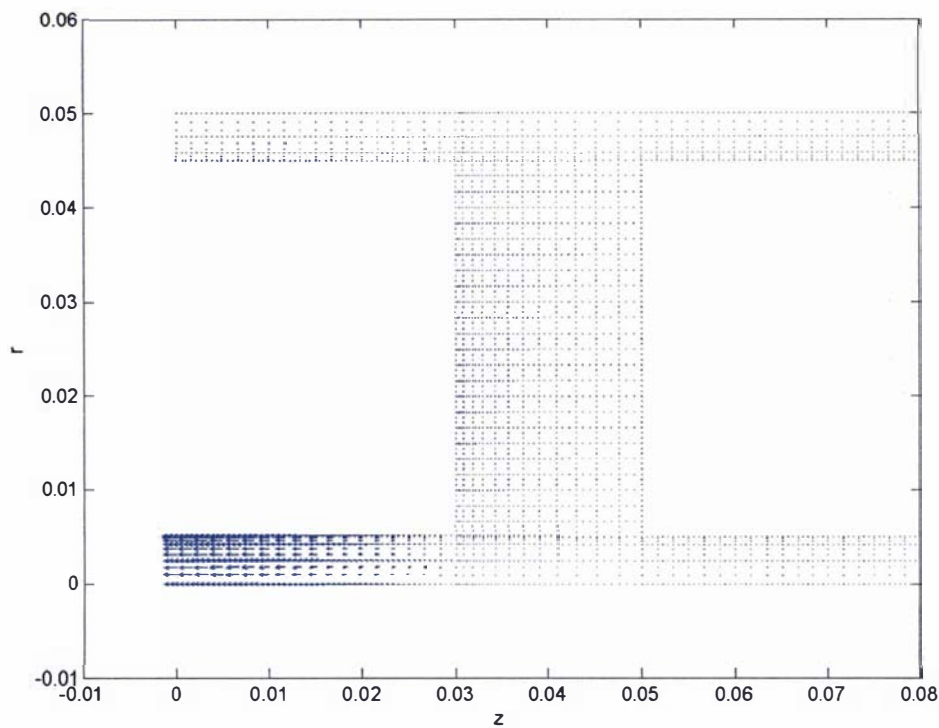


Figure 4.25: Vector plot of the magnetic vector potential A within the overall conductive regions at $t=0.7\mu s$, for numerical test 1.

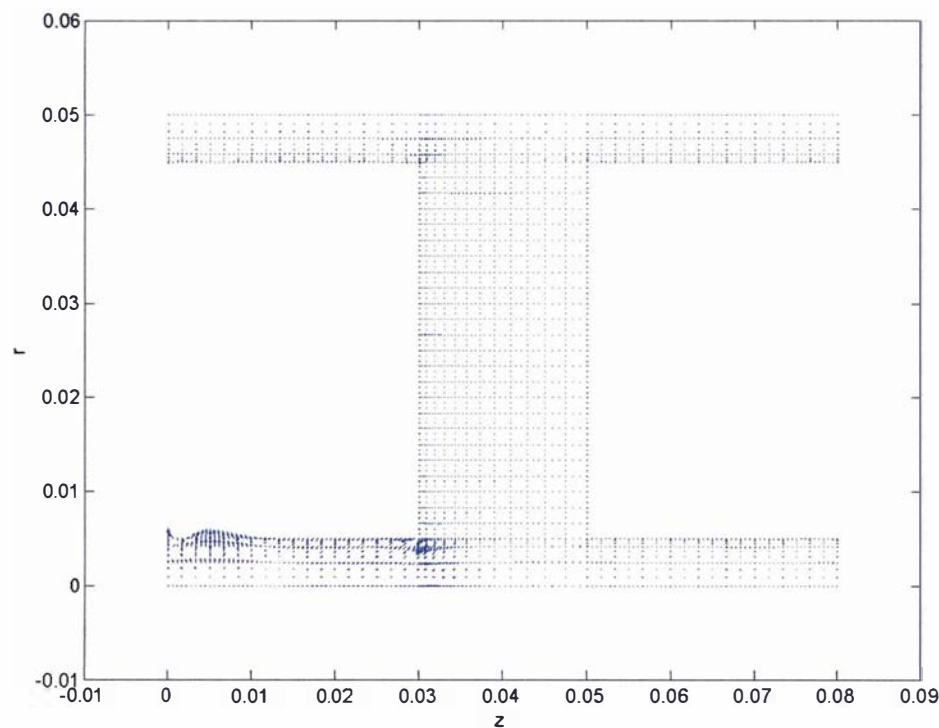
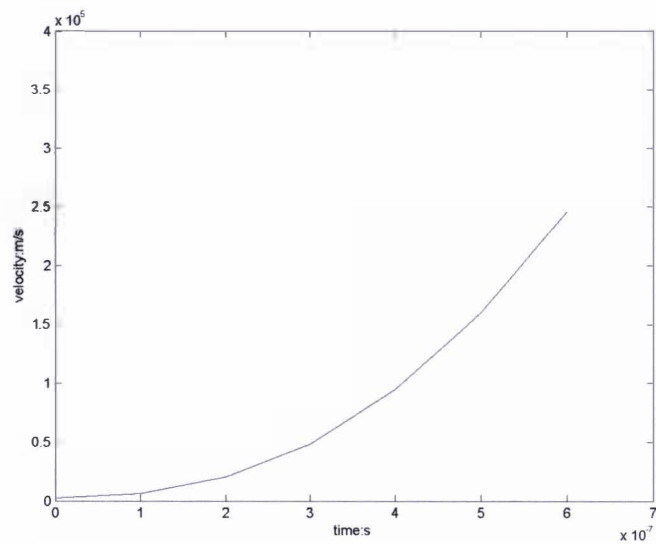


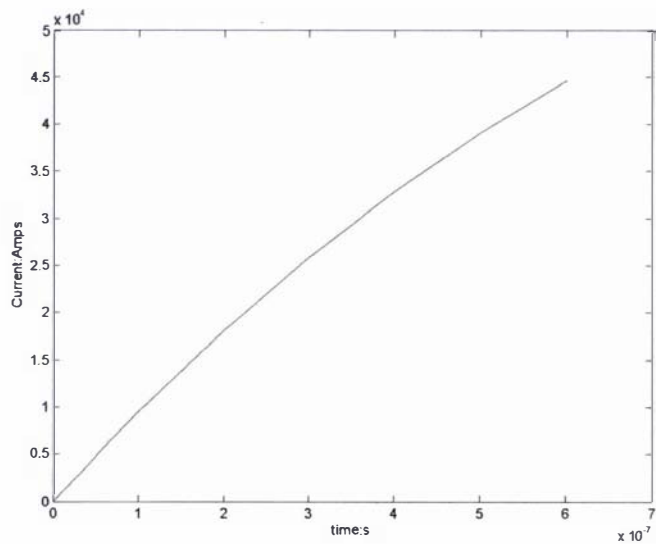
Figure 4.26: Vector plot of the gradient of the electric scalar potential ∇V within the overall conductive regions at $t=0.7\mu s$, for numerical test 1.

Results for Numerical test 2

The velocity and current as functions of time are displayed in graphs 4.14 and 4.15. Vector plots of the current density across the plasma are presented for three selected times in figures 4.27 to 4.29. Vector plots of the magnetic field across the plasma (in which the magnitude and sign of B_θ is presented as a vector value in the z direction) are shown in figures 4.30 to 4.32. The overall vector plot of the current density is presented for two selected times in figures 4.33 and 4.34. The corresponding magnetic field within the conductive regions is also presented at these selected times in figures 4.35 and 4.36. Vector plots of A and ∇V at $t=0.6\mu s$ within (the overall) conductive region are presented in figures 4.37 and 4.38.



Graph 4.14: Graph of the velocity of the plasma as a function of time, for numerical test 2



Graph 4.15: Graph of the current as a function of time, for numerical test 2

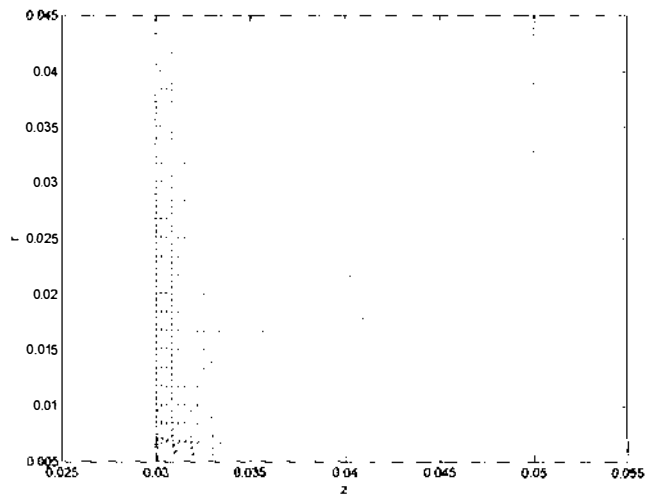


Figure 4.27: Vector plot of the current density across the plasma at $t=0.1\mu s$, for numerical test 2.

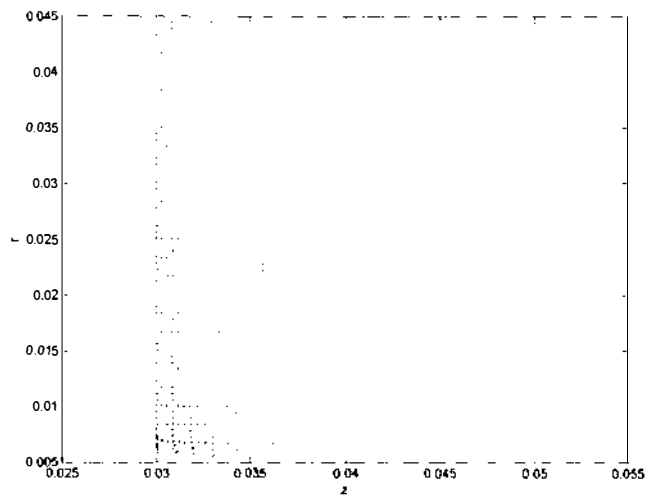


Figure 4.28: Vector plot of the current density across the plasma at $t=0.3\mu s$, for numerical test 2.

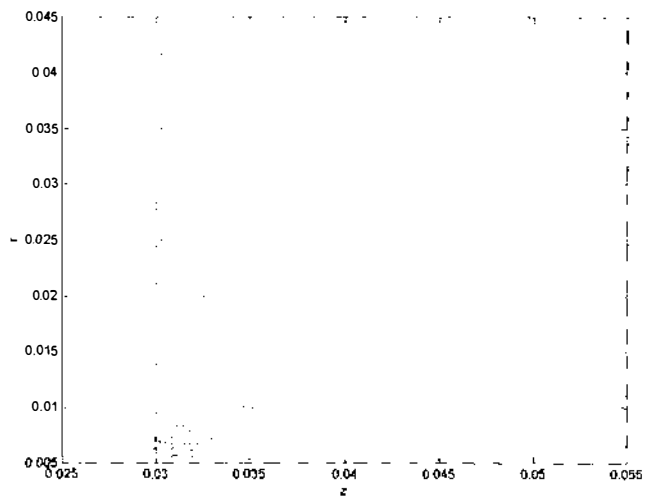


Figure 4.29: Vector plot of the current density across the plasma at $t=0.6\mu s$, for numerical test 2.

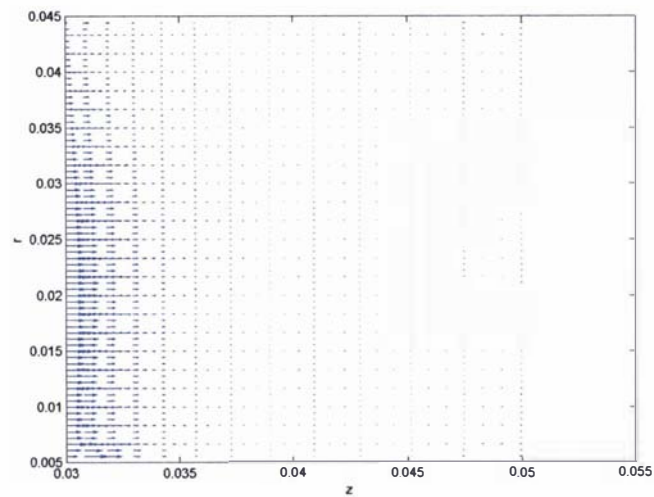


Figure 4.30: Vector plot showing the magnetic field distribution across the plasma at $t=0.1\mu s$, for numerical test 2.

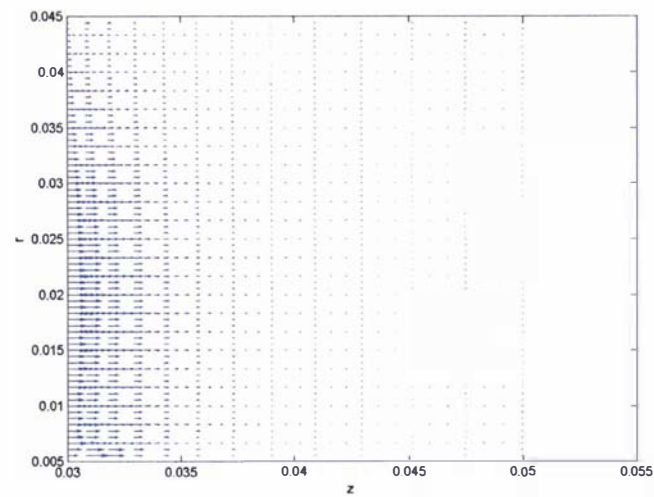


Figure 4.31: Vector plot showing the magnetic field distribution across the plasma at $t=0.3\mu s$, for numerical test 2.

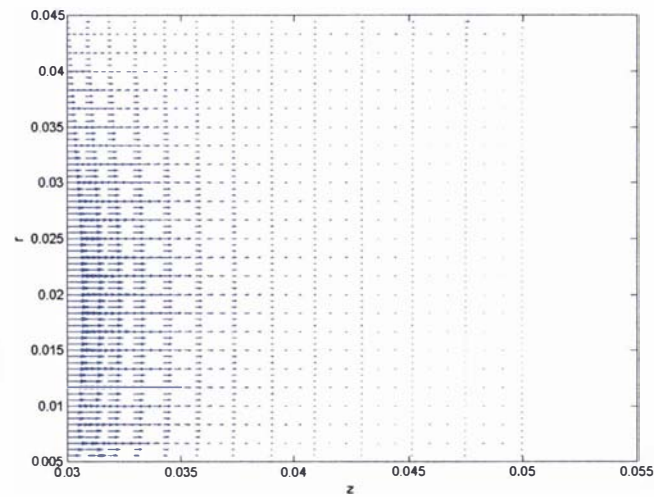


Figure 4.32: Vector plot showing the magnetic field distribution across the plasma at $t=0.6\mu s$, for numerical test 2.

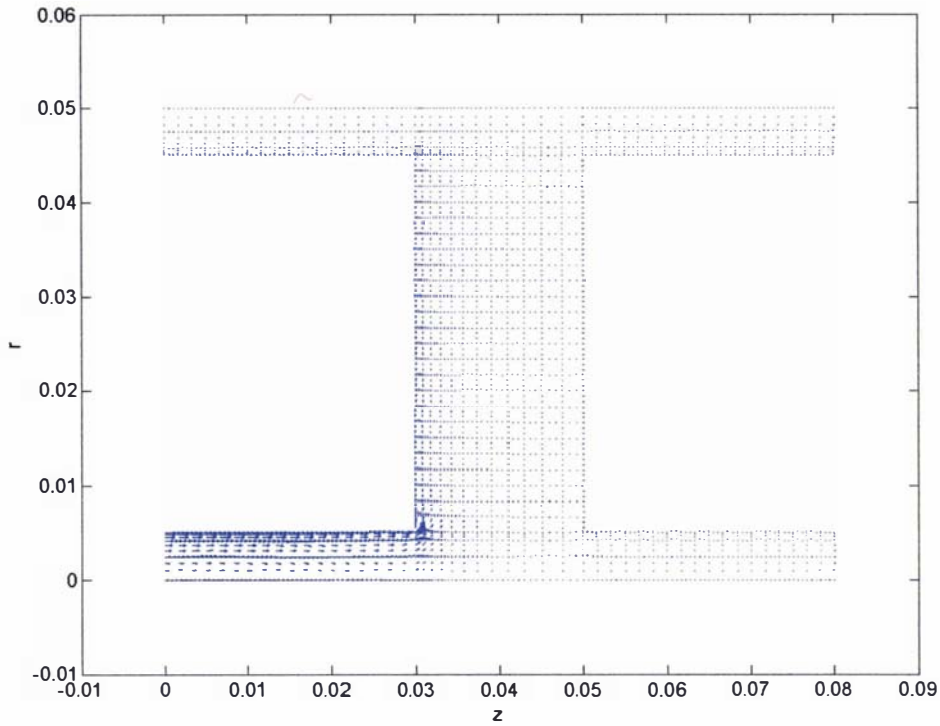


Figure 4.33: Vector plot of the overall current density at $t=0.1\mu\text{s}$, for numerical test 2

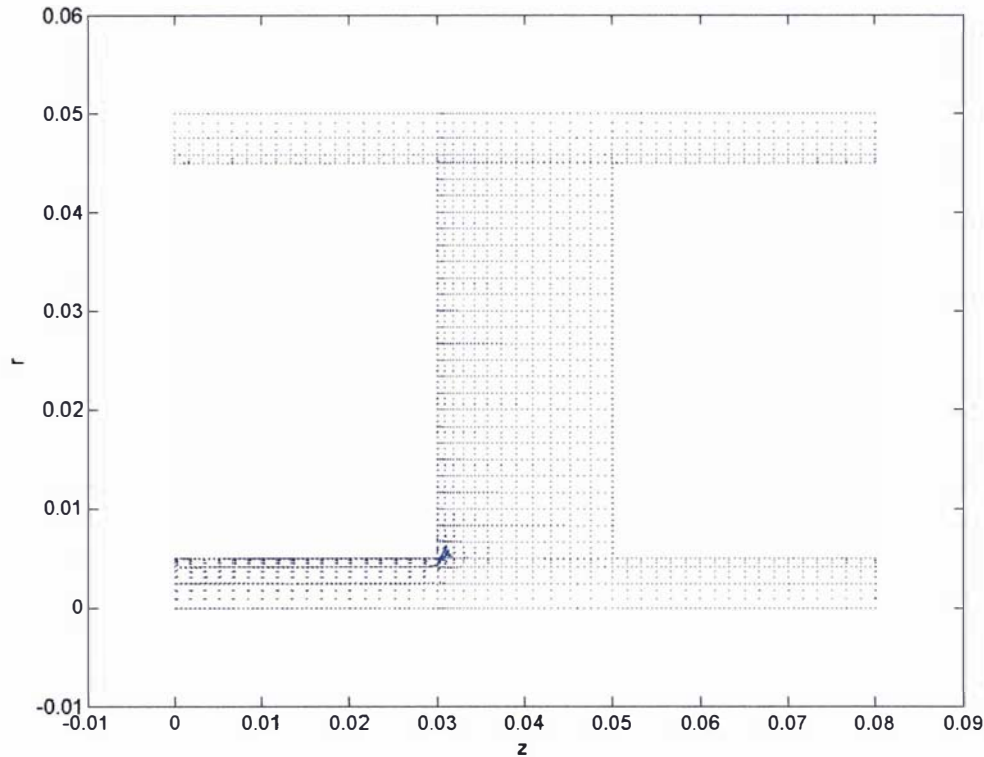


Figure 4.34: Vector plot of the overall current density at $t=0.6\mu\text{s}$ showing the formation of errors within the solution, for numerical test 2.

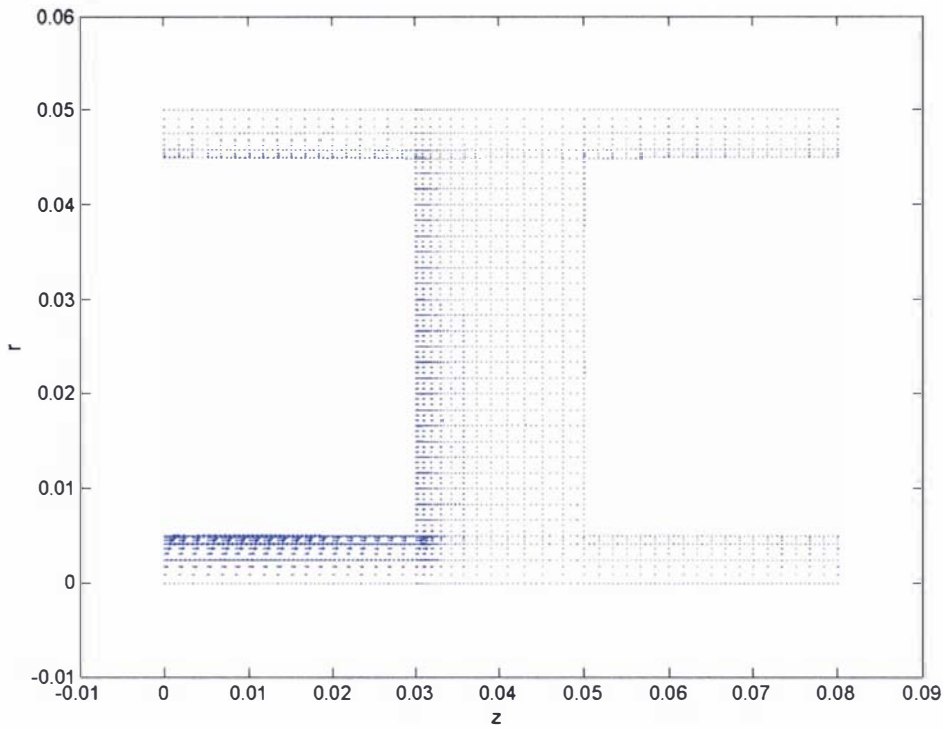


Figure 4.35: Vector plot of the magnetic field within the conductive region at $t=0.1\mu\text{s}$, for numerical test 2.

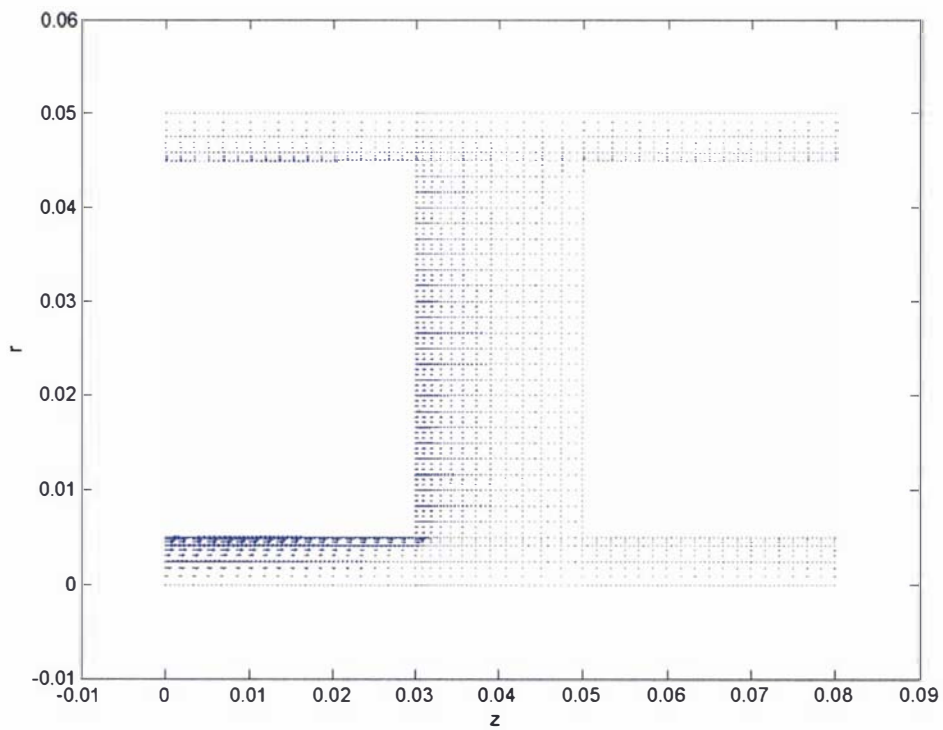


Figure 4.36: Vector plot of the magnetic field within the conductive region at $t=0.6\mu\text{s}$ showing the formation of errors within the solution, for numerical test 2.

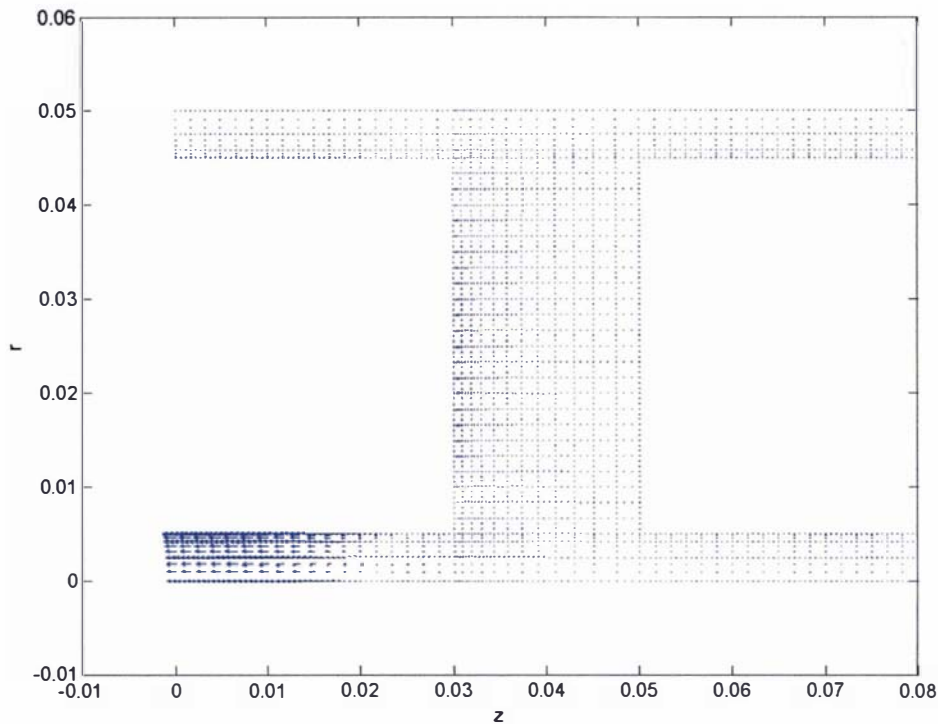


Figure 4.37: Vector plot of the magnetic vector potential A within the overall conductive regions at $t=0.6\mu s$, for numerical test 2.

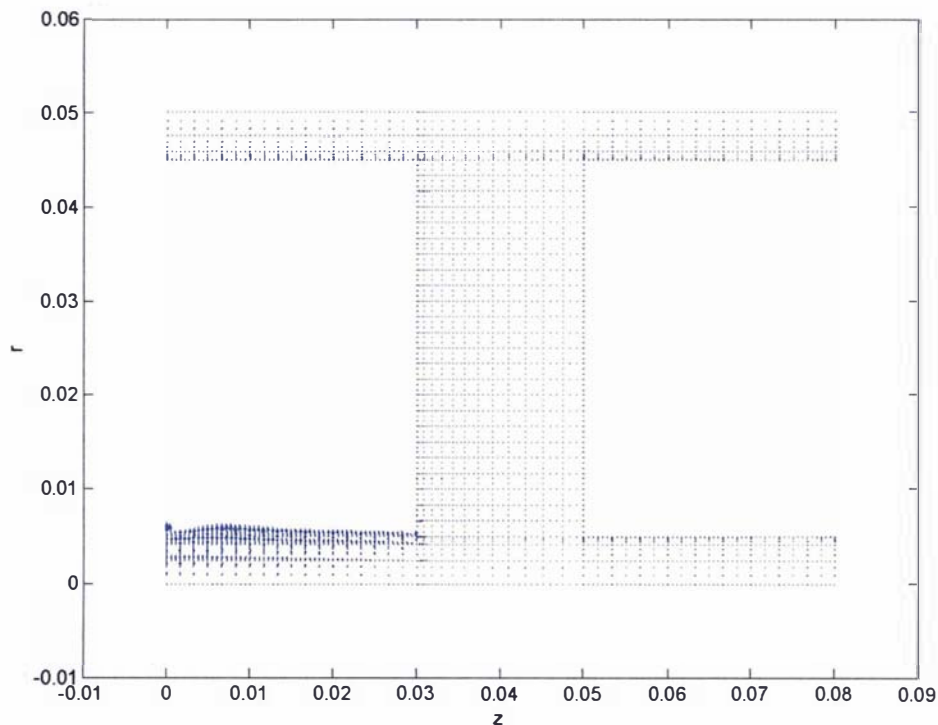


Figure 4.38: Vector plot of the gradient of the electric scalar potential ∇V within the overall conductive regions at $t=0.6\mu s$, for numerical test 2.

4.3.15:Results of the numerical model MATAC – Comparison initial MATAC results with first order model

Comparison of the initial MATAC test results with the first order model and the situation of a fixed velocity in the electrodes

A comparison between the test results of MATAC and the first order model (discussed in section 4.2) is made in table 4.5. The first order one dimensional model was run using the circuit parameters (R_o , L_o , C and V), plasma mass and acceleration distance displayed in table 4.5.

Name	Mass: mg	Acceleration distance: m	Plasma Length: cm	Total Ro: Ω	Total Lo: nH	C: μ F	Charging Voltage: V	Initial velocity: km/s	Final velocity km/s	Acceleration time μ s
Numerical test 1	0.0003	0.05	2	0.01	10	500	1000	2.6	159	0.70
Numerical test 2	0.0003	0.05	2	0.01	10	500	1000	2.6	246	0.60
First order model	0.0003	0.05	Not applicable	0.01	10	500	1000	2.6	311	0.58

Table 4.5: Comparison of results of the MATAC and the first order model.

One final numerical test was conducted using MATAC, in which the velocity imposed upon the electrodes was held at a constant value. This test was conducted using the parameters displayed in table 4.6. Essentially this test is the same as numerical test 2, with the exception that the velocity values within the electrodes was fixed.

Numerical test number	Mass: mg	Acceleration distance: m	Plasma Length: cm	Total Ro: Ω	Total Lo: nH	C: μ F	Charging Voltage: V	Conductivity Value: $1/(\Omega m)$	Fixed velocity in the electrodes km/s	Time step: μ s
3	0.0003	0.05	2	0.01	10	500	1000	16000	2.6	0.1

Table 4.4: Parameters used to test the MATAC program with a fixed velocity value within the electrode regions.

The program was run for the same time period as numerical test 2. The current density across the plasma is shown for two selected times in figures 4.39 and 4.40. The corresponding magnetic field distribution across the plasma (in which the magnitude and sign of B_θ is presented as a vector value in the z direction) for these times is presented in figures 4.41 and 4.42. The overall current density and magnetic field within the conductive regions at the end of the calculated time period are presented in figures 4.43 and 4.44 respectively.

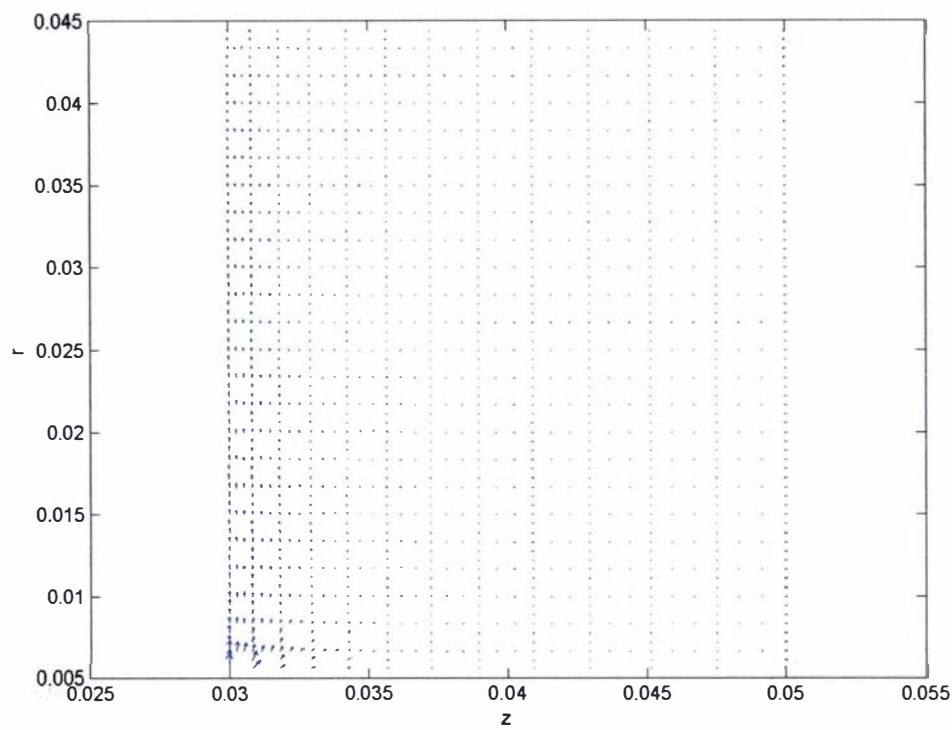


Figure 4.39: Vector plot of the current density across the plasma at $t=0.1\mu\text{s}$, for numerical test 3

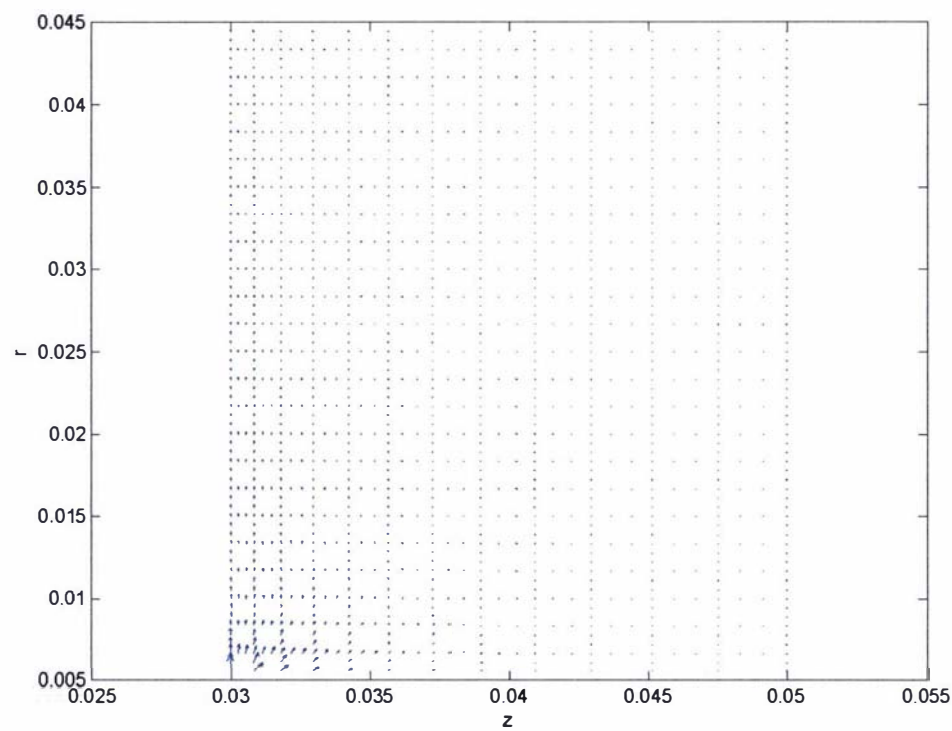


Figure 4.40: Vector plot of the current density across the plasma at $t=0.6\mu\text{s}$, for numerical test 3

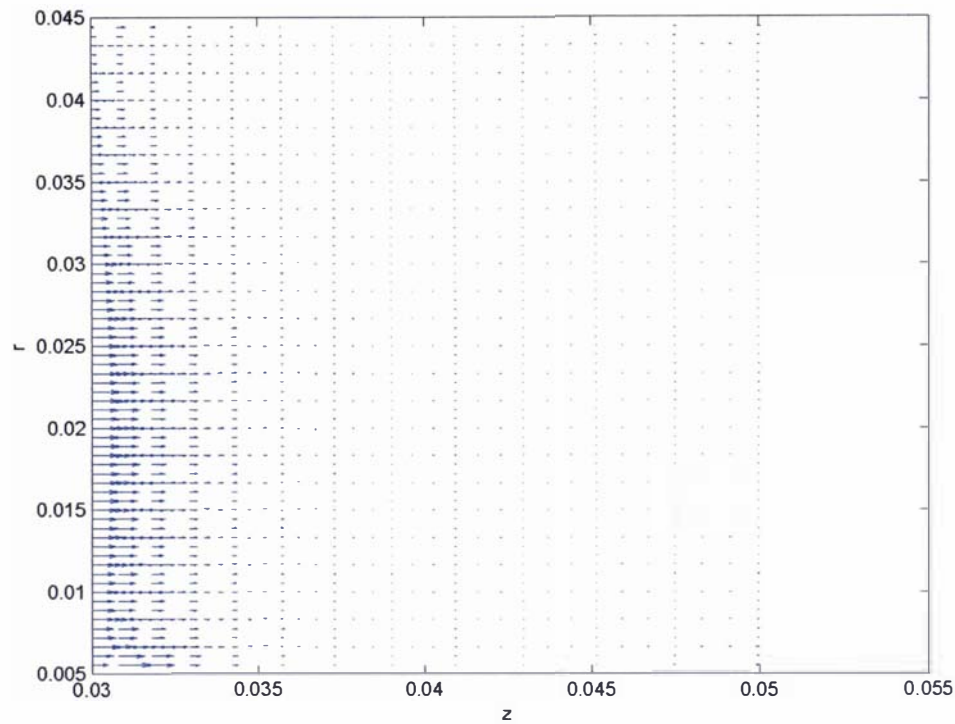


Figure 4.41: Vector plot showing the magnetic field distribution across the plasma at $t=0.1\mu s$, for numerical test 3

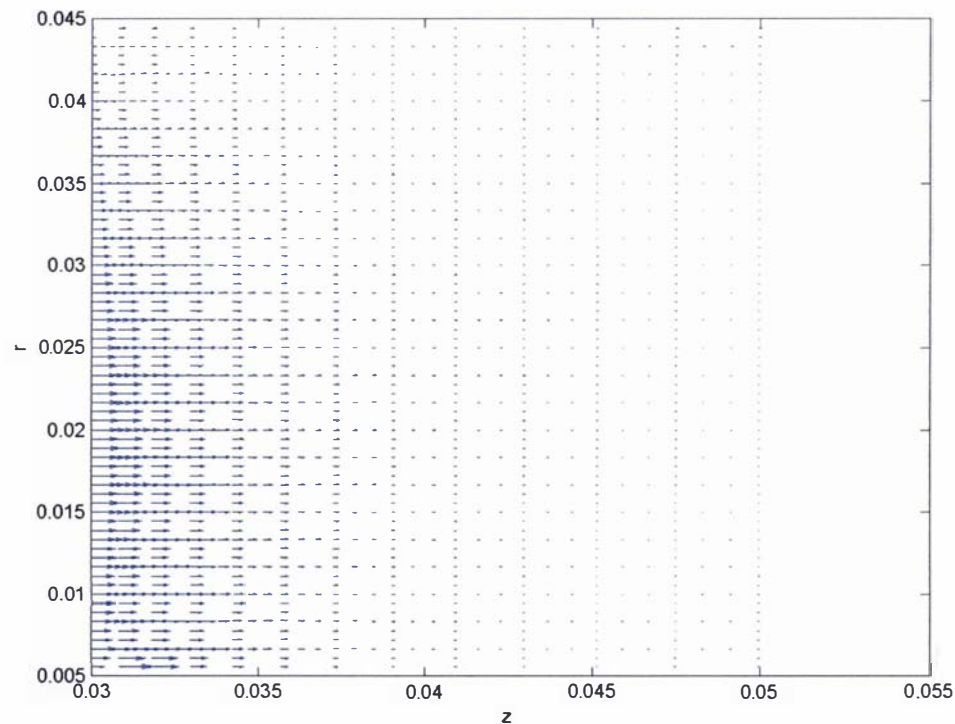


Figure 4.42: Vector plot showing the magnetic field distribution across the plasma at $t=0.6\mu s$, for numerical test 3

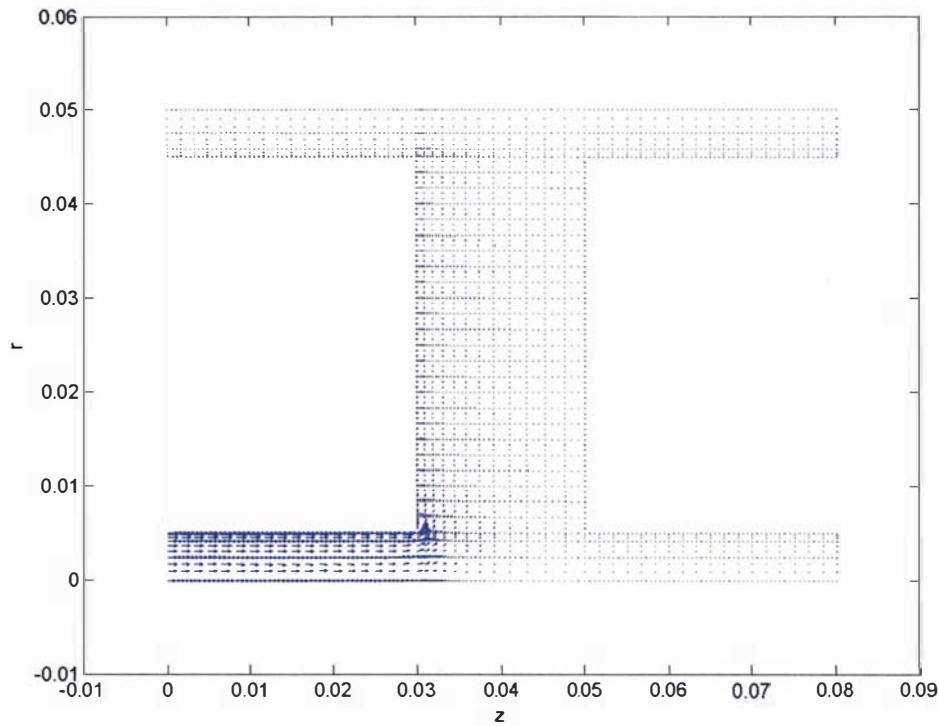


Figure 4.43: Vector plot of the overall current density at $t=0.6\mu s$ (showing the correctly predicted current density in the electrodes), for numerical test 3

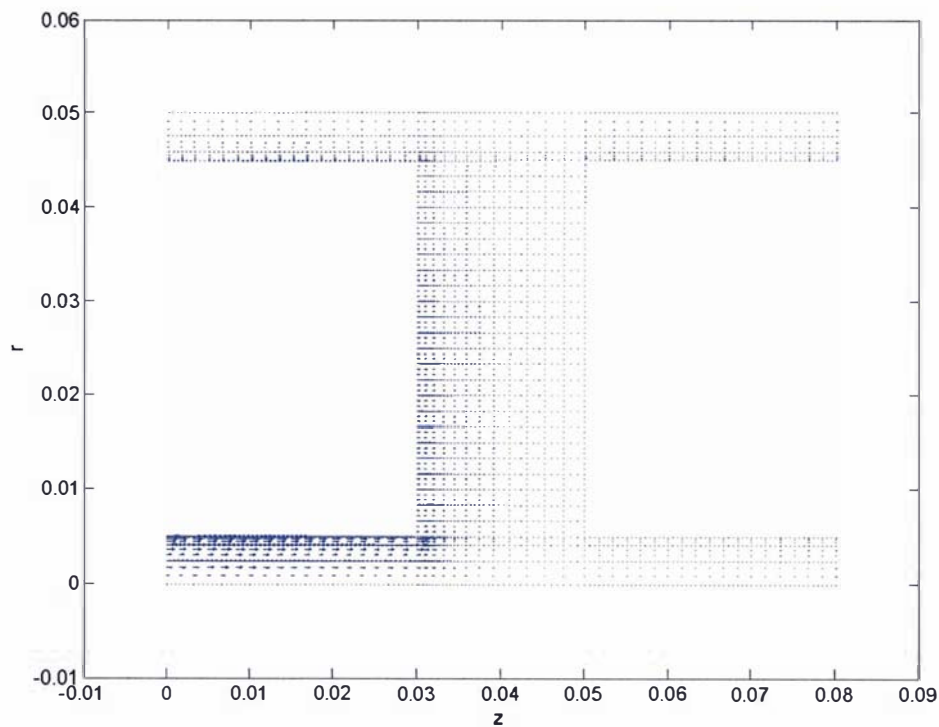


Figure 4.44: Vector plot of the magnetic field within the conductive regions at $t=0.6\mu s$ (showing the correctly predicted magnetic field in the electrodes), for numerical test 3

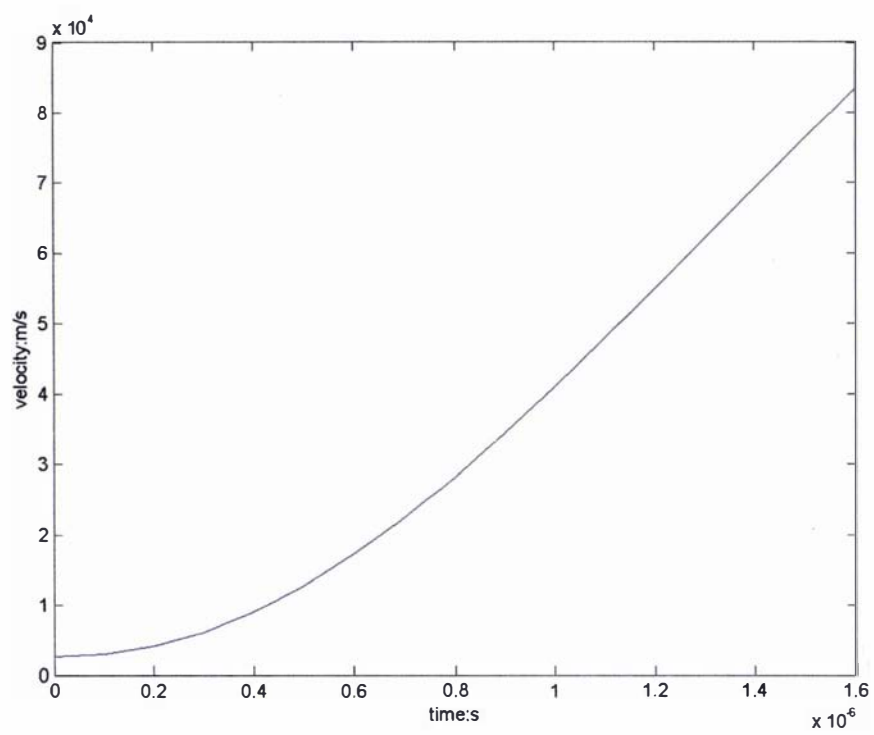
Results of the MATAC program applied to the operation of the Lica

The performance of the Lica fitted with a 5cm in length positive electrode was calculated using the MATAC program (with the techniques and restrictions discussed in section 4.3.14) and employs the same parameters that were used in the first order model (refer to table 4.1 of section 4.2.2). A conductivity value of $340\Omega^{-1}m^{-1}$ was applied to all conductive regions, because in its current form MATAC requires a constant conductivity value within these regions (refer to section 4.3.14). This conductivity value was derived from the average calculated conductivity value from graph 3.18 in section 3.3.8, under the assumption that the average temperature of the plasma is 5000K. The plasma within the accelerator is derived from the assumption that the plasma is created from the FWHH of the neutral hydrogen gas pulse from the piezoelectric valve; in order for the plasma to fit into the accelerator the length of the plasma block was rounded to being 5cm in length. MATAC was run using a mesh constructed on 30 elements in the r direction (i.e. ELEM2=30, refer to appendix 4F) and the parameters summarized in table 4.7.

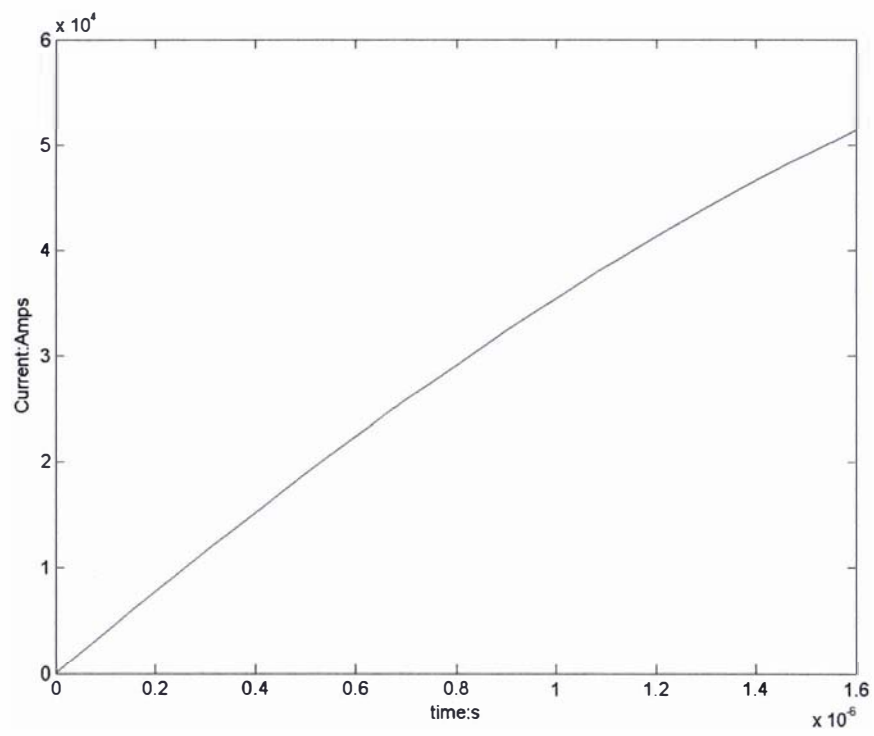
Mass: mg	Acceleration distance: m	Plasma Length: cm	Total Ro: Ω	Total Lo: nH	C: μ F	Charging Voltage: V	Conductivity Value: $1/(\Omega m)$	Initial velocity: km/s	Time step: μ s
0.00014	0.05	5	0.0086	64.6	17.5	10000	340	2.6	0.1

Table 4.7: Parameters used to calculate the performance of the Lica fitted with a 5cm in length positive electrode using the MATAC program

The velocity and current as functions of time are presented in graphs 4.16 and 4.17. Vector plots of the current density across the plasma are displayed for three selected times in figures 4.45 to 4.47. The corresponding magnetic field distribution across the plasma (in which the magnitude and sign of B_{θ} is presented as a vector value in the z direction) is displayed in figures 4.48 to 4.50. The current density across the entire conductive region is exhibited in figures 4.51 to 4.53 for these selected times. Vector plots for the magnetic field within the conductive regions are displayed, for two selected times, in figures 4.54 and 4.55.



Graph 4.16: Graph of the velocity as a function of time, simulating the operation of the Lica fitted with a 5cm in length positive electrode, calculated using MATAC and the calculated plasma electrical conductivity at 5000K of 340 siemens/m.



Graph 4.17: Graph of current as a function of time, simulating the operation of the Lica fitted with a 5cm in length positive electrode, calculated using MATAC and the calculated plasma electrical conductivity at 5000K of 340 siemens/m.

4.3.15: Results of the numerical model MATAC – Lica simulation

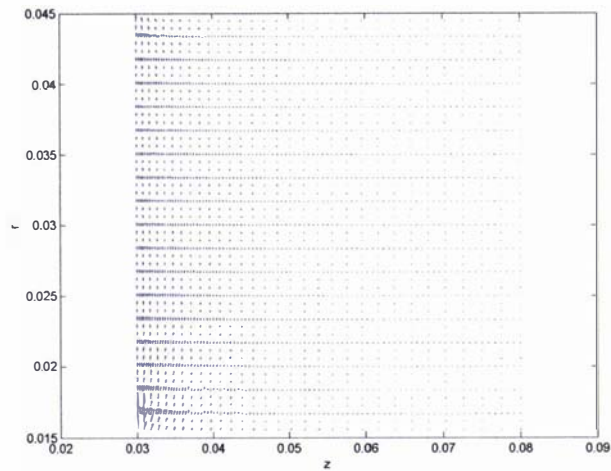


Figure 4.45: Vector plot of the current density across the plasma at $t=0.1\mu s$, obtained from a simulation of the operation of the Lica fitted with a 5cm in length positive electrode, calculated using MATAC and the calculated plasma electrical conductivity at 5000K of 340 siemens/m.

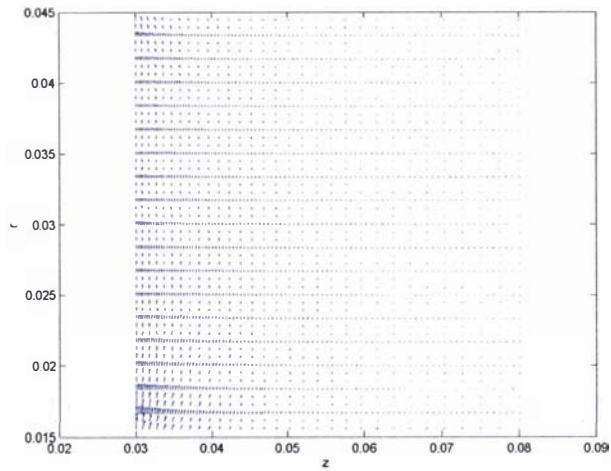


Figure 4.46: Vector plot of the current density across the plasma at $t=0.8\mu s$, obtained from a simulation of the operation of the Lica fitted with a 5cm in length positive electrode, calculated using MATAC. and the calculated plasma electrical conductivity at 5000K of 340 siemens/m.

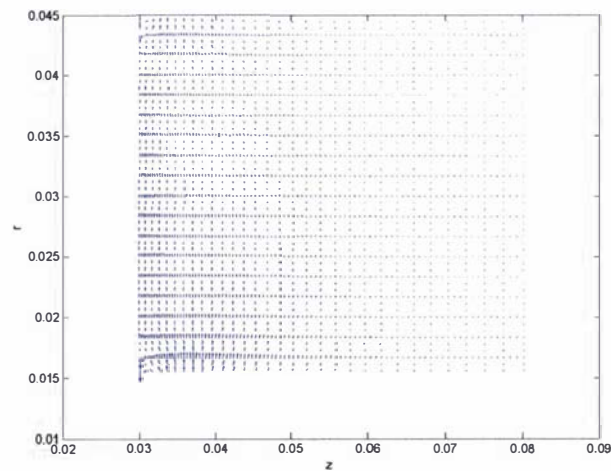


Figure 4.47: Vector plot of the current density across the plasma at $t=1.6\mu s$, obtained from a simulation of the operation of the Lica fitted with a 5cm in length positive electrode, calculated using MATAC and the calculated plasma electrical conductivity at 5000K of 340 siemens/m.

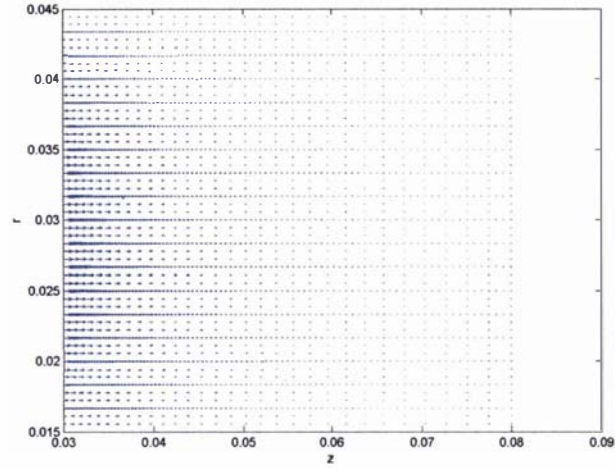


Figure 4.48: Vector plot showing the magnetic field distribution across the plasma at $t=0.1\mu\text{s}$, obtained from a simulation of the operation of the Lica fitted with a 5cm in length positive electrode, calculated using MATAC. and the calculated plasma electrical conductivity at 5000K of 340 siemens/m.

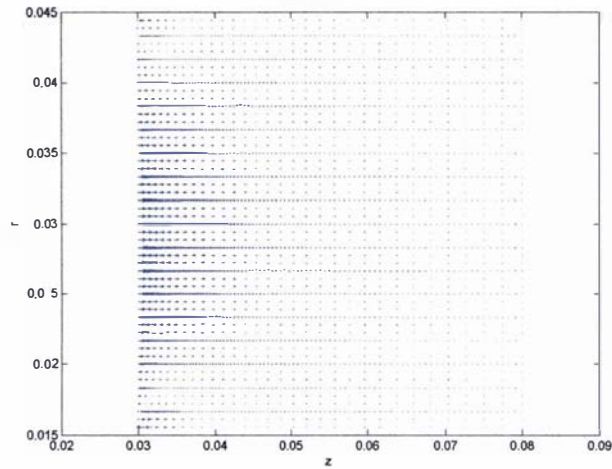


Figure 4.49: Vector plot showing the magnetic field distribution across the plasma at $t=0.8\mu\text{s}$, obtained from a simulation of the operation of the Lica fitted with a 5cm in length positive electrode, calculated using MATAC. and the calculated plasma electrical conductivity at 5000K of 340 siemens/m.

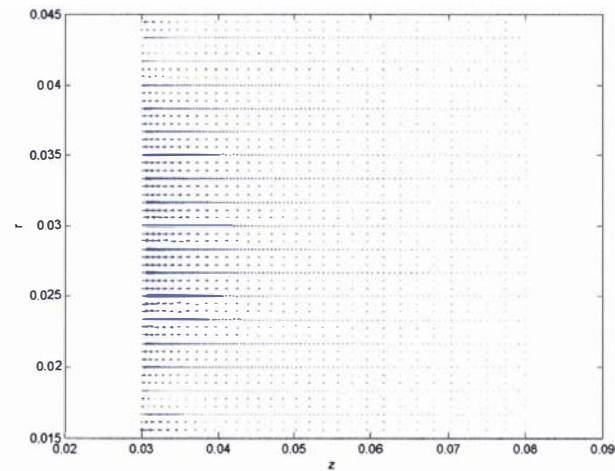


Figure 4.50: Vector plot showing the magnetic field distribution across the plasma at $t=1.6\mu\text{s}$, obtained from a simulation of the operation of the Lica fitted with a 5cm in length positive electrode, calculated using MATAC. and the calculated plasma electrical conductivity at 5000K of 340 siemens/m.

4.3.15: Results of the numerical model MATAC – Lica simulation

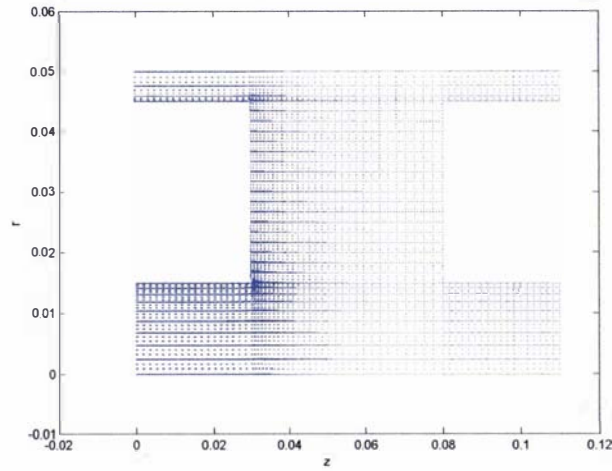


Figure 4.51: Vector plot of the overall current density at $t=0.1\mu\text{s}$, obtained from a simulation of the operation of the Lica fitted with a 5cm in length positive electrode, calculated using MATAC. and the calculated plasma electrical conductivity at 5000K of 340 siemens/m.

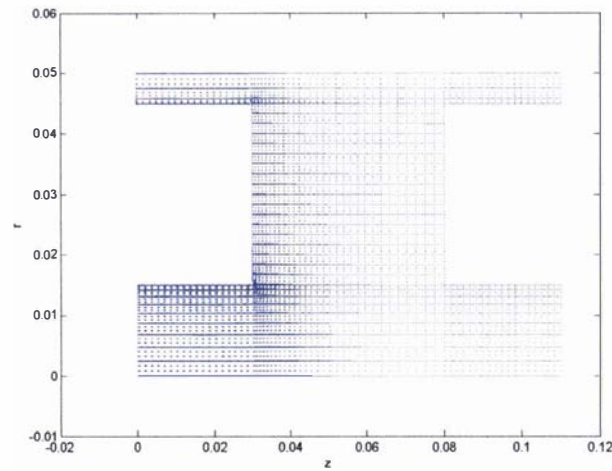


Figure 4.52: Vector plot of the overall current density at $t=0.8\mu\text{s}$, obtained from a simulation of the operation of the Lica fitted with a 5cm in length positive electrode, calculated using MATAC. and the calculated plasma electrical conductivity at 5000K of 340 siemens/m.

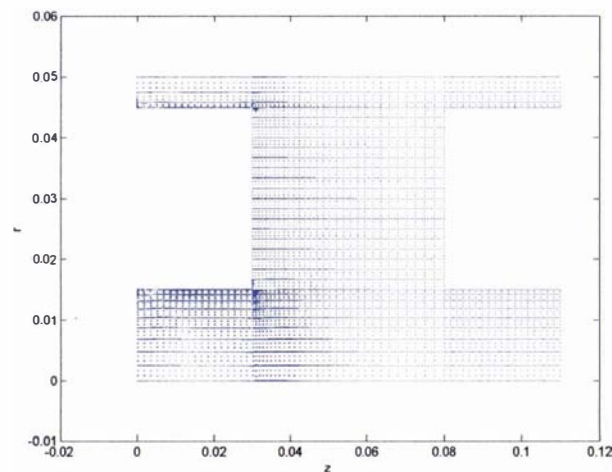


Figure 4.53: Vector plot of the overall current density at $t=1.6\mu\text{s}$ showing the formation of errors within the solution, obtained from a simulation of the operation of the Lica fitted with a 5cm in length positive electrode, calculated using MATAC. and the calculated plasma electrical conductivity at 5000K of 340 siemens/m.

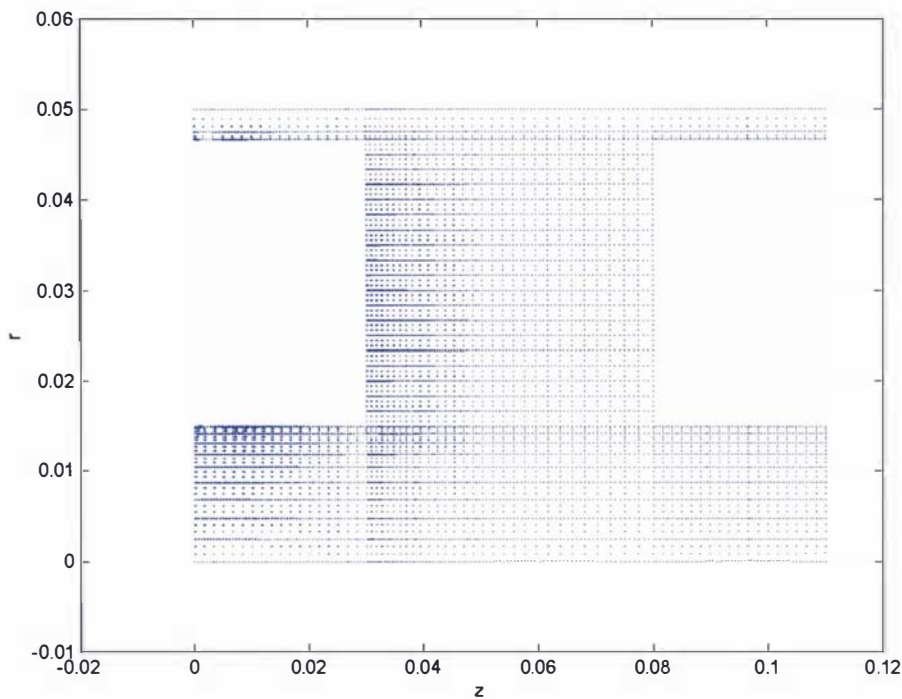


Figure 4.54: Vector plot of the magnetic field within the conductive regions at $t=0.1\mu s$, obtained from a simulation of the operation of the Lica fitted with a 5cm in length positive electrode, calculated using MATAC and the calculated plasma electrical conductivity at 5000K of 340 siemens/m.

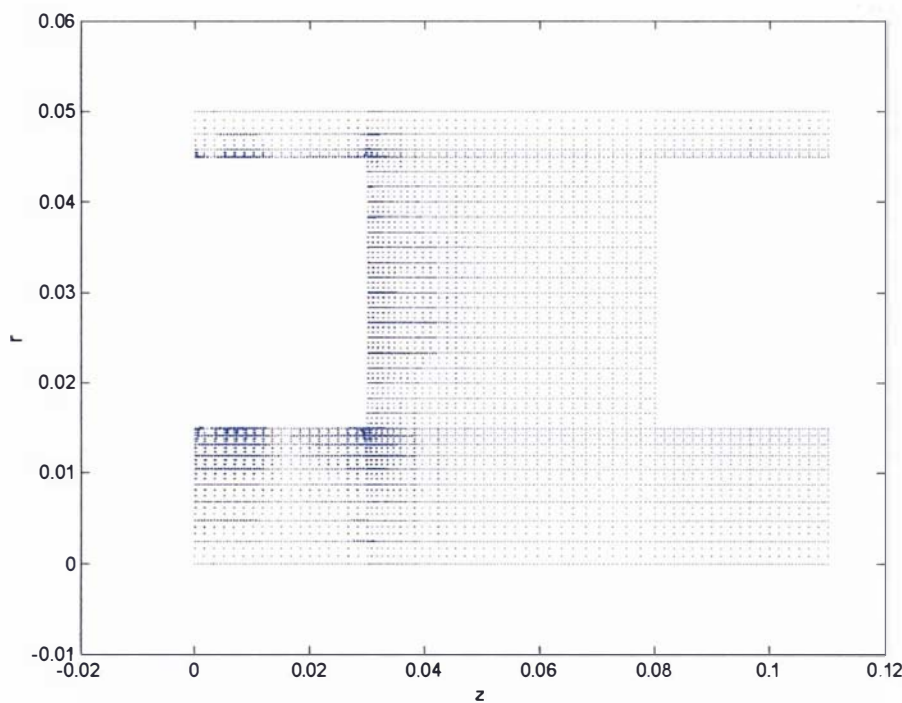


Figure 4.55: Vector plot of the magnetic field within the conductive regions at $t=1.6\mu s$ showing the formation of errors within the solution, obtained from a simulation of the operation of the Lica fitted with a 5cm in length positive electrode, calculated using MATAC and the calculated plasma electrical conductivity at 5000K of 340 siemens/m.

4.3.16: Discussion on the MATAC numerical model

It is apparent from the results displayed in table 4.5 that the MATAC program is more accurately able to model a pulsed coaxial plasma accelerator than the simply derived first order model (which assumes the motion of the plasma is the result of a filament current). MATAC is primarily more accurate than a first order model because it is able to account for the current density and magnetic field distributions across the plasma, including both the skin effect and velocity skin effect. Naturally as the conductivity of the plasma increases its exit velocity also increases and the current density and magnetic field distributions within the plasma will increase and tend towards the filament current model; this is observed in the results presented in table 4.5 and in figures 4.15 to 4.17, 4.18 to 4.20, 4.27 to 4.29 and 4.30 to 4.32. This effect is most noticeable when the magnetic field distributions across the plasma for numerical test 1 ($\sigma = 300\Omega^{-1}m^{-1}$) and numerical test 2 ($\sigma = 16000\Omega^{-1}m^{-1}$) are compared (i.e. compare figures 4.18, 4.19 and 4.20 with figures 4.30, 4.31 and 4.32).

However in the initial numerical test cases (numerical test 1 and 2) the appearance of errors within the overall current density and magnetic field were noticed, the effects of these errors can be viewed in figures 4.22 and 4.24 for numerical test 1 and figures 4.34 and 4.36 for numerical test 2. These numerical errors appear to be the product of the fineness of the mesh, the time step and how quickly the velocity changes from one time step to another (within the calculation). The numerical errors appear to be most prevalent in the ∇V calculation, particularly near the breech (where $\nabla V = -v_z B_\theta$ is enforced each time step) and at the re-entrant corners (i.e. where the current density is solely described by the ∇V term). The numerical errors (in both the calculated current density and magnetic fields) within the conductive regions do not appear in the numerical trial in which the velocity within the conductor was fixed (refer to the results in figures 4.4.3 and 4.4.4 of numerical test 3).

Unfortunately, as discussed in section 4.3.15, MATAC does not contain any error improvement schemes that could be used to prevent such errors from occurring. In its current form MATAC is solely dependent upon the user choosing a fine enough mesh and a small enough time step to prevent these errors. The problem is further compounded by the fact that the time derivatives of A are based upon a FD scheme, the error of which is particularly dependent upon the time step chosen. On the whole most of the non-physical effects of these errors are within the electrode regions and the results presented here concerning the final velocity of the plasma can be assumed to be reasonably accurate because of this.

The MATAC program appears to give physical results such as the skin effect and the effect of current diffusion within the moving armature as a result of the velocity skin effect and induced

current; both of these effects were noted in [115] (a rail gun calculation paper). A current density vector plot from [115] is shown in diagram 4.18.

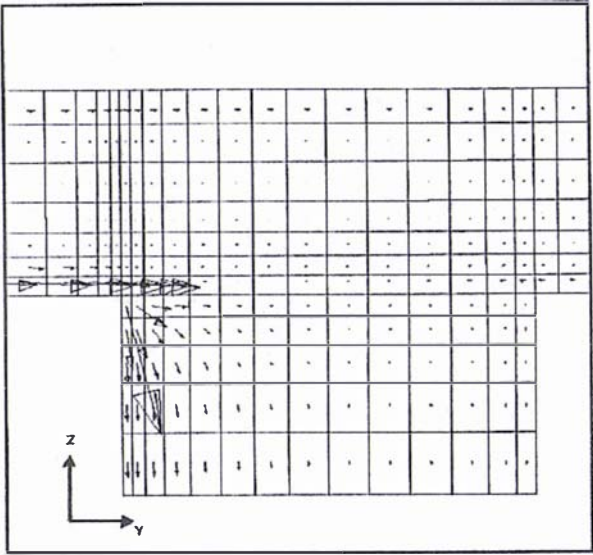


Diagram 4.18: Vector plot of the current density (cross sectional view) in a moving rail gun armature [115] (the armature is moving at a velocity of 500m/s)

Despite the lack of an error improvement strategy, the MATAC program was applied to simulating the operation of the Lica fitted with a 5cm in length positive electrode (the results of which can be found in section 4.3.15). The end results of this are summarized in table 4.8 with the first order model results (refer to table 4.1 in section 4.2.2) and the experimentally obtained results.

Name	Mass: mg	Acceleration distance: m	Final velocity for the bulk of the plasma: km/s	Total acceleration time: μ s
First order model	0.00014	0.05	456	0.42
MATAC	0.00014	0.05	83.6	1.6
Average experimental results for the perceived bulk of the plasma	Assumed to be 0.00014	0.05	40 to 50	Acceleration time for the bulk of the plasma unknown. Full acceleration time (from voltage trace) between 22 to 33

Table 4.8: Comparison of the results of the first order model and MATAC to the average experimentally obtained results for the bulk of the plasma, relating to the Lica fitted with a 5cm in length positive electrode.

At present it can be seen from the MATAC result that the premise that the plasma being accelerated in the Lica is formed from the bulk of the neutral hydrogen gas pulse (at FWHH) from the piezoelectric valve (having a temperature of 5000K and a conductivity determined by using the Spitzer formula) is incorrect, because the results fail to correctly predict the experimentally observed (full) acceleration time. Despite this fact, the numerically predicted final plasma velocity is in the region of the experimentally observed results; that is to say the experimentally observed results show three distinct plasma (peak) velocity regions of 40km/s, 50km/s and 60km/s to 80km/s and the numerically obtained result could lie within any of these regions if other effects (refer to section 1.3) were taken into account. Especially since the chemical makeup of the plasma pulses has yet to be determined experimentally.

It is quite possible, from the observed ablation marks on the accelerator electrodes (refer to sections 3.3.4, 3.3.5 and 3.3.6) and the numerical result, that the operation of the Lica is very dependent upon ablative effects.

Unfortunately the MATAC program is unable to explain the anomalies in the operation of the Lica; such as why there appears to be a series of plasma sheaths, why the final exit velocity of the plasma appears to be independent of the positive electrode length and the phenomena of misfires. These are aspects that necessitate the need for magnetohydrodynamic and ion models. MATAC provides an initial frame-work to which magnetohydrodynamic and ion models could be added. The author of this thesis suggests the use of either a FV [113], [114] or more preferably an ALE algorithm [153], [154] to solve the magnetohydrodynamic aspects of the problem.

Chapter 5

Miscellaneous experiments and procedures

There were a number of experiments and techniques used in this thesis which have not been covered, either because of their failings or because they do not directly relate to the main purpose of this research; however they are worth a brief mention here.

A chopper wheel was used in some TOF experiments conducted with the piezoelectric valve. The chopper wheel consisted of a thin metal disk with two 0.7mm rectangular slits placed directly opposite to each other on the circumference of the wheel. The chopper wheel was synchronized with the pulse generator by using the experimentally determined speed of revolution (of the chopper wheel) as a function of the applied voltage to the chopper wheel motor. The chopper wheel was used to conduct a series of experiments in which attempts were made to extract various portions of the gas pulse (produced from the valve). These experiments generally confirmed that the gas pulses produced from the valve were very short and well defined.

The gas pulse characteristics for several gases other than H_2 that include N_2 , O_2 , dry air and Ar were used in the experiments conducted with the piezoelectric valve. It is important to mention that special care needs to be taken when working with noble gases, such as Ar , in that the piezoelectric crystal should not be operated at too high a driving voltage, to prevent the dielectric breakdown of the noble gas and damage to the piezoelectric crystal.

As previously alluded to in some of the preceding chapters, both a set of photomultipliers and an interferometer were tried as means of determining the velocity of the plasma. As can be seen in diagrams 3.5, 3.8 and 3.11 there are two T-sections on the flight tube which are 1m apart. It was here that the two photomultipliers were positioned; the multipliers were housed in blacked 1m long tubes that had 1mm slits facing onto the flight tube. Special windows were placed on the ends of the T-sections to allow light to be emitted to the photomultipliers. The two photomultipliers were Hamamatsu R375 photomultiplier tubes, which have a spectral range of 160nm to 850nm and have synthetic silica windows. Because a lot of light is expected to be emitted from the plasma, including a lot of UV light, this attribute could be used to determine the velocity of the plasma. The concept of determining the velocity using this method was simple, the passage of the hydrogen plasma passed each photomultiplier would be recorded and the delay between the recorded times would allow the velocity of the plasma to be ascertained (from the basic TOF concept). Unfortunately the initial discharge of the plasma accelerator (the

breakdown of the preionized gas into a plasma) caused the first photomultiplier (the one closest to the plasma accelerator) to become oversaturated, and the velocity distribution of the plasma could not be determined. A longer flight tube and a greater distance between the first multiplier and the plasma accelerator would be required for this method to work; this aspect was deferred for future upgraded versions of the Lica. In general, all the photomultipliers were capable of confirming the time at which the preionized gas was converted into a plasma.

An interferometer formed from a Helium Neon laser and a series of mirrors inside the flight tube was also tried as a means of determining the velocity of the plasma. In theory the passage of the plasma should have broken the collimated laser beam at either of the T-sections, and the velocity of the plasma would have then been determined in much the same fashion as that used for the photomultipliers. Unfortunately there was no sign of either laser beam deflection or phase shift in the beams. All that could be observed was the background vibration of the flight tube as a result of the mechanical pumps; so this method could not be employed to determine the velocity of the plasma.

Materials other than steel were trialled in the Lica. An Aluminium positive electrode 32.8cm in length and 3.12cm in diameter, machined with a sharp edge at its backmost point (refer to section 3.1) was also trialled in the Lica. Use of Aluminium as an electrode material was discontinued, due to the large amount of ablation damage incurred using this electrode material. A lot of the tests conducted on the Lica used what shall be referred to as “burst mode”. In burst mode a series of gas pulses followed by preionization pulses were introduced into the plasma accelerator. Using this method it was discovered that lower charging voltages on the capacitor could be used to cause the subsequent breakdown and acceleration of the hydrogen gas. Either two or three gas pulses were used for this purpose. The results from using burst mode showed that it was possible to initiate the breakdown of hydrogen gas pulse using a charging voltage as low as 1.6kV on the capacitor. The time delays between the gas pulses produced from the valve and the preionization pulses were staggered, as can be seen in diagram 5.1. The number of gas pulses, driving pulse length and the frequency at which these gas pulses succeed one another were all set using the pulse generator. The time delay placed upon the preionization pulse was typically set between 270 μ s to 330 μ s, with a preionization pulse duration between 50 μ s and 100 μ s. An example of one of the results obtained using burst mode with a 20cm in length 3cm in diameter 316 stainless steel positive electrode is displayed in graphs 5.1.a to 5.1.c. The parameters used to generate these results are presented in table 5.1.

Number of shots	Hydrogen backing pressure: kPa	Gas pulse frequency : Hz	Driving pulse length: μ s	Preionization time delay: μ s	Preionization length: μ s	Capacitor voltage: kV	Multichannel scaler bin width: μ s	Oscilloscope sampling frequency: MHz
3	447	1800	180	250	50	2.5	5.12	2.5

Table 5.1: Settings on the various pieces of experimental used to conduct a burst mode test on the *Lica* fitted with a 20cm in length 3cm in diameter stainless steel electrode

A diagram diagrammatically representing the various time delays involved in this particular experiment is displayed in diagram 5.1.

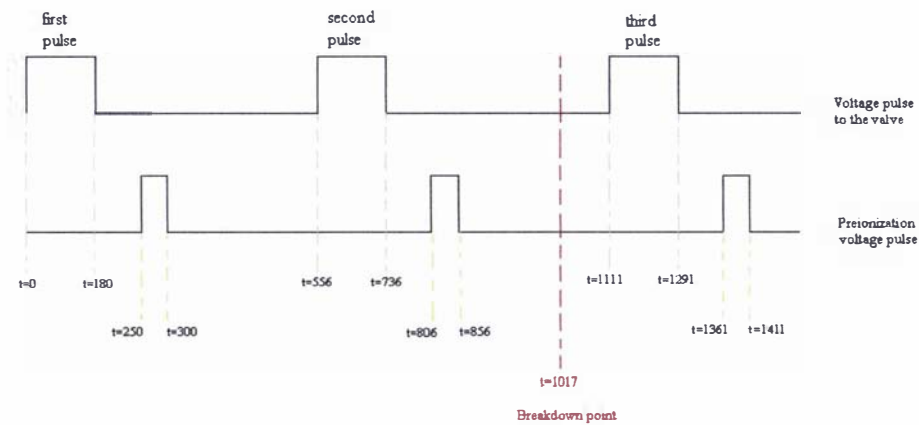
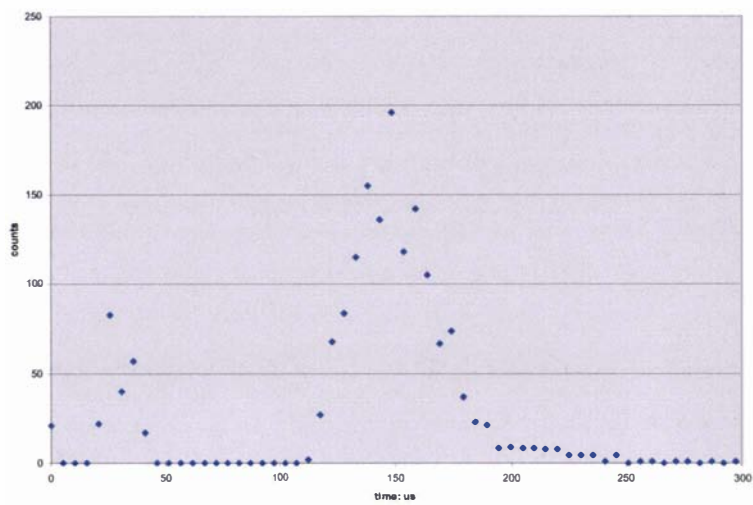
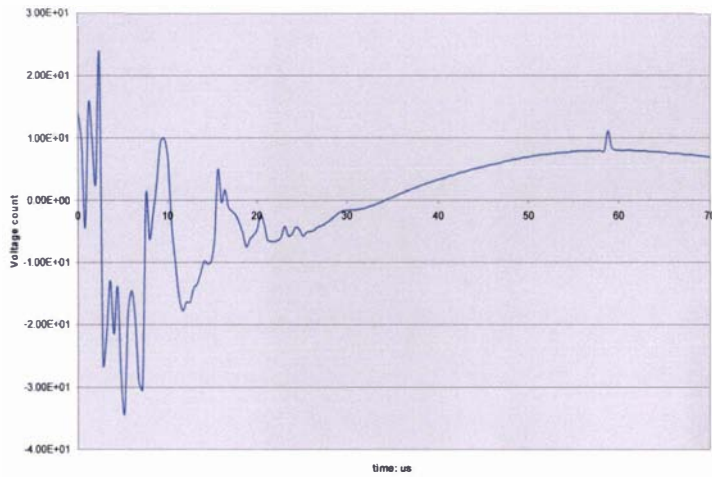


Diagram 5.1: Diagram representing the timing of various voltage pulses for the *Lica* operated in burst mode, using the parameters listed in table 5.1. All times are referenced from $t=0$ (the time when a voltage pulse is sent from the pulse generator to the valve), the point at which the preionized gas breaks down is also displayed.

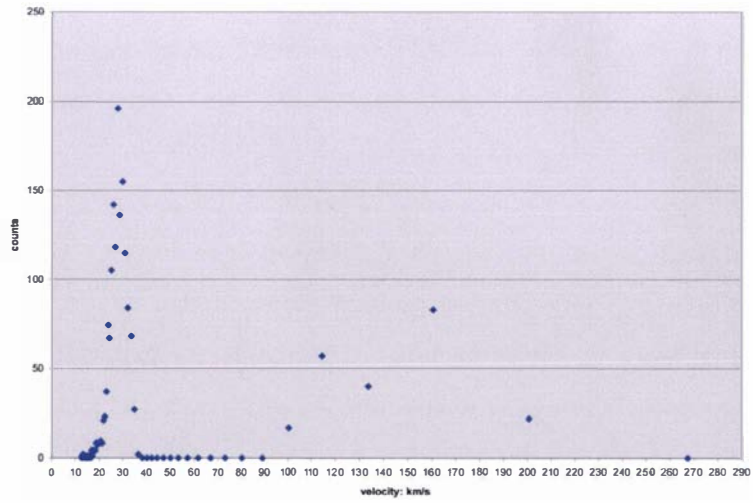
For this particular set of results it was experimentally determined, from both the voltage trace and the results from the photomultipliers, that the preionized gas breaks down at $t=1.017$ ms; the breakdown time has also been included in diagram 5.1. This shows that the capacitor was discharged using the second gas pulse. It has been theorized that the burst mode of operation relies upon scattered gas from previous pulses (remaining in the plasma accelerator) interacting with the succeeding gas pulses, lowering the breakdown conditions required to discharge the capacitor. The breakdown conditions are probably lowered due to the combination of the increased gas density; scattered gas interacting and increasing the temperature of the preceding gas pulses; and the contribution and interactions of stray ions and electrons created from previous pulses.



Graph 5.1.a: Graph of raw data as a function of time, using burst mode and the parameters given in table 5.1



Graph 5.1.b: Graph of the voltage trace as a function of time, using burst mode and the parameters given in table 5.1



Graph 5.1.a: Graph of the velocity distribution of the plasma as a function of time, using burst mode and the parameters given in table 5.1

The velocity distributions and voltage traces shown above are quite typical for this mode of operation. The velocity distribution shows two distinct velocity ranges, which can be likened to misfire results of section 3.3.7. Unfortunately when using the burst mode of operation it is difficult to determine the amount of hydrogen gas being accelerated and the exact point within the plasma accelerator at which the preionized breaks down.

The direct comparison of the results obtained using burst mode, such as the results presented here, cannot be directly compared to those obtained from accelerating a single gas pulse (i.e. the results of section 3.3 in its entirety), because of the different energies (stored in the capacitor) and plasma masses involved in the acceleration processes.

Chapter 6

Future directions

Both the piezoelectric valve and the Lica apparatus are prototype devices, which have yet to be fully optimized for use in the MTF scheme discussed in section 1.1. There are a number of techniques that could be used to improve their performance. Also there are a certain number of experimental aspects of these devices that were not fully investigated or explored, either because of the time constraints placed upon this thesis or because they were overlooked in the frenzied pursuit that is the PhD experience.

The numerical model MATAC that was developed in this thesis is merely capable of solving the electromagnetic equations of the plasma accelerator. In its current form it is little more than a solid armature rail gun program. There are many improvements and additions that could be made to the numerical model.

Once again it is important to mention that there was a need to develop the MATAC program, because specially written plasma accelerator programs such as MACH3 are export controlled and ordinarily cannot be obtained. Freeware rail gun programs are generally inadequate and are not as developed as MATAC. And finally, commercially available electromagnetic (PDEase) or fluid flow (PHOENICS, FLUENT or PHYSICA+) programs are either very expensive (to obtain a licence) or they are unable to be applied to the plasma accelerator problem, because they cannot model or account for certain aspects. Commercial programs as a rule are “black box” in nature (so access to their source code is forbidden) this can further complicate the problem of trying to model the plasma accelerator problem if the commercial program does not contain or acknowledge certain physical aspects, such as an energy balance equations in MHD, or allow the import of data (results) from other programs.

6.1: Future development and experimentation of the piezoelectric valve

The prototype piezoelectric valve (by itself) is capable of generating hydrogen gas pulses less than 2K in (longitudinal) temperature, with pulses widths in the order of 10 μ s at the FWHH (at 42.9cm from the valve). This is very advantageous from the experimental point of view of a pulsed plasma accelerator, as alluded to in section 2.4.10.

However the mass output from the prototype valve is below the 0.2mg of hydrogen gas required for the MTF scheme discussed in section 1.1. Currently the un-skimmed maximum output of the valve is about one tenth of the required amount (refer to section 2.3.6). The possibility of using

either an array of piezoelectric valves or by cryogenic means to increase the mass output from the valve was briefly mentioned in section 2.3.8.

Simply arranging six piezoelectric valves around the axis of the plasma accelerator (i.e. all facing in the direction of the plasma accelerator) and operating them simultaneously, possibly using the same driving unit, would increase the mass introduced into the plasma accelerator. But this scheme would complicate matters by introducing a certain amount of turbulence from the merging of several free jet expansions. A simpler scheme which would only require the modification of the current piezoelectric valve is to use cryogenic means to increase the mass output. Work has tentatively begun on this scheme; the first alteration to existing valve that must be made is to replace the O-ring seal on the poppet, because under cryogenic temperatures O-ring seals do not work properly. The O-ring seal needs to be replaced with a knife edge copper gasket that seals onto a Teflon washer. The prototype cryogenic valve is currently cooled with a copper heat sink connecting the valve housing to a liquid nitrogen reservoir. Other cryogenic options include using a cryogenic reservoir to cool the high pressure gas introduced to the valve.

The current prototype piezoelectric valve also has to be redesigned to prevent the loss in output from its long term operation (refer to section 2.3.8), as a result of the loosening of the screws connecting the spring washers and the face plate to the valve housing, because these screws are not locked in place. Redesigning the valve so that these screws are locked in place (to the valve housing) will prevent this loss in performance.

The effect on the mass output of the fully tensioned valve as a result of varying the driving pulse length and backing pressure needs to be investigated. This will be similar to the extended mass output results of the valve conducted after its three year working period, as shown in section 2.3.7.

6.2: Future development of the Lica

An improved version of the Lica is planned which will be referred to as the Spica (which stands for: Supersonically pulse injected coaxial accelerator). The Spica will have several features which were lacking in the Lica:

- 1) A longer flight distance
- 2) B-dot probes to experimentally determine the current flowing in the plasma accelerator
- 3) Photomultipliers to confirm the velocity of the plasma pulses
- 4) The use of diffraction gratings [85], [86], [87] to experimentally determine both the composition of the plasma and its temperature

- 5) Investigation of the effects of using different electrode materials to improve the operation of the plasma accelerator
- 6) Removing the skimmer attachment in front of the piezoelectric valve and increasing the mass of hydrogen introduced into the plasma accelerator.

Analysing the anomaly of misfires was difficult to make using the 4m long flight distance in the Lica apparatus, because only a few data points could be collected. Spica is intended to have a flight distance between 8 to 10 metres. This extended flight distance will allow more data to be collected over a wider number of bins, allowing more detail on the velocity distributions in misfires to be collected.

A short coming of the Lica apparatus was that it was only equipped with a voltage divider. Without the use of B-dot probes to experimentally determine the current flowing in the plasma accelerator, the resistance of the plasma could not be determined. In most rail guns, that use plasma armatures, B-dot probes are used to experimentally measure the current [167], [168], [169], [170] and [171]. In Spica the main B-dot used to determine the current flowing in the plasma accelerator will be placed at an equal distance from the positive electrode struts and the start of the grounded electrode. Placing the B-dot probe in this position should minimise the influence of other magnetic fields, produced from the plasma and the electrode struts, on the results from the B-dot probe. A series of insulated B-dot probes placed near the grounded electrode will be used to provide a rough means of measuring both the velocity and current distribution across the plasma.

Photomultipliers were tried as a means of measuring the velocity of the plasma in the Lica; however the photomultipliers were placed too close together and the first photomultiplier was placed too close to the discharge of the plasma accelerator to be of any diagnostic use. Since the Spica has an extended flight distance, the photomultipliers are intended to be placed approximately 4 or 5 metres apart and be positioned further from the plasma accelerator (to limit the effects of the initial discharge on the photomultipliers).

The addition of diffraction gratings will allow the composition of the plasma and a measure of the amount of ablation to be determined. The temperature of the plasma will also be able to be determined using this equipment. It may also be possible to experimentally observe the evolution and acceleration of the plasma, and note the effect of ablation as a function of time.

The use of different electrode materials to try and minimise the effects of ablation are planned for investigation in the Spica. Because of the skin effect, the surface layer (less than 1mm) of the electrode conducts the bulk of the current density. This means that the positive stainless steel electrode could be coated with the intended material at a fraction of the cost of manufacturing the entire electrode from the material. One of the materials of interest is the use of graphite coatings, which since it is conductive and has a low Z value has the added

advantage that the minimum ignition temperature for a fusion reaction will be less affected by the amount of the ablated material produced from such an electrode as compared to an electrode made from a higher Z material (refer to section 1.1).

The amount of hydrogen plasma accelerated in the plasma accelerator is also planned to be increased, firstly by removing the skimmer attachment in front of the valve and directly injecting the hydrogen gas pulse into the accelerator. Then the prototype cryogenic valve discussed in section 6.1 will be trialled in the accelerator.

6.3: Future development of the numerical modelling process and the MATAC program

It has been demonstrated in chapter 4 that MATAC is capable of solving the basic electromagnetic equations of a plasma accelerator. The first change that needs to be implemented in MATAC is to use the full AVA formulation, refer to section 4.3.14. This will involve altering the temporal variation and system matrices, and including a one dimensional FEM model to determine the value of the electric scalar V at the breech of the plasma accelerator. This one dimensional FEM model needs to be included so that the Dirichlet value for V can be used to remove the need to include the surface flux boundary conditions described by equation (4.184) (refer to the discussion given in section 4.3.13). This one dimensional model consists of first solving the magnetic field and then using equation (4.E.37) (refer to appendix 4E) to obtain the value for V . This alteration to MATAC will allow the proper conductivity of both the plasma and the electrode materials to be used in the formulation.

The next alteration that needs to be made is to include an error improvement strategy within the time marching scheme [107] and the mesh [155] (refer to section 4.3.14). Currently trials of error evaluation at half time steps [107] have been trialled using the various test cases in section 4.3.13; however these trials showed that the use of half time step analysis was found to be less important than the fineness of the mesh. The possibility of using an eigenvalue analysis scheme [108] to solve the temporal dependence of the equations (although computationally more expensive but far more accurate than a time marching scheme) is also a consideration. An adapted mesh to prevent numerical error appearing will also be trialled.

A full MHD model consisting of either a FV [113], [114] or possibly an ALE algorithm [153], [154] is planned to be added to the MATAC program. This addition is necessary to account for the motional and energy aspects of the plasma. Due to the conservation of mass considerations an FEM approach cannot be applied to the MHD equations without a great deal of difficulty.

Further intentions of adding an ion and ablation model to MATAC will have to be deferred until the full MHD model has been completed. The use of commercially available fluid flow programs to solve the MHD equations of the plasma accelerator will not be used, because of the

6.3 Future development of the numerical modelling process and the MATAC program

reasons conveyed in the introductory discussion at the start of this chapter. The possibility of adding or altering a freeware MHD program has not yet been fully investigated.

Other electromagnetic considerations such as the effect of plasma instabilities on the motion of the plasma, which were numerically shown to be of importance in [65], cannot be considered until the MHD model has been included in the MATAC program.

Chapter 7

Conclusions

The piezoelectric valve developed in this thesis is capable of a maximum output of 0.022mg of hydrogen gas per pulse (produced using a 200 μ s driving pulse at a backing pressure of 750kpa). Unfortunately this output is only one tenth of that required by the proposed MTF scheme. Two methods that could be used to increase this output to that required for the MTF scheme would be either to use an array of piezoelectric valves or by cryogenic means, both these methods remain the subject of future research.

The results of the gas pulse characteristics experiments revealed that the very short gas pulses, with an average pulse width of 10 μ s, longitudinal temperatures below 2K and with terminal speed ratios between 23 and 28 could be produced. Optimum gas pulses, without the presence of peak splitting, were generated within the 160 μ s to 200 μ s driving pulse range. The peak splitting observed in the density profiles can probably be attributed to the bouncing of the O-ring seal.

The skimmer and preionizer attachment had a noticeable effect on the gas pulses produced from the valve; the hydrogen gas pulses produced in this manner (using driving pulses between 150 μ s to 200 μ s) were warmer and broader than those produced without the attachment. Gas pulses produced in this fashion had temperatures in the range of 10K to 12K, with average pulse widths between 25 μ s and 34 μ s, and terminal speed ratios between the values of 8 to 10. The broadening of these gas pulses can be attributed to scattered gas from the preionizer attachment. The gas pulses introduced into a coaxial plasma accelerator using the currently developed piezoelectric valve are superior to those produced from the traditionally used solenoid valves. Solenoid valves operate on a millisecond time scale and tend to quasi-statically fill pulsed plasma accelerators resulting in the snowplough mode of operation. The prototype piezoelectric valve operates on a microsecond time scale, and with the preionizer attachment in front of the valve, it generates hydrogen gas pulses approximately 5.89cm in length (at FWHH) at distance of 36.5cm from the valve (generated using a 180 μ s driving pulse with a longitudinal temperature of 12.1K). Since the gas pulses produced from the valve (even with the preionizer attachment) are very short it may be possible to develop a plasma accelerator that operates in the sought after plasma block mode of operation rather than the typically encountered snowplough mode of operation.

Despite the fact that the piezoelectric valve is yet to achieve the required mass output for the proposed MTF scheme, it has been shown that the piezoelectric valve has several desirable properties compared to those of solenoid valves, which would be advantageous in the proposed MTF scheme.

The unique prototype Lica plasma accelerator has been shown to be a practical working plasma accelerator. The novel use of supporting the central electrode through the use of four tensioned conducting struts, the unconventional preionization method and the use of a piezoelectric valve have been demonstrated to be practical options in the construction of a pulsed plasma accelerator.

The Lica was typically operated using a charging voltage of 10kV and a driving pulse length of 180 μ s. Because of the skimmer attachment in front of the valve, the actual amount of hydrogen gas that is injected into the plasma accelerator is calculated as being approximately 1.88×10^{-3} mg. It is presently unclear on the exact breakdown and plasma acceleration processes present within the Lica apparatus. What was discovered was that the use of longer positive electrodes made little difference to the velocity of the resulting plasma, which is the opposite of what one would expect. It has therefore been hypothesised that the Lica operates by accelerating a series of plasma pulses; this hypothesis was partially based upon the analysis of the velocity distributions. The hypothesis is further confirmed by the separation of the perceived peak structure at the higher charging voltage of 14kV; however more tests are needed to confirm this observation. There appears to be at least three main peaks in the perceived peak structure in the regions of 40km/s, 50km/s and 60km/s to 80km/s, with the bulk of the plasma travelling in the 40km/s to 50km/s range. The total acceleration time for all the plasma is between 22 μ s and 33 μ s.

Unfortunately due to a lack of funding, experimental means of determining the temperature of the plasma was not possible. So the temperature of the plasma was calculated by fitting a Maxwell – Boltzmann distribution to the velocity distribution of the plasma, with the assumptions that the plasma is entirely composed of hydrogen and that it has achieved a thermal equilibrium by the time it reached the detector. The average temperature of the plasma pulses calculated in this fashion was determined to be in the region of 3000K to 5000K. Even though the robustness of the linear least squares fits used to calculate the temperature of the plasma pulses were not entirely reliable (the average R^2 value of the fits was 0.75) they were more robust than simply assuming a single peak structure, lending further credence to hypothesis that the Lica operates by accelerating a series of plasma pulses.

The anomaly of the high velocity plasma in the region of 150km/s to 250km/s, which have been referred to as misfires, cannot be adequately explained at present and remain the subject of speculation.

The Lica has some experimental flaws. Firstly it was not equipped with any B-dot probes so the current could not be experimentally determined and neither could an estimation of the plasma resistivity. And secondly, the Lica only contains one means of determining the velocity distribution of the plasma; there were no other experimental means of confirming this

distribution. These and other improvements need to be implemented in an upgraded version of the Lica.

A numerical modelling approach was used as a means of trying to understand and recreate the operation of the plasma accelerator. The unavailability of specially written plasma accelerator program; the associated cost and problems of commercially available programs; and the limitations of freeware rail gun programs necessitated the need to develop the mathematical models presented in this thesis.

In analytical terms it was not possible to develop anything more than a lump sum model based upon the solution to the circuit equations and the assumption that the plasma accelerator operates by the acceleration of a filament current as a result of the Lorentz force acting upon it. This analytical model was found to be too inadequate in describing the complicated operation of the Lica.

The one dimensional Runge-Kutta numerical model that was developed to extend the results gained from the analytical model allowed other effects such as a simple ablation model to be incorporated into it; however this model too was unable to describe the operation of the Lica. The one dimensional first order models (both analytical and numerical) that were developed were unable to model such effects as the correct current distribution across the plasma, the velocity skin effect and compressional effects. These one dimensional models effectively represent an upper limit to the velocity that could be obtained from a plasma accelerator accelerating an infinitely conductive plasma.

Because of these limitations the two dimensional electromagnetic model called MATAC was developed. MATAC can be likened to essentially being a sliding contact rail gun program, because there was not enough time to incorporate a full MHD solver into its framework. Despite this, it does not detract from the fact that MATAC is a fully functional FEM electromagnetic plasma accelerator program that has been designed to overcome many of the numerical problems associated with solving the electromagnetics of a plasma accelerator.

A spin off from the numerical modelling efforts was the extension of the upwinding scheme of Hughes [157] to quadratic and cubic elements. It was found that there was little difference between the linear and quadratic upwinding schemes; it appears that the cubic upwinding scheme was the least accurate of all the schemes, where the main error in the upwinded cubic solution is associated with nodes immediately before the high gradient jump in the solution.

The MATAC program despite the lack of an error improvement scheme, in either the time marching scheme or the mesh, gives physically meaningful results. The program shows such effects as the skin effect, and current diffusion within the moving armature as a result of the velocity skin effect and induced current.

The appearance of numerical errors in MATAC seem to be a product of the fineness of the mesh, the time step and how quickly the velocity changes from one time step to another. These numerical errors, in the current density and magnetic fields, are most prevalent in the ∇V calculation, most notably at the breech and at re-entrant corners. Since the current density is solely dependent upon ∇V at re-entrant corners, where the traditional finite elements used in MATAC are unable to correctly model the singular solution at this point (i.e. inherent errors will be present at these points), this is not an unexpected effect.

The MATAC program was run for the situation of the Lica fitted with a 5cm in length positive electrode accelerating a pure hydrogen plasma, operating in the plasma block mode of operation (for initial purposes), in which the program was run using the physical and electrical properties of the plasma calculated using the FWHH of the neutral hydrogen gas pulse. The conductivity of the plasma was calculated using the experimentally determined temperature of 5000K and the ad hoc assumption that the plasma is at a thermal equilibrium, primarily due to the lack of experimental information and the necessity to simplify the initial problem. Using these assumptions the plasma was determined to be an ideal, non-degenerate plasma, with an electron density in the range of 8.9×10^{16} electrons/m³ to 1.8×10^{17} electrons/m³; the conductivity of this plasma was calculated using the Spitzer formula [59].

Using the previously discussed parameters, the MATAC program predicts that the bulk of the plasma will obtain a final velocity of 82.6km/s after a 1.6 μ s acceleration period. This numerical prediction is unable to correctly match the experimental results (despite the possibility that with the inclusion of other factors the numerical result could be said to lie within any of the normally observed experimentally determined velocity regions). This tends to suggest that a larger mass than what has previously been assumed is being accelerated and that ablation plays a larger role in the operation of the plasma accelerator than has been considered. This will have a noticeable effect on the previously made assumptions made about the plasma, including its composition, conductivity and temperature. However these questions remain the subject of further experimental and numerical work. So the hypothesis that the Lica operates by accelerating a series of plasma sheaths remains unconfirmed.

Both the piezoelectric valve and the plasma accelerator developed in this thesis have not yet been fully optimized for the purposes of the proposed MTF scheme, in which a plasma accelerator is required to be capable of accelerating a 0.2mg hydrogen gas pulse to a velocity in excess of 200km/s, with reproducible results and be able to operate at a firing rate of 10Hz. Developing a plasma accelerator that is capable of these results is still a matter for future research; what has been demonstrated in this thesis is that both the plasma accelerator and the

valve that have been developed are both viable options that may, with future development, be of interest to the proposed MTF scheme.

Appendices for Chapter 4

Appendix 4A: Vector calculus

General vector relationships

Given the vectors F and G and the scalars v and u , where F and G are defined in the coordinate directions of i , j and k as:

$$F = ai + bj + ck \quad (4.A.1)$$

$$G = pi + qj + rk \quad (4.A.2)$$

The dot product of the two vectors F and G is given as:

$$F \cdot G = ap + bq + cr \quad (4.A.3)$$

The cross product of the two vectors F and G is given by:

$$F \times G = (br - cq)i + (cp - ar)j + (aq - bp)k \quad (4.A.4)$$

Operations on scalars and vectors

$$\nabla(vu) = u\nabla v + v\nabla u \quad (4.A.5)$$

$$\nabla(F \cdot G) = F \times \nabla \times G + G \times \nabla \times F + (F \cdot \nabla)G + (G \cdot \nabla)F \quad (4.A.6)$$

$$\nabla \cdot (vF) = v\nabla \cdot F + F \cdot \nabla v \quad (4.A.7)$$

$$\nabla \cdot (F \times G) = G \cdot \nabla \times F - F \cdot \nabla \times G \quad (4.A.8)$$

$$\nabla \times (vF) = v\nabla \times F + \nabla v \times F \quad (4.A.9)$$

$$\nabla \times (F \times G) = F\nabla \cdot G - G\nabla \cdot F + (G \cdot \nabla)F - (F \cdot \nabla)G \quad (4.A.10)$$

Integral formulae

The Divergence theorem is given as:

$$\int \nabla \cdot F d\Omega = \int F \cdot \partial\Gamma = \int F \cdot n d\Gamma \quad (4.A.11)$$

Stokes theorem is given by:

$$\int \nabla \times F \cdot \partial\Gamma = \int F \cdot \partial c = \int F \times n dc \quad (4.A.12)$$

Greens formulas are given as:

$$\int (\nabla^2 u + \nabla v \cdot \nabla u) \delta\Omega = \int v \nabla u \cdot n \delta\Gamma \quad (4.A.13)$$

$$\int (\nabla^2 u - u \cdot \nabla^2 v) \delta\Omega = \int (v \nabla u - u \nabla v) \cdot n \delta\Gamma \quad (4.A.14)$$

Expanded vector relations in different coordinate systems

Rectangular coordinates (x, y, z)

$$\nabla v = \frac{\partial v}{\partial x} i + \frac{\partial v}{\partial y} j + \frac{\partial v}{\partial z} k \quad (4.A.15)$$

$$\nabla \cdot F = \frac{\partial F_x}{\partial x} + \frac{\partial F_y}{\partial y} + \frac{\partial F_z}{\partial z} \quad (4.A.16)$$

$$\nabla \times F = \left(\frac{\partial F_z}{\partial y} - \frac{\partial F_y}{\partial z} \right) i + \left(\frac{\partial F_x}{\partial z} - \frac{\partial F_z}{\partial x} \right) j + \left(\frac{\partial F_y}{\partial x} - \frac{\partial F_x}{\partial y} \right) k \quad (4.A.17)$$

$$\nabla^2 v = \frac{\partial^2 v}{\partial x^2} i + \frac{\partial^2 v}{\partial y^2} j + \frac{\partial^2 v}{\partial z^2} k \quad (4.A.18)$$

$$\nabla^2 F = \nabla^2 F_x i + \nabla^2 F_y j + \nabla^2 F_z k \quad (4.A.19)$$

Cylindrical coordinates (r, θ , z)

$$\nabla v = \frac{\partial v}{\partial r} i + \frac{1}{r} \frac{\partial v}{\partial \theta} j + \frac{\partial v}{\partial z} k \quad (4.A.20)$$

$$\nabla \cdot F = \frac{1}{r} \frac{\partial}{\partial r} (r F_r) + \frac{1}{r} \frac{\partial F_\theta}{\partial \theta} + \frac{\partial F_z}{\partial z} \quad (4.A.21)$$

$$\nabla \times F = \left(\frac{1}{r} \frac{\partial F_z}{\partial \theta} - \frac{\partial F_\theta}{\partial z} \right) i + \left(\frac{\partial F_r}{\partial z} - \frac{\partial F_z}{\partial r} \right) j + \left(\frac{1}{r} \left(\frac{\partial}{\partial r} (r F_\theta) - \frac{\partial F_r}{\partial \theta} \right) \right) k \quad (4.A.22)$$

$$\nabla^2 v = \frac{1}{r} \frac{\partial}{\partial r} \left(r \frac{\partial v}{\partial r} \right) i + \frac{1}{r^2} \frac{\partial^2 v}{\partial \theta^2} j + \frac{\partial^2 v}{\partial z^2} k \quad (4.A.23)$$

$$\nabla^2 F = \left(\nabla^2 F_r - \frac{2}{r^2} \frac{\partial F_\theta}{\partial \theta} - \frac{F_r}{r^2} \right) i + \left(\nabla^2 F_\theta - \frac{2}{r^2} \frac{\partial F_r}{\partial \theta} - \frac{F_\theta}{r^2} \right) j + \nabla^2 F_z k \quad (4.A.24)$$

Appendix 4B: Lagrange multipliers

Lagrange multipliers have traditionally found uses in optimisation problems, in applying boundary conditions and constraint equations [172]. In the Lagrange multiplier technique the stationary solution is augmented by a function known as the Lagrangian function:

$$F(u, \lambda) = f_T(u) + \lambda g(u) \quad (4.B.1)$$

In equation (4.B.1) λ is the Lagrange multiplier, $g(u)$ is the constraint or boundary condition that is to be imposed, $f_T(u)$ is the function which is to be constrained and $F(u, \lambda)$ is the minimised function. When $F(u, \lambda)$ is minimised with respect to the solution u the Lagrange multiplier will be maximised. A general proof of the Lagrange multiplier technique relating to the minimisation of equation (4.B.1) can be found in [78].

Traditionally Lagrange multipliers are used in the finite element method, either to impose boundary conditions or in applying constraint equations. When imposing constraint boundary conditions the boundary conditions are introduced into the formulation through the multiplication of a Lagrange multiplier.

$$f_T(u) + \lambda g(u) \quad (4.B.2)$$

After minimising equation (4.B.2) with respect to the solution variable u the following weak formulation is derived:

$$k(u) - f(u) + \lambda g'(\lambda) = 0 \quad (4.B.3)$$

In equation (4.B.3) $k(u)$ is the weak formulation system matrix, $f(u)$ is the resulting weak formulation system vector and g is the imposed set of boundary conditions. A second equation is needed to describe the Lagrange multiplier, this is done by minimising equation (4.B.2) with respect to the Lagrange multiplier resulting in equation (4.B.4).

$$g(u) = 0 \quad (4.B.4)$$

Equations (4.B.3) and (4.B.4) are written in matrix form as:

$$\begin{bmatrix} k, g' \\ g, 0 \end{bmatrix} \begin{Bmatrix} u \\ \lambda \end{Bmatrix} = \begin{bmatrix} f \\ 0 \end{bmatrix} \quad (4.B.5)$$

When imposing discrete constraint conditions (such as $\nabla \cdot u = 0$) in the Galerkin weighted residual method using Lagrange multipliers, the constraint is added to the formulation after multiplication with a Lagrange multiplier, this is represented by equation (4.B.6).

$$f_T(u) + \lambda g(u) \quad (4.B.6)$$

After multiplying equation (4.B.6) with a test function W for u and minimisation with respect to u results in the following equation:

$$k(u) - f(u) + \int \lambda' W g(u) \partial \Omega = 0 \quad (4.B.7)$$

The second equation describing the Lagrange multiplier is found by minimising equation (4.B.6) with respect to the Lagrange multiplier (after it has been multiplied with a test function) resulting in:

$$\int W g(u) \partial \Omega = 0 \quad (4.B.8)$$

Equations (4.B.7) and (4.B.8) can be represented in matrix form as:

$$\begin{bmatrix} k, \int W g' \partial \Omega \\ \int W g \partial \Omega, 0 \end{bmatrix} \begin{Bmatrix} u \\ \lambda \end{Bmatrix} = \begin{bmatrix} f \\ 0 \end{bmatrix} \quad (4.B.9)$$

It can be clearly seen that the matrices (4.B.5) and (4.B.9) are symmetrical (providing that the system matrix given by k is also symmetrical), so are amenable to solution by the use of the biconjugate method (provided the matrix is positive definite) or the use of the general residual method [78]. However to prevent pivoting problems from the zero term on the central diagonal of the matrices, which would give a singular matrix, a small slack variable is added to the diagonal. Typically this term is very small approximately 1×10^{-6} [172]. The addition of the slack variable β to matrices (4.B.5) and (4.B.9) is given by matrices (4.B.10) and (4.B.11) respectively.

$$\begin{bmatrix} k, g' \\ g, \beta \end{bmatrix} \begin{Bmatrix} u \\ \lambda \end{Bmatrix} = \begin{bmatrix} f \\ 0 \end{bmatrix} \quad (4.B.10)$$

$$\begin{bmatrix} k, \int W g' \partial \Omega \\ \int W g \partial \Omega, \beta \end{bmatrix} \begin{Bmatrix} u \\ \lambda \end{Bmatrix} = \begin{bmatrix} f \\ 0 \end{bmatrix} \quad (4.B.11)$$

If a non-discrete constraint is imposed using a Lagrange multiplier (such as $\nabla \times u = w$ where w is a forcing constraint) then equation (4.B.8) is modified as:

$$\int W g(u) \partial \Omega = f_\lambda \quad (4.B.12)$$

This non-discrete constraint is represented in matrix form by combining equations (4.B.12) and (4.B.11), with slack variables on the diagonals, resulting in equation (4.B.13).

$$\begin{bmatrix} k, \int W g' \partial \Omega \\ \int W g \partial \Omega, \beta \end{bmatrix} \begin{Bmatrix} u \\ \lambda \end{Bmatrix} = \begin{bmatrix} f \\ f_\lambda \end{bmatrix} \quad (4.B.13)$$

When matrices (4.B.10), (4.B.11) and (4.B.13) are solved for values of u and λ , the actual value of λ may have no physical significance. It is only in some formulations such as optimization or the Stokes equation [172] where the Lagrange multiplier is a sort after part of the solution. In the Stokes equation the pressure term may be considered to be a Lagrange multiplier (a sort after solution).

Appendix 4C: Matrix values for the new cubic upwinding scheme

$$v_{11} = \sum_{i=1}^3 \left(-\frac{9}{16}\xi_i^3 + \frac{9}{16}\xi_i^2 + \frac{1}{16}\xi_i - \frac{1}{16} \right) \left(-\frac{27}{16}\xi_i^2 + \frac{18}{16}\xi_i + \frac{1}{16} \right) \frac{h}{2} W_i \quad (4.C.1)$$

$$v_{12} = \sum_{i=1}^3 \left(-\frac{9}{16}\xi_i^3 + \frac{9}{16}\xi_i^2 + \frac{1}{16}\xi_i - \frac{1}{16} \right) \left(\frac{81}{16}\xi_i^2 - \frac{18}{16}\xi_i - \frac{27}{16} \right) \frac{h}{2} W_i \quad (4.C.2)$$

$$v_{13} = \sum_{i=1}^3 \left(-\frac{9}{16}\xi_i^3 + \frac{9}{16}\xi_i^2 + \frac{1}{16}\xi_i - \frac{1}{16} \right) \left(-\frac{81}{16}\xi_i^2 - \frac{18}{16}\xi_i + \frac{27}{16} \right) \frac{h}{2} W_i \quad (4.C.3)$$

$$v_{14} = \sum_{i=1}^3 \left(-\frac{9}{16}\xi_i^3 + \frac{9}{16}\xi_i^2 + \frac{1}{16}\xi_i - \frac{1}{16} \right) \left(\frac{27}{16}\xi_i^2 + \frac{18}{16}\xi_i - \frac{1}{16} \right) \frac{h}{2} W_i \quad (4.C.4)$$

$$v_{21} = \sum_{i=1}^3 \left(\frac{27}{16}\xi_i^3 - \frac{9}{16}\xi_i^2 - \frac{27}{16}\xi_i + \frac{9}{16} \right) \left(-\frac{27}{16}\xi_i^2 + \frac{18}{16}\xi_i + \frac{1}{16} \right) \frac{h}{2} W_i \quad (4.C.5)$$

$$v_{22} = \sum_{i=1}^3 \left(\frac{27}{16}\xi_i^3 - \frac{9}{16}\xi_i^2 - \frac{27}{16}\xi_i + \frac{9}{16} \right) \left(\frac{81}{16}\xi_i^2 - \frac{18}{16}\xi_i - \frac{27}{16} \right) \frac{h}{2} W_i \quad (4.C.6)$$

$$v_{23} = \sum_{i=1}^3 \left(\frac{27}{16}\xi_i^3 - \frac{9}{16}\xi_i^2 - \frac{27}{16}\xi_i + \frac{9}{16} \right) \left(-\frac{81}{16}\xi_i^2 - \frac{18}{16}\xi_i + \frac{27}{16} \right) \frac{h}{2} W_i \quad (4.C.7)$$

$$v_{24} = \sum_{i=1}^3 \left(\frac{27}{16}\xi_i^3 - \frac{9}{16}\xi_i^2 - \frac{27}{16}\xi_i + \frac{9}{16} \right) \left(\frac{27}{16}\xi_i^2 + \frac{18}{16}\xi_i - \frac{1}{16} \right) \frac{h}{2} W_i \quad (4.C.8)$$

$$v_{31} = \sum_{i=1}^3 \left(-\frac{27}{16}\xi_i^3 - \frac{9}{16}\xi_i^2 + \frac{27}{16}\xi_i + \frac{9}{16} \right) \left(-\frac{27}{16}\xi_i^2 + \frac{18}{16}\xi_i + \frac{1}{16} \right) \frac{h}{2} W_i \quad (4.C.9)$$

$$v_{32} = \sum_{i=1}^3 \left(-\frac{27}{16}\xi_i^3 - \frac{9}{16}\xi_i^2 + \frac{27}{16}\xi_i + \frac{9}{16} \right) \left(\frac{81}{16}\xi_i^2 - \frac{18}{16}\xi_i - \frac{27}{16} \right) \frac{h}{2} W_i \quad (4.C.10)$$

$$v_{33} = \sum_{i=1}^3 \left(-\frac{27}{16}\xi_i^3 - \frac{9}{16}\xi_i^2 + \frac{27}{16}\xi_i + \frac{9}{16} \right) \left(-\frac{81}{16}\xi_i^2 - \frac{18}{16}\xi_i + \frac{27}{16} \right) \frac{h}{2} W_i \quad (4.C.11)$$

$$v_{34} = \sum_{i=1}^3 \left(-\frac{27}{16}\xi_i^3 - \frac{9}{16}\xi_i^2 + \frac{27}{16}\xi_i + \frac{9}{16} \right) \left(\frac{27}{16}\xi_i^2 + \frac{18}{16}\xi_i - \frac{1}{16} \right) \frac{h}{2} W_i \quad (4.C.12)$$

$$v_{41} = \sum_{i=1}^3 \left(\frac{9}{16}\xi_i^3 + \frac{9}{16}\xi_i^2 - \frac{1}{16}\xi_i - \frac{1}{16} \right) \left(-\frac{27}{16}\xi_i^2 + \frac{18}{16}\xi_i + \frac{1}{16} \right) \frac{h}{2} W_i \quad (4.C.13)$$

$$v_{42} = \sum_{i=1}^3 \left(\frac{9}{16}\xi_i^3 + \frac{9}{16}\xi_i^2 - \frac{1}{16}\xi_i - \frac{1}{16} \right) \left(\frac{81}{16}\xi_i^2 - \frac{18}{16}\xi_i - \frac{27}{16} \right) \frac{h}{2} W_i \quad (4.C.14)$$

$$v_{43} = \sum_{i=1}^3 \left(\frac{9}{16}\xi_i^3 + \frac{9}{16}\xi_i^2 - \frac{1}{16}\xi_i - \frac{1}{16} \right) \left(-\frac{81}{16}\xi_i^2 - \frac{18}{16}\xi_i + \frac{27}{16} \right) \frac{h}{2} W_i \quad (4.C.15)$$

$$v_{44} = \sum_{i=1}^3 \left(\frac{9}{16}\xi_i^3 + \frac{9}{16}\xi_i^2 - \frac{1}{16}\xi_i - \frac{1}{16} \right) \left(\frac{27}{16}\xi_i^2 + \frac{18}{16}\xi_i - \frac{1}{16} \right) \frac{h}{2} W_i \quad (4.C.16)$$

Appendix 4D: Bessel functions

The following formulas under the headings of “General Formulas for Bessel Functions” and “Modified Bessel Functions” were taken from [173].

General Formulas for Bessel Functions

An m -th order Bessel function is defined as $Z_m(z) = aJ_m(z) + bY_m(z)$, in which a , b and α are constants that are independent of “ m ” and “ z ”.

$$\frac{1}{z} \frac{\partial}{\partial z} \left(z \frac{\partial Z_m}{\partial z} \right) + \left(1 - \frac{m^2}{z^2} \right) Z_m = 0 \quad (4.D.1)$$

$$\frac{2m}{z} Z_m(z) = Z_{m-1}(z) + Z_{m+1}(z) \quad (4.D.2)$$

$$2 \frac{\partial}{\partial z} Z_m(z) = Z_{m-1} - Z_{m+1} \quad (4.D.3)$$

$$\int z^{m+1} Z_m(z) dz = z^{m+1} Z_{m+1}(z) \quad (4.D.4)$$

$$\int z^{-m+1} Z_m(z) dz = -z^{-m+1} Z_{m+1}(z) \quad (4.D.5)$$

$$\int [Z_0(\alpha z)]^2 z dz = \frac{1}{2} z^2 [Z_0^2(\alpha z) + Z_1^2(\alpha z)] \quad (4.D.6)$$

$$\int [Z_m(\alpha z)]^2 z dz = \frac{1}{2} z^2 [Z_m^2(\alpha z) - Z_{m-1}(\alpha z) Z_{m+1}(\alpha z)] \quad (4.D.7)$$

$$\frac{\partial}{\partial z} [z^{m+1} Z_{m+1}(z)] = z^{m+1} Z_m(z) \quad (4.D.8)$$

$$\frac{\partial}{\partial z} [z^{-m+1} Z_{m-1}(z)] = -z^{-m+1} Z_m(z) \quad (4.D.9)$$

Modified Bessel Functions

An m -th order modified Bessel function K_m is defined by equation (4.D.10).

$$K_m(z) = \frac{1}{2} \pi i^{m+1} [J_m(iz) + iY_m(iz)] \quad (4.D.10)$$

$$I_m(z) = \frac{1}{i^m} J_m(z) \quad (4.D.11)$$

$$I_{-m}(z) = I_m(z) \quad (4.D.12)$$

$$K_{-m}(z) = K_m(z) \quad (4.D.13)$$

$$I_m(z) K_{m-1}(z) + I_{m-1}(z) K_m(z) = \frac{1}{z} \quad (4.D.14)$$

$$I_{m-1}(z) - I_{m+1}(z) = \left(\frac{2m}{z} \right) I_m(z) \quad (4.D.15)$$

$$I_{m-1}(z) + I_{m+1}(z) = 2 \frac{\partial}{\partial z} I_m(z) \quad (4.D.16)$$

Modified Bessel functions proofs

The following are proofs and relationships of Bessel and Modified Bessel functions, some of which (equations (4.D.19), (4.D.20) and (4.D.21)) have not been found in the literature and have been derived using equations (4.D.1) to (4.D.16).

The integration of $\int z J_0(\alpha z) dz$

For $\int z J_0(\alpha z) dz$ let $x = \alpha z$; hence $dx = \alpha dz$ so:

$$\int \frac{x}{\alpha} J_0(x) \frac{dx}{\alpha} = \frac{1}{\alpha^2} \int x J_0(x) dx$$

Using equation (4.D.4) the above equation becomes:

$$\frac{1}{\alpha^2} \int x J_0(x) dx = \frac{1}{\alpha^2} x J_1(x)$$

Substituting back in the values for “x” gives:

$$\int z J_0(\alpha z) dz = \frac{1}{\alpha} z J_1(\alpha z) \quad (4.D.17)$$

The integration of $\int z J_0(i\alpha z) dz$ or the integration of $\int z I_0(\alpha z) dz$

For the integration of $\int z J_0(i\alpha z) dz$ let $x = i\alpha z$; hence $dx = i\alpha dz$ so:

$$\int \frac{x}{i\alpha} J_0(x) \frac{dx}{i\alpha} = \frac{1}{i^2 \alpha^2} \int x J_0(x) dx$$

Using equation (4.D.4) then the above equation becomes

$$\frac{1}{i^2 \alpha^2} \int x J_0(x) dx = \frac{1}{i\alpha} x J_1(x)$$

Given the relationship between I_n and J_n in equation (4.D.11) then substituting the values for “x” and values for n gives

for n=0

$$I_0(\alpha z) = J_0(i\alpha z)$$

and for n=1

$$I_1(\alpha z) = \frac{1}{i} J_1(i\alpha z)$$

Substituting these values (for $n=0$ and $n=1$) into the derived solution for the integral gives:

$$\int z I_0(\alpha z) dz = \frac{1}{\alpha} z I_1(\alpha z) \quad (4.D.18)$$

The integration of $\int \frac{1}{i} J_1(i\alpha z) dz$ or the integration of $\int I_1(\alpha z) dz$

For the integration of $\int \frac{1}{i} J_1(i\alpha z) dz$ let $x = i\alpha z$; hence $dx = i\alpha dz$ so:

$$\int \frac{1}{i\alpha} J_1(x) \frac{dx}{i\alpha} = \frac{1}{i^2\alpha} \int J_1(x) dx$$

Using equation (4.D.5) the above equation becomes:

$$\frac{1}{i^2\alpha} \int J_1(x) dx = -\frac{1}{i^2\alpha} J_0(x)$$

Substituting the values for “x” into the above equation gives:

$$\frac{1}{i^2\alpha} \int J_1(i\alpha z) i\alpha dz = -\frac{1}{i^2\alpha} J_0(i\alpha z)$$

$$\therefore \int \frac{1}{i} J_1(i\alpha z) dz = -\frac{1}{i^2\alpha} J_0(i\alpha z)$$

Using the relationship between I_n and J_n in equation (4.D.11) and then substituting the values for “x” and values for n gives

for $n=0$

$$I_0(\alpha z) = J_0(i\alpha z)$$

and for $n=1$

$$I_1(\alpha z) = \frac{1}{i} J_1(i\alpha z)$$

Substituting these values (for $n=0$ and $n=1$) into the derived solution for the integral gives:

$$\int I_1(\alpha z) dz = \frac{1}{\alpha} I_0(\alpha z) \quad (4.D.19)$$

The integration of $\int z K_0(\alpha z) dz$

From equation (4.D.10) if $x = \alpha z$ and $n=0$ then this equation becomes:

$$K_0(\alpha z) = \frac{1}{2} \pi i [J_0(i\alpha z) + iY_0(i\alpha z)]$$

Using the above equation $\int z K_0(\alpha z) dz$ is defined as being:

$$\int z K_0(\alpha z) dz = \int \frac{1}{2} \pi i [z J_0(i\alpha z) + iz Y_0(i\alpha z)] dz$$

In the above equation (using equations (4.D.18) and (4.D.11))

$$\int \frac{1}{2} \pi i z J_0(i\alpha z) dz = \frac{1}{2\alpha} \pi z J_1(i\alpha z)$$

and

$$i^2 \int \frac{1}{2} \pi i z Y_0(i\alpha z) dz = \frac{i}{2\alpha} \pi z Y_1(i\alpha z)$$

; hence

$$\int z K_0(\alpha z) dz = \frac{1}{2\alpha} \pi [J_1(i\alpha z) + iY_1(i\alpha z)]$$

From equation (4.D.10) if $x = \alpha z$ and $n=1$ then this equation becomes:

$$K_1(\alpha z) = \frac{1}{2} \pi i^2 [J_1(i\alpha z) + iY_1(i\alpha z)]$$

Substituting this into the working solution produces:

$$\int z K_0(\alpha z) dz = -\frac{1}{\alpha} z K_1(\alpha z) \quad (4.D.20)$$

The integration of $\int K_1(z) dz$

From equation (4.D.10) if $n=1$ then this equation becomes:

$$K_1(z) = \frac{1}{2} \pi i^2 [J_1(iz) + iY_1(iz)]$$

Hence using the above equation $\int K_1(\alpha z) dz$ is given as:

$$\int K_1(z) dz = \int \frac{1}{2} \pi^2 [J_1(iz) + iY_1(iz)] dz$$

In the above equation (with the use of equation (4.D.5))

$$\int \frac{1}{2} \pi^2 J_1(iz) dz = -\frac{1}{2} \pi i J_0(iz)$$

and

$$\int \frac{1}{2} \pi^3 Y_1(iz) dz = -\frac{1}{2} \pi^2 Y_1(iz)$$

Substituting these into the working solution gives:

$$\int K_1(z) dz = -\frac{1}{2} \pi [J_0(iz) - iY_0(iz)]$$

From equation (4.D.10) if $n=0$ then this equation becomes:

$$K_0(z) = \frac{1}{2} \pi [J_0(iz) + iY_0(iz)]$$

Substituting this into the working solution results in:

$$\int K_1(z) dz = -K_0(z) \quad (4.D.21)$$

Appendix 4E: Test cases

When dealing with any numerically solved system it is always prudent to conduct a test on a suitable problem that has an analytical solution, to gauge the accuracy and any possible numerical errors. For the problem of modelling the plasma accelerator there is no analytical solution in the literature, however there are three simple test cases that can be used to test the numerical formulation. The three test cases are an infinitely long conductive wire, an infinitely long conductive coaxial cable, and an infinitely long conductive wire set in a moving reference frame. All three test cases will be treated as eddy current problems and will be calculated using the assumption that the electrical system is overdamped; the reason for this is that all three have modified Bessel functions as their solutions, which require the time dependent term be a constant (in an underdamped system the term in front of the time dependent term is not a constant). The current in an overdamped RLC circuit is given by the following formula:

$$i = (e^{Et} - e^{Ft})F \frac{Q}{\left(1 - \frac{F}{E}\right)} \quad (4.E.1)$$

In the above equation E and F are constants defined as:

$$E = -\frac{Ro}{2Lo} + \frac{1}{2Lo} \sqrt{Ro^2 - \frac{4Lo}{C}}$$

$$F = -\frac{Ro}{2Lo} - \frac{1}{2Lo} \sqrt{Ro^2 - \frac{4Lo}{C}}$$

Hence the time derivative of the current is derived as:

$$\frac{\partial i}{\partial t} = (E - F)i \quad (4.E.2)$$

Because the current density is proportional to the current, if the time coordinate is separated from the spatial coordinates then the time derivatives of the current and the current density will be proportional; hence the time derivative of the current density is obtained as equation (4.E.3).

$$\frac{\partial J}{\partial t} = (E - F)J \quad (4.E.3)$$

Case1: an infinitely long conductive wire

In this test case the problem of an infinitely long conductive wire with a constant conductivity is subjected to a time dependent current (from an overdamped RLC circuit).

Solving the current density equation

The equation to be solved (derived from the rearrangement of equation (4.67), the use of equations (4.66) and (4.55) and the vector relationships in terms of cylindrical coordinates given in Appendix 4A) is:

$$\frac{\partial^2 J_z}{\partial r^2} + \frac{1}{r} \frac{\partial J_z}{\partial r} - \sigma \mu_o \frac{\partial J_z}{\partial t} = 0 \quad (4.E.4)$$

Substituting equation (4.E.3) into equation (4.E.4) gives:

$$\frac{\partial^2 J_z}{\partial r^2} + \frac{1}{r} \frac{\partial J_z}{\partial r} - \alpha J_z = 0 \quad (4.E.5)$$

In the above equation $\alpha = \sigma\mu_o(E - F)$, the solution to equation (4.E.5) is a zero order modified Bessel function, as given in Appendix 4D (refer to equation (4.D.1)). So the current density has the form of:

$$J_z = AI_0(\alpha r) + BK_0(\alpha r) \quad (4.E.6)$$

In equation (4.E.6) A and B are both constants to be determined by the boundary conditions. The boundary conditions for this problem are defined by either the current (equations (4.E.7) and (4.E.8)) or magnetic field (equations (4.E.9) and (4.E.10)) values on the conducting surface boundaries:

$$i(0) = 0 \quad (4.E.7)$$

$$i(R_1) = i \quad (4.E.8)$$

and

$$B_\theta(0) = 0 \quad (4.E.9)$$

$$B_\theta(R_1) = \frac{\mu_o i}{2\pi R_1} \quad (4.E.10)$$

Either of these boundary conditions can be used to solve the system. Traditionally the magnetic field boundary conditions are used [110]; however in this instance, the boundary conditions given by equations (4.E.7) and (4.E.8) will be used (in which i is the inputted current into the infinitely long wire; this current is defined by equation (4.E.1)).

At $r = 0$ the value for the current density must have a finite value; hence the constant B in equation (4.E.6) must be equal to zero and equation (4.E.6) is reduced to:

$$J_z = AI_0(\alpha r) \quad (4.E.11)$$

The relationship between the current density, in the z direction, and the current is defined by:

$$2\pi \int r J_z \partial r = i \quad (4.E.12)$$

Substituting equation (4.E.11) into equation (4.E.12) and using equation (4.D.18) given in appendix 4D results in equation (4.E.13), in which C_J is an integration constant.

$$2\pi \int A r I_0(\alpha r) \partial r = 2\pi A \frac{1}{\alpha} r I_1(\alpha r) + C_J = i \quad (4.E.13)$$

Using the boundary condition given by equation (4.E.7) results in $C_J = 0$, because $I_1(0) = 0$. The remaining boundary condition, given by equation (4.E.8), gives the solution for the constant A as:

$$A = \frac{i\alpha}{2\pi R I_1(\alpha R)} \quad (4.E.14)$$

Solving the magnetic field equation

The equation for the magnetic field (derived from expanding equation (4.54) using the vector relationships in terms of cylindrical coordinates given in Appendix 4A) is given as:

$$\frac{1}{r} \left(\frac{\partial}{\partial r} (r B_\theta) \right) = \mu_o J_z \quad (4.E.15)$$

The current density in equation (4.E.15) is defined by equation (4.E.11). Integrating equation (4.E.15) with respect to the r coordinate (after multiplying both sides by r since the problem is in cylindrical coordinates) and using equation (4.D.18) (refer to Appendix 4D) produces:

$$B_\theta = \frac{D}{\alpha} I_1(\alpha r) + \frac{C_B}{r} \quad (4.E.16)$$

In equation (4.E.16) C_B is an integration constant, and D is defined as:

$$D = \frac{\mu_o i \alpha}{2\pi R I_1(\alpha R)} \quad (4.E.17)$$

The integration constant C_B is solved by applying boundary conditions (4.E.9) and (4.E.10) to equation (4.E.16). Because of the boundary condition defined by equation (4.E.9) and the fact that the magnetic field must have a finite value at $r = 0$ results in $C_B = 0$ (the same result obtained by applying the boundary condition given in equation (4.E.10) to equation (4.E.16)); hence the magnetic field is obtained as:

$$B_\theta = \frac{D}{\alpha} I_1(\alpha r) \quad (4.E.18)$$

Solutions of the Magnetic vector potential and the electric scalar potential

The analytical solution in terms of the magnetic vector potential A and the electric scalar potential V can be derived from the previously determined solution for the current density (equation (4.E.11)), the use of equations (4.66), (4.55) and the current continuity equation (either equation (4.66) or (4.68)). A suitable solution (for these quantities) is obtained when equation (4.68) is considered with respect to the boundary conditions generated from equation (4.63) and the boundary conditions described in section 4.3.2. If V is considered to be some arbitrary constant, say equal to zero, then A will be defined by the following equation:

$$\frac{\partial A}{\partial t} = -\frac{1}{\sigma} J_z \quad (4.E.19)$$

Integration of equation (4.E.19) leads to:

$$A_z = -\frac{1}{\sigma(E - F)} J_z \quad (4.E.20)$$

Substituting the value for J_z defined by equation (4.E.11) results in:

$$A_z = -\frac{1}{\sigma(E - F)} A I_0(\alpha r) \quad (4.E.21)$$

Case2: an infinitely long conductive coaxial cable

In this test case the problem of an infinitely long coaxial cable with a constant conductivity is subjected to a time dependent current from an overdamped RLC circuit; the region between the cathode and anode will be considered as a vacuum region (to simplify the problem). The solution to this problem consists of solving equations (4.67) and (4.68) within the three separate regions (cathode, vacuum, and anode regions). The cathode region will be defined as being $0 < r < R_1$ (R_1 is the radius of the cathode); this region will have the same solution as that obtained for an infinitely long conductive wire (Test Case 1). The vacuum region is defined as being $R_1 < r < R_2$ (R_2 is the inner radius of the anode). Within this region the magnetic field is given as:

$$B_\theta = \frac{\mu_o i}{2\pi r} \quad (4.E.22)$$

Because this region is a vacuum the current density and the ∇V term are irrelevant; however the solution for A does not have a straightforward analytical solution. This statement is easily verified if equations (4.64) and (4.68) are considered in terms of both the A_r and A_z components and the boundary conditions given in section 4.3.2. But, since the A variable is merely a means to an end (i.e. in obtaining J and B_θ) and the flux boundary conditions for this variable (on the computational surface of this of this region) are defined by equation (4.E.22), the correct value for B_θ within this region will be obtained from a FEM program that solves equations (4.67) and (4.68). The anode region is defined as being $R_2 < r < R_3$ (R_3 is the outer radius of the anode).

Solving the current density equation within the anode region

The current density equation to be solved within the anode region is given by equation (4.E.5); hence the current density is defined by equation (4.E.6), which will be rewritten to prevent confusion with the previously defined constants A and B as:

$$J_z = A_1 I_0(\alpha r) + B_1 K_0(\alpha r) \quad (4.E.23)$$

In equation (4.E.23) A_1 and B_1 are constants, the boundary conditions within this region are:

$$i(R_2) = 0 \quad (4.E.24)$$

$$i(R_3) = -i \quad (4.E.25)$$

and

$$B_\theta(R_2) = \frac{\mu_o i}{2\pi R_2} \quad (4.E.26)$$

$$B_\theta(R_3) = 0 \quad (4.E.27)$$

Equation (4.E.23) together with the boundary conditions (4.E.24) and (4.E.25) forms an ill posed problem, because integrating equation (4.E.23) using the relationship given in equation (4.E.11) results in equation (4.E.28) (in which equations (4.D.18) and (4.D.20) have been employed).

$$\left[A_1 \frac{1}{\alpha} r I_1(\alpha r) - B_1 \frac{1}{\alpha} r K_1(\alpha r) \right]_{R_2}^{R_3} = -\frac{i\alpha}{2\pi}$$

$$\therefore A_1 \left(\frac{1}{\alpha} R_3 I_1(\alpha R_3) - \frac{1}{\alpha} R_2 I_1(\alpha R_2) \right) + B_1 \left(\frac{1}{\alpha} R_2 K_1(\alpha R_2) - \frac{1}{\alpha} R_3 K_1(\alpha R_3) \right) = -\frac{i\alpha}{2\pi} \quad (4.E.28)$$

This equation cannot be solved, unless either A_1 or B_1 are defined by the user or another boundary condition; however an approximate solution (that approximately satisfies all the boundary conditions for this problem) is obtained if $A_1 = 0$, which simplifies equation (4.E.23) to:

$$J_z = B_1 K_0(\alpha r) \quad (4.E.29)$$

The constant B_1 is then obtained from equation (4.E.28) as:

$$B_1 = \frac{-i\mu_o}{R_2 K_1(\alpha R_2) - R_3 K_1(\alpha R_3)} \quad (4.E.30)$$

Solving the magnetic field equation within the anode region

The magnetic field equation to be solved within the anode region is obtained from equation (4.E.15), in which the current density within this region is defined by equation (4.E.29). Integration of equation (4.E.15) with respect to the r coordinate (after multiplying both sides by r , because the problem is in cylindrical coordinates) and using equation (4.D.20) produces:

$$B_\theta = \frac{-\mu_o B_1}{\alpha} K_1(\alpha r) + \frac{G_B}{r} \quad (4.E.31)$$

In equation (4.E.31) G_B is an integration constant. This integration constant can be found by using the known boundary condition given by equation (4.E.26) as:

$$G_B = \frac{\mu_o i}{2\pi} + \frac{\mu_o B_1 R_2}{\alpha} K_1(\alpha R_2) \quad (4.E.32)$$

For values of $\alpha \gg \gg 1$ the second boundary condition for the magnetic field given by equation (4.E.27) is satisfied because equation (4.E.31) is reduced to:

$$B_\theta = \frac{i\mu_o}{2\pi R_2 K_1(\alpha R_2)} K_1(\alpha r) \quad (4.E.33)$$

If $\alpha \gg \gg 1$ then the above equation is approximately equal to zero at $r = R_3$, because $\frac{K_1(\alpha R_3)}{K_1(\alpha R_2)} \sim 0$.

Solutions of the Magnetic vector potential and the electric scalar potential

A suitable solution for the these variables (when equation (4.67) is considered with respect to the boundary conditions resulting from equation (4.63) and the boundary conditions described in section 4.3.2) is to consider V as being an arbitrary constant, so let $V = 0$; hence A will be defined by equation (4.E.20), which leads to the following expression for A :

$$A_z = -\frac{1}{\sigma(E - F)} B_1 K_0(\alpha r) \quad (4.E.34)$$

Case 3: an infinitely long conductive wire set in a moving reference frame

In this test case the problem of an infinite long conductive wire set within a reference frame moving in the z direction with a constant velocity is subjected to a time dependent current from an overdamped RLC circuit. The solutions to the current density and the magnetic field will be the same as the solutions derived for Test Case 1. However the magnetic vector potential and the electric scalar potential are therefore velocity dependent terms, as can be seen in equations (4.141) and (4.142) (refer to section 4.3.9). A suitable solution for these variables which will satisfy the boundary conditions and the current continuity equation is to take the value for V as an arbitrary constant, so let $V = 0$. Due to this choice for V , the magnetic vector potential is defined by the following equation (to satisfy the normal component of the current density on the conductive surfaces and the current continuity equation, in other words to satisfy the solution of $J_r = 0$ within the problem region):

$$\frac{\partial A_r}{\partial t} = -v_z B_\theta \quad (4.E.35)$$

Substituting the equation for the magnetic field, equation (4.E.18), into equation (4.E.35) results in the following equation:

$$A_r = -v_z \frac{D}{\alpha(E-F)} I_1(\alpha r) \quad (4.E.36)$$

An alternative to the solution of equation (4.E.36) is to let $A_r = 0$. Because of this choice, the gradient of the electric scalar potential, in the r direction, must be defined by equation (4.E.37) in order to satisfy the solution of $J_r = 0$ within the problem domain.

$$\frac{\partial V}{\partial r} = -v_z B_\theta \quad (4.E.37)$$

Substituting the equation for the magnetic field, equation (4.E.18), into equation (4.E.37) results in:

$$\frac{\partial V}{\partial r} = -v_z \frac{D}{\alpha} I_1(\alpha r) \quad (4.E.38)$$

The equation for the electric scalar potential V is derived by integrating equation (4.E.38) with respect to the r direction using equation (4.D.19) (refer to appendix 4D), which results in:

$$V = -v_z \frac{D}{\alpha^2} I_0(\alpha r) + C_V \quad (4.E.39)$$

In equation (4.E.39) C_V is an integration constant, which can be set to any arbitrary value.

Appendix 4F: MATAC

A MATLAB windows based version of MATAC (version 1) can be found on the disk accompanying this thesis. The program resides in the folder marked MATAC. Also contained in the disk are the test cases, spurious test case, and upwinding trial programs that were used to generate some results in this thesis (these are contained in self explanatory folders). To run the MATAC program make sure that the current directory in MATLAB is changed to one that contains the MATAC program, then enter MATAC1 in the command window. Most of the lines in MATAC and its supporting subroutines also contain notes explaining to the user the purpose of the variable or task being performed. A brief description of the MATAC program is described below with supporting excerpts from the program.

Line 19 in MATAC inputs the physical data variables into the program using the subroutine "GetParametersMATAC". "GetParametersMATAC" neatly stores variables, such as conductivity values, allowing the user to easily change any or all of the physical variables.

Lines 42 to 67 describe the basic mesh parameters for the magnetic vector potential (A) elements. The number of elements in the r direction "ELEM2" is a user defined variable on line 42. This variable defines the overall fineness of the mesh. The time parameters are described on lines 75 to 80. MATAC uses a user defined fixed time step "tstep" on line 75. A total number of time steps "nstep" on line 79 is used as a safety measure to terminate the program after a user defined number of time steps have been completed. The mesh used in the anode, cathode, and plasma regions can be altered to either a logarithmic or a linear changing mesh (refer to section 4.3.13) using the tags on lines 92 to 94; if these tags are set to a value of 1 by the user then the mesh will be altered to the chosen mesh scheme. If "MeshLog=1" then a logarithmic mesh will be used in both the anode and cathode regions, while the setting of "Meshlinearchange=1" will implement a linear changing mesh in these regions. If "MeshlinearPlasma=1" then a linear changing mesh will be used in the plasma region and the anode and cathode regions around the plasma. Lines 251 to 285 set the basic mesh parameters relating to the electric scalar potential (V), within the conductive regions of the overall mesh.

The overall mesh (for the magnetic vector potential) is an algebraic mesh, constructed using cubic serendipity elements and stored as a vector called "gcoord". This mesh is constructed using the information given in lines 297 to 441. Once the overall mesh has been constructed the physical data relating to the conductivity and velocity at each node is stored in a vector "NodeRealData" in lines 448 to 486. Depending upon the user defined tags set on lines 91 to 94 (discussed in the preceding paragraph), certain regions of the mesh will be redefined using either a logarithmic or linear changing mesh. This is implemented in lines 506 to 1176.

Information relating to nodes that will also contain a solution for the electric scalar potential (i.e. nodes within a conductive region) are determined from the overall mesh in lines 1189 to 1300. In this process nodes within a conductive region are indexed within a vector called "VApoint", these points are also indexed with respect to the overall mesh using the vector "AVpoint". Data relating to the position of these conductive nodes is stored in the "Vgcoord" vector and the physical data is stored in the "VNodeRealData" vector, both these vectors use the index values presented in the "VApoint" index vector.

The elements for the overall FEM process are formed and stored in lines 1313 to 1460. Elements for the overall mesh are formed from the indexed nodes (for each element) in lines 1334 to 1345, in which the vector "nodes" indexes the nodes that will be used to form an element. The physical data of each element is determined from its position in the overall mesh and is stored in the vector "ELEMRealData" in lines 1349 to 1398. If the element is determined to be in a conductive region, from the statement given on line 1411, then the nodes used in the elements construction are also indexed with respect to the "AVpoint" index using the "nodesAV" vector; these nodes are stored with respect to the index vector "VApoint" in the "Vnodes" vector. This process occurs in lines 1411 to 1446 and is used in the FEM loop to index nodes within a conductive element with respect to the electric scalar potential variable's position within the temporal and system matrices.

Lines 1476 to 1601 set up the nodal connectivity that is used in the FV scheme. The FV mesh is indexed using the nodes in the "Volnodes" vector. The nodes within the plasma region calculated using the FEM mesh are extracted and indexed using the "Volnodes" vector. The coordinates of the FV mesh are stored in a vector called "Volgcoord" in lines 1561 to 1571. The FV elements are formed in lines 1574 to 1577 from the "Volnodes" index and stored in the "VolnodesId" vector.

The sparse matrices used in the AVA FEM loop are defined (i.e. their overall size is set as a sparse matrix containing zeros) in lines 1606 to 1717. The basic storage vectors in the FEM loop are first defined as vectors containing zeros in lines 1739 to 1759. The sparse matrices in the gradV FEM loop are first defined, using zero values, on lines 1771 to 1819. Lines 1862 to 1928 are used to create storage vectors

that will be used to visually present the results of the MATAC program as a series of graphs and vector plots.

The initial solutions for all the variables used in the MATAC program are calculated at “ $t=t_0$ ” in lines 1942 to 2047, in which the FEM variables are stored in the solution vector “fsol” and the initial FV variables are stored in the “Solution” solution vector.

The time loop, which encompasses both the FEM and the FV calculations, is started on line 2072 (it finishes on line 3424). The stopping condition for the MATAC program is defined as an “if” condition on line 2081, in which the program is run until either the plasma has left the accelerator (i.e. defined by the stopping distance on line 2064, which is a combination of a user defined stopping distance and the boundary distance used to approximate the far field boundary conditions of the plasma) or the maximum number of time steps “nstep” (defined by the user on line 78) has been reached.

The current time “t” is updated on line 2085 and the previous solution is stored in the vector “fso12”. The value “t2” is updated on line 2086; this variable is used in the FV loop as the end time used in the Runge-Kutta integration. In lines 2094 to 2108 the working temporal matrix, system matrix and system vector are all reset (i.e. reset equal to zero). The current at time “t” is calculated on lines 2117 to 2145, this value is used as an input for the boundary conditions in the AVA calculation. User defined tags determine whether or not a Dirichlet condition will be set for a component, on a particular boundary in the AVA calculation, on lines 2174 to 2278 (these tags are self explanatory). If the user sets a tag equal to 1 then a Dirichlet boundary condition, for that component, will be set on the chosen boundary. The singular points of the problem (for the AVA calculation) can also be set for the A_r and A_z components on lines 2251 to 2271. The user defined Dirichlet conditions are calculated using the “Boundary9section” subroutine on line 2291 and stored as the output vectors “bcdof”, “bint”, “bmark” and “btype”. “bcdof” is a node index vector, “bcval” is the Dirichlet value, “bint” is an index containing the boundary number and both “bmark” and “btype” are used to index the A and V variables in the temporal and system matrices using the boundary subroutine on line 2637. The Neumann (flux) boundary conditions are defined by the user defined tags on lines 2350 to 2351; if these tags are set equal to 1 then a flux boundary condition will be imposed (these tags are self explanatory). The flux boundary conditions are calculated on lines 2355 to 2412. The nodes to which the flux conditions reside are indexed using the vectors “Fluxn1” to “Fluxn4” with their corresponding positions using the vectors “Fluxr1” to “Fluxr4”. The actual flux boundary value is stored in the “QF” vector.

The AVA FEM loop encompasses lines 2447 to 2650. The integration is carried out using Gauss Legendre numerical integration, the FEM loop is presented below in excerpt 4.F.1 with selected subroutines in excerpts 4.F.2 to 4.F.14. The FEM calculation starts by first determining whether or not the current element is in a conductive region on line 2453 (i.e. should V be included in the calculation within the element). The degrees of freedom are set for the current element in lines 2455 to 2465. The coordinates and nodes that make up the current element, and the indexing of these nodes, are determined on lines 2467 to 2497. The Gauss Legendre integration points and weights are determined on line 2530. The numerical integration is conducted within lines 2518 to 2594. Within this loop the shape function is defined on line 2549, the Jacobian of the transformation is calculated on line 2552 and the isoparametric shape functions and their derivatives (with respect to the physical coordinate system) are calculated on lines 2563 to 2567. The nodes used within an element (and the variables solved at the nodes) are indexed on line 2559. The system vector is calculated on line 2579, the system matrix is determined on line 2586 and the temporal system matrix is defined on line 2592 (for the current element). The calculated matrices and vector are assembled into the temporal matrix, system matrix and system vector on lines 2595 to 2603. The flux boundary conditions are implemented on line 2622. The overall system vector is formed on line 2628, using the backwards time integration formulation. Then the Dirichlet conditions are implemented on line 2637. Finally, the system is solved (for the current time step) using the sparse MATLAB LU solver on line 2650. The solution values for A_r , A_z and B_θ are extracted within the conductive region on lines 2667 to 2709. The extracted B_θ values are used as part of the boundary conditions in the gradV FEM loop. The gradV FEM loop lies between lines 2713 to 2949. The boundary conditions for the gradV loop are calculated through lines 2767 to 2796, in which the subroutine “Boundary9sectionVr” and “Boundary9sectionVz” are used to calculate the Dirichlet conditions in much the same manner that “Boundary9section” does. The gradV FEM calculation is conducted in-between lines 2760 to 2949, using the same basic techniques and subroutines that are used in the AVA FEM loop. Lines 3012 to 3019 calculate the current density and magnetic field within the conductive region. The current density and magnetic field within the plasma region is used in the FV loop to calculate the force acting on the plasma at the current time “t”. A graphical display of the current density and magnetic field plots is presented for each time step on lines 3107 to 3135.

The FV loop, presented in excerpt 4.F.15 (with selected subroutines 4.F.16 to 4.F.18), is used to calculate the force on the plasma at the current time “t” and from this value the velocity and distance travelled by the plasma (within the current time step) is calculated using a fifth order Runge-Kutta solver. The FV loop is conducted on lines 3143 to 3215. The FV elements are determined on lines 3164 to 3180 and the current density and the magnetic field for the current FV element is extracted on lines 3175 to 3180. The product of $\mathbf{J} \times \mathbf{B}$ is calculated on line 3196. After the sum of $\mathbf{J} \times \mathbf{B}$ across the plasma has been determined a fifth order Runge-Kutta solver (the MATLAB “ode45” algorithm) and the “JrBoMove” subroutine determines the velocity and the distance travelled by the plasma in the current time step. Finally, the velocity of the moving conductors (i.e. the anode and cathode regions) is updated for use in the next time step in lines 3276 to 3411. The remainder of the MATAC program, lines 3447 to 3750 are used to graphically display the end results of the program in a series of graphs and vector plots.

Selected excerpts from MATAC

```
%loop for elemental matrices and vectors
for iel=1:EELEM          %loop for elements

    iel;

    %Determine properties of the current element
    ELEMTtype=ELEMRealData(iel,3);      %if ELEMTtype==1 then is in a conductive region and "V" is included

    %Set degrees of freedom for current element - determined by ELEMTtype

    %conductive region "A" and "V"
    if (ELEMTtype==1)
        ELEMndof=ndof1;
    end;

    %non-conductive region "A" only
    if (ELEMTtype==0)
        ELEMndof=ndof2;
    end;

    %Extract nodes for current element, "nd" describes the nodes related
    %to the "A" mesh and "vnd" describes the nodes related to the "V"
    %mesh. "vnd" is only set for conductive regions.

    nd=zeros(nnel,1);
    vnd=zeros(nnel,1);

    r1=zeros(nnel,1);
    r2=zeros(nnel,1);

    for itel=1:nnel

        %Set "nd" and "vnd" for conductive regions
        if (ELEMTtype==1)
            nd(itel)=nodes(iel,itel);
            vnd(itel)=nodesAV(iel,itel);
        end;

        %Set "nd" only for non-conductive regions
        if (ELEMTtype==0)
            nd(itel)=nodes(iel,itel);
        end;

        %extract coordinates
        r1(itel)=gcoord(nd(itel),1);      %extract z coordinate for itel node
        r2(itel)=gcoord(nd(itel),2);      %extract r coordinate for itel node

    end;    %end nnel loop

%Set tag to display ELEMTtype, ELEMndof, "nd" and "vnd" for current element
DisplayElementindexnodes=0;
```

```

if (DisplayElementindexnodes==1)
iel
ELEMType
ELEMndof
r1
r2
nd'
vnd'
end;

%Set value of sigma for current element

sigma=ELEMRealData(iel,2);      %extract element sigma value
vz=ELEMRealData(iel,4);        %extract element velocity value

%
%

%Determine points and weighting coefficients for Gaussian Legendre
%quadrature

[point2,weight2]=Guass2D(numberintpointx,numberintpointy);

%numerical integration loop

%extract points and weighting coefficients for each element node
for ix=1:numberintpointx

    %set normal points and weights in x
    x=point2(ix,1);
    weightx=weight2(ix,1);

    for iy=1:numberintpointy

        %set normal points and weights in y
        y=point2(iy,2);
        weighty=weight2(iy,2);

        [shape,dshape,dshapedn]=Shape12(x,y);

        [Jacobian2D]=Jacobian2DlinearRectangle(nnel,dshape,dshapedn,r1,r2);

        %Jacobian2D=Jacobian2DlinearRectangle(nnel,dshape,dshapedn,r1,r2);

        detJacob=det(Jacobian2D);

        invJacob=inv(Jacobian2D);

        %Determine isoparametric shape functions with respect to the
        %physical coordinate system

        [H]=HShape(nnel,shape,weightx,weighty,detJacob);

        [dHdx]=DerivativeHShapeDerivativeX(nnel,dshape,dshapedn,invJacob,weightx,weighty,detJacob);

        [dHdy]=DerivativeHShapeDerivativeY(nnel,dshape,dshapedn,invJacob,weightx,weighty,detJacob);

        indexAVA=extractsysdof2DAVA(nd,vnd,ELEMType,ELEMndof,VNodeStart,ndof,Vndof,nnel); %extract system dofs
        indexAVA;

        %f=isosteadyvectorAVABol2point(H,dHdx,dHdy,r1,r2,sigma,uo,E,F,ELEMType,ELEMndof,nnel); %compute vector matrix "F"
        f=isosteadyvectorAVABol2point2(H,dHdx,dHdy,r1,r2,sigma,uo,ELEMType,ELEMndof,nnel); %compute vector matrix "F"

        k=isoKBackelementmatrix2DAVABoSKKR6b(H,dHdx,dHdy,r1,r2,S,sigma,uo,ELEMType,ELEMndof,ndof,Vndof,nnel,tstep); %compute element
        matrix "K"

        k=k*weightx*weighty*detJacob;

```

```

m=isoMBackelementmatrix2DAVABoSKKR6VelocityTest1b(H,dHdx,dHdy,r1,r2,S,vz,sigma,uo,ELEMTtype,ELEMndof,ndof,Vndof,nnel,tstep);

m=m*weightx*weighty*detJacob;

kk=kassemble(kk,k,indexAVA);           %assemble system matrix

kk;

mm=massemble(mm,m,indexAVA);           %assemble system matrix

mm;

ff=fassemble(ff,f,indexAVA);           %assemble system vector

ff;

end; %end Gaussian numberintpointsy loop
end; %end Gaussian numberintpointsx loop

end; %end element loop

%
%
%

%Apply Flux boundary conditions

[ff]=isoSurfaceFlux3sectionAz12point(ff,QF,Fluxn1,Fluxn2,Fluxn3,Fluxn4,Fluxmark,Fluxr1,Fluxr2,Fluxr3,Fluxr4,FluxTypeBoundary,numberlineintp
oints,nlinear,ndof);

%Form overall matrices and vectors

gg=tstep*ff+kk*fsol; %form system vector

%
%

%Apply boundary conditions

[mm,gg]=boundarycondition2ComAVA(mm,gg,bcdof,bcval,bmark,btype,VNodeStart,ndof,Vndof);
%[mm,gg]=boundarycondition2ComSymAVA(mm,gg,bcdof,bcval,bmark,btype,VNodeStart,ndof,Vndof);

ff;
ff1;
gg;
kk;
mm;

fsol=mm\gg; %compute solution

```

Excerpt 4.F.1: Excerpt containing the FEM loop used to solve the AVA system in MATAC

```

function [point2,weight2]=Guassian2D(numberintpointsx,numberintpointsy)

%This m-file calculates the integration points and weighting coefficients
%for the Gaussian Legendre quadrature for 2D integration by using the 1D
%Gaussian Legendre quadrature routine Guassian1D

%Determine the size of the points and weighting coefficients matrix. Both
%point2 and weight2 are two column matrices, which state both the x and y
%components.

%Determine size of matrices
if (numberintpointsx>numberintpointsy)

```

```

    numberpoints=numberintpointsx;
else
    numberpoints=numberintpointsy;
end;

%initialise matrices

point2=zeros(numberpoints,2);
weight2=zeros(numberpoints,2);

%find points and weighting coefficients

%for x coordinate using 1D Gaussian Legendre quadrature

[pointx,weightx]=Guassian1D(numberintpointsx);

%for y coordinate using 1D Gaussian Legendre quadrature

[pointy,weighty]=Guassian1D(numberintpointsy);

%store x values for points and weights
for ix=1:numberintpointsx
    point2(ix,1)=pointx(ix);
    weight2(ix,1)=weightx(ix);
end;

%store y values for points and weights
for iy=1:numberintpointsy
    point2(iy,2)=pointy(iy);
    weight2(iy,2)=weighty(iy);
end;

```

Excerpt 4.F.2: Subroutine used to conduct a two dimensional Gauss Legendre integration used in MATAC

```

function [point1,weight1]=Guassian1D(numberintpoints)

%This m-file calculates the integration points and weighting coefficients
%for the Gaussian-Legendre quadrature for 1D integration where a function
%f(x) is integrated as follows:
%Int(f(x))=Sum(f(x)*W)
%Where "W" is the weighting coefficient and "x" is the integration point
%The Gaussian-Legendre quadrature gives exact answers for a polynomial
%of order "2n-1" by an "n" number of points.

point1=zeros(numberintpoints,1);
weight1=zeros(numberintpoints,1);

%Derive weighting for given point of Gaussian-Legendre

%1 point quadrature

if (numberintpoints==1)
    point1(1)=0;
    weight1(1)=2;
end;

%2 point quadrature

if (numberintpoints==2)
    point1(1)=-1/(sqrt(3));
    point1(2)=1*point1(1);
    weight1(1)=1;
    weight1(2)=weight1(1);
end;

%3 point quadrature

if (numberintpoints==3)
    point1(1)=-0.774596669241483;
    point1(2)=0;
    point1(3)=point1(1);
    weight1(1)=0.555555555555556;
    weight1(2)=0.888888888888889;
    weight1(3)=weight1(1);
end;

%4 point quadrature

if (numberintpoints==4)

```

```

point1(1)=-0.861136311594053;
point1(2)=-0.339981043584856;
point1(3)=-point1(2);
point1(4)=point1(1);
weight1(1)=0.347854845137454;
weight1(2)=0.652145154862546;
weight1(3)=weight1(2);
weight1(4)=weight1(1);
end;

```

Excerpt 4.F.3: Subroutine used to conduct a one dimensional Gauss Legendre numerical integration in MATAC

```

function [shape,dshapede,dshapedn]=Shape12(evalue,nvalue)

%This m-file calculates the isoparametric shape functions for a linear
%rectangular shape

%Overall shape functions

shape(1)=(1/32)*(1-evalue)*(1-nvalue)*(9*(evalue^2+nvalue^2)-10);
shape(2)=(1/32)*(1+evalue)*(1-nvalue)*(9*(evalue^2+nvalue^2)-10);
shape(3)=(1/32)*(1+evalue)*(1+nvalue)*(9*(evalue^2+nvalue^2)-10);
shape(4)=(1/32)*(1-evalue)*(1+nvalue)*(9*(evalue^2+nvalue^2)-10);
shape(5)=(9/32)*(1-nvalue)*(1-evalue^2)*(1-3*evalue);
shape(6)=(9/32)*(1-nvalue)*(1-evalue^2)*(1+3*evalue);
shape(7)=(9/32)*(1+evalue)*(1-nvalue^2)*(1-3*nvalue);
shape(8)=(9/32)*(1+evalue)*(1-nvalue^2)*(1+3*nvalue);
shape(9)=(9/32)*(1+nvalue)*(1-evalue^2)*(1+3*evalue);
shape(10)=(9/32)*(1+nvalue)*(1-evalue^2)*(1-3*evalue);
shape(11)=(9/32)*(1-evalue)*(1-nvalue^2)*(1+3*nvalue);
shape(12)=(9/32)*(1-evalue)*(1-nvalue^2)*(1-3*nvalue);

%Derivative of shape function with respect to e coordinate

dshapede(1)=(1/32)*(-1)*(1-nvalue)*(9*(evalue^2+nvalue^2)-10)+(1/32)*(1-evalue)*(1-nvalue)*(9*(2*evalue));
dshapede(2)=(1/32)*(1)*(1-nvalue)*(9*(evalue^2+nvalue^2)-10)+(1/32)*(1+evalue)*(1-nvalue)*(9*(2*evalue));
dshapede(3)=(1/32)*(1)*(1+nvalue)*(9*(evalue^2+nvalue^2)-10)+(1/32)*(1+evalue)*(1+nvalue)*(9*(2*evalue));
dshapede(4)=(1/32)*(-1)*(1+nvalue)*(9*(evalue^2+nvalue^2)-10)+(1/32)*(1-evalue)*(1+nvalue)*(9*(2*evalue));
dshapede(5)=(9/32)*(1-nvalue)*(-2*evalue)*(1-3*evalue)+(9/32)*(1-nvalue)*(1-evalue^2)*(-3);
dshapede(6)=(9/32)*(1-nvalue)*(-2*evalue)*(1+3*evalue)+(9/32)*(1-nvalue)*(1-evalue^2)*(3);
dshapede(7)=(9/32)*(1)*(1-nvalue^2)*(1-3*nvalue);
dshapede(8)=(9/32)*(1)*(1-nvalue^2)*(1+3*nvalue);
dshapede(9)=(9/32)*(1+nvalue)*(-2*evalue)*(1+3*evalue)+(9/32)*(1+nvalue)*(1-evalue^2)*(3);
dshapede(10)=(9/32)*(1+nvalue)*(-2*evalue)*(1-3*evalue)+(9/32)*(1+nvalue)*(1-evalue^2)*(-3);
dshapede(11)=(9/32)*(-1)*(1-nvalue^2)*(1+3*nvalue);
dshapede(12)=(9/32)*(-1)*(1-nvalue^2)*(1-3*nvalue);

%Derivative of shape function with respect to n coordinate

dshapedn(1)=(1/32)*(1-evalue)*(-1)*(9*(evalue^2+nvalue^2)-10)+(1/32)*(1-evalue)*(1-nvalue)*(9*(2*nvalue));
dshapedn(2)=(1/32)*(1+evalue)*(-1)*(9*(evalue^2+nvalue^2)-10)+(1/32)*(1+evalue)*(1-nvalue)*(9*(2*nvalue));
dshapedn(3)=(1/32)*(1+evalue)*(1)*(9*(evalue^2+nvalue^2)-10)+(1/32)*(1+evalue)*(1+nvalue)*(9*(2*nvalue));
dshapedn(4)=(1/32)*(1-evalue)*(1)*(9*(evalue^2+nvalue^2)-10)+(1/32)*(1-evalue)*(1+nvalue)*(9*(2*nvalue));
dshapedn(5)=(9/32)*(-1)*(1-evalue^2)*(1-3*evalue);
dshapedn(6)=(9/32)*(-1)*(1-evalue^2)*(1+3*evalue);
dshapedn(7)=(9/32)*(1+evalue)*(-2*nvalue)*(1-3*nvalue)+(9/32)*(1+evalue)*(1-nvalue^2)*(-3);
dshapedn(8)=(9/32)*(1+evalue)*(-2*nvalue)*(1+3*nvalue)+(9/32)*(1+evalue)*(1-nvalue^2)*(3);
dshapedn(9)=(9/32)*(1)*(1-evalue^2)*(1+3*evalue);
dshapedn(10)=(9/32)*(1)*(1-evalue^2)*(1-3*evalue);
dshapedn(11)=(9/32)*(1-evalue)*(-2*nvalue)*(1+3*nvalue)+(9/32)*(1-evalue)*(1-nvalue^2)*(3);
dshapedn(12)=(9/32)*(1-evalue)*(-2*nvalue)*(1-3*nvalue)+(9/32)*(1-evalue)*(1-nvalue^2)*(-3);

```

Excerpt 4.F.4: Subroutine “Shape12” contains the shape functions used in the cubic serendipity isoparametric elements used in MATAC

```

function [Jacobian2D]=Jacobian2DlinearRectangle(nnel,dshapede,dshapedn,r1,r2)

%This m-file calculates the Jacobian for a two dimensional rectangular element
%
%J11=dxde=Sum(dHde*x)
%J12=dyde=Sum(dHde*y)
%J21=dxdn=Sum(dHdn*x)
%J22=dydn=Sum(dHdn*y)

Jacobian2D=zeros(2,2);

```

```
%loop for Jacobian
for it=1:nnel
    Jacobian2D(1,1)=Jacobian2D(1,1)+r1(it)*dshapede(it);
    Jacobian2D(1,2)=Jacobian2D(1,2)+r2(it)*dshapede(it);
    Jacobian2D(2,1)=Jacobian2D(2,1)+r1(it)*dshapedn(it);
    Jacobian2D(2,2)=Jacobian2D(2,2)+r2(it)*dshapedn(it);
end;
```

Excerpt 4.F.5: Subroutine used to calculate the Jacobian of the elements used in MATAC

```
function [H]=HShape(nnel,shape,weightx,weighty,detJacob)

%This m-file calculates the isoparametric shape functions with respect to
%the physical coordinates

for it=1:nnel
    H(it)=shape(it);
end;
```

Excerpt 4.F.6: Subroutine used to calculate the isoparametric shape functions in the physical coordinate system

```
function [dHdx]=DerivativeHShapeDerivative(nnel,dshapede,dshapedn,invJacob,weightx,weighty,detJacob)

%This m-file calculates the derivative of the isoparametric shape function
%with respect to the first coordinate in the physical coordinate system

for it=1:nnel
    dHdx(it)=invJacob(1,1)*dshapede(it)+invJacob(1,2)*dshapedn(it);
end;
```

Excerpt 4.F.7: Subroutine used to calculate the derivative of the isoparametric shape functions, with respect to the z coordinate, in the physical coordinate system

```
function [dHdy]=DerivativeHShapeDerivativey(nnel,dshapede,dshapedn,invJacob,weightx,weighty,detJacob)

%This m-file calculates the derivative of the isoparametric shape function
%with respect to the second coordinate in the physical coordinate system

for it=1:nnel
    dHdy(it)=invJacob(2,1)*dshapede(it)+invJacob(2,2)*dshapedn(it);
end;
```

Excerpt 4.F.8: Subroutine used to calculate the derivative of the isoparametric shape functions, with respect to the r coordinate, in the physical coordinate system

```
function [f]=isosteadyvectorAVABol2point2(H,dHdx,dHdy,r1,r2,sigma,uo,ELEMTtype,ELEMndof,nnel)

%This function calculates the element vector "f" for the current element iel,
%for the AVA formulation. The value of ELEMTtype will determine the value
%and size of "f". For conducting regions both "A" and "V" are included, but
%for non-conducting regions only "A" is included.

%set "f" for a conducting region
```

[illegible]

Excerpt 4.F.9: Subroutine used to calculate the system vector for an element

```
function [k]=isoKBackelementmatrix2DAVBBoSKKR6b(H,dHdx,dHy,r1,r2,S,sigma,uo,ELEMTType,ELEMndof,ndof,Vndof,nnel,tstep)

%This function computes the elemental matrix "K" for the current element
%iel for the AVA formulation. The value of ELEMTType will determine the
%values and size of "k". In conducting regions "A" and "V" are included. In
%non-conducting regions only "A" is included.

%calculate rc

lengthrc=length(r2);
rc=0;

for this=1:lengthrc
    rc=(1/lengthrc)*r2(this)+rc;
end;

%Matrix K

%Set "k" for a conducting region i.e. ELEMTType==1

if (ELEMTType==1)

for i1=1:nnel
    for i2=1:nnel

        %matrix points for component 1: Az
        p1node=(i1-1)*ELEMndof+1;
        p2node=(i2-1)*ELEMndof+1;

        %matrix points for component 2: Ar
        q1node=(i1-1)*ELEMndof+2;
        q2node=(i2-1)*ELEMndof+1;

        %matrix points for component 4: Bo
        s1node=(i1-1)*ELEMndof+3;
        s2node=(i2-1)*ELEMndof+1;

        %matrix points for component 3: V
        r1node=(i1-1)*ELEMndof+4;
        r2node=(i2-1)*ELEMndof+1;

%component 1: Az
k(p1node,p2node)=rc*(sigma)*(H(i1)*H(i2));
k(p1node,(p2node+1))=0;
k(p1node,(p2node+2))=0;
k(p1node,(p2node+3))=0;

%component 2: Ar
k(q1node,q2node)=0;
k(q1node,(q2node+1))=rc^3*(sigma)*(H(i1)*H(i2));
k(q1node,(q2node+2))=0;
k(q1node,(q2node+3))=0;

%component 4: Bo
k(s1node,s2node)=0;
k(s1node,(s2node+1))=0;
k(s1node,(s2node+2))=0;

end
end
end
```



```

k(s1node,(s2node+3))=0;

%component 3: V
k(r1node,r2node)=-rc*sigma*H(i1)*dHdx(i2);
k(r1node,(r2node+1))=-2*rc*sigma*H(i1)*H(i2)-rc^2*sigma*H(i1)*dHdy(i2);
k(r1node,(r2node+2))=0;
k(r1node,(r2node+3))=0;

    end;
end;

end;    %end if statement for ELEMTtype==1

%Set "k" for a non-conductive region i.e. ELEMTtype==0

if (ELEMTtype==0)

for i1=1:nnel
    for i2=1:nnel

        %matrix points for component 1: Az
        p1node=(i1-1)*ELEMndof+1;
        p2node=(i2-1)*ELEMndof+1;

        %matrix points for component 2: Ar
        q1node=(i1-1)*ELEMndof+2;
        q2node=(i2-1)*ELEMndof+1;

        %matrix points for component 4: Bo
        s1node=(i1-1)*ELEMndof+3;
        s2node=(i2-1)*ELEMndof+1;

        %component 1: Az
        k(p1node,p2node)=rc*(sigma)*(H(i1)*H(i2));
        k(p1node,(p2node+1))=0;
        k(p1node,(p2node+2))=0;

        %component 2: Ar
        k(q1node,q2node)=0;
        k(q1node,(q2node+1))=rc^3*(sigma)*(H(i1)*H(i2));
        k(q1node,(q2node+2))=0;

        %component 4: Bo
        k(s1node,s2node)=0;
        k(s1node,(s2node+1))=0;
        k(s1node,(s2node+2))=0;

    end;
end;

end;    %end if statement for ELEMTtype==0

```

Excerpt 4.F.10: Subroutine used to calculate the system matrix for an element

```

function
[m]=isoMBackelementmatrix2DAVABoSKKR6VelocityTest1b(H,dHdx,dHdy,r1,r2,S,vz,sigma,uo,ELEMTtype,ELEMndof,ndof,Vndof,nnel,tstep)

%This function computes the elemental matrix "M" for the current element
%iel for the AVA formulation. The value of ELEMTtype will determine the
%values and size of "k". In conducting regions "A" and "V" are included. In
%non-conducting regions only "A" is included.

%calculate rc

lengthrc=length(r2);
rc=0;

for this=1:lengthrc
    rc=(1/lengthrc)*r2(this)+rc;
end;

```

```

%Matrix M

%Set "m" for a conducting region i.e. ELEMType==1

if(ELEMType==1)

for i1=1:nnel
    for i2=1:nnel

        %matrix points for component 1: Az
        p1node=(i1-1)*ELEMndof+1;
        p2node=(i2-1)*ELEMndof+1;

        %matrix points for component 2: Ar
        q1node=(i1-1)*ELEMndof+2;
        q2node=(i2-1)*ELEMndof+1;

        %matrix points for component 4: Bo
        s1node=(i1-1)*ELEMndof+3;
        s2node=(i2-1)*ELEMndof+1;

        %matrix points for component 3: V
        r1node=(i1-1)*ELEMndof+4;
        r2node=(i2-1)*ELEMndof+1;

%component 1: Az
m(p1node,p2node)=(rc*(dHdy(i1)*dHdy(i2))+S*(rc*(dHdx(i1)*dHdx(i2))))*(tstep/uo)+rc*(sigma)*(H(i1)*H(i2));
m(p1node,(p2node+1))=(-rc^2*(dHdy(i1)*dHdx(i2))+S*(2*rc*(dHdx(i1)*H(i2))+rc^2*(dHdx(i1)*dHdy(i2))))*(tstep/uo);
m(p1node,(p2node+2))=0;
m(p1node,(p2node+3))=rc*(sigma)*H(i1)*dHdx(i2)*tstep;

%component 2: Ar
m(q1node,q2node)=(-rc^2*(dHdx(i1)*dHdy(i2))+S*(2*rc*(H(i1)*dHdx(i2))+rc^2*(dHdy(i1)*dHdx(i2))))*(tstep/uo)-
rc^2*sigma*vz*H(i1)*dHdy(i2)*tstep;
m(q1node,(q2node+1))=(rc^3*(dHdx(i1)*dHdx(i2))+S*(4*rc*(H(i1)*H(i2))+2*rc^2*(H(i1)*dHdy(i2))+2*rc^2*(dHdy(i1)*H(i2))+rc^3*(dHdy(i1)*dHdy(i2))))*(tstep/uo)+rc^3*(sigma)*(H(i1)*H(i2))+rc^3*sigma*vz*H(i1)*dHdx(i2)*tstep;
m(q1node,(q2node+2))=0;
m(q1node,(q2node+3))=rc^2*(sigma)*H(i1)*dHdy(i2)*tstep;

%component 4: Bo
m(s1node,s2node)=rc*H(i1)*dHdy(i2);
m(s1node,(s2node+1))=-rc^2*H(i1)*dHdx(i2);
m(s1node,(s2node+2))=rc*H(i1)*H(i2);
m(s1node,(s2node+3))=0;

%component 3: V
m(r1node,r2node)=-rc*sigma*vz*dHdy(i1)*dHdy(i2)*tstep-rc*sigma*H(i1)*dHdx(i2);
m(r1node,(r2node+1))=rc^2*sigma*vz*dHdy(i1)*dHdx(i2)*tstep-2*rc*sigma*H(i1)*H(i2)-rc^2*sigma*H(i1)*dHdy(i2);
m(r1node,(r2node+2))=0;
m(r1node,(r2node+3))=rc*sigma*dHdx(i1)*dHdx(i2)*tstep+rc*sigma*dHdy(i1)*dHdy(i2)*tstep;

    end;
end;

end;    %end if statement for ELEMType==1

%Set "m" for a non-conductive region i.e. ELEMType==0

if(ELEMType==0)

for i1=1:nnel
    for i2=1:nnel

        %matrix points for component 1: Az
        p1node=(i1-1)*ELEMndof+1;
        p2node=(i2-1)*ELEMndof+1;

        %matrix points for component 2: Ar
        q1node=(i1-1)*ELEMndof+2;
        q2node=(i2-1)*ELEMndof+1;

        %matrix points for component 4: Bo
        s1node=(i1-1)*ELEMndof+3;
        s2node=(i2-1)*ELEMndof+1;

```

```

%component 1: Az
m(p1node,p2node)=(rc*(dHdy(i1)*dHdy(i2))+S*(rc*(dHdx(i1)*dHdx(i2))))*(tstep/uo)+rc*(sigma)*(H(i1)*H(i2));
m(p1node,(p2node+1))=(-rc^2*(dHdy(i1)*dHdx(i2))+S*(2*rc*(dHdx(i1)*H(i2))+rc^2*(dHdx(i1)*dHdy(i2))))*(tstep/uo);
m(p1node,(p2node+2))=0;

%component 2: Ar
m(q1node,q2node)=(-rc^2*(dHdx(i1)*dHdy(i2))+S*(2*rc*(H(i1)*dHdx(i2))+rc^2*(dHdy(i1)*dHdx(i2))))*(tstep/uo)-
rc*sigma*vz*H(i1)*dHdy(i2)*tstep;
m(q1node,(q2node+1))=(rc^3*(dHdx(i1)*dHdx(i2))+S*(4*rc*(H(i1)*H(i2))+2*rc^2*(H(i1)*dHdy(i2))+2*rc^2*(dHdy(i1)*H(i2))+rc^3*(dHdy(i1)*d
Hdy(i2))))*(tstep/uo)+rc^3*(sigma)*(H(i1)*H(i2))+rc^2*sigma*vz*H(i1)*dHdx(i2)*tstep;
m(q1node,(q2node+2))=0;

%component 4: Bo
m(s1node,s2node)=rc*H(i1)*dHdy(i2);
m(s1node,(s2node+1))=-rc^2*H(i1)*dHdx(i2);
m(s1node,(s2node+2))=rc*H(i1)*H(i2);

end;
end;

end;    %end if statement for ELEMType==0

```

Excerpt 4.F.11: Subroutine used to calculate the temporal system matrix for an element

```

function
[ff]=isoSurfaceFlux3sectionAz12point(ff,Q,Fluxn1,Fluxn2,Fluxn3,Fluxn4,Fluxmark,Fluxr1,Fluxr2,Fluxr3,Fluxr4,FluxTypeBoundary,numberlineintpo
ints,nlinear,ndof)

%This functions inputs the flux across a surface for the case of Int(W*Q)dS
%where "W" is the test function across the boundary and "Q" is the average
%Flux

this=length(Fluxmark);

Displayinput=0;

if (Displayinput==1)
Fluxn1
Fluxn2
Fluxn3
Fluxn4
Fluxr1
Fluxr2
Fluxr3
Fluxr4
Fluxmark
FluxTypeBoundary
Q
end;

for i=1:this

[linepoint1,lineweight1]=Gaussian1D(numberlineintpoints);

for im=1:numberlineintpoints

rlinear=zeros(4,1);

rlinear(1)=Fluxr1(i);
rlinear(2)=Fluxr2(i);
rlinear(3)=Fluxr3(i);
rlinear(4)=Fluxr4(i);

rlinear;

FluxType=FluxTypeBoundary(i);    %determine flux boundary type

xline=linepoint1(im);
weightxline=lineweight1(im);

[lineshape,linedshapede]=Shapeline4(xline);

Jacobian1D=Jacobian1D3point(nlinear,linedshapede,rlinear);

[Hline]=HShapeline(nlinear,lineshape,weightxline);

```

```

%display flux variable values

DisplayFluxVariables=0;
if DisplayFluxVariables==1
    i
    FluxType
    weightxline
    JacobianID
    Hline
end;

%calculate system vector

node1=(Fluxn1(i)-1)*ndof+Fluxmark(i);
node2=(Fluxn2(i)-1)*ndof+Fluxmark(i);
node3=(Fluxn3(i)-1)*ndof+Fluxmark(i);
node4=(Fluxn4(i)-1)*ndof+Fluxmark(i);

ff(node1)=ff(node1)+Q(i)*Hline(1)*(JacobianID*weightxline);
ff(node2)=ff(node2)+Q(i)*Hline(2)*(JacobianID*weightxline);
ff(node3)=ff(node3)+Q(i)*Hline(3)*(JacobianID*weightxline);
ff(node4)=ff(node4)+Q(i)*Hline(4)*(JacobianID*weightxline);

ff;

end;

end;

```

Excerpt 4.F.12: Subroutine used to calculate the flux boundary conditions

```

function [Hline]=HShapeLine(nlinear,lineshape,weightxline)

%This m-file calculates the linear isoparametric shape functions with respect to
%the physical coordinates

for it=1:nlinear
    Hline(it)=lineshape(it);
end;

```

Excerpt 4.F.13: Subroutine used to calculate the linear shape functions for the flux boundary elements

```

function [kk,ff]=boundarycondition2ComAVA(kk,ff,bcdof,bcval,bmark,btype,VNodeStart,ndof,Vndof)

%This function applies the boundary conditions to the effective system
%matrix and vector for the case of the AVA formulation. This is based upon
%the value of btype which determines where the value is placed. If btype=1
%then it is an "A" value, if btype=2 then it is a "V" value.
%
%This function applies boundary conditions unsymmetrically

n1=length(bcdof);
sdof=size(kk);

for i=1:n1

    %Set "A" values

    if (btype(i)==1)

        c=bcdof(i);
        d=bmark(i);
        point=(c-1)*ndof+d;

        for j=1:sdof
            kk(point,j)=0;
        end;
    end;
end;

```

```

kk(point,point)=1;
ff(point)=bcval(i);

end; %end if statement for btype==1

%Set "V" values

if (btype(i)==2)

c=bcdoef(i);
d=bmark(i);
point=(c-1)*Vndof+d+VNodeStart;

for j=1:sdof
    kk(point,j)=0;
end;

kk(point,point)=1;
ff(point)=bcval(i);

end; %end if statement for btype==2

end; %end loop to set boundary conditions

```

Excerpt 4.F.14: Subroutine used to input Dirichlet conditions into the temporal system matrix

```

%Finite Volume Sum loop to calculate Force on the plasma block

%initialisation Sum

VolSum=0;

%loop for elemental matrices and vectors
for iel=1:VolEELEM %loop for elements

    Volr1=zeros(Volnnel,1);
    Volr2=zeros(Volnnel,1);
    Volnd=zeros(Volnnel,1);
    VolVnd=zeros(Vnnel,1);
    VolJr=zeros(Vnnel,1);
    VolBo=zeros(Vnnel,1);

    %extract current volume nodes

    for itel=1:Volnnel
        Volnd(itel)=Volnodes(iel,itel); %extract first node for element itel
        Volr1(itel)=Volgcoord(Volnd(itel),1); %extract z coordinate for itel node
        Volr2(itel)=Volgcoord(Volnd(itel),2); %extract r coordinate for itel node
    end;

    iel;
    Volnd;
    Volr1;
    Volr2;

    %extract current V nodes with respect to the volume nodes
    for item=1:Vnnel
        VolVnd(item)=VolnodesV(iel,item);
        VolJr(item)=Jr(VolnodesV(iel,item));
        VolBo(item)=BoConductor(VolnodesV(iel,item));
    end;

    VolVnd;
    VolJr;
    VolBo;

    %set VolELEMDataTag for current element
    VolELEMDataTag=VolELEMRealData(iel,1);

    iel;

```

```

VolELEMDDataTag;

%Extract Average of values for current element
XSum=AverageSumJrBo2(VolVnd,VolJr,VolBo,VolELEMDDataTag);

%Compute Area of current element volume
Area=VolShapeArea(Volr1,Volr2);

%Compute Average "r" value "rc" for the current element
lengthVolrc=length(Volr2);
Volrc=0;

for thisrc=1:lengthVolrc
    Volrc=(1/lengthVolrc)*Volr2(thisrc)+Volrc;
end;

%Compute VolSum
VolSum=VolSum+2*pi*Volrc*Area*XSum;

end;

%Update value for the force on the plasma block before VolSum is reset
ForceBlock=VolSum

%
%
%

%Calculate velocity and distance travelled by the plasma block in the
%current time step using ode45

[tt,X]=ode45('JrBoMove',[t1,t2],X0);

%extract current values for distance travelled and velocity
sizeX=length(X);

Distance=X(sizeX,1)
vo=-X(sizeX,2)

%Reset initial solution for the calculation of velocity and distance in
%ode45
X0=[Distance,-vo];
t1=t2;

clear X
clear tt

%Update Solution
Solution(ntake,1)=t;
Solution(ntake,2)=i;
Solution(ntake,3)=-vo;
Solution(ntake,4)=Distance;
Solution(ntake,5)=ForceBlock;

```

Excerpt 4.F.15: Excerpt containing the FV loop used to determine the velocity and distance moved by the plasma for the current time step

```

function XSum=AverageSumJrBo2(VolVnd,VolJr,VolBo,VolELEMDDataTag)

%This function calculates the average value of the fore term which is a
%product of Jr and Bo for a linear rectangular finite volume element. This
%is done by extracting the input values for the VolVnd element nodes of the
%V mesh and then averaging them.

sizeVolnd=length(VolVnd);

XSum=0;

```

```
%Set values for inner elements

if (VolELEMDataTag==0)
for gm=1:sizeVolInd
    XSum=XSum+(1/sizeVolInd)*VolJr(gm)*VolBo(gm);
end;
end;

%Set values for cathode/plasma elements

if (VolELEMDataTag==1)
for gm=1:sizeVolInd

    if (gm==1 | gm==2 | gm==5 | gm==6)
        VolJrNow=0;
        VolBoNow=0;
    else
        VolJrNow=VolJr(gm);
        VolBoNow=VolBo(gm);
    end;

    XSum=XSum+(1/sizeVolInd)*VolJrNow*VolBoNow;

end;
end;

%Set values for anode/plasma elements

if (VolELEMDataTag==2)
for gm=1:sizeVolInd

    if (gm==3 | gm==4 | gm==9 | gm==10)
        VolJrNow=0;
        VolBoNow=0;
    else
        VolJrNow=VolJr(gm);
        VolBoNow=VolBo(gm);
    end;

    XSum=XSum+(1/sizeVolInd)*VolJrNow*VolBoNow;

end;
end;
```

Excerpt 4.F.16: Subroutine used to calculate $J \times B$ for a FV element

[illegible]

Excerpt 4.F.17: Subroutine used to calculate the area of a FV element


```
function MjrBo=JrBoMove(t,x)

%This function calculates the velocity and distance travelled by the plasma
%block from the given input parameters of Force and mass at the current
%time step t. This function is used as a part of ode45 with the previously
%calculated values as initial conditions for the current time range of to to
%t. The equations to be solved are distance "d" and velocity "v" where
%d(d)/d(t)=v and d(v)/d(t)=Force(t)/mass.

global ForceBlock mass
ForceBlock;
mass;

MjrBo=[x(2);(ForceBlock/mass)];
```

Excerpt 4.F.18: Subroutine used to input data into the MATLAB ode45 algorithm. This subroutine is used to determine the velocity and the distance travelled by the plasma within the current time step.

References

- [1] R. A. Gross
'Fusion Energy'
(New York, Brisbane: Wiley, 1984)
- [2] P. W. Atkins and J. A. Baron
'General chemistry', second edition
(New York: Scientific American Books: Distributed by W. H. Freeman, 1992)
- [3] R. C. Kirkpaterick, R. Lindemuth and M. S. Ward
Fusion technology, **27**, 201 (1995)
- [4] Y. C. F. Thio, C. E. Knapp, R. C. Kirkpaterick, R. E. Siemon and P. J. Turchi
Journal of fusion energy. **20**, 1 (2002)
- [5] J. H. Pegnan, R. E. Peterkin Jr, G. P. Baca, J. D. Beason, D. E. Bell, M. E. Dearborn, D. Dietz, M. R. Douglas, S. E. Englert, T. J. Englert, K. E. Hackett, J. H. Holmes, T. W. Hussey, G. F. Kiuttu, F. M. Lehr, G. J. Marklin, B. W. Mullins, D. W. Price, N. F. Roderick, E. L. Ruden, C. R. Sovinec, P. J. Turchi, G. Bird, S. K. Coffey, S. W. Seiler, Y. G. Chen, D. Gale, J. D. Graham, M. Scott and W. Sommars
Phys Fluids B. **5**, 2938 (1993)
- [6] J. H. Degnan, W. L. Cowan, J. D. Graham, J. L. Holmes, E. A. Lopez, D. W. Price and N. F. Roderick
Fusion Technology. **35**, 354 (1999)
- [7] G. W. Sutton and A. Sherman
'Engineering magnetohydrodynamics'
(New York: McGraw-Hill, 1965)
- [8] J. A. Browning
Journal of thermal spray technology. **8**, 351 (1999)
- [9] P. M. Mostov, J. L. Neuringer and D. S. Rigney
The physics of fluids. **4**, 1097 (1961)
- [10] P. J. Hart
The physics of fluids. **5**, 38 (1961)
- [11] D. Dietz
Journal of applied physics. **62**, 2669 (1987)
- [12] E. Igenbergs
IEEE transactions on magnetics. **27**, 650 (1991)
- [13] I. R. McNab
IEEE transactions on magnetics. **35**, 250 (1999)
- [14] S. Williamson and C. D. Home
IEEE transactions on magnetics. **31**, 516 (1995)
- [15] D. A. Bresie and J. A. Andrews
IEEE transactions on magnetics. **27**, 623 (1991)
- [16] A. J. McPhee
Pulsed Power conference, 1995. IEEE International. **2**, 781(1995)
- [17] J. H. Gully
IEEE transactions on magnetics. **27**, 329 (1991)

References

- [18] M. Rott and E. Igenbergs
IEEE transactions on magnetics. **37**, 232 (2001)
- [19] R. Dethlefsen, I. McNab, C. Dobbie, T. Bernhardt, R. Puterbaugh, F. LeVine, T. Coradeschi and V. Rinaldi
IEEE transactions on magnetics. **29**, 934 (1993)
- [20] B. L. Maas and N. D. Clements
IEEE transactions on magnetics. **29**, 1017 (1993)
- [21] E. Spahn, G. Buderer and F. Hatterer
IEEE transactions on magnetics. **31**, 78(1995)
- [22] E. Spahn, G. Buderer, J. Wey, V. Wegner and F. Jamet
IEEE transactions on magnetics. **29**, 1060 (1993)
- [23] R. D. Ford and R. D. Hudson
IEEE transactions on magnetics. **29** , 949 (1993)
- [24] M. E. Parten
IEEE transactions on magnetics. **25**, 425 (1989)
- [25] A. Yamori, M. Kohno and N. Kawashima
IEEE transactions on magnetics. **35**, 497 (1999)
- [26] T. Maruo, K. Fujioka, K. Nagaoka, A. Okamoto, K. Ikuta and K. Nemoto
IEEE transactions on magnetics. **27**, 65 (1991)
- [27] J. V. Parker
IEEE transactions on magnetics. **27** , 80 (1991)
- [28] M.Rott
IEEE transactions on magnetics. **27**, 601 (1991)
- [29] P. Thomas and M. Rott
IEEE transactions on magnetics. **33**, 384 (1997)
- [30] U. Shumiak, T. W. Hussey and R. E. Peterkin Jr
IEEE Transaction on plasma science. **23**, 83 (1995)
- [31] J. T. Scheuer, K. F. Schoenberg, R. A. Gerwin, R. P. Hoyt, I. Henins, D. C. Black, R. M. Mayo and R. W. Moses Jr
IEEE transactions on plasma science. **22**, 1015 (1994)
- [32] S. S. Bushman, R. L. Burton
Journal of propulsion and power. **17**, 959 (2001)
- [33] R. P. Hoyt, J. T. Scheuer, K. F. Schoenberg, R. A. Gerwin, R. W. Moses Jr, I. Henins
IEEE transactions on plasma science. **23**, 481 (1995)
- [34] S. Yao, E. Suzuki and A. Nakayama
Thin solid films. **390**, 165 (2001)
- [35] P. Thomas, E. Igenbergs, H. Tamura and A. B. Sawakoa
IEEE transactions on magnetics. **19**, 609 (1993)
- [36] A. Hudepohl, M. Rott and E. Igenbergs
IEEE transactions on magnetics. **25**, 232 (1989)

References

- [37] J. V. Parker
IEEE transactions on magnetics. **25**, 418 (1989)
- [38] B. M. Smirnov
'Physics of ionized gases'
(New York, Chichester: Wiley, 2001)
- [39] M. Shahinpoor
IEEE transactions on magnetics. **25**, 508 (1989)
- [40] D. A. Weeks, W. F. Weldon and R. C. Zowarka
IEEE transactions on plasma science. **17**, 403 (1989)
- [41] G. C. Boynton and M. A. Huerta
IEEE transactions on magnetics. **31**, 564 (1995)
- [42] G. C. Boynton and M. A. Huerta
IEEE transactions on plasma science. **17**, 486 (1989)
- [43] N. P. Orton and J. G. Gilligan
IEEE transactions on magnetics. **31**, 640 (1995)
- [44] M. A. Huerta and G. C. Boynton
IEEE transactions on magnetics. **25**, 238 (1989)
- [45] G. C. Boynton, M. A. Huerta and Y. C. Thio
IEEE transactions on magnetics. **29**, 751 (1993)
- [46] D. Hahn and J. G. Gilligan
IEEE transactions on magnetics. **27**, 251 (1991)
- [47] R. J. Zollweg
IEEE transactions on magnetics. **25**, 648 (1989)
- [48] M. H. Fresa
IEEE transactions on magnetics. **27**, 233 (1991)
- [49] G. L. Katulka, J. Kolodzey and J. Olowolafe
IEEE transactions on magnetics. **35**, 356 (1999)
- [50] A. Poltanov, N. Jygailo, M. Bykov, A. Glinov, A. Svobodov, A. Belyakov and N. Chernetskaya
IEEE transactions on magnetics. **33**, 406 (1997)
- [51] C. Persad
IEEE transactions on magnetics. **35**, 300 (1999)
- [52] J. R. Hull
IEEE transactions on magnetics. **25**, 243 (1989)
- [53] K. F. Schenberg
Physics of plasmas. **5**, 2090 (1998)
- [54] E. E. O'Donnell
IEEE transactions on plasma science. **17**, 484 (1989)
- [55] P. A. Drake and C. E. Rathmann
IEEE transactions on magnetics. **22**, 1448 (1986)
- [56] S. H. Le, G. Bisson, P. J. Leonard, D. Rodger and C. Leyden
IEEE transactions on magnetics. **29**, 1102 (1993)

References

- [57] J. R. Auton, C. R. Grant, R. L. Houghton and H. P. Thompson
IEEE transactions on magnetics. **25**, 63 (1989)
- [58] P. A. Drake and C. E. Rathmann
IEEE transactions on magnetics. **27**, 61 (1991)
- [59] D. Diver
'A plasma formulary for physics, technology and astrophysics'
(Berlin, New York: Wiley-VCH, 2001)
- [60] T. J. M. Boyd and J. J. Sanderson
'The physics of plasmas'
(Cambridge: Cambridge University Press, 2003)
- [61] H. P. Wagner, H. J. Kaeppler and M Auweter-Kurtz
Journal of physics D: Applied physics. **31**, 519 (1998)
- [62] M. Bourouis, M. A. Huerta and F. Rodrigues-Trelles
IEEE transactions on magnetics. **29**, 1113 (1993)
- [63] M. A .Huerta and J. L. Castillo
IEEE transactions on magnetics. **31**, 610 (1995)
- [64] M. A. Huerta and M. Bourouis
IEEE transactions on magnetics. **27**, 257 (1991)
- [65] A. A. Kondratyev
Laser and particle beams. **18**, 269 (2000)
- [66] G. A. Shuestsov, V. D. Kurguzov, G. V. Ivanov and S. A. Anisimov
IEEE transactions on magnetics. **31**, 657 (1995)
- [67] G. Scoles
'Atomic and molecular beam methods: Volume 1'
(New York: Oxford University Press, 1988)
- [68] H. Pauly
'Atom molecule and cluster beams 1: Basic theory production and detection of thermal energy beams'
(Berlin, London: Springer, 2000)
- [69] J. Marshall
Proceedings of the second United Nations international conference on peaceful uses of atomic energy (United Nations, Geneva). **31**, 341 (1958)
- [70] D. C. Hagerman and J. E. Osher
The review of scientific instruments. **34**, 56 (1963)
- [71] A. Auerbech and R. McDiarmid
Rev. Sci. Instrum. **51**, 1273 (1980)
- [72] J. B. Cross and J. J. Valentini
Rev. Sci. Instrum. **53**, 38 (1982)
- [73] D. Proch and T. Trickl
Rev. Sci. Instrum. **60**, 713 (1989)

References

- [74] T. Ikeda
'Fundamentals of piezoelectricity'
(Oxford, New York: Oxford University Press, 1996)
- [75] Physik Instrumente, Nanopositioning 1998 (catalogue), (refer to <http://www.physikinstrumente>)
- [76] P. W. Atkins
'Physical chemistry', fifth edition
(Oxford, New York: Oxford University Press, 1994)
- [77] P. Felder
'Photofragment translational spectroscopy'
(Dissertation University of Zurich 1993)
- [78] W. H. Press, S. A. Teukolsky, W. T. Vetterling and B. P. Flannery
'Numerical recipes in Fortran 77, Volume 1', second edition
(Cambridge (England), New York, NY, USA: Cambridge University Press, 1992)
- [79] P. R. Bevington and D. K. Robinson
'Data reduction and error analysis for the physical sciences', second edition
(New York: McGraw-Hill, 1992)
- [80] P. W. Harland and B. R. Cameron
J. Chem. Soc. Faraday Trans. **87**, 1069 (1991)
- [81] <http://www.thinkSRS.com>
- [82] J. D. Kraus
'Electromagnetics', fourth edition
(New York: McGraw-Hill, 1991)
- [83] W. S. Zaengl and E. Kuffel
'High voltage engineering fundamentals'
(Oxford (Oxfordshire), New York: Pergamon Press, 1983)
- [84] H. Deutsch, K. Becker, S. Matt and T. D. Mark
International Journal of Mass Spectrometry. **197**, 37 (2000)
- [85] V. Kowalenko and G. A. Clark
J. Phys. D: Appl.Phys. **33**, 230 (2000)
- [86] A. Sedghinasab, D. R. Keefer and H. L. Crowder
IEEE transactions on plasma science. **17**, 360 (1989)
- [87] P. Lehmann, J. Wey, H. Mach, A. Eichhorn and K. Daree
IEEE transactions on plasma science. **17**, 371 (1989)
- [88] F. F. Chen
'Introduction to plasma physics and controlled fusion Volume 1: Plasma physics', second edition
(New York: Plenum Press, 1984)
- [89] H. Pauly
'Atom molecule and cluster beams II: Cluster beams, fast and slow beams, accessory equipment and applications'
(Berlin, New York: Springer, 2000)
- [90] P. Thomas
IEEE transactions on magnetics. **31**, 661 (1995)

References

- [91] P. Thomas
IEEE transactions on magnetics. **33**, 272 (1997)
- [92] A. Esser, R. Redmer and G. Ropke
Contributions to plasma physics. **43**, 33 (2003)
- [93] G. Ropke
Physical review A. **38** 3001 (1988)
- [94] S. Ichimaru and S. Tanaka
Physical review A. **32**, 1790 (1985)
- [95] R. A. Serway
'Physics for scientists and engineers, Volume 2', fourth edition
(Philadelphia: Saunders College Publishers, 1996)
- [96] J. D. Jackson
'Classical electrodynamics', second edition
(New York: Wiley, 1975)
- [97] F. E. Ehlers
American Rocket Society Journal. **30**, 334 (1961)
- [98] H. Bo, H. Min and W. Xinxin
Proceedings of the 6th international conference on the properties and applications of dielectric materials June 21-26 2000. **1**, 391 (2000)
- [99] W. Reininghaus
J.Phys D: Appl. Phys. **6**, 14863 (1973)
- [100] J. P. Novak and R. Bartnikas
IEEE transactions on plasma science. **19**, 95 (1991)
- [101] N. Wiegart, L. Niemeyer, F. Pinnekamp, W. Boeck, J. Kindersberger, R. Morrow, W. Zaengl, M. Zwicky, I. Gallimberti and S. A. Boggs
IEEE transactions on power delivery. **3**, 923 (1988)
- [102] N.Wiegart, L. Niemeyer, F. Pinnekamp, W. Boeck, J. Kindersberger, R. Morrow, W. Zaengl, M. Zwicky, I. Gallimberti and S. A. Boggs
IEEE transactions on power delivery. **3**, 931 (1988)
- [103] N.Wiegart, L. Niemeyer, F. Pinnekamp, W. Boeck, J. Kindersberger, R. Morrow, W. Zaengl, M. Zwicky, I. Gallimberti and S. A. Boggs
IEEE transactions on power delivery. **3**, 939- (1988)
- [104] K. K. Cobb, N. E. Taconi Jr, C. R. Heddings
IEEE transactions on magnetics. **29**, 1137 (1993)
- [105] P. P. Silvester and R. L. Ferrari
'Finite elements for electrical engineers', third edition
(New York: Cambridge University Press, 1996)
- [106] J. Jin
'The finite element method in electromagnetics'
(New York: Wiley, 1993)
- [107] K. J. Binns, P. J. Lawrenson and C. W. Trowbridge
'The analytical and numerical solution of electric and magnetic fields'
(Chichester (England), New York: Wiley, 1992)

References

- [108] K. H. Huebner, E. A. Thornton and T. G. Byrom
'The finite element method for engineers', third edition
(New York: Wiley, 1995)
- [109] P. P. Silvester and G. Pelosi
'Finite elements for wave electromagnetics methods and techniques'
(New York: Institute of Electrical and Electronics Engineers, 1994)
- [110] P. Zhou
'Numerical analysis of electromagnetic fields'
(Berlin, New York: Springer-Verlag, 1993)
- [111] G. Sewell
'The numerical solution of ordinary and partial differential equations'
(San Diego, CA: Academic Press, Boston: Harcourt Brace Jovanovich, 1988)
- [112] M. N. O. Sadiku
'Numerical techniques in electromagnetics'
(Boca Raton Fla: CRC Press, 1992)
- [113] C. A. J. Fletcher
'Computational techniques for fluid dynamics, Volume 1: fundamental and general techniques'
(Berlin New York: Springer-Verlag, 1991)
- [114] C. Hirsch
'Numerical computation of internal and external flows, Volume 1: Fundamentals of numerical discretization'
(Chichester (England), New York: Wiley, 1988)
- [115] D. Kondrashov and D. Keefer
IEEE transactions on magnetics. **33**, 254 (1997)
- [116] C. W. Crowley, P. P. Silvester and H. Hurwitz Jr
IEEE transactions on magnetics. **24**, 397 (1988)
- [117] C. W. Crowley
'Mixed order covariant projection finite elements for vector fields'
Thesis, McGill University, Montreal, Canada 1988
- [118] J. P. Webb
IEEE transactions on magnetics. **29**, 1460 (1993)
- [119] G. Mur
IEEE transactions on magnetics. **30**, 3552 (1994)
- [120] G. Mur
IEEE transactions on magnetics. **34**, 3244 (1998)
- [121] Y. W. Kwon and H. Bang
'The finite element method using MATLAB'
(Boca Raton: CRC Press, 1997)
- [122] S. C. Brenner and L. R. Scott
'The mathematical theory of finite element methods'
(New York, NY: Springer-Verlag, 2002)
- [123] C. T. F. Ross
'Advanced applied finite element methods'
(Chichester: Horwood, 1998)

References

- [124] T. J. M. Boyd and J. J. Sanderson
'The physics of plasmas'
(Cambridge, UK, New York: Cambridge University Press, 2003)
- [125] O. Biro and K. Preis
IEEE transactions on magnetics. **25**, 3145 (1989)
- [126] C. R. I. Emson and J. Sikin
IEEE transactions on magnetics. **19**, 2450 (1983)
- [127] P. J. Lenard and D. Roger
IEEE transactions on magnetics. **24**, 90 (1988)
- [128] T. Morisue
IEEE transactions on magnetics. **18**, 531 (1982)
- [129] A. Kameari
IEEE transactions on magnetics. **24**, 118 (1988)
- [130] G. Drago, P. Girdinio, M. Nervi, R. A. Orlando, G. L. Sabbi, G. Secondo and P. Fernandes
IEEE transactions on magnetics. **30**, 2976 (1994)
- [131] C. F. Bryant, C. R. I. Emson and C. W. Trowbridge
IEEE transactions on magnetics. **26**, 430 (1990)
- [132] C. F. Bryant, B. Dillon, C. R. I. Emson, J. Simkin and C. W. Trowbridge
IEEE transactions on magnetics. **28**, 1182 (1992)
- [133] C. F. Bryant, C. R. I. Emson and C. W. Trowbridge
IEEE transactions on magnetics. **26**, 2373 (1990)
- [134] B. M. A. Rathman and J. B. Davies
IEEE transactions on microwave theory techniques. **32**, 922 (1984)
- [135] K. D. Paulsen and D. R. Lynch
IEEE transactions on microwave theory techniques. **39**, 395 (1991)
- [136] M. M. Taheri and D. M.-Syahkal
IEEE transactions on microwave theory techniques. **37**, 1536 (1989)
- [137] K. Hayata, M. Eguchi, M. Koshiba and M. Suzuki
Journal of lightwave technology. **4**, 1090 (1986)
- [138] J. P. Webb
IEEE transactions on microwave theory techniques. **33**, 635 (1985)
- [139] J. P. Webb
IEEE transactions on magnetics. **24**, 162 (1988)
- [140] A. H. Sameh and J. A. Wisniewski
SIAM J.Numer. Anal. **19**, 1243 (1982)
- [141] C. L. Chang and J. J. Nelson
SIAM J.Numer. Anal. **34**, 480 (1997)
- [142] J. E. Akin
'Application and implementation of finite element methods'
(London, New York: Academic Press, 1982)

References

- [143] J. V. Bladel
IEEE transactions on antennas and propagation. **33**, 450 (1985)
- [144] M. Haas and G. Kuhn
Computational Mechanics. **28**, 250 (2002)
- [145] J. P. Webb
IEEE transactions on microwave theory techniques. **36**, 1819 (1988)
- [146] A.S. B. B. Dhia, C. Hazard and S. Lohrengel
SIAM J.Appl. Math. **59**, 2028 (1999)
- [147] D. Givoli and L. Rivkin
International journal for numerical methods in engineering. **35**, 1329 (1992)
- [148] T. Apel and S. Nicaise
Mathematical methods in applied sciences. **21**, 519 (1998)
- [149] K. Muramatsu, T. Nakata, N. Takahashi and K. Fujiwara
IEEE transactions on magnetics. **28**, 1186 (1992)
- [150] K. Muramatsu, N. Takahashi and T. Hashio
IEEE transactions on energy conversion. **14**, 1312 (1999)
- [151] K. Muramatsu, T. Nakata, N. Takahashi and K. Fujiwara
IEEE transactions on magnetics. **32**, 749 (1996)
- [152] K. Muramatsu, N. Takahashi, C. Yamada, S. Kobayashi and T. Kuwahara
Electric machines and devices conference record, IEEE international 1997. *pg MC1/5.1-MC1/5.3* (1997)
- [153] L. G. Margolin
Introduction to “An Arbitrary Lagrangian-Eulerian computing method for all flow speeds”
Journal of computational physics. **135**, 198 (1997)
- [154] C. W. Hirt, A. A. Amsden and J. L. Cook
Journal of computational physics. **135**, 203 (1997)
- [155] E. S. Oran and J. P. Boris
‘Numerical simulation of reactive flow’, second edition
(Cambridge, U.K. , New York, NY: Cambridge University Press, 2001)
- [156] J. N. Reddy and D. K. Gartling
‘The finite element method in heat transfer and fluid dynamics’, second edition
(Boca Raton, FL: CRC Press, 2001)
- [157] Thomas J. R. Hughes
International Journal for numerical methods in engineering. **12**, 1359 (1978)
- [158] I. Christie, D. F. Griffiths, A. R. Mitchell and O. C. Zienkiewicz
International Journal for numerical methods in engineering. **10**, 1389 (1976)
- [159] J. C. Heinrich, P. S. Huyakorn, O. C. Zienkiewicz and A. R. Mitchell
International Journal for numerical methods in engineering. **11**, 1313 (1977)
- [160] L. R. Abrahamsson, H. B. Keller and H. O. Kreiss
Numer. Math. **22**, 367 (1974)
- [161] S. Kurz, J. Fetzner and G. Lehner
IEEE transactions on magnetics. **31**, 1737 (1995)

References

- [162] Y. Saad and M. H. Schultz
SIAM journal on scientific and statistical computing. **7**, 856 (1986)
- [163] M. Benzi, J. C. Haws and M. Tuma
SIAM Journal of Scientific computing. **22**, 1333 (2000)
- [164] H. J. Kim, K. Choi, H. B. Lee, H. K. Jung and S. Y. Hahn
IEEE transactions on magnetics. **32**, 1373 (1996)
- [165] Darren Redfern and Colin Campbell
'The MATLAB 5 handbook'
(New York: Springer, 1998)
- [166] J. R. Gilber, C. Moler and R. Schreiber
SIAM J.Matrix Anal. App. **13**, 333 (1992)
- [167] J. V. Parker
IEEE transactions on plasma science. **17**, 487 (1989)
- [168] K. K. Cobb
IEEE transactions on plasma science. **17**, 507 (1989)
- [169] L. M. Smith and D. R. Keefer
IEEE transactions on plasma science. **17**, 501 (1989)
- [170] B. U. Bouvier
IEEE transactions on plasma science. **17**, 516 (1989)
- [171] B. .J. Evans and L. M. Smith
IEEE transactions on plasma science. **19**, 516 (1991)
- [172] G. A. Mohr
'Finite elements for solids, fluids, and optimization'
(Oxford (England), New York: Oxford University Press, 1992)
- [173] P. M. Morse and H. Feshbach
'Methods of theoretical physics, Part 2'
(New York, McGraw-Hill, 1953)

Bibliographies

John A. Harrison

Dr Harrison is well known within the Physical Chemistry/Chemical Physics community in New Zealand and has good linkages with a number of highly respected international research groups in Switzerland, Japan, England and the USA. Co-author of 18 articles in international peer reviewed journals including one publication in the highly rated journal "Science".

Founded Chemistry at the Albany Campus, 1995

John A. Harrison

Curriculum Vitae

- | | |
|------------------|--|
| 1989 | PhD in Physical Chemistry (1989) University of Canterbury Supervisor: Prof Leon F. Phillips |
| 1989 – 91 | Adolph C and Mary Sprague Miller Institute for Basic Research in Science Postdoctoral Fellowship at the University of California Berkeley. (Highest postdoctoral award for science at UC Berkeley, awarded to only ten people per year across all of the sciences) |
| 1991-92 | Postdoctoral fellow, College of Chemistry, UC Berkeley |
| 1990, 92, 93, 94 | Visiting Scientist at the Institute for Physical Chemistry, University of Zurich, Switzerland (Laboratory for Molecular Dynamics and Laser Spectroscopy) 1992 visit funded by the Swiss National Science Foundation. |
| 1993 – 98 | Lecturer, Massey University. |
| 1996 – present | Head of the Institute of Fundamental Sciences at Massey University, Albany section. |
| 1997 | Presidential Invited visitor to the Institute of Molecular Science, Okazaki, Japan |
| 1999 – present | Senior Lecturer. |
| 2000 – 01 | Visiting Professor at the Laboratory for Molecular Dynamics and Laser Spectroscopy, Institute for Physical Chemistry, University of Zurich, Switzerland (funded by Swiss National Science Foundation). |

Bibliographies

Ian R.R. Shinton

Candidate for PhD

Ian R.R. Shinton

Curriculum Vitae

- 2001 BTech Materials (1st Class Honours) (2001) Auckland University
The BTech Materials degree was a degree offered at Auckland University as conjoint degree between Chemistry and Chemical/Material engineering.
- 2001 – 2004 Awarded Bright Futures Top Achievers Doctoral Scholarship (TAD 680)
- 2001-2005 Candidate for PhD
- 2004 Invited speaker at 2004 IEEE International conference on plasma science:
- Harrison. J, Shinton. I, Thelen. M.A, Dingley. G
Development of a plasma gun for application in MTF: the LICA (linearly injected coaxial accelerator)
IEEE International conference on plasma science (ICOPS 2004), Conference abstracts, (2004) pg 161
- Invited poster session at 2004 IEEE International conference on plasma science:
- Shinton. I
Preliminary numerical modelling of the LICA (linearly injected coaxial accelerator)
IEEE International conference on plasma science (ICOPS 2004), Conference abstracts, (2004) pg 383